ASSESSING THE SEISMIC PERFORMANCE OF EXISTING REINFORCED CONCRETE BUILDINGS: FROM STANDARD-BASED METHODS TO FULL PROBABILISTIC APPROACHES

A Dissertation
Submitted to the Faculty of Engineering of the University of Porto
In partial fulfilment of the requirements
For the degree of
Doctor of Philosophy
by

Nuno Manuel da Silva Pereira

2019

Supervisor: Prof. Xavier das Neves Romão
Department of Civil Engineering
Faculty of Engineering of the University of Porto
Porto, Portugal

ii

Thesis Examining Committee

The present thesis has been examined on March 1, 2019, at the Faculty of Engineering of the University of Porto, by the following committee:

President:

Dr. Humberto Salazar Amorim Varum, Full Professor at the Faculty of Engineering of the University of Porto, Portugal

Examiners:

Dr. Rui Jorge Silva Moura Pinho, Associate Professor at the University of Pavia, Italy.

Dr. Dimitrios Vamvatsikos, Assistant Professor at the National Technical University of Athens, Greece.

Dr. António Santos Carvalho Cabral Araújo Correia, Assistant Researcher at the National Laboratory for Civil Engineering, Lisbon, Portugal

Dr. José Miguel de Freitas Castro, Assistant Professor at the Faculty of Engineering of the University of Porto, Portugal

Dr. Xavier das Neves Romão, Assistant Professor at the Faculty of Engineering of the University of Porto, Portugal (Supervisor)

Pure mathematics is, in its way,
the poetry of logical ideas.

ALBERT EINSTEIN.
[New York Times May 5, 1935]

Acknowledgements

In a world where logical ideas become poetry, this would be the limit where we divide everything by *x* and, asymptotically, we reach the infinite of my thoughts. An infinite road populated by all of you that, throughout the years, have marked me with your words, with your thoughts, ideas and actions. This is where I will try to find a simple, logical and unified form to acknowledge all the people who made this journey possible, and made every day not just another day at the office. I have to begin by expressing my sincere gratitude and admiration to my supervisor Professor Xavier Romão for his unconditional support, constant encouragement and for having such a positive impact in my life. I can say that you recovered an old dream from my bucket list. I would never be writing this lines without your belief, without your support, without your technical guidance, without your true friendship.

I am deeply grateful to Professor José Miguel Castro for his sympathy, constant support, guidance and for being a role-model. I will never forget the countless technical discussions we had at airports and while travelling, along with the many advices you gave me that ultimately shaped my own life.

Over the past few years I greatly benefited, both technically and personally, from the interaction with many colleagues and friends from the University of Porto and abroad. I am truly thankful to the high speed rail team, namely Alejandro Tejada, João Rocha, João Francisco Rocha, Joel Malveiro, Nuno Ribeiro, Pedro Montenegro, etc… for showing me how not to derail when crossing at very high speeds all the bridges we build in our lives...and to my colleagues Ádám Zsarnóczay, António Silva, Despoina Skoulidou, Filipe Ribeiro, Hossamelden Ahmed, Luís Martins, Mário Marques, Miguel Araújo and my G311/G312 office mates for showing me how safe it would be to cross all those bridges with them by my side. I thank João Pacheco de Almeida and Alexandre Costa for the kind words and time they always had for me.

This journey started and crossed paths later again with a group of very special people I admire technically and personally. To the NCREP team, namely Filipe Neves, Bruno Quelhas, Tiago Ilharco and Valter Lopes, I express my gratitude for their help, and for setting an important example in my life. A special word of thanks goes to my great colleague and friend Luís Macedo. Your encouragement and optimism were fundamental during this journey.

A todos os meus amigos pelos traços e passos que nos unem e que sempre tiveram nas palavras, nas mãos, a solução de todos os problemas, a razão de todas as verdades. Ao meu irmão por estar sempre do meu lado. A Lidia e Manuel Araújo, por todo o apoio e amor. Aos meus pais pela admiração, paciência, esforço e amor que sempre me fizeram seguir e sentir, todos os dias. Ao meu pai, por tudo o que sempre me deu e por sempre achar que eu seria capaz. A ti, Ana Maria, a ti os meus olhos, os meus sonhos para poderes sonhar. A ti o tempo a vida e o poema. A tua parte de mim.

Nuno Pereira

Abstract

The proposed thesis addresses several topics in the field of seismic safety and performance assessment of existing reinforced concrete (RC) buildings. The seismic performance assessment of existing RC buildings is affected by several sources of aleatory and epistemic uncertainty which can be explicitly incorporated in full probabilistic approaches. However, including these uncertainties into the framework of standard-based methods is usually achieved through the development of scalar safety factors and closed-form verifications. Due to incompatibilities found between standard-based methods and full probabilistic approaches, both from a conceptual and practical point of view, the main objective of this thesis is to propose a new set of methods and of safety coefficients that are consistent with the full probabilistic treatment of all sources of uncertainty affecting the assessment of the seismic safety.

In light of this wide-scope objective, the thesis focusses on the assessment and management of three types of uncertainties: the uncertainty associated with the available knowledge about the structural and material properties of the existing building, the uncertainties in the models selected to simulate the nonlinear behaviour of the energy dissipative components of the structure, and the uncertainty about the objectives of the seismic performance assessment, including the adequacy of the methods that are used to perform the safety assessment.

The first part of the dissertation focuses on evaluating the adequacy of current standard-based methods for the survey and assessment of the structural and material properties of existing RC buildings. A finite population statistics-based approach is proposed to be the core of the uncertainty assessment strategy that is established. The development of this strategy starts by integrating the referred statistical approach into a procedure for assessing concrete strength in existing RC buildings. A methodology for estimating the variability of the concrete strength in existing buildings using the proposed paradigm is then also developed, and a set of material safety factors that provide a conservative estimate of the mean concrete strength is then proposed. These factors are also defined for the reinforcing steel yield strength based on experimental tests that were carried out and on literature values. A set of testing levels and the corresponding compatible material safety factors are then proposed based on these approaches. Finally, the finite population paradigm is extended to cover the uncertainty about the construction details by introducing the concept of conformity factor. This factor is defined as a continuous variable that is used to treat the binary character of the uncertainty about these elements.

The second part of the thesis focusses on assessing the uncertainties associated with the correlation between the physical measurable properties addressed in the first part and the constitutive models that are adopted to analyse the seismic safety. Focusing on the flexural response of beam-column components, an in-depth analysis of the plastic hinge mechanism

development and rotation is presented, focusing its conceptual aspects that require particular attention when defining the localization length and selecting constitutive material models to be used with distributed inelasticity modelling approaches. A comprehensive analysis of the effects of model and constitutive parameter selection is presented, including a proposal about adequate material models that can simulate the response up to collapse.

Finally, the third part of the dissertation connects the concepts involved in the definition of the numerical model, in the characterization of the structural and material properties of the building with the performance objectives and limit state conditions proposed in current standard-based methods. A new methodology is proposed to derive safety factors for the capacity of RC frame elements including the level of knowledge that exists about the building properties and the capacity limits. This method ensures the consistent definition of demand and capacity by using the same behaviour model to compute demand and capacity, thus also accounting for the modelling uncertainty at the component level. An extension of this method is then proposed to account for potential inconsistencies between demand and capacity. Finally, an application is performed to assess the adequacy of component-based limit state conditions in light of the full probabilistic PEER performance based earthquake engineering methodology.

Resumo

A presente dissertação aborda vários tópicos no contexto da avaliação da segurança e do desempenho sísmico de edifícios existentes em betão armado (BA). A avaliação do desempenho sísmico deste tipo de edifícios em BAé afectada por várias fontes de incerteza de natureza aleatória e epistémica, as quais são explicitamente incluídas em abordagens puramente probabilísticas ou indirectamente introduzidas, como acontece no caso das abordagens regulamentares actuais. Neste sentido, o principal objectivo desta dissertação consiste em propor um novo conjunto de métodos e de coeficientes de segurança que possam ser utilizados no desenvolvimento de procedimentos regulamentares e que são consistentes com o tratamento probabilístico completo de todas as fontes de incerteza incluídas na avaliação da segurança sísmica.

De acordo com o objectivo global estabelecido, a presente dissertação foca a avaliação de três tipos diferentes de incertezas: a incerteza associada ao conhecimento sobre as propriedades estruturais e materiais do edifício existente, a incerteza relacionada com a modelação do comportamento não linear dos principais elementos da estrutura e a incerteza associada aos objectivos da avaliação do desempenho sísmico e aos métodos utilizados para a sua quantificação.

A primeira parte da dissertação foca-se na avaliação da adequabilidade dos métodos propostos nos regulamentos de avaliação da segurança sísmica actuais para o levantamento e a quantificação das propriedades estruturais e materiais de edifícios de BA. Propõe-se uma abordagem baseada em estatísticas de população finita que será o núcleo da estratégia proposta para a avaliação da incerteza. A abordagem é primeiramente analisada no âmbito da avaliação da resistência à compressão do betão em edifícios existentes de BA. Seguidamente, estabelece-se uma metodologia para estimar a variabilidade da resistência à compressão do betão em edifícios existentes usando o paradigma proposto, sendo proposto um conjunto de fatores de segurança que permitem a definição de uma estimativa conservativa da resistência média do betão. Estes factores são igualmente definidos para a tensão de cedência do aço. O número de ensaios de caracterização material a realizar bem como os factores de segurança compatíveis com esses ensaios são posteriormente propostos com base na referida abordagem. Finalmente, o paradigma da população finita é estendido para cobrir a incerteza relacionada com a pormenorização de armaduras, introduzindo a noção de fator de conformidade, definida como uma variável contínua usada para tratar as características binárias da incerteza detas propriedades.

A segunda parte da dissertação foca-se na avaliação das incertezas associadas à correlação entre as propriedades físicas tratadas na primeira parte e os modelos constitutivos adoptados para analisar a resposta do edifício. É dado um ênfase particular na análise da resposta à flexão de elementos lineares do tipo pilar-viga, apresentando-se e uma análise do processo de formação do

mecanismo de rótula plástica e das rotações desenvolvidas. Nesta análise, focam-se aspectos conceptuais que requerem atenção particular aquando da definição do comprimento de localização e da selecção das leis constitutivas dos materiais em modelos de plasticidade distribuída. Apresenta-se uma análise abrangente dos efeitos da selecção do modelo e dos parâmetros constitutivos que culmina na proposta de leis uniaxiais adequadas para a simulação da resposta dos componentes estruturais até ao colapso.

Finalmente, a terceira parte da dissertação aborda a ligação entre os conceitos envolvidos na definição do modelo numérico, na caracterização das propriedades estruturais e materiais do edifício e os objetivos de desempenho e condições de estado limite propostas nos regulamentos estruturais. Propõe-se uma nova metodologia que permite derivar factores de segurança para a capacidade dos elementos estruturais que inclui o nível de conhecimento existente acerca das propriedades do edifício e dos limites de capacidade. O método proposto permite uma definição consistente da resposta e da capacidade, dado que usa o mesmo modelo para calcular estas quantidades, considerando portanto a incerteza relacionada com a abordagem seleccionada para a modelação estrutural ao nível dos componentes estruturais. Propõe-se ainda uma extensão deste método que permitir corrigir possíveis inconsistências entre a metodologia definida para estimar a resposta e a estratégia seguida para a quantificação da capacidade. Finalmente, apresenta-se um caso de estudo em que se avalia a adequabilidade da condição de estado limite definida à luz da metodologia probabilística do PEER-PBEE (performance based earthquake engineering), i.e. da avaliação da segurança com base em perdas económicas.

Contents

5. Derivation of closed-form safety factors for component-based limit-states of RC frame buildings

Chapter 1

Introduction

1.1 Motivation

A dramatic increase in the consequences of natural disasters has been observed worldwide over the past decades. These significant impacts were translated into severe human and economic losses, revealing the large exposure of societies to unexpected levels of natural hazards together with significant levels of unpreparedness and vulnerability. The reasons for the high level of losses are manifold, but some well-known specific aspects play a decisive role. The population increase in clustered areas has led to the development of the so-called megacities (thus increasing the level of exposure to hazards), contributing to the rapid growth of construction in such areas complemented, many times, by the building of structures and infrastructures having inadequate levels of quality and safety (thus increasing the level of vulnerability to hazards). Furthermore, the lack of adequate preparedness and awareness has led to insufficient resilience levels, jeopardising the response and recovery after disasters.

Natural disasters are often associated to the occurrence of extreme events such as earthquakes, hurricanes or floods. These events not only have a considerable immediate impact due to the vulnerability of buildings and lifelines to ground shaking, wind speed or water rise, but subsequent events, such as aftershocks, tsunamis, urban fires or storm surges, also induce large levels of human, economic, social and cultural losses. Countless examples are available worldwide and history if full of tragic memories of this type of events. The 1755 Lisbon earthquake is an example of how a major earthquake may generate consequences resulting not only from the ground motion itself but also from all the consequent events that followed the major ground shaking.

Over the past years, a sequence of major earthquakes striking at different places worldwide and generating impressive records with respect to fatalities, economic, social and cultural losses has

been witnessed. The 2011 Japan and New Zealand events led to record-breaking observations of losses, including those related with downtime and household, along with numerous other tangible and intangible losses [1-2]. In other cases (e.g. the Haiti earthquake of 2010), the levels of physical damage were devastating with most of the constructions exhibiting inadequate performance and leading to fatalities due to structural collapse. This scenario cannot be expected to occur only in the Haiti case since many of today's large or expanding cities across the world are located in earthquake-prone regions [3-4]. Nonetheless, even in the case of a similar earthquake event, different societies experience different level of consequences, particularly due to the distinct levels of preparedness of some countries when compared with that of others. While, countries with a lower Gross Domestic Product (GDP) per capita are said to be more exposed to economic losses due to the effects of natural hazards [5], emerging economies can also sustain high impacts [6]. Furthermore, poor countries are also associated to low societal resilience to disasters and to inadequate standards with respect to construction, a fact that increases their vulnerability to extreme natural events such as earthquakes [7].

In southern Europe, the losses associated to earthquakes have also been considerable over the past 30 years. In Italy, it is estimated that the 2012 Emilia Romagna earthquake caused direct losses in the range of US$ 225M [8], with additional losses expected due to downtime and production loss (to a total of 16.000M US$), while the financial efforts and rebuilding costs due to the 2009 L'Aquila Earthquake were estimated to exceed 2500M US$. These two events are the most significant events that occurred in the past 15 years in southern European countries. Conversely, the number of homeless persons after the 2009 L'Aquila earthquake was considerably higher than in the case of the 2012 Emilia Romagna, which may be related to the difference between the indirect costs observed in the two events.

In the specific case of Portugal, earthquake risk has a significant importance in the national economic context. According to Aon Benfield [9], losses of about 6300M US$ can be expected from a 250 years return period earthquake, which puts a significant pressure on the banking sector due to mortgage obligations. Hence, assessing the state of existing buildings and improving their seismic performance may represent a high priority issue not only for building owners but also for public authorities and societies, since the consequences of an event will spread to all sectors.

The post-earthquake scenarios found after some of the recent earthquakes (e.g. Wenchuan, 2008; Haiti, 2010) have shown the lack of preparedness of the existing constructions and populations. If a comparison is made between the Haiti 2010 and the New Zealand 2010 earthquake consequences, it is possible to see that the global losses were very similar (8000M US$ in Haiti and 6500M US$ in the New Zealand earthquake sequence). Nonetheless, the difference between the GDPs of these two countries reflects very distinct consequences of similar monetary losses. As a proof, the high number of fatalities in Haiti gives an idea about the number of building collapses that were observed, while the lower number of collapses in New Zealand show that

losses were more related to damage consequences and business interruption instead of structural collapses. Furthermore, the level of preparedness can be measured by the percentage of the total losses that are estimated to be insured. The 77% insurance coverage of New Zealand against the 3% of Haiti clearly demonstrates the differences in seismic risk awareness in both countries. In addition, the lack of awareness problem of Haiti was also enhanced by the lack of earthquake activity over the past 250 years, a clearly different scenario than those connected to hurricanes and floods that occur almost every year.

Due to the importance of reinforced concrete (RC) buildings in the development of modern cities, their vulnerability to ground shaking can have a significant impact, not only due to the potential losses but also due to the number of people affected by those losses. Therefore, the scale of the vulnerability of these buildings can assume disastrous proportions. In the post-earthquake scenario of the 2010 Haiti earthquake, reconnaissance reports indicated that constructions exhibited a complete lack of seismic design principles [10], leading to multiple structural collapses and fatalities. Nevertheless, the numerous deadly collapses found in Haiti contrast with the few (2) cases found in reinforced concrete (RC) structures on the aftermath of the Christchurch earthquake sequence of 2010/11. Therefore, the clear importance of these structures in life safety is self-evident. If losses are considered instead of fatalities, the two scenarios registered similar economic consequences. Although the November 2010 Christchurch earthquake only caused moderate damages, the February 2011 earthquake caused severe damage on 16% of the 833 RC buildings, exceeding life-safety performance objectives [11]. Moreover, the Christchurch earthquake sequence clearly highlighted also the difference in the performance of the pre-1970 RC buildings (designed without seismic provisions) and the modern and safer buildings [12]. Following the earthquake sequence, 57% of the pre-1970 RC frame buildings were either yellow or red-tagged [12]. As documented for the case of 2009 L'Aquila earthquake in Italy [13], a large part of the population lived in multi-residential units in mid- or high-rise compounds (38%) that were severely damaged by the 2009 earthquake. As in other earthquakes (particularly the recent NZ events), this damage was not only related with the lack of ductility of structural components but also with the performance of non-structural components such as ceilings, electrical and piping systems, infill and partition walls. This extensive damage can lead to the demolition of the building even if collapse was avoided and the building complies with traditional building seismic design approaches. This implies that, for societies, the impact of the financial losses related with damage on buildings, on their contents, and with downtime has the same importance as life safety conditions in the seismic performance of buildings.

Dating back from the aftermath of the 1994 Northridge earthquake, many ask if life safety and irreparable building scenarios should be valid performance targets [12]. Traditionally, earthquake engineering considers the so-called Engineering Demand Parameters (EDP) to evaluate the seismic performance of structural and geotechnical structures. Although providing an indication

to the engineering community about the life safety conditions, EDPs give limited information to stakeholders (governments, insurance companies and building owners). In order to provide adequate engineering information to societal demands regarding the inclusion of loss limitation principles into the seismic assessment provisions, recent proposals started to include a set of objective decision variables (DVs) that are expected to provide relevant information to stakeholders. Since this effective risk communication can only be achieved by using a consequence-based (e.g. performance-based) approach, this implies the need to have variables and performance objectives that make sense to stakeholders (mean annual frequencies of exceedance (MAF), risk, expected annual cost, net present value) and simultaneously fulfil the necessary structural safety requirements imposed by engineering practice [14]. Hence, one of the main challenges currently faced by the earthquake engineering community is to develop adequate practice-oriented procedures to evaluate the safety of existing buildings that include these decision variables, along with the evaluation of their range in a given region for particular seismic scenarios. These procedures should be able to retain the necessary simplicity of current seismic safety assessment and design standards, but they should also provide ways to control the existing uncertainties, an aspect which is possible almost only when using full-probabilistic approaches, namely those developed under the umbrella of the PEER Performance Based Earthquake Engineering (PBEE) framework [15].

1.2 The role of uncertainties in the seismic assessment of RC buildings

The development of standard-based methods that are able to provide the necessary DVs to assess seismic retrofitting needs involves a complex interaction between the probabilistic occurrence of the ground motions and the careful evaluation of the impact of the uncertainty sources inherent to the overall assessment process. On the one hand, statistical analyses of the parameters and the corresponding distributions are instrumental for the quantification of uncertainties in seismic loss or safety evaluations. Generally, uncertainties about the basic parameters and methods must be propagated to the structural response, damage and loss assessments, either in terms of central values, dispersions and probability distributions or using uncertainty factors to account for the existing variability. On the other hand, in order to get an integrated analysis of the physical phenomena at hand, engineering judgement must also be adopted in some steps of the uncertainty assessment and propagation. Hence, the balance between these two types of analysis (probability and engineering) will yield a coherent methodology that agrees with the physics of the problem and conserves the main probabilistic principles associated to the assessment of existing uncertainties.

Over the years, the search for this balance led to the development of several code and guideline methods for the design and assessment of the seismic safety of buildings introducing different levels of simplification to deal with uncertainties. The FEMA P-58 guidelines [16] propose the

use of a deterministic model approach that accounts for record-to-record variability and considers predefined values for the modelling uncertainties. Conversely, the CNR guidelines [17] adopt a logic tree approach that includes, as an option, the possibility to explicitly account for all sources of uncertainty. Adopting a logic tree approach can be computationally exhaustive, particularly when considering nonlinear time history analysis and uncertainty propagation methods accounting for the aleatory uncertainty and multiple ground motion records.

Instead of adopting the time consuming path of the logic tree approach, uncertainty factors can be derived (also using a logic tree approach) and adopted as benchmark values for specific types of structures. As previously referred, FEMA P-58 proposes a set of uncertainty factors that must be used to increase the record-to-record variability of the EDPs. In fact, the use of these uncertainty factors is of the upmost importance when developing a practice-oriented strategy since they are in line with the approach followed by standard-based methods in earthquake engineering. Current standard-based methods use deterministic factors (like the confidence factor (CF) of Part 3 of Eurocode 8 (EC8/3) [18] or the knowledge factor k of ASCE 41-13 [19]) as a way to incorporate uncertainties into the limit state capacity of structural components. As pointed by Franchin *et al.* [20], the CF cannot explicitly account for all the sources of uncertainty both in theory and in practice. Despite being also limited, applying a factor directly to the EDP capacity, as proposed by ASCE 41-13 [19], is conceptually more intuitive than applying a factor only to the material properties, but its connection to the different uncertainties affecting the seismic safety verification is not clear. Bradley [21] performed a review of these uncertainties, disaggregating them among three main classes, namely:

- Uncertainties associated to the input ground motions;
- Uncertainties associated to the numerical simulation of the seismic response;
- Uncertainties about the goals of PBEE and the accuracy of the adopted framework.

1.2.1 Uncertainties in the ground motion input

The uncertainties associated to the ground motion input depend essentially on three factors. The first is associated to the type of ground motions that is selected, which depends on the type of analysis that is performed. The PEER-PBEE formulation follows a multiple ground motion intensity framework where ground motions are selected and scaled for different values of a certain intensity measure (IM). Alternatively, a single intensity-based assessment can be performed, enabling the derivation of the EDP-IM correlation for a single ground motion intensity. Cases may occur in which the seismological knowledge about the site may allow for a scenario-based assessment, where the rupture of a specific fault is used to assess the seismic performance.

The second factor is associated to the process of ground motion selection. Typically, when a multiple intensity-based assessment is conducted, ground motions are selected and scaled to each

ground motion intensity level, following the principles of incremental dynamic analysis (IDA) [22]. The derivation of an EDP-IM correlation using this method is consistent for ground motion intensity measure IM that is used for scaling but is not consistent for other IMs. Conditional ground motion selection [23-24] at each IM level considered in the analysis may overcome the previous issues, enabling the ground motion selection process to be fully compatible with the ground motion hazard. These methods have the advantage of including the different rates at which different IMs change with return periods. Uniform scaling, on the other hand, will increase the value of other IMs in ways that might be inconsistent with the hazard at the site. Recent studies analysed the use of the average spectral acceleration (AvgSa) as an efficient and sufficient IM (see e.g. [25]), which provides better consistency with the hazard and reduces the structure dependency of the fragility, especially when used with a consistent record selection (see e.g. [26]). The third issue regarding the seismic input uncertainties is associated with the number of ground motion records used in the analysis. The robustness of the response estimators is affected by the number of ground motions due to bias-variance trade-off problems, as pointed by Bradley [27].

1.2.2 Structural modelling uncertainties

As discussed by Bradley [21], the ability to consider the uncertainty associated to numerical modelling in PBEE results is currently at a very early stage of development. The information about modelling uncertainties provided by previous studies [28-32] is vague and, in some cases, contradictory. Most of the available conclusions are from studies where ground motion uncertainties are clearly dominant with respect to modelling uncertainties [29; 32]). These conclusions are biased by the overestimation of record-to-record variability due to the inadequate selection of ground motions and by the underestimation of modelling uncertainties given that some of the more important effects are not included [21]. More integrated studies [30; 33-38] have shown that modelling uncertainties and ground motion input uncertainties can have similar weights in the outcome of the fragility analysis, changing not only the variability but also its central value. Bradley [21] defined modelling uncertainties according to four classes, namely:

- *i)* Uncertainty about the physical properties of the structure, e.g. it depends on the quality of the physical characterization process of the structure;
- *ii)* Uncertainties about the constitutive modelling parameter uncertainty, e.g. the effect of the correlation between the estimated physical properties and their idealized model representation;
- *iii)* Uncertainty about the selection of the constitutive model for the numerical analysis;
- *iv)* Uncertainty about the level of simplification of the selected structural model e.g. the simplifications assumed when considering a single degree of freedom, a planar or a tri-

dimensional model of the structure, when defining a certain level of damping or simplified boundary conditions.

Most studies to date [29-31; 35] only address type (*i*) and (*ii*) uncertainties and, consequently, do not address the global combination of all uncertainties. This fact is indicated in Bradley [21] as one of the possible factors for the lack of knowledge about the importance of modelling uncertainties. A general comparison of the uncertainties included in different literature studies made in [36] has shown that no study consistently addressed all the sources of uncertainty that affect the seismic safety assessment results. Noteworthy exceptions to this observation are the recent studies by Gokkaya *et al.* [37] and by O'Reilly and Sullivan [38], with both cases highlighting the importance of modelling uncertainties. Gokkaya *et al.* [37] also studied the impact of correlations on modelling uncertainties, while O'Reilly and Sullivan [39] proposed predefined values of modelling uncertainties for Italian RC buildings, comparing them with those provided in current guidelines (i.e. FEMA P-58).

Conceptually, some of the previously mentioned uncertainties can be classified as aleatory and other as epistemic uncertainties (see [40] for a conceptual distinction). While some of the uncertainties can be included in the analysis as probability distributions, others have to be included as a binary option, with some probability or factor reflecting the merits of each option due to the existing lack of knowledge. The first type is generally associated with material and geometric properties. Still, Bradley [21] remarked the fact that the spatial distribution of material properties is currently not considered in seismic response studies. The second type can be introduced in the analysis by adopting a logic tree approach (e.g. [41-44]), following concepts commonly seen in seismology to calculate the mean hazard curve for a given site. According to the logic tree approach, each branch of the tree will require the construction of a different numerical simulation model and will lead to a different set of EDP values for each ground motion. In theory, replications of these models must also be adopted using a sufficient number of simulations to cover the probability distributions of the remaining variables of the problem.

1.2.1.1 Uncertainty about the characterization of the physical properties of the building
The fundamental difference between the design of a building and the assessment of an existing one is related with the type of uncertainty about the material properties, geometry and construction details. In the design case, standard values are assumed for the physical properties, which account for a certain level of uncertainty whose magnitude is guaranteed by quality control operations. In existing buildings, particularly in older ones, the safety assessment needs to be carried out using realistic values of the physical properties in order to reflect what is actually built. Although some of these properties can be surveyed relatively easy (e.g. geometrical properties), others will need

more resources for an effective and reliable characterization (e.g. the mechanical properties of the materials).

The survey of existing structures often demonstrates the difficulties of determining their physical characteristics. For example, it is known that design assumptions can sometimes change during construction, and physical properties are also often seen to deviate drastically, sometimes randomly, from the expected ones. The lack of knowledge is, in some cases, associated to the construction phases while in others it can be due to outdated or missing design documents and blueprints. Hence, it is instrumental in any assessment (not limited to the case of seismic safety) to conduct a structural survey to characterize the physical structural properties to be used in numerical modelling. From the suite of Eurocodes, only EC8/3 provides indications on how to estimate and reflect the uncertainties about the physical structural properties of an existing RC building. Specific indications are given regarding the number of tests that need to be carried out and the percentage of structural members that have to be checked in order to achieve a certain level of confidence about the structure. However, the connection between the EC8/3 knowledge levels (KLs) and CF values has been criticized (e.g. see [20; 44]) due to the lack of objectivity behind the CF values.

With respect to the survey framework, no statistically-based approach has been so far proposed integrating all the variables affecting the material assessment problem and no statistical background is provided to define the necessary number of tests. Statistical models are available to represent the materials properties in existing buildings but it is important to distinguish some of the available proposals. One type of proposals found in the literature refers to the statistical distribution of the concrete strength within a region, including tests from multiple buildings [43; 45]. While these proposals may be important to define the dispersion of the mean strength in portfolio analysis, the structure-specific variability of the material strength may be significantly different from the dispersion observed with large datasets including multiple buildings. With respect to the uncertainty about the structural details, to the author's knowledge only the approach adopted by Jalayer *et al.* [46] has been formulated, which uses the binomial distribution to include the probability of observing a defect in structural members.

1.2.1.2 Uncertainties about constitutive parameters and model selection

In the 2011 and 2012 surveys carried out by the American Society of Civil Engineers [47], 70% of the respondents (most of them practitioners) acknowledged that nonlinear dynamic analysis is part of their practice. Still, they also stated there is currently a lack of adequate guidelines addressing the modelling of nonlinear structural elements. The main issue associated to modelling is the multitude of options for the numerical modelling of elements and structural subsystems [48]. An example of this issue can be seen in the results of a recent blind prediction test [49] that show a considerable dispersion, even when experienced researchers are involved. Therefore, there

is a need for extensive guidelines on how to develop adequate models and include their corresponding uncertainty. Mitra [50] analysed the impact of constitutive modelling and other high-level uncertainties and concluded that analysts must be aware of the uncertainties associated with the adoption of different concrete strength envelopes, integration rules and type of distributed inelasticity models. In an engineering-based uncertainty assessment, Calabrese et al. [51] show the impact of numerical localization in the response of RC columns and provide a qualitative assessment of the uncertainties that can result from the analysis. From a statistical viewpoint, Yazgan and Dazio [52-53] have analysed the uncertainty in the response of columns and RC walls tested in a shaking table. Using the results obtained with different frame modelling techniques, the authors derived median factors and coefficients of variation for the maximum and residual rotations. Both element- and section-level hystereses were varied but only a fibre, a bilinear and a Takeda model without constitutive parameter uncertainty were included.

With respect to RC columns subjected to uniaxial loads, a recent study [48] quantified uncertainty distributions for initial stiffness, dissipated energy and peak strength using frame and finite element models. An extensive number of columns (320) was used in this study but the constitutive modelling parameters were kept constant in the simulations and response degradation was not analysed. Another study carried out by Rodrigues et al. [54] compared the performance of different distributed inelasticity models (force-based and displacement-based models) when simulating RC columns under biaxial loading, but it did not specify uncertainty factors nor included constitutive parameter modelling uncertainties. Nonetheless, this study performs the biaxial analysis of a considerable set of columns similar to those found in existing buildings in Europe (in low to mid-rise frames). Zeris et al. [55] also analysed the variability of the global response of a RC building when considering different frame models but only includes the flexural behaviour of the elements. Other studies have also included the effect of brittle failure modes in RC frame elements. In most cases, these mechanisms (flexure/flexure-shear failure, shear failure, axial failure, bond-slip) are modelled by spring elements where the response degradation is concentrated. The works of Haselton et al. [56] and Zhu et al. [57] present flexure moment-rotation spring models that are useful since they provide not only the mean correlation between the physical properties and the constitutive models, but also the corresponding uncertainties. However, the boundary conditions of the model (derived mainly for cantilever columns) may affect its application in more general cases. Regarding brittle failure modes, Elwood [58], Leborgne and Gannoum [59] and Baradaran Shoraka and Elwood [60] presented strategies to include failure criteria into beam-column elements.

Multiple modelling choices are also available for beam-column joints. Celik and Ellingwood [61] compared various joint models proposing an additional solution to model the shear-distortion behaviour of the joint. However, the comparison was made using elements with small length near the joint regions, which may induce strain localization and therefore lead to calibrated joint model

that is dependent on the adopted frame modelling strategy. Also, material degradation was left out of the referred study. Conversely, Birely *et al.* [61] used a dual-hinge model incorporated into a lumped plasticity beam–column element which combines two rotational springs in series to simulate the inelastic deformations of the beam and the joint. More recently, Lima *et al.* [62] calibrated expressions for exterior joints while Hassan and Mohele [63] proposed a beam-column joint model specifically for existing RC buildings, simulating experimentally the lack of joint reinforcement typically found in older constructions. Similar experiments were conducted by Park and Mosalam [64-65] and a model for unreinforced corner joints was then also proposed. O'Reilly and Sullivan [39] have also recently proposed models for beam-column joints of older RC buildings in Italy.

1.2.1.3 Uncertainties about macro-modelling decisions

Apart from the subsystem modelling analysis addressed before, decisions made at the macro-level (as opposed to the micro-level involving the correlation between the physical properties and the constitutive numerical modelling considerations) may also have a considerable impact in the seismic response of RC buildings. Aspects regarding the inclusion of joint flexibility, infill behaviour, shear deformations and brittle failure modes, or simply the consideration of 3D effects by rigid diaphragms or spatial variability of mass and stiffness, are some of the effects that require careful consideration. Celik *et al.* [67] and Jeong *et al.* [68] have shown the impact of some of these aspects in the seismic fragility of RC frames. Some studies in the literature focused on assessing the influence of introducing the irregularities and the distribution of infill panels (e.g. see [69-77]), among which Sattar and Liel [78], Haldar *et al.* [79] and D'Ayala and Meslem [36] have shown the direct effect these issues on fragility curves. Ricci *et al.* [88] analysed the impact of infill distributions in the seismic response of RC buildings while Sousa *et al.* [89] studied the impact of modelling infills panels, different slab assumptions and mass representation. Pinho *et al.* [80] addressed the modelling of rigid diaphragm analysing the impact of adopting different numerical alternatives.

1.2.2 Uncertainties about the goals of the seismic performance assessment

The complexity and the objectives of the assessment procedures of the PEER-PBEE framework focus on the quantification and management of uncertainties while failing, in some cases, to provide a consistent understanding about the deficiencies of a building. While DVs are provided for decision-making, in some sense, they also lack a safety-based approach, since the generic approach benefits stakeholder decision-making but, at the same time, gives rise to multiple interpretations of the same results. Therefore, the PEER-PBEE methodology does not comply with common safety-based proposals (e.g. the limit states in the Eurocodes) involving threshold conditions. Also, the basic procedure of the PEER-PBEE methodology can be seen as a complex

and cumbersome approach, whose simplification by the adoption of simpler procedures may generate also uncertainty. Currently, multiple concepts are followed by seismic safety assessment codes worldwide, raising the uncertainty on how compatible they are between themselves and, particularly, where they stand when compared with modern PEER-PBEE concepts and outcomes. Interpretations of the interaction between statistical assessment and engineering judgment about structural conditions are of the upmost importance in the assessment of existing RC buildings. Not only the assessment must show how buildings may perform but also, in a mitigation and preparedness sense, it must inform potential decisions to improve the seismic performance of the building.

Another type of uncertainty derives from the scale at which the seismic assessment is performed. While it may be possible to apply directly the PEER-PBEE methodology to a single building, portfolio analysis require the use of simplified methods (e.g. see [16; 81-84]). Hence, it is necessary to guarantee that the same level of accuracy and that similar outcomes to those of the PEER-PBEE can be extracted from the analysis performed using these simplified methods. At least the reliability of these simplified methods must be assessed and the corresponding uncertainties should be quantified. Conservatism when quantifying the DVs is acceptable within the context of portfolio analysis, where one is more interested in global loss and risk metrics. Conversely, in structure-specific assessments, one is interested in deciding about the type of retrofitting that needs to be implemented which demands very accurate DVs due to its importance for stakeholder decision-making.

1.3 Scope and Objectives

The major goal of this thesis is to develop a methodology that unifies the multiple concepts involved in the seismic safety assessment of existing RC buildings, addressing the need for compatibility between the current standard-based methods and full probabilistic approaches such as the PEER-PBEE methodology. In light of this, the thesis analyses the strengths of probabilistic methods and shows how they can be applied in a practical way within the scope of current code-based methods. The consistency of code-based methods is addressed, involving the individual analysis and the combination of all the sources of uncertainty that affect the seismic performance assessment problem. The connection between the standard-based load and capacity factored (DCFD) approach and the full probabilistic analysis of the uncertainties about the materials, the geometric properties, the way the component response and its intrinsic nonlinearity are introduced in the seismic assessment procedure, and the main objectives of the assessment are addressed. Regarding the structural characterization, the thesis provides a methodological approach to answer the question "which structure is one assessing?" and reviews current code-based methods for the in-situ survey of the structural and material properties. As an outcome, it derives safety factors for component capacities that are compatible with the adopted survey plan and the inherent

epistemic uncertainty. With respect to the modelling uncertainties, the thesis addresses the Bayesian question "Given that the structure is known, what is the uncertainty associated with the adoption of different modelling schemes, and how will it affect the goal of the seismic performance assessment?". Using the main observations made regarding the previous questions, this thesis also addresses the question "How can simple DCFD approaches be improved in order consistently incorporate uncertainties?". Finally, after defining a standard-based framework consistent with full probabilistic approaches, the thesis revisits the code definition of seismic performance assessment and introduces a framework consistent with the modern PEER-PBEE approach to address the question "Are standard-based performance objectives compatible with limit state compliance criteria?".

1.4 Organization and Outline

Following the proposed objectives, this thesis was divided into ten chapters. All chapters were designed to be self-contained and include the cited respective references. Nevertheless, the thesis should be read as a continuous sequence of chapters to understand the scope of the developments proposed in each chapter, namely the main reasoning behind each development. Given the format choices, some repetitions may be found from one chapter to another. Apologies are given due to any inconvenience it may cause in the course of reading the thesis.

Chapter 1, as seen before, addresses the necessary background that frames the following chapters, namely by discussing the main differences between standard-based methods and full probabilistic approaches and by defining, in light of the state-of-the-art, the main research questions that will be analysed herein.

One of the great earthquake engineers I know owns a metaphoric car-dealership. Famously and deservedly known for having built a Batmobile and a mighty "Toyota" out of a Ferrari, this engineer kept working on giving us all the tools necessary to reduce the very expensive maintenance cost of the Batmobile. We are now entering his car dealership, but for some reason our eyes are not drawn to the Batmobile (full probabilistic PBEE/loss assessment) but rather to the Alfas (standard-based methods such as EC8/3 and DCFD equations). Long story-short…We bought a classic Alfa, but it broke instantly. How can we fix it?

Chapter 2 proposes a finite population strategy to calibrate probabilistically sampling plans to estimate the strength of material properties and to assess the conformity of the structural details in existing RC buildings. The main principles that may be used to disaggregate finite populations of structural elements are formulated. Furthermore, the uncertainties associated with the assessment are described, and a ranking of their importance is discussed. Non-destructive tests are used to evaluate the expected variability of material strength at the building storey level, and the estimates obtained by the proposed methodology are compared with real datasets. The variability of non-destructive tests is compared with that obtained based on destructive tests, and

the efficiency of using an indirect estimate for the coefficient of variation in the estimation of the mean concrete strength is assessed.

This is where we start looking at the main components of our Alfa (the standard-based method) and we try to figure out what's wrong with it. We start by assessing the state of the car engine (physical properties of the building). Ideally we could fix each part individually (assess each structural component), but we may eventually end up fixing too many parts (due to excessive number of destructive tests), which is obviously economically unfeasible. So here we see how many parts we must really fix in order to have a car that will be able to make on average a few kilometres per year in the Summer.

Chapter 3 extends the principles adopted in Chapter 2 by proposing a new set of prior estimators for concrete strength variability based on non-destructive tests. These estimators are derived using a database of empirical data and are fully consistent with the physical properties of the non-destructive tests and with the correlations found for the concrete compressive strength. Both ultrasonic pulse velocities and rebound hammer test results were considered in the study. Expressions are proposed to estimate the standard deviation and the coefficient of variation of the concrete strength in a given region where the material properties are expected to be homogeneous (as defined in Chapter 2) based solely on the results of non-destructive tests.

Luckily, we found a place where we are able to buy some cheap spare parts (non-destructive tests) to replace some of the old ones (to replace destructive tests). Furthermore, we found a talented mechanic (indirect variability estimators) that agreed to recondition the engine (physical properties of the building) to its original state.

Chapter 4 addresses possible applications of the finite population methods derived in Chapter 2 to overcome the limitations of existing code-based strategies to assess material properties in RC buildings. Simplified code-methods use alternative ways to reflect the physical parameter uncertainties in the assessment. With this in mind, a safety coefficient (CF_{mat}) representing the uncertainty about the mean material properties is defined, following recent interpretations about the EC8/3 confidence factor. The proposed values of CF_{mat} and the corresponding sampling plans that are also defined enable the total control of the bias and variability associated to the survey operations in existing RC buildings. Furthermore, CF_{mat} is in line with the current code-based assessment methods.

At this stage, we were confident that all the problems we had could be solved. So we replaced some old parts (destructive tests) by the spare parts we got (non-destructive tests) and put the talented mechanic (indirect estimators for the variability) to work. Although we knew that everything would look brand new from the inside of the engine (adequate estimates for the mean), we decided to add a few new components (CFmat) just to be safe and avoid possible future issues identified by the mechanic (indirect variability estimators).

Chapter 5 integrates the principles addressed in Chapters 2, 3 and 4 and defines a complete and consistent framework to include the uncertainties about the structural properties into the estimate of the capacity of RC members. The proposed framework is formulated based on the demand-capacity factored design (DCFD) format embedded in the EC8/3 and ASCE 41 frameworks. A

consistent set of empirical models representing ductile and non-ductile failure modes are evaluated, and capacity safety factors are proposed based on the uncertainties about these models and on the testing and survey operation levels adopted in the assessment. The closed-form safety factors depend on the results and properties of the survey/testing plan and can be adjusted for each component individually to reflect the actual amount of information about the physical properties of a given component. Furthermore, the use of limit state conditions based of the adopted DCFD approach enables modelling uncertainties to be included by accounting for the uncertainty about the damage state of the component and by using the same modelling strategy to assess the demand and the capacity.

Fantastic, our shiny Alfa is ready to go and… it doesn't. It turned out that our mechanic found out that at very high speeds (nonlinear analysis), we do not need new engine parts (CF$_{mat}$), instead we need a new clutch (DCFD limit state condition) and some additional reconditioning work (capacity safety factors). This is where we fix the clutch making it compatible with the properties of the reconditioned engine (the physical structural properties). An advice to you, Alfa enthusiast... Always make sure you check your clutch (DCFD limit state condition)) before fixing the engine (assessing the structural properties). It might save you some time and money in the process.

Chapter 6 analyses experimental evidence about the damaged region in RC elements under cyclic loading. A mechanical interpretation of the main mechanisms affecting the hinge formation and the consequent damage evolution is discussed based on a database of experimental damage length reports. A sensitivity analysis of the main physical parameters involved in the damage mechanisms is performed, and compound variables representative of these mechanisms are then also analysed. Empirical approximations for the length of the damaged region in RC frame componenets are proposed. The length of the damaged region is further correlated with the expected ductility and with the type of mechanism that may lead to the damage localization and to the collapse of the frame component.

A new decision had to be made. The driving shaft (the concentrated plasticity model) fell off and broke when fixing the clutch (DCFD limit state condition) and we found that we need to replace it. We found an alternative class of driving shafts (distributed inelasticity models), but to be able to buy one we first need to check the specs (ductility, mechanism and damaged region length) of the selected driving shaft of our Alfa.

Chapter 7 analyses a consistent local formulation modelling approach for the simulation of the post-peak response of RC beam-column components. This formulation combines the relevant principles discussed in Chapter 6 regarding the localization of damage in RC frame elements, the available regularization techniques for force-based elements and the mechanics associated to hinge formation and rotation. The proposed modelling approach is a regularized local force-based frame element and a modified fibre-based local plasticity model that generates equivalent strains and curvatures after the softening of the uniaxial materials. The stress-strain curves of these materials are defined based on the rationale behind the expected failure mode of the component. Furthermore, they also include a regularization of the strains based on the size-dependent

properties of the materials given the differences between the size of the specimen tested to evaluate the uniaxial material properties and the real size of the plastic hinge. The proposed modelling approach was developed using the models available in the software OpenSees and its performance was analysed for a suite of 36 experimental tests.

Ok. The new driving shaft (distributed inelasticity model) appears to be compatible, provided that we ensure that all the specs (ductility, mechanism and damaged region length) of the original one are adopted.

Chapter 8 analyses the compatibility between the seismic demands obtained with the reference concentrated plasticity model adopted for the definition of the limit state conditions discussed in Chapter 5 with those obtained with the distributed inelasticity model analysed in Chapter 7. Compatibility factors for the seismic demand obtained by these two modelling approaches are then developed. These compatibility factors are calibrated for nonlinear static and dynamic analysis and are based on component-level results obtained for 48 RC frames with four storeys and with different levels of lateral capacity and ductility. The limit state condition introduced in Chapter 5 for seismic safety assessment is revised in order to account for this compatibility factor, and generic values of the factor are proposed for ductile and brittle limit state assessment.

The new driving shaft (distributed inelasticity model) cannot be directly fitted to the clutch and minor adjustments (compatibility factors) to have to be made again by our mechanic to prevent future problems. After doing so, our work is done. Houston, we have an Alfa…

Chapter 9 analyses the equivalence of standard-based methods and probabilistic approaches in a more global way instead of a case-by-case situation. Based on the nonlinear dynamic analysis of three 3D RC frame buildings, the consistency between the results obtained with the DCFD condition and the qualitative description of the performance objectives in current standards is evaluated. This consistency is evaluated by considering a DCFD condition defined in terms of losses. The considered loss assessment procedure involves a simplified loss assessment approach derived from storey-based loss assessment methods. The use of this simplified method supports the development of a more generalized analysis of the referred equivalence, since it considers general loss functions that avoid the need for an extensive inventory of building components. The equivalence is analysed by comparing the statistical distributions of the values of the average spectral acceleration obtained for different loss thresholds and for component-based criteria. This comparison indicates the level of expected losses that, on average, corresponds to the DCFD condition.

Hold on…I told you that all the components were working, but is it safe to drive? Here that's where we check the performance of the new/old-like engine, just to see how fast it runs with respect to its original top speed.

Chapter 10 summarizes the main conclusions and contributions of this thesis. Additionally, its main limitations, future developments and further research needs are also discussed.

Here we show the main steps, pitfalls and directions we followed to put our mighty Alfa to run again. We point the major issues and weaknesses, and recognize the need for a future full of Alfas, but with a few electric ones as well.

1.5 References

1   Goda K, *et al*, (2013). Ground motion characteristics and shaking damage of the 11th March 2011 Mw 9.0 Great East Japan Earthquake. Bulletin of Earthquake Engineering; 13(1): 1-30.

2   Wilkinson S, *et al.*, (2013). Observations and implications of damage from the magnitude Mw 6.3 Christchurch, New Zealand earthquake of 22 February 2011. Bulletin of Earthquake Engineering; 13(1): 1-35.

3   Lall SV, Deichmann U, (2009). Density and disasters: Economics of urban hazard risk. Policy Research Working, The World Bank.

4   He C, Huang Q, Dou Y, Tu Q, Liu J (2017). The population in Chinas's earthquake-prone areas has increased by over 32 million along with the rapid urbanization. Environmental Research letters; 11(7):1-13.

5   Ghesquiere F, Mahul O, (2010). Financial Protection of the State against Natural Disasters – A Primer, Policy Research Working Paper 5429, The World Bank.

6   MunichRE. Beilharz H, Rauch B, Wallner C, (2013). Economic consequences of natural catastrophes: Emerging and developing economies particularly affected –Insurance cover is essential

7   Ferreira M, (2012). Seismic Risk of Urban Systems (in Portuguese). PhD Dissertation. Instituto Superior Tecnico. Universidade Tecnica de Lisboa.

8   Ioannou I, *et al*., (2012). The 29th May 2012 Emilia Romagna Earthquake. EPICentre field observation report. University College of London.

9   Aon Benfield, (2012). Aon Benfield Impact Forecasting: Seismic risk in Portugal. (http://www.lloyds.com/~/media/files/lloyds/offices/spain/cob%20lisbon%20sept%2012/g oran%20trendafiloski.pdf accessed April, 2014)

10 Fierro E, Perry K, (2010). Preliminary Reconnaissance report – 12 January 2010 Haiti earthquake.(http://peer.berkeley.edu/publications/Haiti_2010/documents/Haiti_Reconnaiss ance.pdf)

11 Elwood K, Pampanin S, Kam WY, (2011). 22 February 2011 Christchurch earthquake and implications for the design of concrete structures. Proceedings of the International Symposium on Engineering Lessons Learned from the 2011 Great East Japan Earthquake, March 1-4, 2012, Tokyo, Japan.

12 Kam WY, Pampanin S, (2011). The seismic performance of RC buildings in the 22 February 2011 Christchurch earthquake. Structural Concrete; 12(4): 223–233.

13 Liel A, Lynch K, (2012). Vulnerability of Reinforced-Concrete-Frame Buildings and Their Occupants in the 2009 L'Aquila, Italy, Earthquake. Natural Hazards Review; 13(1): 11–23.

14 Fragiadakis M, Vamvatsikos D, Karlaftis M, Lagaros N, (2015). Seismic assessment of structures and lifelines. Journal of Sound and Vibration; 334: 29-56

15 Cornell CA, Krawinkler H, (2000). Progress and challenges in seismic performance assessment, PEER Centre News 3(2):1-3.

16 FEMA (2012). Next-Generation Methodology for Seismic Performance Assessment of Buildings, prepared by the Applied Technology Council for the Federal Emergency Management Agency, Report No. FEMA P-58, Washington, D.C

17 CNR (2014). CNR DT 212/2013. Istruzioni per la Valutazione Affidabilistica della Sicurezza Sismica degli Edifici Esistent. Consiglio Nazionalle delle Ricerche – Commisione de studio per la predisposizione e l'analisi di norme technique relative alle construzioni. Roma. May, 2014.

18 CEN (2005). Eurocode 8: design of structures for earthquake resistance. Part 3: Assessment and retrofitting of buildings. Brussels, 2005

19 ASCE (2007). Seismic rehabilitation of existing buildings (ASCE/SEI 41-06). American Society of Civil Engineers, Reston, Virginia, USA.

20 Franchin P, Pinto PE, Rajeev P, (2010). Confidence factor?. Journal Earthquake Engineering; 14 (7): 989–1007.

21 Bradley BA, (2013). A critical examination of seismic response uncertainty analysis in earthquake engineering. Earthquake Engineering and Structural Dynamics; 42(11): 1717-1729.

22 Vamvatsikos D, Cornell CA, (2002). Incremental dynamic analysis. Earthquake Engineering and Structural Dynamics; 31 (3): 491-514.

23 Baker J, (2011). Conditional Mean Spectrum: Tool for ground motion selection. Journal of Structural Engineering; 137(3): 322-331.

24 Bradley BA, (2012). A ground motion selection algorithm based on the generalized conditional intensity measure. Soil Dynamics and Earthquake Engineering; 40:48-61.

25 Kohrangi M, Vamvatsikos D, Bazzurro P, (2017). Site dependence and record selection schemes for building fragility and regional loss assessment. Earthquake Engineering and Structural Dynamics; 46(10): 1625-1643

26 Kohrangi M, Bazzurro P, Vamvatsikos D, Spillatura A, (2018). Conditional spectrum based ground motion record selection using average spectral acceleration. Earthquake Engineering and Structural Dynamics; 47(1): 265-265.

27 Bradley BA, (2013). A comparison of intensity-based demand distributions and the seismic demand hazard for seismic performance assessment. Earthquake Engineering & Structural Dynamics; 42(15): 2235-2253.

28 Ibarra L, Krawinkler H, (2005). Global Collapse of Frame Structures under Seismic Excitations. Report. John A. Blume Earthquake Engineering Research Centre. Stanford University. Stanford, California

29 Lee T, Mosalam K, (2006). Probabilistic seismic evaluation of reinforced concrete structural components and systems, PEER Technical Report 2006/04, Aug. 2006.

30 Liel A, Haselton C, Deierlein G, Baker J, (2009). Incorporating modelling uncertainties in the assessment of seismic collapse risk of buildings. Structural Safety 2009; 31(2):197–211.

31 Fragiadakis M, Vamvatsikos D, Karlaftis M, Lagaros N, (2015). Seismic assessment of structures and lifelines. Journal of Sound and Vibration; 334: 29-56

32 Kwon, O. and Elnashai, A. (2006). The effect of material and ground motion uncertainty on the seismic vulnerability curves of RC structure. Engineering Structures 28 (2): 289-303

33 Haselton C. (2006). Assessing Seismic Collapse Safety of Modern Reinforced Concrete Moment Frame Buildings. Ph.D. Dissertation, Department of Civil and Environmental Engineering, Stanford University.

34 Celarek D, Dolšek M, (2013). Practice-oriented probabilistic seismic performance assessment of infilled frames with consideration of shear failure of columns, Earthquake Engineering and Structural Dynamics; 42:1339–1360.

35 Dolsek M, (2009). Incremental dynamic analysis with consideration of modelling uncertainties. Earthquake Engineering and Structural Dynamics; 38(6):805–825.

36 D'Ayala D, Meslem A, (2013). Sensitivity of analytical fragility functions to capacity-related parameters, GEM Technical Report 2013-X, GEM Foundation, Pavia, Italy.

37 Gokkaya BU, Baker JW, Deierlein GG, (2016). Quantifying the impacts of modeling uncertainties on the seismic drift demands and collapse risk of buildings with implications on seismic design checks. Earthquake Engineering and Structural Dynamics; 45(10): 1661-1683.

38 O'Reilly GJ, Sullivan TJ, (2018). Quantification of modelling uncertainty in existing Italian RC frames. Earthquake Engineering and Structural Dynamics; 47(4): 1054-1074.

39 O'Reilly GJ, Sullivan TJ, (2017). Modeling techniques for the seismic assessment of the existing Italian RC Frame Structures. Journal of Earthquake Engineering: 1-35.

40 Der Kiureghian A, Ditlevsen O (2009). Aleatory or epistemic? Does it matter? Structural Safety; 31(2):105-112.

41 Pinto PE, Franchin P, (2014) Existing Buildings: The New Italian Provisions for Probabilistic Seismic Assessment, in A. Ansal (ed.), Perspectives on European Earthquake Engineering and Seismology, Geotechnical, Geological and Earthquake Engineering 34.

42 Rota *et al.* (2014). A framework for the seismic assessment of masonry buildings taking into account different sources of uncertainty. Earthquake Engineering and Structural Dynamics; 43(7):1045–1066

43 Silva V, (2013). Development of open-source tools for seismic risk assessment: application to Portugal, PhD Thesis, University of Aveiro, Portugal.

44 Elefante L, (2010). Dealing with uncertainties in the assessment of existing RC buildings. PhD Thesis, Università degli Studi di Napoli Federico II, Naples, Italy.

45 Cristofaro MT. (2009). Metodi di valutazioni della resistenza a compressione del calcestruzzo di structure di c.a. esistenti. PhD dissertation. Universitá di Firenze. Italy.

46 Jalayer F, Petruzzelli F, Iervolino I, Manfredi G, (2010). Accounting for the effect of in-situ tests and inspections on the performance assessment of existing buildings. Proceedings of the 14th European Conference on Earthquake Engineering, Ohrid, Macedonia.

47 Head M, Dennis S, Muthukumar S, Nielson B, Mackie K, (2014). Nonlinear analysis in modern earthquake engineering practice. ASCE Structure Magazine:16–20.

48 Huang X, Kwon O, (2014). Numerical models of RC elements and their impacts on seismic performance assessment. Earthquake Engineering and Structural Dynamics; 44:283–298.

49 Terzic V, Schoettler M., Restrepo J, Mahin S, (2015). Concrete Column Blind Prediction Contest 2010: Outcomes and Observations. PEER Report No. 2015/01. Pacific Earthquake Engineering Research Centre. University of California, Berkeley.

50 Mitra N, (2008). Uncertainty in analytical structural response associated with high level modelling decisions. The 14th World Conference on Earthquake Engineering. Beijing, China

51 Calabrese A, Almeida JP, Pinho R. (2010). Numerical Issues in Distributed Inelasticity Modelling of RC Frame Elements for Seismic Analysis. Journal of Earthquake Engineering; 14(S1), 38-68.

52 Yazgan U, Dazio A, (2011). Simulating Maximum and Residual Displacements of RC Structures: I. Accuracy, Earthquake Spectra; 25(4). 1187-1202.

53 Yazgan U, Dazio A, (2011). Simulating Maximum and Residual Displacements of RC Structures: II. Sensitivity, Earthquake Spectra; 25(4):1203-1218.

54 Rodrigues H, Varum H, Arêde A, Costa A, (2012). Comparative efficiency analysis of different nonlinear modelling strategies to simulate the biaxial response of RC columns. Earthquake Engineering and Engineering Vibration; 11: 553-566.

55 Zeris C, Vamvatsikos D, Giannitsa P, Alexandropoulos K, (2007). Impact of FE modeling in the seismic performance prediction of existing RC buildings. Proceedings of the COMPDYN2007 Conference on Computational Methods in Structural Dynamics and Earthquake Engineering, Rethymno, Greece.

56 Haselton CB, Liel AB, Taylor-Lange SC, Deierlein GG. (2016). Calibration of Model to Simulate Response of Reinforced Concrete Beam-Columns to Collapse. ACI Structural Journal; 113(6): 1141-1152.

57 Zhu L, Elwood KJ, Haukaas T, (2007). Classification and Seismic Safety Evaluation of Existing Reinforced Concrete Columns, Journal of Structural Engineering; 133 (9):1316-1330.

58 Elwood KJ. (2004). Modelling failures in existing reinforced concrete columns. Canadian Journal of Civil Engineering; 31(5): 846-859.

59 LeBorgne M, Ghannoum W, (2014). Calibrated analytical element for lateral-strength degradation of reinforced concrete columns. Engineering Structures; 81:35-48.

60 Baradaran Shoraka M, Elwood K, (2013). Mechanical Model for Non Ductile Reinforced Concrete Columns Journal of Earthquake Engineering; 17(7): 937-957.

61 Celik O, Ellingwood B. (2008). Modeling Beam-Column Joints in Fragility Assessment of Gravity Load Designed Reinforced Concrete Frames. Journal of Earthquake Engineering; 12(3): 357-381.

62 Birely A, Lowes L, Lehman D. (2012). A model for the practical nonlinear analysis of reinforced-concrete frames including joint flexibility. Engineering Structures; 34:455–465

63 Lima C, Martinelli E, Faella C, (2012). Capacity models for shear strength of exterior joints in RC frames: state-of-the-art and synoptic examination. Bulletin of Earthquake Engineering; 10(3): 967-983.

64 Hassan W, Moehle J, (2012). A Cyclic Nonlinear Macro Model for Numerical Simulation of Beam-Column Joints in Existing Concrete Buildings. 15th World Conference on Earthquake Engineering, Lisbon, Portugal.

65 Park S, Mosalam K, (2012). Analytical Model for Predicting the Shear Strength of Unreinforced Exterior Beam-Column Joints. ACI Structural Journal; 102(2): 149-160

66 Park S, Mosalam K, (2013). Simulation of Reinforced Concrete Frames with Non-Ductile Beam-Column Joints. Earthquake Spectra;29(1): 1-25.

67 Celik OC, Ellingwood BR (2010). Seismic fragilities for non-ductile reinforced concrete frames–Role of aleatoric and epistemic uncertainties. Structural Safety; 32(1): 1-12.

68 Jeon JS, Lowes LN, DesRoches R, Brilakis I, (2015). Fragility curves for non-ductile reinforced concrete frames that exhibit different component response mechanisms. Engineering Structures; 85: 127-143.

69 Asteris P, Antoniou S, Sophianopoulos D, Chrysostomou C, (2011). Mathematical Macromodeling of Infilled Frames: State of the Art. Journal of Structural Engineering; 137(12): 1508–1517.

70 Mondal G, Tesfamariam S, (2014). Effects of vertical irregularity and thickness of unreinforced masonry infill on the robustness of RC framed buildings. Earthquake Engineering and Structural Dynamics; 43(2): 205–223.

71 Uva G, Porco F, Fiore A, (2012). Appraisal of masonry infill walls effect in the seismic response of RC framed buildings: a case study. Engineering Structures; 34:514–26.

72 Uva G, Raffaele D, Porco F, Fiore A, (2012). On the role of equivalent strut models in the seismic assessment of infilled RC buildings. Engineering Structures; 42:83–94.

73 Dymiotis C, Kappos AJ, Chryssanthopoulos MK, (1999). Seismic Reliability of RC Frames with Uncertain Drift and Member Capacity, Journal of Structural Engineering, ASCE; 125(9): 1038–1047.

74 Ellul F, (2006). Static nonlinear finite element analysis of low engineered masonry infilled reinforced concrete frames for seismic assessment, PhD Thesis, University of Bath. UK.

75 Dolšek M, Fajfar P, (2008). The effect of masonry infills on the seismic response of a four-storey reinforced concrete frame – a deterministic assessment, Engineering Structures; 30: 1991-2001

76 Mulgund G, Kulkarni A, (2011). Seismic assessment of RC frame buildings with brick masonry infills. International Journal of Advanced Engineering Sciences and Technologies; 2:140-147.

77 Burton H, Deierlein G, (2014). Simulation of Seismic Collapse in Non-Ductile Reinforced Concrete Frame Buildings with Masonry Infills. Journal of Structural Engineering; 140, SPECIAL ISSUE: Computational Simulation in Structural Engineering.

78 Sattar S, Liel AB, (2010). Seismic performance of reinforced concrete frame structures with and without masonry infill walls. 9th U.S. National and 10th Canadian Conference on Earthquake Engineering, Toronto, Canada.

79 Haldar P, Singh Y, Paul D, (2012). Effect of URM infills on seismic vulnerability of Indian code designed RC frame buildings, Earthquake Engineering and Engineering Vibration; 11: 233-241.

80 Pinho R, Bhatt C, Antoniou S, Bento R, (2008). Modelling of the horizontal slab of a 3D irregular building for nonlinear static assessment. Proceedings of the 14th World Conference on Earthquake Engineering, Beijing, China.

81 Vamvatsikos D, Cornell CA, (2005). Direct estimation of the seismic demand and capacity of MDOF systems through incremental dynamic analysis of an SDOF approximation. ASCE Journal of Structural Engineering; 131(4):589–599.

82 Silva V, Crowley H, Pinho R, Varum H, (2013). Extending displacement-based earthquake loss assessment (DBELA) for the computation of fragility curves, Engineering Structures; 56:343-356.

83 Welch D, Sullivan TJ, Calvi GM, (2014). Developing Direct Displacement-Based Procedures for Simplified Loss Assessment in Performance-Based Earthquake Engineering. Journal of Earthquake Engineering; 18(2).

84 Rossetto T, Elnashai A, (2005). A new analytical procedure for the derivation of displacement-based vulnerability curves for populations of RC structures. Engineering Structures; 27(3):397–409.

Chapter 2

Uncertainty in the assessment of the concrete strength using a finite population approach

Scope and objectives

Quantifying and managing uncertainties is a fundamental building block of any seismic safety assessment procedure, irrespectively of the complexity of the adopted methodology. Particularly, modelling uncertainties represent important aspects in any building assessment (not only for the specific case of seismic safety). Considering modelling uncertainties requires the involvement of four classes of interconnected uncertainty sources (see Chapter 1), all related to the physical properties. Physical modelling uncertainties aggregate the uncertainties about all the building characteristics whose properties or state is unknown. As opposed to the design case where predefined values are implicit for these uncertainties, in existing structures the actual properties can and must be identified, particularly due to the lack of knowledge about the construction quality at the time of construction. In RC structures, the geometric characteristics of the structural system and its components, the reinforcing steel details and the composition and spatial variability of the structural material properties (concrete and steel) are among these properties. In addition, the assessment of all the non-structural components (infill properties) may also be of interest. Hence, consistent survey plans must be developed that address the variability of the material properties and of the detailing with the same level of depth. In the present Chapter, a finite population paradigm is proposed to assess material and structural properties in existing RC buildings. Focus is given herein to the assessment of the concrete strength by proposing a complete framework to assess its variability using destructive and non-destructive tests and to control the reliability of the estimates of its central tendency.

2.1 Introduction

In the safety assessment of existing buildings, quantifying the "as-built" material properties is of the utmost importance due to the impact that it has on the subsequent application of safety assessment methods. In the case of reinforced concrete (RC) buildings, the concrete compressive strength is a material property that requires careful consideration [1] due to its inherent variability. This fact leads to the usual consideration of the concrete strength as being a random variable that has a certain (unknown) level of aleatory uncertainty [2]. This aleatory uncertainty is related to the inherent variability of the hardened concrete strength in existing structures [3] which can reach large values [4-5], often exceeding a coefficient of variation (CoV) of 20% [6]. Among other factors, this variability is associated with mix, casting and curing operations, which require a significant level of workmanship. Several studies (e.g. see [3; 7-8]) have analysed the impact of workmanship on the strength of hardened concrete and found that it can induce several types of variability depending on the structural system being analysed. Primarily, expected variations can be associated to batch-to-batch variability, involving the randomness related mainly with the construction management and planning and with quality control. Likewise, member-to-member variability can occur due to the influence of workmanship in casting operations. Variations of the concrete strength can also be expected within each structural member due to the previously mentioned factors. Moreover, a recent study [9] also described cracking, damage and the selection of the testing positions within the length of a structural element as sources of potential variability. In addition to the aleatory uncertainty associated with the concrete strength, epistemic uncertainty will also be generated due to the lack of knowledge associated with non-surveyed structural elements. Since survey plans only comprise tests on a few structural members in order to minimize the damage and the cost of inspection operations, the selection of a given set of elements to be tested instead of another will generate uncertainty. This uncertainty is even more important due to the low number of material tests that are generally carried out in existing buildings, a trend partially supported by existing norms (e.g. [10-13]). Often, standards regulating the assessment of existing buildings require a limited number of tests/inspections to be performed at each storey and for each type of primary component that is part of the building in order to obtain estimates of the mean values of the material properties. Nonetheless, as referred in [14], current building codes do not address the uncertainty level in the survey results and neglect the impact that sampling may have on the estimate of the dispersion of concrete strength (specifically on the estimate of the CoV) and on the corresponding estimate of the mean value. Therefore, controlling the epistemic uncertainty about the CoV of the concrete strength is a key component of a survey framework since it will affect the variability of the estimate (i.e. its precision), especially when it is based on a reduced number of tests. Moreover, this uncertainty is also seen to depend on the relation between the number of structural elements that are not tested during survey operations and the total number of structural elements of the population.

To control the extent of this uncertainty in survey operations and its impact on the estimate of the mean value of the concrete compressive strength in existing buildings, a method based on finite population statistics is proposed herein. The proposed approach will enable to effectively control the uncertainty in the estimates of the variability and of the mean value of the concrete strength in a population to improve their reliability. By accounting for the number of structural elements that are not tested during survey operations, the proposed method overcomes limitations of current standard methods and enables the development of more consistent survey frameworks to assess concrete strength in existing buildings.

2.2 Assessing statistical parameters in finite populations

In statistics, a population is said to be finite when it is possible to count all its elements. Statistical parameters characterizing these populations have specific features, which are associated to finite size conditions. To evaluate the exact value of these parameters, knowledge about all the N independent elements of the population is required. If all the N elements are observed, the population mean is then:

$$\bar{x}_U = \frac{1}{N} \cdot \sum_{k=1}^{N} x_k \qquad (1)$$

where U represents the population, N is the finite population size and x_k is an individual element of U. By the same principles, the variance of the population is given by:

$$S_U = \frac{1}{N-1} \cdot \sum_{k=1}^{N} (x_k - \bar{x}_U)^2 \qquad (2)$$

If instead of observing all the N elements of the finite population, a sample with size n ($n < N$) is observed, estimates for $\bar{x}_U$ and S_U can be computed. Assuming a simple random sampling of n elements without replacement from an unordered population of size N, M combinations of n elements can be defined, with M being given by:

$$M = \binom{N}{n} = \frac{N!}{n!(N-n)!} \qquad (3)$$

The main characteristic of finite population statistics resides in the conditional correlation between the probabilities of observing different values that is introduced by sampling. In finite populations, increasing the sample size n will affect the estimates of the statistical parameters since the observation of element x_k will affect the probability of observing the next element in

the sample, i.e. x_{k+1}. This fact leads to sampling probabilities that depend on n, thus reducing the level of statistical uncertainty (that is implicit when considering a sample to represent the population) in the estimators for the statistical parameters when compared to that of infinite populations.

In a finite population with N elements, an estimate $\hat{\bar{x}}_U$ for the real mean $\bar{x}_U$ obtained using a sample with n elements is defined by:

$$\hat{\bar{x}}_U = \frac{1}{n} \cdot \sum_{k=1}^{n} x_k \tag{4}$$

The theoretical variance of the estimator $\hat{\bar{x}}_U$ obtained with a sample of n elements is defined by:

$$S(\hat{\bar{x}}_U) = \frac{1}{n} \cdot \left(\frac{N-n}{N-1}\right) \cdot S_U \tag{5}$$

where $\left(\frac{N-n}{N-1}\right)$ is the squared value of the finite population correction factor [15]. Based on Eq. (5), the variance of the estimate of the mean can be seen to converge to zero as n converges to N, which implies that the sample mean will converge to the true population mean at a rate given by the finite population correction factor. Therefore, this factor is seen as a representation of the statistical uncertainty in the estimate for the finite population mean. Still, in a general case where $n < N$, the variance of the estimate of the mean will be a direct function of S_U, thus showing the importance of knowing the variability of the concrete strength in order to control the uncertainty in the estimate of the mean. However, since the population variance S_U is always unknown, it needs to be replaced by its estimator $\hat{S}_U$ which, for a finite population, is given by [15]:

$$\hat{S}_U = \frac{1}{n} \cdot \frac{N}{N-1} \cdot \sum_{k=1}^{n} (x_k - \hat{\bar{x}}_U)^2 \tag{6}$$

The variance of the estimator $\hat{S}_U$ depends on the selected sample (i.e. on the values x_k of the n elements observed) and is given by [15]:

$$S(\hat{S}_U) = \left(\frac{N}{N-1}\right)^2 \cdot \left(\frac{1-(n/N)}{n}\right) \cdot \frac{1}{n-1} \cdot \sum_{k=1}^{n} \left[(x_k - \hat{\bar{x}}_U)^2 - \frac{1}{n} \cdot \sum_{k=1}^{n} (x_k - \hat{\bar{x}}_U)^2\right]^2 \tag{7}$$

An approximation for the confidence interval of the finite population standard deviation has been proposed by O'Neill [16], whereby the CI for the variance can be written as:

$$\text{CI}\left(S_U^2\right) = \left[\left(\frac{n-1}{N-1} + \frac{N-n}{N-1} \cdot \frac{1}{F_{1-\theta, DF_n, DF_C}^*}\right) \cdot \hat{S}_U^2, \left(\frac{n-1}{N-1} + \frac{N-n}{N-1} \cdot \frac{1}{F_{\alpha-\theta, DF_n, DF_C}^*}\right) \cdot \hat{S}_U^2\right], \qquad (8)$$

where F_{a, DF_n, DF_C}^* represents the a-percentile of the F-distribution with $DF_n = n - 1$ and $DF_n = N - n$ degrees of freedom.

2.3 Using finite population statistics to assess concrete strength in existing RC buildings

2.3.1 Discretizing the concrete strength and disaggregating its variability

By depending on both n and N, finite population statistics enable to control the epistemic uncertainty about the estimates of the mean and of the variability of a population using data provided by a ratio of n/N elements. This approach is somehow similar to the uncertainty reduction principle that underlines the procedures in current standards (e.g. see [10]) where it is implicit that an increase in the number of structural elements that are tested during survey operations will lead to a reduction of the uncertainty about the estimate of the mean value of the material property. Therefore, a procedure based on finite population statistics like the one proposed herein is found to be consistent with current standard assessment procedures.

Adopting finite population principles to assess the concrete strength in existing buildings requires additional considerations to define what can be considered a finite population of concrete strength values (i.e. a group of N values where homogeneity is expected). To discretize the concrete strength values in a RC building and disaggregate them into finite populations, concrete strength variability was assumed the result of four components [3]: 1) within-test variability, 2) within-member variability, 3) between-member variability and 4) batch-to-batch variability. Systematic between-member (3) variability and batch-to-batch variability (4) were assumed to be dominant when compared with the other two components [3], despite their known effects (e.g. see [9; 14;17]). This fact allows for the definition of a concrete strength discretization criterion where it is assumed that each structural member of the building is represented by a single concrete strength value. For the purpose of the proposed method, it is also considered that the concrete strength value of a given member can be assessed from a compression test performed on a concrete core extracted from the member. Using this discretization of the concrete strength values, the disaggregation of the (discrete) structure into finite populations of N structural members can then be defined by analysing the nature of the actual construction process of a building. It is noted that

a similar rationale was adopted in [18] to disaggregate the concrete strength in existing RC buildings where the material properties were assumed to be homogeneous at each floor to reflect the construction timeline. Therefore, structural regions (where a region designates any cluster of structural elements that are believed to have similar physical properties, hence defining a finite population) can be established to reflect the expected batch-to-batch variability. These regions can be made by all the members of a given type in a storey (e.g. all the beams or all the columns), by a portion of the members of a given type in a storey or even by combining multiple types of elements in multiple storeys. A disaggregation following this strategy can be seen to be in agreement with the material property assessment procedures defined by current seismic safety assessment standards (e.g. see [10, 11, 13]). According to these procedures, the characterization of the concrete strength in a building must include data collected from each storey, from each type of structural element (e.g. columns, beams) and over an area with a limited size.

By disaggregating the concrete strength using this rationale, a number of regions can be defined within the building. Each one of these regions is a finite population with N elements where concrete strength is expected to be homogeneous. Finite population statistics can then be used to assess the concrete strength in each region, namely by defining sampling plans in terms of the ratio n/N, i.e. the number of structural members of the region where the concrete strength is evaluated (n) which is a fraction of the corresponding total number of structural members in the region (N). Therefore, by defining statistics of the concrete strength (e.g. the mean value or other parameters) as a function of n/N, the level of epistemic uncertainty in the concrete strength assessment becomes explicitly controlled.

2.3.2 Assessing the mean and the CoV of concrete strength using finite population statistics

In order to see how finite population statistics can be applied to assess the mean value of the concrete strength, a simulation study is presented in the following where 8 datasets (referred hereon as CH1-CH8) were analysed. Datasets CH1-CH8 have total sizes of 27, 30, 32, 22, 25, 19, 25 and 27 and were extracted from [19] where further statistical details and analyses on these datasets can be found. The study presented herein replicates real conditions: an analyst must select a certain number of candidate structural elements (n) of a region where the material strength will be assessed and no information about the remaining ($N - n$) members will be available. For each dataset and for a given value of n, a number of samples were defined which correspond to the minimum between the number of possible combinations of n elements extracted from the N elements and 10 million random samples of size n extracted from the N elements. For each dataset, the lowest value of n that was adopted was 2 and the largest was N.

In order to examine the sampling uncertainty about the mean estimate of the concrete strength due to the ($N - n$) non-surveyed structural elements, the ratio χ_m was defined:

$$\chi_m = \frac{\hat{\bar{x}}_U}{\bar{x}_U} \tag{9}$$

where $\hat{\bar{x}}_U$ is the sample estimate of the mean (Eq. (4)) and $\bar{x}_U$ is the true population mean (Eq. (1)). Hence, for each size n, a dataset of χ_m values was created. In order to analyse how the sampling uncertainty about the mean is correlated with the global population variability, two parameters were analysed: $\beta_{m,m}$ which is the mean of the χ_m ratios and $\beta_{CoV,m}$ which is defined by:

$$\beta_{CoV,m} = \frac{\text{CoV}\chi_m}{\text{CoV}_U} \tag{10}$$

where $\text{CoV}\chi_m$ is the CoV of χ_m and CoV_U is the true population CoV. Parameter $\beta_{CoV,m}$ is closely related to the theoretical factor $\beta_{CoV,m*}$ which depends on the finite population correction factor and is defined by:

$$\beta_{CoV,m*} = \frac{1}{\sqrt{n}} \cdot \sqrt{\frac{N-n}{N-1}} \tag{11}$$

The results of the simulation study indicate that $\beta_{m,m}$ is 1.0 for all the considered sample sizes, which means that, on average, the population mean will be obtained from the samples, irrespectively of the adopted sample size (i.e. on average, $\chi_m=1$). With respect to the variability of χ_m, Fig. 1 shows the evolution of $\beta_{CoV,m}$ for increasing values of the ratio n/N and for the datasets CH1-CH8 simultaneously, and compares it with the evolution of $\beta_{CoV,m*}$ calculated for different values of N (from 10 to 40 in steps of 5).

As expected, the variability of χ_m decreases as the sample size increases. The rate of this reduction follows the evolution of $\beta_{CoV,m*}$ (evaluated for N equal to the corresponding population size) and reduces $\beta_{CoV,m}$ as n/N converges to 1. The value of $\beta_{CoV,m}$ is also expected to vary significantly with the population size N, as can be seen from the $\beta_{CoV,m*}$ curves. It can be seen that, for a given value of n/N, $\beta_{CoV,m*}$ becomes lower as N increases. This reduction is due to the fact that, for a given value of n/N, as N increases, n also increases proportionally and the $1/\sqrt{n}$ factor of Eq. (11) controls the $\beta_{CoV,m*}$ reduction rate.
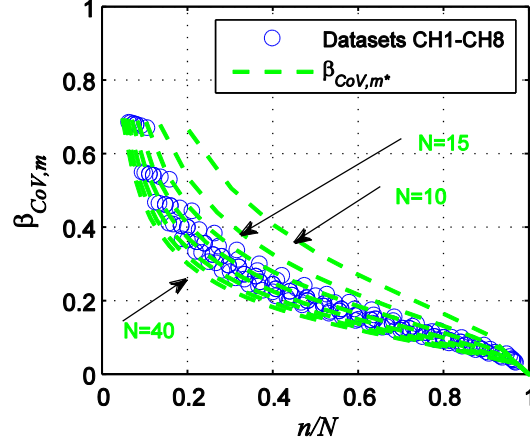
Figure 1. Comparison between the $\beta_{CoV,m}$ values obtained from the simulations (datasets CH1-CH8) and the values of β_{CoV,m^*} for different values of N.

Although, in the previous results, the estimate for the mean was analysed assuming that S_U (more precisely CoV_U) was known (see Eq. (5)), often this value is not known and has to be estimated based on the sample results. Hence, it is also expected that statistical uncertainty will affect the estimate of S_U obtained from a given sample due to the possibility of multiple combinations of n out of N test results (e.g. see Eq. (7)). The data that was simulated to analyse the ratio χ_m was therefore reused in order to examine the sampling uncertainty in the estimate of the population CoV, i.e. CoV_U. Parameter CoV_U was selected as a measure of the population dispersion instead of the variance S_U since it quantifies the variability without scaling effects, i.e. without depending on the range of values of the population. This new analysis examined the ratio χ_{CoV} defined by:

$$\chi_{CoV} = \frac{\widehat{CoV}_U}{CoV_U} \tag{12}$$

where $\widehat{CoV}_U$ is the CoV estimated using the sampled data and CoV_U is the corresponding true population value. The mean and the CoV of χ_{CoV} were analysed for different values of n/N to verify the rate at which $\widehat{CoV}_U$ converges to the real value CoV_U in typical populations of concrete core strength values. Figure 2a presents the evolution of the mean of χ_{CoV} and Fig. 2b presents the evolution of the CoV of χ_{CoV} for increasing values of n/N. In both cases, analytical approximations were fitted to evaluate the evolution of the mean and of the CoV of χ_{CoV} as a function of n/N.

2.8
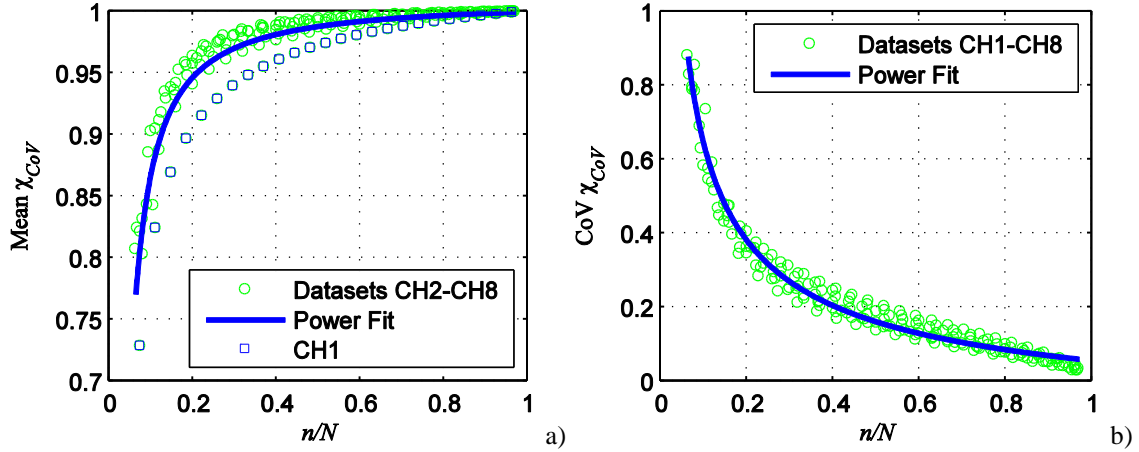
Figure 2. Evaluation of Meanχ_{CoV} (a) and CoVχ_{CoV} (b) for different values of n/N for the datasets CH1-CH8 and corresponding fits defined by Eq. (13) and Eq. (14), respectively.

From Fig. 2a, it can be seen that only the results of dataset CH1 are not in close agreement with the trend line established for the mean of χ_{CoV} which is defined by the power model given by:

$$\text{Mean}\chi_{CoV} = 1.01 - 0.01 \cdot (n/N)^{-1.16} \qquad (13)$$

As can be seen in Fig. 2a, a mean ratio of 0.95 is obtained for n/N equal to 0.2, while for the CH1 dataset a mean ratio of 0.95 requires an increase of n/N up to 0.35. For the variability of χ_{CoV}, its power decay with the increase of n/N can be defined by:

$$\text{CoV}\chi_{CoV} = 0.22 \cdot (n/N)^{-0.56} - 0.16 \qquad (14)$$

For this case, the trend line that was found is consistent with all the datasets. As can be seen from Fig. 2b, the uncertainty about the estimate of the population CoV requires higher sample sizes in order to achieve acceptable levels of precision. For example, at least 40% of the total number of structural elements have to be tested in order to get a minimum CoVχ_{CoV} of 0.20.

To further illustrate the impact of sampling in the assessment of the CoV, Fig. 3 shows the boxplots of χ_{CoV}, obtained for all the datasets when adopting ratios of *3/N* (Fig. 3a) and *6/N* (Fig. 3b). These two ratios were selected because they correspond to the minimum sample sizes proposed in [11].

As shown in Fig. 3, the distribution of the sampling CoV (in this case represented by the ratio χ_{CoV}) is considerably asymmetric. Furthermore, this visual asymmetry is seen to reduce when the sample size increases from $n = 3$ (Fig 3a) to $n = 6$ (Fig3b). Based on these results, it becomes clear that taking a small sample of values from a population of concrete cores may lead to a significant overestimation or underestimation of the concrete strength variability.
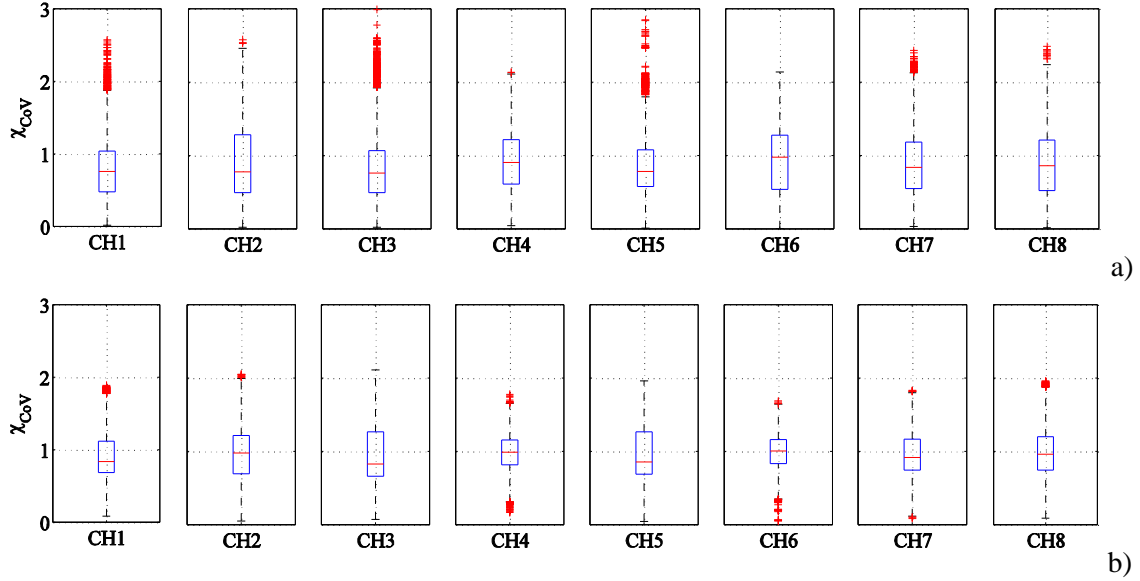
Figure 3. Boxplots of the χ_{CoV} ratios obtained when sampling from CH1-CH8 with sizes a) $n = 3$ and b) $n = 6$.

In the overall, the simulation study results indicate that adopting the proposed finite structure paradigm and using finite population principles to assess concrete strength statistics provides important information regarding the reduction of uncertainty when increasing the ratio n/N. Furthermore, the results also show that a high (and often impractical) number of destructive tests is required to reduce the epistemic uncertainty to acceptable levels (i.e. for CoVχ_{CoV} to be around 0.10). Therefore, alternative methods must be defined to estimate the concrete strength variability in a finite population and overcome the need to carry out a high number of destructive tests.

2.4 An alternative method to estimate the finite population CoV of concrete strength

An alternative approach is proposed herein to estimate the variability (i.e. the CoV) of a finite population concrete strength values using auxiliary information obtained from non-destructive tests (NDTs). These tests are often used in survey campaigns since they induce limited levels of damage to the structural components and can be used in a larger number of elements usually at a lower cost. An example of this kind of methods is the surface hardness determination test using the rebound hammer. The results of this test have been shown to correlate well with the concrete compressive strength and multiple correlation models have already been proposed (e.g. see [20]). When using adequately calibrated models, the measured rebound numbers (RNs) can be converted into compressive strength estimates. Still, it is noted that current standards (e.g. [21]) do not allow the use of these correlations without a preliminary calibration involving destructive tests results (at least 9) obtained from concrete cores collected from the building under survey. In general, standard-based methods recommend the use of NDTs as a complementary source of information to assess existing structures. As an example, Masi and Vona [6] recommended

conducting NDTs in 8% to 15% of the total number of elements *per* storey, with an absolute minimum of 6 to 10 tests. For example, in a region that has 20 structural elements, this leads to a minimum number of tests corresponding to $n/N = 0.30$.

Instead of converting the RN test results into concrete strength values, the proposed method defines a direct correlation between the CoV of destructive tests (CoV_{fc}) and the CoV of the RNs (CoV_{RN}) evaluated for the same structural elements. Pairs of data comprising CoVs of populations of RNs and concrete core compressive test results were selected from existing literature studies [22-24] to establish the proposed model. A total of 24 CoV_{fc}-CoV_{RN} pairs were used, each one comprising more than 8 locations/readings of both tests. Figure 4 shows the correlation obtained for the considered data, together with the 75% prediction bounds of the model [25]. The correlation was derived using a robust regression model with a bi-squared weighting function. The global correlation model that was obtained has an adjusted-R^2 of 0.72, a root mean squared error (RMSE) of 0.06 and is expressed by:

$$\widehat{CoV}_{fc} = 1.042 \cdot CoV_{RN} + 0.123 \tag{15}$$

The model requires the variability of the RN values to be known, i.e. an adequate estimate must be defined for CoV_{RN} and the indicative sample sizes proposed in [6] can be used as a reference to establish this estimate. Accordingly, for the ranges proposed (6 to 10 tests *per* storey, which, under the finite population paradigm, means *per* finite population), it is assumed that values of n/N in the range 0.30-0.40 will yield acceptable estimates of CoV_{RN}.
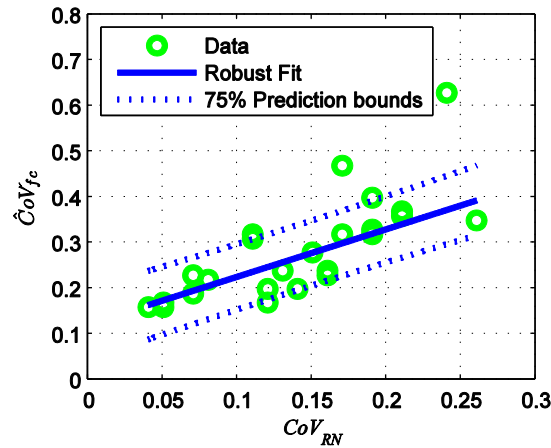
Figure 4. Correlation between $\widehat{CoV}_{fc}$ and CoV_{RN} along with the corresponding 75% prediction bounds.

The purpose of defining this general model correlating the variability of both tests was to check if it was possible to derive a tool that would, without any calibration, provide an indication of the variability that an analyst may expect prior to the design of the destructive test campaign. Hence, a naïve approximation for the CoV_{fc} was analysed to check what would be the possible

improvements on the quality of the estimation of the variability or the mean when compared with other strategies. It must be noticed that the developed approximation [Eq. (14)] was used hereon as a benchmark due to the limited amount of datasets available in literature. The data used to construct was extracted from populations of data from experimental campaigns performed in the laboratory or in situ, using possibly multiple types of equipment and different operation quality. Hence, the proposed law may only be seen as a general methodology and future improvements using results from experimental campaigns performed locally at each country in portfolios of existing buildings may significantly improve the robustness and reduce the generality of the benchmark adopted herein.

Finally, by assuming that $\widehat{CoV}_{fc}$ provides an adequate estimate of CoV_U and considering that $\beta_{CoV,m*}$ represents the theoretical evolution of $\beta_{CoV,m}$ (Fig. 1), a reliable estimate of the sampling variability of the mean estimate for the concrete strength $CoV\left(\widehat{\overline{x}}_{fc}\right)$ in typical storeys (i.e. with N structural elements in the range of 15-30) is obtained by combining Eq. (15) and Eq. (11):

$$\beta_{CoV,m} = \frac{CoV\chi_m}{CoV_U} = \frac{CoV\left(\widehat{\overline{x}}_{fc}\right)}{CoV_U} \Leftrightarrow CoV\left(\widehat{\overline{x}}_{fc}\right) = \beta_{CoV,m*} \cdot CoV_U \Leftrightarrow$$

$$\Leftrightarrow CoV\left(\widehat{\overline{x}}_{fc}\right) = \left(\frac{1}{\sqrt{n}} \cdot \sqrt{\frac{N-n}{N-1}}\right) \cdot (1.042 \cdot CoV_{RN} + 0.123) \tag{16}$$

where CoV_{RN} needs to be determined from a minimum of $n/N = 0.30$ tests and ideally should cover the highest number of structural elements possible (see Appendix 1).

2.5 Validation of the proposed procedure using experimental data

To assess the validity of the proposed finite population approximations defined by Eqs. (15) and (16), five additional datasets of RN and core strength values were considered. Datasets C1-C4 correspond to pairs of data extracted from multi-storey RC buildings constructed in the mid-1990s that were surveyed within the present study. Each pair has a core strength value evaluated in a structural element and a RN value from the same location. Since dataset C4 presented a wide range of concrete strength values (from 20.75 MPa to 64.81 MPa) a subset of C4 (termed C4*) was additionally defined where the top five values were removed in order to obtain a more homogeneous dataset. Dataset C5 was obtained from [26] and comprises RN and concrete core strength values extracted from an existing building. Table 1 summarizes the selected datasets.

Table 1. Statistical parameters of the six datasets considered in the validation study

Dataset	N	$\bar{x}_U$ (MPa)	CoV_{fc}	CoV_{RN}
C1	19	27.46	0.29	0.17
C2	27	28.11	0.36	0.21
C3	20	30.14	0.38	0.16
C4	25	35.99	0.34	0.14
C4*	20	30.66	0.18	0.12
C5	21	19.74	0.19	0.08

A simulation study was performed to evaluate the reliability of the proposed correlation defined by Eq. (15) to estimate the variability of the concrete strength $\widehat{Co}V_{fc}$ by analysing the empirical cumulative distribution function (ECDF) of the ratio ψ_{CoV} defined by:

$$\psi_{\mathrm{CoV}} = \frac{\widehat{Co}V_{fc}}{CoV_{fc}} \tag{17}$$

Where $\widehat{Co}V_{fc}$ represents the estimate of the real variability CoV_{fc} obtained for each dataset when assessing n out of N randomly selected structural elements without having information on the remaining N-n structural elements. To estimate $\widehat{Co}V_{fc}$ for each dataset (C1-C5), M samples (see Eq. (3)) with sizes $n/N = 0.30$ were extracted (i.e. n equal to 6, 8, 6, 8, 6, and 6 tests for datasets C1-C5, respectively). For each sample, the value of CoV_{RN} was converted into the estimate $\widehat{Co}V_{fc}$ using two different models: Model RMP1 which corresponds to the correlation defined by Eq. (15), and model RMP2 which is a variant of this model that considers a 50% upper confidence bound of the regression, assuming the normality of the residuals and adding 0.6745*RMSE to the mean prediction, and is given by:

$$\widehat{Co}V_{fc} = 1.042 \cdot CoV_{RN} + 0.163 \tag{18}$$

Based on this regression model, a rationale similar to the one leading to Eq. (16) can also be established to define a new estimate for $CoV(\hat{\bar{x}}_{fc})$ now given by:

$$CoV(\hat{\bar{x}}_{fc}) = \left(\frac{1}{\sqrt{n}} \cdot \sqrt{\frac{N-n}{N-1}} \right) \cdot (1.042 \cdot CoV_{RN} + 0.163) \tag{19}$$

In order to compare the uncertainty associated to these strategies with others that involve the use of correlation models converting each value of RN into a point estimate for the concrete strength

f_c, the simulated results of ψ_{CoV} for the RMP1 and RMP2 models were reused for a secondary analysis. In this case, the objective was to derive the ECDF of the ψ_{CoV} ratios after converting the n RN values of the M samples into f_c values using correlation models (RM) from the literature. After converting the RN values, statistical analyses of each sample were performed and M possible estimates of $\widehat{CoV}_{fc}$ were computed. Again, the ψ_{CoV} values were calculated by normalizing the M $\widehat{CoV}_{fc}$ values by the CoV_{fc} of the corresponding dataset. Three different RM models were considered to convert the RN values into f_c values. The RM1 And RM3 correlation models were selected because they were derived using data that is believed to be similar to the datasets C1-C5 considered herein. The correlation model RM2 was selected due to its alternative form. Model RM1 is a power model proposed in [27] and defined by:

$$f_{c,RM1} = 0.00917 \cdot (RN)^{2.27} \tag{20}$$

Model RM2 is the calibration curve proposed in [28] assuming $f_{c,ref}=30$ and $RN_{ref}=35$, given by:

$$f_{c,RM2} = f_{c,ref} \cdot \left(\frac{RN}{RN_{ref}}\right)^{2.38} \tag{21}$$

The model termed RM3 is the power model fitted to the dataset C5 in [26] and defined by:

$$f_{c,RM3} = 0.00645 \cdot (RN)^{2.23} \tag{22}$$

Although the proposed procedure focusses on quantifying $\widehat{CoV}_{fc}$, the analysis of the RM models also allows for the computation of an estimate for the mean concrete strength of each dataset, $\widehat{\bar{x}}_{fc}$. Due to the importance of having an estimate for this statistical parameter, the reliability of RM1, RM2 and RM3 was also evaluated with respect to $\widehat{\bar{x}}_{fc}$. This additional analysis only requires computing the mean of the n converted values of f_c for each one of the M samples. To evaluate the statistical uncertainty associated with $\widehat{\bar{x}}_{fc}$, the ECDF of the M ratios ψ_m was analysed, where ψ_m is given by:

$$\psi_m = \frac{\widehat{\bar{x}}_{fc}}{\bar{x}_{fc}} \tag{23}$$

in which $\bar{x}_{fc}$ is the mean of the concrete strength of the corresponding dataset (C1-C5).

It is noted that the objective of using the selected correlation models was to verify how the estimates of ψ_m and ψ_{CoV} would compare in terms of sampling uncertainty with that of core

samples with sizes $n = 3$ and $n = 6$. These sample sizes were selected as benchmarks because standards often refer them as values for the minimum number of tests that need to be carried out under several situations (e.g. see [10-13]). Furthermore, for the selected datasets, $n = 3$ corresponds to an average value of n/N equal to 0.14 while $n = 6$ corresponds to an average value of n/N equal to 0.28. The M combinations of destructive test results (i.e. core strength values f_c) were extracted from datasets C1-C5 and for each one of the M samples, the estimates of $\widehat{CoV}_{fc}$, $\widehat{\bar{x}}_{fc}$, ψ_m and ψ_{CoV} were computed. In addition, the ECDF of the M ψ_m and ψ_{CoV} ratios was computed for each dataset to compare them with those calculated based on RMP1, RMP2, RM1, RM2 and RM3.

Finally, the efficiency of Eqs. (16) and (19) to estimate the real sampling uncertainty of the mean was also analysed. The values of $\widehat{CoV}_{fc}$ were used as an input in Eqs. (16) and (19) to estimate $CoV\left(\widehat{\bar{x}}_{fc}\right)$. This analysis involved four models: $\text{SIM}_{n=3}$ which involve the estimate of $CoV\left(\widehat{\bar{x}}_{fc}\right)$ obtained using Eq. (16) (RMP1) and $n = 3$, $\text{SIM*}_{n=3}$ which involve the estimate of $CoV\left(\widehat{\bar{x}}_{fc}\right)$ obtained with Eq. (19) (RMP2) and $n = 3$, $\text{SIM}_{n=6}$ which involve the estimate of $CoV\left(\widehat{\bar{x}}_{fc}\right)$ obtained with Eq. (16) (RMP1) and $n = 6$ and $\text{SIM}_{n=6}$ which involve the estimate of $CoV\left(\widehat{\bar{x}}_{fc}\right)$ obtained with Eq. (19) (RMP2) and $n = 6$. The ECDF of the M $CoV\left(\widehat{\bar{x}}_{fc}\right)$ values that result from the M possible estimates of $\widehat{CoV}_{fc}$ was then calculated for all these models. To analyse the performance of Eq. (16), the EDCF curves were compared with the $CoV\left(\widehat{\bar{x}}_{fc}\right)$ (a scalar value) obtained when computing the CoV of all the M estimates of $\widehat{\bar{x}}_{fc}$ when using 3 destructive tests ($\text{Real}_{n=3}$) and 6 destructive tests ($\text{Real}_{n=6}$).

2.6 Results and discussion

2.6.1 Analysis of the ψ_{CoV} ratios

Figure 5 presents the ECDFs of the ψ_{CoV} ratios obtained using the different strategies defined in the previous Section (i.e. RMP1, RMP2, RM1, RM2 and RM3). As mentioned before, all the computed ECDFs are conditioned to a sample size corresponding to $n/N = 0.30$. Hence, the presented ECDFs reflect the sampling uncertainty associated with the selection of different test locations for the rebound hammer test within a given finite population.
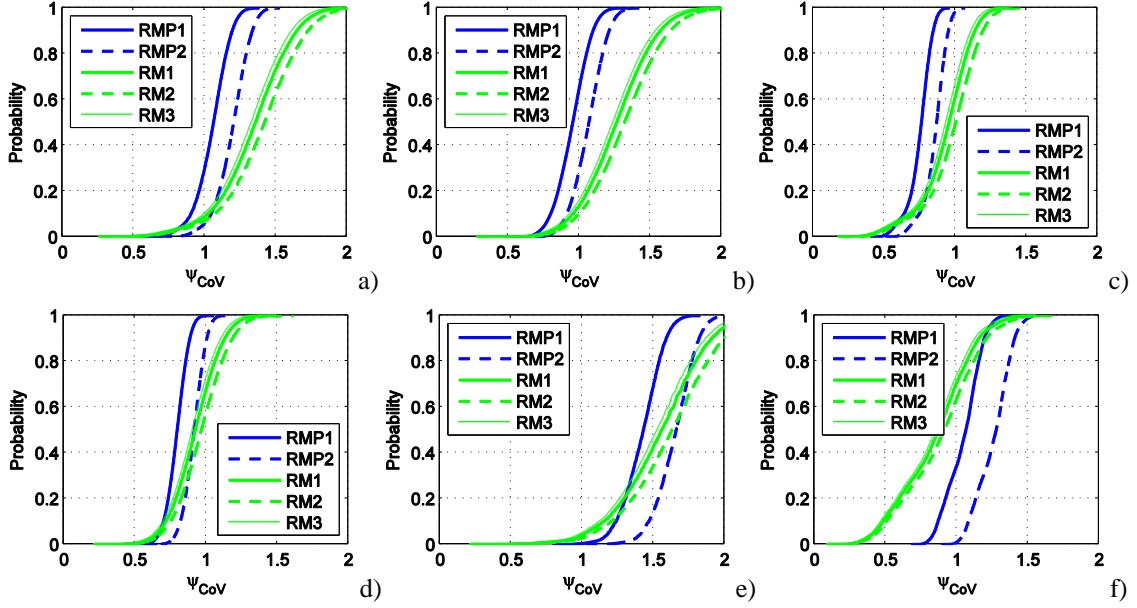
Figure 5. Comparison of the ECDFs of the ψ_{CoV} ratios considering multiple samples of RN values with a size $n/N = 0.30$ for dataset a) C1, b) C2, c) C3, d) C4, e) C4* and f) C5.

The results show that the RMP1 and RMP2 models lead to data with a lower dispersion when compared with that obtained from models RM1, RM2 and RM3. This trend can be observed by analysing the steepness of the ECDFs, which is higher for the RMP1 and RMP2 models than for the other cases. The median estimate obtained for ψ_{CoV} with RMP1 changes with the considered dataset. In some cases it is higher than 1.0 (Fig. 5e) while in others it is lower than 1.0 (Figs. 5c and 5d). In the overall, the RMP2 model provided results that are more conservative than the RMP1 model which underestimated the median ratio for datasets C3 and C4 (Figs. 5c and 5d). Regarding model RM3, it should be noted that the sampling uncertainty has a significant effect in the estimation of the CoV even for dataset C5 (the dataset for which the RM3 model was calibrated), (Fig. 5f). From Fig. 5, it can also be seen that models RM1 and RM2 lead to data with a dispersion similar to that of RM3, possibly due to the closeness of the exponents of the power term. It is noted, however, that the models RM1, RM2 and RM3 that were selected are not representative of all possible models. To demonstrate the impact of selecting different regression models (i.e. with different values of the fitted parameters) in the estimate of ψ_{CoV}, an additional analysis was performed using artificial power models (RMb) ax^b simulating different values of the fitted parameters. Power models with an exponent term b between 1.0 and 3.0 in steps of 0.25 were simulated. The term a was estimated for each value of b using the correlation between the coefficients derived in the meta-analysis presented in [28] (i.e. b = 1.0307-0.259·ln(a)).

Figure 6 shows the ECDFs of the ψ_{CoV} that were obtained for datasets C1, C3 and C5 using the several RMb correlation models. For comparison purposes, the ECDFs of the ψ_{CoV} that were obtained with RMP1 and RMP2 are also shown. These results indicate that a lower dispersion of ψ_{CoV} can be obtained when selecting a value b equal to 1.75, 2.25 and 3.0 for datasets C1, C3 and

C5, respectively. From these results, it can be seen that estimating the variability of the concrete strength using predefined correlation models (i.e. with uncalibrated values of *a* and *b*) can lead to large and unreliable values.
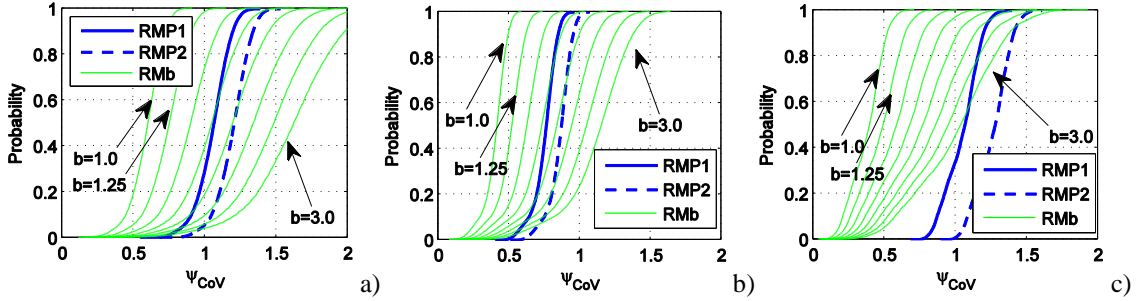
Figure 6. Comparison of the ECDFs of the ψ_{CoV} ratios considering multiple samples of RN values with a size *n*/N=0.30 for different type of models (*b*=1.0 to 3.0) for dataset a) C1, b) C3 and c) C5.

Figure 7 presents the comparison of the ECDFs of the ψ_{CoV} ratios obtained using the RMP1 and RMP2 models and using all the possible samples with $n = 3$ and $n = 6$ cores of each dataset.
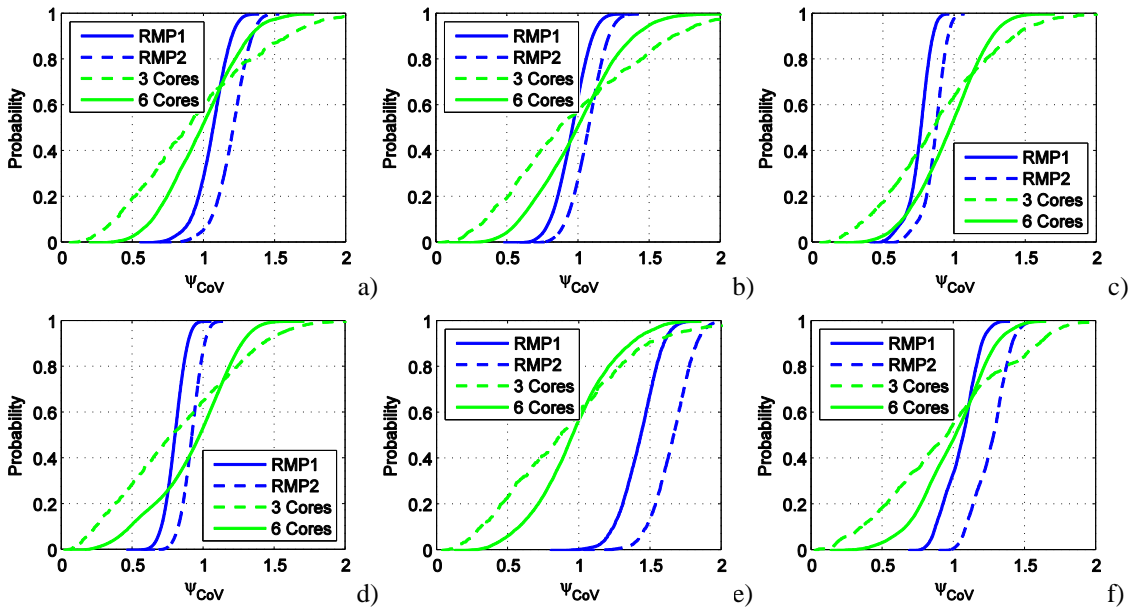
Figure 7. Comparison of the ECDFs of the ψ_{CoV} ratios for the proposed approaches and for classical sample sizes suggested in current standard for datasets a) C1, b) C2, c) C3, d) C4, e) C4* and f) C5.

The observations that can be made regarding these results are twofold. Firstly, it can be seen that blindly selecting a small sample of cores within a finite population (an approach that is in agreement with current standards) may lead to inadequate estimates of the variability since the dispersion exhibited by the corresponding ECDF curves is very large. These observations are consistent across all the datasets, irrespective of the fact that they might have a higher (e.g. C1 to C4) or a lower (e.g. C5) dispersion.

Secondly, when comparing these results with the proposed strategies (RMP1 and RMP2), it can be seen that the statistical uncertainty is adequately managed when using the RN values to estimate the variability. This confirms the suggestion in [14] that highlights the potential use of NDTs to complement the use of core strength values to assess the concrete strength in existing buildings. The results presented herein are not only in agreement with [14] but also show that the proposed methodology improves the previous use of NDTs since it reduces the uncertainty in the estimation of the concrete strength variability.

To further highlight this conclusion, Fig. 8 shows a global parametric comparison between the results obtained by the RMP1, RMP2, RM1, RM2 and RM3 models and the core-based strategies with $n = 3$ and $n = 6$. This comparison is performed for the Meanψ_{CoV}(Fig. 8a) and the CoVψ_{CoV} (Fig. 8b).
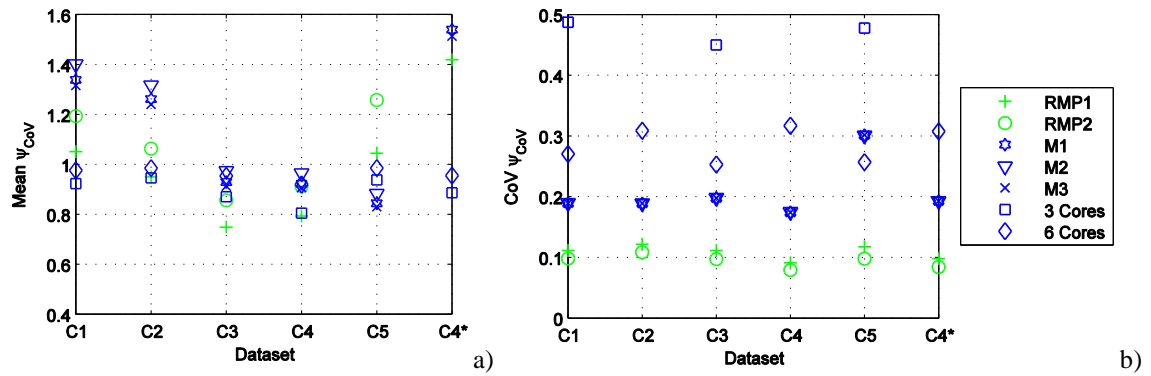
Figure 8. Statistical analysis of ψ_{CoV} for different models and datasets: a) analysis of the Mean ψ_{CoV} , b) analysis of the CoV ψ_{CoV}

The analysis of these parameters indicates that the RMP1 and RMP2 models provide adequate results, especially in terms of controlling the uncertainty given by CoVψ_{CoV} (Fig 8b). With respect to the Meanψ_{CoV}, RMP1 underestimates the expected value of the population CoV (the range of Meanψ_{CoV} is 0.75-1.05) while RMP2 provides more conservative results (the range of Meanψ_{CoV} is 0.86-1.26). The best average response was observed when using the $n = 6$ cores approach (the range of Mean ψ_{CoV} is 0.92-0.99). Nevertheless, if, on average, an adequate estimate of the population CoV can be obtained when using the strength results of 6 cores, analysing the expected variability (Fig. 8b) shows otherwise. The values of CoVψ_{CoV} for this approach range from 0.25 to 0.31 which indicates that taking a random sample of size 6 from all the possible structural elements may yield significantly variable estimates of the population CoV. Still, the worst results in terms of CoVψ_{CoV} are observed when samples with $n = 3$ cores are considered since the range of CoVψ_{CoV} is now 0.45-0.54. On the contrary, the most precise estimates of ψ_{CoV} are given by the RMP1 and RMP2 models, which exhibit values of CoVψ_{CoV} that range from 0.09 to 0.11 and from 0.08 to 0.11, respectively.

2.6.2 Analysis of the ψ_m ratios

With respect to the results of the ψ_m ratios, Fig. 9 presents the ECDFs of the estimates obtained using the samples of RN values and the models RM1, RM2 and RM3. These curves are compared with those obtained with the core-based strategies with $n = 3$ and $n = 6$ in order to verify if the use of predefined models selected would lead to a lower sampling variability when compared to that which is obtained using with core samples with sizes $n = 3$ and $n = 6$. It can be seen that, on average, the RM1, RM2 and RM3 models fail to predict the true mean of the population since the median value of the ECDFs is, in most cases, shifted away from the ratio $\psi_m=1$. The core-based strategies with $n = 3$ and $n = 6$ provided adequate estimates for the mean of the finite population. Furthermore, no significant differences have been found between the results for $n = 3$ or $n = 6$ cores.
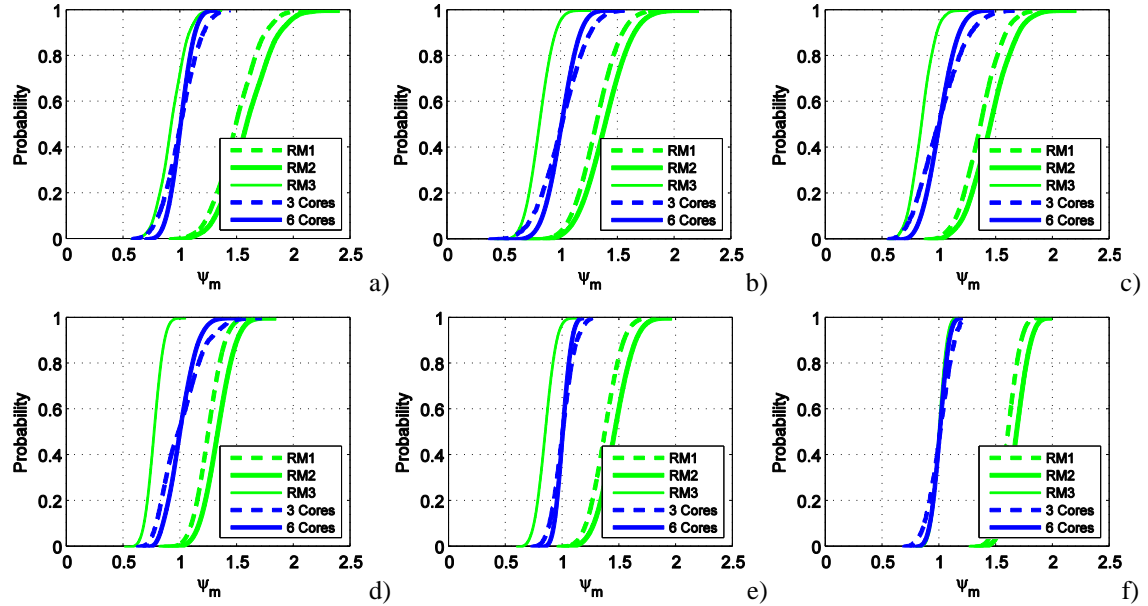
Figure 9. Cumulative distribution of the ψ_m ratios considering multiple samples of RN values with a size $n/N=030$ for dataset a) C1, b) C2, c) C3, d) C4, e) C4* and f) C5.

Finally, Fig. 10 shows the comparison between the values of $CoV\left(\hat{\bar{x}}_{fc}\right)$ obtained with the core-based strategies with $n = 3$ and $n = 6$ and the corresponding ECDF curves involving different samples of RN values, i.e. RMP1 (Eq. (16)) and RMP2 (Eq. (19)). The results show that, for all the cases and models considered, the ECDFs have a small variability and the difference between their median value and the CoV of the sample mean is usually within a range of 0.05, thus demonstrating the adequacy of the proposed approaches. The differences found are a direct consequence of the main limitation of the proposed methods, i.e. they rely on empirical correlations (i.e. Eqs. (15) and (18)). Consequently, the proposed methods can be improved by adding more data. With respect to the differences between the curves obtained with $n = 3$ and $n = 6$ cores, it can be seen that, although these approaches provided good results regarding the estimate of the mean concrete strength, the sampling variability almost doubles when the lower

sample size is adopted. Therefore, these approaches are not adequate to provide an effective control of the uncertainty in the estimate of the mean value of the concrete strength.
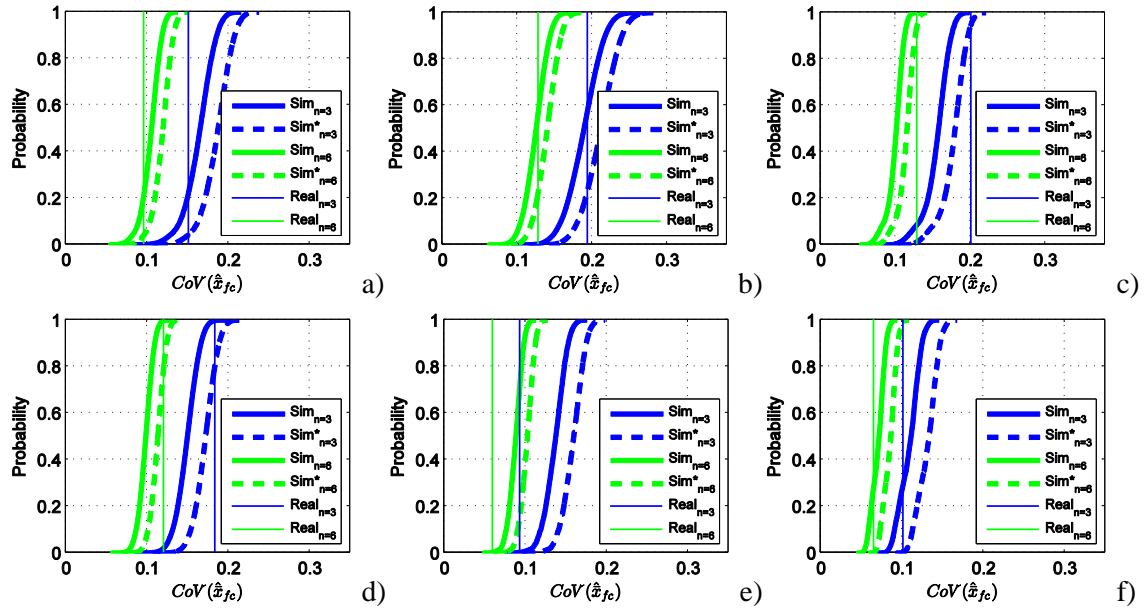
Figure 10. Cumulative distribution of $CoV\left(\hat{\bar{x}}_{fc}\right)$ estimated using Eq. (16) with $n=3$ ($Sim_{n=3}$) and $n=6$ ($Sim_{n=6}$), Eq. (19) $n=3$ ($Sim*_{n=3}$) and $n=6$ ($Sim*_{n=6}$) and comparison with the real sampling uncertainty about the mean using 3 ($Real_{n=3}$) and 6 ($Real_{n=3}$) core samples for datasets a) C1, b) C2, c) C3, d) C4 e) C4* and f) C5.

2.7 Conclusions

A finite population statistics-based approach that uses auxiliary information for the assessment of concrete strength in existing RC buildings has been presented in this study. The proposed approach effectively controls the uncertainty in the estimate of the variability of the concrete strength in a population as well as the uncertainty in the estimate of the mean value of the concrete strength. The approach relies on a discretization of the concrete strength distribution within the building considering that a single concrete strength value can be assigned to each structural element, thus making the variability a direct representation of the member-to-member heterogeneity. Other sources of variability such as within member variability and the uncertainty related to the test procedure were excluded from the proposed approach. However, analysing the importance of these factors is recommended by repeating tests whenever possible. To assess the variability of a finite population of concrete strength values, an empirical model was proposed that correlates the CoV of concrete core strength values and the CoV of populations of RN values assessed in the same locations. The adequacy of the proposed empirical model to estimate the CoV of the concrete strength using indirect measurements of the concrete strength has been shown using five datasets involving core strength results and RN values. These results showed that the proposed method enhances the use of NDTs for the assessment of the concrete strength in existing buildings since it leads to a reduction of the uncertainty in the estimation of the concrete strength

variability. It is noted that the empirical model that was developed does not account for test repeatability issues that may affect the regression. Such approach was selected to reflect scenarios where the number of tests that can be carried out is limited.

Regarding the estimate of the mean value of the concrete strength, the simulations carried out within the present study showed that, on average, the mean value of a region can be estimated with an acceptable uncertainty using a number of core compression tests obtained from 15% to 30% of the members in the region. However, this approach leads to inadequate estimates of the mean concrete strength variability. The proposed method also provides a better estimate of the mean concrete strength variability, assuming that NDTs can capture the expected variability of the concrete strength of a finite population of structural elements where the concrete strength is assumed to be homogeneous.

In conclusion, the presented study highlights the importance of using auxiliary data provided by NDTs when assessing the concrete compressive strength of an existing building and proposes the use of a strategy based on finite population principles to manage the uncertainty in the estimation of concrete strength statistics.

2.8 Appendix

The relation $n/N = 30\%$ that is proposed for the number of NDTs that must be performed in order to estimate the CoV of NDTs ($CoV_{N,NDTs}$) is a possible recommendation combining simplicity and accuracy. In order to assess the implications of this assumption, the confidence interval for the sample variance of a finite population proposed by O'Neill [16] can be used to construct the variance ratio S_N^2/S_n^2, yielding:

$$\frac{S_N^2}{S_n^2} = \left(\frac{n-1}{N-1}\right) + \left(\frac{N-n}{N-1}\right) \cdot \frac{1}{F_{\alpha/2}^*\left(n-1, N-n\right)},$$
(A.1)

where $F_{1-\alpha/2}^*\left(k_1, k_2\right)$ is the $\alpha/2$ percentile of the F-distribution with k_1 and k_2 degrees of freedom. After some mathematical manipulation, this expression can be used to obtain the ratio between the sample and the finite population standard deviation as:

$$\frac{S_n}{S_N} = \frac{1}{\sqrt{\left(\frac{n-1}{N-1}\right) + \left(\frac{N-n}{N-1}\right) \cdot \frac{1}{F_{\alpha/2}^*\left(DF_n, DF_C\right)}}},$$
(A.2)

By assuming that the NDT test results (in this case the RN values) follow a lognormal distribution, the standard deviation of the RN in the logarithmic space can be approximately defined by its CoV in the natural space. As a result, Eq. A.2 can be approximately re-written as:

$$\frac{CoV_n}{CoV_N} = \frac{1}{\sqrt{\left(\dfrac{n-1}{N-1}\right)+\left(\dfrac{N-n}{N-1}\right)\cdot\dfrac{1}{F^*_{\alpha/2}\left(DF_n, DF_C\right)}}}\ , \qquad (A.3)$$

Figure 11 shows the variation of the ratio between the sample and the population coefficient of variation for different α levels obtained by simulating expression A.3 for different levels of *n* and *N*.
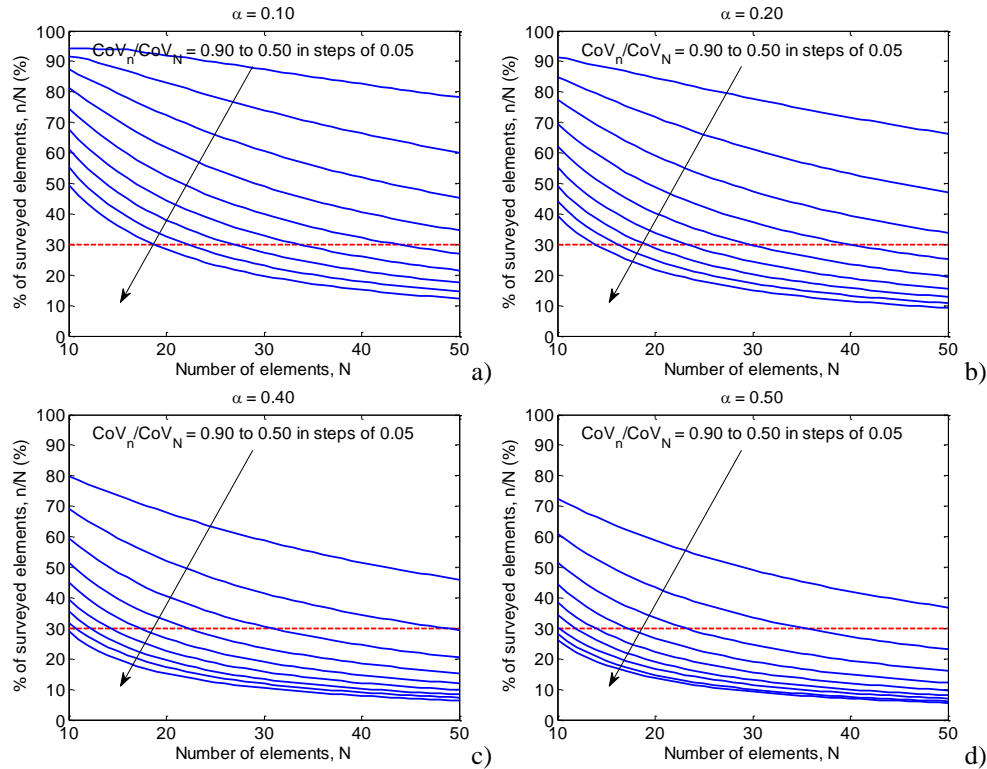
Figure 11. Correlation between the percentages (*n/N*) of structural elements where NDTs must be performed for different finite numbers of *N* elements in order to ensure pre-defined CoV_n/CoV_N ratios associated to a confidence level of α=0.10 (a), α=0.20 (b), α=0.40 (c), and α=0.50 (d).

Since the CoV_N of NDTs is typically lower (values between 5% and 15% can be often obtained) than that of the concrete strength (values between 10% and 30% can be often obtained), it can be assumed that a larger confidence interval (and therefore α value) can be assumed than the typical 5% value. Under that assumption, it can be seen that, for a typical range of N associated with a homogeneous concrete properties (10-20 structural elements), a ratio of 75% can be expected when α = 0.20 is adopted, which decreases to 60% for α = 0.10. As a result, although the assumptions made lead to a controlled estimate of $CoV_{N,NDTs}$, increasing the percentage of

elements that are surveyed will rapidly increase the accuracy of the estimated values. Therefore, the use of Fig. 11 is recommended in order to balance the cost and the accuracy of the survey results.

2.9 References

1   Caspeele R, Taerwe L (2012). Influence of concrete strength estimation on the structural safety assessment of existing structures. Construction and Building Materials; 62:77-84.

2   Der Kiureghian A, Ditlevsen, O. (2009). Aleatory or epistemic? Does it matter?. Structural Safety; 31(2):105-112.

3   Bartlett FM, MacGregor JG (1993). Statistical analysis of the compressive strength of concrete structures. ACI Materials Journal; 93(2):158-168.

4   Cristofaro MT, D'Ambrisi A, De Stefano M, Pucinotti R, Tanganelli M, (2012). Studio sulla Dispersione dei Valori di Resistenza a Compressione del Calcestruzzo di Edifici Esistenti. Il Giornale delle Prove non Distruttive Monitoraggio e Diagnostica; 2 (in Italian).

5   Shimizu Y, Hirosawa M, Zhou J (2000). Statistical Analysis of Concrete Strength in Existing Reinforced Concrete Buildings. In: Proceedings of 12th world conference on earthquake engineering, Japan; 2000.

6   Masi A, Vona M (2009). Estimation of the in-situ concrete strength: provisions of the European and Italian seismic codes and possible improvements. In: Cosenza E, editor. Eurocode 8 perspectives from the Italian standpoint workshop, 67–77, Doppiavoce, Naples, Italy.

7   Drysdale RC, (1973). Variation of concrete strength in existing buildings. Magazine of Concrete Research; 25(85):201-207.

8   Stewart MG, (1995). Workmanship and its influence on probabilistic models of concrete compressive strength. ACI Materials Journal; 92(4):361–372.

9   Masi A, Chiauzzi L, (2013). An experimental study on the within-member variability of in situ concrete strength in RC building structures. Construction and Building Materials; 47:951-961.

10 CEN (2005). Eurocode 8: design of structures for earthquake resistance. Part 3: Assessment and retrofitting of buildings. Brussels, Belgium.

11 ASCE (2014). Seismic Evaluation and Retrofit of Existing Buildings (ASCE/SEI 41-13). American Society of Civil Engineers, Reston, Virginia, USA.

12 Code of Interventions (2011). Organization for Earthquake Resistant Planning and Protection, Ministry of Environment Planning and Public Works, Greece.

13 Circolare 2 febbraio 2009. n. 617 Approvata dal consiglio superiore dei Lavori Pubblici. Istruzioni per l'applicazione delle ''Nuove norme tecniche per le costruzioni'' di cui al decreto ministeriale 14 gennaio; 2008–2009 [in Italian].

14 Fiore A, Porco F, Uva G, Mezzina M (2013). On the dispersion of data collected by in situ diagnostic of the existing concrete. Construction and Building Materials; 47:208-217.

15 Sarndal C, Swensson B, Wretman J (2003). Model assisted survey sampling. Springer-Verlag New York.

16 O'Neill B, (2014). Some Useful Moment Results in Sampling Problems, The American Statistician; 68:4, 282-296

17 Uva G, Porco F, Fiore A, Mezzina M (2013). Proposal of a methodology of in situ concrete tests and improving the estimate of the compressive strength. Construction and Building Materials; 38(1):72–83.

18 Jalayer F, Petruzzelli F, Iervolino I, Manfredi G (2010). Accounting for the effect of in-situ tests and inspections on the performance assessment of existing buildings. Proceedings of the 14th European Conference on Earthquake Engineering, Ohrid, Macedonia.

19 Chen X, Wu S, Zhou J (2014). Variability of Compressive Strength of Concrete Cores. Journal of Performance of Constructed Facilities; 28(4):.

20 Breysse D (2012). Non-destructive evaluation of concrete strength: An historical review and a new perspective by combining NDT methods. Construction and Building Materials; 33:139–63.

21 CEN (2007). EN 13791-Assessment of in situ compressive strength in structures and precast concrete components. European Standard; Brussels, Belgium.

22 Szilágyi K (2013). Rebound Surface hardness and related properties of concrete. PhD Dissertation. Budapest University of Technology and Economics. Budapest, Hungary.

23 Fabbrocino G, Di Fusco A, Manfredi G (2005). In Situ evaluation of concrete strength for existing constructions: critical issues and perspectives of NDT methods. In: fib Symposium "Keep Concrete Attractive", Budapest, Hungary.

24 Brognolli M (2007). Prove e controlli non distruttivi per la verifica degli edifici esistenti secondo la normativa sismicae le norme tecniche per le costruzioni. In: Convegno presso l'Ordine degli Ingegneri della Provincia di Brescia, Italy.

25 Montgomery DC, Runger GC (2003). Applied statistics and probability for engineers, 3rd edn. Wiley, New York.

26 Monteiro A, Gonçalves A (2009). Assessment of characteristic strength in structures by the rebound hammer test according to EN 13791:2007. In: Proceedings of NDTCE'09 Conference, Nantes, France.

27 Biondi S, Candigliota E (2008). In situ tests for seismic assessment of RC structures. In: Proceedings of 14th world conference on earthquake engineering, Beijing, China.

28 Soutsos MN, Breysse D, Garnier V, Goncalves A, Monteiro AV (2012). Estimation of on-site compressive strength of concrete. In: Breysse D, editor. Non-Destructive Assessment of Concrete Structures: Reliability and Limits of Single and Combined Techniques. RILEM State of the Art Reports, Springer Netherlands: 119-186.

29 Breysse D, Martínez-Fernández J (2014). Assessing concrete strength with rebound hammer: review of key issues and ideas for more reliable conclusions. Materials and Structures; 47:1589–1604.

Chapter 3

Prior estimators for the concrete strength variability in existing structures based on indirect tests

Scope and objectives

The previous chapter has presented a finite population strategy to control the uncertainty about the mean of the concrete strength in existing buildings. It was shown that the use of non-destructive tests can significantly improve the results obtained in a survey campaign to characterize the actual concrete properties of a building. Furthermore, it has been shown that the use of an empirical prior model could significantly improve the estimate made for the variability, and that a limited number of cores could be used to estimate the mean of a given population. As pointed out, the use of non-destructive tests is usually associated with the adoption of a calibrated model to convert the results of non-destructive tests into estimates for the concrete strength. Nevertheless, such approach, which is within the scope of current state-of-the-art guidelines, was not studied in the previous formulation of the method. Thus, the present chapter aims to improve the previously proposed finite population strategy by adopting a consistent model to estimate the variability including the use of calibrated models to correlate destructive and non-destructive tests. Moreover, it aims to analyse in detail the adequacy of using an approximation for the variability that is consistent with the current practice when using NDTs to assess the concrete strength in existing structures.

3.1 Introduction

Over the past few years, repairing and upgrading existing reinforced concrete (RC) structures has been recognized as an important priority [1-2]. A crucial part of assessing the conservation state and the structural performance of these structures involves evaluating their actual mechanical properties [3]. Among these, evaluating the concrete compressive strength (f_c) is particularly important given its impact in the structural performance and the known issues associated with its assessment, as highlighted in Chapter 2 (e.g. see also [4]).

Characterizing f_c in existing buildings usually involves determining two specific parameters: a location parameter, often the mean value of concrete strength μ, and a variability parameter, usually either the standard deviation σ or the coefficient of variation (CoV) of the data [5]. Given the properties of these parameters, the uncertainty associated with estimating μ can be seen to be related with the uncertainty associated with estimating the variability. Thus, estimating μ requires a reliable estimate of the inherent variability (i.e. σ or CoV) of concrete strength, which can attain very large values (e.g. see [6]) due to the effect of workmanship ([7- 8]) among other factors. Other authors (e.g. 9, 10) highlighted the importance of the uncertainty associated with core testing and within-member variability when assessing in-situ concrete strength. Furthermore, previous research 5 has also shown the effect of sampling uncertainty (mainly focusing on member-to-member variability) associated with the use of samples of small size. The authors highlighted that even when adopting a finite population strategy to control the statistical uncertainty, large size samples of concrete core strength test results are required to get a reliable estimate of the variability.

The need for a large number of concrete core strength test results to accurately estimate concrete strength variability has led to the use of alternative methods involving additional sources of information. Bayesian methods have been proposed as possible approaches to incorporate the information of different sources when estimating the σ or CoV of concrete strength ([1, 2, 11]) or to quantify material safety factors ([12-13]). In some cases, prior information can also be established using data about σ or CoV based on past studies. For example, Caspeele and Taerwe [1] proposed a set of informative priors for different concrete classes based on concrete production data from Germany. Although their strategy can be adapted to different countries, its applicability to older RC structures for which there is no information regarding the expected concrete class may be difficult without preliminary in situ testing to estimate the concrete variability. In another case, Jalayer *et al.* [11] used a prior concrete strength distribution defined by a lognormal distribution with a median of 16.18 MPa and a CoV of 0.15 to represent typical values found in post-world war II construction in Italy. Alternatively, prior information can account for the results provided by non-destructive test (NDT) results. Giannini *et al.* [2] proposed a systematic framework combining concrete core and NDT results that requires a given number of cores to develop a case-specific regression model to convert NDT results into f_c estimates.

It has been shown that NDTs can be used to reduce the epistemic uncertainty, despite having as a main drawback the fact that they require the use of a conversion model [2]. Recently, Alwash *et al*. [14] analysed the uncertainties associated with destructive tests, NDT results and with the models that are used to convert NDT results into concrete strength estimates. In terms of conversion models, these authors analysed the efficiency of specific regressions, calibrating prior models (such as those in [15]) and the bi-objective approach [5]. They concluded that all the approaches can efficiently (i.e. using a low number of core strength test results) provide adequate estimates for the mean, but only the bi-objective approach was seen as a reliable method to estimate the variability. The bi-objective approach is a method proposed by Alwash *et al* [5] where the first and second statistical moments of the in situ distribution of f_c are directly related to those obtained from the sample of NDT results. Therefore, this method provides an alternative estimate of the conversion model parameters based on aggregated data instead of using the classical approach based on individual test results.

Despite the significance of NDTs towards reducing the uncertainty in the concrete strength assessment process and reducing the number of destructive tests that need to be performed, no universal conversion model can be defined between the test results of a certain type of NDT and f_c ([16, 19]). However, the possibility of developing empirical expressions that are able to provide estimates of the in situ concrete strength variability using NDT results has not been analysed so far. Therefore, the present paper addresses this issue by combining the main rationale behind the prior distributions proposed in [11] and the principles of the bi-objective approach. In particular, this paper analyses if empirical models correlating the statistical parameters of a population of concrete core strength test results and those of a population of rebound hammer test results (*RN*) or ultrasonic pulse velocity test results (*UPV*) can be used to establish initial estimates for the variability of the in situ concrete strength. Furthermore, the results of the study also provide information that can be used to improve the selection of conversion models for the bi-objective approach or for specific regression methods.

3.2 Determining the statistical parameters of the concrete strength distribution based on NDTs

3.2.1 Brief review of existing conversion models

The variability of concrete strength in existing RC structures, particularly in older RC buildings, can be associated with multiple factors. Some of the factors affect not only the concrete strength but also the NDT results ([14, 16]). As such, the conversion models that are established between NDT reslts and f_c are also significantly affected by those factors. Therefore, as referred by Breysse *et al*. [17], an adequate conversion model can only be developed when based on data collected in situ. Among others, [18-19] present a thorough review of different types of conversion models that are available to correlate *RN* test results or *UPV* test results with f_c. Figure 1 shows the

distribution of the type of conversion models adopted in past studies based on the surveys in [16] and [19].
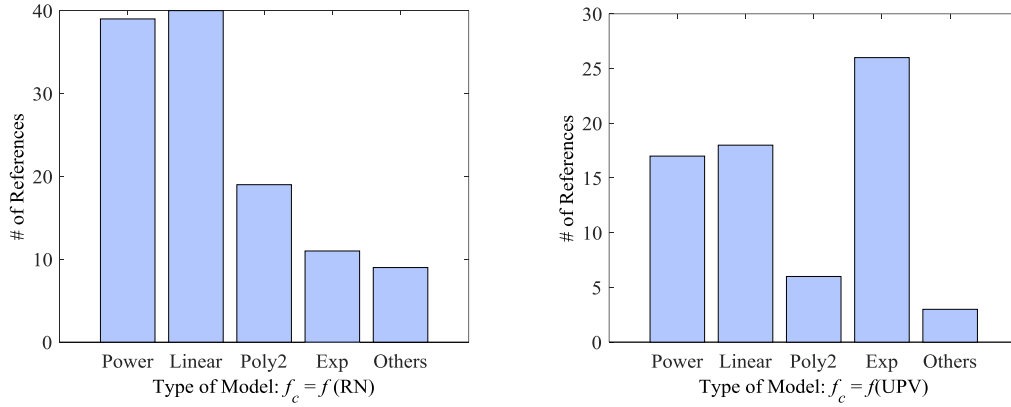
Figure 1. Variety of models adopted to correlate f_c with *RN* or *UPV* based on the surveys in [16] and [19] (Power, Linear Poly2 and Exp stand for power, linear, polynomial and exponential model, respectively).

As shown in Fig. 1, linear models correlating f_c with *RN* or *UPV* are often adopted. These models usually establish a linear conversion function between the NDT results (T_i) and the core strength test results $f_{c,i}$ similar to:

$$f_{c,i} = a \cdot T_i + b. \tag{1}$$

According to the data presented in Fig. 1, the number of studies using linear conversion models is approximately the same as the number of cases that consider a power model instead. The performance of this type of model was analysed by Breysse and Fernández-Martinez [19] who considered the use of a power correlation model between *RN* and f_c with regression coefficients c and d such as:

$$f_{c,i} = c \cdot RN_i^d, \tag{2}$$

which is equivalent to the following linear correlation model on a log-log space:

$$\ln(f_{c,i}) = \ln(c) + d \cdot \ln(RN_i). \tag{3}$$

After analysing several models, these authors also found there is a correlation between the values of the regression coefficients c and d, with coefficient d being able to be defined as a function of c by $d = 1.031 - 0.259 \cdot \ln(c)$. Furthermore, in a different study, Breysse [16] observed that the coefficient d of a power model correlating *UPV* and f_c such as:

$$f_{c,i} = c \cdot UPV_i^d, \tag{4}$$

could be approximated by the relation $d = \alpha - \delta \cdot \ln(c)$, with $\alpha = 2.393$ and $\delta = 0.684$. The range of d values for the power models indicated by Breysse (16; Tables 7 & 9) are 2.22-6.29 and 1.16-2.47 for *UPV* and *RN* test results, respectively.

Figure 1 also shows that among the strategies adopted to correlate *UPV* and f_c, it is also common to select an exponential model expressed by:

$$f_{c,i} = r \cdot e^{q \cdot UPV}, \tag{5}$$

which is equivalent to the following linear correlation model on a log-log space:

$$\ln\left(f_{c,i}\right) = \ln(r) + q \cdot UPV_i. \tag{6}$$

Apart from the previous models that individually use *RN* or *UPV* to establish a correlation with f_c, other models can also be found in the literature where combinations of these NDTs are used. Among those, the model combining both *RN* and *UPV*, usually known as the SonReb method, is one of the most popular [16]. According to [16], the most commonly found models that combine NDTs can be seen to either follow a bilinear model defined by:

$$f_{c,i} = \alpha + \beta \cdot RN_i + \chi \cdot UPV_i. \tag{7}$$

or a double power model defined by:

$$f_{c,i} = \delta \cdot RN_i^{\varepsilon} \cdot UPV_i^{\phi}. \tag{8}$$

which is equivalent to the following linear form:

$$\ln\left(f_{c,i}\right) = \ln(\delta) + \varepsilon \cdot \ln\left(RN_i\right) + \phi \cdot \ln\left(UPV_i\right). \tag{9}$$

Irrespective of the selected type of model or of the number of NDTs that are used, the coefficients of the model have to be determined by regression analysis using in situ data. After determining the regression parameters, the model can be used to obtain pointwise (e.g. in a member of the structure) estimates of concrete strength values based on additional NDT results. These estimated f_c values are then used to estimate the mean and the dispersion of the concrete strength, which, in turn, can be used to assess the characteristic value of the concrete strength ([15, 20]). These were the main principles adopted in [5] to establish the bi-objective approach, which defines a

conversion model between f_c and the NDTs not as a function of their pointwise values, but as a function of their mean and standard deviation instead. This approach was shown to be more effective than using classical pointwise conversion models to obtain reliable estimates of the mean and standard deviation of concrete strength since it requires less data. Therefore, this correlation approach also enables the analysis of the correlation problem in terms of random variables and statistical distributions.

3.2.2 Using the bi-objective approach to establish the statistical parameters of the concrete strength distribution

The bi-objective approach developed in [5] can be interpreted as a method that establishes the regression parameters as a function of random variables defined by the concrete strength f_c and the NDT results T ([21]; *pp.*180). For the case where a linear correlation like Eq. (1) is assumed between variables T and f_c, the bi-objective approach establishes the regression parameters as:

$$b = \mu_{f_c} - a \cdot \mu_T \tag{10}$$

$$a = \frac{s_{f_c}}{s_T} \tag{11}$$

where μ_{f_c} and s_{f_c} represent the mean and the standard deviation of f_c, respectively, and μ_T and s_T represent the mean and the standard deviation of T, respectively. Hence, if the random variable f_c is defined by a general function $f_c = g(T)$, the expected value μ_{f_c} and the variance $s_{f_c}^2$ of f_c can be obtained using a Taylor series expansion which, by using only the first order terms, simplifies to ([21]; *pp.*183):

$$\mu_{f_c} \approx g\left(\mu_T\right) \tag{12}$$

$$s_{f_c}^2 \approx s_T^2 \cdot \left(\frac{\partial g\left(\mu_T\right)}{\partial T}\right)^2. \tag{13}$$

Equations (12) and (13) become Eqs. (10) and (11) when function g is assumed to be linear. If a power function similar to Eq. (2) is assumed instead, Eqs. (12) and (13) can be re-written as:

$$d = \frac{ln\left(\dfrac{\mu_{f_c}}{c}\right)}{ln\left(\mu_T\right)} \tag{14}$$

$$c = \frac{s_{f_c}}{s_T} \cdot \frac{1}{d \cdot \mu_T^{d-1}} \tag{15}$$

Alternatively, by considering the linear version of the power model on a log-log space, function g then takes a form similar to Eq. (6), which yields:

$$\ln\left(c^*\right) = \mu_{\ln f_c} - d^* \cdot \mu_{\ln T} \tag{16}$$

$$d^* = \frac{s_{\ln f_c}}{s_{\ln T}} \tag{17}$$

where $\mu_{\ln f_c}$ and $s_{\ln f_c}$ represent the mean and the standard deviation of the natural logarithm of f_c, respectively, and $\mu_{\ln T}$ and $s_{\ln T}$ represent the mean and the standard deviation of the natural logarithm of T, respectively. Additionally, if both random variables T and f_c are assumed to follow a lognormal distribution, it is possible to re-write Eqs. (16) and (17) as ([21]; $pp.$102):

$$\ln\left(c^*\right) = \mu_{\ln f_c} - d^* \cdot \mu_{\ln T} \approx \left(\ln \mu_{f_c} - \frac{1}{2}CoV_{f_c}^2\right) - d^* \cdot \left(\ln \mu_T - \frac{1}{2}CoV_T^2\right) \tag{18}$$

$$d^* \approx \frac{CoV_{f_c}}{CoV_T} \tag{19}$$

The approximations involved in Eqs. (18) and (19) consider that $s_{\ln f_c} = \sqrt{\ln\left(1 + CoV_{f_c}^2\right)} \approx CoV_{f_c}$ and $s_{\ln T} = \sqrt{\ln\left(1 + CoV_T^2\right)} \approx CoV_T$. These approximations can be shown to lead to an error below 7% as long as the standard deviation of the natural logarithm of the data is smaller than 0.5.

Finally, in case of adopting an exponential correlation model, the corresponding function g is similar to Eq. (5) and leads to a bi-objective approach that yields the following regression parameters:

$$q = \frac{\ln\left(\dfrac{\mu_{f_c}}{r}\right)}{\mu_T} \tag{20}$$

$$r = \frac{s_{f_c}}{s_T} \cdot \frac{1}{q \cdot e^{(q \cdot \bar{x}_T)}}, \tag{21}$$

By considering a linearized version of function g similar to Eq. (6) instead, and simultaneously assuming that f_c follows a lognormal distribution and that T follows a normal distribution, the following regression parameters are obtained:

$$ln\left(r^*\right) = \mu_{ln f_c} - q^* \cdot \mu_T \tag{22}$$

$$q^* = \frac{s_{\ln f_c}}{s_T} \approx \frac{CoV_{f_c}}{s_T}, \tag{23}$$

which also considers that $s_{\ln f_c} \approx CoV_{f_c}$. Equations (10) to (23) can be seen to represent simplified statistical moment-based bi-objective conditions that are compatible with commonly adopted models defining the relation between concrete strength and NDT results. The possibility of correlating statistical descriptors of the data in a way that is consistent with typical conversion models is one of the advantages of considering the bi-objective approach. Simultaneously, these descriptors are also estimators of the parameters of probabilistic distributions that are commonly considered for the material properties in later stages of the safety assessment of a structure. This aspect is particularly relevant when trying to extend the bi-objective approach to conversion models that involve more than two parameters, such as the SonReb approach (see Eqs. (7)-(9)). In these cases, deriving a multi-objective approach would require information about the third statistical moment. However, within the scope of a concrete strength assessment framework similar to the one proposed in [5] in which samples of data with relatively small sizes are normally involved, deriving such multi-objective approach may be inadequate. Estimates of third order or higher order statistical moments are known to be highly dependent on the sample size (22) and reliable estimates can only be obtained with sample sizes that will seldom be compatible with typical concrete strength assessment practice. In light of these arguments, a multi-objective approach is not developed herein for the SonReb approach. Nevertheless, regression models involving the variability of concrete strength and NDT results using a SonReb-like approach can be developed and tested, as seen in the following.

3.2.3 Development of general models for the concrete strength variability based on NDTs

Given that developing an adequate survey plan to characterize the concrete strength of an existing building requires information about the variability of the concrete strength, it is important to have methods capable of providing a preliminary estimate of this property.

By following principles similar to those attempting to establish generic strength-NDT laws, general variability relations compatible with the strength-NDT laws presented in the previous section are developed herein to provide preliminary estimates of the concrete strength variability. The importance of these general models, as referred before, lies in their ability to provide

information for defining the minimum number of destructive tests necessary to evaluate concrete strength ([4]) based on an estimate of the concrete strength variability. The functional form of the candidate models that are developed based on the previously analysed strength-NDT laws and the corresponding terminology that was considered to reference them hereon are presented in Table 1.

Table 1. Candidate models selected to evaluate the potential correlation between the variability estimators of RN, UPV and f_c test results.

Reference	Correlation functions compatible with typical regression models	Based on	Hypothesis
M1-RN	$s_{f_c} = a \cdot s_{RN}$	Eq. (11)	Linear regression between NDT and f_c
M1-UPV	$s_{f_c} = a \cdot s_{UPV}$		
M2-RN	$\dfrac{s_{f_c}}{s_{RN}} = c \cdot d \cdot \mu_{RN}{}^{d-1}$	Eq. (15)	Power regression between NDT and f_c
M2-UPV	$\dfrac{s_{f_c}}{s_{UPV}} = c \cdot d \cdot \mu_{UPV}{}^{d-1}$		
M3-RN	$CoV_{f_c} = d^* \cdot CoV_{RN}$	Eq. (19)	Power regression between NDT and f_c and both variables assumed to follow a lognormal distribution.
M3-UPV	$CoV_{f_c} = d^* \cdot CoV_{UPV}$		
M4-RN	$\ln\left(\dfrac{s_{f_c}}{s_{RN}}\right) = \ln(r) + \ln(q) + q \cdot \mu_{RN}$	Eq. (21)	Exponential regression between NDT and f_c
M4-UPV	$\ln\left(\dfrac{s_{f_c}}{s_{UPV}}\right) = \ln(r) + \ln(q) + q \cdot \mu_{UPV}$		
M5-RN	$CoV_{f_c} = q^* \cdot s_{RN}$	Eq. (23)	Exponential regression between NDT and f_c where f_c and the NDT are assumed to follow a lognormal and a normal distribution, respectively
M5-UPV	$CoV_{f_c} = q^* \cdot s_{UPV}$		

Parameters μ_j, s_j and CoV_j stand for the mean, standard deviation and coefficient of variation of a given data j, respectively, where j can be defined by f_c, *RN* or *UPV* test results. Parameters *a*, *c*, *d*, d^*, *r*, q and q^* are the model coefficients obtained by regression analysis. It is noted that second order polynomial models are not among the considered candidate approaches given their limitations in modelling the physical phenomena that are involved (i.e. they don't provide fully monotonic relations between the dependent and independent variables of the model, in this case the variability of f_c and that of the selected NDT). Additionally to the models presented in Table 1, general relations involving SonReb-like approaches were also developed considering that the most common SonReb-like models involve a linear combination of *RN* and *UPV* or a double power model, as referred in 16. Following the principles that were considered for the case where

a single NDT is used, the general form of Eq. (13) can be used to write a first order variance estimate given by ([21]; *pp*.186):

$$s_{f_c}^2 \approx s_{RN}^2 \cdot \left(\frac{\partial g\left(\mu_{RN}\right)}{\partial RN} \right)^2 + s_{UPV}^2 \cdot \left(\frac{\partial g\left(\mu_{UPV}\right)}{\partial UPV} \right)^2 + \rho_{RN,UPV} \cdot s_{RN} \cdot s_{UPV} \left(\frac{\partial^2 g\left(\mu_{RN},\mu_{UPV}\right)}{\partial RN \cdot \partial UPV} \right). \tag{24}$$

As can be seen, this expression requires the correlation factor $\rho_{RN,UPV}$ between *RN* and *UPV* to be known. However, it must be noted that this parameter is rarely (if ever) available from studies involving the development of a regression model by the SonReb method. Table 2 shows the candidate models that can be developed using Eq. (24) based on the different *g* functions presented before (Eqs. (7)-(9)).

Table 2. Candidate models selected to evaluate the potential correlation between the variability estimators of RN, UPV and f$_c$ test results using SonReb-like approaches.

Ref.	Correlation functions compatible with typical regression models	Hypothesis
M1-SonReb	$s_{f_c}^2 = \left(\beta \cdot s_{RN}\right)^2 + \left(\chi \cdot s_{UPV}\right)^2$	Variance approximation for the SonReb model according to Eq. (7).
M2-SonReb	$s_{f_c}^2 = \left(\varepsilon \cdot \delta \cdot s_{RN} \cdot \mu_{RN}^{(\varepsilon-1)} \cdot \mu_{UPV}^{\phi}\right)^2 + \left(\phi \cdot \delta \cdot s_{UPV} \cdot \mu_{RN}^{\varepsilon} \cdot \mu_{RN}^{(\phi-1)}\right)^2 +$ $+ \rho_{RN,UPV} \cdot s_{RN} \cdot s_{UPV} \cdot \left(\varepsilon \cdot \delta \cdot \phi \cdot \mu_{RN}^{(\varepsilon-1)} \cdot \mu_{RN}^{(\phi-1)}\right)$	Variance approximation for the SonReb model according to Eq. (8).
M2*-SonReb	$s_{f_c}^2 \approx \left(\varepsilon \cdot \delta \cdot s_{RN} \cdot \mu_{RN}^{(\varepsilon-1)} \cdot \mu_{UPV}^{\phi}\right)^2 + \left(\phi \cdot \delta \cdot s_{UPV} \cdot \mu_{RN}^{\varepsilon} \cdot \mu_{RN}^{(\phi-1)}\right)^2$	Similar to M2- SonReb but assuming that *UPV* and *RN* are uncorrelated.
M3-SonReb	$CoV_{f_c}^2 \approx \left(\varepsilon^* \cdot CoV_{RN}\right)^2 + \left(\phi^* \cdot CoV_{UPV}\right)^2$	CoV approximation for the SonReb model according to Eq. (9) assuming that all variables are lognormally distributed.

M1-SonReb is the first order Taylor approximation for the variance using a linear combination similar to Eq. (7) which can be seen to be independent of the value of $\rho_{RN,UPV}$. On the other hand, M2-SonReb is the first order approximation obtained using a double power model and depends on $\rho_{RN,UPV}$. The case where f_c, *UPV* and *RN* are uncorrelated is represented by the expression of model M2*-SonReb (a special case of M2-SonReb). Finally, model M3-SonReb extends the assumptions of M2*-SonReb by also assuming that f_c, *UPV* and *RN* follow lognormal distributions.

3.3 Methodology adopted to evaluate the generalized estimators for the concrete strength variability

3.3.1 Selected datasets of test results

The validity of the selected candidate models for establishing preliminary estimates of the concrete strength variability was analysed using a series of datasets comprising test results of core strength f_c, *RN* and *UPV* obtained from different in situ and laboratory tests. The database of selected results involves statistical parameters (μ, s, *CoV* and sample size) extracted from the test campaign data obtained from [4], [2], [23-50], some of which have also been used in the study conducted in [51]. In total, the database contains 78 sets of data, where 68 sets have statistical data from f_c and *RN* test results, and 50 sets have statistical data from f_c and *UPV* test results. Among these datasets, a total of 40 have test results of f_c and simultaneously of *RN* and *UPV*. Since information regarding the correlation between the *RN* and *UPV* test results was not available for these 40 datasets, only models not involving information about this parameter were analysed herein (M1-SonReb, M2*-SonReb and M3-SonReb). The full database of statistical parameters adopted, along with the corresponding references can be found in the Appendix.

3.3.2 Regression analysis

The models estimating concrete strength variability were defined based on the three-step ROUT (robust regression and outlier removal) procedure proposed in [52]. The first step of the procedure involves fitting a robust curve to the data. In the second step, the residuals of the robust fit are analysed to determine if one or more values are trend outliers. In the third step, the data identified as trend outliers in the second step are removed and an ordinary least squares regression is performed on the remaining data. The detection process considered in the second step is based on an outlier identification test adapted from the False Discovery Rate approach for testing multiple comparisons, as proposed in [52]. To analyse the sensitivity of the results of this second step to the type of weight function considered in the robust fitting, different functions were tested (e.g. see [53; 54]). These preliminary analyses indicated that the outlier identification process was not sensitive to the selected weight function. Therefore, the robust fits were all performed using Tukey's bisquare function. Furthermore, the outlier identification process also depends on the value selected for the false discovery rate. This value was set as 10% based on the discussion presented in [52] and to account for the uncertainty of the measured data (e.g. repeatability and reproducibility issues, variability due to environmental conditions). By selecting a 10% threshold, the final regression analyses will be more clearly focussed on fitting the bulk of the data, thus emphasizing the average character of the models that are envisioned. The adjusted coefficient of determination (adj-R^2) was used as the goodness-of-fit measure of the model obtained from the final regression. To emphasize these results, the corresponding fits that would be obtained without removing the outlying data (i.e. without applying the ROUT procedure) are also presented, along

with their value of adj-R^2. For the more relevant cases, this goodness-of-fit analysis is also complemented by examining the root mean squared error (RMSE) and by examining the ratios between the predictions made by the model and the corresponding real values of the concrete strength variability. For the M2* SonReb model, a nonlinear fitting procedure was adopted to adjust the multi-parameter curve.

3.4 Results obtained from the correlation analyses

3.4.1 Overview

The following sections present the results obtained by fitting the models identified in Section 2 to the experimental data defined in Section 3.3 using regression analysis with and without removing the outlying data. In the following plots, the outlying data are represented by squares while the data considered in the regression analysis are represented by circles. In total, 68 pairs of f_c and RN data were used in the results shown in Section 3.4.2, 50 pairs of f_c and UPV data in those shown in Section 3.4.3, and 40 triplets of f_c, RN and UPV data in those presented in Section 3.4.4. Details of the adopted datasets are available in the Appendix, as referred before. Section 3.5 presents the overall analysis of the regression results using relations between predicted and real values due to difficulties in representing the surface plots that are obtained from the regression analyses. Still, the goodness of the regression results is discussed using the principles adopted in Sections 3.3.2 and 3.3.3.

3.4.2 Results obtained for the correlation between the variability of f_c and RN

The regression results obtained with model M1-RN are presented in Fig. 2. The quality of the regression that is obtained without the ROUT procedure (Fig. 2a) shows there is no correlation between s_{f_c} and s_{RN} (the value of adj-R^2 is negative, which means that the fit provides results that are worse than a horizontal line equal to the mean value of the data). When applying the ROUT method, one outlying value is excluded from the final regression (Fig. 2b) but the properties of the correlation remain similar to the previous case.

Figure 3 shows the regression results obtained using the power-based correlation defined by model M2-RN. In this case, the level of correlation found between the compound variable s_{f_c}/s_{RN} and the mean of the RN test results μ_{RN} without the ROUT procedure (Fig3a) is larger than the one observed when using the linear regression model (adj-R^2 is 0.36). However, when applying the ROUT procedure, five outlying values are excluded from the final regression (Fig. 3b) and only a minor change is observed in the correlation level (adj-R^2 is now 0.35).

Figure 2. Results of the regression analysis for model M1-RN without the ROUT procedure (a) and with the ROUT procedure (b).

Figure 3. Results of the regression analysis for model M2-RN without the ROUT procedure (a) and with the ROUT procedure (b).

When analysing model M3-RN (which considers that both f_c and RN follow a lognormal distribution) the results shown in Fig. 4 are obtained. As can be seen, there is a noticeable linear correlation between CoV_{f_c} and CoV_{RN}. On average, it can be seen that CoV_{f_c} is approximately two times the estimated value of CoV_{RN}. Still, the fit that was obtained without the ROUT procedure (Fig. 4a) has a value of adj-R^2 which is low (0.17). However, after applying the ROUT procedure (Fig. 4b), four outlying values are excluded from the regression and the value of adj-R^2 increases up to 0.50. For this case, parameter d^* was found to have an expected value of 1.94 with a 95% confidence interval (CI$_{95\%}$) of [1.84, 2.04]. The value of the RMSE for this regression is 0.056, which is lower than the value that was obtained without the ROUT procedure (0.090).

When fitting an exponential-based correlation between f_c and RN defined by model M4-RN, the regression results shown in Fig. 5 are obtained. The correlation was established on a semi-log space in order to reduce the nonlinearity of the regression model and try to improve the quality of the fit. In this case, the ROUT procedure identified one outlying value, which improved the correlation level and lead to an increase of the adj-R^2 from 0.33 to 0.38.

3.13

Figure 4. Results of the regression analysis for model M3-RN without the ROUT procedure (a) and with the ROUT procedure (b).
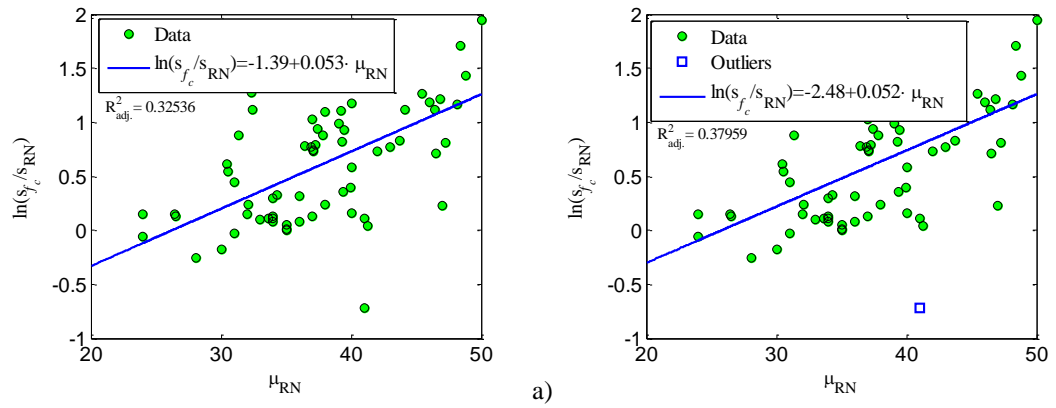
Figure 5. Results of the regression analysis for model M4-RN without the ROUT procedure (a) and with the ROUT procedure (b).

Figure 6 shows the results obtained by fitting model M5-RN derived from an exponential-based correlation between f_c and RN, and considering that f_c and RN follow a lognormal distribution and a normal distribution, respectively. The level of correlation improves after applying the ROUT procedure. When the regression is performed without applying the ROUT procedure (Fig. 6a), adj-R^2 is 0.19. After applying the procedure (Fig. 6b), three outlying values are excluded and the correlation level of the new fit has now an adj-R^2 value of 0.29.
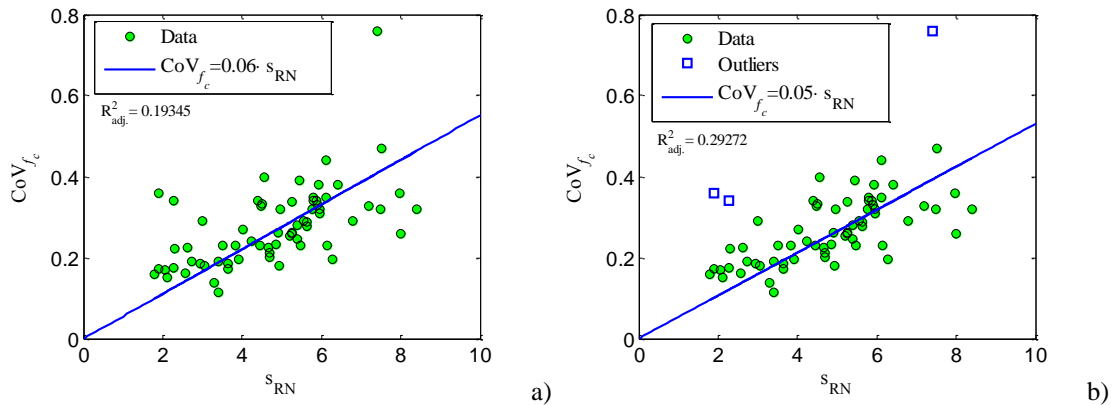
Figure 6. Results of the regression analysis for model M5-RN without the ROUT procedure (a) and with the ROUT procedure (b).

3.14

3.4.3 Results obtained for the correlation between the variability of f_c and UPV

The regression results obtained with model M1-UPV are shown in Fig. 7. The trends that were found in the regressions obtained with and without applying the ROUT procedure show there is no correlation between s_{f_c} and s_{UPV} (negative values of adj-R^2s were obtained).

Unlike for the previous model, a significant level of correlation was observed when analysing the power-based model M2-UPV, as shown in Fig. 8. The correlation level found without applying the ROUT procedure (Fig. 8a) yielded a value of adj-R^2 of 0.54 and a RMSE of 18.61, which indicates that s_{f_c} and s_{UPV} are moderately correlated when using model M2-UPV. This correlation improved further by applying the ROUT procedure and excluding three trend outliers, leading to an adj-R^2 of 0.66 and a RMSE of 9.20. The model that best fitted the data yielded an expected value for parameter c of 0.063 (with a $CI_{95\%}$ of [-0.0192, 0.146]) and an expected value for parameter d of 4.35 (with a $CI_{95\%}$ of [3.574, 5.117]).
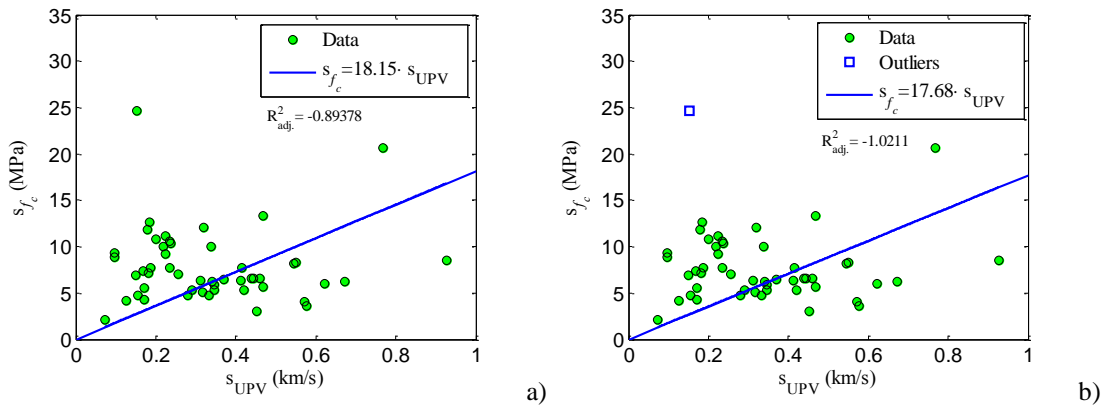
Figure 7. Results of the regression analysis for model M1-UPV without the ROUT procedure (a) and with the ROUT procedure (b).
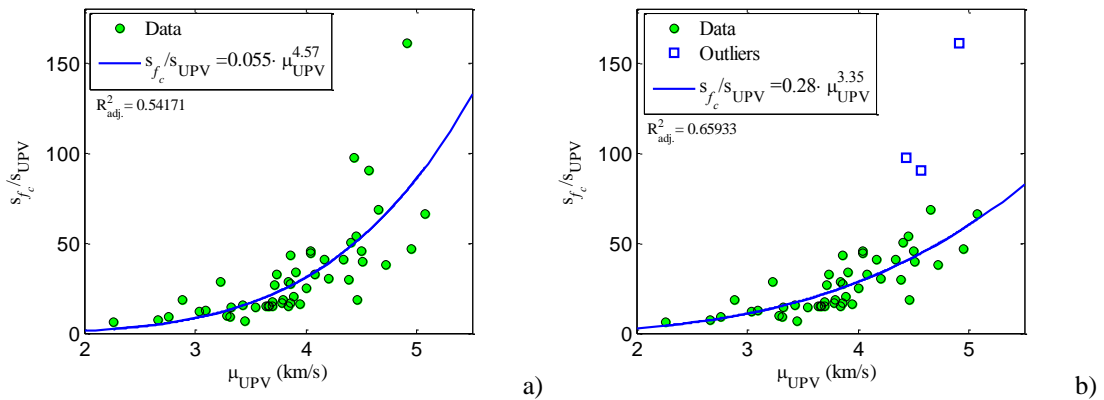
Figure 8. Results of the regression analysis for model M2-UPV without the ROUT procedure (a) and with the ROUT procedure (b).

When analysing model M3-UPV, which also considers a power-based correlation but assumes that f_c and *UPV* follow a lognormal distribution, the results shown in Fig. 9 are obtained. In this case, the ROUT procedure identified two trend outlier data. Contrary to what was seen for model M3-RN, no meaningful correlation was observed when using model M3-UPV (the value of adj-R^2 is negative), even after excluding the identified outliers.
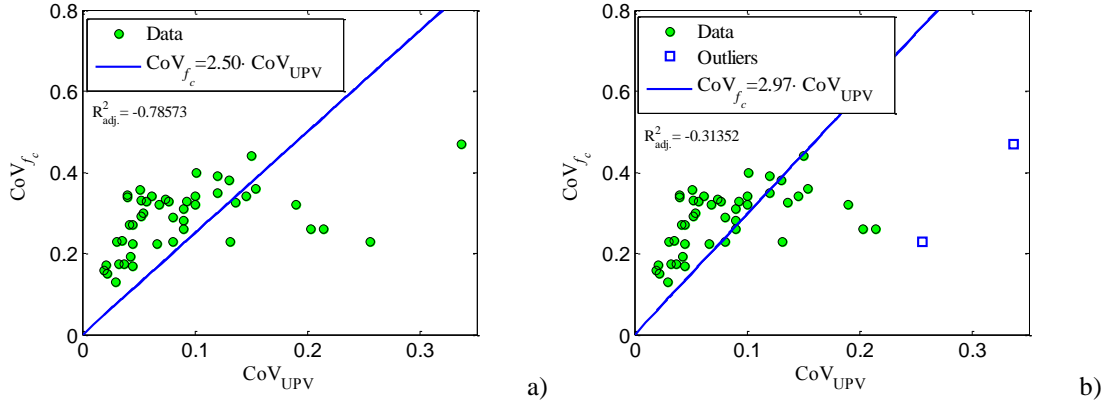
Figure 9. Results of the regression analysis for model M3-UPV without the ROUT procedure (a) and with the ROUT procedure (b).

Similar to what was found for model M2-UPV, a better correlation was obtained when analysing the exponential-based relation considered by model M4-UPV. In this case, the ROUT procedure was unable to identify outlying data. Therefore, the final regression presented in Fig. 10 corresponds to the ordinary least squares fit obtained for the entire data. As can be seen, model M4-UPV leads to a high correlation level (the adj-R^2 is 0.68 and the RMSE is 0.40). The model fit yielded an expected value for parameter *q* of 0.981 (with a $CI_{95\%}$ of [0.790, 1.171]) and an expected value for parameter *r* of 0.563 (with a $CI_{95\%}$ of [0.220, 1.442]).
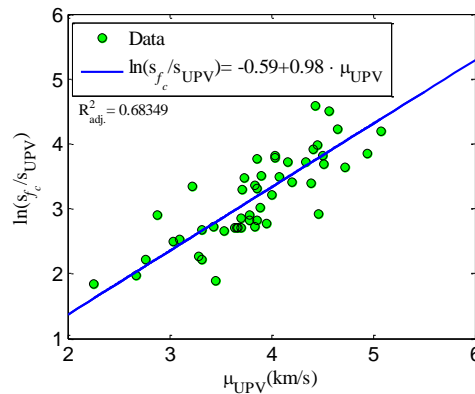
Figure 10. Results of the regression analysis for model M4-UPV without the ROUT procedure since no outliers were identified.

When analysing model M5-UPV, which considers that f_c follows a lognormal distribution and that *UPV* follows a normal distribution, the regression results presented in Fig. 11 do not show an improvement in the level of correlation when compared to the results shown in Fig. 10. The results

of Fig. 1 are only better than those shown in Fig. 9 for model M3-UPV that also involves distribution assumptions. The correlation level that is found without applying the ROUT procedure is very low (the value of adj-R^2 is 0.08). After applying the ROUT procedure, no outlier value was found.
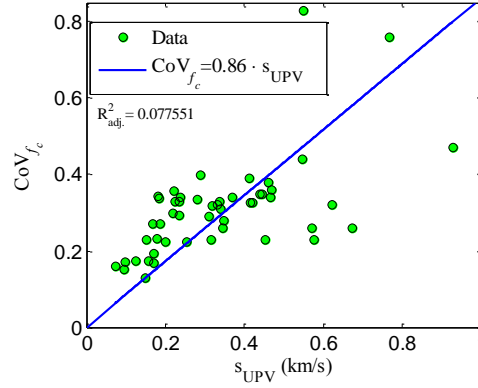
Figure 11. Results of the regression analysis for model M5-UPV without the ROUT procedure since no outliers were identified.

3.4.4 Results obtained using the SonReb-like approaches

As mentioned before, regression results for the SonReb-like approaches are presented using plots displaying predicted *vs* real values. It is also noted that RMSE values appearing in those plots correspond to variance or CoV^2 RMSE values, depending on the regression model under analysis. Figure 12 presents the results obtained for model M1-SonReb in terms of the predicted standard deviation against its real value. As seen in Fig. 12b, the ROUT procedure excluded four outlying values. The comparison of both regression results highlights the larger sensitivity of this model to variations of the standard deviation of *RN* than to those of the standard deviation of *UPV* (β is considerably larger than χ). Although similar coefficients were found before and after applying the ROUT procedure, the latter leads to a smaller RMSE but also to a lower $R^2_{adj.}$

Figure 13 shows the results obtained using model M2*-SonReb, assuming that *UPV* and *RN* are uncorrelated. The results obtained after excluding four outliers (Fig. 13b) identified using the ROUT procedure indicate that concrete strength variability estimated using M2*-SonReb is more sensitive to the *UPV* data (the power coefficient of *UPV* is higher than that of *RN*). After applying the ROUT procedure, the regression results show a similar coefficient of determination but lead to a reduction of the RMSE to about one third.
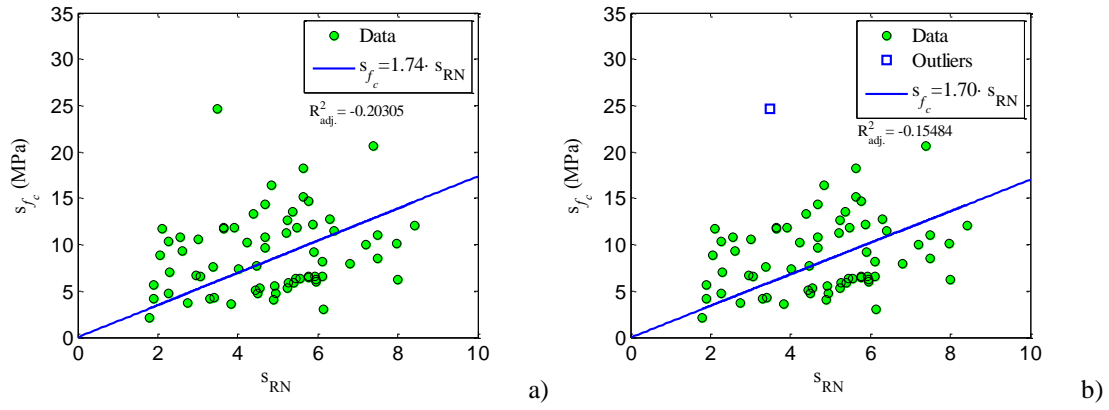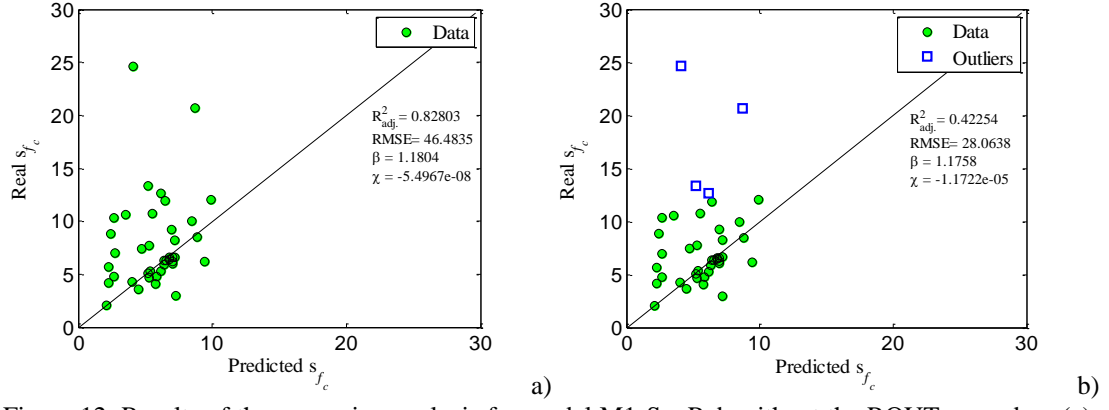
Figure 12. Results of the regression analysis for model M1-SonReb without the ROUT procedure (a) and with the ROUT procedure (b).
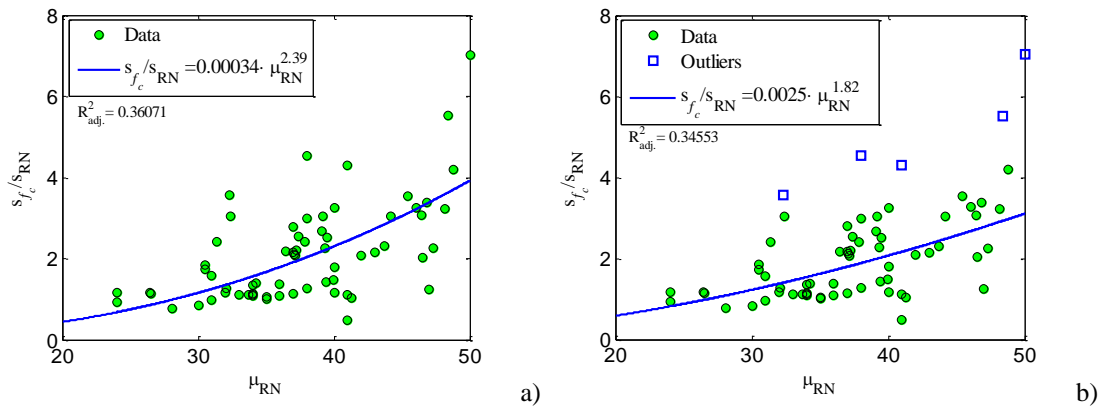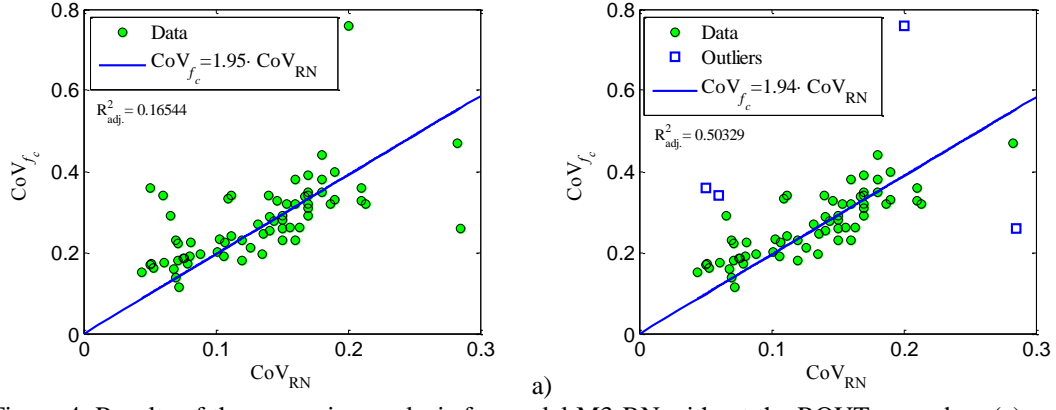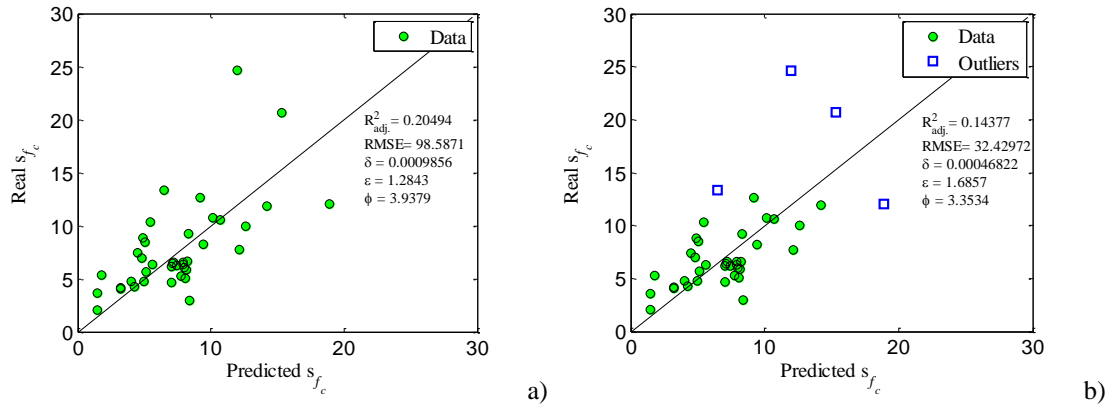

Figure 13. Results of the regression analysis for model M2*-SonReb without the ROUT procedure (a) and with the ROUT procedure (b).

Finally, Fig. 14 shows the results obtained for model M3-SonReb with and without applying the ROUT procedure. This model considers the same hypothesis of M2*-SonReb while also considering that *UPV*, *RN* and f_c follow lognormal distributions.
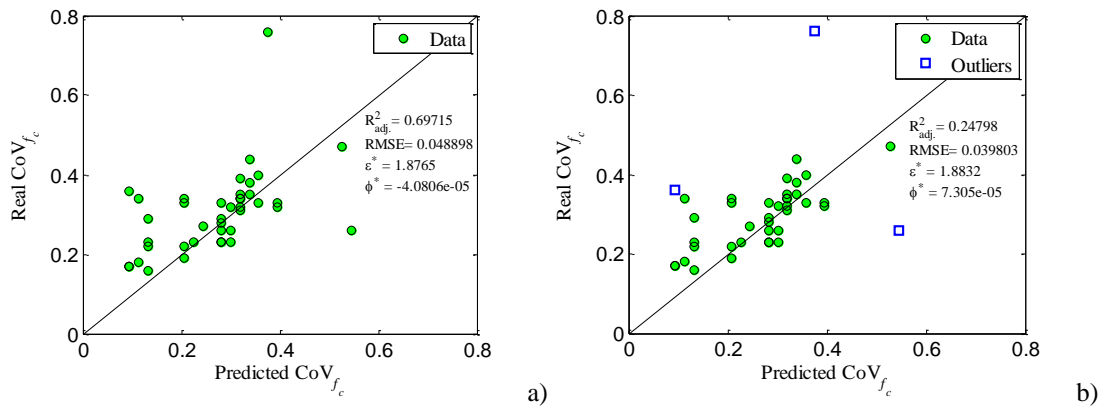
Figure 14. Results of the regression analysis for model M3-SonReb without the ROUT procedure (a) and with the ROUT procedure (b).

As seen in Fig. 14, the *RN* coefficient ε* only changes slightly between the cases where outliers are excluded or not. Conversely, the *UPV* coefficient φ* indicates the contribution of *UPV* to be irrelevant when estimating $CoV_{f_c}^2$ using this model. Applying the ROUT procedure leads to regression results that have a lower coefficient of determination but also a lower RMSE. It can be seen that a reduction of the RMSE of $CoV_{f_c}^2$ from 0.049 to 0.040 is equivalent to a reduction of the RMSE of CoV_{f_c} from 0.22 to 0.20.

3.5 Discussion of the results

3.5.1 Results obtained for the correlation between the variability of f_c and RN

Figure 2 has shown that the regression coefficient *a* (that has a value close to 1.70) obtained for model M1-RN is within the range of expected values, according to [15]. However, the correlation level found in the analysis does not support the adoption of a linear model to correlate the variability of f_c and *RN*. Although the use of linear conversion models can be found in previous studies available in the literature, such models are only expected to provide adequate results if the fitting range is chosen to be narrow [18].

Using the power-based model M2-RN improves the level of correlation found between the variability of f_c and *RN*. This result reflects the main issues reported in [19] where a systematic review of conversion models suggested the use of power models in this case. However, the stronger correlation level was found for this type of model when f_c and *RN* are assumed to follow a lognormal distribution, i.e. for model M3-RN. The value of adj-R^2 that was obtained is 0.50, which corresponds to a Pearson correlation coefficient of 71%. Furthermore, the expected value of the coefficient d^* that was found to be 1.94 is seen to be in line with values available from previous studies addressing conversion models of this type and that range from 1.0 to 4.0, with an average value of 2.10 [16]. It can therefore be concluded that model M3-RN provides an adequate indicator for the variability of f_c based on the variability of *RN*.

Although the use of an exponential-based conversion model is not as common as the power-based approach, the former was found to be used in several cases according to the review in [18]. Still, given that the level of correlation that was obtained with model M3-RN is larger than the one observed for M4-RN, M3-RN is considered more adequate to estimate concrete variability. For the case of model MR5-RN, the regression coefficient that was found for the correlation between CoV_{f_c} and s_{RN} when *RN* and f_c are assumed to follow a normal and a lognormal distribution, respectively, ($q^* = 0.05$) is compatible with the values found in [18], which range between 0.06 and 0.08. However, the quality of the fit obtained with this model is lower than the one obtained with model M4-RN, making it also less reliable than M3-RN to estimate concrete variability.

In the overall, model M3-RN is seen as an adequate relation to establish a preliminary estimate for CoV_{f_c} due to the relevant correlation level that was found. The estimates obtained with this model are associated with the assumption that both f_c and RN follow a lognormal distribution. Since RN test results usually have a lower bound limit of 20, the likelihood of RN having an asymmetric distribution is high, particularly when lower values of f_c are involved.

To complement the analysis presented for model M3-RN, its reliability was also examined by analysing the distribution of the ratios $\eta_{CoV_{f_c}}$ between the predictions made for CoV_{f_c} and the corresponding real values of the concrete strength variability. Figure 15 shows the probability plot of the $\eta_{CoV_{f_c}}$ values that were obtained using model M3-RN and considering all the data (i.e. without removing the trend outliers).
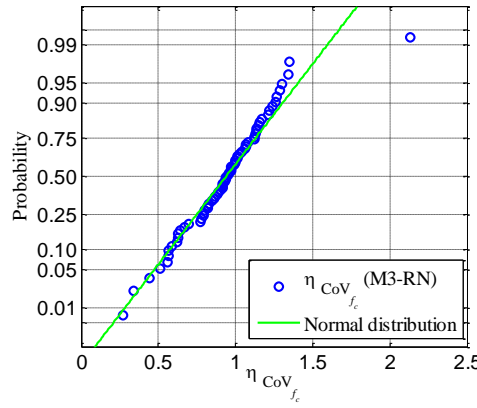
Figure 15. Probability plot of the ratio between the estimates made with model M3-RN and the real values of CoV_{f_c}.

The plot assumes the $\eta_{CoV_{f_c}}$ values follow a normal distribution but a visual assessment of the plot indicates there is large deviation in the upper tail of the data due to one $\eta_{CoV_{f_c}}$ value that invalidates this assumption. The Shapiro-Wilk goodness-of-fit test [55] was also applied to the $\eta_{CoV_{f_c}}$ ratios and the result showed that the normality assumption was rejected for a confidence level of 95%. Nevertheless, the normal distribution fits the majority of the data, exhibiting a mean value of 0.94 and a standard deviation of 0.28. Given this mean value, it can be seen that model M3-RN is able to provide relatively unbiased estimates of CoV_{f_c}.

3.5.2 Results obtained for the correlation between the variability of f_c and UPV

The results presented in Fig. 7 (model M1-UPV) confirmed the inadequacy of using a linear model to correlate the variability of f_c with that of UPV, given the lack of trend that was observed. This observation is in line with the expected relation between the physical properties of UPV and

f_c. As pointed out by Breysse [16] the modification of concrete strength with time is not captured by a linear relation involving *UPV* test results. As such, in matured concrete, a change in concrete strength is not followed by a significant change in the *UPV* values. Therefore, a linear correlation between the standard deviations of f_c and *UPV* is not expected to provide a significant result. As mentioned also in [16] the non-proportionality between the increase of *UPV* with f_c implies that most studies define the relation between these parameters using power models with a large power coefficient or exponential models.

With respect to the performance of the power model, the results obtained with model M2-UPV provided the best fit among the multiple alternatives analysed for both NDTs. The power coefficient ($d = 4.35$) can be seen to be within the range of values identified by Breysse [16] (i.e. 1.7447-12.809) and corroborates the high level of nonlinearity of the relation between f_c and *UPV*. However, unlike the results found for *RN*, considering the power model relation and assuming that both *UPV* and f_c follow a lognormal distribution (model M3-UPV) was not seen as an adequate approach.

The adequacy of using an exponential model instead of a power model to correlate the variability of f_c with that of *UPV* was also confirmed, as seen in Fig. 10 (model M4-UPV). Even though the correlation level found for this model (adj-$R^2 = 0.68$) is similar to that of M2-UPV (adj-$R^2 = 0.66$), the correlation level of model M4-UPV was obtained without removing any outlier. Hence, model M4-UPV is preferred instead. Furthermore, introducing the additional assumptions that f_c follows a lognormal distribution and that *UPV* follows a normal distribution (model M5-UPV) was not seen to yield an adequate level of correlation (Fig. 11). Although the values of q^* that were obtained are in line with the range of expected values referred [16] (i.e. 0.60-2.27 s/km), the fitting results led to an inadequate value of adj-R^2 due to the very large variation of the data with respect to the trend line. This variation of the data is further illustrated in Fig. 16a where the mean value of the *UPV* dataset corresponding to each s_{UPV} value is also represented, providing an additional scale to assess the nonlinearity issues previously discussed. Together with these data points, three linear correlation ranges are also shown. As can be seen, when accounting for the mean value of the *UPV* datasets μ_{UPV}, the ratio between CoV_{f_c} and s_{UPV} follows a different trend depending on the value of μ_{UPV}. As such, approximate trend lines can be defined for three ranges of μ_{UPV}. For μ_{UPV} values larger than 4.0km/s, the trend line proposed by Turgut [0] with a coefficient q of 1.29 s/km is suggested. For μ_{UPV} values lower than 3.5 km/s, a trend line with a coefficient q close to the minimum value defined by Breysse [16] is considered. For μ_{UPV} values between 3.5km/s and 4.0km/s, a trend line with a coefficient q of 0.91 km/s was defined which corresponds to the robust average trend found for the data that is not covered by the two other trend lines. The

multi-linear correlation model between CoV_{f_c} and s_{UPV} is represented in Fig. 16b and summarized in Eq. (25).
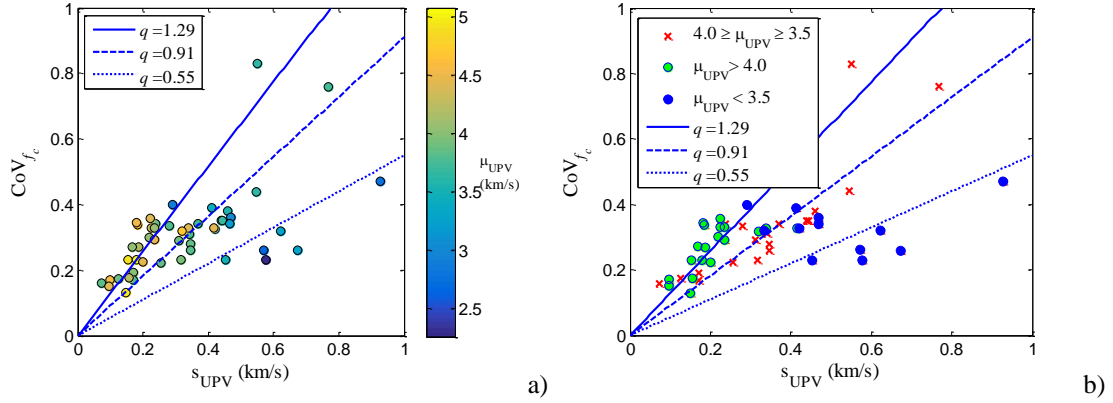
Figure 16. Disaggregation of the s_{UPV} data according to the mean value of the corresponding dataset (a) and representation of the proposed multi-linear correlation model (b).

$$CoV_{f_c} = \begin{cases} 1.29 \times s_{UPV} & \mu_{UPV} > 4\,km/s \\ 0.91 \times s_{UPV} & 4\,km/s \geq \mu_{UPV} \geq 3.5\,km/s \\ 0.55 \times s_{UPV} & \mu_{UPV} < 3.5\,km/s \end{cases} \qquad (25)$$

As carried out for model M3-RN, a complementary analysis was performed to quantify the relation between the model predictions and the real values of the concrete strength variability. Therefore, for model M4-UPV, the ratios $\eta_{s_{f_c}}$ between the predictions made for s_{f_c} and the corresponding real values were analysed (Fig. 17a). For the model defined by Eq. (25), the ratios $\eta_{CoV_{f_c}}$ between the predictions made for CoV_{f_c} and the corresponding real values were also analysed (Fig. 17b). As for the corresponding plot involving *RN* test results, the plots of Fig. 17 were also obtained considering all the data (i.e. without removing the trend outliers).

A visual assessment of the plots indicates there are small deviations between the probability plots of the reference normal distributions and those of $\eta_{s_{f_c}}$ and $\eta_{CoV_{f_c}}$. After applying the Shapiro-Wilk goodness-of-fit test 55 to the $\eta_{s_{f_c}}$ and $\eta_{CoV_{f_c}}$ ratios, the results indicate that the normality assumption could not be rejected for a confidence level of 95%. The normal distribution fitted to the $\eta_{s_{f_c}}$ ratios for model M4-UPV has a mean value of 1.08 and a standard deviation of 0.43, while for the model defined by Eq. (25) the mean value of $\eta_{CoV_{f_c}}$ is 0.96 and the standard deviation is 0.27. Given the mean values that were obtained, both models are seen to lead to relatively unbiased estimates of the concrete strength variability.
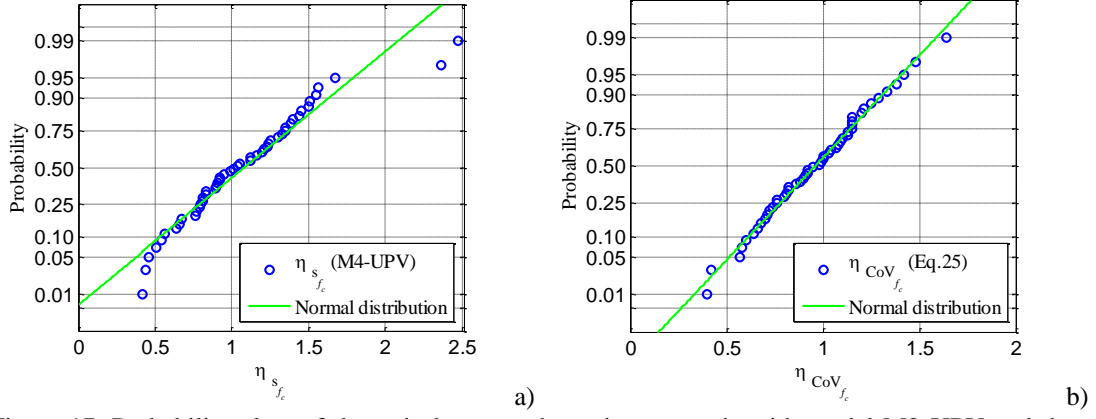
Figure 17. Probability plots of the ratio between the estimates made with model M2-UPV and the real values of s_{f_c} (a), and with Eq.(25) and the real values of CoV_{f_c} (b).

3.5.3 Results obtained for the SonReb-like approaches approach

Given the larger complexity of the SonReb-like approaches (i.e. the correlation models now involve three variables instead of two), the number of data triplets considered in the regressions analyses (i.e. 40) may be insufficient to perform a detailed analysis of their adequacy. Therefore, this limitation must be accounted for when examining the trends that are discussed herein. Nevertheless, some of the results that were obtained show a considerable level of consistency with the correlation models analysed in the previous sections and with the main observations in the review performed by Breysse [16]. Regarding the linear correlation model M1-SonReb, Fig. 12 shows that a linear correlation between s_{f_c} and s_{UPV} is unable to be established, given the large sensitivity of the model to s_{RN}. The value of coefficient β (1.18, see Fig. 12) is of the same order of magnitude as the regression coefficient that was obtained with model M1-RN (1.70, see Fig. 2) while coefficient χ is almost zero (see Fig.7 and the results of model M1-UPV). Thus, the results obtained with M1-SonReb are in line with those observed in Sections 4.2 e 4.3.

A similar level of consistency is observed when analysing the results obtained using model M3-SonReb. In this case, the correlation between CoV_{f_c} and CoV_{RN} is clearly dominant, and the value of the regression coefficient ε^* that is found (1.88, see Fig. 14) is also of the same order of magnitude as the regression coefficient that was obtained with model M3-RN that involves the same conditions (1.94, see Fig. 4). This connection between CoV_{f_c} and CoV_{RN} is further highlighted given the value of the regression coefficient ϕ^* (close to zero, see Fig. 14), which implies that model M3-SonReb behaves like M3-RN, irrespective of the *UPV* data being involved. The most commonly found SonReb-like conversion models have the functional form of model M2*-SonReb (e.g. see [16] and references therein). Still, the general form of this model (i.e. M2-SonReb) was unable to be analysed given the lack of information regarding the correlation between the *RN* and *UPV* data in each of the considered cases. As such, only the particular case

where both parameters are assumed to be uncorrelated was evaluated (i.e. model M2*-SonReb). Unlike for the results of M1-SonReb and M3-SonReb, the results obtained with M2*-SonReb show that a general model of this type has the potential to be developed, namely given the significant values that were obtained for the *RN* and *UPV* regression coefficients. Despite the limitations surrounding the use of this model, it is nevertheless interesting to notice that the regression coefficients obtained for M2*-SonReb are within the average of twelve models analysed by Breysse [16]. Still, further studies with an extensive number of datasets have to be carried out to evaluate consistently the advantages of model M2*-SonReb.

3.6 Conclusions

The presented study analysed the possibility of developing generalized empirical expressions to obtain an estimate of the in situ concrete strength variability using NDT results. The study analysed the performance of several correlation models between different estimators of the variability of concrete strength and NDT results. In addition, the models were also associated with assumptions regarding the statistical distributions of f_c and of the NDT results.

By analysing the performance of the selected correlation models using several sets of variability data for f_c and NDT results, it was concluded that several general empirical expressions can be established. When *RN* test results are available, a preliminary estimate for the variability of concrete strength can be obtained by the expression $CoV_{f_c} = 1.94 \cdot CoV_{RN}$ which assumes that both f_c and *RN* follow a lognormal distribution. However, no reliable correlation was found that would allow estimating the standard deviation of f_c, s_{f_c}, using *RN* test results.

When using *UPV* test results, expressions were obtained to define preliminary estimates of both s_{f_c} and CoV_{f_c}. The expression $s_{f_c} = s_{UPV} \cdot \exp\left(0.98 \cdot \mu_{UPV} - 0.59\right)$ was seen to provide reliable estimates of s_{f_c} but needs to also involve the mean value of the *UPV* test results in order to capture the effect of the nonlinear relation between *UPV* and f_c. Since no reliable expression was found to correlate CoV_{f_c} with a measure of the variability of *UPV* without involving μ_{UPV}, a multi-linear model was proposed instead. This multi-linear model estimates CoV_{f_c} as a function of s_{UPV} and three different ranges of μ_{UPV} (Eq. (25)). This model is seen to provide a level of reliability similar to that provided by the model involving s_{f_c}. Results obtained using SonReb-like models confirmed some of the trends that were identified by the single NDT models. Still, no statistically significant SonReb-like model was identified. This conclusion is mostly related to limitations associated to the available data. As such, further research needs to address the development of SonReb-like models such as those analysed herein, namely to assess, among other factors, the sensitivity of the models to the correlation between *RN* and *UPV*.

Finally, the results obtained from the study that was performed highlight several aspects regarding the selection of adequate conversion models between NDTs and f_c results when using specific regression methods or a bi-objective approach. The results indicate that an adequate conversion model between NDTs and f_c results should involve a power or an exponential model, especially in existing structures where the CoV_{f_c} is expected to be above 10%. In particular, the results that were obtained confirm the conclusions in [16] that suggest the use of exponential or power models with large power coefficients for *UPV-f_c* conversion and the use of power models for *RN-f_c* conversion.

3.7 Appendix

Database adopted for the study of general models for the concrete strength variability.

N	$f_{c,mean}$	UPV_{mean}	RN_{mean}	s_{fc}	s_{UPV}	s_{RN}	CoV_{fc}	CoV_{UPV}	CoV_{RN}	REF.
19	27.46	-	40	7.96	-	6.80	0.29	-	0.17	[4]
27	28.11	-	38	10.12	-	7.98	0.36	-	0.21	[4]
20	30.14	-	40	11.45	-	6.40	0.38	-	0.16	[4]
25	35.99	-	42	12.24	-	5.88	0.34	-	0.14	[4]
20	30.66	-	41	5.52	-	4.92	0.18	-	0.12	[4]
21	19.74	-	36	3.75	-	2.74	0.19	-	0.08	[24]
145	18.80	3.67	34	6.58	0.44	5.78	0.35	0.12	0.17	[23]
83	17.30	3.54	33	6.57	0.46	5.94	0.38	0.13	0.18	[23]
62	20.90	3.86	36	5.85	0.35	5.40	0.28	0.09	0.15	[23]
27	18.70	3.64	34	8.23	0.55	6.12	0.44	0.15	0.18	[23]
26	18.90	3.70	34	6.43	0.37	5.78	0.34	0.10	0.17	[23]
30	15.00	3.32	31	4.80	0.33	4.96	0.32	0.10	0.16	[23]
32	20.10	3.79	35	6.23	0.34	5.95	0.31	0.09	0.17	[23]
30	21.90	3.95	37	5.04	0.32	4.44	0.23	0.08	0.12	[23]
24	18.90	3.70	34	6.62	0.44	6.12	0.35	0.12	0.18	[23]
59	16.20	3.43	32	6.32	0.41	5.44	0.39	0.12	0.17	[23]
46	21.80	3.89	37	6.32	0.31	5.55	0.29	0.08	0.15	[23]
16	20.30	3.84	35	5.28	0.35	5.25	0.26	0.09	0.15	[23]
9	30.06	-	47	4.12	-	3.29	0.14	-	0.07	[25]
48	13.30	2.88	24	5.32	0.29	4.56	0.40	0.10	0.19	[38]
67	27.20	3.72	37	20.67	0.77	7.40	0.76	0.21	0.20	[38]
8	30.40	3.86	38	10.34	0.24	2.28	0.34	0.06	0.06	[38]
8	52.00	4.57	41	8.84	0.10	2.05	0.17	0.02	0.05	[38]
21	28.00	4.34	31	9.24	0.23	5.89	0.33	0.05	0.19	[38]
6	15.80	3.04	38	5.69	0.47	1.90	0.36	0.15	0.05	[38]
16	15.70	2.26	24	3.61	0.58	3.84	0.23	0.25	0.16	[38]
13	13.00	3.45	41	2.99	0.45	6.15	0.23	0.13	0.15	[38]
14	18.80	3.29	35	6.02	0.62	5.95	0.32	0.19	0.17	[38]
21	107.00	4.91	50	24.61	0.15	3.50	0.23	0.03	0.07	[38]
40	10.00	3.66	-	8.30	0.55	-	0.83	0.15	-	[38]
26	28.60	4.17	-	7.72	0.19	-	0.27	0.05	-	[38]
13	53.60	4.95	-	6.97	0.15	-	0.13	0.03	-	[38]
7	33.30	4.04	-	9.99	0.22	-	0.30	0.05	-	[38]
207	23.40	4.08	-	7.70	0.23	-	0.33	0.06	-	[38]
144	35.95	-	39	6.69	-	2.95	0.19	-	0.08	[26]
118	63.30	-	48	11.74	-	3.64	0.19	-	0.08	[26]
114	41.73	-	32	9.35	-	2.62	0.22	-	0.08	[26]
144	77.41	-	48	11.70	-	2.12	0.15	-	0.04	[26]
100	67.19	-	47	7.65	-	3.39	0.11	-	0.07	[26]
136	45.78	-	37	9.71	-	4.68	0.21	-	0.13	[26]
120	44.50	-	37	11.29	-	5.21	0.25	-	0.14	[26]
120	42.62	-	38	10.26	-	4.24	0.24	-	0.11	[26]

Database adopted for the study of general models for the concrete strength variability (continued)

N	$f_{c,mean}$	UPV_{mean}	RN_{mean}	s_{fc}	s_{UPV}	s_{RN}	CoV_{fc}	CoV_{UPV}	CoV_{RN}	REF.
118	65.35	-	47	12.77	-	6.29	0.20	-	0.14	[26]
172	69.20	-	46	11.88	-	3.64	0.17	-	0.08	[26]
208	71.12	-	46	14.34	-	4.68	0.20	-	0.10	[26]
216	70.25	-	47	16.38	-	4.84	0.23	-	0.10	[26]
160	60.72	-	44	11.87	-	3.90	0.20	-	0.09	[26]
212	54.71	-	39	15.13	-	5.64	0.28	-	0.14	[26]
212	45.82	-	37	14.71	-	5.77	0.32	-	0.15	[26]
204	63.55	-	40	18.30	-	5.64	0.29	-	0.14	[26]
136	55.16	-	39	13.57	-	5.38	0.25	-	0.14	[26]
167	34.69	-	40	11.08	-	7.49	0.32	-	0.19	[26]
130	66.74	-	49	10.78	-	2.57	0.16	-	0.05	[26]
13	36.30	4.50	45	10.60	0.23	3.00	0.29	0.05	0.07	[27]
10	15.71	2.67	30	4.10	0.57	4.90	0.26	0.21	0.16	[28]
18	18.09	2.76	27	8.50	0.93	7.50	0.47	0.34	0.28	[29]
25	31.39	3.86	32	7.00	0.26	2.30	0.22	0.07	0.07	[30]
20	22.40	4.00	32	4.30	0.17	3.40	0.19	0.04	0.11	[31]
19	24.28	3.91	37	4.20	0.13	1.90	0.17	0.03	0.05	[31]
23	14.07	3.78	41	4.70	0.28	4.50	0.33	0.07	0.11	[33]
14	23.85	3.32	28	6.20	0.67	8.00	0.26	0.20	0.29	[34]
32	30.49	4.39	34	10.00	0.34	7.20	0.33	0.08	0.21	[35]
19	13.21	3.84	26	2.10	0.07	1.80	0.16	0.02	0.07	[36]
31	36.78	-	43	6.58	-	3.05	0.18	-	0.07	[38]
22	16.21	3.10	-	5.29	0.42	-	0.33	0.14	-	[2]
21	32.57	3.74	-	5.51	0.17	-	0.17	0.05	-	[2]
16	26.26	3.23	39	13.33	0.47	4.39	0.34	0.14	0.11	[39]
80	51.53	5.08	36	11.89	0.18	5.47	0.23	0.04	0.15	[40]
63	27.17	4.21	37	4.76	0.16	2.26	0.18	0.04	0.06	[41]
60	23.61	4.46	31	7.73	0.42	4.47	0.33	0.09	0.15	[42]
40	37.70	4.72	39	12.04	0.32	8.41	0.32	0.07	0.21	[43]
30	47.94	4.45	44	10.76	0.20	4.67	0.22	0.04	0.11	[44]
20	27.35	4.04	30	7.42	0.17	4.01	0.27	0.04	0.13	[45]
16	37.33	4.66	31	12.63	0.18	5.25	0.34	0.04	0.17	[46]
120	31.37	4.41	-	11.16	0.22	-	0.36	0.05	-	[47]
60	61.83	4.44	-	9.36	0.10	-	0.15	0.02	-	[48]
24	20.96	4.51	-	7.20	0.18	-	0.34	0.04	-	[49]
120	22.45	-	34	5.88	-	5.26	0.26	-	0.16	[50]

3.8 References

1   Caspeele R, Taerwe L, (2012). Bayesian assessment of the characteristic concrete compressive strength using combined vague-informative priors. Construction and Building Materials; 28:342–50.

2   Giannini R, Sguerri L, Paolacci F, Alessandri S, (2014) Assessment of concrete strength combining direct and NDT measures via Bayesian inference. Engineering Structures 64:68-77.

3   Fiore A, Porco F, Uva G, Mezzina M, (2013). On the dispersion of data collected by in situ diagnostic of the existing concrete, Construction and Building Materials; 47:208-217.

4   Pereira N, Romão X, (2016). Assessment of the concrete strength in existing buildings using finite population approach. Construction and Building Materials; 110: 106–116.

5   Alwash M, Sbartaï ZM, Breysse D, (2016). Non-destructive assessment of both mean strength and variability of concrete: a new bi-objective approach. Construction and Building Materials 113:880–889.

6   Cristofaro MT, D'Ambrisi A, De Stefano M, Pucinotti R, Tanganelli M (2012). Studio sulla Dispersione dei Valori di Resistenza a Compressione del Calcestruzzo di Edifici Esistenti. Il Giornale delle Prove non Distruttive Monitoraggio e Diagnostica; 2 (in Italian).

7   Stewart MG, (1995). Workmanship and its influence on probabilistic models of concrete compressive strength, ACI Materials Journal; 92(4):361–372.

8   Bartlett FM, MacGregor JG, (1999). Variation of in-place concrete strength in structures, ACI Materials Journal; 96(2):261–270.

9   Uva G, Porco F, Fiore A, Mezzina M, (2013). Proposal of a methodology of in situ concrete tests and improving the estimate of the compressive strength. Construction and Building Materials; 38(1):72–83.

10 Masi A, Chiauzzi L, (2013). An experimental study on the within-member variability of in situ concrete strength in RC building structures. Construction and Building Materials; 47:951-961

11 Jalayer F, Elefante L, Iervolino I, Manfredi G, (2011). Knowledge-based performance assessment of existing RC buildings, Journal of Earthquake Engineering; 15:362-389.

12 Monti G, Alessandri S, (2009). Application of Bayesian techniques to material strength evaluation and calibration of confidence factors, in: E. Cosenza (Ed.), Eurocode 8 Perspectives From the Italian Standpoint Workshop, Doppiavoce, Naples, Italy, 67-77

13 Romão X, Gonçalves R, Costa A, Delgado R, (2012). Evaluation of the EC8-3 confidence factors for the characterization of concrete strength in existing structures; Materials and Structures; 45.

14 Alwash M, Breysse D, Sbartaï ZM, Szilágyi K, Borosnyói A, (2017). Factors affecting the reliability of assessing the concrete strength by rebound hammer and cores. Construction and Building Materials; 140(1): 354-363.

15 CEN, (2007). EN 13791-Assessment of in situ compressive strength in structures and precast concrete. CEN, Brussels, Belgium.

16 Breysse D, (2012). Nondestructive evaluation of concrete strength: an historical review and new perspective by combining NDT methods, Construction and Building Materials; 33 :139-163.

17 Breysse D, Soutsos M, Moczko A, Laurens S, (2010). Quantitative non-destructive assessment of in situ concrete properties: the key question of calibration, Structural faults and repair, Edinburgh, 15–17.

18 Szilágyi K, Borosnyói A, (2009). 50 years of experience with the Schmidt Rebound hammer, Concr. Struct 10: 46–56.

19 Breysse D, Martinez-Fernandez J, (2014). Assessing concrete strength with rebound hammer: review of key issues and ideas for more reliable conclusions, Materials and Structures; 47: 1589-1604.

20 ACI (2003). ACI 228.1R-03 - In-Place Methods to Estimate Concrete Strength, American Concrete Institute, USA.

21 Ang AHS, Tang WH, (2006). Probability Concepts in Engineering: Emphasis on Applications to Civil and Environmental Engineering (vol.1), second ed., John Wiley and Sons.

22 Bao Y, (2013). On sample Skewness and Kurtosis. Econometric Reviews, 32(4): 415-448.

23 Ali-Benyahiaa K, Sbartaï ZM, Breysse D, Kenaid S, Ghricia M, (2017). Analysis of the single and combined non-destructive test approaches for on-site concrete strength assessment: General statements based on a real case study. Case Studies in Construction Materials 6: 109-119.

24 Monteiro A, Gonçalves A, (2009). Assessment of characteristic strength in structures by the rebound hammer test according to EN 13791:2007, Proceedings of NDTCE'09 Conference, Nantes, France.

25 Soutsos M, Breysse D, Garnier V, Goncalves A, Monteiro A, (2012). Estimation of on-site compressive strength of concrete. In Non-Destructive Assessment of Concrete Structures: Reliability and Limits of Single and Combined Techniques. Springer Netherlands.

26 Szilágyi K, (2013). Rebound surface hardness and related properties of concrete. Ph. D. thesis, University of Technology and Economics Budapest, Hungary.

27 Gennaro-Santori A, (2005). NDT measurements on the concrete elements of the bridges – Technical Report n. 74.05, CND Controlli NonDistruttivi s.r.l., ANAS – SS761 Val Seriana.

28 Brognoli M, (2007). Prove e controlli non distruttivi per la verifica degli edifici esistenti secondo la normativa sismica e le norme tecniche per le costruzioni, Brescia, Italy.

29 Masi A, Vona M, (2009). La Stima della Resistenza del Calcestruzzo In-Situ: Impostazione delle Indagini ed Eleborazione dei Risultati, Progettazione sismica, n° 1/2009, IUSS Press, ISSN 1973-7432, 2009.

30 Masi A, Dolce M, Vona M, Nigro D, Pace G, Ferrini M, (2007). Indagini sperimentali su elementi strutturali estratti da una scuola esistente in c.a., XII ANIDS conference, Pisa, Italy.

31 Dolce M, Masi A, Ferrini M, (2006). Estimation of the actual in-place concrete strength in assessing existing RC structures, 2nd International FIB Conference, Napoli, Italy

32 Han HS, (1992). Estimation of In-situ concrete strength by combined Non-Destructive Method. Magazine of the Korea Concrete Institute 4(4): 57-66.

33 Pucinotti R, (2015). Reinforced concrete structure: Non-destructive in situ strength assessment of concrete, Construction and Building Materials; 75: 331-341.

34 Masi A, Chiauzzi L, Manfredi V, (2016). Criteria for identifying concrete homogeneous areas for the estimation of in-situ strength in RC buildings. Construction and Building Materials; 121: 576-587.

35 Nada Mahdi F, Abd Muttalib IS, Ali Khalid J, (2013). Prediction of compressive strength of reinforced concrete structural elements by using combined non-destructive tests, Journal of Engineering; 19(10):1189-1211.

36 Hannachi S, Guetteche N, (2011). Le contrôle non destructif des ouvrages en béton – évaluation de la résistance à la compression du béton sur site – utilisation de la méthode combinée, 29èmes Rencontres AUGC, Tlemcen, 28-30.

37 Scanlon A, Mikhailovsky L, (1987). Strength evaluation of an existing concrete bridge based on core and non-destructive test data. Canadian Journal of Civil Engineering 14: 145-154.

38 Fabbrocino G, Di Fusco A, Manfredi G, (2005). In situ evaluation of concrete strength for existing constructions: critical issues and perspectives of NDT methods, fib symposium, keep attractive concrete. Budapest, Hungary.

39 Nobile L, (2015). Prediction of concrete compressive strength by combined non-destructive methods. Meccanica, 50(2): 411-417.

40 Cianfrone F, Facaoaru I, (1979). Study on the introduction into Italy on the combined nondestructive method, for the determination of in situ concrete strength. Matériaux et Constructions, 12(71): 413-424.

41 Knaze P, Beno P, (1984). The use of combined non-destructive testing methods to determine the compressive strength of concrete. Matériaux et Constructions, 17(3): 207- 210.

42 Oktar O, Moral H, Taşdemir M, (1996). Sensitivity of concrete properties to the pore structure of hardened cement paste. Cement and concrete research, 26(11): 1619-1627.

43 Jain A, Kathuria A, Kumar A, Verma Y, Murari K, (2013). Combined use of non-destructive tests for assessment of strength of concrete in structure. Procedia Engineering, 54:241-251.

44 Rojas-Henao L, Fernández-Gómez J, López-Agüí J, (2012). Rebound Hammer, Pulse Velocity, and Core Tests in Self-Consolidating Concrete. ACI Materials Journal, 109(2): 235-243.

45 Nikhil V, Balki Minal R, Deep S, Vijay D, Vishal S, Patil S, (2015). The use of combined non-destructive testing in the concrete strength assessment from laboratory specimens and existing buildings. International Journal of Current Engineering and Scientific Research, 2(5): 55-59.

46 Sbartaï Z, Breysse D, Larget M, Balayssac JP, (2012). Combining NDT techniques for improved evaluation of concrete properties. Cement and Concrete Composites 34: 725–733.

47 Musmar M, Abedalhadi N, (2008). Relationship between ultrasonic pulse velocity and standard concrete cube crushing strength. Journal of Engineering Sciences, Assiut University, 36(1): 51-59.

48 El Mir A, Nehme S, (2016). A comparative study on ultrasonic pulse velocity for normally vibrated and self-compacting concretes. Concrete Structures, 17: 8-12.

49 del Rio L, Jiménez A, Lopez F, Rosa F, Rufo M, Paniagua J, (2004). Characterization and hardening of concrete with ultrasonic testing. Ultrasonics, 42: 527-530.

50 Hajjeh, H, (2012). Correlation between destructive and non-destructive strengths of concrete cubes using regression analysis. Contemporary engineering sciences, 5(10): 493-509.

51 Alwash M, (2017). Assessment of concrete strength in existing structures using non-destructive tests and cores: analysis of current methodology and recommendations for more reliable assessment. PhD. Dissertation, University of Bordeaux, France.

52 Motulsky H, Brown R, (2006). Detecting outliers when fitting data with nonlinear regression – a new method based on robust nonlinear regression and the false discovery rate. BMC bioinformatics, 7(1): 123-143.

53 O'Leary D, (1990) Robust regression computation using iteratively reweighted least squares. SIAM Journal on Matrix Analysis and Applications, 11(3): 466-480.

54 Wilcox R, (2005). Introduction to robust estimation and hypothesis testing. Elsevier Academic Press, London, UK.

55 Shapiro S, Wilk M, (1965). An analysis of variance test for normality (complete samples). Biometrika 52(3/4): 591-611.

Turgut P, (2004). Research into the correlation between concrete strength and UPV value. NDT.net (12).

Chapter 4

Safety factors for material properties in existing reinforced concrete buildings

Scope and objectives

In the previous chapters, a finite population paradigm was explored to control the epistemic uncertainty in the assessment of the physical properties of existing reinforced concrete (RC) buildings. Despite having shown that the indirect measure of the variability of the material properties could be useful to estimate the mean concrete strength, no specific sampling plans were proposed. Hence, the current chapter uses the concepts previously developed for the derivation of statistically based sampling plans to assess the material properties in existing buildings. The proposed sampling plans will therefore be consistent with the finite population strategy defined before. Although full probabilistic nonlinear methods rely on the definition of statistical distributions for the material properties, simplified methods involving storey-based mean values of the material properties can benefit from the definition of an interval of values bounding the real mean. This concept is fundamental in current seismic safety codes, but limited guidance usually provided in these standards. Based on these arguments, the concepts derived in Chapter 2 were extended to propose a new set of Knowledge Levels and adaptive safety factors (CF_{mat}) that can be used in simplified verifications such as the methods available in EC8/3. CF_{mat} values and sampling plans are proposed herein for both the concrete strength and the reinforcing steel yield strength, overcoming the main limitations of the current EC8/3 proposal and presenting an integrated survey framework that significantly improves the current standard-based approaches.

4.1 Introduction

Assessing the seismic performance of existing structures is a matter of high priority in earthquake prone areas. As recognized by earthquake engineering experts and public authorities, evaluating the safety of existing buildings and infrastructures is fundamental. Therefore, specific code-based methods must be developed to address these issues and an adequate calibration of these methods must be carried out to analyse their ability to be used in practice. As such, several standards (e.g. [1-6]) have been recently developed to address the specifics of the seismic safety assessment of existing structures and studies analysing some of their procedures have started to appear [7-11]. One important issue that affects the evaluation of the seismic performance of existing buildings is related to the definition of their material properties, since the original construction quality levels and design standards may be very different from those currently in use. Characterizing these material properties can be achieved in different ways which may lead to different levels of knowledge, depending on the level of detail provided by the survey plans and on the availability and reliability of information about the design. Therefore, the reliability of the structural properties considered in the seismic safety assessment will depend on the correlation between the amount of knowledge gathered about the structure and the confidence about that data. Still, to account for the existing uncertainty, the structural properties need to be defined with values that are on the "safe side".

The current European standard for the seismic safety assessment of existing buildings is the Eurocode 8-Part 3 (EC8/3) [1]. This standard specifies explicit rules regarding the assessment of structural properties in existing buildings, namely regarding the geometry, the structural details and the material properties. Survey plans are specified for all these components in order to conform to qualitative knowledge levels (KLs). Associated to each KL, EC8/3 defines a coefficient termed confidence factor (CF) that factors the mean material strength values in order to establish values that are on the "safe side" and to reduce the admissible capacity of the structural elements due to the uncertainty. The connection between the KLs and the CF values has been criticized (e.g. see [7-8]) due to the lack of objectivity behind the CF values. By only affecting the mean material properties, the CF does not reflect explicitly the remaining uncertainties, a fact that led to alternative interpretations of this parameter that consider the CF to be a factor only able to represent the uncertainty about the material properties. Rota *et al.* [9] modified the CF concept proposed by the EC8/3 and by the Italian standard NTC-08 [5] and defined a coefficient accounting only for the uncertainty in the material properties. The framework they developed assumed that a multiple uncertainty approach would be more adequate than the methodology proposed by the standards. Monti and Alessandri [10] and Romão *et al.* [11] presented two generic methods that provide a probability-based approach to calibrate a coefficient CF_{mat} accounting for the uncertainty in the material properties. These generic methods formulate coefficients that

depend on the statistical analysis of a given number of tests that are performed in the structure to assess the material properties.

The present study follows the fundamental concepts adopted in [11] to derive an alternative safety factor CF_{mat} for the mean value of a material strength in existing reinforced concrete (RC) buildings. The fact that the approach in [11] does not include explicitly the sampling uncertainty and material strength disaggregation will be addressed by the methodology proposed herein. This approach will introduce an adaptive probability-based formulation defining a set of sampling plans and CF_{mat} values (similar to the concepts of KLs proposed in EC8/3) based on finite population statistics. A comparison will be also made with the original CF values proposed by EC8/3 in order to check the maximum variability level of the material properties (represented by the coefficient of variation, CoV) that is compatible with the approach presented in the code. Furthermore, a survey framework will be presented that includes the definition of different CF_{mat} values for the concrete compressive strength and for the reinforcing steel yield strength and that specifies the different number of tests that have to be performed to characterize these material properties.

4.2 Brief review of current standard-based methods to assess material properties in existing buildings

Standards for the seismic safety assessment of existing RC buildings establish that a given number of tests must be carried out in a structure to determine the material properties, namely to characterize the concrete compressive strength and the yield strength of the reinforcement. According to these standards, material properties can be characterized by performing destructive tests on a number of material samples extracted from the structural members. Due to the destructive nature of this approach and the costs that it may involve (both direct and indirect), standards also suggest the use of non-destructive tests (NDTs) to complement the data obtained from destructive testing. Still, no specific rules on how to include these auxiliary results are defined. To provide additional details regarding the context of the present study, the procedures proposed by some of these standards are briefly reviewed in the following.

4.2.1 Eurocode 8 – Part 3

EC8/3 defines the minimum number of material samples that must be tested by defining, for each storey and each type of member, the number of tests that guarantees a certain KL. EC8/3 establishes three KLs: KL1, KL2 and KL3, which are termed Limited, Comprehensive and Full, respectively. For each KL, EC8/3 assigns a CF that will act as a safety factor for the mean value of the material properties accounting for the uncertainty induced by the material sampling plan. The values of the CFs proposed by EC8/3 are 1.35, 1.20 and 1.00 for KL1, KL2 and KL3, respectively. No distinction is made in the code between the concrete compressive strength and

the reinforcing steel yield strength regarding the number of tests that need to be performed and the CF values that are adopted for these two properties. For KL3, three concrete cores and three samples of reinforcing steel bars from each storey and from each type of element must be tested. The number of samples that must be tested is reduced to two and to one for KL2 and KL1, respectively.

4.2.2 Italian standard NTC-08

The Italian standard NTC-08 [5] follows a strategy that is similar to that of EC8/3 by proposing the same three KLs. For the case of the concrete strength, this standard also introduces a guidance related to what can be regarded as an area with a potentially homogeneous concrete strength. This standard states that the minimum number of material tests must be performed over surface areas smaller than 300 m^2. Accordingly, for KL1, one core test must be performed for each type of element, for each storey and for each 300 m^2 of construction surface area. For KL2 and KL3, the number of concrete cores that have to be tested is two and three, respectively. To characterize reinforcing steel, the minimum number of tests set by the standard is the same as for concrete but without enforcing the surface area limitation criterion. The values defined by EC8/3 for the CFs of KL1, KL2 and KL3 are also adopted by the Italian standard.

4.2.3 Romanian standard P100-3

The Romanian standard P100-3 [12] follows a material assessment approach similar to that of NTC-08 but sets different minimum values for some of the parameters. The minimum number of concrete core tests that need to be carried out and that P100-3 adopts are referred to a construction area that must not be larger than 1000 m^2. Furthermore, these minimum number of tests are now two, four and six for KL1, KL2 and KL3, respectively, for each type of element and for each 1000m^2 of construction surface area. Still, the CF values proposed by EC8/3 are also adopted by P100-3.

4.2.4 ASCE 41-13

The standard ASCE 41-13 [13] defines the material property assessment procedures according to two levels (termed Usual and Comprehensive). Furthermore, it also includes different survey plans to assess the concrete compressive strength and the yield strength of reinforcing steel. For the Usual material assessment level, the evaluation of the concrete strength can be divided in two cases. If the analyst has information about the concrete design strength, at least one core must be extracted from structural components of each different concrete class and the minimum number of cores that need to be tested from the building is three. When the design strength is unknown, at least one core must be extracted from each type of structural component and the minimum number of cores that need to be tested from the building is now six. For reinforcing steel, two

cases are also defined for the Usual material assessment level. If design information is available, nominal values of the yield strength can be adopted without the need for testing. If such design data is unavailable, at least two reinforcing steel bars must be extracted from the building for testing.

Regarding the second level of material assessment defined by ASCE 41-13 (Comprehensive), the minimum number of concrete cores that need to be tested is also divided in cases where design information is available and where it is missing. If the concrete strength specified in the design is known but no additional test data is available, a minimum of three cores must be tested from each storey, each 306 m^3 of concrete or each 929 m² of surface area. When the design concrete strength is unknown and no additional information exists, a minimum of six cores must be tested instead for the same conditions regarding location, surface area and concrete volume. In addition, this standard also specifies that if the CoV of the concrete core test results is higher than 0.20, additional tests must be performed until it is lower than or equal to 0.20. If the additional tests do not reduce the CoV, a knowledge factor of 0.75 must be used to reduce the structural element capacity in the seismic safety assessment (this standard does not reduce the material strength values as the previously analysed standards). To assess the reinforcing steel characteristics, three cases are distinguished for the Comprehensive material assessment. If construction documents are available, at least three reinforcing steel samples must be tested for each type of element. When no information is available about the reinforcing steel grade but the date of the construction is known and the expected reinforcing steel properties are confirmed, at least three samples must be tested for every three storeys and for each type of element. Finally, if the construction date is unknown, at least six steel samples must be tested for every three storeys.

4.3 Scope of the proposed CF$_{mat}$ safety factor for the mean material strength

It can be seen from the previous section that existing standards for the seismic safety assessment of existing RC buildings do not provide a unified approach to assess material strength properties and none of the available approaches controls adequately the uncertainty of the in-situ assessment. More specifically, the referred standards involve different approaches to establish the number of tests that need to be performed to estimate the material strength properties and do not address the statistical uncertainty associated to these survey plans. Furthermore, it is likely that different materials may require different assessment approaches given the differences in their expected variability. ASCE 41-13 addresses this aspect by defining different testing plans for the concrete compressive strength and the reinforcing steel yield strength, but does not provide a specific rationale to justify those survey plans. Conversely, since the procedure defined by EC8/3 to assess the material properties is disaggregated by storey and by structural element, only the expected construction sequence of a building is likely to be reflected. Since EC8/3 assigns the same CF

values for the concrete strength and the reinforcing steel yield strength, the CF values are disconnected from the expected variability of the materials. Romão *et al.* [11] addressed this situation by proposing CF$_{mat}$ factors for the reduction of the mean material strength according to the expected statistical distribution of the material strength and to the number of tests (*n*) being performed. The proposed methodology was generic and was used to calibrate specific factors for the mean value of the concrete compressive strength. Nonetheless, in this framework as in others (e.g. see14]), the uncertainty in the estimates of the material properties depends only on *n* and does not include any reference to the size and the number of structural elements of the building. However, if the total number of structural elements *N* is accounted for when defining the survey framework, an explicit control of the sampling uncertainty associated to the number of structural elements where the material strength is not assessed can be achieved.

The methodology proposed herein to derive CF$_{mat}$ safety factors extends the original methodology proposed in [11] to include the fact that a building or a region of the building can be divided into *N* structural elements having an expected homogeneous class of the material strength under assessment (as discussed in Chapter 2 and in [18]). By assuming this finite number of elements, finite population statistics can be considered to define safety factors for the mean value of material strength that account for the uncertainty associated to the survey sampling. When defining *N*, the *discrete structure* concept is also adopted where each structural member is assumed to be represented by a single strength value, which can be obtained from a reliable (destructive) test performed on a material sample from that element. Therefore, for each disaggregated region of *N* structural elements, the CF$_{mat}$ safety factors are defined considering that only a sample of *n* out of *N* structural elements are tested and that a prior estimate for the material variability (i.e. the CoV) in that region is available.

To derive the referred CF$_{mat}$ safety factors, a critical situation in terms of safety also has to be defined. As mentioned before, EC8/3 refers that the estimates of the mean material strength must be divided by the CF in order to obtain values that have an adequate safety level. Furthermore, the value of CF is seen to be larger when there is less knowledge about the material. Hence, the underlying critical safety condition justifying the need for the CF reflects a situation where the estimate for the mean material strength overestimates the real value. Therefore, this critical safety condition also needs to be included in the probabilistic quantification of the CF$_{mat}$ safety factors proposed herein. Finally, it is noted that the development of the CF$_{mat}$ safety factors presented in the following assumes that the statistical distribution of the material strength can be represented by a normal or a lognormal distribution.

4.4 Definition of the CF$_{mat}$ safety factor for the mean material strength

4.4.1 Definition of CF$_{mat}$ for the case of a normal distributed strength with known variance

The proposed CF$_{mat}$ safety factor addresses the material strength assessment of a finite population of N members by establishing a confidence interval for the finite population mean. This interval is similar to the common confidence interval for the mean but with the addition of a finite population correction factor which reflects the importance of the relative size of the sample. This correction is based on the fact that when selecting a sample of size n from a finite population of size N that follows a normal distribution, the sample mean $\hat{\bar{x}}_U$ follows a normal distribution with a mean equal to the true mean $\bar{x}_U$ of the population and a standard deviation $\sigma_{\hat{\bar{x}}_U}$ given by [15]:

$$\sigma_{\hat{\bar{x}}_U} = \sqrt{S(\hat{\bar{x}}_U)} = \sigma_U \cdot \frac{1}{\sqrt{n}} \cdot \sqrt{\frac{N-n}{N-1}} = \sigma_U \cdot \beta_{CoV} \tag{1}$$

where σ_U is the standard deviation of the population of size N, $S(\hat{\bar{x}}_U)$ is the variance of the sampling mean and β_{CoV} is an uncertainty factor that reflects the uncertainty in the estimate of the finite population mean. By standardizing $\hat{\bar{x}}_U$, variable Z is obtained:

$$Z = \frac{\hat{\bar{x}}_U - \bar{x}_U}{\sigma_U \cdot \frac{1}{\sqrt{n}} \cdot \sqrt{\frac{N-n}{N-1}}} = \frac{\hat{\bar{x}}_U - \bar{x}_U}{\sigma_U \cdot \beta_{CoV}} \tag{2}$$

which follows the standard normal distribution. Using this distribution, the following probability can be obtained:

$$P\left(-z_{1-\frac{\alpha}{2}} \leq \frac{\hat{\bar{x}}_U - \bar{x}_U}{\sigma_U \cdot \beta_{CoV}} \leq z_{1-\frac{\alpha}{2}}\right) = 1 - \alpha \tag{3}$$

where $z_{1-\frac{\alpha}{2}}$ is the $(1-\frac{\alpha}{2})$ percentage point of the standard normal distribution. Alternatively, if only a one-sided lower bound is needed, the following probability is obtained by modifying Eq. (3):

$$P\left(\frac{\hat{\bar{x}}_U - \bar{x}_U}{\sigma_U \cdot \beta_{CoV}} \leq z_{1-\alpha}\right) = 1 - \alpha \tag{4}$$

where $z_{1-\alpha}$ is the $(1-\alpha)$ percentage point of the standard normal distribution.

Based on the critical safety condition previously defined where the estimate for the mean $\hat{\bar{x}}_U$ is expected to exceed its real value $\bar{x}_U$, it is seen that the CF$_{mat}$ safety factor must verify the condition:

$$\frac{\bar{x}_U}{\text{CF}_{mat}} \le \bar{x}_U \leftrightarrow \text{CF}_{mat} \ge \frac{\hat{\bar{x}}_U}{\bar{x}_U} \tag{5}$$

Therefore, the minimum value of CF_{mat} that still verifies the critical safety condition is:

$$\text{CF}_{mat} = \frac{\hat{\bar{x}}_U}{\bar{x}_U} \tag{6}$$

Combining Eq. (6) with Eq. (4) yields:

$$P\left(\text{CF}_{mat} \le 1 + z_{1-\alpha} \cdot \text{CoV}_U \cdot \beta_{\text{CoV}}\right) = 1 - \alpha \tag{7}$$

where CoV_U is the CoV of the N material strength values. Eq. (7) states that, for an expected value of the population CoV_U there is a $(1-\alpha)$ probability that $\text{CF}_{mat} \le 1 + z_{1-\alpha} \cdot \text{CoV}_U \cdot \beta_{\text{CoV}}$ if $\bar{x}_U = \frac{\hat{\bar{x}}_U}{\text{CF}_{mat}}$. Accordingly, the $(1-\alpha)$ upper confidence bound for CF_{mat} is given by:

$$\text{CF}_{mat} \le 1 + z_{1-\alpha} \cdot \text{CoV}_U \cdot \beta_{\text{CoV}} \tag{8}$$

Since one is interested in establishing a safety factor that will define a limiting value for the mean material strength that is consistent with the critical safety condition previously defined, the maximum value of CF_{mat} conforming to the condition set by Eq. (8) must then be adopted:

$$\text{CF}_{mat} = 1 + z_{1-\alpha} \cdot \text{CoV}_U \cdot \beta_{\text{CoV}} \tag{9}$$

Therefore, for a given survey plan (involving n out of N structural elements where the material strength is evaluated), CF_{mat} establishes a safety factor for the mean value of the material strength that is compatible with the lower limit of the $(1-\alpha)$ confidence interval that is believed to include the real mean $\bar{x}_U$ (Eq. (4)). To quantify CF_{mat}, CoV_U needs to be known, but a realistic estimate $\text{CoV}|N$ of its expected value can be used instead. This estimate can be defined using values from the literature or survey data from different types of material property tests. Further details regarding the definition of $\text{CoV}|N$ for specific materials will be addressed in a later section. In order to simplify the applicability of the formulation, the following approximation was introduced that removes the dependence of β_{CoV} on N:

$$\beta_{\text{CoV}} = \frac{\left(0.20 - 0.14\frac{n}{N}\right)}{\left(0.22 + \frac{n}{N}\right)} \tag{10}$$

The approximation yields adequate estimates of β_{CoV} for N values between 12 and 30 which represents a typical value for the number of structural elements that is expected to be found in a region (e.g. a storey) in RC frame buildings. In order to observe the evolution of CF_{mat}, Fig. 1 presents the evaluation of Eq. (9) for different values of CoV|N (from 0.10 to 0.45 in steps of 0.05), for different values of the relative sample size n/N and for different values of the $(1-\alpha)$ confidence level. The minimum value of CoV|N was set to 0.10 since a given material strength will always be affected by multiple sources of uncertainty and it is considered that eliminating all these sources is not feasible for materials used in RC buildings. The maximum value of CoV|N was set to a conservative value of 0.45 that reflects a case with significant heterogeneity in the material properties of a building (e.g. due to a lack of construction or material quality). Four $(1-\alpha)$ confidence levels were also considered to calculate the values for CF_{mat}: 0.75, 0.85, 0.90 and 0.95.

Figure 1. Evolution of CF_{mat} for different variability levels and confidence levels assuming that the material strength follows a normal distribution: a) $1-\alpha = 0.95$, b) $1-\alpha = 0.90$, c) $1-\alpha = 0.85$ and d) $1-\alpha = 0.75$.

As discussed in [11], even though there is no evident rationale for the use of these values, they are often referred in the literature as adequate values for ordinary and important structures [16-17]. As expected, the results of Fig. 1 indicate that, irrespective of the selected confidence level, CF_{mat} will tend to 1.0 as the ratio n/N also approaches 1.0. Furthermore, it can also be seen that

depending on the selected confidence level and on the expected value of CoV|N, CF$_{mat}$ can take values that are higher than the CF values proposed by the standards previously referred.

4.4.2 Definition of CF$_{mat}$ for the case of a lognormal distributed strength with known variance

When considering that the material strength follows a lognormal distribution with known variance, an approach similar to that of the normal distribution can be adopted. When considering a random sample of a variable Y extracted from a population having N elements that follow a lognormal distribution with unknown population mean $\bar{y}_U$ and known standard deviation σ_{Uy}, the variable X = ln(Y) will follow a normal distribution with mean $\bar{x}_{Ux}$ and standard deviation σ_{Ux}. From the confidence interval defined by Eq. (4), it is known that:

$$\hat{\bar{x}}_{Ux} - z_{1-\alpha} \cdot \sigma_{Ux} \cdot \beta_{CoV} \leq \bar{x}_{Ux} \tag{11}$$

which, by adding $\sigma_{Ux}^2/2$ to both sides and applying the exponential transformation, leads to:

$$e^{\hat{\bar{x}}_{Ux} + \frac{\sigma_{Ux}^2}{2}} \cdot \frac{1}{e^{z_{1-\alpha} \cdot \sigma_{Ux} \cdot \beta_{CoV}}} \leq e^{\bar{x}_{Ux} + \frac{\sigma_{Ux}^2}{2}} \tag{12}$$

where $e^{\hat{\bar{x}}_{Ux} + \frac{\sigma_{Ux}^2}{2}}$ represents parameter $\bar{y}_U$, i.e. the mean of the lognormal variable Y. Similarly, $e^{\hat{\bar{x}}_{Ux} + \frac{\sigma_{Ux}^2}{2}}$ is the sampling estimate for the mean of variable Y, i.e. $\hat{\bar{y}}_U$. Therefore, Eq. (12) can be rewritten as:

$$\hat{\bar{y}}_U \cdot \frac{1}{e^{z_{1-\alpha} \cdot \sigma_{Ux} \cdot \beta_{CoV}}} \leq \bar{y}_U \tag{13}$$

By the properties of the lognormal distribution, the standard deviation of the associated normal variable X can be replaced by:

$$\sigma_{Ux} = \sqrt{\ln\left(CoV_{Uy}^2 + 1\right)} \tag{14}$$

where CoV_{Uy} is the CoV of Y. Combining Eq. (13) with Eq. (14) then leads to:

$$\hat{\bar{y}}_U \leq \bar{y}_U \cdot e^{z_{1-\alpha} \cdot \sqrt{\ln\left(CoV_{Uy}^2 + 1\right)} \cdot \beta_{CoV}} \tag{15}$$

Considering that the critical safety condition is now defined as the case where the estimate of the mean $\hat{\bar{y}}_U$ exceeds its real value $\bar{y}_U$, the CF$_{mat}$ safety factor must verify the condition:

4.10

$$\frac{\hat{\bar{y}}_U}{CF_{mat}} \leq \bar{y}_U \leftrightarrow CF_{mat} \geq \frac{\hat{\bar{y}}_U}{\bar{y}_U} \tag{16}$$

As before, the minimum value of CF_{mat} that still verifies the critical safety condition is:

$$CF_{mat} = \frac{\hat{\bar{y}}_U}{\bar{y}_U} \tag{17}$$

Combining Eq. (17) with Eq. (15) and considering a rationale similar to the one that was assumed for the case where the material strength follows a normal distribution (see Eqs. (7) and (8)) yields:

$$CF_{mat} = e^{z_{1-\alpha} \cdot \sqrt{\ln(CoV_{Uy}^2 + 1)} \cdot \beta_{CoV}} \tag{18}$$

As in the case of the normally distributed material strength, the parametric definition of CF_{mat} depends on the expected value of CoV_{Uy} which is also termed CoV|N herein. In order to observe the evolution of CF_{mat} for this case, Fig. 2 presents the evaluation of Eq. (18) following the same considerations that were assumed for the case where the material strength follows a normal distribution regarding the range of the selected values for the confidence levels and for CoV|N.
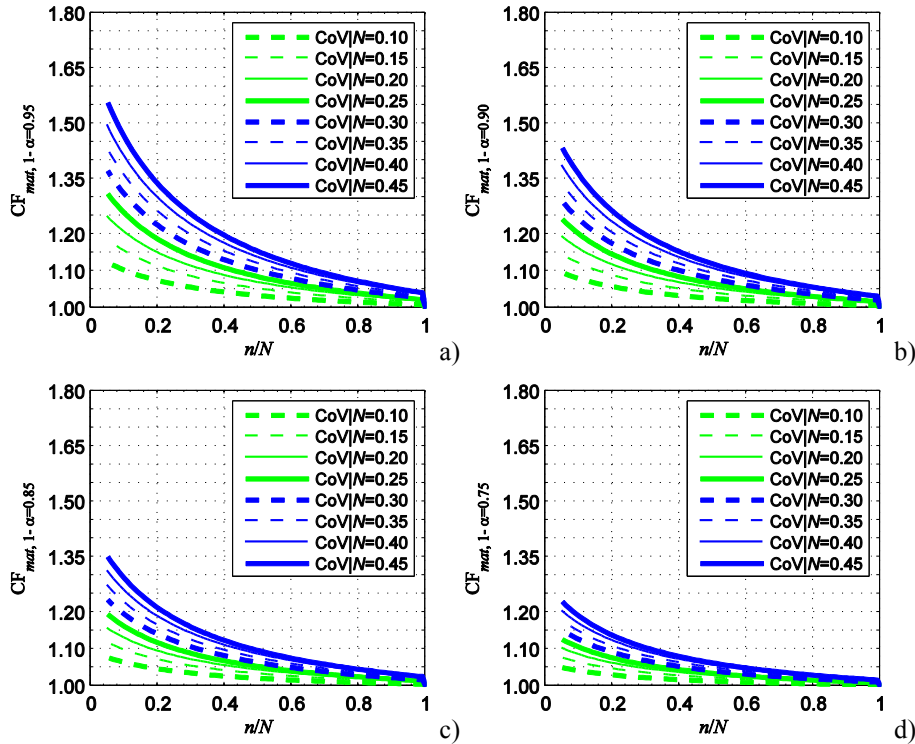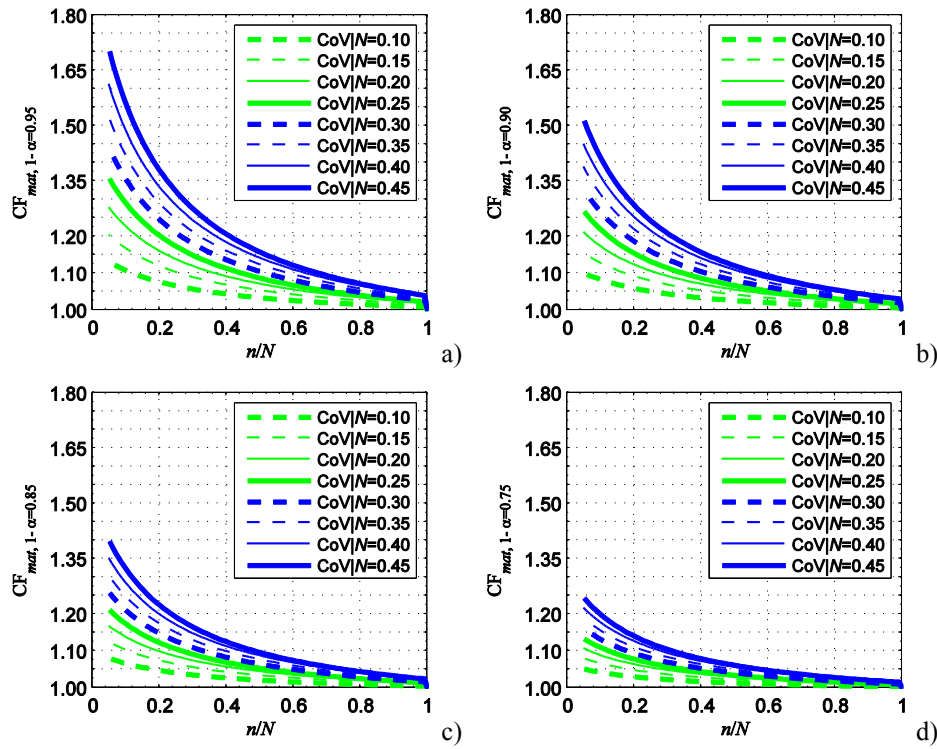

Figure 2. Evolution of CF_{mat} for different variability levels and confidence levels assuming that the material strength follows a lognormal distribution: a) 1-α=0.95, b) 1-α=0.90, c) 1-α=0.85 and d) 1-α=0.75.

The results of Fig. 2 can be seen to exhibit an evolution trend similar to that of the results presented in Fig. 1. However, the CF_{mat} values are seen to be larger in this case than for the case of the normally distributed material strength, especially for lower values of the ratio n/N and for the higher values of CoV|N.

4.5 Calibration of a survey framework to assess material strength in RC buildings

Since the formulation for the proposed CF_{mat} safety factor is similar to the interpretation made by several authors [10-11] regarding the CF proposed by EC8/3, a survey framework compatible with EC8/3 based on the CF_{mat} safety factor was analysed herein. The survey framework includes a direct connection between the CF_{mat} safety factors and the KLs and assumes that, for the seismic safety assessment, the mean value of the material strength needs to be factored by CF_{mat} to quantify certain parameters, as defined by EC8/3.

The fundamental change that is introduced by the proposed survey framework refers to the connection between the characteristics of the survey plan and the value of the adopted CF_{mat} safety factor. Currently, EC8/3 considers CFs that factor the mean value of the material strength independently of the type of material and that are connected to predefined sampling plans. Instead, a new set of CF_{mat} safety factors that depend on a prior estimate of the variability (thus depending on the material) and on the relative number of tested structural components, n/N, is proposed. This proposal overcomes inconsistencies found in the EC8/3 framework that does not account for the total number of structural elements under assessment and does not consider any information about the variability of the material strength to establish the CFs. The proposed survey plans are first discussed in the current section without associating them to a specific material being assessed. The applicability of this general approach to the cases of concrete compressive strength and reinforcing steel yield strength is discussed in Section 4.6.

4.5.1 Alternative definition of the minimum number of tests for each knowledge level (KL)

The proposed survey plans are established for regions of a building where the material properties are believed to be physically homogeneous. An example of these regions refers to the storey differentiation referred in EC8/3, which reflects the expected construction sequence of a building or the disaggregation in groups of storeys proposed by ASCE 41-13 to assess the reinforcing steel properties. Each one of these regions is made of N structural elements, and each element is assumed to have a single material strength value.

For each region made of N structural elements, a different relative number of tested elements can be defined that will reflect different KLs about the material properties. Therefore, the proposed procedure establishes minimum values for this relative number of tests n/N for the three KLs of EC8/3 instead of proposing an absolute number of tests that has to be carried out. The proposed

survey plans involve the assessment of the material properties in a minimum number of elements corresponding to n/N ratios equal to 0.1, 0.2 and 0.3 for KL1, KL2 and KL3, respectively. Hence, a higher level of knowledge is obtained when going from KL1 to KL3. For KL3, the relative sample size of $n/N = 0.3$ was established in order to provide a balanced solution between the uncertainty in the estimate for the mean material strength and the structural damage induced to the building during the survey operations [18]. Based on the n/N value set for KL3, values for KL2 and KL1 were defined in order to reflect a reduction in the amount of collected information that would be compatible with the corresponding reduction in the KL. Hence, the suggested sampling plans involving relative sample sizes of $n/N = 0.2$ and $n/N = 0.1$ reflect a proportional reduction in the number of tests from KL3 to KL2 and from KL2 to KL1, respectively.

To illustrate the proposed survey plans, Fig. 3 presents the evolution of the minimum number n of structural members that need to be tested in regions with a different total number of members (i.e. different values of N). The values of n presented in Fig. 3 were obtained by rounding up the product between the proposed n/N ratios and each value of N to the nearest following integer. In addition, a complementary condition setting that n must not be lower than two was also enforced for all KLs (two structural members have to be tested to be able to compute the mean value).
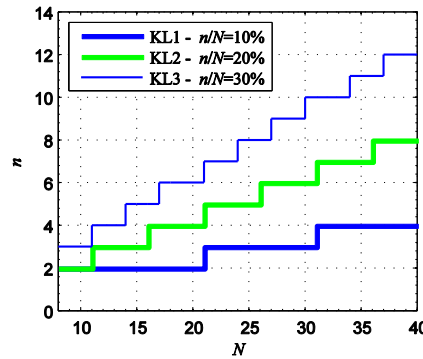
Figure 3. Variation of the absolute number of tests n for the proposed KLs according to the total number of elements N in the region where the material strength needs to be assessed.

Results show that for KL1 the number of tests n that is required increases when the value of N increases by ten, e.g. for $11 \leq N \leq 20$, n is 2, for $21 \leq N \leq 30$, n is 3, etc. The relation found for KL2 shows the increase in the number of tests that is required occurs when the value of N increases by five, e.g. for $8 \leq N \leq 10$, n is 2, for $11 \leq N \leq 15$, n is 3, etc. For the case of KL3, the relation found shows the required number of tests increases when the value of N increases by three or four, e.g. for $11 \leq N \leq 13$, n is 4, for $14 \leq N \leq 16$, n is 5, for $17 \leq N \leq 20$, n is 5, etc. These trends were only analysed up to an N value of forty since it was assumed that an N value in this range is representative of the maximum number of structural members of the same type that may be found in an area of 320 m^2 (the maximum admissible size of a homogeneous region according to the limit suggested in the Italian standard [5]). If only eight or less structural members are

present in the region, a minimum of two tests is always necessary for KL1 and KL2, and a minimum of three tests is required for KL3. As an example, considering a building storey with twenty structural members (i.e. $N = 20$), a minimum of two tests is required for KL1, four tests for KL2 and six tests for KL3.

4.5.2 Definition of CF_{mat} compatible with the proposed knowledge levels and survey plans

To complete the integrated KL-CF_{mat} method proposed herein, a correlation has to be made between the formulation proposed for the CF_{mat} safety factors and the survey plans/knowledge levels defined in the previous section. To analyse this correlation, Fig. 4 presents the evolution of the CF_{mat} values as a function of increasing values of CoV|N, for different (1-α) confidence levels ranging from 0.75 to 0.95, in steps of 0.05, and for the three KLs previously defined in terms of n/N.
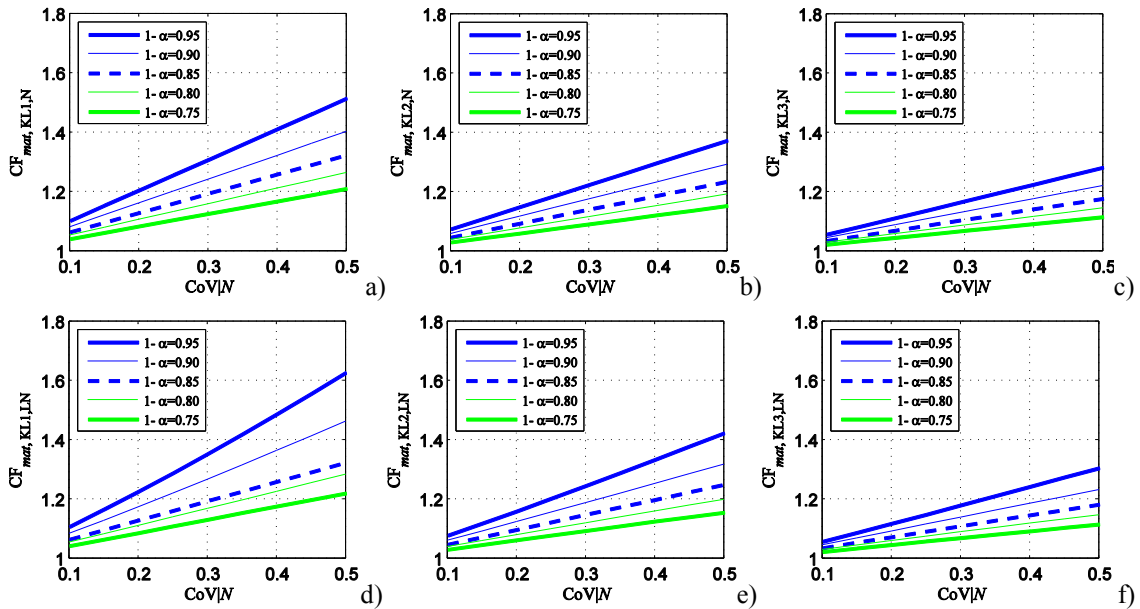
Figure 4. Evolution of CF_{mat} for different KLs assuming a normal distribution (KL1, (a); KL2, (b); KL3, (c)) and a lognormal distribution (KL1, (d); KL2, (e); KL3, (f)).

The results based on the normal distribution (i.e. Eq. (10)) are presented in Fig. 4a (KL1), Fig. 4b (KL2) and Fig. 4c (KL3), while those based on the lognormal distribution (i.e. Eq. (18)) are presented in Fig. 4d (KL1), Fig. 4e (KL2) and Fig. 4f (KL3). A global analysis of the results of Fig. 4 indicates that, for each KL and for all the selected confidence levels, the values of CF_{mat} are larger when assuming a lognormal distribution. These differences, and the fact that it represents a more conservative approach, indicate that this model is more adequate to define the values of CF_{mat} within a safety assessment perspective where no information about the distribution shape is available. After setting this condition, it is necessary to decide which confidence level should be assigned to each KL. Little guidance can be found with respect to the selection of an adequate confidence level to establish material strength values. Still, some rationale seems to exist

regarding the bounds for possible values of the confidence level. As referred in [11], a minimum confidence level of 0.75 is generally considered in the context of structural assessment. On the other hand, it is common to find the value of 0.95 being suggested as a maximum value for all practical purposes. As can be seen from Fig. 4, all KLs exhibit significant differences between the CF_{mat} values obtained for the 0.95 and 0.75 confidence levels. On the other hand, the results obtained for the 0.85 and the 0.80 confidence levels are very similar. In addition, the results obtained for the 0.85 confidence level are closer to those obtained for the 0.75 confidence level than to those of the 0.95 confidence level.

Given these results, the maximum confidence level analysed, i.e. 0.95, could be recommended in order to be more confident that the true unknown mean will not be lower than the estimate corrected by the CF_{mat}. Figure 5a presents the three curves representing the interconnection between the KL and CF_{mat} assuming a constant 0.95 confidence level for all KLs. However, since the three KLs are associated with three different amounts of available data, the case where the confidence level associated to the CF_{mat} of each KL could be different was also analysed.
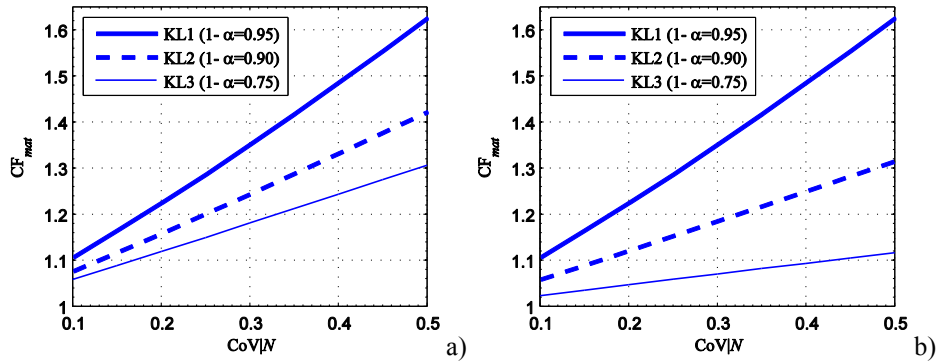
Figure 5. Evolution of CF_{mat} for the selected KL levels assuming a) a 0.95 confidence level and b) variable confidence levels depending on the amount of information provided by the survey plan compatible with the KL.

Therefore, instead of selecting the same confidence level for all the KLs, one may alternatively require a higher confidence level (i.e. a larger confidence interval) for KL1 since there is less information for that KL. For the remaining KLs, lower confidence levels (i.e. with smaller confidence intervals) may be progressively established. This fact can be analysed bearing in mind the reduction of the sampling uncertainty about the mean that is obtained when n/N increases. Hence, if one assumes a maximum confidence level of 0.95 for the case where n/N is lower (i.e. KL1), the minimum confidence level of 0.75 can be associated to the case where n/N is larger (KL3). An intermediate confidence level may then be established for KL2. Since the reduction of CF_{mat} is approximately 50% from a confidence level of 0.90 to a confidence level of 0.75, the value of 0.90 was assumed for the intermediate level of knowledge (KL2). Figure 5b presents the three curves representing the interconnection between the KL and CF_{mat} assuming different

confidence levels for each KL. As expected, this approach leads to lower CF_{mat} safety factors for KL2 and KL3 than the one where a confidence level of 0.95 is assumed (Fig. 5a).

4.6 Comparison between the EC8/3 CF values and the proposed CF_{mat} values

The CF_{mat} safety factor established for the three KLs can be compared with the CF values proposed by other standards. As referred before, EC8/3 and the Italian code propose a similar approach regarding the survey operations that are needed to assess material strength. Still, it must be noted that the CF value proposed by these standards for KL3 (CF = 1.0) is unrealistic unless the material strength is assessed in all the structural members. Given the CF values these standards propose for KL2 and KL1, 1.20 and 1.35, respectively, a reference value of 1.10 is proposed for the CF of KL3 for the purpose of the following analysis. To analyse the two approaches, Fig. 6 shows the comparison of the (fixed) CF-KL1$_{EC8/3}$, CF-KL2$_{EC8/3}$ and CF-KL3$_{EC8/3}$ factors associated to the KLs according to EC8/3, and the (variable) CF_{mat} safety factors considering the different confidence levels previously assigned.
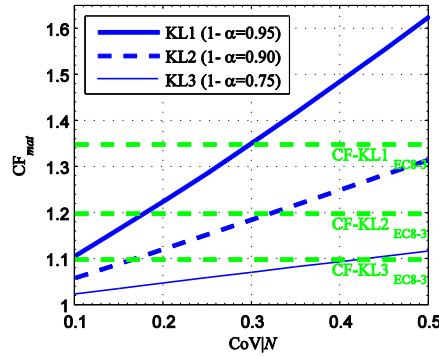
Figure 6. Evolution of CF_{mat} for the selected confidence levels of each KL and comparison with the CFs proposed by EC8/3 and the Italian standard considering variable confidence levels.

By comparing the CF values and the evolution of the proposed CF_{mat} safety factors, it can be seen that for both approaches to be compatible, the admissible variability of the material property (i.e. CoV|N) must be limited. By analysing the range of CoVs for which CF-KL1$_{EC8/3}$ and CF-KL2$_{EC8/3}$ cross their corresponding CF_{mat} curve (CF-KL3$_{EC8/3}$ was left out since 1.10 is not the true value proposed by the standards), it can be seen that CoV|N should be limited to a value around 0.30. For KL1, a CoV|N of 0.30 leads to a CF_{mat} value of 1.34 while, for KL2, a CF_{mat} value of 1.18 is obtained. For KL3, the CF_{mat} value corresponding to a CoV|N of 0.30 is 1.07.

Based on this analysis, the CF values proposed by EC8/3 and the Italian standard for KL1 and KL2 can only be found to be acceptable for the purpose of defining a safe value of the mean material strength as long as CoV|N is lower than 0.30. For the case of KL3, the proposed approach based on CF_{mat} leads to a more statistically sound proposal since the CF value of 1.0 proposed by

the EC8/3 and the Italian standard is unrealistic. Nonetheless, the standard-based CF values will lead to over conservative values of the mean material strength when $\text{CoV}|N$ is significantly lower than the referred limit of 0.30. Therefore, an approach defining a CF_{mat} that varies according to the level of material strength variability that is found (or expected) during the assessment is seen to be more flexible and useful. As such, this approach enables the definition of different CF_{mat} values for different types of materials.

4.7 Defining CF*mat* safety factors for concrete and reinforcing steel

EC8/3 defines KLs and CFs for the assessment of material properties without distinguishing the type of material. Therefore, according to the European code, the same number of structural elements should be tested in each storey of a RC building for the quantification of the concrete compressive strength and the reinforcing steel yield strength. On the contrary, since the proposed integrated KL-CF$_{mat}$ method depends on an estimate of the material strength variability $\text{CoV}|N$, different strategies and different CF$_{mat}$ values can be defined for these two different materials.

For the case of the concrete compressive strength, a CF$_{mat}$ termed CF$_{conc}$ can be defined which will depend directly on the estimate of the dispersion of the N concrete stength values $\text{CoV}_{fc}|N$. As shown in previous studies [18-19], estimating the $\text{CoV}_{fc}|N$ using a small sample of results from concrete core tests may lead to estimates that do not reflect the real variability of the concrete strength. This fact is even more relevant due to the high value of the concrete strength $\text{CoV}_{fc}|N$ that is usually found in existing buildings [20-23], often exceeding a value of 0.20 [24]. A methodology improving the accuracy of the estimate of $\text{CoV}_{fc}|N$ by using rebound hammer tests was proposed in Chapter 3. Using results of the rebound hammer test, i.e the rebound numbers (RNs), carried out in a minimum number of $n/N = 0.30$ elements in a region, the methodology determines their variability, $\text{CoV}_{RN}|n$, and converts it into an equivalent value of $\text{CoV}_{fc}|N$ using an empirical model. Details on the adequacy of this methodology to estimate the concrete strength variability can be found in Chapter 2. Alternatively, a conservative approach can be adopted to establish generic values for CF$_{conc}$. Given the range of values reported in the literature (e.g. see [20-24]), a $\text{CoV}_{fc}|N$ of 0.30 can be considered to be a conservative estimate of the concrete strength variability. According to Fig. 6 and to the assumptions it involves (see Sections 4.5.2 and 4.5.3), the CF$_{conc}$ values that are obtained by considering a $\text{CoV}_{fc}|N$ of 0.30 are 1.34, 1.18 and 1.07, for KL1, KL2 and KL3, respectively. However, for simplicity, it is suggested to round these values and define the CF$_{conc}$ values as 1.35, 1.20 and 1.10 for KL1, KL2 and KL3, respectively.

For the case of reinforcing steel, common values for the $\text{CoV}|N$ of the rebar yield strength are generally less than 0.10. Several studies characterizing the steel yield strength can be found in the literature to support this level of variability. For example, experimental results from [25] showed that for reinforcing steel bars with a nominal strength of 280 MPa, a CoV of 0.107 was found,

while for a nominal strength of 410 MPa, the variability decreased to 0.093. Moreover, experimental results from [26] showed that for reinforcing steel bars of the European class S400, a CoV of 0.047 was found, while for reinforcing steel bars of the European class S500, a CoV of 0.052 was obtained. The analysis of experimental results obtained by the autors from tensile tests of reinforcing steel bars extracted from an existing building led to the yield strength variations shown in Fig. 7. The tests were performed in reinforcing bars with Ø16 (mm) which were expected to conform with the European Class S500. A mean yield strength of 515MPa was found for the 31 tested samples, with a CoV of 0.06. Although these values can be assumed as a reference, a conservative estimate for CoV|N with a value of 0.10 might be more adequate for existing structures due to potential alterations in the characteristics of the reinforcing bars.
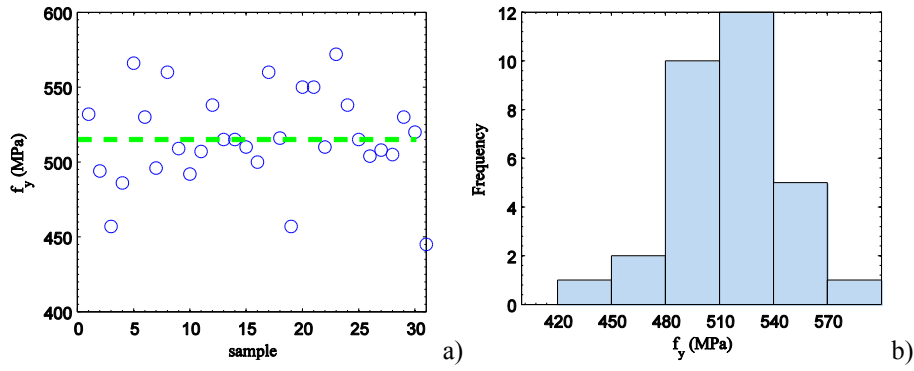
Figure 7. Experimental data representing the differences between the yield strength from reinforcing steel samples extracted from an existing RC building and the mean yield strength (dashed line) (a) and corresponding histogram of the experimental data (b).

Considering a CoV|N with a value of 0.10 for the reinforcing steel yield strength, CF$_{mat}$ (in this case termed CF$_{rs}$) values of 1.10, 1.06 and 1.02, for KL1, KL2 and KL3, respectively, are found to be compatible with Fig. 6 and the assumptions it involves. However, since repairing the damage caused by extracting reinforcing steel bar samples from a RC structure for testing is expected to be more expensive than repairing the holes left after extracting concrete cores (additional concrete needs to be removed to provide adequate lap splicing and formwork will also be needed), there are some practical advantages in revising the values of n/N that are proposed for the different KLs. Therefore, instead of considering n/N values of 0.10, 0.20 and 0.30 for KL1, KL2 and KL3, respectively, to characterize the reinforcing steel yield strength, a constant n/N value of 0.05 is now suggested. By analysing the results of Fig. 2 for a CoV|N of 0.10, it can be seen that the CF$_{mat}$ values corresponding to $n/N = 0.05$ are 1.13, 1.10 and 1.05, for KL1, KL2 and KL3, respectively. These CF$_{mat}$ values can be seen to be slightly larger than those obtained for the previous n/N values and suggest that CF$_{rs}$ values of 1.15, 1.10 and 1.05 can be proposed for KL1, KL2 and KL3, respectively, to characterize the mean yield strength of reinforcing steel involving the assessment of only $n/N = 0.05$ structural elements for all the KLs. It is noted that for lower values of N, the n/N=0.05 condition can lead to the need of only one test to estimate the reinforcing steel

yield strength in a region. Still, conceptually, a minimum of two tests is required to compute an estimate for the mean.

Based on the CF_{conc} and CF_{rs} values that were defined for the several KLs, Table 1 summarizes a proposal for a survey framework that can be used in a standard-based approach to assess the concrete compressive strength and the steel yield strength in existing RC buildings. This proposal defines sampling plans for concrete NDTs, concrete core compression tests and reinforcing steel sample tensile tests by specifying the minimum n/N number of tests that needs to be performed at each region made of N structural members (e.g. a storey) and for each type of structural element.

Table 1. Number of tests to be performed at each region made of N structural members

Knowledge Level	Concrete NDTs[*] (n/N)	Concrete Core Tests (n/N)	CF_{conc}[†]	Reinforcing Steel Tensile Tests (n/N)	CF_{rs}[‡]
(KL1) Limited	0.30	0.10	1.35	0.05	1.15
(KL2) Comprehensive	0.30	0.20	1.20	0.05	1.10
(KL3) Full	0.30	0.30	1.10	0.05	1.05

[*] Suggested values assume that NDTs are rebound hammer tests but other NDTs can also be used.
[†] Assuming that CoV|N of the concrete compressive strength is lower than 0.30.
[‡] Assuming that CoV|N of the steel yield strength is lower than 0.10.

4.8 Conclusions

The present study proposed an adaptive probability-based framework defining test sampling plans for existing RC buildings and new CF_{mat} material safety factors leading to mean material strength values that are on the "safe side". The development of the framework is also based on two essential concepts: 1) a building can be divided into one or more regions, where each region has N structural elements and is expected to exhibit a homogeneous class of the material strength under assessment; 2) each structural element from a given region is defined by a single value of the material strength under assessment. By assuming this finite number of elements and of material strength values in each region, the proposed framework uses finite population statistics to define CF_{mat} safety factors that consider the uncertainty associated to the number of tested structural elements in a region and the inherent variability of the material strength under analysis. Analytical expressions were defined for the CF_{mat} safety factors for the case where the material property is assumed to follow a normal distribution and for the case where it is assumed to follow a lognormal distribution. These expressions rely on the possibility of quantifying the expected material strength variability and possible approaches were discussed to estimate this variability.

The proposed framework was developed in order to be compatible with seismic safety assessment procedures defined by current standards such as EC8/3, namely by also considering the concept of KL and by defining test sampling plans and CF_{mat} safety factors in agreement with the KLs established by these standards. For these KLs, the definition of the CF_{mat} safety factors was analysed for different values of the expected material variability and for different confidence

levels. Based on these analyses, confidence levels of 0.95, 0.90 and 0.75 were proposed for KL1, KL2 and KL3, respectively, to establish a connection between the values of CF_{mat} and the KLs. A comparison between the proposed CF_{mat} safety factors and the CF values defined by EC8/3 showed that the latter can only provide conservative results (i.e. on the safe side) if the CoV of the material in the region being assessed is below 0.30.

Specific CF_{mat} safety factors were then defined for the concrete compressive strength and for the reinforcing steel yield strength, termed CF_{conc} and CF_{rs}, respectively that account for their different variability. Finally, specific values of the minimum number of destructive and non-destructive tests that have to be performed in a region of a RC building to characterise these material strength properties were also established. The format of the proposed test sampling plans and of the CF_{conc} and CF_{rs} safety factors is suitable for integration in standard-based procedures such as those of EC8/3 and overcomes some of their previously highlighted limitations.

4.9 References

1 CEN. Eurocode 8: design of structures for earthquake resistance. Part 3: Assessment and retrofitting of buildings. Brussels; 2005.

2 NZSEE. Assessment and Improvement of the Structural Performance of Buildings in Earthquake. Recommendations of a NZSEE Study Group on Earthquake Risk Buildings, New Zealand Society for Earthquake Engineering, New Zealand; 2006.

3 ASCE. Seismic evaluation of existing buildings (ASCE/SEI 31-03). American Society of Civil Engineers, Reston, Virginia, USA; 2004.

4 ASCE. Seismic rehabilitation of buildings (ASCE/SEI 41-06). American Society of Civil Engineers, Reston, Virginia, USA; 2007.

5 Circolare 2 febbraio 2009. n. 617 Approvata dal consiglio superiore dei Lavori Pubblici. Istruzioni per l'applicazione delle ''Nuove norme tecniche per le costruzioni'' di cui al decreto ministeriale 14 gennaio; 2008–2009 [in Italian].

6 ATC. Quantification of building system performance and response parameters. Applied Technology Council, Redwood City, California, USA; 2009.

7 Elefante L. Dealing with uncertainties in the assessment of existing RC buildings. PhD Dissertation, Università degli Studi di Napoli Federico II, Naples, Italy; 2009.

8 Franchin P, Pinto P, Rajeev P. Confidence factor?. J Earthq Eng 2010;14(7): 989–1007.

9 Rota M, Penna A, Magenes G. A framework for the seismic assessment of masonry buildings taking into account different sources of uncertainty. J Earthq Eng Struct Dyn 2014;43(7):1045–1066.

10 Monti G, Alessandri S. Application of Bayesian techniques to material strength evaluation and calibration of confidence factors. In: Cosenza E, editor. Eurocode 8 perspectives from the Italian standpoint workshop, 67–77, Doppiavoce, Naples, Italy; 2009.

11 Romão X, Gonçalves R, Costa A, Delgado R. Evaluation of the EC8-3 confidence factors for the characterization of concrete strength in existing structures. Mater Struct 2012;45(11):1737-1758.

12 MDRT. Seismic Design Code. Part III. Seismic assessment of existing buildings, Monitorul Oficial No. 647 bis (P 100-3/2008); 2009.

13 ASCE. Seismic Evaluation and Retrofit of Existing Buildings (ASCE/SEI 41-13). American Society of Civil Engineers, Reston, Virginia, USA; 2014.

14 Kog Y. Sample size for determining in situ strength of concrete in structures. Mag Concr Res 2012;64(11):1045–1048.

15 Levy P, Lemeshow J. Sampling of Populations: Methods and Applications, 4th ed. Wiley, New York; 2008.

16 Hindo K, Bergstrom W. Statistical Evaluation of the In-Place Compressive Strength of Concrete. Concr Int 1985;7(2):44-48.

17 Wong WF, Chiew SP, Ho NY .Evaluation of in situ test data from existing concrete structures. In: Dhir RK, Jones MR (eds) Proceedings of the symposium concrete 2000: economic and durable construction through excellence, vol 2. E & FN Spon, London; 1993.

18 Pereira N, Romão X. Assessment of the concrete strength in existing buildings using a finite population approach. Construct Build Mater 2016; 110:106-116.

19 Fiore A, Porco F, Uva G, Mezzina M. On the dispersion of data collected by in situ diagnostic of the existing concrete. Construct Build Mater 2013;47:208-217.

20 Shimizu Y, Hirosawa M, Zhou J. Statistical Analysis of Concrete Strength in Existing Reinforced Concrete Buildings. In: Proceedings of 12th world conference on earthquake engineering, Japan; 2000.

21 Cristofaro MT, D'Ambrisi A, De Stefano M, Pucinotti R, Tanganelli M. Studio sulla Dispersione dei Valori di Resistenza a Compressione del Calcestruzzo di Edifici Esistenti. Il Giornale delle Prove non Distruttive Monitoraggio e Diagnostica 2012;2 (in Italian).

22 Masi A, Digrisolo A, Santarsiero G. Concrete Strength Variability in Italian RC Buildings: Analysis of a Large Database of Core Tests, Applied Mechanics and Materials, 2014;597: 283-290.

23 Masi A, Chiauzzi L. An experimental study on the within-member variability of in situ concrete strength in RC building structures, Constr. Build Mater, 2013; 47:951–961.

24 Masi A, Vona M. Estimation of the in-situ concrete strength: provisions of the European and Italian seismic codes and possible improvements. In: Cosenza E, editor. Eurocode 8 perspectives from the Italian standpoint workshop, 67–77, Doppiavoce, Naples, Italy; 2009.

25 Mirza S, MacGregor JG. Variability of the mechanical properties of reinforcing bars. J. Struct. Div 1979; 105:921-937.

26 Pipa M. Ductilidade de elementos de betão armado sujeitos a ações cíclicas: Influencia das características mecânicas das armaduras. PhD Dissertation. Universidade Técnica de Lisboa, Lisbon, Portugal; 1993. (in Portuguese).

[This page was intentionally left blank]

Chapter 5

Derivation of closed-form safety factors for component-based limit-states of RC frame buildings

Scope and objectives

The previous chapters have shown how a finite population approach could be used to survey material properties in existing RC buildings, and presented a new set of material strength safety factors and compatible survey plans to efficiently control the epistemic uncertainty about these parameters. Nevertheless, the combination of the proposed approach with the actual safety assessment procedure as it is currently defined in current seismic safety assessment standards was not addressed. These standards, such as the EN1998-3 (EU) or ASCE 41-13 (USA), follow a component-based approach, with the limit-state acceptance criteria being defined based on chord rotation and shear force capacities. These capacity variables are defined in order to verify ductile and brittle failure modes, respectively. Despite the similar limit-state philosophy, both codes have different conceptual ways on how to introduce the effects of uncertainties, with the EN1998-3 focusing on the adoption of confidence factors (CF) used to factorize the material mean strength values and ASCE 41-13 introducing a knowledge factor (k) used to reduce the element capacity. This approach allows for a direct reduction of the capacity, while the CF-based safety checks may lead to unknown safety factors that may not reflect neither the impact of all the uncertainties about the different parameters nor the sensitivity of different capacity models to these parameters. This chapter aims to provide an alternative set of safety factors following the approach defined in ASCE 41-13, and to combine these values with recent capacity models, their uncertainties and the uncertainty management strategy derived in the previous chapters.

5.1 Introduction

Eurocode 8 - Part 3 (EC8/3) [1] emerged as the first European standard for the seismic safety assessment of existing structures and included methods to deal with the specific features of this domain for the earthquake and structural engineering fields. Due to the novel character of the standard in the European context, several studies and applications were developed following its publication, highlighting some issues related with this global framework. In one of these studies, Romão *et al.* [2] made a comparative application of the EC8/3 procedures highlighting the difficulties in meeting the criterion that allows for the validation of linear elastic results, showing that its applicability should be limited to the limit state of damage limitation. Similar conclusions regarding this issue have been drawn by Pinto and Franchin [3], Mpampatsikos *et al.* [4], Caprili *et al.* [5], Araújo and Castro [6] and Manfredi and Masi [7], highlighting also other strengths and limitations of linear elastic analysis methods. Mpampatsikos *et al.* [4] also compared assessment results obtained with different assumptions regarding the ductile and the brittle capacity of structural elements in reinforced concrete (RC) buildings. The authors observed the impact of different definitions for the initial stiffness of structural elements and for the length of the shear span in the verification of the referred failure modes. Romão *et al.* [8] and Araújo and Castro [9] complemented these observations by showing the influence of exact and approximated methods to quantify the seismic demand of beam-column elements in RC and in steel moment resisting frames, respectively.

Romão *et al.* [2] also showed that selecting different knowledge levels for the structural properties may lead to significant differences on the seismic demand and capacity results. The correlation between the confidence factors (CFs) and the knowledge levels (KLs) for different limit states was analysed by Jalayer *et al*. [10] and Franchin *et al*. [11]. The study by Jalayer *et al*. [10] focussed on assessing if the CFs applied solely to the mean material properties would be able to reflect the effect of other uncertainties. Following the same principle, Franchin *et al*. [11] performed a conceptual analysis of the CF role in the EC8/3 framework. After a consistent and extensive study, the authors identified the main issues associated with the current safety assessment format of the standard that include the inability to differentiate CF values as a function of different analysis methods and structural typologies (e.g. in terms of load resisting systems, size of the building, construction materials), the non-conservative character of averaging the material properties, and the lack of rationale behind the assumption of a state of complete knowledge when only a sample of structural elements is surveyed. This last issue was also noted by Monti and Alessandri [12] and Romão *et al*. [13] who revised the formulation of the CF values based on statistical models and on the uncertainty about the mean material properties.

Chapters 2 and 4 (see also [14, 15]) focused on improving the in situ quantification of concrete and reinforcing steel properties by proposing a strategy based on finite population statistics to assess the uncertainty about the mean value of these variables. Next, a coefficient (CF_{mat}) was

proposed to correlate the uncertainty about the mean, the number of in situ tests performed and the expected level of the inherent variability that led to a conservative value for the mean. A set of simplified models were then also developed in Chapter 3 (see also [16]) to define an estimate of the concrete strength variability based solely on non-destructive tests. This approach is in line with the procedure of ASCE 41-13 [17] that recommends using a lower quantile of the sampling distribution of the concrete strength when the corresponding coefficient of variation (CoV) exceeds a given value. Aside from this connection between a representative value of the concrete strength and the CoV of it distribution, this standard also considers a knowledge factor κ which is used to factor the deformation or strength capacity limits. These limits are associated with qualitative inspection and testing plans, but are not connected to the results of the survey. To address this additional issue, the present study provides a methodology that explicitly correlates the results of the survey, the corresponding epistemic uncertainty and the values of the a global safety factor, SF_R, with properties similar to those of κ, that can be used to factor the deformation or strength capacity limits associated to acceptance criteria for different performance levels.

5.2 Brief comparison between ASCE 41-13 and EC8/3 procedures

5.2.1 Performance levels, rehabilitation objectives and importance classes

EC8/3 [1] and ASCE 41-13 [17] are seismic safety assessment standards that are part of the last generation of performance-based earthquake engineering codes and guidelines. Therefore, both codes consider a performance-based assessment approach, incorporating a set of performance and rehabilitation objectives, along with several aspects related with uncertainty characterisation and propagation. EC8/3 provides a set of performance objectives involving the pairing of specific levels of damage for structural and non-structural components and selected seismic hazard levels. Three different levels are defined in EC8/3: Near Collapse (NC), Significant Damage (SD) and Damage Limitation (DL). In the case of ASCE 41-13, similar principles are followed but performance objectives are defined as Operational (OP), Immediate Occupancy (IO), Life Safety (LS) and Collapse Prevention (CP). Nonetheless, while EC8/3 defines a set of performance objectives associated to specific seismicity levels, ASCE 41-13 sets different pairs of hazard and performance levels that can be considered, depending on the rehabilitation objectives. Figure 1 shows a direct comparison of the different rehabilitation objectives (i.e. combination of hazard levels and performance requirements) defined according to the ASCE 41-13 approach and the EC8/3 for ordinary buildings.

As seen in Fig. 1, while ASCE 41-13 establishes multiple combinations of performance levels and seismicity levels to define the rehabilitation objectives, EC8/3 only defines a single combination. In EC8/3, the rehabilitation objectives only change with the importance class of the

building, but these modifications are introduced by increasing the return period at which the performance level is verified.

ASCE 41-13	Performance Level				EC8/3	Limit state			
	OP	IO	LS	CP		-	DL	SD	NC
50% in 50 years	*a*	*b*	*c*	*d*	50% in 50 years	-	-	-	-
20% in 50 years	*e*	*f*	*g*	*h*	20% in 50 years	-	**x**	-	-
10% in 50 years	*i*	*j*	*k*	*l*	10% in 50 years	-	-	**x**	-
2% in 50 years	*m*	*n*	*o*	*p*	2% in 50 years	-	-	-	x

Figure 1. Comparison of the ASCE41-13 and the EC8/3 combinations of performance levels and the corresponding hazard levels of the ground motion intensity associated to different rehabilitation objectives (adapted from [18]). *a* to *p* are combinations of performance levels and seismic hazard scenarios to be assessed in order to comply with a given set of performance objectives according to ASCE 41-13. The **x** markers presented refer to the combinations recommended in the general document of EC8/3, which can be changed in National Annexes.

5.2.2 Data collection, level of in situ testing and safety factors

Existing RC buildings differ from new ones because knowledge about the design assumptions is often unavailable and the quality control employed during the construction stage is also usually unknown. As a result, in situ properties often exhibit significant deviations from current best practices or from the design documentation, particularly in older buildings. Therefore, there is a significant uncertainty when characterizing these properties, depending on factors such as the intrinsic variability of the material characteristics or the conformity level between documentation and in situ properties. In general, the in situ properties of RC structures can be disaggregated among 3 classes: 1) parameters related to the global and sectional geometry of the structural components (class X_G); 2) parameters related to the reinforcement detailing such as the number of longitudinal bars or the stirrup diameter and spacing (class X_D); 3) parameters related to the material properties of the structural component, typically the concrete compressive strength and the reinforcing steel yield strength (class X_M). Class X_M can therefore be further decomposed into the subclasses X_{fc} (concrete compressive strength) and X_{fy} (reinforcing steel yield strength). Given these classes, the overall uncertainty of as-built data can also be disaggregated into uncertainties associated to these classes of parameters reflecting the existing knowledge about these properties.

5.2.2.1 Accounting for uncertainty in ASCE 41-13

ASCE 41-13 accounts for the uncertainty in the referred classes by establishing specific KLs for which particular uncertainty factors are provided. The KLs are defined based on the amount of information available from the building records (design drawings, construction documents, material reports), on the type of condition assessment that was adopted (visual or comprehensive) and on the selected level of in situ testing (None, Usual or Comprehensive). Depending on the amount of information gathered during the inventory and survey campaigns, the corresponding

KL will: 1) specify the knowledge factor (κ) that can be adopted, i.e. a factor used to reduce the capacity of each individual component due to the lack of knowledge about its properties; 2) constrain the method of analysis that can be used; 3) limit the performance levels that can be assessed. Table 1 presents the levels of information and testing associated to different KLs and their corresponding knowledge factors (κ), admissible methods of analysis and maximum performance levels that can be analysed.

Table 1. ASCE 41-13 correlation between the KL, the performance levels and κ

Data	Level of knowledge						
	Minimum			Usual		Comprehensive	
Performance level	Life safety or lower			Life safety or lower		Greater than Life safety	
Analysis procedure	Linear			All		All	
Drawings (X_G)	DE2		DE1	DE2		DE3	
Inspection (X_D)	CA1	CA1	CA2	CA1	CA2	CA1	CA2
Materials (X_M)	M1	M2	M1	M3	M4	M5	M6
In-situ testing (X_M)	No			Usual		Comprehensive	
Knowledge factor κ	0.75	0.90[a,b]	0.75	1.00	1.00	1.00	1.00

DE1: None; DE2: Design drawings or equivalent; DE3: Construction documents or equivalent; CA1: Visual; CA2: Comprehensive; M1: From default values; M2: From design drawings; M3: From design drawings and tests; M4: From usual tests; M5: From documents and tests; M6: From comprehensive tests; [a] If the building meets certain requirements specified in the code, κ=1.0 can be adopted; [b] If inspection or testing records are available to substantiate the design drawings, κ=1.0.

As seen in Table 1, if a Performance Level greater than LS is to be considered, the Comprehensive KL must be guaranteed which considers that construction documents or equivalent are available, that a visual (CA1) or a comprehensive (CA2) condition assessment is performed (covering geometric variables (X_G) and variables related to construction details (X_D)), and that documents regarding the material properties (X_M) and tests are available or a comprehensive in situ test campaign is performed. Table 2 shows the inspection levels defined in ASCE 41-13 and the corresponding number of structural components that must be surveyed. The condition assessment (inspection level) CA1 implies that a direct visual inspection of accessible and representative primary components and connections has to be performed. For CA2 (comprehensive), the condition assessment implies the local removal of cover concrete to inspect reinforcement details. Specific sampling plans are proposed in ASCE 41-13 for the material properties (X_M) that define two levels of testing (Usual and Comprehensive). Table 3 summarizes the number of structural elements where concrete samples and reinforcing steel coupons must be collected from and tested. Furthermore, ASCE 41-13 indicates that a κ value of 0.75 must be considered when: 1) components are found to be damaged or their condition is damaged during the assessment; 2) the coefficient of variation (CoV) of the mechanical properties exceeds 20% or 3) components contain archaic or proprietary material and the condition is uncertain.

Table 2. ASCE 41-13 inspection levels (IL) and minimum number of components that must be surveyed in RC structures.

IL	Design drawings	Number of tests
CA1	-	Visual inspection of at least 20% of the components and connections at each floor level. It can be increased to 40% when degradation is found in some components.
CA2	Detailed design drawings available	At least 3 different connections (including one of each type: beam–column, column–foundation, and beam–diaphragm). If deviations are found, at least 25% of the specific connection type shall be inspected to identify the extent of deviation.
CA2	Detailed design drawings not available	At least three connections of each type of primary connection shall be exposed for inspection. If common detailing is observed, consider it representative of installed conditions. If variations are observed among similar connections, additional connections shall be inspected until an accurate understanding of the building construction is gained.

Table 3. ASCE 41-13 testing levels (TL) and minimum number of tests that must be conducted in RC structures.

TL	Parameters	Design strength	Number of tests
Usual	X_c	Known	1 core from samples of each different concrete strength, with a minimum of 3 for the entire building
Usual	X_c	Unknown	1 core from each type of seismic force-resisting component, with a minimum of 6 for the entire building.
Usual	X_{RS}	Known	-
Usual	X_{RS}	Unknown	At least 2 coupons for the entire building
Comprehensive	X_c	Known*	A minimum of 3 cores shall be extracted for each floor level, 306m^3 of concrete, or 930 m^2 of surface area.
Comprehensive	X_c	Unknown*	A minimum of 6 cores shall be extracted for each floor level, 306m^3 of concrete, or 930 m^2 of surface area.
Comprehensive	X_{RS}	Known	3 coupons from each element or component type for the entire building.
Comprehensive	X_{RS}	Unknown	3 coupons from each element or component type every 3 floors if the date of construction is known. 6 coupons from each element/component type every 3 floors otherwise.

5.2.2.2 Accounting for uncertainty in EC8/3

EC8/3 considers the epistemic uncertainty about the building properties by defining specific testing and inspection levels which are then associated to a confidence factor (CF). The CF reflects the level of confidence that exists about the values adopted for each parameter X_G, X_D and X_M. EC8/3 proposes 3 values for the CF that are connected to 3 KLs: limited (KL1), extended (KL2) and comprehensive (KL3). The correlation between the CF and the KLs established in EC8/3 is shown in Table 4.

With respect to the X_G variables, EC8/3 specifies that a visual survey of the overall geometry of the structure and sectional dimensions can be carried out to check the conformity with outline construction documents. If discrepancies are observed, a full survey must be carried out to produce a new set of structural drawings, identifying the components and their dimensions.

Table 4. EC8/3 correlation between the KL, the performance levels and CF

Data	Level of knowledge		
	Limited (KL1)	Normal (KL2)	Full (KL3)
Performance level	-	-	-
Analysis procedure	Linear	All	All
Outline Drawings (X_G)	Visual or Full survey (if visual detects discrepancies)		
Drawings (X_D)	DE1	DE2 | DE1	DE3 | DE1, DE2
Inspection (X_D)	Limited	Limited | Extended	Limited | Comprehensive
Materials (X_M)	M1	M2 | M1	M3| M2, M1
In-situ testing	Limited	Limited | Extended	Limited | Comprehensive
Confidence factor, CF	1.35	1.20	1.00

DE1: Simulated design; DE2: Incomplete original detailed construction drawings; DE3: original detailed construction drawings; M1: default values according to standards at the time of construction; M2: from original design specifications; M3: from original test reports.

For the construction details (X_D), three different inspection levels are considered: Limited, Extended and Comprehensive. The amount of structural elements to be surveyed for each inspection level is shown in Table 5.

Table 5. EC8/3 inspection levels (IL) and minimum number of components that must be surveyed.

IL	Design drawings	Number of tests
Limited	Simulated design	20 % of elements checked for details
Extended	Incomplete original construction drawings	20 % of elements checked for details
	Simulated design	50 % of elements checked for details
Comprehensive	Original construction drawings	20 % of elements checked for details
	Simulated design	80 % of elements checked for details

As opposed to the inspection levels, which incorporate relative quantities (i.e. surveying *n* out of *N* components), the testing levels specify absolute values for the number of elements where concrete cores and reinforcing steel coupons have to be extracted and tested. Table 6 shows the number of tests associated to the EC8/3 testing levels.

Table 6. EC8/3 testing levels and minimum number of tests that must be conducted in RC structures.

TL	Parameter	Design strength	Number of tests (per floor, for each type of element)
Limited	X_c	Default values	1 core
	X_{RS}	Default values	1 reinforcing steel coupon
Extended	X_c	Design specifications	1 core
		Default values	2 cores
	X_{RS}	Design specifications	1 reinforcing steel coupon
		Default values	2 reinforcing steel coupon
Comprehensive	X_c	Original tests reports	1 core
		Default values	3 cores
	X_{RS}	Original tests reports	1 reinforcing steel coupon
		Default values	3 reinforcing steel coupon

5.2.2.3 Acceptance criteria and structure of the safety assessment methodology

ASCE 41-13 proposes a safety assessment methodology that is divided into three tiers: Tier 1 and 2 refer to a simplified screening and to a deficiency-based evaluation procedure, while Tier 3 is a comprehensive analytical procedure. On the contrary, EC8/3 only has one tier that is similar to Tier 3 in ASCE 41-13. In these two cases, the safety verifications for the limit state conditions and the associated performance objectives are based on the analysis of acceptance criteria for individual structural elements. Although the same principle is considered by both standards, the format of the safety inequality that must be verified is not the same, as shown in Fig. 2 for the case where nonlinear analysis is considered in the assessment.

ASCE 41-13	Acceptance criterion
	Nonlinear analysis
Failure mode — Ductile / Brittle	$S\left(X_G, X_D, \hat{\bar{X}}_M{}^{*a}\right) \le \kappa \cdot R\left(X_G, X_D, \hat{\bar{X}}_M{}^{*a}\right)$

EC8/3 2005	Acceptance criterion
	Nonlinear analysis
Failure mode — Ductile / Brittle	$S\left(X_G, X_D, \hat{\bar{X}}_M\right) \le \dfrac{1}{\gamma_{el}} \cdot R\left(X_G, X_D, \dfrac{\hat{\bar{X}}_M}{\zeta \cdot CF}\right)$

*a the concrete properties may be defined by the mean value or the mean minus one standard deviation.

Figure 2. Comparison of the limit state conditions defined in ASCE 41-13 and EC8/3. The parameter ζ is a partial safety factor that depends on the type of mechanism, γ_{el} is a factor that varies with the performance level analysed and $\hat{\bar{X}}_M$ is the estimate made for the expected value of the material properties.

According to both standards, a demand value *S* must be quantified using either linear or nonlinear methods of analysis. In ASCE 41-13, when nonlinear analysis is considered, the demand values must be obtained using the mean material properties or a reduced value, particularly for the case of concrete strength when it exhibits a high variability. The same expected mean value of the material properties are adopted to quantify the capacity R. No particular information is provided regarding which values should be adopted for parameters of class X_G and class X_D. The uncertainty is accounted for by multiplying the capacity *R*, either in terms of plastic rotations (defined by specific values) or shear strength (computed using an analytical model), by the knowledge factor κ. As a result, the uncertainty is included directly and establishes a lower bound of the capacity *R* of each component. Furthermore, for the plastic rotation capacity, ASCE 41-13 directly correlates the acceptance criteria of each structural component with the corresponding behaviour modelling approach, which corresponds to the generalized backbone model represented in Fig. 3 for the case of RC components.
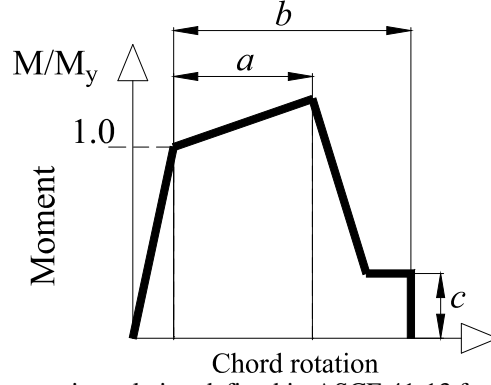
Figure 3. Generalized moment-rotation relation defined in ASCE 41-13 for RC frame elements.

By providing values for each model parameter (a, b and c in Fig. 3), ASCE 41-13 ensures a complete compatibility between the modelling approach and the acceptance criteria by defining them as a function of a and b. For example, for a RC column whose behaviour is not controlled by inadequate development or splicing [17], the limit state criterion for IO is defined by a plastic rotation equal to 15% of a, while for LS and CP, the acceptance criteria are set as 50% of b and 70% of b, respectively.

As opposed to the ASCE 41-13 approach, the CF defined by EC8/3 is not applied globally to R. Instead, the CF is used to factor the concrete compressive strength and the reinforcing steel yielding strength in the analytical expressions that define R. As shown in Fig. 2, when nonlinear analysis is adopted, the capacity R of the element is computed using mean material properties that have to be divided by CF and by a partial safety factor ζ. The partial safety factor ζ has a value equal to 1.0 when ductile mechanisms are analysed, and is equal to γ_c and γ_s for the peak concrete compressive strength and the reinforcing steel yield strength, respectively, when R refers to the capacity associated to brittle mechanisms. For both mechanisms, the value of R is also divided by an additional factor γ_{el} which is independent of the KL. The factor γ_{el} depends on the performance level (as κ indirectly does in ASCE 41-13) and varies according to the type of mechanism. Therefore, the EC8/3 acceptance criteria include a factor γ_{el} that reduces the capacity R independently of the adopted KL. The KL is embedded in the concept of CF, which is expected to represent the epistemic uncertainty about the mean value adopted for the material properties (since the CF only affects class X_M) and, therefore, only reflects the KL about the materials. Furthermore, parameter ζ factors the mean material properties to define a lower quantile of the expected distribution while the role of γ_{el} can be associated with the empirical nature of the R models defined by EC8/3. As mentioned by Franchin and Pagnoni [27], R can be defined by:

$$R = \hat{R}\left(X_G, X_D, X_{f_c}, X_{f_y}\right) \cdot \varepsilon_R,$$ (1)

where $\hat{R}$ is an analytical function that defines the median value of the resistance based on the input vectors X_G, X_D, X_{f_c} and X_{f_y}, and ε_R is a lognormal random variable representing the epistemic error of the model of $\hat{R}$ with median $\hat{\varepsilon}_R$ and logarithmic standard deviation $\sigma_{\ln R}$. Based on this assumption, when the real values of X_G, X_D, X_{f_c} and X_{f_y} are known, there is a certain quantile of ε_R that, when multiplied by the value obtained by the model R defined by the standard, leads to the equality:

$$\frac{1}{\gamma_{el}} \cdot \hat{R}\left(X_G, X_D, X_{f_c}, X_{f_y}\right) = \hat{R}\left(X_G, X_D, X_{f_c}, X_{f_y}\right) \cdot \left(\varepsilon_R\right)_q \Leftrightarrow \frac{1}{\gamma_{el}} = \left(\varepsilon_R\right)_q, \tag{2}$$

Due to the format of the EC8/3 limit state assessment framework, the CF is assumed to implicitly account also for the lack of knowledge or the uncertainties about the geometric variables (X_G) and the construction details (X_D). However, neither EC8/3 nor ASCE 41-13 indicate how to account for differences found between expected data (e.g. from design documents) and surveyed data. Furthermore, unlike in the limit state assessment of ASCE 41-13, the role of the CF, γ_{el} and ζ in EC8/3 is more difficult to interpret and to correlate with the existing uncertainties. The previous discussion suggests that γ_{el} could be interpreted as a safety factor (SF_R), similar to κ in ASCE 41-13, while CF is seen to be a measure of the reliability of the estimate of the mean properties of the materials. Nonetheless, the latter should be redefined individually for parameters X_G, X_D, X_{f_c} and X_{f_y}, since EC8/3 currently proposes a single CF for all parameters. Therefore, a consistent safety assessment framework must be defined and include a consistent derivation of SF_R factors, as well as a new set of variables that can be used to adequately estimate the mean properties.

5.3 Proposed component-based limit-state assessment framework

5.3.1 Definition of groups of variables with similar properties and their uncertainties

The limit state assessment framework proposed herein combines the strengths of the ASCE 41-13 and EC8/3 methodologies and introduces the key elements that support the definition of more consistent probability-based limit state acceptance criteria. In both methodologies, the capacity of a structural component is defined by a set of variables belonging to the four classes of parameters previously defined: X_G, X_D, X_{f_c} and X_{f_y}. These variables have different properties and need to be framed into the safety assessment framework in different ways. Parameters X_{f_c}

and X_{f_y} are continuous properties defined by sets of N values (N is the number of structural components) termed $x_{f_c,j}$ and $x_{f_y,j}$ for the jth component. These values follow probability distributions that can be defined by mean values μ_{f_c} and μ_{f_y}, respectively, and by standard deviations σ_{f_c} and σ_{f_y}, respectively. As opposed to these material properties, X_G and X_D represent variables that are discrete and, in some cases, are completely unknown. While variables belonging to X_G are usually fairly easy to characterize, this is often not the case for those belonging to class X_D. However, if the X_G variables are known, the use of simulated design can overcome the lack of knowledge associated to X_D. resulting from the unavailability of design data and drawings or the difficulty in carrying out in situ surveys. In light of this, it is assumed that having complete knowledge about X_G is a necessary condition to be able to carry out a safety assessment involving the EC8/3 or the ASCE 41-13 Tier 3 methods. Otherwise, only simplified methods of analysis (such as those of Tier 1 in ASCE 41-13) should be adopted due to insufficient knowledge about the structural properties. When design documents are unavailable and a complete characterization of X_G has been performed, a reference set of parameters $X_{D,ref}$ can be established using simulated design. Based on these reference values, the uncertainty can be estimated by adopting a tailored inspection to verify the adequacy of $X_{D,ref}$. The uncertainty about $X_{D,ref}$ can be divided into that associated to the transverse reinforcement, $X_{D,w}$, and that associated to the longitudinal reinforcement, $X_{D,l}$. These two variables can then be used to define conformity indexes $k_{D,w}$ and $k_{D,l}$ whose distributions across the structure can be assumed to be continuous and defined by the ratios between $X_{D,w}$ and $X_{D,l}$ and their corresponding reference values $X_{D,w,ref}$ and $X_{D,l,ref}$, respectively, for all the structural components. The conformity indexes $k_{D,w}$ and $k_{D,l}$ of a given structural component j can be defined as:

$$
\begin{aligned}
k_{D,w,j} &= \frac{x_{D,w,j}}{x_{D,w,ref,j}}, \\
k_{D,l,j} &= \frac{x_{D,l,j}}{x_{D,l,ref,j}}
\end{aligned}
\qquad , \tag{3}
$$

where $x_{D,w,j}$, $x_{D,l,j}$, $x_{D,w,ref,j}$ and $x_{D,l,ref,j}$ are the jth components of $X_{D,w}$, $X_{D,l}$, $X_{D,w,ref}$ and $X_{D,l,ref}$, respectively. After surveying the N components of the building, the statistical distribution of $k_{D,w}$ and $k_{D,l}$ can then be established based on their mean values ($\mu_{k_{D_w}}$, $\mu_{k_{D_l}}$) and

standard deviations ($\sigma_{k_{Dw}}$, $\sigma_{k_{Dl}}$). If all the structural components are surveyed and their properties match $X_{D,ref}$, the mean values of $\mu_{k_{Dw}}$ and $\mu_{k_{Dl}}$ are 1.0, and their variability is either assigned a value reflecting the uncertainty associated to the survey methodology or is not considered (i.e. $\sigma_{k_{Dw}}$ and $\sigma_{k_{Dl}}$ are 0). For a given structural component j, an instance y_j can be defined as:

$$y_j = \left\{ x_{D,w,ref,j}, x_{D,l,ref,j}, x_{G,j}, k_{D,w,j}, k_{D,l,j}, x_{f_c,j}, x_{f_y,j} \right\},$$ (4)

which can be re-written by considering a generic variable Z_i as:

$$y_j = \left\{ (Z_i)_j \right\}, i = 1 : \dim(Y).$$ (5)

where Y is a matrix containing the N values of each variable Z_i (Z_i is equal to $X_{D,w,ref}$, $X_{D,l,ref}$, X_G, k_{D_w}, k_{Dl}, X_{f_c} or X_{f_y}) that can be fully established when all the N components are surveyed. In this case, the corresponding statistical parameters (mean μ_Y and standard deviation σ_Y) can be defined as:

$$\mu_Y = \left\{ X_{D,w,ref}, X_{D,l,ref}, X_G, \mu_{k_{Dw}}, \mu_{k_{Dl}}, \mu_{f_c}, \mu_{f_y} \right\},$$ (6)

and

$$\sigma_Y = \left\{ \sigma_{D,w,ref}, \sigma_{D,l,ref}, \sigma_G, \sigma_{k_{Dw}}, \sigma_{k_{Dl}}, \sigma_{f_c}, \sigma_{f_y} \right\}.$$ (7)

where $\sigma_{D,w,ref}$, $\sigma_{D,l,ref}$ and σ_G are zero given that $X_{D,w,ref}$, $X_{D,l,ref}$ and X_G are constant parameters that must be known for all the N components

5.3.2 Distinction between the properties of surveyed and of non-surveyed components
When assessing the properties of an existing building, only a subset of n out of the N structural components of the structure are usually surveyed. As a result, matrix Y is incomplete since only n parameters $Z_i \in Y$ are characterized while the remaining ones have missing data. Since matrix Y needs to be fully defined to perform the safety assessment of the structure, estimates for the missing values have to be obtained. The strategy that is proposed to deal with these missing data involves using the information collected from the n surveyed components to infer the properties of the remaining non-surveyed $N - n$ components. More precisely, the proposed method uses

the information about all the n out of N components where Z_i observations are available to quantify the sampling mean m_{Z_i} and standard deviation s_{Z_i} about Z_i. Based on m_{Z_i} and s_{Z_i}, estimates can be obtained for the real mean μ_{Z_i} and for the real standard deviation σ_{Z_i} of each generic variable Z_i. The correlation between any σ_{Z_i} and s_{Z_i} can be defined as:

$$\sigma_{Z_i} = VF_{Z_i} \cdot s_{Z_i}, \tag{8}$$

where VF_{Z_i} is a variability factor accounting for the uncertainty about s_{Z_i} due to the number of non-surveyed components. Similarly, μ_{Z_i} can be estimated based on m_{Z_i} by:

$$\mu_{Z_i} = MF_{Z_i} \cdot m_{Z_i}, \tag{9}$$

where MF_{Z_i} is a mean factor used to define the probabilistic range μ_{Z_i} may assume given the estimate made based on m_{Z_i}. Both MF_{Z_i} and VF_{Z_i} introduce the effect of uncertainty on the estimation of the mean and of the variance, and can be associated to a confidence interval (CI). The CI about the mean μ_{Z_i} can be established following the principles outlined in [14] and in [15]. Accordingly, by testing/surveying n out of N structural components, where N represents the total number of structural components of a given region (see [14] for a discussion about the concept of region), a finite population confidence interval for the mean of each parameter Z_i can be established by (considering that the standard deviation is unknown):

$$\mu_{Z_i} = m_{Z_i} \pm t_{n-1} \frac{1}{\sqrt{n}} \cdot \sqrt{\frac{N-n}{N-1}} \cdot s_{Z_i}, \tag{10}$$

which, by dividing both sides by m_{Z_i}, becomes:

$$\mu_{Z_i} = \left(1 \pm t_{n-1} \frac{1}{\sqrt{n}} \cdot \sqrt{\frac{N-n}{N-1}} \cdot CoV_{Z_i} \right) \cdot m_{Z_i}, \tag{11}$$

and consequently leads to the uncertainty factor MF_{Z_i} which depends on the unknown coefficient of variation estimated based on n out of N structural components where the physical properties are surveyed, i.e.:

$$MF_{Z_i} = 1 \pm t_{n-1,1-\alpha/2} \frac{1}{\sqrt{n}} \cdot \sqrt{\frac{N-n}{N-1}} \cdot CoV_{Z_i},$$ (12)

In case a sufficiently accurate approximation for CoV_{Z_i} can be established, MF_{Z_i} can be calculated assuming that σ_{Z_i} is known, yielding:

$$MF_{Z_i} = 1 \pm z_{1-\alpha/2} \frac{1}{\sqrt{n}} \cdot \sqrt{\frac{N-n}{N-1}} \cdot CoV_{Z_i},$$ (13)

where $z_{1-\alpha/2}$ is the $1-\alpha/2$ quantile of the standard normal distribution. By following the same principles, the CI for the standard deviation σ_{Z_i} can be established following the principles defined by O'Neill (2014) [26], yielding:

$$\sigma_{Z_i}^2 = \left(\left(\frac{n-1}{N-1} \right) + \left(\frac{N-n}{N-1} \right) \cdot \frac{1}{F_\alpha(n-1,N-n)} \right) \cdot s_{Z_i}^2,$$ (14)

where F_α is the α quantile of the F distribution with $(n-1)$ and $(N-n)$ degrees of freedom. Based on Eq. (14), the value of VF_{Z_i} can be obtained by:

$$VF_{Z_i} = \sqrt{ \left(\frac{n-1}{N-1} \right) + \left(\frac{N-n}{N-1} \right) \cdot \frac{1}{F_\alpha(n-1,N-n)} },$$ (15)

Using the proposed approach, the $N-n$ structural components that are left without specific information from the survey have to be treated differently from the n components that were surveyed. For the latter, values directly obtained from the surveys can be used to estimate the capacity R, since the existing uncertainty is only the one related with the test procedure and its accuracy. On the other hand, for the unsurveyed components, the lack of knowledge implies that the only available information is that defined by the interval of values that μ_{Z_i} and σ_{Z_i} can assume. Hence, when formulating a safety factor SF_R for each component, as discussed before within the context of Eq. (2), a vector of $(SF_R)_j$ values has to be considered that will have different values depending on the available level of knowledge for a given component j. Vector SF_R is therefore created as illustrated in Fig. 4, where the value for a given component j $(SF_R)_j$

is either of class $SF_{R,kno}$ (in the case all Z_i are assessed) or of class $SF_{R,unk}$ (otherwise). Consequently, following the principle outlined in Eq. (2), two classes of capacity variables are also possible, R_{kno} and R_{unk}, for the cases where the member properties are surveyed and otherwise, respectively.
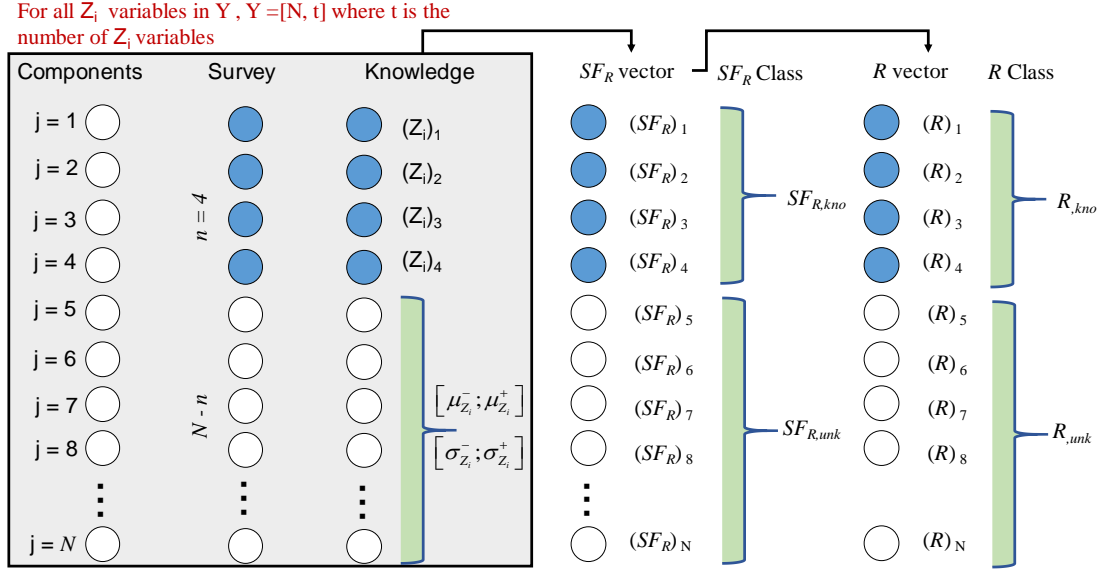
Figure 4. Disaggregation between surveyed and unsurveyed structural components and indication of the information gathered for each component j and the corresponding value and class of the safety factor that must be associated when formulating the limit state condition.

5.3.3 Proposed component-based acceptance criteria for generic performance levels

The safety inequality defined in Eq. (2) can be written based on the elements of the Y matrix as:

$$\frac{D\left(y_j\right)}{R\left(y_j\right)} \leq 1.0\,, \tag{16}$$

where $D\left(y_j\right)$ represents the structural demand of component j with properties y_j obtained by a numerical model used to compute the response of the N components of the structure, and $R\left(y_j\right)$ is the corresponding capacity obtained from a mathematical model R. Considering the averaging and safety principles embedded in codes targeting the assessment of existing buildings, Eq. (16) can be set as:

$$\frac{\hat{D}\left(y_j\right)}{R_q\left(y_j\right)} \leq 1.0\,, \tag{17}$$

where $\hat{D}(y_j)$ is the median demand obtained with the expected values of y_j and $R_q(y_j)$ is the qth percentile of the distribution of capacity $R(y_j)$. The median demand $\hat{D}(y_j)$ is an unbiased estimator of the expected value of the demand $D(y_j)$. With respect to $R_q(y_j)$, the definition of a low percentile to represent the assessment (or design) value of the capacity $R(y_j)$ is common to many safety assessment codes, and can be alternatively defined based on the median $\hat{R}(y_j)$ and SF_R as:

$$R_q(y_j) = \frac{\hat{R}(y_j)}{(SF_R)_j}, \tag{18}$$

which can be re-written assuming the capacity follows a lognormal distribution (as considered in [27] when defining component safety factors), as:

$$(SF_R)_j = \frac{\exp(\mu_{\ln R(y_j)})}{\exp(\mu_{\ln R(y_j)} + \Phi(q) \cdot \sqrt{\sigma^2_{\ln R(y_j)}})}. \tag{19}$$

where $\Phi(q)$ is the number of standard deviations away from the logarithmic mean of the qth percentile of the distribution of $\ln R(y_j)$ for each structural component, and $\sigma_{\ln R(y_j)}$ is the corresponding standard deviation. The selection of the qth percentile can be associated with the rehabilitation objectives (in ASCE 41-13) or the importance class (in EC8/3) adopted in the analysis. By doing so, a direct correlation can be defined between the mandatory level of safety (at the component level) and the adopted performance levels (i.e. the admissible damage state). Tentative values of $\Phi(q)$ are proposed in Table 7, where these factors are defined as a function of the importance classes defined in Eurocode 8 - Part 1 (EC8/1) [19], assuming that, for ordinary buildings, the 16% percentile provides an adequate reliability level.

Table 7. Variation of the factor $\Phi(q)$ with the accepted level of safety for different importance classes

Importance Class	Buildings	q	$\gamma_I = -\Phi(q)$
I	RC buildings with minor importance	25%	0.85
II	Ordinary RC buildings	16%	1.00
II	Important RC buildings	5%	1.65
III	Vital/Essential RC buildings	2%	2.00

By assuming a unique γ_I for the entire structure, differences in the SF_R values calculated for the N components of the building will depend on the existing uncertainty about the structural properties of each individual component. As a result, the vector of SF_R values (as shown in Fig. 4) will depend on the available knowledge about each component, namely on the uncertainty values (represented by $\sigma_{\ln R(y_j)}$) defined according to the survey that was performed, since:

$$(SF_R)_j = \exp\left(-\Phi(q) \cdot \sqrt{\sigma^2_{\ln R(y_j)}}\right). \tag{20}$$

As shown in Fig. 4, when all the Z_i properties of a component j are surveyed, $(SF_R)_j$ is of the class $SF_{R,kno}$, which implies that the uncertainty $\sigma_{\ln R(y_j)}$ is only proportional to the uncertainty of the capacity model itself, which depends on the properties of ε_R. Conversely, when the properties of the structural component are not surveyed, the value of $\sigma_{\ln R(y_j)}$ has to be defined based on $y_{j=1\to n}$ properties of the n surveyed components. This implies that the SF_R of the class $SF_{R,unk}$ will depend not only on ε_R, but also on the estimates made for the global values of $\mu_{\ln R(Y)}$ and $\sigma^2_{\ln R(Y)}$, following the principles defined by Eqs. (6) to (15).

5.3.4 Definition of SF_R for a given component as a function of random variables

The key aspect for calibrating SF_R is the quantification of the mean and the dispersion of $\ln R(y_j)$. Given that $R(y_j)$ is assumed to follow a lognormal distribution, $\ln R(y_j)$ can be treated as a normal variable and estimated as a function of y_j and $\varepsilon_{\ln R}$. The expected value and the variability of $\ln R(y_j)$ can be established by the Taylor series expansion about the mean value of y_j, μ_{y_j}, truncated after the first order terms. According to Ang and Tang ([20]; *p.* 186), $\mu_{\ln R(y_j)}$ and $\sigma^2_{\ln R(y_j)}$ can be defined by:

$$\mu_{\ln R(y_j)} = \ln\left(R\left(\mu_{y_j}\right)\right) + \overline{\varepsilon}_{\ln R} \tag{21}$$

$$\sigma^2_{\ln R(y_j)} \cong \sum_{i=1}^{t} \left(\sigma^2_{Z_i}\right)_j \cdot \left(\frac{\partial \ln R\left(\mu_{y_j}\right)}{\partial Z_i}\right)^2 + \sigma^2_{\ln \varepsilon_R} \tag{22}$$

where $\partial / \partial_{Z_i}$ is the partial derivative of $\ln R$ with respect to the generic variable $Z_i \in Y$ evaluated at the vector of mean values μ_{y_j}, and $t = \dim(y_j)$ is the number of elements of Y. Thus, the generic format of $(SF_R)_j$ can be established by:

$$(SF_R)_j = \exp\left(-\Phi(q) \cdot \sqrt{\sum_{i=1}^{t} (\sigma_{Z_i}^2)_j \cdot \left(\frac{\partial \ln R(\mu_{y_j})}{\partial Z_i}\right)^2 + \sigma_{\ln \varepsilon_R}^2}\right). \tag{23}$$

Equation (23) provides the framework for calculating any $(SF_R)_j$ given any testing or survey level of the component, including the cases where the component is unsurveyed or is surveyed. In the latter case, all the Z_i characteristics of the structural component j are assessed, which means that $(\sigma_{f_c})_j \cong 0$, $(\sigma_{f_y})_j \cong 0$, $(\sigma_{k_{D,w}})_j \cong 0$ and $(\sigma_{k,l})_j \cong 0$. In this particular case, y_j is fully known and $(SF_R)_j$ belongs to the class $SF_{R,kno}$ and simplifies to:

$$(SF_R)_j = \exp\left(-\Phi(q) \cdot \sigma_{\ln \varepsilon_R}\right). \tag{24}$$

5.4 SF_R factors for different limit states of RC columns

5.4.1 Capacity models for RC frame components in ASCE 41-13 and EC8/3

The application of the framework proposed in the previous section implies that there must be a direct correlation between the modelling techniques used to quantify the median demand of component j, $\hat{D}(y_j)$ and the corresponding resistance defined by Eq. (18). In current standards, the seismic performance assessment of RC frame buildings is analysed for a set of deformation-controlled mechanisms, usually defined by chord rotation limits, and additional force-controlled mechanisms, defined in terms of shear and axial force limits. ASCE 41-13 defines an explicit hinge model for beam-column components, providing modelling parameters and limit state acceptance criteria for different performance levels. The modelling parameters are the effective flexural stiffness, EI_{eff}, the pre-capping plastic rotation capacity (*a*) the total plastic rotation (*b*) until a given residual moment ratio (*c* times the yielding moment M_y) is reached. The limit state criteria corresponding to the performance levels of Immediate Occupancy (IO), Life Safety (LS) and Collapse Prevention (CP) are defined as function of *a* and *b*. Tables of values are provided in the standard for these limits for beams, column and beam-column joints, but continuous analytical models are not explicitly defined.

Conversely, EC8/3 provides limit state values for chord rotations of beams and columns associated to different performance levels. The first limit state defines the yielding chord rotation (θ_{DL}), and corresponds to the Damage Limitation (DL) performance level. The Near Collapse limit state is characterised by the rotation (θ_{NC}) corresponding to a decay of 20% from the maximum moment M_c, whereas the significant damage limit state criterion (θ_{SD}) is defined by a chord rotation with a value equal to ¾ of θ_{NC}. None of the codes includes an ultimate collapse limit state (C), which can be considered as the rotation corresponding to a zero bending capacity. Modelling parameters and performance level acceptance criteria defined in ASCE 41-13 are constant values associated with specific conditions regarding stirrup spacing, axial load level, amount of transverse reinforcing steel and correlation with the shear failure capacity. Among the effects that critically govern the response of RC frame elements, the most relevant are the use of smooth reinforcing steel bars and the likely occurrence of brittle failure modes induced by pure shear or flexure-shear mechanisms. Pure shear refers to the type of failure mechanism included in the force-controlled limit state defined in both EC8/3 and ASCE 41-13. Therefore, these standards can be seen to define only one force-controlled limit state that is associated to a maximum value of shear force and one performance level (NC in EC8/3), unlike the deformation-controlled mechanisms which are established for several performance levels.

5.4.2 Capacity models for RC columns with different characteristics

The models adopted in the present study were selected in order to allow for the definition of the numerical model used to compute the demands and the limit state criteria, as done in ASCE 41-13 and shown in Fig. 5a.
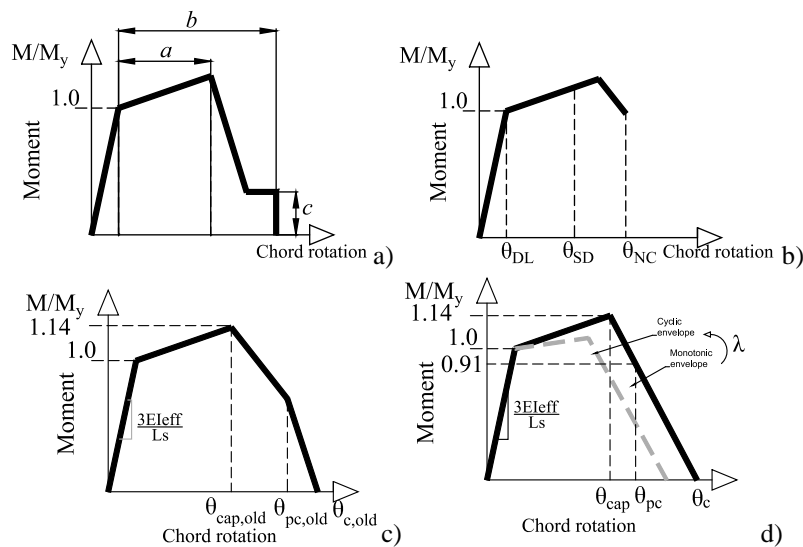

Figure 5. Generalized moment-rotation model and identification of the component limit states defined by ASCE 41-13 [17] (a), limit state values proposed by EC8/3 [1] (b) and representation of the modelling/limit state criteria adopted in this study for beam-column elements with smooth (c) and ribbed (d) steel bars.

A similar rationale can be used to construct a moment-rotation backbone model based on the limit states presented in EC8/3, as shown in Fig.5b. Recent studies ([21, 22]) have highlighted the differences between the seismic response of RC components with ribbed and smooth steel bars. Therefore, since the proposed seismic assessment framework must be able to address all the possible existing RC frame buildings, a distinction is introduced herein between the old RC components (with smooth bars) and modern components (with ribbed bars). The corresponding generalized moment-rotation models assumed in this study are shown in Fig. 5c and in Fig. 5d. The rotation capacity of RC frame elements with smooth bars was studied by Verderame and Ricci [22] due to the importance that old RC building typologies may have in the existing building stock – these correspond to most of the buildings constructed prior to the 1960s in Europe. The modelling parameters suggested in [22] include a quadrilinear cyclic backbone model (Fig. 5c) defined by the flexural stiffness $EI_{eff,old}$, the capping rotation $\theta_{cap,old}$, the near collapse post-capping rotation $\theta_{pc,old}$ and the collapse post-capping rotation $\theta_{c,old}$. The empirical relations developed by Verderame and Ricci [22] for the abovementioned parameters are:

$$EI_{eff,old} = 0.074 \cdot 8.1^{v} \cdot \left(1 + 0.3 \cdot \frac{L_s}{d}\right) \cdot EI_g \cdot \varepsilon_{EI_{eff,old}} \rightarrow K_{eff,old} = \frac{3 \cdot EI_{eff,old}}{L_s}, \qquad (25)$$

$$\theta_{cap,old} = 0.0097 \cdot 0.27^{v} \cdot \left(1 + 0.28 \cdot \frac{L_s}{d}\right) \cdot \left(0.58 + 0.42 \cdot \frac{\min\left(\frac{l_0}{d_b};50\right)}{50}\right) \cdot \varepsilon_{\theta_{cap,old}}, \qquad (26)$$

$$\theta_{pc,old} = 0.037 \cdot 0.042^{v} \cdot \omega_w^{0.19} \cdot \left(1 + 0.5 \cdot \frac{L_s}{d}\right) \cdot \left(0.84 + 0.16 \cdot \frac{\min\left(\frac{l_0}{d_b};50\right)}{50}\right) \cdot \varepsilon_{\theta_{pc,old}}, \qquad (27)$$

$$\theta_{c,old} = 0.086 \cdot 0.024^{v} \cdot 44^{100 \cdot \rho_w} \cdot \varepsilon_{\theta_{c,old}}, \qquad (28)$$

where EI_g is the flexural stiffness of the gross cross section, v represents the axial load ratio, L_s is the shear span length ($L_s = M / V$), d is the effective cross-section depth, l_0 is the longitudinal reinforcement splice length, d_b is the longitudinal bar diameter, ρ_w is the geometrical transverse reinforcement ratio, ω_w is mechanical transverse reinforcement ratio and $\varepsilon_{EI_{eff,old}}$, $\varepsilon_{\theta_{cap,old}}$, $\varepsilon_{\theta_{pc,old}}$ and $\varepsilon_{\theta_{c,old}}$ are random error terms. The parameters defining the lognormal distribution of the error terms for these models are shown in Table 8.

Table 8. Median and logarithmic standard deviation of the models defined by Eqs. (27)-(30)

Parameter	median	$\sigma_{\ln \varepsilon}$
$\varepsilon_{EI_{eff},old}$	1.04	0.24
$\varepsilon_{\theta_{cap},old}$	1.00	0.30
$\varepsilon_{\theta_{pc},old}$	1.03	0.25
$\varepsilon_{\theta_{c},old}$	0.96	0.39

Given this modelling approach for a component, the limit state associated to the DL performance level can be defined by the condition involving the secant stiffness (M/θ) exceeding the value of $K_{eff,old}$ defined in Eq. (25) for the double-bending case. The limit state compatible with the performance level SD can be defined by the occurrence the chord rotation $\theta_{cap,old}$ (Eq. (26)), while for the NC and C (collapse) performance levels, the occurrence of the chord rotations $\theta_{pc,old}$ (Eq. (27)) and $\theta_{c,old}$ (Eq. (28)) can be used as limit state conditions, respectively.

In European buildings constructed after the 1960s, the occurrence of smooth bars is limited. As discussed by Verderame and Ricci [22], although the model developed by Haselton *et al*. [23] may be inadequate to model RC frame columns with smooth bars, it is an adequate modelling approach for columns of more recent buildings. The model defined by Haselton *et al*. [23] for this type of components was calibrated based on experimental cyclic results in beam-column elements and is defined by a trilinear backbone curve (Fig. 4d). This backbone curve is defined by the yielding moment M_y and the initial stiffness based on EI_{eff}, the plastic rotation corresponding to the capping point $\theta_{cap,pl}$, which corresponds to the difference between θ_{cap} and the yield rotation, the post-capping plastic rotation $\theta_{pc,pl}$ which corresponds to the difference between the collapse rotation θ_c and θ_{cap} (see Fig. 4d). The main parameters of the model are defined based on Eqs. (29)-(32),

$$EI_{eff} = 0.30 \cdot \left(1+\nu\right)^{0.80} \cdot \left(\frac{L_s}{H}\right)^{0.72} \cdot E_c \cdot I_g \cdot \varepsilon_{EI_{eff}} \rightarrow K_{eff} = \frac{3 \cdot EI_{eff}}{L_s}, \quad (29)$$

$$\theta_{cap} = 0.14 \cdot \left(1+0.4 \cdot a_{sl}\right) \cdot \left(0.19\right)^{\nu} \cdot \left(0.02+40 \cdot \rho_w\right)^{0.54} \cdot \left(0.62\right)^{\frac{f_c}{100}} \cdot \varepsilon_{\theta_{cap}}, \quad (30)$$

$$\theta_{pc} = 4/3 \cdot \theta_{cap} \quad (31)$$

$$\theta_c = \theta_{cap} + \theta_{pc,pl} = \theta_{cap} + 0.76 \cdot \left(0.031\right)^{\nu} \cdot \left(0.02+40\rho_w\right)^{1.02} \cdot \varepsilon_{\theta_{pc,pl}} \quad (32)$$

5.21

where f_c is the concrete compressive strength (in MPa), a_{sl} is a binary factor equal to 1.0 when case fixed-end rotations due to bar pull out are expected and 0.0 otherwise, and $\varepsilon_{EI_{eff}}$, $\varepsilon_{\theta_{cap}}$, $\varepsilon_{\theta_{pc,pl}}$ are random error terms. The medians and logarithmic standard deviations of $\varepsilon_{EI_{eff}}$, $\varepsilon_{\theta_{cap}}$, $\varepsilon_{\theta_{pc,pl}}$ are shown in Table 9.

Table 9. Median and logarithmic standard deviation of the models shown in Eqs. (29)-(32)

Parameter	median	$\sigma_{\ln \varepsilon}$
$\varepsilon_{EI_{eff}}$	1.11	0.21
$\varepsilon_{\theta_{cap}}$	1.00	0.45
$\varepsilon_{\theta_{pc,pl}}$	1.00	0.72

The value of θ_{pc} can be associated to a decay of 20% in the maximum bending moment in order to be consistent with the EC8/3 NC performance level. The backbone proposed by Haselton *et al*. [23] is a monotonic envelope to which a cyclic degradation parameter is added to introduce this cyclic effect.

Due to the effect of cyclic degradation, Haselton *et al*. [23] proposed replacing $\theta_{pc,pl}$ by $\theta_{pc,pl,cyclic}$ defined as 50% of $\theta_{pc,pl}$ and $\theta_{cap,pl}$ by $\theta_{cap,pl,cyclic}$ defined as 70% of $\theta_{cap,pl}$. In light of this, the limit state acceptance criterion for the DL performance level can be defined based on the effective stiffness of the moment-rotation model, as done above using $K_{eff,old}$, while for the SD performance level the maximum rotation can be limited to $\theta_{SD} = 0.80 \cdot \theta_{cap}$. For the NC and C performance levels, the acceptance criteria can be defined by the rotation limits $\theta_{NC} = 4/3 \cdot \theta_{SD}$ and $\theta_C = \theta_{SD} + 0.50 \cdot \theta_{pc,pl}$, respectively.

Apart from the deformation-controlled mechanisms, force-controlled mechanisms also need to be analysed to account for the effect of brittle failure modes. In RC beam-column elements, this usually involves analysing a limit state that controls the maximum shear force. Based on ASCE 41-13, the shear force capacity of of RC beam-column elements can be defined by:

$$V_n = k \cdot \left[\frac{A_{sw} \cdot f_y \cdot 0.8 \cdot H}{s_w} + \left(\frac{0.5\sqrt{f_c}}{L_s / (0.8 \cdot H)} \cdot \sqrt{1 + \frac{N}{0.5 \cdot \sqrt{f_c} \cdot B \cdot H}} \right) \cdot 0.8 \cdot B \cdot H \right], \qquad (33)$$

where k is equal to $1.0 - 0.075 \cdot \left(\mu_\Delta^{pl} - 2 \right) \geq 0.70$. Since the model calibration presented in [23] included rectangular cross section columns failing in a flexural mode (220 tests) and in a

combined flexure-shear mode (35 tests), and excluded elements where brittle shear failure was observed, V_n can be used to capture shear failure prior or at the onset of yielding in flexure. Similar considerations can be made regarding the elements with smooth bars, since it is not expected that flexure-shear failure will be dominant due to the effect of bond-slip deformations. As a result, factor k can be assumed equal to 1.0, since the flexure-shear failure is captured by the moment-rotation phenomenological law. Such hypothesis is also more consistent with the uncorrelated properties adopted by Gokkaya et al. [24] and leads to the simplification of Eq. (33) into:

$$V_n = \frac{A_{sw}}{s_w} \cdot f_y \cdot 0.8 \cdot H + \left(\frac{0.5\sqrt{f_c}}{L_s/(0.8 \cdot H)} \cdot \sqrt{1 + \frac{N}{0.5 \cdot \sqrt{f_c} \cdot B \cdot H}} \right) \cdot 0.8 \cdot B \cdot H , \qquad (34)$$

5.4.3 Derivation of SF_R for deformation-controlled mechanisms with smooth bars

The computation of ∂/∂_{Z_i} for the deformation-controlled limit states based on Eqs. (25) to (28) was performed by computing the partial derivatives with respect to the relevant variables. For all limit states, the limit state values of a given component depend on several geometrical variables such as L_s, $\sigma_N = N/(B \cdot H)$ and the corresponding parameters N, B, and H), considered herein as known so the seismic analysis of the building can be performed. Furthermore, they also depend on the value of the concrete compressive strength f_c, the reinforcing steel yield strength f_y, the area of transverse reinforcement per meter A_{sw}/s_w and l_0/d_b. Parameter A_{sw}/s_w has a reference value of $(A_{sw}/s_w)_{ref}$ and its corresponding conformity index is $k_{D,w} = (A_{sw}/s_w)_{obs}/(A_{sw}/s_w)_{ref}$. On the other hand, parameter l_0/d_b has an expected value of $(l_0/d_b)_{ref}$ that must be corrected by the observed $k_{D,l}$ value given by $(l_0/d_b)_{obs}/(l_0/d_b)_{ref}$. Based on these conditions, the value of $SF_{DL,old}$ that is used to assess the DL performance level based on $K_{eff,old}$ and the values of $SF_{SD,old}$, $SF_{NC,old}$ and $SF_{C,old}$ that are used to assess the SD, NC and C performance levels, respectively, can be defined as:

$$SF_{DL,old} = \exp\left(-\Phi(q) \cdot \sqrt{\left(\frac{0.50 \cdot (mf_c - 4.18 \cdot \sigma_N)}{(mf_c)^2} \right)^2 \cdot (v_{f_c})^2 + \sigma^2_{\ln \varepsilon_{El_{eff},old}}} \right), \qquad (35)$$

$$SF_{SD,old} = \exp\left(-\Phi(q) \cdot \sqrt{\left(\frac{1.31 \cdot \sigma_N}{\left(mf_c\right)^2}\right)^2 \cdot v_{f_c}^2 + \left(\frac{0.0084 \cdot \left(l_0/d_b\right)_{ref}}{0.58 + 0.0084 \cdot \left(l_0/d_b\right)_{ref} \cdot mk_{D,l}}\right)^2 \cdot v_{k_{D_l}}^2 + \sigma_{\ln \varepsilon_{cap,old}}^2}\right), \tag{36}$$

$$SF_{NC,old} = \exp\left(-\Phi(q) \cdot \sqrt{\begin{array}{l}\left(\frac{3.17 \cdot \sigma_N - 0.19 \cdot mf_c}{mf_c^2}\right)^2 \cdot v_{f_c}^2 + \left(\frac{0.19}{mf_y}\right)^2 \cdot v_{f_y}^2 + \left(\frac{0.19}{mk_{D,w}}\right)^2 \cdot v_{k_{Dw}}^2 + \\ + \left(\frac{0.0032 \cdot \left(l_0/d_b\right)_{ref}}{0.84 + 0.0032 \cdot \left(l_0/d_b\right)_{ref} \cdot mk_{D,l}}\right)^2 \cdot v_{k_{D_l}}^2 + \sigma_{\ln \varepsilon_{pc,old}}^2\end{array}}\right), \tag{37}$$

$$SF_{C,old} = \exp\left(-\Phi(q) \cdot \sqrt{\left(\frac{3.73 \cdot \sigma_N}{mf_c^2}\right)^2 \cdot v_{f_c}^2 + \left(3.78 \cdot \frac{1}{B} \cdot \left(\frac{A_{sw}}{s_w}\right)_{ref}\right)^2 \cdot v_{k_{D,w}}^2 + \sigma_{\ln \varepsilon_{C,old}}^2}\right), \tag{38}$$

where mf_c represents the range of the concrete strength sampling mean $MF_{f_c} \cdot \overline{f}_c$, mf_y is the range of the reinforcing steel yield strength sampling mean, $MF_{f_y} \cdot \overline{f}_y$, $mk_{D,w}$ is the range of the mean of the conformity index $k_{D,w}$, $MF_{k_{D,w}} \cdot \overline{k}_{D,w}$ and $mk_{D,l}$ is the range of the mean of $k_{D,l}$, $MF_{k_{D,l}} \cdot \overline{k}_{D,l}$. The ranges of the variability terms $VF_{f_c} \cdot s_{f_c}$, $VF_{f_y} \cdot s_{f_y}$, $VF_{k_{D,w}} \cdot s_{k_{D,w}}$ and $VF_{k_{D,l}} \cdot s_{k_{D,l}}$ are represented in Eqs. (35)-(38) by the terms v_{f_c}, v_{f_y}, $v_{k_{D,l}}$ and $v_{k_{D,w}}$, respectively.

5.4.4 Derivation of SF_R for deformation-controlled mechanisms with ribbed bars

For the case of components with ribbed bars, the derivation of SF_{DL} used to assess the DL performance level based on K_{eff} and of SF_{SD}, SF_{NC} and SF_C used to assess the SD, NC and C performance level, respectively, followed principles similar to those outlined for the case of components with smooth bars. The relevant parameters for this case are also L_s, σ_N (i.e. N, B, and H), f_c, f_y and A_{sw}/s_w. Using the capacity models presented in Eqs. (29)-(32) and applying Eqs. (20) and (22), the following safety factors were obtained:

$$SF_{DL} = \exp\left(-\Phi(q) \cdot \sqrt{\left(\frac{0.5 \cdot mf_c - 0.30 \cdot \sigma_N}{mf_c \cdot \left(\sigma_N + mf_c\right)}\right)^2 \cdot v_{f_c}^2 + \sigma_{\ln \varepsilon_{El_{eff}}}^2}\right), \tag{39}$$

$$SF_{SD} = \exp\left(-\Phi(q) \cdot \sqrt{\left(\frac{1.66 \cdot \sigma_N}{mf_c^2} - 0.0048\right)^2 \cdot v_{f_c}^2 + \left(\frac{\frac{21.6}{B} \cdot \left(\frac{A_{sw}}{s_w}\right)_{ref}}{0.02 + \frac{40}{B} \cdot \left(\frac{A_{sw}}{s_w}\right)_{ref} \cdot mk_{D,w}}\right)^2 \cdot v_{k_{D,w}}^2 + \sigma_{\ln \varepsilon_{cap}}^2}\right), \tag{40}$$

5.24

$$SF_{NC} = SF_{SD}, \tag{41}$$

$$SF_C = \exp\left(-\Phi(q)\cdot\sqrt{\left(\dfrac{(0.076+0.030\cdot a_{sl})\cdot\dfrac{40}{B}\cdot\left(\dfrac{A_{sw}}{s_w}\right)_{ref}+u_1\cdot u_2^{0.48}\cdot\dfrac{31.2}{B}\cdot\left(\dfrac{A_{sw}}{s_w}\right)_{ref}}{(0.14+0.056\cdot a_{sl})\cdot u_2+0.76\cdot u_1\cdot u_2^{1.48}}\right)^2\cdot v_{f_c}^2+\sigma_{\ln\varepsilon_C}^2 + \left(\dfrac{(0.14+0.056\cdot a_{sl})\cdot(1.66\cdot\sigma_N-0.0048)\cdot u_2^{0.54}+3.47\cdot u_1\cdot\sigma_N\cdot mk_{D,w}\cdot u_2^{1.02}}{mf_c^2\cdot\left((0.076+0.030\cdot a_{sl})\cdot u_2^{0.54}+0.76\cdot u_1\cdot u_2^{1.02}\right)}\right)^2\cdot v_{k_{D,w}}^2}\right), \tag{42}$$

where u_1, u_2 and $\sigma_{\ln\varepsilon_C}^2$ (excluding the correlation between $\varepsilon_{\theta_{cap}}$ and $\varepsilon_{\theta_{pc,pl}}$) are given by:

$$u_1 = 2.72^{0.0048\cdot mf_c-1.81\cdot\sigma_N/mf_c}$$

$$u_2 = 0.02 + \frac{40}{B}\cdot\left(\frac{A_{sw}}{s_w}\right)_{ref}\cdot mk_{D,w}, \tag{43}$$

$$\sigma_{\ln\varepsilon_C}^2 = \sigma_{\ln\varepsilon_{cap}}^2 + \sigma_{\ln\varepsilon_{pc,pl}}^2$$

5.4.5 Derivation of SF_R for force-controlled mechanisms

The safety factors defined for force-controlled mechanisms are associated to the NC performance level irrespective of the remaining performance levels under analysis in a given seismic assessment procedure. Based on the capacity model defined in Eq. (34), the relevant safety factor $SF_{NC,V}$ can be defined as:

$$SF_{NC,V} = \exp\left(-\Phi(q)\cdot\sqrt{\left(a_1\right)^2\cdot v_{f_c}^2+\left(a_2\right)^2\cdot v_{f_y}^2+\left(\frac{mf_y}{mk_{D,w}}\cdot a_2\right)^2\cdot v_{k_{Dw}}^2+\sigma_{\ln\varepsilon_{NC,V}}^2}\right), \tag{44}$$

where

$$a_1 = \frac{0.64\cdot B\cdot H^2\cdot\left(\sigma_N+\sqrt{mf_c}\right)}{L_s\cdot mf_c\cdot\left(3.2\cdot H\cdot\dfrac{A_{sw}}{s_w}\cdot mf_y\cdot mk_{D,w}\cdot\sqrt{1+\dfrac{2\cdot\sigma_N}{\sqrt{mf_c}}}+2.56\cdot\dfrac{B\cdot H^2}{L_s}\cdot\left(\sigma_N+\sqrt{mf_c}\right)\right)}, \tag{45}$$

$$a_2 = \frac{1}{mf_y+0.40\cdot\dfrac{B\cdot H}{mk_{D,w}\cdot\left(\dfrac{A_{sw}}{s_w}\right)_{ref}\cdot L_s}\cdot\sqrt{mf_c}\cdot\sqrt{1+\dfrac{2\cdot\sigma_N}{\sqrt{mf_c}}}}\cdot \tag{46}$$

5.5 SF_R factors for different limit states of RC beams

The case of RC beams can be analysed as a particular case of the previously analysed models for columns, the main differences being the inexistence of axial load and the existence of asymmetric longitudinal reinforcement layouts. The former is covered by the cases where very low or zero axial load are considered. Based on [23], the latter can be accounted for by considering the correction term CT proposed by Biskinis and Fardis [25] when quantifying $\theta_{SD,old}$, $\theta_{NC,old}$, $\theta_{C,old}$, θ_{SD}, θ_{NC} and θ_C that is given by:

$$CT = \left(\frac{\max\left(0.01; \omega_l^{'}\right)}{\max\left(0.01; \omega_l^{tot} - \omega_l^{'}\right)} \right)^{0.225} \approx \left(\frac{A_{sl}^{'}}{A_{sl}} \right)^{0.225} \tag{47}$$

where $A_{sl}^{'}/A_{sl}$ is the ratio between the area of longitudinal reinforcing steel in compression $A_{sl}^{'}$ and in tension A_{sl}. The correction term CT is therefore affected by the conformity index $k_{D,\rho}$, associated with the longitudinal reinforcement. By introducing these two aspects into Eqs. (24)-(27), revised versions of the SF_R factors presented in Eqs. (35)-(38) were obtained assuming that the variability parameters $\sigma_{\ln\varepsilon}^2$ are approximately the same as those in Eqs. (25)-(28):

$$SF_{DL,old} = \exp\left(-\Phi(q) \cdot \sqrt{\left(\frac{1}{2 \cdot mf_c}\right)^2 \cdot \left(v_{f_c}\right)^2 + \sigma_{\ln\varepsilon_{EI_{eff},old}}^2} \right), \tag{48}$$

$$SF_{SD,old} = \exp\left(-\Phi(q) \cdot \sqrt{\left(\frac{0.0084 \cdot \left(l_0/d_b\right)_{ref}}{0.58 + 0.0084 \cdot \left(l_0/d_b\right)_{ref} \cdot mk_{D,l}}\right)^2 \cdot v_{k_{D,l}}^2 + \left(\frac{0.225}{mk_{D,\rho}}\right)^2 \cdot v_{k_{D,\rho}}^2 + \sigma_{\ln\varepsilon_{cap,old}}^2} \right), \tag{49}$$

$$SF_{NC,old} = \exp\left(-\Phi(q) \cdot \sqrt{ \begin{array}{l} -\left(\frac{0.19}{mf_c}\right)^2 \cdot v_{f_c}^2 + \left(\frac{0.19}{mf_y}\right)^2 \cdot v_{f_y}^2 + \left(\frac{0.225}{mk_{D,\rho}}\right)^2 \cdot v_{k_{D,\rho}}^2 + \sigma_{\ln\varepsilon_{pc,old}}^2 \\ + \left(\frac{0.0032 \cdot \left(l_0/d_b\right)_{ref}}{0.84 + 0.0032 \cdot \left(l_0/d_b\right)_{ref} \cdot mk_{D,l}}\right)^2 \cdot v_{k_{D,l}}^2 \end{array} } \right), \tag{50}$$

$$SF_{C,old} = \exp\left(-\Phi(q) \cdot \sqrt{ +\left(3.78 \cdot \frac{1}{B} \cdot \left(\frac{A_{sw}}{s_w}\right)_{ref}\right)^2 \cdot v_{k_{D,w}}^2 + \sigma_{\ln\varepsilon_{C,old}}^2} \right). \tag{51}$$

Considering the models described before for the case of columns with ribbed bars, revised versions of the SF_R factors can also be obtained for beams following the same principles outlined before regarding the axial load, the asymmetric reinforcement and the $\sigma^2_{\ln \varepsilon}$ terms. Based on Eqs. (39)-(42), SF_{DL}, SF_{SD}, SF_{NC} and SF_C can be rewritten as:

$$SF_{DL} = \exp\left(-\Phi(q) \cdot \sqrt{\left(\frac{1}{2 \cdot mf_c}\right)^2 \cdot \left(v_{f_c}\right)^2 + \sigma^2_{\ln \varepsilon_{EI_{eff}}}} \right), \tag{52}$$

$$SF_{SD} = \exp\left(-\Phi(q) \cdot \sqrt{\left(-0.0048\right)^2 \cdot v_{f_c}^2 + \left(\frac{\frac{21.6}{B} \cdot \left(\frac{A_{sw}}{s_w}\right)_{ref}}{0.02 + \frac{40}{B} \cdot \left(\frac{A_{sw}}{s_w}\right)_{ref} \cdot mk_{D,w}}\right)^2 \cdot v_{k_{D,w}}^2 + \left(\frac{1}{mk_{D,\rho}}\right)^2 \cdot v_{k_{D,\rho}}^2 + \sigma^2_{\ln \varepsilon_{cap}}} \right), \tag{53}$$

$$SF_{NC} = SF_{SD}, \tag{54}$$

$$SF_C = \exp\left(-\Phi(q) \cdot \sqrt{\left(\frac{-0.067 \cdot 0.62^{mf_c} \cdot \left(1 + 0.4 \cdot a_{sl}\right) \cdot u_1^{0.54}}{-0.14 \cdot 0.62^{mf_c} \cdot \left(1 + 0.4 \cdot a_{sl}\right) \cdot u_1^{0.54} + 100 \cdot \left(\frac{A'_{sl}}{A_{sl}}\right)_{ref} \cdot u_1^{1.02}}\right)^2 \cdot v_{f_c}^2 + \frac{1}{mk_{D,\rho}} + \left(\frac{0.54 \cdot u_2 + 1.02 \cdot \frac{40}{B} \cdot \left(\frac{A_{sw}}{s_w}\right)_{ref} \cdot u_1^{0.48}}{u_2 \cdot u_1 + \left(\frac{A_{sw}}{s_w}\right)_{ref} \cdot u_1^{1.48}}\right)^2 \cdot v_{k_{D,w}}^2 + \sigma^2_{\ln \varepsilon_C}} \right), \tag{55}$$

where u_1, u_2 and $\sigma^2_{\ln \varepsilon_C}$ are given by:

$$u_1 = 0.14 \cdot \left(1 + 0.4 \cdot a_{sl}\right) \cdot 0.62^{mf_c} \cdot u_2^{0.54}$$
$$u_2 = 0.02 + \frac{40}{B} \cdot \left(\frac{A_{sw}}{s_w}\right)_{ref} \cdot mk_{D,w} \tag{56}$$
$$\sigma^2_{\ln \varepsilon_C} = \sigma^2_{\ln \varepsilon_{cap}} + \sigma^2_{\ln \varepsilon_{pc,pl}}$$

Finally, for the case of shear force limit state, $SF_{NC,V}$ can be simplified according to the following expression:

$$SF_{NC,V} = \exp\left(-\Phi(q) \cdot \sqrt{\left(a_1\right)^2 \cdot v_{f_c}^2 + \left(a_2\right)^2 \cdot v_{f_y}^2 + \left(\frac{mf_y}{mk_{D,w}} \cdot a_2\right)^2 \cdot v_{k_{Dw}}^2 + \sigma^2_{\ln \varepsilon_{NC,V}}} \right), \tag{57}$$

where

5.27

$$a_1 = \frac{0.32 \cdot B \cdot H^2}{L_s \cdot mf_c \cdot \left(1.6 \cdot H \cdot \left(\frac{A_{sw}}{s_w} \right)_{ref} \cdot mf_y \cdot mk_{D,w} \cdot \sqrt{mf_c} + \frac{0.32 \cdot H^2 \cdot mf_c}{L_s} \right)}, \tag{58}$$

$$a_2 = \left(1 + \frac{0.40 \cdot H \cdot \sqrt{f_c}}{L_s \cdot \left(\frac{A_{sw}}{s_w} \right)_{ref} \cdot mk_{D,w}} \right)^{-1}, \tag{59}$$

5.6 Simplified standard-based inspection and testing levels

Although the presented formulation can be adopted for multiple combinations of uncertainties, testing and inspection plans can be used to formulate simplified approaches more compatible with standard-based methods. By considering the testing plans proposed in [15], limit values for MF_{Z_i} and VF_{Z_i} can be defined by separating the Z_i variables according to the type of survey operations they require to be determined. Accordingly, the elements of X_{f_c} and X_{f_y} require destructive testing and must, therefore, be connected to a certain testing plan that includes the number of structural components where concrete cores and reinforcing steel coupons need to be extracted for testing. Conversely, elements of k_{D_w} and k_{D_l} only require a non-destructive survey (i.e. only covering materials need to be removed) and they also need to be associated to an inspection plan that includes the number of structural elements that should be surveyed with rebar detectors.

By considering the analysis made in [15], three inspection (IL) and testing levels (TL) can be proposed. The TLs suggested herein follow what is proposed in [15], including the increase in the confidence level as more tests are performed ($\alpha = 0.05$, $\alpha = 0.10$ and $\alpha = 0.25$ for TL1, TL2 and TL3), to quantify the mean value of the material properties. Furthermore, it is considered that an indirect estimate of CoV_{f_c} can be obtained based on non-destructive tests (NDTs) (see Chapter 3 and [16]), which typically may be up to 0.30. For CoV_{f_y}, an upper level estimate of 0.10 can be assumed instead. Table 10 shows the testing levels that are obtained using this approach and the corresponding uncertainty factors that are based on the previously referred considerations.

Table 10. Testing levels and corresponding uncertainty factors

Testing Level	Cores (n/N)	Confidence level, α	$[MF_{f_c}^{low}; MF_{f_c}^{up}]$	Coupons (n/N)	$[MF_{f_y}^{low}; MF_{f_y}^{up}]$
TL1	10%	0.05	$[0.54 \cdot N^{0.13}; 1.54 \cdot N^{-0.085}]$	0.05	[0.80; 1.20]
TL2	20%	0.10	$[0.52 \cdot N^{0.14}; 1.58 \cdot N^{-0.09}]$	0.05	[0.85; 1.15]
TL3	30%	0.25	$[0.72 \cdot N^{0.07}; 1.31 \cdot N^{-0.055}]$	0.05	[0.90; 1.10]

The interval $[MF_{f_c}^{low}; MF_{f_c}^{up}]$ involves several approximations and considers a CoV_{f_c} of 0.30 as a limit case, as shown in Fig. 6.

Figure 6. Approximations for the correlation between the number of components N and $MF_{f_c}^{up}$ for TL1 (a), TL2 (b) and TL3 (c) and between N and $MF_{f_c}^{low}$ for TL1 (d), TL2 (e) and TL3 (f).

It can be seen that when an average case is considered (i.e. for a number of components N of 20), the values of $MF_{f_y}^{low}$ are approximately the inverse of the CF_{fc} factors (obtained based on a one-sided confidence interval for the lognormal mean) indicated in Chapter 4.

Conversely to f_c, and since CoV_{f_y} is typically limited to a value not larger than 0.10, constant values are adopted for $[MF_{f_y}^{low}; MF_{f_y}^{up}]$ based on the analysis shown in Fig. 7.

Figure 7. Approximations for the correlation between the number of components N and $MF_{f_y}^{up}$ for TL1 (a), TL2 (b) and TL3 (c) and between N and $MF_{f_y}^{low}$ for TL1 (d), TL2 (e) and TL3 (f).

5.29

With respect to the ILs, a similar simplification can be introduced but, in this case, a larger percentage of surveyed components decreases the impact of n/N on the mean, when compared to what happens with the proposed TLs. Hence, even though $CoV_{k_{D,l}}$ and $CoV_{k_{D,w}}$ are unknown, the larger variability is connected to the quantification of $\sigma_{k_{D,l}}$ and $\sigma_{k_{D,w}}$. Therefore, by assuming a α_F of 0.16 (and $1-\alpha_F = 0.84$) to quantify $[VF_k^{low};VF_k^{up}]$ (let k represent either $k_{D,l}$ or $k_{D,w}$) and considering the same rationale that was adopted to estimate $[MF_k^{low};MF_k^{up}]$, i.e. assuming an upper value of 0.30 for CoV_k and a variable confidence level but using in this case Eq. (21) instead of Eq. (22), Table 11 was obtained for the different proposed ILs.

Table 11. Inspection levels and corresponding uncertainty factors

Inspection Level	(n/N)	$[MF_k^{low};MF_k^{up}]$	$[VF_k^{low};VF_k^{up}]$
IL1	30%	$[0.15 \cdot N^{0.48}; 2.54 \cdot N^{-0.21}]$	$[0.60 \cdot N^{0.10}; 3.87 \cdot N^{-0.33}]$
IL2	50%	$[0.54 \cdot N^{0.145}; 1.58 \cdot N^{-0.10}]$	$[0.69 \cdot N^{0.07}; 1.98 \cdot N^{-0.16}]$
IL3	70%	$[0.82 \cdot N^{0.04}; 1.20 \cdot N^{-0.037}]$	$[0.80 \cdot N^{0.04}; 1.40 \cdot N^{-0.07}]$

The approximate models developed for $[MF_k^{low};MF_k^{up}]$ and for $[VF_k^{low};VF_k^{up}]$ are shown in Figs. 8 and 9.
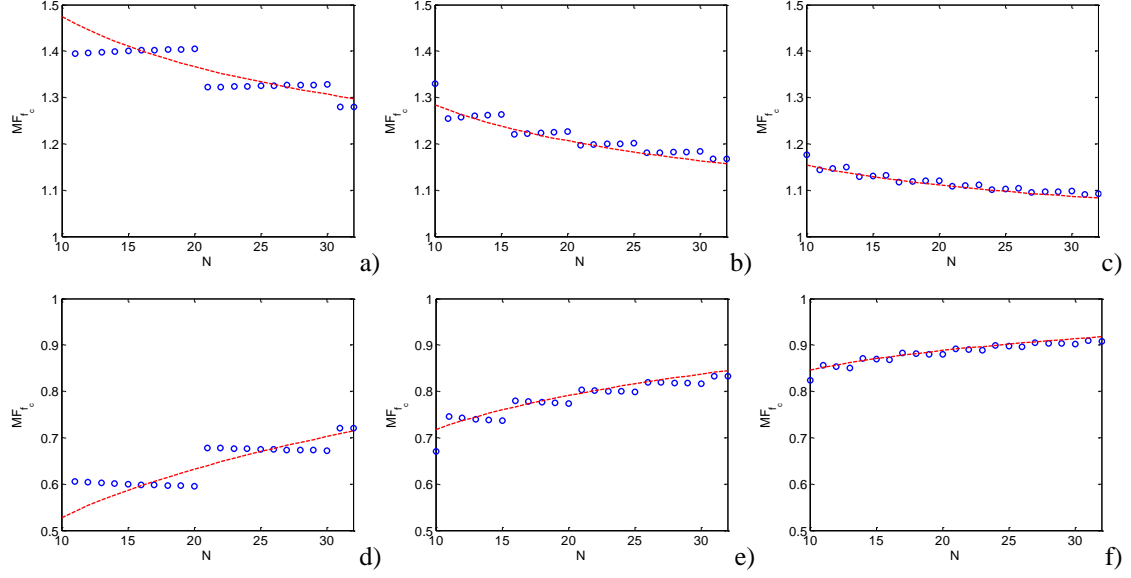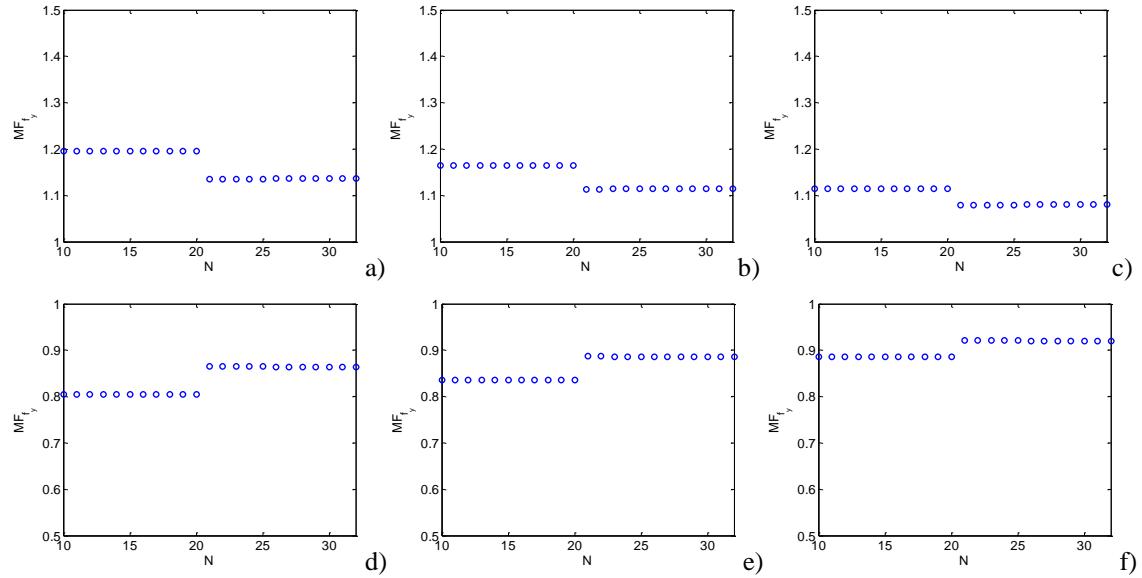

Figure 8. Approximations for the correlation between the number of components N and MF_k^{up} for TL1 (a), TL2 (b) and TL3 (c) and between N and MF_k^{low} for TL1 (d), TL2 (e) and TL3 (f).
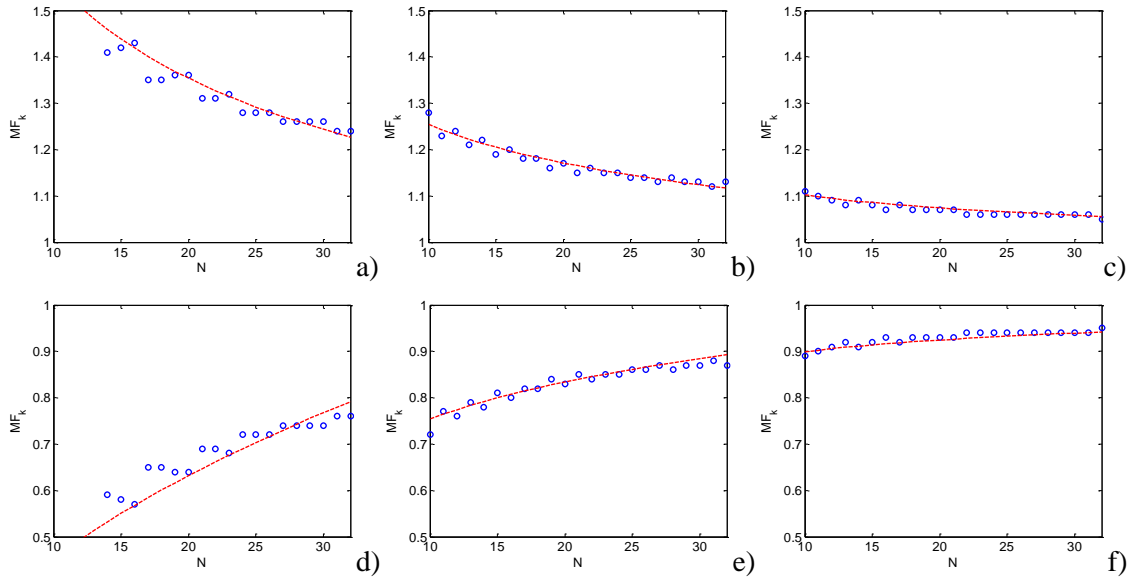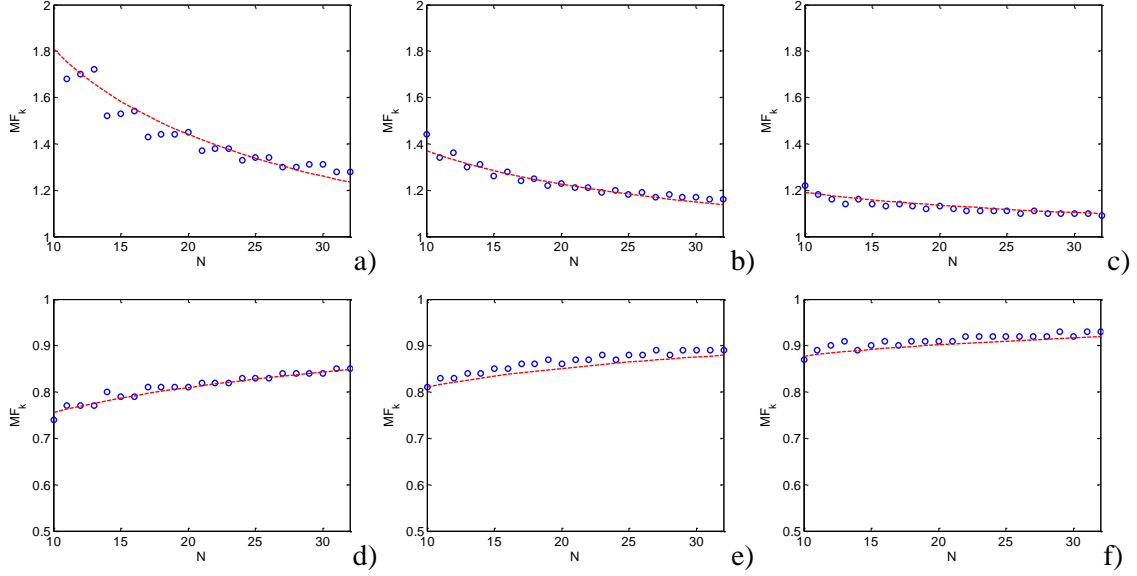
Figure 9. Approximations for the correlation between the number of components N and VF_k^{up} for TL1 (a), TL2 (b) and TL3 (c) and between N and VF_k^{low} for TL1 (d), TL2 (e) and TL3 (f).

5.7 Application example

A five storey RC frame building was adopted herein to demonstrate the calculation of the different SF_R factors that were proposed in the previous sections, and to demonstrate the impact that different types of variables and survey uncertainties may have in their values. The columns of the ground storey of the building are taken as the region under evaluation. As pointed in [14], a separation of regions in the building by storey and by floor may favour the ability to capture potential zones with homogenous properties and that reflect the systematization of construction practice (namely workmanship and construction quality). The plan layout of the storey analysed herein is shown in Fig. 10.

The selected building is assumed to be a residential building and was designed for a minimum lateral force equal to 2% of the total weight. The real properties of the columns are shown in Table 12, including the geometry of the sections, the reinforcement details and the material properties of each column of the storey. In the table, RN refers to the rebound hammer number, while $N\psi_2$ is the axial load (kN) that is expected for the seismic combination of loads. The presented values of RN and f_c are results of tests performed in a real building (dataset D5 reported in Chapter 2), while the dataset f_y refers to steel yield strength values obtained for 16mm diameter bars collected from an existing building in Portugal. The longitudinal and transversal bar diameters were randomly generated by adding to the nominal values (16 mm and 6mm, respectively) a uniform error ranging between -1.2 mm and 1.2 mm. The spacing of the transversal reinforcement was randomly generated by adding to the nominal value (0.15 m) a uniform error ranging

between -4 cm and 4 cm. The selected building is a residential building, the value of $-\Phi(q)$ is equal to 1.00 (see Table 7). The real median values of the capacity of the columns for the SD, NC and C performance levels are shown in Fig. 11, while the corresponding SF_R values obtained for the case when only the uncertainty about the limit state models is considered ($\varepsilon_{\ln R}$) are shown in Fig. 12. For the purpose of this application example, none of the material properties were assumed to be known prior to the survey, while the geometry of the building is assumed to be fully known. It is also assumed that design documents are available, indicating that all columns are supposed to have 4 smooth longitudinal steel bars with a 16mm diameter (d_b) and that the corresponding embedment length (l_0) is designed to be at least 35 times the longitudinal bar diameter (i.e. $(l_0/d_b)_{ref} = 35$). Information about the transverse reinforcement of the columns is also assumed to be available from the design documents, indicating that it should be made of stirrups with 6 mm diameter steel bars and a spacing of 15 cm in the bottom and top regions of each column, i.e. $(A_{sw}/s_w)_{ref} = 0.000377$. Furthermore, a region that includes all the 20 columns of the storey was considered ($N = 20$).
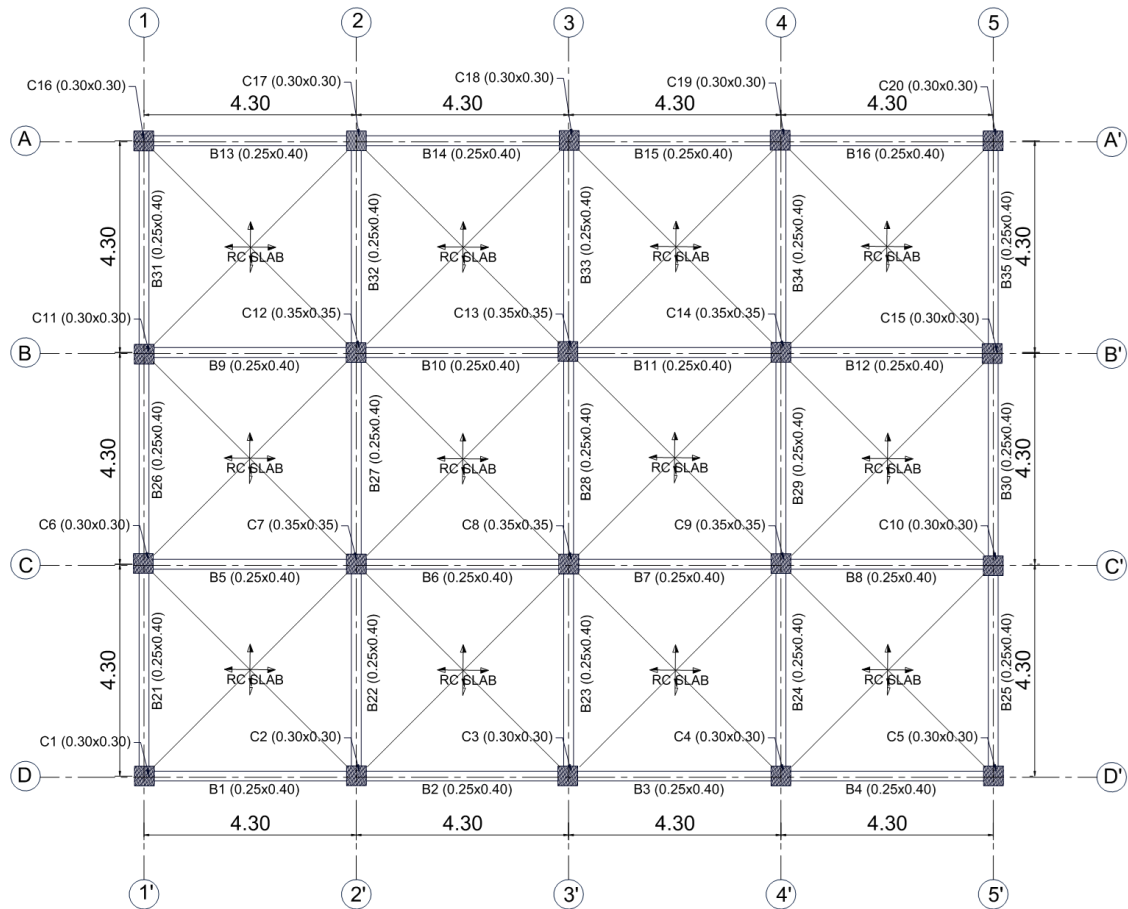

Figure 10. Layout of the structural system considered in the example application involving 20 columns and 31 beams and that represent one storey of a residential building.

Table 12. Real properties of the 1st storey of a residential building with five storeys designed for a minimum lateral force equal to 2% of the total weight.

Variable	X_g	X_g	-	X_{fc}	X_{fy}	$X_{D,\rho}$	$X_{D,w}$	$X_{D,l}$	X_g	X_g
Column	H	B	RN	f_c	f_y	A_{sl}[a]	As_w // s_w[b]	l_o/d_b	L	$N\psi_2$
Units	m	m	-	MPa	MPa	-; mm	mm; m	-	m	kN
C1	0.30	0.30	41	24.9	532	4Ø15.6	Ø 6.0 // 0.14	28.0	2.8	138.7
C2	0.30	0.30	37	19.3	494	4Ø15.3	Ø 5.9 // 0.16	21.0	2.8	277.4
C3	0.30	0.30	38	23.9	457	4Ø16.3	Ø 5.9 // 0.15	27.3	2.8	277.4
C4	0.30	0.30	37	20.2	486	4Ø15.4	Ø 6.7 // 0.16	16.6	2.8	277.4
C5	0.30	0.30	39	22.5	530	4Ø15.6	Ø 6.0 // 0.16	10.2	2.8	138.7
C6	0.35	0.35	38	22.6	496	4Ø15.7	Ø 5.8 // 0.14	24.3	2.8	277.4
C7	0.35	0.35	39	19.7	560	4Ø15.8	Ø 6.0 // 0.18	29.6	2.8	554.7
C8	0.35	0.35	37	23.6	509	4Ø16.7	Ø 7.0 // 0.14	21.5	2.8	554.7
C9	0.30	0.30	31	13.2	492	4Ø15.4	Ø 5.9 // 0.16	20.0	2.8	554.7
C10	0.30	0.30	31	15.3	507	4Ø15.9	Ø 5.8 // 0.15	24.5	2.8	277.4
C11	0.35	0.35	35	16.6	538	4Ø16.3	Ø 6.5 // 0.16	16.5	2.8	277.4
C12	0.35	0.35	36	22.2	515	4Ø15.9	Ø 7.1 // 0.13	17.5	2.8	554.7
C13	0.35	0.35	34	17.7	515	4Ø17.2	Ø 6.3 // 0.13	13.1	2.8	554.7
C14	0.30	0.30	36	15.5	510	4Ø15.4	Ø 6.6 // 0.12	12.7	2.8	554.7
C15	0.30	0.30	38	23.7	500	4Ø15.2	Ø 5.0 // 0.14	28.3	2.8	277.4
C16	0.30	0.30	38	18.4	560	4Ø16.5	Ø 5.4 // 0.15	18.6	2.8	138.7
C17	0.30	0.30	35	16.3	516	4Ø16.3	Ø 6.3 // 0.16	10.3	2.8	277.4
C18	0.30	0.30	36	20.9	457	4Ø16.3	Ø 6.6 // 0.19	21.3	2.8	277.4
C19	0.30	0.30	39	23.5	550	4Ø16.8	Ø 5.7 // 0.14	23.1	2.8	277.4
C20	0.30	0.30	40	22.3	550	4Ø15.7	Ø 5.3 // 0.17	28.3	2.8	138.7

[a] MØX represents M bars with a diameter of X mms; [b] MØX represents M bars with a diameter of X mm; [a] ØY//Z refers to square stirrups (2 x 2 legs) with a diameter of Y mms and a spacing of Z meters.
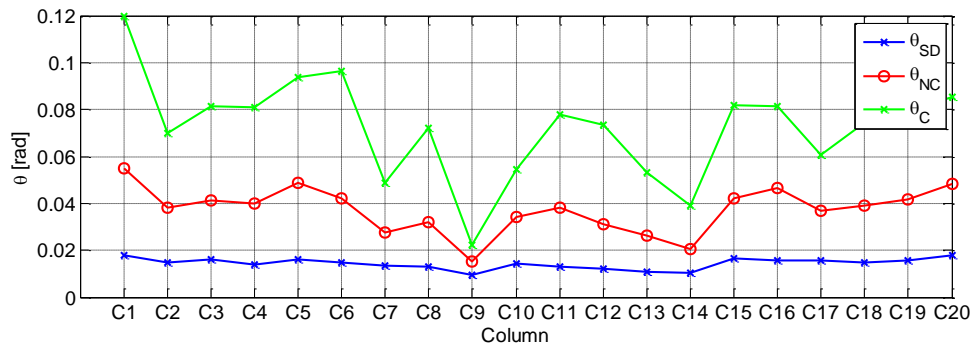

Figure 11. Median values of the capacity of the columns for the SD, NC and C performance levels.
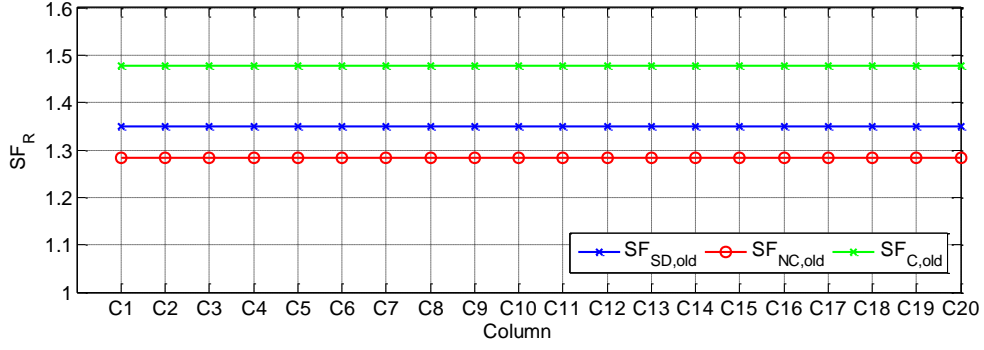
5.33

Figure 12. SF_R values obtained for the case when only the uncertainty about the limit state models is considered ($\varepsilon_{\ln R}$).

The inspection and the testing levels that were selected are IT1 and IL1, respectively. As a result, the following are obtained from Tables 10 and 11:

Table 13. Real properties of the 1st storey of a residential building with 5 storeys designed with a minimum.

N	n_{fc}	n_{insp}	n_{fy}	VF_k^{low}	VF_k^{up}	MF_k^{low}	MF_k^{up}	$MF_{f_c}^{low}$	$MF_{f_c}^{up}$	$MF_{f_y}^{low}$	$MF_{f_y}^{up}$
20	2	6	1	0.81	1.44	0.63	1.35	*0.80*	1.19	0.80	1.20

Furthermore, based on IL1 and IT1, 6 out the 20 columns have to be surveyed for details and using concrete NDTs, while 2 concrete cores and 1 reinforcing steel coupon must be extracted and tested.

The survey campaign can be simulated from the real values of the properties by randomly selecting 6 columns to survey the longitudinal and transverse reinforcement layouts, and by randomly selecting the material properties corresponding to the results that would be obtained from the destructive tests performed in 3 out of those 6 elements (2 concrete cores + 1 reinforcing steel coupon). By randomly selecting 6 out of 20 columns, RN results were also obtained and the corresponding coefficient of variation CoV_{RN} was estimated. An estimate of CoV_{f_c} was then obtained using the proposal in [16], i.e. $CoV_{f_c} \approx 1.95 \cdot CoV_{RN}$. As a result, all possible combinations of 6 components out of 30 and from each a random combination of 3 components out of 6 were considered, which resulted in multiple estimates of $\theta_{SD,old}$, $\theta_{NC,old}$, $\theta_{C,old}$ and of the corresponding safety factors $SF_{SD,old}$, $SF_{NC,old}$, $SF_{C,old}$. For both parameters, their values were obtained by considering an upper estimate of the variability factors v_x^2 and a lower estimate of the mean factors m_x. This means that values VF_k^{up}, MF_k^{low}, $MF_{f_c}^{low}$ and $MF_{f_y}^{low}$ were adopted from Tables 10 and 11 to compute m_x and v_x^2. Figures 13-15 show the histograms of $SF_{SD,old}$, $SF_{NC,old}$ and $SF_{C,old}$ obtained from the different survey plans compatible with IL1 and TL1.
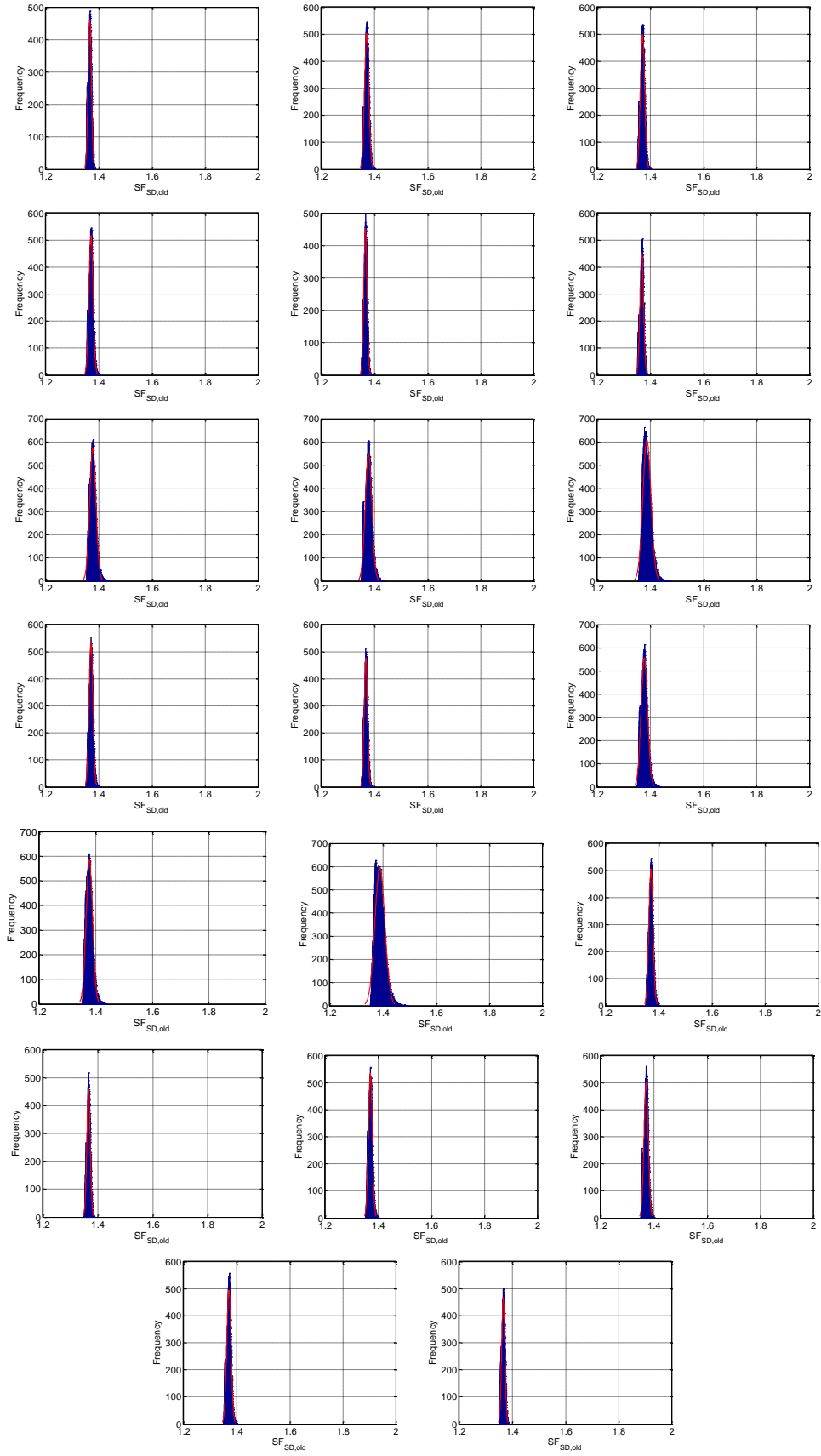
Figure 13. Histograms of $SF_{SD,old}$ obtained for each column considering different possible survey and testing plans compatible with TL1 and IL1.
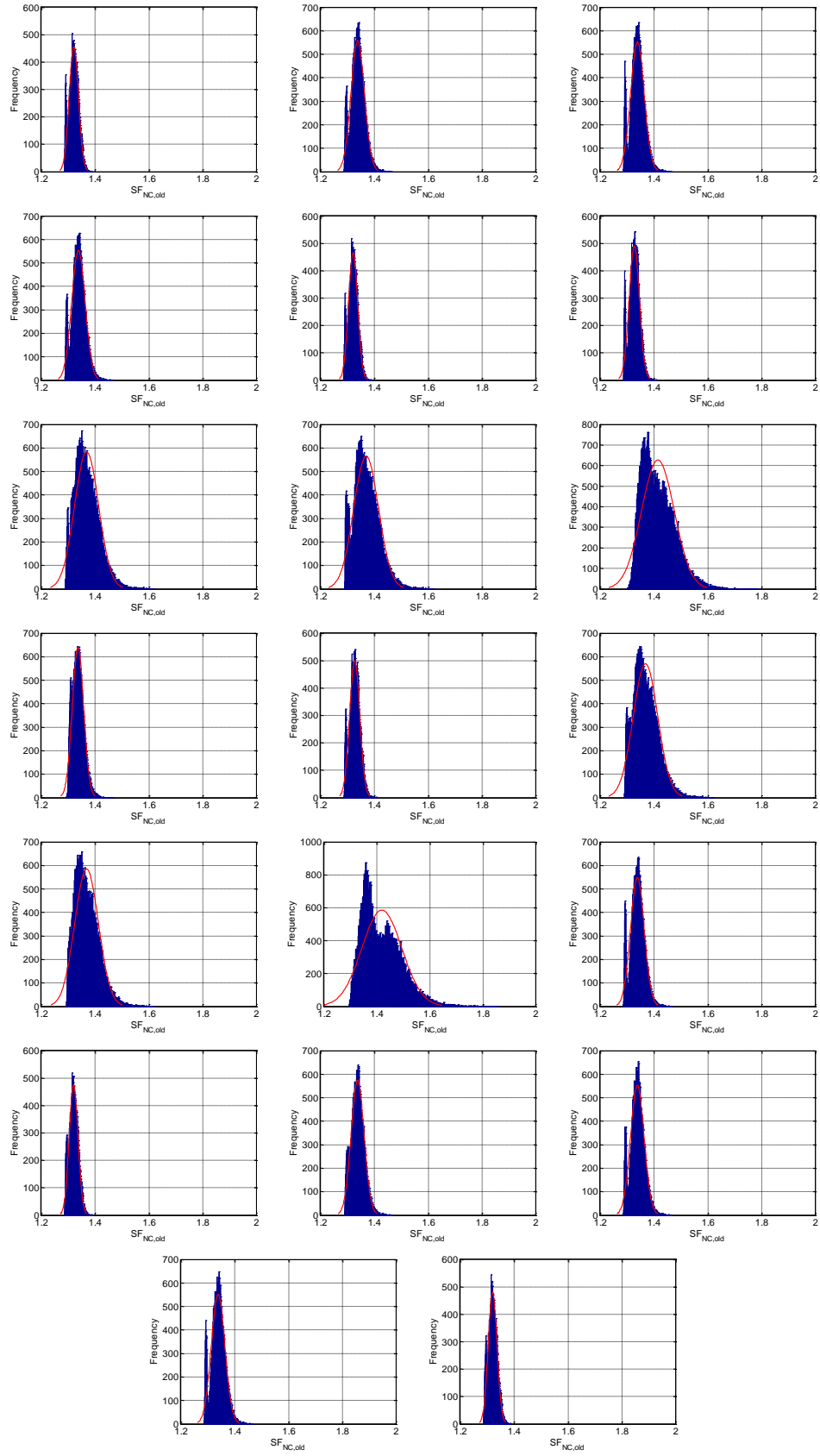
Figure 14. Histograms of $SF_{NC,old}$ obtained for each column considering different possible survey and testing plans compatible with TL1 and IL1.

5.36
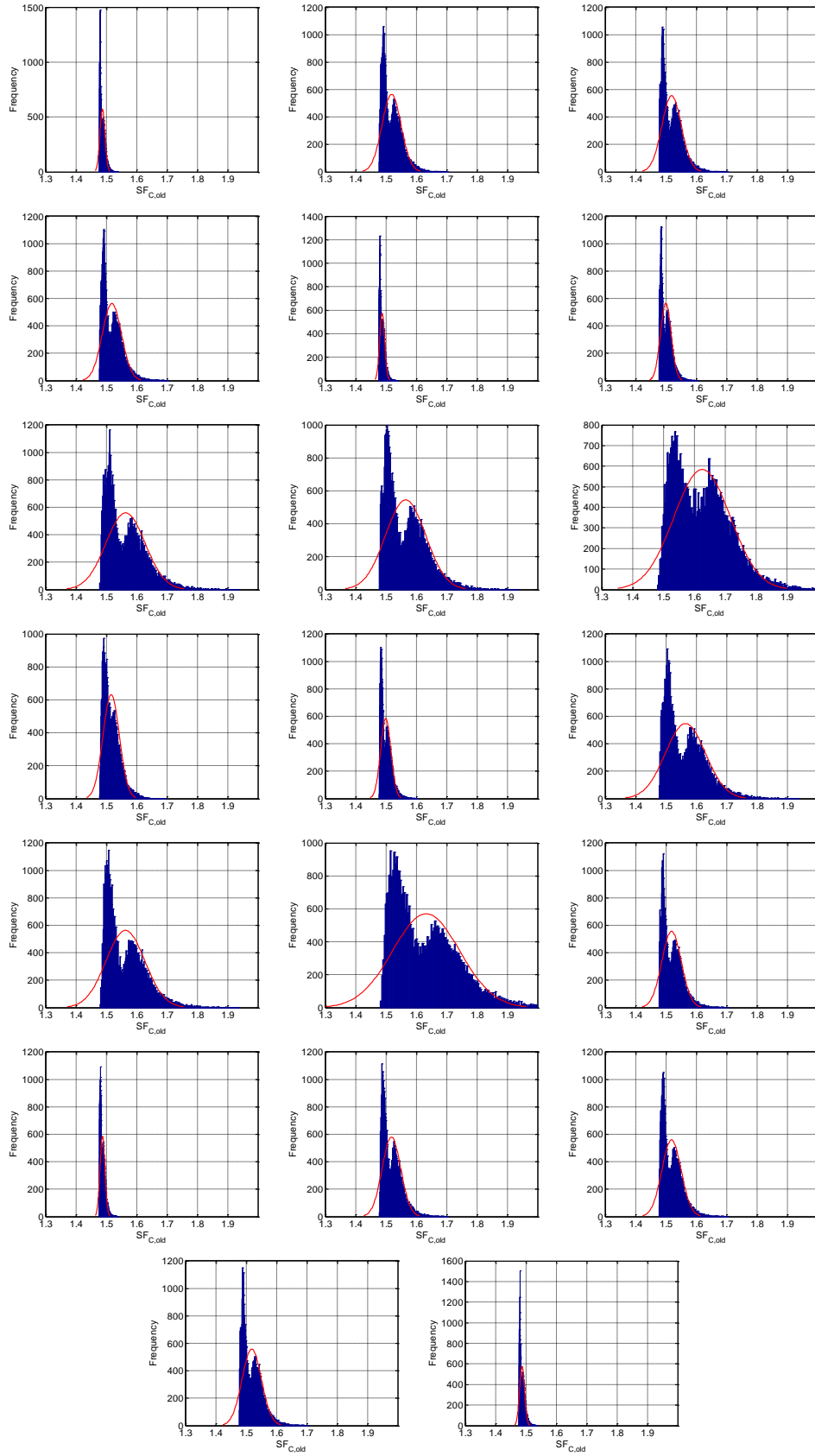
Figure 15. Histograms of $SF_{C,old}$ obtained for each column considering different possible survey and testing plans compatible with TL1 and IL1.

5.37

As seen from these histograms, $SF_{SD,old}$ has a smaller variation and leads to values that are closer to the value only obtained only with $\varepsilon_{\ln R}$ (see Fig. 12). The remaining cases show that an increase of the axial load level (i.e. of factor σ_N) leads to different weights being assigned to the uncertainty about the concrete properties and, therefore, leads to larger and more disperse values for $SF_{NC,old}$ and for $SF_{C,old}$. Figure 16 shows the boxplots of the ratio between the rotations θ_{SD} ,θ_{NC} and θ_{C} determined from Eq. (16) and the rotations $\theta_{SD,real}$,$\theta_{NC,real}$ and $\theta_{C,real}$ obtained using the real values of the parameters divided by the safety factor defined by Eq. (17).
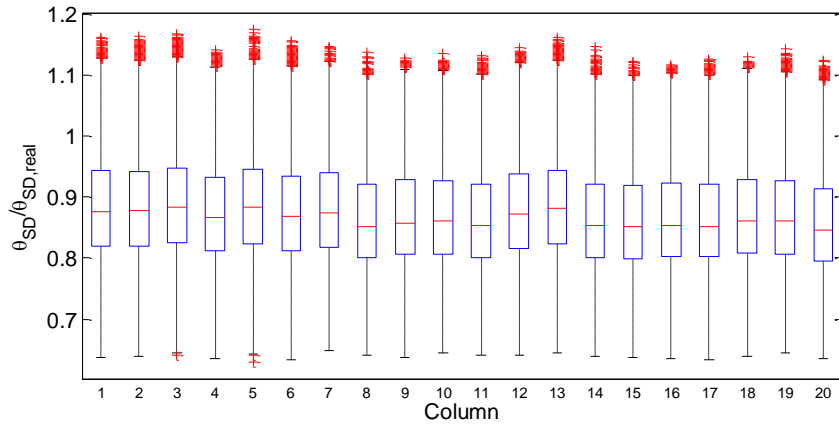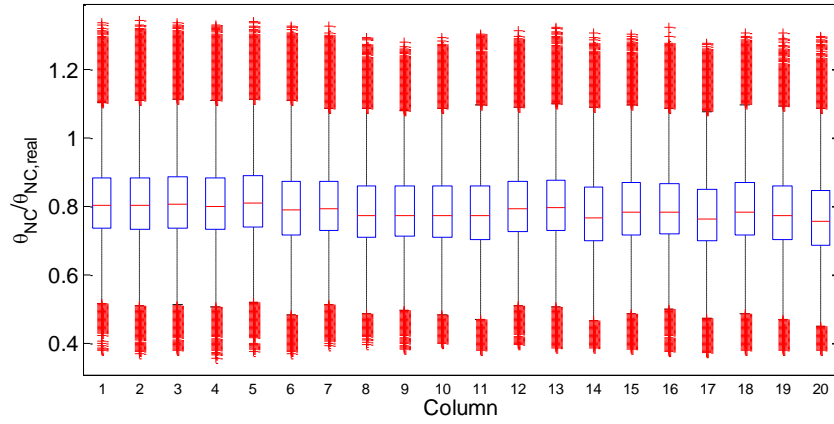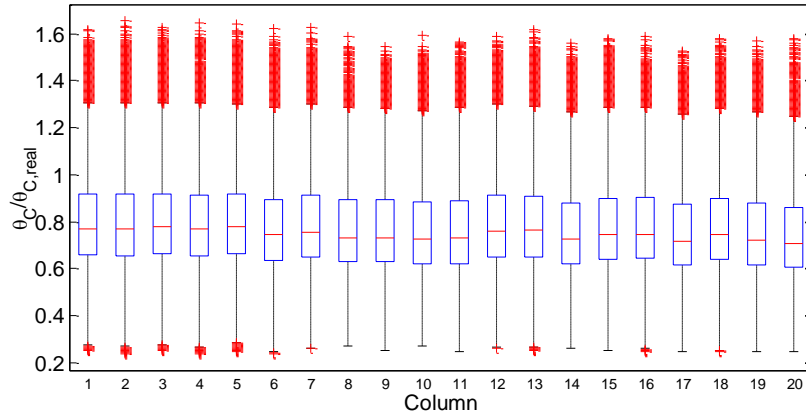
Figure 16. Boxplots of the ratio between the rotations determined from Eq. (16) and the rotations obtained using the real values of the parameters X, divided by the safety factor introduced in Eq. (17).

5.38

As shown in Fig. 16, the median ratios that were obtained are around 0.90, 0.80 and 0.80 for $\theta_{SD}/\theta_{SD,real}$, $\theta_{NC}/\theta_{NC,real}$ and $\theta_C/\theta_{C,real}$, respectively. These results also show that the bulk of the data is concentrated around these values, with the 25% quartile being found for ratios larger than 0.80, 0.70 and 0.65 for $\theta_{SD}/\theta_{SD,real}$, $\theta_{NC}/\theta_{NC,real}$ and $\theta_C/\theta_{C,real}$, respectively. Thus, the adopted IL and TL are able to control the probability of underestimating the rotation capacity, even for the current case where the lower levels of testing and inspection that were proposed (TL1 and IL1) were adopted.

5.8 Conclusions

This chapter proposed a new framework for the safety assessment of existing RC buildings. This proposal is an alternative to the original EC8/3 framework proposed in [1] and focusses on providing a more adequate characterization of the uncertainty in the limit state capacities. The proposed methodology provides the basis for defining flexible survey plans of a building, while controlling the uncertainty of the relevant parameters and focusing the outputs on the endpoint of the assessment, i.e. an adequate definition of the component capacities that will be used in the safety assessment verifications. Furthermore, the framework merges the main strengths of the ASCE 41-13 safety assessment approach regarding the definition of global safety factors, the connection between the admissible analysis methods and the available knowledge, between numerical models and acceptance criteria.

Based on the limitations identified in [11] and other previous studies, this proposal presents a new formulation for the limit state verification that shifts from the use of CF values to a format that involves global safety factors (SF$_R$) that factor the capacity of RC frame building components. These safety factors were calibrated for RC beams and columns with smooth and ribbed bars and were formulated for different levels of uncertainty of the parameters involved in the assessment. The selected parameters were divided in classes corresponding to the concrete strength, reinforcing steel strength, geometric properties and reinforcement details. The calibration that was performed provides a direct link between the testing and inspection plans that can be adopted and the admissible range of values for the mean properties of the variables. In order to solve the difficulties associated with the assessment of reinforcement details and their uncertainty, a new methodology was proposed that involves defining a reference structure based on the available design documents or on simulated design. The uncertainty of reinforcement details is then analysed by estimating the average conformity between the reference structure and what is observed in the real building.

5.9 References

1   CEN (2005). Eurocode 8: design of structures for earthquake resistance. Part 3: Assessment and retrofitting of buildings. Brussels, 2005.

2   Romão X, Delgado R, Costa A. (2010). A comparative application of different EC8-3 procedures for the seismic safety assessment of existing structures. Bulletin of Earthquake Engineering; 8(1): 91.

3   Pinto PE, Franchin P, (2008) Assessing existing buildings with Eurocode 8 part 3: a discussion with some proposals. Background documents for the Worksop: Eurocodes: background and applications. Brussels, Belgium.

4   Mpampatsikos V, Nascimbene R, Petrini L, (2008). A critical review of the R.C. frame existing building assessment procedure according to Eurocode 8 and Italian seismic code. Journal of Earthquake Engineering, 12: 52–82.

5   Caprili S, Nardini L, Salvatore W, (2012). Evaluation of seismic vulnerability of a complex RC existing building by linear and nonlinear modeling approaches. Bulletin of Earthquake Engineering; 10: 913-954.

6   Araújo M, Castro JM, (2016). On the quantification of local deformation demands and adequacy of linear analysis procedures for the seismic assessment of existing steel buildings to EC8-3. Bulletin of Earthquake Engineering 14 (6): 1613-1642.

7   Manfredi V, Masi A, (2017). Consistency of analysis methods considered in EC8-3 for the seismic assessment of RC existing buildings. Bulletin of Earthquake Engineering, 15(7): 3027-3051.

8   Romão X, Delgado R, Costa A, (2010) Practical aspects of demand and capacity evaluation of RC members in the context of EC8-3. Earthquake Engineering and Structural Dynamics; 39:473–99.

9   Araújo M, Castro JM, (2017). Simplified procedure for the estimation of local inelastic deformation demands for seismic performance assessment of buildings. Earthquake Engineering and Structural Dynamics; 46: 491–514.

10 Jalayer F, Elefante L, Iervolino I, Manfredi G, (2011). Knowledge-based performance assessment of existing RC buildings. Journal of Earthquake Engineering;15: 362-389.

11 Franchin P, Pinto PE, Rajeev P, (2010). Confidence factor?, J Earthq. Eng. 14 (7): 989–1007.

12 Monti G, Alessandri S, (2009). Application of Bayesian techniques to material strength evaluation and calibration of confidence factors, in: E. Cosenza (Ed.), Eurocode 8 Perspectives From the Italian Standpoint Workshop, 67-77, Doppiavoce, Naples, Italy, 2009

13 Romão X., Gonçalves R., Costa A., Delgado R. (2012). Evaluation of the EC8-3 confidence factors for the characterization of concrete strength in existing structures, Materials and Structures; 45 (11): 1737–1758.

14 Pereira N, Romão X, (2016). Assessment of the concrete strength in existing buildings using a finite population approach. Construction and Building Materials. 110. 106-116.

15 Pereira N, Romão X, (2016). Material strength safety factors for the seismic safety assessment of existing RC buildings. Construction and Building Materials. 119. 319-328.

16 Pereira N, Romão X, (2018). Assessing concrete strength variability in existing structures based on the results of NDTs. Construction and Building Materials. 173. 786-800.

17 American Society of Civil Engineers (ASCE), (2014). Seismic Evaluation and Retrofit of Existing Buildings (ASCE/SEI 41-13), Reston, VA, USA.

18 Araújo, M., Castro, J. M., Romão, X., Delgado, (2012) Comparative study of the European and American seismic safety assessment procedures for existing steel buildings. Proceedings of the 15th World Conference of Earthquake Engineering. Lisbon, Portugal

19 CEN (2005). Eurocode 8: design of structures for earthquake resistance. Part 1: General rules, seismic actions and rules for buildings. Brussels.

20 Ang AHS, Tang WH, (2006). Probability Concepts in Engineering: Emphasis on Applications to Civil and Environmental Engineering (vol. 1), second ed., John Wiley and Sons.

21 Verderame G, Ricci P, Manfredi G, Cosenza E, (2010). Ultimate chord rotation of RC columns with smooth bars: Some considerations about EC8 prescriptions. Bulletin of Earthquake Engineering, 8: 1351-1373.

22 Verderame G, Ricci P, (2018). An empirical approach for nonlinear modelling and deformation capacity assessment of RC columns with plain bars. Engineering Structures, 176: 539-554.

23 Haselton CB, Liel AB, Taylor-Lange SC, Deierlein GG. (2016). Calibration of model to simulate response of reinforced concrete beam-columns to collapse. ACI Structural journal. 113(6): 1141-1152.

24 Gokkaya BU, Baker JW, Deierlein GG, (2016) Quantifying the impacts of modeling uncertainties on the seismic drift demands and collapse risk of buildings with implications on seismic design checks. Earthquake Engineering and Structural Dynamics; 45: 1661–1683

25 Fardis MN, Biskinis DE, (2003). Deformation Capacity of RC Members, as Controlled by Flexure or Shear. Otani Symposium: 511-530.

26 O'Neill B, (2014) Some Useful Moment Results in Sampling Problems, The American Statistician; 68:4, 282-296

27 Franchin P, Pagnoni T, (2018). A general model of resistance partial factors for seismic assessment and retrofit. Proceedings of the 16th European Conference on Earthquake Engineering, Thessaloniki, Greece.

[This page was intentionally left blank]

Chapter 6

Estimating the damage localization length in RC frame components using experimental evidence and mechanical principles

Scope and objectives

In the previous chapters, focus has been put into the necessary procedures to characterize the real properties of existing RC frame buildings, and a complete framework was defined to account for the corresponding epistemic and aleatory uncertainties. Furthermore, probabilistic safety factors were defined to establish safe estimates of the brittle and ductile capacity of RC frame components and to define acceptance criteria representing certain seismic performance levels. These criteria were defined as threshold capacity values for component deformations that have to be compared with estimates of the corresponding demand. This demand quantification usually relies on finite element methods that quantify the nonlinear response of the building. A cornerstone of the behaviour models that are often used to quantify this response is the definition of the element ductility that depends on the mechanism and damage states of the component. The full development of the mechanism is often assumed to occur when reaching the loss of load bearing capacity of the component, which is connected to the concentration of damage within a finite length of the element where nonlocal deformations occur and where the Euler-Bernoulli hypotheses are violated. The length of this damaged region is therefore the length where relative displacements or inelastic rotations are concentrated, as a result of several physical phenomena leading to the localization of the deformations. The current chapter presents a critical analysis of the characteristics of the damage region length in RC frame components, and correlates its magnitude with the ductility and the kinematics of the region where severe nonlinear behaviour and damage localization is expected.

6.1 Introduction

The response of RC building components under monotonic or cyclic loading exhibits a variety of ductility levels depending on the properties of the materials, geometry, reinforcement details and loading conditions. Observations made in several experimental campaigns conducted in the past have shown that adequate confinement improves ductility (e.g. [1, 2]) and the shear capacity of the element. This is why seismic design and assessment standards enforce specific rules for the minimum transverse reinforcement of RC elements, thus ensuring minimum confinement and ductility levels and avoiding the occurrence of brittle failure modes. Recent studies (i.e. [3]) proposed the complementary adoption of anti-buckling design criteria in order to increase the collapse capacity of RC elements. The proposed criteria are based on minimum values for the slenderness ratio $\lambda = s_w/d_b$, where s_w is the stirrup spacing and d_b is the diameter of the longitudinal bars. The minimum values proposed by the authors were 8.4, 7.0 and 6.3 for a steel yielding strength f_{sy} of 275MPa, 400MPa and 500MPa, respectively, when targeting full ductility ([3]). These minimum values increase to 11, 9 and 8 when designing for a limited ductility scenario. The anti-buckling rules can therefore be seen to complement typical confinement-based design guidelines by introducing a factor that explicitly controls ductility based on the buckling of the reinforcement. The efficiency of these design principles is further enhanced when all bars are restrained by a cross tie, an important condition also noted by Saatcioglu and Ozcebe [2]. Apart from the effects of shear capacity, confinement and buckling resistance, many studies (e.g. [4-7]) have shown that ductility is also considerably affected by the axial load level and by the loading conditions, with considerable differences being found between the results obtained from monotonic and cyclic loads [8, 9].

Generally speaking, the typical flexural response of RC frame components under lateral loading exhibits an initial elastic branch up to the yielding moment of the section, followed by a hardening branch that extends until the behaviour capping point is reached (controlled either by the maximum bending moment or the admissible shear force). After that, a softening branch towards the total loss of strength capacity is typically observed. As a result, exploring the inelastic response (i.e. the ductility) of RC frame components leads to damage accumulation due to the formation of mechanisms that involve differential transversal displacements, sliding and widening of diagonal shear cracks up to the maximum deformation capacity of the element (i.e. maximum displacement and/or rotation with respect to the chord). This fact implies that, when designing the RC component, the ductility prescriptions are associated to the quantification of a finite length of the member over which damage is expected to be concentrated. In the evaluation of pre- or post-event retrofitting needs, assessing the extent of this length (which must be repaired/retrofitted using techniques such as RC, steel or FRP jacketing to increase confinement and anti-buckling resistance) is paramount. Pam and Ho [10] defined this length as the critical region length L_{cr}, i.e. the length of the RC frame member that requires adequate transverse

reinforcement compatible with a given ductility level. This critical region was defined as the length of the element where yielding of the longitudinal reinforcement, extensive concrete cover spalling with damage propagation to the concrete core, large deformations, and buckling and fracture of steel longitudinal steel bars are observed.

When the confinement or the shear capacity of the element is insufficient (i.e. non-ductile components), the definition of L_{cr} is strictly related to the extent of the element where the shear deformations are concentrated. For other levels of ductility, a strict connection between the plastic deformation capacity and L_{cr} can be established. Past research has developed simplified models for L_{cr} based on measurements performed using experimental data, including the component of the deformation related to the inelastic deformations and that related to interface effects such as bar pull out and strain penetration. These empirical models are based on the definition of an equivalent plastic hinge length, $L_{p,eq}$, which represents the height of the rectangular block where the localization of inelastic deformations is expected to occur. According to Priestley and Park [11], $L_{p,eq}$ depends on the displacement ductility, on the curvature ductility and on the length L of the element. As pointed out by Tarquini *et al.* [12] and Goodnight *et al.* [13], $L_{p,eq}$ is not a physical parameter but rather an analytical convenience associated with the indirect quantification of the global deformations of the element by integrating local deformations over the plastic hinge length. Goodnight *et al.* [13] recently reviewed these methods based on experimental observations and proposed the decoupling of the fixed-end rotations from the element internal deformations along with the adoption of a linear evolution for the inelastic curvatures. The first condition is intrinsically connected to the definition of the physical plastic hinge length, L_{pH}, which bounds the area where nonlocal deformations may be observed due to the high concentration of compressive strains near the section of maximum moment and due to the tension shift effect [14]. Nonlocal deformations (e.g. see [15]) violate the Euler-Bernoulli hypothesis (EBH) and are connected to the occurrence of horizontal cracks, to the sliding of concrete wedges in diagonal cracks and to the buckling of the longitudinal reinforcement. Due to the plastic nature of these mechanisms, the violations of the EBH can be associated with the concentration of damage at the damaged region length L_D, which converges to L_{PH} after the full hinge mechanism is formed. Therefore, after observing the softening of the global element response, the damaged region length L_D remains constant and the damage accumulation depends on nonlocal deformations at the critical region.

Although it is clear from the previous analysis that damage accumulation is driven by the concentration of nonlocal deformation-based effects that violate the EBH, typical empirical models do not explicitly incorporate the hinge mechanics into the formulation of L_D (or even $L_{p,eq}$). Instead, these models use a set of parameters that are expected to reflect the general properties of the moment gradient and of the tension shift effects (e.g. see [16]), irrespective of the ductility of the element. As an alternative to these empirical methods, it would be necessary

to establish the mechanical principles of the damage patterns and the mechanics of the element response and identify the correlation that may exist between them and direct measurements of L_D in experimental tests (involving different ductility levels). This idea was recently followed by Zimos *et al.* [17] who analysed the post-test damage patterns of non-ductile components in order to quantify L_D and the inclination of the diagonal shear cracks. The semi-empirical methodology that was proposed can only cover a subset of existing RC frame components and must, therefore, be extended to cover components belonging to different ductility classes. In light of this, the present study extends the principles used in [17] to propose a mechanical interpretation for the definition of L_{PH} using experimental measurements of L_D from ductile RC frame components. In particular, the study provides a possible classification for the global ductility of beam-column RC components with a rectangular cross section and correlates it with the expected length of the damaged region L_D, an essential task to define retrofitting solutions to increase seismic capacity or to establish repair needs after an earthquake.

6.2 Criteria for the ductility classification for RC frame components

As discussed in the previous section, the ductility of RC components is influenced by multiple factors. Experimental evidence has shown that shear capacity, the confinement properties, the buckling resistance and the axial load level are among the key variables to define the ductility of RC frame components. Therefore, these variables must be used when defining a classification scheme to predict the expected ductility of the component. The classification system proposed herein includes four different ductility classes: non-ductile (NDO), low ductility (DUCL), moderate ductility (DUCM) and high ductility (DUCH). In order to have a consistent definition of the ductility level, a general criterion to detect the expected failure mode of the component was first established. The adopted criterion is based on the proposal by Zhu *et al.* [18] who separated the response and failure of RC columns among two different regions: the flexural dominated cases (Zone F) and the shear dominated cases (Zone S). The authors selected two variables as the key inputs to distinguish between cases belonging to Zone S or to Zone F. The first variable is the transverse reinforcement ratio, $\rho_{sh} = A_{sh}/B \times s_w$, where B is the cross section dimension perpendicular to the loading direction and A_{sh} is the area of the transverse reinforcement bars parallel to the direction of loading, i.e. $A_{sh} = n_{legs} \times 1/4 \times \pi \times d_w^2$ where n_{legs} represents the number of stirrup legs and d_w the diameter of the stirrup. The second condition adopted by Zhu *et al.* [18] includes the ratio of shear demand to capacity (V_p/V_n) and the aspect ratio of the component (L_s/d). The first variable (V_p/V_n) compares the maximum shear demand (V_p) estimated by the maximum moment M_{max} (computed using the capping-to-yielding moment ratio defined in Haselton *et al.* [19] and the yielding moment computed according to [20] divided by the shear span L_s) and the corresponding capacity V_n, which can be estimated from ASCE41-17 [21] as:

$$V_n = \varsigma \cdot k \cdot \left(\frac{0.5 \cdot f_c}{L_s / d} \sqrt{1 + \frac{N}{0.5\sqrt{f_c \cdot A_c}}} \right) \cdot 0.8 \cdot A_g + k \cdot \frac{A_w \cdot f_{y,w} \cdot d}{s_w} \qquad (1)$$

where N represents the axial load in the column (in MN), f_c is the concrete compressive strength (in MPa), A_c is the gross cross section area (B×H in m^2), $f_{y,w}$ is the transverse reinforcement steel yield strength (in MPa), d is depth of the cross section measured from the extreme compressive fibre to the centreline of the transverse reinforcement, k is a strength degradation coefficient that depends on the ductility demand (varying linearly from 1.0, for a ductility level lower than 2.0, to 0.7 for ductility levels higher or equal to 6) and ς is 0.75 or 1.00 if the element is made of lightweight or normal weight concrete, respectively. The second variable is the aspect ratio (L_s/d) of the column. Based on these two variables, [18] established the global criteria that are represented in Fig. 1 to identify the type of failure in columns.
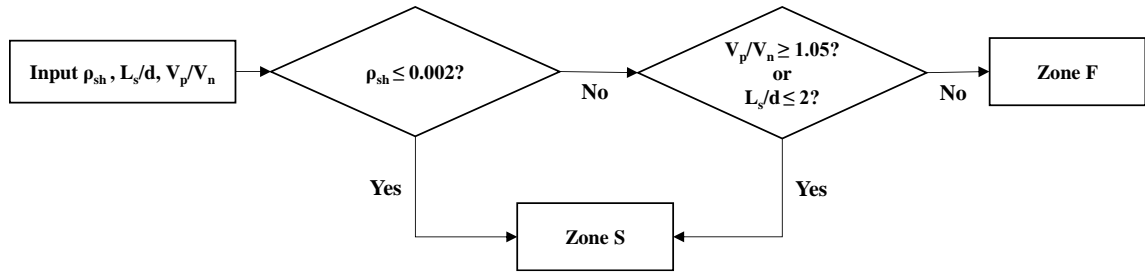
Figure 1. Criteria to distinguish between flexure- and shear-dominated RC components proposed in [18]

As seen in Fig. 1, zone S, that involves components with failure controlled by shear, is defined by factors ρ_{sh} lower than 0.002 and/or L_s/d lower than 2 (short columns). Beam-column components assumed to have predominantly shear failure have no ductility and, consequently, the L_s/d and ρ_{sh} criteria define components belonging to the NDO ductility class. The remaining cases (Zone F) correspond to components where flexural failure modes are expected according to the Zhu *et al.* ([18]) classification. In this case, components can exhibit several ductility levels depending on their characteristics and on the loading conditions. In order to establish a condition that could separate structural components with low ductility from those that are expected to have larger inelastic capacity, the main assumptions included in the Eurocode framework (e.g. [22, 23]) were considered herein. Following [23], the axial load level (ν) and the longitudinal rebar slenderness ratio ($\lambda = s_w/d_b$) were adopted as key variables to distinguish DUCL, DUCM and DUCH components. Based on the conditions defined in that standard, the axial load ratio ν should be limited to 0.65 and to 0.55 in DUCM and DUCH components, respectively. Furthermore, λ cannot exceed values of 8 and 6 in DUCM and DUCH components, respectively. Due to the closeness of the criteria defining DUCM and DUCH components, a simplified version of these

criteria was considered herein to define a single class DUCM/DUCH of components separated from the DUCL components. Therefore, DUCM/DUCH components were identified by considering threshold values for λ and ν of 6 and 0.55, respectively. Aside from these criteria, an additional condition was also considered to separate DUCL components. This condition is associated to the interaction between the shear and flexure mechanisms and is based on the ratio V_p/V_n that must be larger than 0.75 to ensure a pure flexural ductile response compatible with the DUCM/DUCH class. From these criteria, the flowchart presented in Fig. 2 is obtained.
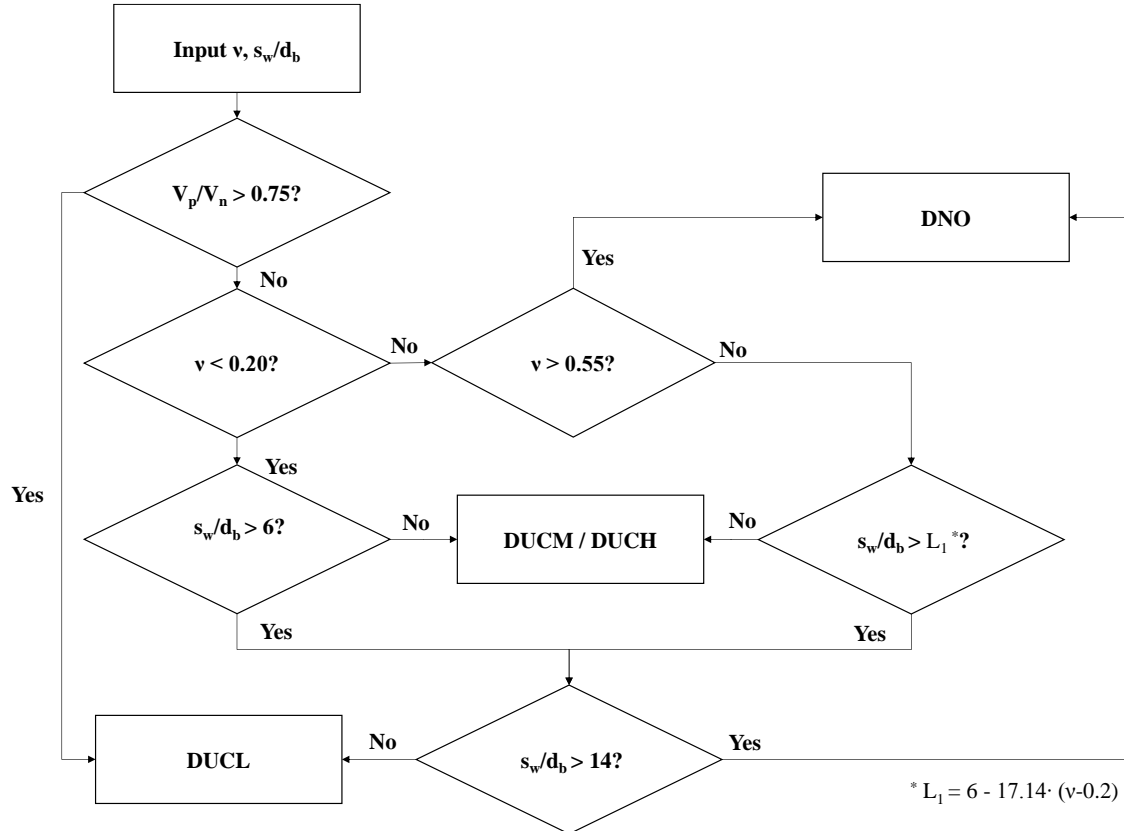
Figure 2. Criteria to distinguish between RC components meeting the DUCL and DUCM/DUCH conditions

As seen from the flowchart of Fig. 2 (combined with the flowchart of Fig. 1), RC components with $0.75 > V_p/V_n \geq 1.05$ are assumed to have a flexure-shear failure mechanism occurring for limited ductility levels such as those considered for class DUCL. For V_p/V_n ratios below 0.75, if excessive axial load levels are found (ν exceeding 0.55) or if s_w/d_b exceeds 14, the component is expected to be of class DNO. Conversely, if ν is lower than 0.20 and λ is lower than 6, RC components are assumed to belong to the ductility class DUCM/DUCH. The $\lambda \leq 6$ condition was defined based on the lowest possible value established by Dhakal and Su [3]. The 0.20 limit of ν was defined in order to represent the transition between columns that typically start to exhibit softening or mild hardening force-displacement envelopes instead of hardening. From this point on, the axial load level and the existence of second order effects were considered to limit the ductility, even when adequate confinement is considered. This condition was represented by a

linear threshold defined for ν between 0.20 and 0.55 that includes the components with $s_w/d_b \leq 6\text{-}17.14\cdot(\nu\text{-}0.20)$. This intermediate region between the linear threshold and the DNO zone defines cases belonging to the ductility class DUCL. By combining the conditions in Figs. 1 and 2, the overall classification scheme defined by the flowchart of Fig. 3 is obtained.

Figure 3. Criteria to distinguish between RC components meeting the DNO, DUCL and DUCM/DUCH conditions.

The SERIES column database [24] was adopted to verify the adequacy of the proposed classification to distinguish DNO, DUCL and DUCM/DUCH components. A total of 343 columns were considered involving multiple combinations of axial load levels, failure modes,

geometrical properties and reinforcement configurations. The failure modes reported in the database were used directly as a reference in order to evaluate the DNO condition. To evaluate the adequacy of the DUCL condition, the rotation ductility of each specimen was estimated by quantifying the plastic capping rotation following the proposal of Haselton *et al.* [19], to which the yielding rotation computed according to [25] was added. The sum of the two rotations was then divided by the latter. Figure 4a presents the comparison between the DNO and DUCL/DUCM/DUCH division obtained by applying the criteria presented in Fig. 3 and the type of failure reported in the database. The Flexure class represents components that were seen to exhibit a flexural failure mode or a flexure-shear failure mode, while the Shear class represents all the components failing in pure shear. Considering only the columns classified within the Flexure class, Fig. 4b shows the criteria defined in Fig. 3 to distinguish the DUCL and DUCM/DUCH classes. In addition, Fig. 4b also identifies the database components with an expected ductility level lower or equal than 3 ($\mu_\theta \leq 4$) and higher than 3 ($\mu_\theta > 4$).
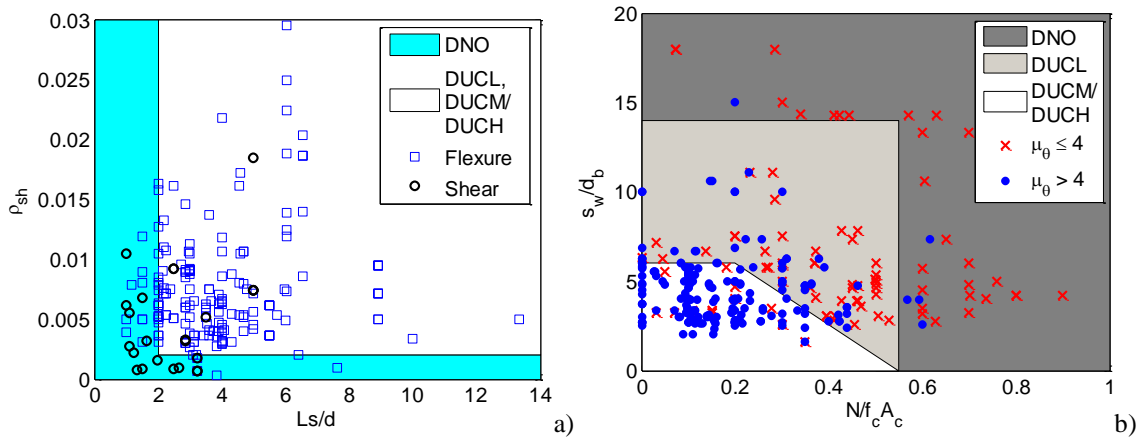
Figure 4. Comparison of the criteria adopted to define DNO conditions a) and the conditions established to separate DUCL and DUCM/DUCH cases.

As seen in Fig. 4a, most of the tests identified as shear-dominated fall inside the region defined by the criteria proposed by Zhu *et al.* [18]. Similarly, Fig. 4b shows that the majority of the tests whose ductility is expected to be lower than or equal to 3 fall inside the region defined by the criteria of the DUCL cases, thus implying that components verifying the conditions established for DUCM/DUCH are expected to have local ductility levels larger than 3. The presence of cases with an expected ductility larger than 4 is very low in the DNO region (3%), moderate in the DUCL region (33%) and high in the DUCM/DUCH region (64%). For the case of an expected ductility level lower or equal to 4, these percentages change to 33% (DNO), 48% (DUCL) and 19% (DUCM/DUCH).

6.3 Mechanical principles to estimate the length of the damaged region

6.3.1 Correlation between the ductility level and the length of the damaged region L_D

One of the key aspects associated with the ductility of RC components is the development of local mechanisms and the subsequent strength and stiffness degradation associated to the violation of the EBH. Given the differences between the ductility classes defined in the previous section, it is expected that both the damage-generating mechanisms and the characteristics of the damage accumulation (location and length) should also be distinct. As stated before, the point where the softening of the element response occurs can be used as a parameter to identify the ductility of the components. An illustrative analysis of possible correlations between the previously defined ductility classes and the failure mechanism is provided in Fig. 5, where Δ represents the lateral displacement of the element and M-θ stands for moment-rotation.
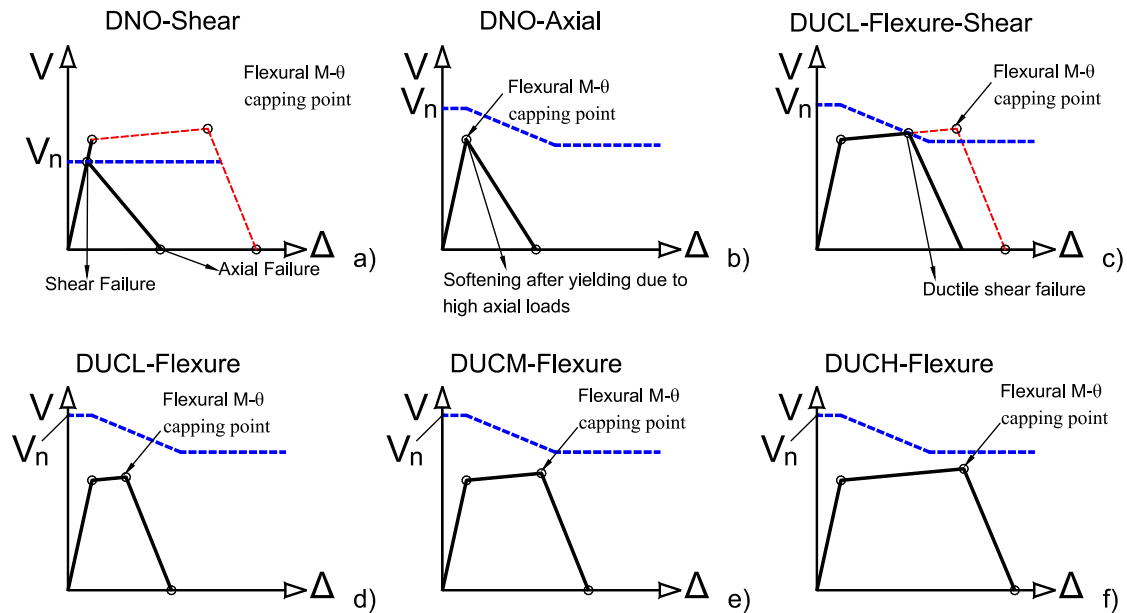
Figure 5. Typical RC member force-displacement responses associated with different ductility classes.

As shown in Fig. 5a, DNO-Shear RC components are governed by the lack of shear strength and minimum confinement, with brittle failure modes occurring prior to yielding in flexure. On the other hand, a critical DNO case can also be defined by including a high axial load scenario (Fig. 5b) that leads to the softening of the component response after yielding in flexure. The RC components with low ductility (DUCL) have either flexure-shear failure modes, where the rotation capacity of the hinges is limited by the shear capacity of the element (Fig. 5c) or low deformation capacity due to a low axial load or lack of anti-buckling resistance (Fig. 5d). Finally, DUCM and DUCH components have a more stable response with pure flexural behaviour, exhibiting a ductile response until the capping point of the moment-rotation is attained (Figs. 5e and 5f). The response of RC frame components can therefore be seen to exhibit several differences

depending on the expected ductility class. The main differences can be connected to the condition triggering the softening of the element force-displacement envelope and its corresponding effect on the damage pattern observed in experimental tests. Based on the responses shown in Fig. 5, failure mechanisms can be grouped into three different mechanisms: the pure shear failure, the flexure-shear failure and the pure flexural failure. These mechanisms can be associated to specific damage localization regions, as shown in Fig. 6 for a cantilever column. As can be seen, a shear failure mode is typically characterized by the formation of diagonal cracks which occur in the internal region of the element in case of a brittle shear failure (DNO, Fig. 6a) or at the ends of the element in case of a ductile flexure-shear failure mode (DUCL, Fig. 6b). In these cases (i.e. the DNO-Shear and DUCL-Shear failure modes of Fig. 5), the accumulation of damage after the capping point of the force-displacement response is associated to the sliding and widening of the diagonal failure planes. Thus, global deformations during the softening of the force-displacement response are mostly controlled by the mechanics of the deformations occurring within $L_{D,shear}$.
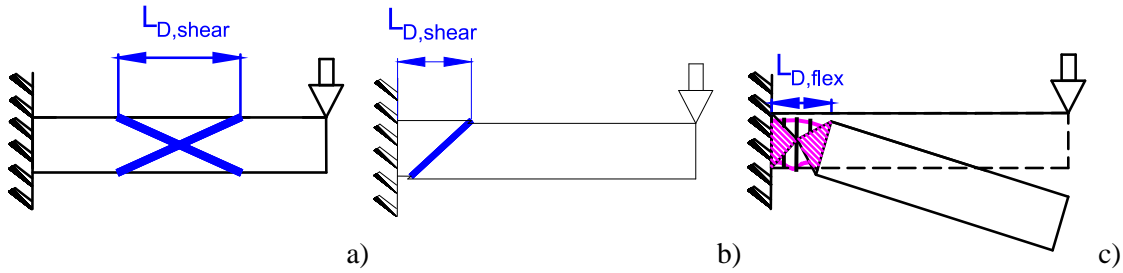

Figure 6. Idealized damage accumulation and extensively damaged region length in RC frame components due to a) a non-ductile pure shear failure, b) a low ductility flexure-shear failure and c) a flexural failure mode.

On the other hand, flexural failure modes due to lateral loading usually imply a concentration of damage at the ends of the components, with ductility demand being mostly related to the deformations observed within those regions. The mechanics of these deformations usually restrict the length of the damaged region to $L_{D,flex}$, (Fig. 6c). As a result, both $L_{D,flex}$ and $L_{D,shear}$ are finite lengths that are connected to the full development of the element's mechanism, which will be responsible for the softening of the force-displacement response for the RC component, as shown in Fig. 5. One key concept in the correlation between ductility and L_D is the consideration of fixed-end rotations associated with bar pull out and strain penetration decoupled from the element response. Feng *et al.* [26] and Goodnight *et al.* [13] pointed out that, when using the equivalent length $L_{p,eq}$, the estimates of material strains are biased and proposed to decouple these interface effects from the material strain levels. A similar approach was also adopted by other authors (e.g. [26-29]) when modelling RC frame components, thus strengthening the idea that the internal equilibrium and curvature demands of the element can be decoupled from deformations associated to rigid body displacements.

6.3.2 Defining L$_{D,shear}$ based on the mechanics of shear failure modes

Based on the principles described in the previous section, Zimos *et al.* [29] analysed the connection between the observed damage patterns in experimental tests and the main principles associated with the softening of the force-displacement response of shear (Fig. 6a) and flexure-shear (Fig. 6b) that governed RC components. The principle adopted to connect these two variables (L$_D$ and the type of component response) was based on the interpretation of the mechanism leading to the damage accumulation along L$_{D,shear}$. Accordingly, Zimos *et al.* [29] proposed a section shear law represented by the quadrilinear model shown in Fig. 7.
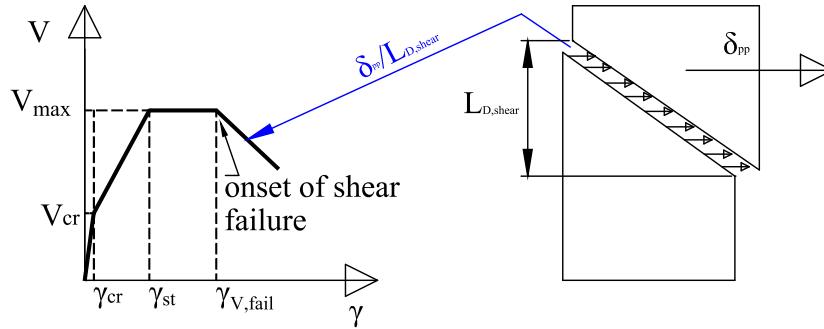

Figure 7. Section shear law proposed by Zimos *et al.* [29] and the condition leading to shear localization.

As seen in Fig. 7, after the onset of shear failure, the shear section law exhibits a softening response in which the shear distortions become dependent on the lateral deformation and on the length of the damaged region, according to the following:

$$\gamma_{eq} = \gamma_{V,fail} + \frac{\delta_{pp}}{L_{D,\text{Shear}}} = \gamma_{V,fail} + \frac{\delta_{pp}}{H \cdot \cot\left(\alpha_{V,cr}\right)}. \tag{2}$$

where γ_{eq} is the equivalent shear distortion in the localization zone, δ_{pp} represents the post-peak total lateral displacement, $\gamma_{V,fail}$ is the shear distortion at the onset of softening, $L_{D,Shear}$ is the vertical projection of the diagonal failure plane where sliding of the concrete wedges occurs and $\alpha_{V,cr}$ is the angle of the idealised failure plane at the onset of shear failure which is different from the initial crack inclination. As seen in Eq. (2), after softening, the region within $L_{D,shear}$ has an nonlocal shear distortion $\left(\delta_{pp}/L_{D,\text{Shear}}\right)$ proportional to the kinematics of the failure mechanism. Therefore $L_{D,shear}$ can be defined as:

$$L_{D,shear} = \frac{H}{\tan\alpha_{V,cr}}. \tag{3}$$

To establish $\alpha_{V,cr}$, Zimos *et al.* [29] analysed experimental data from 68 rectangular RC columns with clear evidence of shear cracking associated with flexure-shear failure and 83 RC columns with pure-shear failure before yielding. By assessing the damage patterns found in the experimental tests, namely by quantifying the geometrical characteristics of the diagonal shear failure planes, the authors proposed the following empirical model for $\alpha_{V,cr}$:

$$\tan^{-1}\left(\frac{H}{2 \cdot L_s}\right) \leq \left\{ \alpha_{V,cr} = \beta_{shear} \cdot \left(\frac{\rho_{sh}^{0.14}}{\sqrt{\nu + 0.90}}\right) \right\} \leq 45°. \tag{4}$$

with β_{shear} representing a factor that is used to separate cases with shear failure ($\beta_{shear} = 66$) and flexure-shear failure ($\beta_{shear} = 75$), ρ_{sh} is the transverse reinforcement ratio and ν is the axial load ratio. This expression can be seen to enable the consistent determination of $L_{D,shear}$ directly from damage patterns and by idealizing the failure mechanisms. By adopting $L_{D,shear}$ and the section shear law of Fig. 7, a consistent post-softening response is then obtained since the coherence between the sectional and the global responses is guaranteed by considering Eq. (2).

6.3.3 Defining $L_{D,flex}$ based on the mechanics of the plastic hinge

The framework of the study proposed by Zimos *et al.* [17] can also be adopted to evaluate $L_{D,flex}$ in flexure-dominated RC components. Nevertheless, in cases governed by flexural behaviour, several mechanisms leading to the development and rotation of hinges have to be considered, since the damage patterns observed in these cases are often more complex that those seen in shear-critical components. Some of these mechanisms involve horizontal and diagonal concrete cracking, formation of sliding planes due to loss of concrete shear friction capacity, slippage of longitudinal steel bars in horizontal cracks and yielding or instability of longitudinal steel bars. Many of these mechanisms violate the EBH and, therefore, require the development of a specific correlation between $L_{D,flex}$ and the section-level condition triggering the softening of the hinge moment-rotation response. The parallelism between the shear localization principles adopted by Zimos *et al.* [17] and those associated with flexure localization is shown in Fig. 8a.

It was previously referred that shear deformations become dependent on the lateral deformation and on $L_{D,shear}$ after the shear distortion $\gamma_{V,fail}$ is attained. Similarly, in flexure-dominated components, reaching the capping curvature (the onset of flexure failure in Fig. 8a) marks the point where the element response starts to depend on $L_{D,flex}$ and is better represented by the hinge rotation θ_{pp}. Therefore, in the same way that equivalent shear distortions become a function of $\delta_{pp}/L_{D,\text{Shear}}$ after reaching $\gamma_{V,fail}$, in flexure dominated components, the equivalent curvature χ_{eq} also becomes proportional to the nonlocal curvature $\theta_{pp}/L_{D,flex}$ after reaching $\chi_{M,Fail}$:

$$\chi_{eq} = \chi_{M,Fail} + \frac{\theta_{pp}}{L_{D,flex}} \tag{5}$$

As also shown in Fig. 8b, the deformations leading to the nonlocal curvatures after $\chi_{M,Fail}$ are conditioned by the concentration of deformations and localized damage that leads to the increase of θ_{pp}. Among the multiple effects that interact in the hinge region and contribute to the development of nonlocal curvatures, longitudinal rebar buckling and the corresponding out-of-the-plane displacement (Δ_{tra} in Fig. 8b) and the development of concrete shear-friction failure planes where sliding displacements occur (Δ_{slid} in Fig. 8b), that leads to the formation of concrete wedges, may be seen as key mechanics to study θ_{pp} and, consequently, to quantify $L_{D,flex}$. The rebar buckling and the concrete diagonal failure plane formation were therefore selected phenomena for the analysis of $L_{D,flex}$.
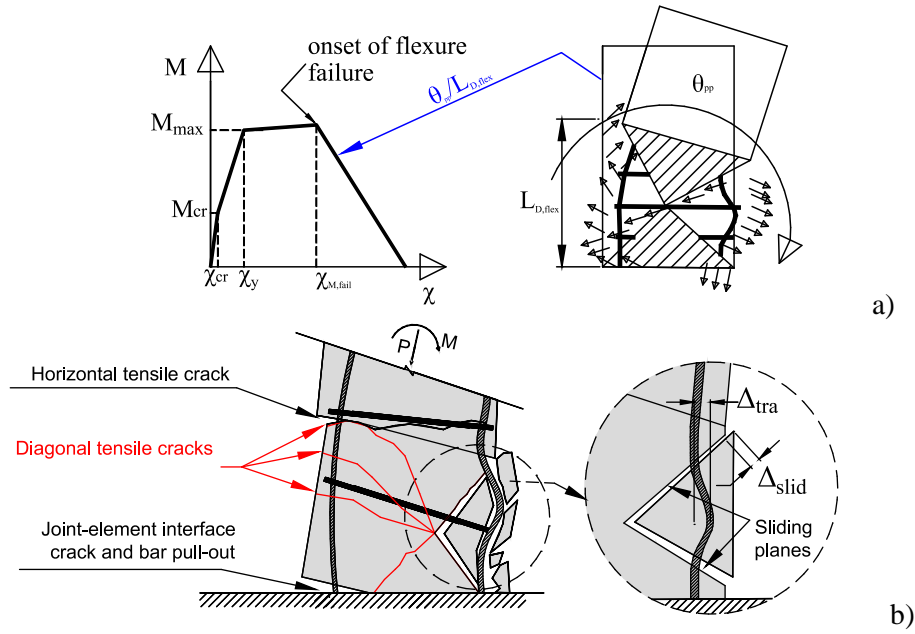
Figure 8. Effect of nonlocal deformations on the section and global deformations of flexure-governed components.

6.3.3.1 Mechanisms based on the instability of the longitudinal steel bars in compression

By assuming that $L_{D,flex}$ is dominated by the damage resulting from the buckling of longitudinal steel bars, the equivalent curvature needs to be defined considering a nonlocal component that is a function of the transversal deformation of the rebar Δ_{tra}:

$$\chi_{eq} = \chi_{M,Fail} + \chi(\Delta_{tra}) \tag{6}$$

where the equivalent curvature χ_{eq} is obtained by summing the curvature $\chi_{M,Fail}$ to the curvature caused by the transverse displacement of the longitudinal bars due to buckling. As a result, by assuming that $\chi(\Delta_{tra,})$ is proportional to $\theta_{pp}(\Delta_{tra})$, $L_{D,flex}$ must converge to the buckling length, L_{buck}. Dhakal and Maekawa [30] proposed an energy method to quantify L_{buck} as a function of the buckling mode n_{buck}, where n_{buck} represents the number of stirrup spacing lengths (s_w) over which the lateral deformations are concentrated. The buckling mode can be correlated with typical metrics characterizing the buckling phenomenon such as those adopted by Pantazoupoulou [31], Dhakal and Maekawa [32], Berry and Eberhard [33], Bae *et al.* [34] or Syntzirma *et al.* [35]. Dhakal and Maekawa [30] proposed a method for calculating n_{buck} based on the equivalent stiffness k_{eq} given by the ratio between the tie stiffness k_t and the normalizing stiffness k of the longitudinal bar. The tie stiffness k_t is defined by:

$$k_t = \frac{E_t \cdot A_t}{l_e} \cdot \frac{n_l}{n_b} \text{ (GPa/cm),} , \qquad (7)$$

where E_t is the Young modulus of the lateral tie, A_t is the cross sectional area of the lateral tie, l_e is the effective leg length of the tie, n_l is the number of ties along the buckling direction and n_b is the number of bars prone to simultaneous buckling. The normalizing stiffness k of the longitudinal bar is given by:

$$k = \frac{\pi^4 \cdot EI_b}{\left(s_w\right)^3}\text{(GPa/cm)}; \quad EI_b = \frac{E_s I_b}{2} \cdot \sqrt{\frac{f_y}{400}} \text{ (GPa/cm}^4\text{)} , \qquad (8)$$

where f_y is the yield strength of the longitudinal reinforcement (in MPa), E_s is the corresponding Young modulus and I_b is the moment of inertia of the longitudinal bar. Figure 9 shows the variation of the buckling mode n_{buck} with k_{eq} found by Dhakal and Maekawa [32] and Dhakal and Su [3], along with a power model fitted to the experimental data.
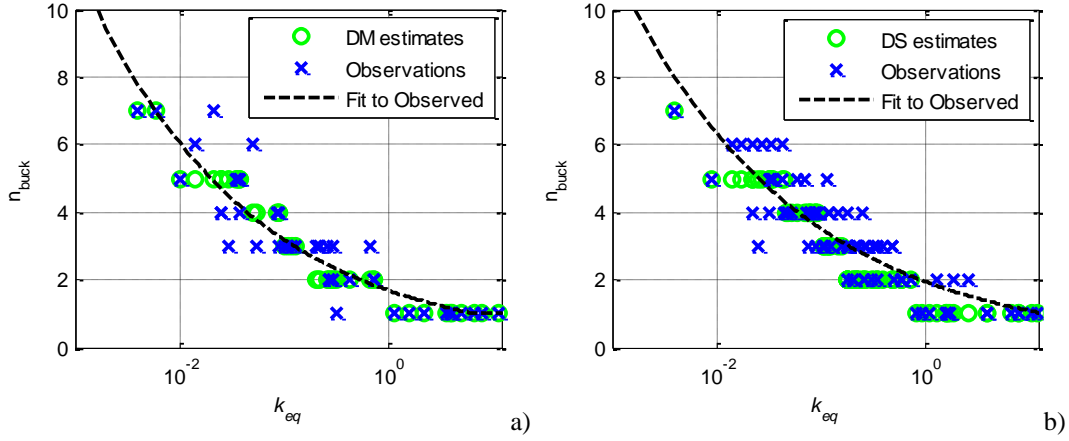
Figure 9. Comparison between experimental buckling modes n_{buck} and (a) estimates DM from Dhakal and Maekawa [30] and (b) estimates DS from Dhakal and Su [3], along with a power model fitted to the observed values.

By assuming that the buckling mechanism is responsible for the nonlocal deformations which increase the equivalent curvatures, $L_{buck} = n_{buck} \times s_w$ can be established as an approximation for $L_{D,flex}$. The two power models that correlate the buckling mode n_{buck} with k_{eq} are continuous approximations which can be used to estimate the damaged region length $L_{D,flex}$ considering the dominance of the buckling effects. Accordingly, $L_{D,flex}$ is approximately given by:

$$L_{D,flex} = \left(c_1 \cdot k_{eq}^{c_2} \right) \cdot s_w, \tag{9}$$

The transverse displacements Δ_{tra}, the buckling length L_{buck} and the nonlocal strains associated with this mechanism have all been studied before by different authors (e.g. [3; 31; 34; 35]). A common aspect of these studies is that they all develop correlations between the slenderness ratio $\lambda = s_w/d_b$ and Δ_{tra} and/or L_{buck}. Hence, by noticing that the interaction diagrams proposed by Syntzirma *et al.* [35] to estimate the steel strain ductility at the onset of buckling ($\eta_{s,cr}$) use a shape function with the form $\eta_{s,cr} = a \cdot \lambda^{-b}$, and that $\eta_{s,cr}$ marks the onset of damage localization, $L_{D,flex}$ can then be defined by:

$$L_{D,flex} = \left[d_1 \cdot \left(\frac{s_w}{d_b} \right)^{-d_2} \right] \cdot s_w. \tag{10}$$

6.3.3.2 Mechanisms based on concrete crushing

When low values of λ are considered, the occurrence of buckling requires a larger number of stirrups to be activated. This situation may lead to a delay in the occurrence of the mechanism or

6.15

to its complete absence due to failure of the surrounding concrete. In this case, the dependence between the nonlocal curvatures and the lateral instability of the reinforcement is surpassed by the lack of capacity of the concrete to sustain the imposed longitudinal and transverse strains. Hence, in this case, the equivalent curvature χ_{eq} does not depend on the nonlocal curvatures generated by Δ_{tra} but, instead, it depends on the nonlocal concrete properties that are typically related to the post-peak strength material properties. As seen in concrete specimens tested under pure compression, failure is often dictated by the loss of tensile strength in the direction perpendicular to the loading (due to the development of splitting cracks) and, particularly, by the loss of concrete shear-friction capacity that leads to the formation of diagonal failure planes and to the occurrence of sliding deformations Δ_{slid}. Visintin *et al.* [36] extended these principles to the analysis of rotating hinges in RC components and their research indicates that χ_{eq} can be obtained by summing the curvature $\chi_{M,Fail}$ with the nonlocal curvature increments due to the sliding on diagonal planes proportional to Δ_{slid} after the onset of sliding (defined by the maximum shear-friction capacity of the element):

$$\chi_{eq} = \chi_{M,Fail} + \chi\left(\Delta_{slid}\right). \tag{11}$$

As for the principles outlined for the reinforcing steel buckling mechanism illustrated in Fig. 8b, after the concrete shear-friction capacity is reached, θ_{pp} becomes proportional to the sliding displacements Δ_{slid} and to the corresponding fragmentation or out-of-the-plane movement of concrete wedges. The effect of the longitudinal cracks in compression is reflected in the size of the detached wedge, since the development of compressive splitting cracks will lead to spalling of the concrete cover. Although the longitudinal splitting cracks cannot change the macroscopic continuum stress state [38], the geometric configuration of the damaged zone may be affected, leading to the development of rectangular concrete wedges, as seen in experimental tests. Consequently, θ_{pp} will be proportional to the height L_{wedge} of the concrete wedge being pushed outwards and, therefore, L_{wedge} can be used to approximate the size of $L_{D,flex}$. Thus, the extensively damaged region $L_{D,flex}$ is associated with spalling or fragmentation of the concrete core material and not to the damage related to the concrete cover spalling resulting from the small transversal deformations and the loss of bonding between the rebar and the concrete cover.

The quantification of L_{wedge} in beams and columns involves conceptual differences. Fantili *et al.* [39] analysed the case of a hinge forming in a four point bending RC beam, following the principles illustrated by the constant moment zone represented in Fig. 10.
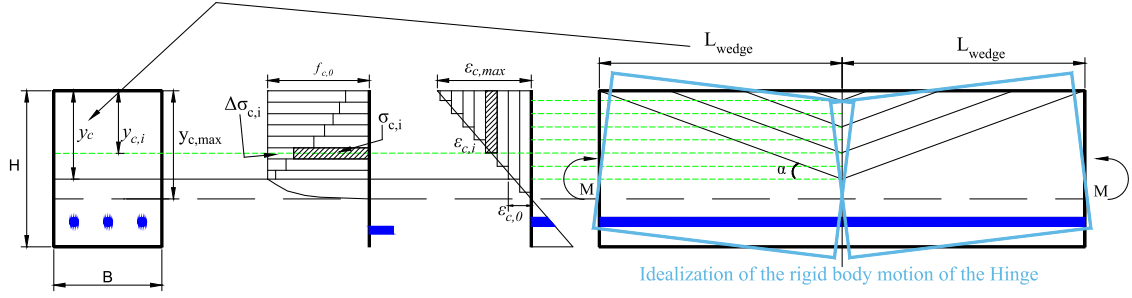
Figure 10. Model proposed by Fantilli *et al.* [39] for the flexural failure of concrete in RC beams: representation of the cross section, the stress profile, the strain profile and of the free-body diagram. The model ensures compatibility between the equivalent strain and stress diagrams, and the multiple failure planes associated with different levels of $y_{c,i}$ that are obtained with the incremental increase of the load forcing the four-point beam mechanism to occur. $y_{c,max}$ represents the depth of the neutral axis, $y_{c,i}$ is the depth of the ith plane associated with the loss of strength $\Delta\sigma_{ci}$ and y_c is the depth of the concrete part in the post-peak softening range.

According to Fantili *et al.* [39], a sliding plane with a length L_{wedge} can be associated to a depth of concrete material with equivalent strains above $\varepsilon_{c,max}$. Thus, to establish an equivalent curvature χ_{eq} consistent with the idealized rigid body rotation of the hinge shown in Fig. 10, the length L_{wedge} of the potential sliding plane is given by:

$$L_{wedge} = \frac{y_c}{\tan\alpha}, \text{ with } y_c = \frac{\varepsilon_{c,max} - \varepsilon_{c,peak}}{\chi_{eq}} . \tag{12}$$

The angle of the sliding plane with respect to the longitudinal axis was proposed by Mohamed Ali [37] as:

$$\alpha = 26° + \frac{\sigma_{con}}{f_{c0}} \cdot 20° \tag{13}$$

where σ_{con} represents an idealized uniform confinement stress and f_{c0} is the peak concrete compressive strength. The value and distribution of σ_{con} is appropriate for the confinement action resulting from external material layers and serves only as an idealization when considering the confinement introduced by stirrups. For the specific case of high strength concrete, Cusson and Paultre [41] proposed the use of a constant angle of 29° (instead of 26°) and a variable factor of 59° (instead of 20°).

Due to the boundary conditions and the location of the idealized hinge in a four point bending RC beam, the damage length $L_{D,flex}$ is twice the value of L_{wedge}:

$$L_{D,flex} = 2 \times L_{wedge} = 2 \times \frac{y_c}{\tan\alpha} . \tag{14}$$

6.17

However, this is not the case when considering RC columns subjected to differential displacements applied at the end points of the element, since hinges form at the ends of the element. Therefore, in this case, $L_{D,flex}$ can be directly associated to L_{wedge}. Visintin *et al.* [36] analysed this particularly case, focusing on the evaluation of the response of a hinge forming at one end of a RC column under axial and bending loads. As presented by Visintin *et al.* [36], the development of concrete wedges at the end of a column component can be analysed according to the diagrams of Fig. 11.
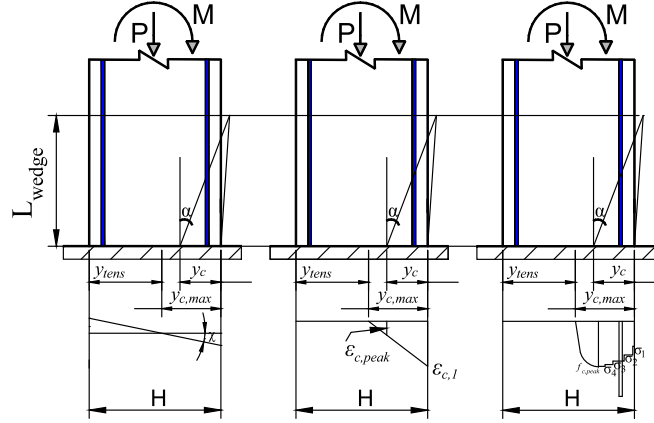
Figure 11. Curvature, strains and stresses in concrete fibres along the section depth associated with the formation of concrete wedges following the moment-rotation model of a plastic hinge proposed by Visintin *et al.* [36].

As shown in Fig. 11, the concrete wedge mechanism adopted by Visintin *et al.* [36] implies that the post-peak behaviour will depend on the sliding along a given diagonal failure plane and, consequently, effective curvatures will result from the deformation along these planes. Hence, $L_{D,flex}$ can be established as in Eq. (14) by:

$$L_{D,flex} = L_{wedge} = \frac{y_c}{\tan \alpha} .$$ (15)

Following the assumed dominance of the wedge sliding mechanism over the hinge damage localization, the length of y_c will vary as the bending moment M increases until $\chi_{M,Fail}$ is reached and will remain constant after that. By assuming that, when $\chi_{M,Fail}$ is reached, the neutral axis depth $y_{c,max}$ is approximately H/3 and considering that Hillerborg [42] referred that y_c could be assumed to be approximately 80% of $y_{c,max}$, $L_{D,flex}$ could then be estimated by:

$$L_{D,flex} = \frac{1}{4} \cdot \frac{H}{\tan \alpha} .$$ (16)

6.3.3.3 The tension-shift effect for components with adequate confinement

The development of wedges described before is intrinsically connected to the flexural response of the element, since the wedges occur due to the localized formation of diagonal cracks associated with the softening of concrete fibres in compression. In many cases, particularly those involving low s_w/d_b ratios, the hinge rotation is further disturbed by a secondary set of diagonal cracks resulting from the transfer of tensile loads to the compression side of the section through a diagonal strut. In this situation, the length y_{TC} is defined as the horizontal distance between the force resultant of the tensile stresses T and the force resultant of the compressive stresses C in the section (Fig. 12). This distance can then be used to estimate the length of the damaged area based on the angle of the shear cracks that occurs due to the load transfer [14]. The geometrical principles needed to determine the length of the element associated with the damage concentration due to the tension-shift effect are shown in Fig. 12a, following Hines *et al.* [14]. Figure 12a also shows the length L_{mg} associated to the development of plasticity in the longitudinal steel bars in tension due to the moment gradient.
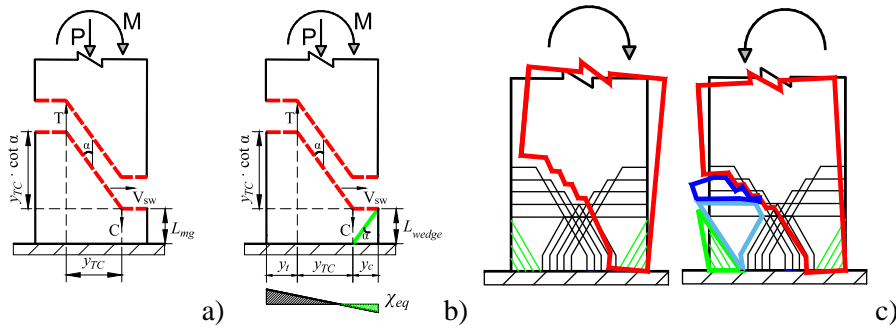
Figure 12. Mechanics of the tension-shift effect based on the principles defined by Hines *et al.* [14] (a), integration of this approach with the development of concrete wedges and the transfer of shear forces due to tension-shift (b) and interaction during cycling loading up to the failure damage pattern (c).

Based on the concept presented in Fig. 12a, the damage localization corresponding to the extent of the section that undergoes most of the damage can be approximated by the vertical progression of the diagonal cracks that are developed when the softening of the moment rotation envelope starts. After developing a fanned crack pattern in the interior part of the section due to the transition between tension and compression, damage will accumulate on the side of the section that is under compression, with the Z-shaped plane (dashed line in Fig. 12) bounding the portion of concrete where crushing will occur. Following the definition of the angle α in Eq. (13), the damage localization length $L_{Z,ts}$ that considers the development of the Z-shaped surface (and its mirror plane developed during cyclic loading) can be defined as:

$$L_{Z,ts} = L_{mg} + \frac{y_{TC}}{\tan\alpha} \tag{17}$$

Figure 12b integrates the concept of $L_{Z,ts}$ with the principle according to which the position of the compression resultant C is defined by the length y_c. Accordingly,

$$L_{Z,ts} = \frac{y_c + y_{TC}}{\tan \alpha} = \frac{2}{3} \cdot \frac{H}{\tan \alpha} \approx L_{D,flex} \tag{18}$$

which assumes that the length $y_c + y_{TC}$ can be approximated by 2/3×H. As often seen in experimental tests, when subjected to reverse loading, the tension-shift cracks lead to the development of wedges and concrete crushing over $L_{Z,ts}$. Hence, $L_{D,flex}$ values defined based on $L_{Z,ts}$ are typically larger than those based on the mechanism leading to L_{wedge} and its interaction with local buckling. Therefore, this threefold mechanism involving compression wedges, tension-shift-based wedges and reinforcement buckling has to be included when assessing $L_{D,flex}$ in RC frame components. The formulation of $L_{D,flex}$ based on $L_{Z,ts}$ is similar to the principles adopted by Goodnight *et al.* [13] where the tension-shift effect (assuming a linear curvature profile) leads to the damage concentration length $L_{PH,t}$ defined by:

$$L_{PH,t} = L_{PH,c} + 0.75 \cdot H \tag{19}$$

where $L_{PH,c}$ is the compressive plastic hinge length that only depends on the moment gradient as a function of the reinforcing steel ultimate-to-yield strength ratio f_u / f_y which can be defined as (due to the assumption of a linear curvature profile):

$$L_{PH,c} = 2 \cdot \min\left\{ 0.2 \cdot \left(\frac{f_u}{f_y} - 1 \right); 0.08 \right\} \cdot L_s \tag{20}$$

where L_s is the shear span. According to Fig. 12, $L_{PH,c}$ defined in Eq. (20) can be interpreted as L_{wedge} on the compression side of the element while $L_{PH,t}$ is similar to $L_{Z,ts}$. In case of cyclic loading, $L_{Z,ts}$ may govern the behaviour since its length is larger than $L_{PH,c}$ when the tension-shift effect and the associated mechanism occur.

6.4 Methodology

6.4.1 General steps

As seen in the previous section, from a mechanical point of view, multiple factors and mechanisms were seen to be related to the length of the damage region, $L_{D,flex}$. To establish a consistent correlation between these mechanisms and the extent of $L_{D,flex}$, a methodology similar to that followed by Zimos *et al.* [17] was adopted. First, a database of experimental data including RC frame components tested under multiple conditions was collected from the literature. The database included the constitutive modelling parameters (i.e. geometrical and construction details) of each column, along with information about the length over which damage was concentrated at after the end of the tests. Subsequently, a sensitivity analysis was conducted to evaluate the correlation between the constitutive modelling parameters and $L_{D,flex}$. Due to the potential connection between the buckling phenomenon and $L_{D,flex}$, a robust regression approach was used to assess the correlation between the damage mode ($L_{D,flex}/s_w$), the rebar slenderness ratio (s_w/d_b) and the equivalent lateral stiffness k_{eq}. The $L_{D,flex}/s_w$ ratio was used as a covariate since it can be associated with all the three damage generating mechanisms analysed before, i.e. the rebar instability, the wedge formation and the tension-shift effect. After performing the correlation analysis, the results obtained were compared with a set of models defined using the mechanical principles analysed in the previous section. In order to analyse the correlation between the ductility classes defined in Section 6.2 and $L_{D,flex}$, the results were disaggregated according to different classes of s_w/d_b.

6.4.2 Database of experimental data

A database comprising the experimental results of 115 RC frame components was analysed in the present study. The majority of the frame components included in the database (92) are those reported by Ning and Li [16] where direct measurements of $L_{D,flex}$ were available. These results refer to datasets collected from Bae and Bayrak [7], Pam and Ho [10], Yang *et al.* [44], Elmenshawi *et al.* [45], Paultre *et al.* [6], Barrera *et al.* [46], Legeron and Paultre [47], Ohno and Nishioka [48] and Ho and Pam [49]. The remaining 23 RC columns added to the database involve the results from the experimental campaign developed by Rodrigues *et al.* [50], including typical RC columns of mid-rise RC residential buildings tested under uniaxial and biaxial load patterns. The original references were verified and the $L_{D,flex}$ measured in Paultre *et al.* [6] and in Legeron and Paultre [47] were set equal to the reported fracture region. For consistency, the $L_{D,flex}$ observations collected from Pam and Ho [10] were modified in order to include those referring to

the direct damaged length observed (instead of the result directly extracted form curvature measurements used in Ning and Li [16]). In the observations made by Ho and Pam [49], the value considered for $L_{D,flex}$ corresponds to the minimum value between those observed on the left hand side and on the right hand side of the component. This last approach was also adopted when analysing the $L_{D,flex}$ values reported by Rodrigues *et al.* [50].

A second version of the database was also created considering that any reliable $L_{D,flex}$ value must be higher or equal to s_w (i.e. it is assumed that s_w should be the minimum length of the damaged region). This second version of the database is termed the filtered dataset hereon. Figure 13 shows the distribution of the main properties of the tested specimens that are included in the selected database.
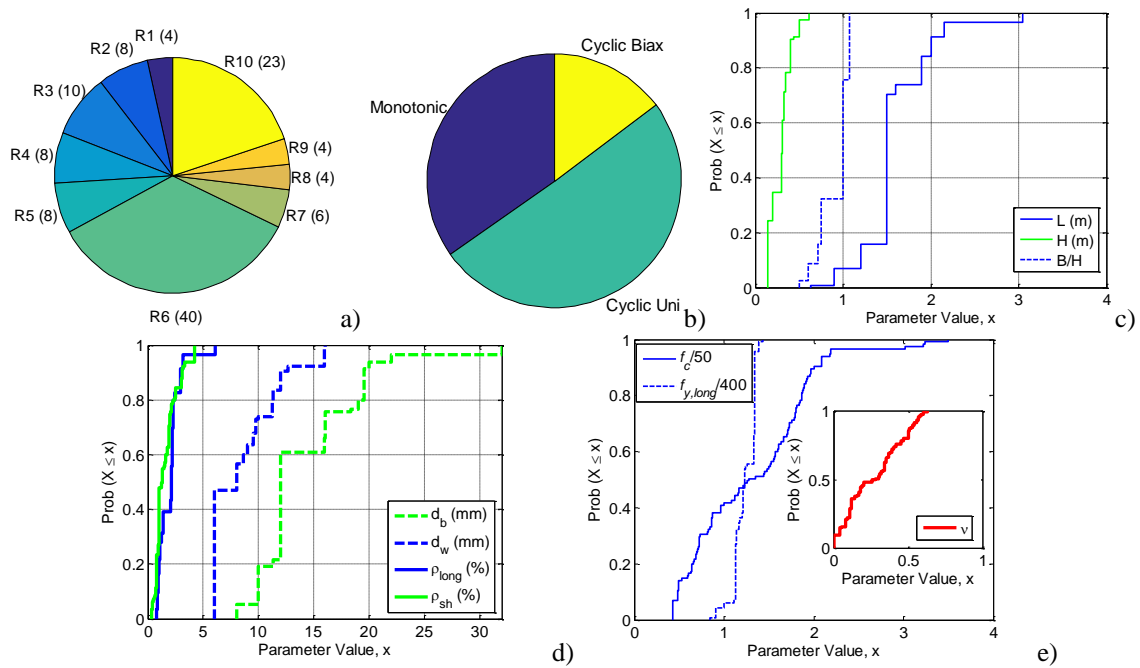

Figure 13. Details of the specimens included in the considered database: a) disaggregation per source of results (R1: Bae and Bayrak [7]; R2: Pam and Ho [10]; R3: Yang *et al.* [44]; R4: Elmenshawi *et al.* [45]; R5: Paultre *et al.* [6]; R6: Barrera *et al.* [46]. R7: Legeron and Paultre [47]; R8: Ohno and Nishioka [48]; R9: Ho and Pam [49]; R10: Rodrigues *et al.* [50]); b) disaggregation by type of loading adopted in the tests, where *monotonic* refers to uniaxial monotonic loading, *cyclic uni* refers to uniaxial cyclic loading and *cyclic biax* refers to biaxial cyclic loading; c) empirical distributions of the length (L), H and B/H ratio for the tested components, d) empirical distributions of longitudinal rebar diameter (d_b), of the stirrup diameter (d_w), of the longitudinal reinforcement ratio (ρ_{long}) and of the transverse reinforcement ratio (ρ_{sh}) for the tested components, and e) empirical distributions of the concrete compressive strength (represented by the ratio between f_c in MPa and 50), of the yielding strength of the longitudinal reinforcing steel (represented by the ratio between the longitudinal steel yield strength $f_{y,long}$ in MPa and 400) and of the axial load level $\nu = N/(A_c \times f_c)$, where N is the axial load and A_c is the area of the cross section.

Datasets R6 and R10 have a larger number of observations than the remaining cases. Nonetheless, their full inclusion in the database is justified by the fact that R6 comprises test results involving monotonic loading and several longitudinal rebar configurations while R10 includes test results

involving several specimens with a similar layout and axial load level but subjected to different uniaxial and biaxial load patterns. The latter enables the effect of the loading conditions to be assessed which has been recently identified as a relevant effect for $L_{p,eq}$ [9] and, therefore, may also affect $L_{D,Flex}$. As can be seen from Fig. 13, the database includes specimens with a wide variety of axial load levels, concrete compressive strength values and reinforcement details. Approximately 70% of the selected specimens have square cross sections and the remaining specimens have rectangular cross sections.

6.4.3 Selected models to represent the length of damage $L_{D,flex}$ RC frame components

Seven models were considered in the present study. Their corresponding designations, formats and the principles related to their development are presented in Table 1.

Table 1. Candidate models selected to approximate the real value of $L_{D,flex}$

Designation	Model	Mechanism
$L_{D,flex} / \lambda$	$L_{D,flex}/s_w = a \cdot \left(\dfrac{s_w}{d_b}\right)^b$	Bar buckling, wedge forming in compression, tension-shift
$L_{D,flex} / \mathrm{k_{eq}}$	$L_{D,flex}/s_w = a \cdot \left(k_{eq}\right)^b$	Bar buckling
L_{buck}	model from Dhakal and Maekawa [30]	Bar buckling
$L_{D,flex,wdg}$	$L_{D,flex,wdg} = \dfrac{y_c}{\tan(\alpha)} = \dfrac{0.25 \cdot H}{\tan(\alpha)}$	Wedge compression
$L_{D,flex,ts}$	$L_{D,flex,ts} = \dfrac{y_c + y_{TC}}{\tan(\alpha)} = \dfrac{0.66 \cdot H}{\tan(\alpha)}$	Tension shift
$L_{PH,c}$	$L_{PH,c} = 2 \cdot \min\left\{0.2 \cdot \left(\dfrac{f_u}{f_y}-1\right); 0.08\right\} \cdot L_s$	Length of the development of plasticity in compression
$L_{PH,t}$	$L_{PH,t} = 2 \cdot \min\left\{0.2 \cdot \left(\dfrac{f_u}{f_y}-1\right); 0.08\right\} \cdot L_s + 0.75H$	Length of the development of plasticity in tension

6.4.4 Statistical methods selected for the analyses

A robust regression analysis using Tukey's bisquare function [51]was performed between numerical estimates and experimental measurements of the length of damage $L_{D,flex}$. Robust regression was selected instead of an ordinary least squares approach in order to account for the potential uncertainty in the measurements of the damage length values reported in the database, given they are based on observations that can be affected by different types of human error. The comparison between estimates and measurements of $L_{D,flex}$ values was performed using Bland-Altman plots [52], considering several goodness-of-fit metrics such as the coefficient of determination (R^2), the root-mean-square error (RMSE), the reproducibility coefficient (RPC, defined as 1.96 times the standard deviation SD) and the corresponding percentage of values within the RPC interval.

6.5 Results and discussion

Figure 14 shows the correlation between the main geometrical and material parameters of the specimens considered in the analysis and the length of the damaged region measured in the experimental tests, $L_{D,flex}$.
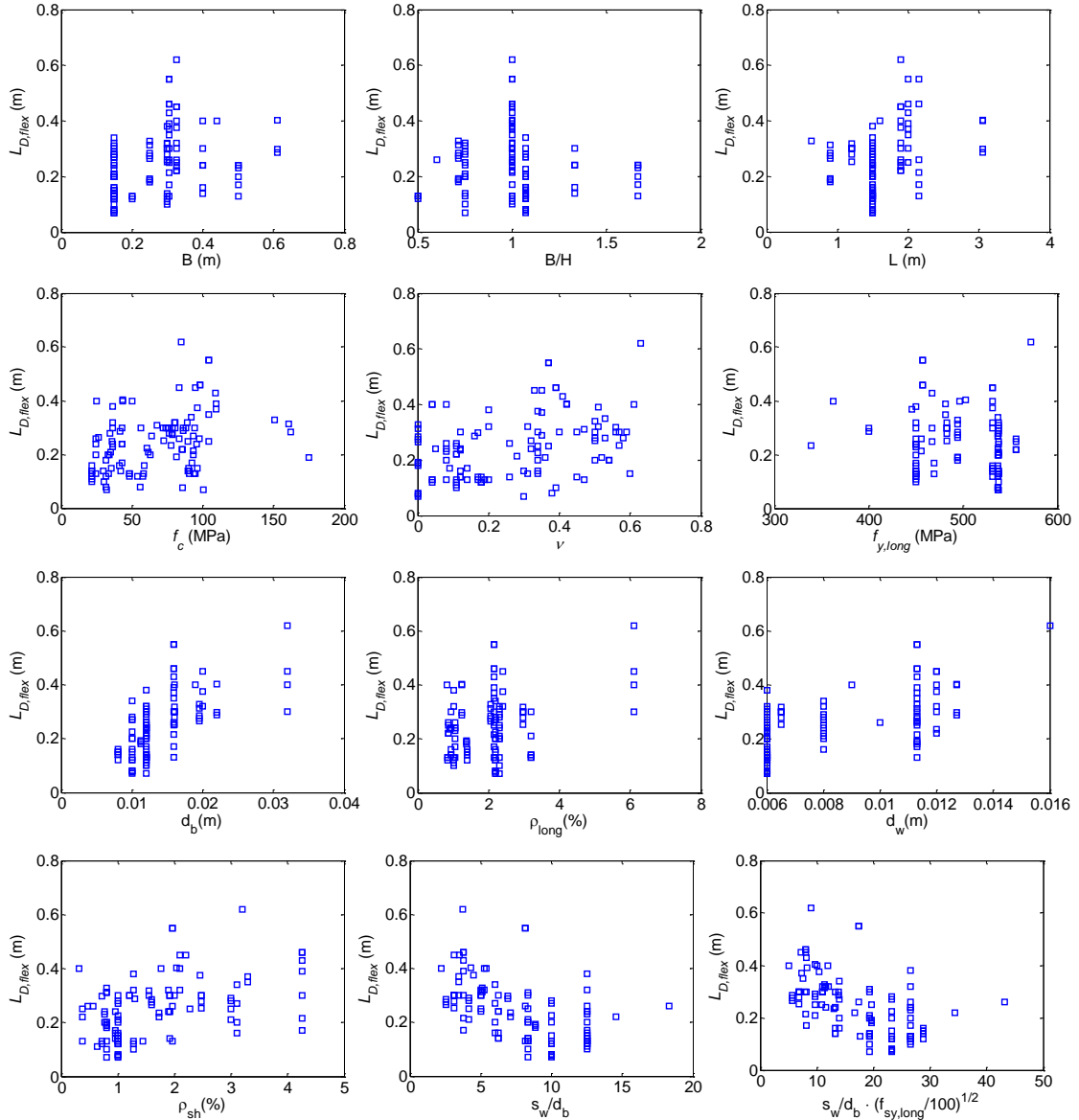
Figure 14. Evaluation of the correlation between $L_{D,flex}$ and several geometrical and material properties.

As seen in Fig. 14, no significant correlation (i.e. in terms of a linear trend) can be observed between the damage length of the components and their corresponding span L. This observation can be extended to the remaining geometrical variables, namely the cross section height H, width B and B/H ratio. Significant scatter can also be found when analysing the correlation between $L_{D,flex}$ and material properties of the section, as well as between $L_{D,flex}$ and several parameters related to the structural details. Some linear trend seems to exist between $L_{D,flex}$ and the longitudinal bar diameter d_b (where d_b was selected as the smallest diameter in a given cross

section) and, to a lower extent, between $L_{D,flex}$ and the stirrup diameter d_w or the transverse reinforcement ratio ρ_{sh}.

Figure 15a shows the correlation results between parameter $L_{D,flex}/s_w$ and the slenderness ratio $\lambda = s_w/d_b$. The slenderness ratio was calculated using the smallest value of d_b in a given cross section. As expected, a decreasing nonlinear trend was found in this case, with larger values of λ leading to lower values of $L_{D,flex}/s_w$, which is consistent with the larger potential for local buckling to occur.

The results of Fig. 15a indicate there is a strong correlation between $L_{D,flex}/s_w$ and s_w/d_b ($R^2=0.73$; RMSE=0.97). The regression analysis shown in Fig. 15b was performed considering the filtered dataset and leads to similar goodness-of-fit results ($R^2=0.75$; RMSE=0.92).

Figure 15. Correlation between L_{Dflex}/s_w and the slenderness ratio λ obtained using the original data (a) and the filtered dataset after including a condition stating that L_{Dflex}/s_w is larger or equal to 1.0 (b).

Similarly to Fig. 15, Fig. 16 shows the correlation results obtained when analysing the relation between $L_{D,flex}/s_w$ and parameter $k_{eq} = k/k_t$. In this case, a higher level of scatter is observed both with the original (Fig. 16a) and the filtered (Fig. 16b) datasets, when compared with the results of Fig. 15. The first case (Fig. 16a) shows a moderate level of correlation ($R^2 = 0.64$; RMSE = 1.12). Similar results are found for the second case (Fig. 16b) that has a R^2 of 0.65 and a RMSE of 1.09.
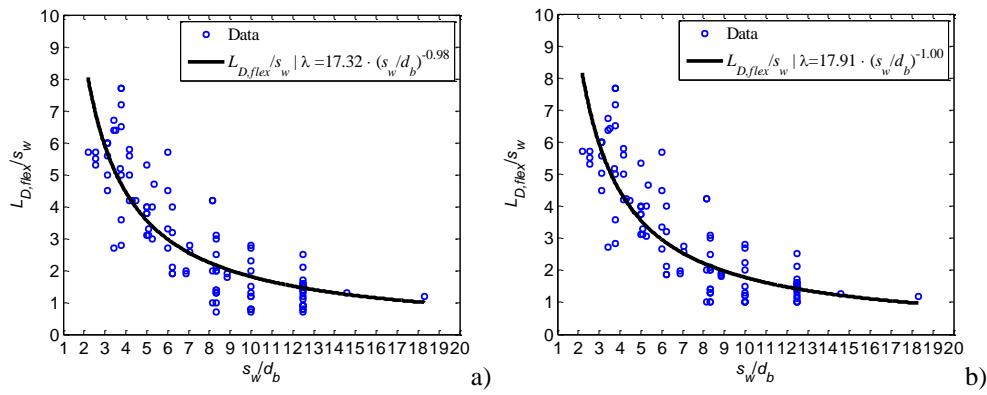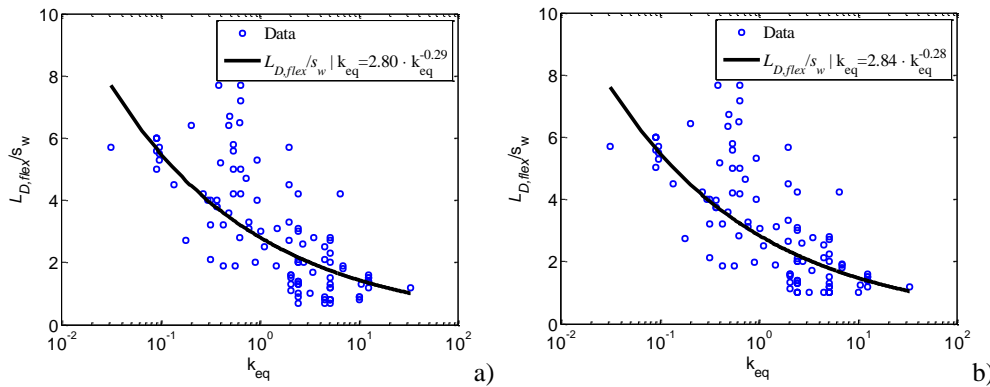

Figure 16. Correlation between L_{Dflex}/s_w and parameter k_{eq} obtained using the original data (a) and the filtered dataset after including a condition stating that L_{Dflex}/s_w is larger or equal to 1.0 (b).

Figure 17 shows the Bland-Altman plots of the damage buckling modes obtained with the approximations $L_{D,flex} / \lambda$, $L_{D,flex} / k_{eq}$, and L_{buck}.
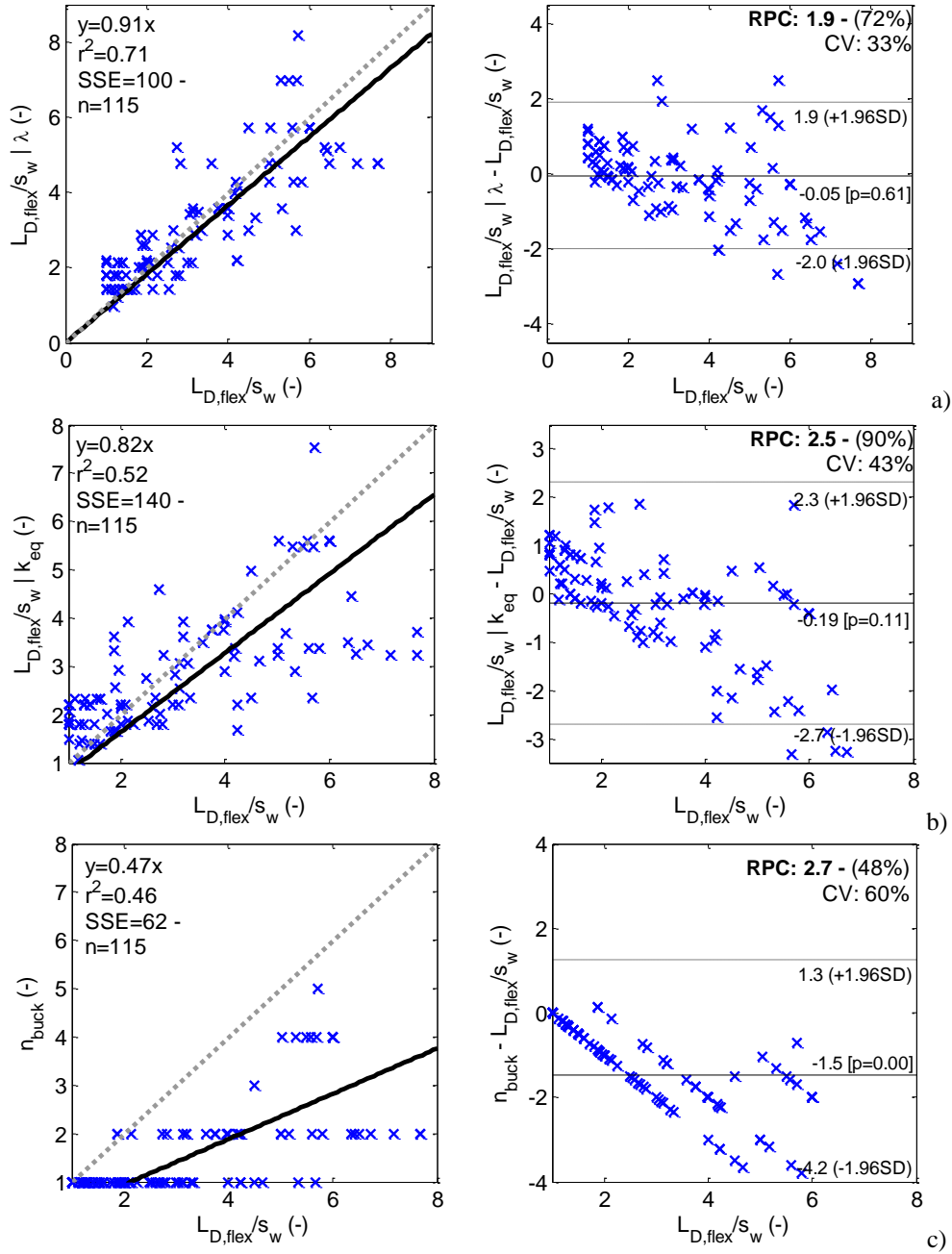
Figure 17. Correlation analysis and Bland-Altman plots obtained using $L_{D,flex}/s_w / \lambda$ (a), $L_{D,flex}/s_w / k_{eq}$ (b), and L_{buck}/s_w (c).

As seen in Fig. 17, the model $L_{D,flex} / \lambda$ is able to provide an adequate estimate for $L_{D,flex}$ (observed-to-predicted ratio y/x = 0.91), while L_{buck} underestimates, on average, the observed values (y/x = 0.47). The Bland-Altman plot obtained for L_{buck} also indicates that when the observed value of L_{dflex} exceeds $3 \times s_w$, the estimates obtained with L_{buck} do not agree with the observed values, as seen by the linear descending pattern, by the asymmetry of the data distribution and by the large coefficient of variation (CV) obtained for the deviations between predicted and observed values

(CV = 0.70). This trend in the distribution of the deviations is common to the three cases analysed, although the observed RCP values increase from 1.9 ($L_{D,flex}$ / λ) to 2.7 (L_{buck}). Overall, the deviations become larger when the observed L_{Dflex}/s$_w$ values are larger than 4. In that case, all models tend to underestimate the real value of L_{Dflex}/s$_w$.

Figure 18 shows the Bland-Altman plots obtained when using the estimates for L_{Dflex} considering the models focusing on mechanisms involving the failure of the concrete core due to the development of diagonal failure planes ($L_{D,flex,wdg}$, $L_{D,flex,ts}$, see Table 1). The results obtained for $L_{D,flex,wdg}$ lead to a Bland-Altman plot that is very similar to the one obtained when using L_{buck} and the underestimation and asymmetry levels exhibited by both models are also comparable. By adding the effect of the diagonal cracking due to the transition between tension and compression ($L_{D,flex,ts}$), the RCP value decreases from 2.8 to 2.6, and the CV of the deviations decreases from 0.64 to 0.39 - values which are closer to those obtained when analysing $L_{D,flex}$/s$_w$ / λ. Since the Bland-Altman plot of model $L_{D,flex,ts}$ does not exhibit the level of asymmetry that is observed for $L_{D,flex,wdg}$, the error distribution has a lower scatter than that obtained for L_{buck} and $L_{D,flex,wdg}$, even for $L_{D,flex}$/s$_w$ values larger than 4.
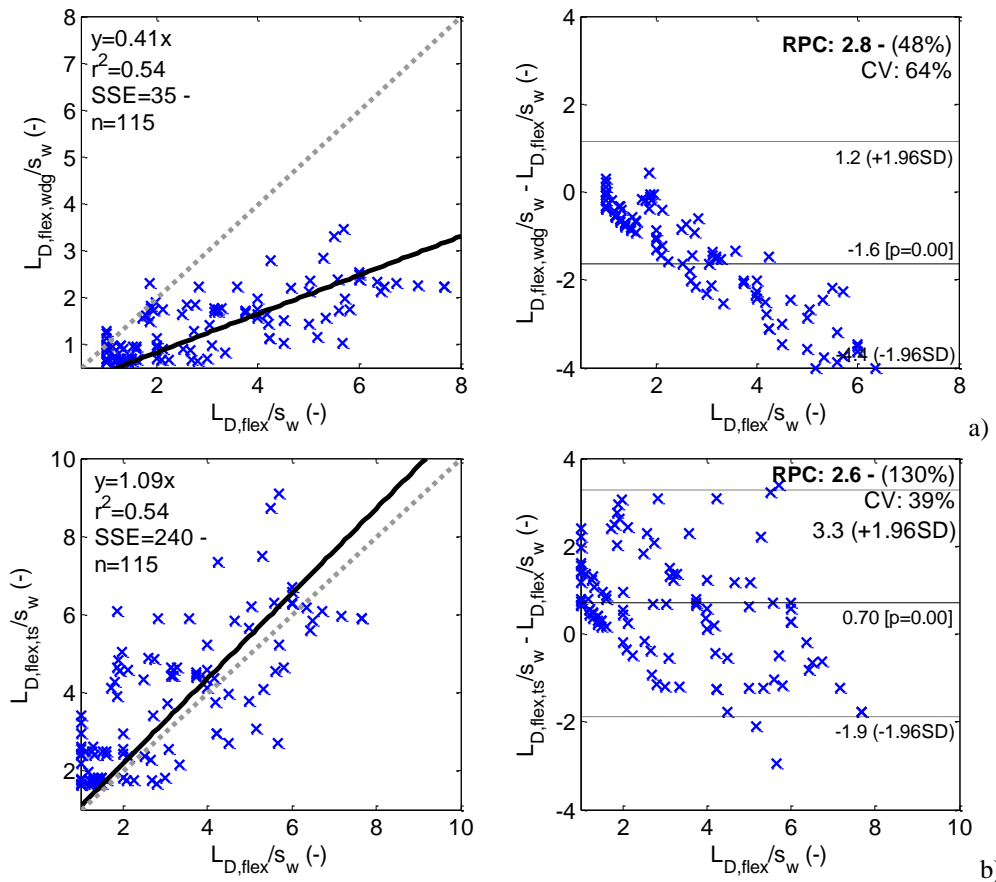

Figure 18. Correlation analysis and Bland-Altman plots obtained using $L_{D,flex,wdg}$ /s$_w$ (a), $L_{D,flex,ts}$ /s$_w$ (b).

Figure 19 presents the Bland-Altman plots obtained using models $L_{PH,c}$ and $L_{PH,t}$, i.e. considering the moment gradient, the tension shift and a linear curvature profile as proposed by Goodnight *et*

al. [13]. As seen in Fig. 19a, model L$_{PH,c}$ underestimates, on average, the value of $L_{D,flex}$/s$_w$. On the contrary, the estimates obtained with L$_{PH,t}$ overestimate the value of $L_{D,flex}$/s$_w$. This dichotomy is clear in the differences between the skewness of the errors shown in Fig. 19 where a positively skewed distribution is seen for the case of L$_{PH,t}$ and a negatively skewed distribution is obtained for L$_{PH,c}$. Furthermore, the results obtained with L$_{PH,c}$ are very close to those found using $L_{D,flex,wdg}$, while the results obtained with L$_{PH,t}$ are closer to those obtained with $L_{D,flex,ts}$. Therefore, $L_{D,flex,ts}$. is seen to be a predictor of the damage pattern for larger values of $L_{D,flex}$/s$_w$, while for $L_{D,flex}$/s$_w$ < 3 compressive instability effects in concrete and longitudinal steel rebars dominate the damage accumulation mechanism.
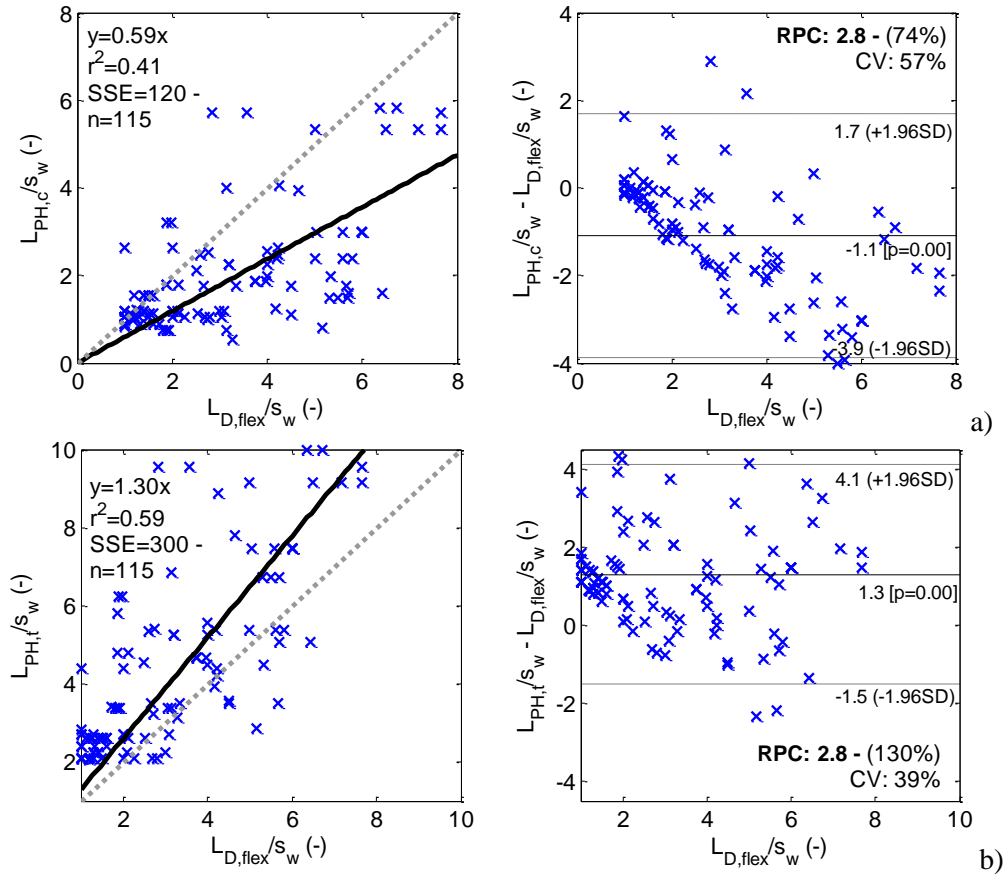
Figure 19. Correlation analysis and Bland-Altman plots obtained using $L_{PH,c}$/s$_w$ (a), $L_{PH,t}$/s$_w$ (b).

In order to evaluate the significance of the differences between the results observed in the analysis of the Bland-Altman plots, and bearing in mind the ductility classification presented in Section 6.2, a complementary cross comparison was performed between the estimates obtained with the models shown in Table 1 and the λ factor of each test. Figure 20 shows the variation of the damage accumulation mode $L_{D,flex}$/s$_w$ as a function of λ, where λ is divided into 4 classes: λ < 4, 4 ≤ λ < 6, 6 ≤ λ < 8 and λ ≥ 8.
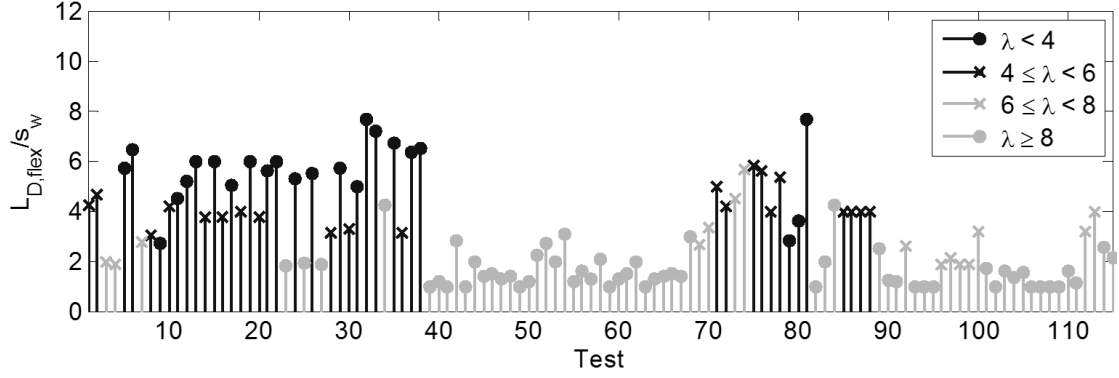
Figure 20. Variation of the damage mode $L_{D,flex}/s_w$ with λ.

As seen in Fig. 20, two different patterns can be observed: for λ values lower than 6, the value of $L_{D,flex}$ is typically between 4 and 6 times the stirrup spacing, s_w. On the other hand, the tests performed on specimens with λ values higher or equal to 6 show a clear trend that converges towards $L_{D,flex}$ values of 1 to 2 times the stirrup spacing, s_w. Based on the results of Fig. 20, Fig. 21 compares the estimates of $L_{D,flex}$ obtained using models L_{buck}, $L_{D,flex,wdg}$, and $L_{PH,c}$ using a similar disaggregation of λ. As seen in Fig. 21, the results computed using L_{buck} are seen to be adequate for the specimens having $\lambda \geq 6$, particularly when higher values of λ are considered. This is evident in the results obtained for the specimens tested by Rodrigues *et al.* [50] (Tests 93-115) and Barrera *et al.* [46] (Tests 39-78). These observations are also in line with the results obtained using the $L_{PH,c}$ approach proposed by Goodnight *et al.* [13], since similar results are observed for $\lambda \geq 6$, although it is also able to provide adequate estimates for some specimens with $\lambda < 6$.

Figure 22 shows the disaggregation of the results for the case when the models associated with diagonal failure planes (i.e. using $L_{D,flex,ts}$ and $L_{PH,t}$). In this case, it can be seen that, when the mechanisms based on the tension-shift effect or the development of diagonal failure plans are considered, the opposite of what was observed in Fig. 21 occurs. The estimates provided by $L_{D,flex,ts}$ and $L_{PH,t}$ are closer to the values of $L_{D,flex}$ observed for tests with $\lambda < 6$ than to those of tests with $\lambda \geq 6$. The results obtained using these models lead to an upper envelope that overestimates the real value of L_D when the specimens have $\lambda \geq 6$. Thus, since specimens with $\lambda < 6$ exhibit failure modes that involve extensive concrete damage and larger buckling modes (as illustrated before in Fig. 21), the use of $L_{PH,t}$ and $L_{D,flex,ts}$ seems to be more consistent with those damage patterns. Figure 23a shows the joint variation of the ratio between $L_{D,flex}$ and L_{buck} with the ratio between $L_{D,flex,ts}$ and $L_{D,flex}$. The observed variations show that, whenever the ratio $L_{D,flex}/L_{buck}$ is closer to 1.0, the maximum value of the ratio $L_{D,flex,ts}/L_{D,flex}$ occurs (values between 2.50 and 4.00). Conversely, for the cases where $L_{D,flex,ts}/L_{D,flex}$ converges to 1.00, an increase in the values of $L_{D,flex}/L_{buck}$ is observed, with particular emphasis for tests with $\lambda < 6$. Nonetheless, there are cases with $\lambda < 6$ that also exhibit values of $L_{D,flex}$ close to L_{buck}. In addition, Fig. 23b shows that in some of the more extreme cases that are observed, either with a zero axial load or with very high axial load levels ($\nu > 0.40$), values of $L_{D,flex}/L_{buck}$ much larger than 1.0 are usually observed.
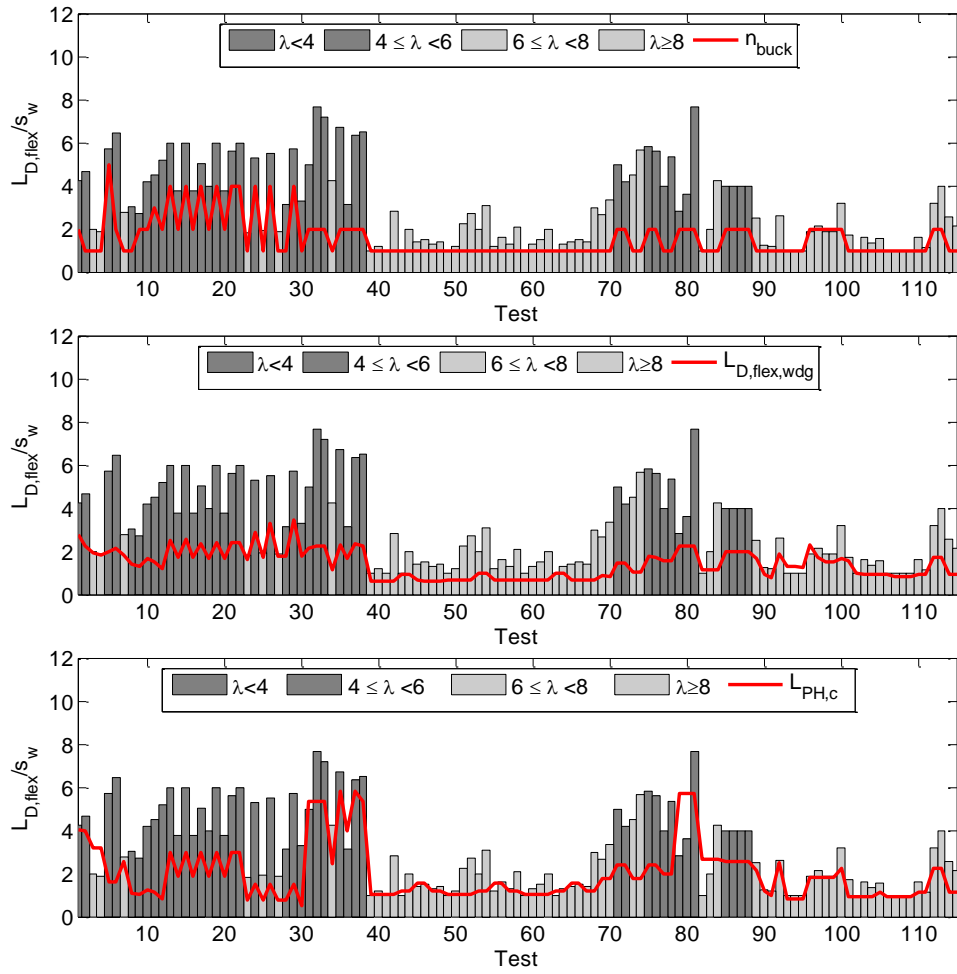
Figure 21. Comparison of the damage mode estimates ($L_{D,flex}/s_w$) obtained for each test specimen using models L_{buck} a), $L_{D,flex,wdg}$ b) and $L_{PH,c}$ c) with $L_{D,flex}$, including the disaggregation of the results according to $\lambda < 6$ and $\lambda \geq 6$.
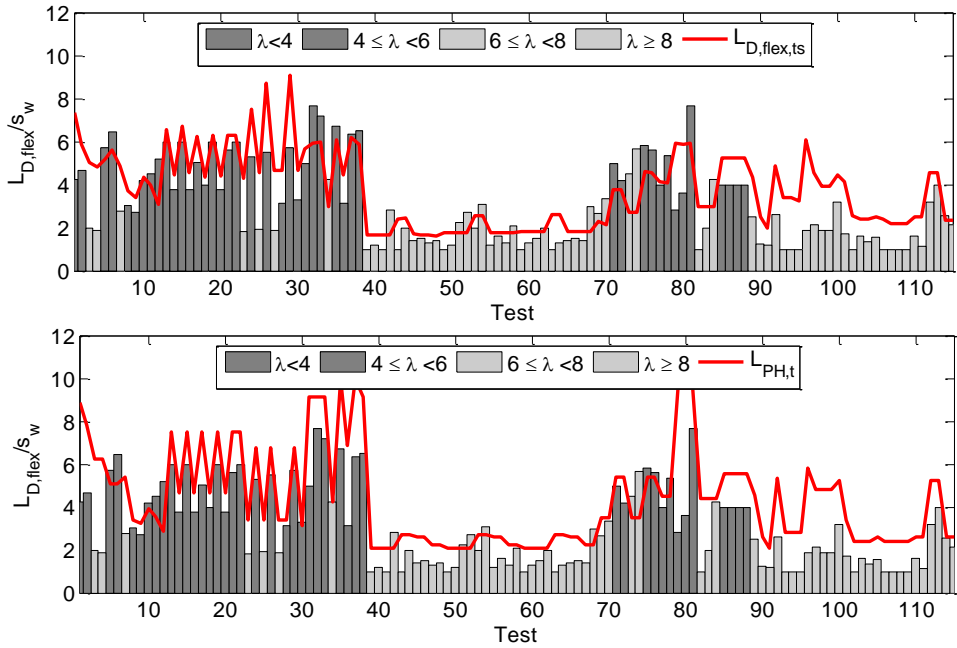
Figure 22. Comparison of the damage mode estimates ($L_{D,flex}/s_w$) obtained for each test specimen using models $L_{D,flex,ts}$ a) and $L_{PH,t}$ b) with $L_{D,flex}$, including the disaggregation of the results according to $\lambda < 6$ and $\lambda \geq 6$.
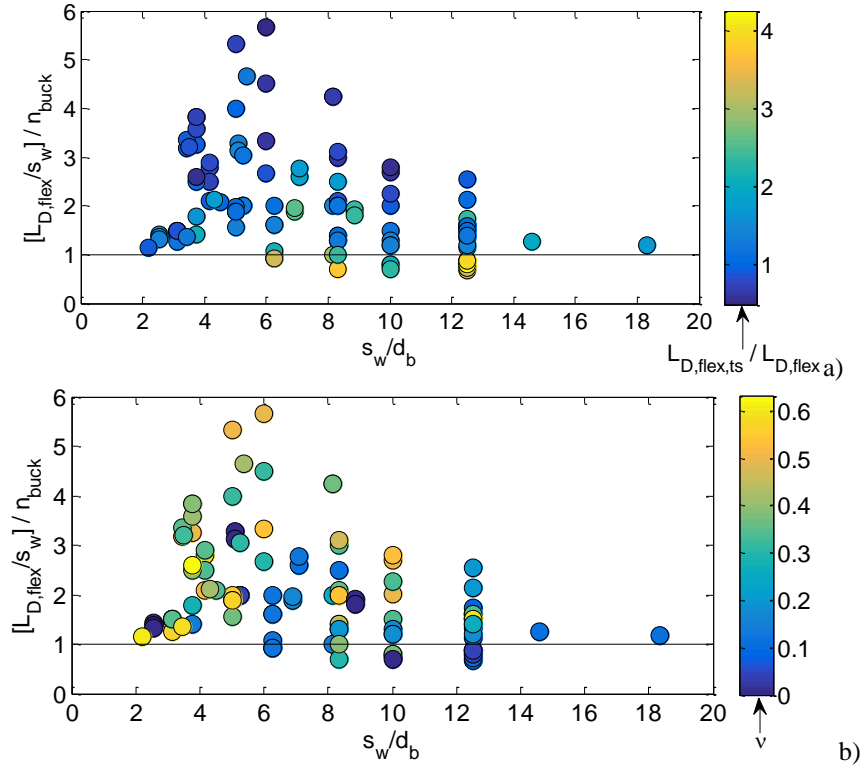
Figure 23. Disaggregation of the deviations from the $L_{D,flex}$ values observed in the experimental tests and L_{buck} and correlation of these values with the deviations of $L_{D,flex}$ from $L_{D,flex,ts}$.

Figure 24 shows the disaggregation of $L_{D,flex} \mid \lambda$ results for $\lambda < 6$ and $\lambda \geq 6$. As shown in the figure, $L_{D,flex} \mid \lambda$ does not provide adequate estimates for some tests since it provides an average estimate minimizing the global deviations. The model $L_{D,flex} \mid \lambda$ can therefore be used to establish an average approximation for $L_{D,flex} \mid \lambda$, instead of adopting different models depending on the value of λ.
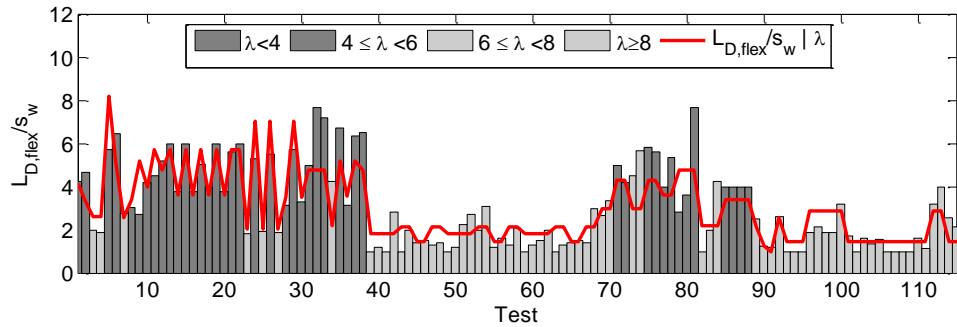
Figure 24. Comparison of the damage mode estimates ($L_{D,flex} / s_w$) obtained for each test specimen using model $L_{D,flex} \mid \lambda$ with $L_{D,flex}$, including the disaggregation of the results according to $\lambda < 6$ and $\lambda \geq 6$.

Figure 25a shows the disaggregation of $L_{D,flex}/s_w$ based on λ and ν, together with the representation of the criteria introduced in Section 6.2 to classify the ductility of RC beam-column components. A linear interpolation function was fitted to the triplets of data and led to a significant coefficient of determination ($R^2 = 0.98$), thus providing a representation of the data that enables the reliable interpretation of the contour plots that were obtained. Similarly, Fig. 25b presents the same plot

6.31

but including a possible association of the types of mechanisms shown in Fig. 5 according to λ, ν and the magnitude of $L_{D,flex}/s_w$.
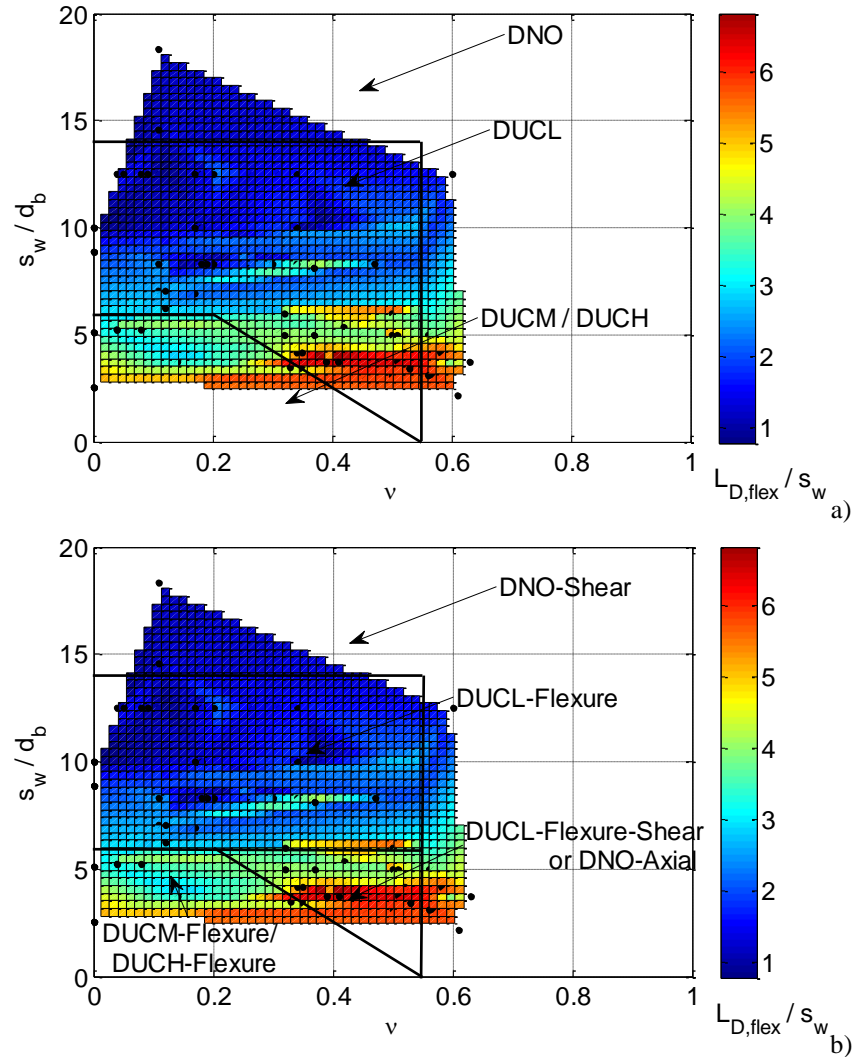
Figure 25. Disaggregation of $L_{D,flex}/s_w$ based on λ and on ν, together with the representation of the criteria introduced in Section 6.2 to classify the ductility of RC beam-column components and a possible association to the mechanisms introduced in Fig. 5

As seen in Fig. 25a, components classified as DUCL can either be associated with a large $L_{D,flex}/s_w$ (between 4 and 6 times s_w) or lower values around 1.0. The limit criterion proposed in Section 6.2 (i.e. the inclined line in Fig. 25) may be seen as a representation of two different mechanisms. On the left hand side of this line, lower values of ν are observed for similar levels of λ ($\lambda < 6$) and lead to mechanisms extending along 3-4 times s_w. On the right hand side of the line, larger values of the $L_{D,flex}/s_w$ ratio are observed, up to the range of 5 to 6 times s_w. As analysed before, when $\lambda \geq 6$ the $L_{D,flex}/s_w$ ratio tends to 1.0 with the increase of λ, irrespective of the axial load level ν. Based on these considerations, Fig. 25b establishes four regions in the plot, defined according to the corresponding mechanism (see Fig. 5 for the corresponding flexure and shear behaviour curves) and the corresponding values of $L_{D,flex}/s_w$, s_w and λ. The region designated by

DUCM-Flexure and *DUCH-Flexure* includes components with a low/moderate axial load level and a low value of λ, which have a considerable anti-buckling capacity and usually exhibit a failure mode involving the combined concrete diagonal cracking (along with tension shift effects) and a buckling mechanism that involves multiple stirrups. The region classified as *DUCL-Flexure-Shear* or *DNO-Axial* includes cases with very high axial load levels and low values of λ, which may induce the development of diagonal cracks in the concrete and accelerate the shear failure and reinforcement buckling, thus increasing $L_{D,flex}$ and decreasing the overall ductility of the element (i.e. the rotation ductility until the global shear force-drift envelope starts softening). Finally, region *DUCL-Flexure* accounts for specimens that exhibit a damage pattern essentially controlled by local buckling (1 to 2 times s_w) and concentrate the damage in a smaller finite region. Hence, in addition to the previous two cases separated before by λ = 6, Fig. 25 can provide a more detailed preliminary estimate of the expected damage mechanism and the damage length, which may then be used to select appropriate retrofitting techniques, fragility functions and repair costs before analysing the building. Furthermore, the proposed classification can also provide important information regarding the nonlinear modelling of RC components when distributed inelasticity models are used, since estimating the length of the damaged region length is a relevant matter when strain-softening issues arise, as mentioned by Sousa *et al.* [53]. Future studies may address this aspect in more detail by analysing the numerical performance of available numerical models separately for components belonging to the different regions defined according to Fig. 25.

6.6 Conclusions

Estimating the extent of the element that may be damaged after an earthquake and the corresponding connection with the ductility and physical mechanisms that lead to damage accumulation is of the upmost importance when deciding retrofitting solutions, evaluating the potential repair cost or even when selecting the nonlinear modelling technique for analysing the seismic behaviour of RC frame buildings. In particular, the combined effect of the concrete crushing mechanisms and the reinforcement instability has to be considered since the occurrence of nonlocal deformations that leads to the softening of the element response, to large rotations and extensive damage accumulation that limits the global ductility.

The presented study started by analysing a set of new rules to be added to those established by [18] in order to identify RC frame components according to their expected level of ductility (i.e. with no ductility, low ductility and moderate/high ductility). The use of the longitudinal rebar slenderness ratio λ = s_w/d_b combined with the axial load level ν = $N/A_c f_c$ were seen to be adequate parameters to identify components with higher and lower levels of ductility. Since ductility is associated with the location of the point of the moment-rotation behaviour or the shear force-displacement behaviour that marks the onset of softening, different mechanisms may occur leading to the violation of the EBH. These nonlocal deformations have implicit that, after the

onset of softening, only moment-rotation or shear force-displacement become objective measures of ductility since the response of the element becomes size-dependent. Thus, each ductility class must be associated with a given condition triggering the onset of softening and associated with a given damage localization length, since the kinematics inside the damaged region will govern the global inelastic deformations. With this in mind, and considering that Zimos *et al* [17] used experimental damage patterns to develop analytical models for the shear damage localization length in NDO components, the current study focused the assessment of DNO, DUCL and DUCM/DUCH flexure-controlled beam-column components using similar principles. Based on the assessment of a set of 115 components, it was concluded that parameter λ that is used to classify the ductility level can also be used to assess the equivalent damage/buckling mode, $L_{D,flex}/s_w$, given the significant correlation that was observed between this variable and λ. When analysing the prediction capabilities of models developed for estimating the reinforcement buckling length, the concrete wedge size, the diagonal cracking associated with concrete shear failure and tension shift effects and an adaptation of the plastic hinge length proposed by Goodnight *et al.* [13], it was concluded, based on statistical analyses, that only the models developed based on λ could provide, on average, adequate estimates of $L_{D,flex}/s_w$. Nevertheless, a posterior analysis has shown that $L_{PH,c}$ or L_{buck} can also be considered to estimate the damaged region length for specimens with $\lambda \geq 6$, while $L_{PH,t}$ and $L_{D,flex,ts}$ can also provide adequate estimates for specimens with $\lambda < 6$. Hence, for DUCL components, the damaged region length can be estimated by L_{buck} following Dhakal and Meakawa [30] and Dhakal and Su [3], while the tension shift based model $L_{PH,t}$ adapted from the proposal of Goodnight *et al.* [13] seems to provide more adequate estimates for DUCM/DUCH components. For DNO components with flexural failure modes, due to the potential shear failure diagonal planes, $L_{PH,t}$ and $L_{D,flex,ts}$ can provide adequate alternatives, but the use of the model proposed by Zimos *et al.* [17] for flexure-shear failure may also be considered in this case. Although these recommendations are supported by the analysis of an extensive set of cases, further studies should be performed using only observations made based on more robust damage monitoring techniques such as those adopted in Goodnight *et al.* [13]. The use of these techniques will reduce the uncertainty/subjectivity of the damage classification that may be found in existing experimental observations.

6.7 References

1   Ozcebe G, Saatcioglu M, (1987). Confinement of concrete columns for seismic loading. ACI Structural Journal; 84(4): 308–315.

2   Saatcioglu M, Ozcebe G, (1989). Response of reinforced concrete columns to simulated seismic loading. ACI Structural Journal; 86: 3-12.

3   Dhakal R, Su J, (2017). Design of transverse reinforcement to avoid premature buckling of main bars. Earthquake Engineerign & Structural Dynamics; 47:147–168.

4   Watson S, Park R, (1994). Simulated seismic load tests on reinforced concrete columns. Journal of Structural Engineering; 120(6): 1825–1849.

5   Bayrak O, Sheikh S, (1988). Confinement reinforcement design considerations for ductile HSC columns. Journal of Structural Engineering, ASCE; 124(9): 999–1010.

6   Paultre P, Légeron F, Mongeau D (2001). Influence of concrete strength and yield strength of ties on the behavior of high-strength concrete columns. ACI Structural Journal; 98(4): 490–501.

7   Bae S, Bayrak O, (2008). Plastic hinge length of reinforced concrete columns ACI Structural Journal; 105(3): 290–300.

8   Haselton CB, Liel AB, Deierlein GG, (2009). Simulating structural collapse due to earthquakes: model idealization, model calibration and numerical solution algorithms. COMPDYN 2009, 2nd International Conference on Computational Methods in Structural Dynamics and Earthquake Engineering. Rhodes, Greece.

9   Yuan F, Wu YF, (2017). Effect of load cycling on plastic hinge length in RC columns. Engineering Structures; 147:90–102.

10   Pam HJ, Ho JC, (2009). Length of critical region for confinement steel in limited ductility high strength reinforced concrete columns. Engineering Structures; 31(12):2896-2908.

11   Priestley MJ, Park R, (1987). Strength and ductility of concrete bridge columns under seismic loading. ACI Structural Journal;84(1): 61-76.

12   Tarquini D, Almeida JP, Beyer K, (2017). Axially equilibrated displacement- based beam element for simulating the cyclic inelastic behaviour of RC members. Earthquake Engineering & Structural Dynamics 46(9): 1471-1492.

13   Goodnight JC, Kowalsky MJ, Nau JM, (2016). Modified plastic-hinge method for circular RC bridge columns. Journal of Structural Engineering; 142(11): 04016103.

14   Hines EM, Restrepo JI, Seible F, (2004). Force-displacement characterization of well confined bridge piers. ACI Structural Journal; 101:537–48.

15   Bazant ZP, Jirasek M, (2002). Nonlocal integral formulations of plasticity and damage: survey of progress. Journal of Engineering Mechanics; 128: 1119–1149.

16   Ning C, Li B, (2015). Probabilistic Approach for Estimating Plastic Hinge Length of Reinforced Concrete Columns. Journal of Structural Engineering; 142(3): 04015164.

17   Zimos DK, Mergos PE, Kappos AJ, (2018). Modelling of R/C members accounting for shear failure localisation: Finite element model and verification. Earthquake Engineering & Structural Dynamics; 47:1631–1650.

18   Zhu L, Elwood KJ, Kaukaas T, (2007). Classification HT. Seismic safety evaluation of existing reinforced concrete columns. Journal of Structural Engineering; 133(9):1316-1330.

19   Haselton CB, Liel AB, Taylor Lange S, Deierlein GG, (2016). Calibration of Reinforced Concrete Beam-Columns for Simulating Seismic Response to Collapse. ACI Structural Journal, 113(6):1141-1152.

20   Panagiotakos TB, Fardis MN, (2001). Deformation of reinforced concrete at yielding and ultimate. ACI Structural Journal;98(2):135–47.

21   American Society of Civil Engineers (ASCE), 2017. Seismic Evaluation and Retrofit of Existing Buildings (ASCE/SEI 41-16), Reston, VA, USA.

22   CEN, (2002). Eurocode 2 - Design of concrete structures - Part 1-1: General rules and rules for buildings. European committee for standardisation, Brussels, Belgium.

23 CEN, (2005) Eurocode 8: design of structures for earthquake resistance. Part 1: General Rules, aseismic actions and rules for buildings. Brussels, Belgium.

24 Peruš I, Fajfar P, Biskinis D, *et al.*, (2013). Enrichment of the distributed database with existing data. Background report accompanying SERIES project Deliverable D2.7. Version: 1.2.

25 CEN, (2005). Eurocode 8: design of structures for earthquake resistance. Part 3: Assessment and retrofitting of buildings. Brussels, Belgium.

26 Feng Y, Kowalsky M, Nau J, (2014). Fiber-Based Modeling of Circular Reinforced Concrete Bridge Columns. Journal of Earthquake Engineering; 18(5):714-734.

27 Zhao J, Sritharan S, (2007). Modeling of strain penetration effects in fiber-based analysis of reinforced concrete structures. ACI Structural Journal; 104(2):133-141.

28 Kashani M, Lowes L, Crewe A, Alexander N, (2016). Nonlinear fibre element modelling of RC bridge piers considering inelastic buckling of reinforcement. Engineering Structures; 116:163-177.

29 Zimos DK, Mergos PE, Kappos AJ. (2015). Shear hysteresis model for reinforced concrete elements including the post-peak range in proceedings of the COMPDYN 2015 5th ECCOMAS Thematic Conference on Computational Methods in Structural Dynamics and Earthquake Engineering, Crete Island, Greece.

30 Dhakal R, Maekawa K, (2002). Reinforcement stability and fracture of cover concrete in reinforced concrete members. Journal of Structural Engineering; 128(10): 1253–1262.

31 Pantazopoulou S, (1998). Detailing for reinforcement stability in RC members. Journal of Structural Engineering; 124(6):623–32.

32 Dhakal R, Maekawa K, (2002). Path-dependent cyclic stress–strain relationship of reinforcing bar including buckling. Engineering Structures; 24:1383–1396.

33 Berry M, Eberhard M, (2005). Practical Performance Model for Bar Buckling. Journal of Structural Engineering 131(7): 1060-1070.

34 Bae S, Mieses A, Bayrak O, (2005). Inelastic Buckling of Reinforcing Bars. Journal of Structural Engineering; 131(2): 314-321.

35 Syntzirma D, Pantazopoulou S, Aschheim M, (2014). Load-History Effects on Deformation Capacity of Flexural Members Limited by Bar Buckling. Journal of Structural Engineering; 136:1-11.

36 Visintin P, Oehlers D, Haskett M, Wu C, (2013). A Mechanics Based Hinge Analysis for Reinforced Concrete Columns. Journal of Structural Engineering. 139(11): 1973-1980.

37 Mohamed Ali MS, Oehlers DJ, Griffith MC (2010). The residual strength of confined concrete. Advances in Structural Engineering; 13(4): 603–618.

38 Markeset G, Hillerborg A, (1995). Softening of concrete in compression - Localization and size effects. Cement and Concrete Research; 25(4): 702–708.

39 Fantilli A, Iori I, Vallini P, (2007). Size effect of compressed concrete in four point bending RC beams. Engineering Fracture Mechanics; 74: 97–108.

40 Visintin P, Chen Y, Oehlers DJ (2015). Size dependent axial and lateral stress strain relationships for actively confined concrete. Advances in Structural Engineering 18 (1), 1-20.

41 Cusson D, Paultre P, (1994). High-Strength Concrete Columns Confined by Rectangular Ties. Journal of Structural Engineering; 120(3):783-804.

42   Hillerborg A, (1990). Fracture mechanics concepts applied to moment capacity and rotational capacity of reinforced concrete beams. Engineering Fracture Mechanics; 35(1/2/3):233–40.

43   Bazant ZP, Xiang Y, (1997). Size effect in compression fracture: splitting crack band propagation. Journal of Engineering Mechanics ASCE; 123(2):162–72.

44   Yang K, Shi QX, Zhao JH, (2013). Plastic hinge length of high strength concrete columns confined by high strength stirrups. Engineering Mechanics;30(2): 254–259.

45   Elmenshawi A, Brown T, El-Metwally S, (2012). Plastic hinge length considering shear reversal in reinforced concrete elements. Journal of Earthquake Engineering; 16(2): 188–210.

46   Barrera AC, Bonet JL, Romero ML, Miguel PF, (2011). Experimental tests of slender reinforced concrete columns under combined axial load and lateral force. Engineering Structures; 33(12): 3676–3689.

47   Legeron F, Paultre P, (2000). Behavior of high-strength concrete columns under cyclic flexure and constant axial load. ACI Structural Journal; 97(4): 591–601.

48   Ohno T, Nishioka T, (1984). An experimental study on energy absorption capacity of columns in reinforced concrete structures. Doboku Gakkai Ronbunshu; 350: 23-33.

49   Ho JCM, Pam HJ, (2003). Inelastic design of low-axially loaded high-strength reinforced concrete columns. Engineering Structures; 25(8):1083–1096.

50   Rodrigues H, Arêde A, Varum H, Costa A, (2013). Damage evolution in reinforced concrete columns subjected to biaxial loading. Bulletin of Earthquake Engineering;11: 1517–1540.

51   Rousseeuw P, Leroy A (1987). Robust regression and outlier detection. Wiley, New York.

52   Bland JM, Altman DG (1999). Measuring agreement in method comparison studies. Statistical Methods in Medical Research. 8 (2): 135–60.

53   Sousa R, Almeida JP, Correia A, Pinho R, (2018). Shake Table Blind Prediction Tests: Contributions for Improved Fiber-based Frame Modelling. Journal of Earthquake Engineering. 1-42. 10.1080/13632469.2018.1466743.

[This page was intentionally left blank]

Chapter 7

Modelling RC frame components using distributed inelasticity elements: towards a consistent model selection

Scope and objectives

In the previous chapter, experimental evidence was used to evaluate the length of the damaged region in RC frame components under seismic loading, defining the ductility and the failure mode leading to significant inelastic rotations based on mechanical principles. It was seen that a distinct damage accumulation pattern is observed when the failure is controlled by shear or by flexural mechanisms. The damage accumulation is a physical localization process defining a region where the major mechanisms that violate the Euler-Bernoulli hypothesis (EBH) are concentrated. Hence, the formation and rotation of plastic hinges depend on nonlocal effects that invalidate this hypothesis, a situation that creates applicability issues with local beam theories requiring the EBH to be valid. To address this issue, the current chapter analyses how these nonlocal effects that invalidate the EBH can be indirectly incorporated into local beam formulations. In particular, conditions are formulated that allow for a consistent model selection and include information about the physical damage localization process, the damage/fracture mechanics of the materials and the strain-localization issues associated to the use of local distributed inelasticity elements. The main objective of the chapter is to define a generalized flowchart for the selection of constitutive models and their parameters that will reduce the uncertainty associated to the model selection decisions made by analysists, as highlighted in recent blind prediction contests.

7.1 Introduction

Over the last decades of earthquake engineering developments, the nonlinear modelling of RC components has been the focus of extensive research and applications. Many reviews and studies [1-8] have been published highlighting the advantages of using frame elements to simulate the behaviour of RC frame components when compared with the use of other finite element (FE) strategies. The balance between accuracy and simplicity provided by frame models allows for an effective integration of material and geometrical nonlinear effects with a lower level of complexity and computational time requirements than other FE strategies. As a result, this modelling strategy is seen to be the preferred approach across a large spectrum of applications involving the simulation of the behaviour of RC frame buildings under earthquake loading. As an example, of the 25 entries submitted to a recent blind-prediction contest [9], 13 (52%) used force-based distributed inelasticity elements (DP-FB), 4 (16%) used displacement-based distributed inelasticity models (DP-DB), 3 (12%) were reported to use finite-length plastic hinge methods (FLPH) and 5 (20%) used concentrated plasticity spring models (CP). Terzig *et al*. [9] also showed that, in some cases, even though similar modelling strategies were considered, significantly different results were obtained. One of the main reasons for this case-to-case variability is associated to the impact that micro-modelling decisions may have on the outcome of the simulations. Some of these micro-modelling decisions may refer to the selection of constitutive models and constitutive model parameters (e.g. see [2, 3, 5]), others to the selected mesh characteristics [4, 10-11], while others are connected to the adopted beam theory [12-14]. Recently, Sousa *et al.* [8] highlighted important points about the main issues that may have led to the large dispersion levels that were found. Among the variables analysed by these authors, the modelling aspects related to the equivalent viscous damping, the strain penetration effects, the element formulation and discretization, and the material constitutive models were found to be the more relevant. Based on the comparisons that were performed, Sousa *et al.* [8] concluded that using a lower number of integration points (IPs) in a DP-FB element and assigning the plastic hinge length as the weight for the extreme IPs can lead to acceptable levels of error, even in cases with no strain localization. Additionally, Calabrese *et al.* [4] performed a sensitivity study and showed that local modelling strategies involving force-based and displacement-based formulations become ill-defined when the sectional response of extreme-end IPs enter into a softening stage. Nonlocal modelling strategies have been proposed in the past by introducing nonlocal strains on the constitutive material models [15] or modifying the post-peak material response based on the fracture energy [16]. Recent studies (e.g. [13-14]) proposed alternative beam theories using nonlocal formulations. The method proposed by Sideris and Salehi 13 can be formulated either respecting or disregarding the Euler-Bernoulli hypothesis (EBH) and, similar to FLPH methods, it is also based on the characteristic length L_c (which becomes the local Navier

beam theory when $L_c = 0$). Conversely, the method proposed by Kenawy *et al.* [14] considers a nonlocal averaging procedure combined with a nonlocal constitutive model for concrete. Coleman and Spacone [16] and Pugh *et al.* [7] use a pure nonlocal technique method that adjusts the material stress-strain properties based on the mesh-properties of force-based elements (i.e. based on the integration scheme since a single element is adopted). Although these two approaches are able to provide an objective global response for the component, mesh-dependent localization is still observed. The regularization of the mesh dependence of local force-based elements has also been analysed by previous research (e.g. see [4, 10,17-20]), namely by manipulating the numerical integration scheme in order to ensure that numerical localization occurs at L_c. For that reason, such DP models are usually termed finite length plastic hinge (FLPH) methods [21], since they resemble frame element formulations with nonlinear springs at the member ends [13]. Physically, the adoption of regularized local force-based elements has implicit that the objective response of the element after entering the softening stage can only be defined in terms of rotations, since nonlocal material properties such as the formation of diagonal sliding planes, of concrete wedges or the lateral deformations of reinforcing steel bars invalidate the EBH. The loss of objectivity of curvature estimates was detailed in Visintin *et al* [22], where rotations were defined as the only objective demand measure after the softening of the materials starts due to nonlocal deformations. As shown in Chapter 6, a mechanical approach can be used to analyse the physical damage localization process (within a length L_D) due to the occurrence of multiple damage-generating mechanisms.

Since the variability of results often found in blind prediction tests has been pointed as one of the major drawbacks for a more widespread implementation of performance-based earthquake engineering in practice [23], guidelines for the adequate modelling of RC components when using local DP elements should be developed. Bearing in mind the existing lack of guidance [24] and the case-to-case variability referred in [9], this chapter proposes a set of guidelines for constitutive parameter and constitutive model selection by combining the main ideas defined in previous studies with the fracture mechanics principles summarized in Chapter 6. The main objective of these guidelines is to help achieving a consistent modelling strategy that combines size-dependent stress-strain models, the physics associated with concrete and steel fracture mechanics and the typical damage accumulation mechanisms of RC frame components.

7.2 Mechanical and physical background of damage localization in RC frame components and constitutive materials

7.2.1 Damage localization in RC frame components under flexure

RC frame components subjected to imposed displacements at their boundaries exhibit very distinct damage patterns depending on the characteristics of the component. When flexural response governs the behaviour of the component, damage localization occurs due to the accumulation of damage in concrete and in reinforcing steel within a finite region of the component. The longitudinal and the transversal deformations caused by the shortening of the steel bars in compression, by the elongation of steel bars in tension, by the widening of concrete cracks or the by the relative displacement between concrete blocks or wedges induce a global rotation of this finite region where damage is concentrated. Such regions are generally called plastic hinges since they aggregate most of the inelastic deformations of the component. Figure 1 shows the main effects leading to damage accumulation in a hinge located at the base of a cantilever column.
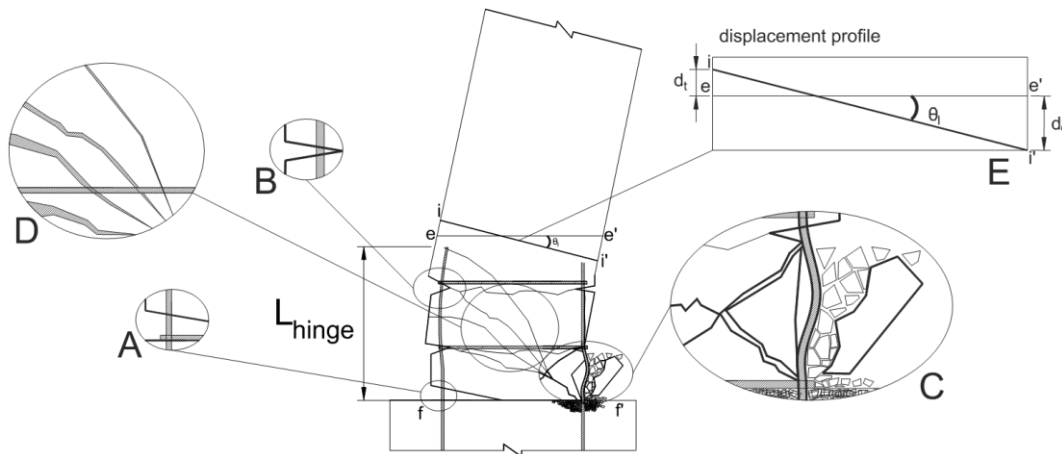
Figure 1. Deformations and damage patterns associated to the formation and rotation of a hinge located at the base of a cantilever column.

As analysed by Visintin *et al.* [22], within the region defined by L_{hinge} (Fig. 1), the principle stating that plane sections remain plane after deformation is only verified at sections e-e' and f-f'. In terms of deformations, a linear displacement profile i-i' (see detail E in Fig. 1) is observed in order to accommodate the overall rotation of the hinge. Equivalent nonlocal strains are usually generated as a result of the vertical deformations d_c and d_t, and can be directly computed by dividing these vertical deformations by the length of the hinge, L_{hinge}. Tensile cracks (details B and D in Fig. 1) are developed and get wider as the displacement at the top of the cantilever column increases, leading to elongation and slippage of the reinforcing bars and, consequently, discrete local rotations. Moreover, a discrete rotation is also generated by the opening of a crack at the interface between the component and the joint (detail A in Fig. 1), which is a rigid body rotation and does not contribute directly to the overall damage of the hinge. The rigid-body

rotations generated by the pull-out of the steel bar from the joint/footing at an early stage can be indirectly added to the element strains by performing the equilibrium in the deformed state, thus including second order effects. In the compressed side of the hinge, concrete wedges are formed and the reinforcing steel bars buckle due to the softening of the concrete and the steel stress-transversal deformation laws. The nonlocal deformations caused by the concrete wedges (vertical component of the sliding displacement of the wedge) and the buckling of the rebar (shortening) introduce a vertical displacement d_c.

As mentioned by Visintin *et al.* [22], the discrete rotations at cracks, the sliding of concrete wedges and the bar buckling are disturbances of the element state that violate the EBH of plane sections and linear strain profiles. As a result, real strains measured by strain gauges are insufficient, as nonlocal strains associated to d_c, d_t and L_{hinge} are not included in what is recorded by these devices. Thus, after these disturbances occur, one can think of equivalent curvatures, equivalent flexural stiffness and equivalent strains that include the nonlocal mechanisms that occur within L_{hinge}. To illustrate these issues, Fig. 2 shows the strain profiles of a hinge located at the basis of a column under compression with and without the formation of tensile cracks.
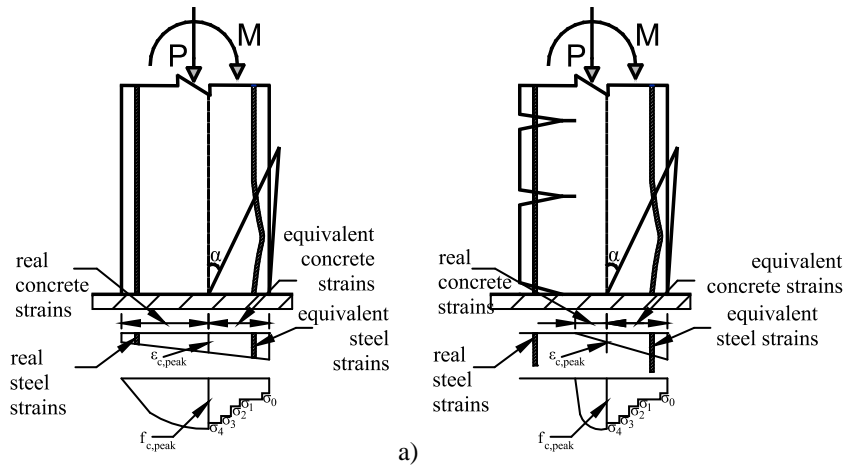
Figure 2. Illustration of the strain profiles of a hinge rotation located at the basis of a column under compression without the formation of tensile cracks (a) and with the formation of tensile cracks (b).

As seen in Fig. 2a, the equivalent material strains depend on the geometrical deformation of concrete and steel in compression, namely on the interaction between the concrete shear friction properties (which are associated to the post-peak softening stress-strain behaviour) and the buckling-restraining capacity of the reinforcing steel bars. Since equivalent strains, ε_{eq}, result from the linear displacement profile i-i' (see detail E in Fig. 1) and are associated with d_c and L_{hinge}, they can be defined by:

$$\varepsilon_{eq} = \varepsilon_{mat} + \frac{d_c}{L_{hinge}} \tag{1}$$

where ε_{mat} represents the real material strains and d_c/L_{hinge} is the nonlocal strain of the materials, i.e. the transverse displacement of the bar at buckling and the sliding of concrete wedges over diagonal sliding planes. These mechanisms are directly correlated with the characteristic length L_c, i.e. the strain resulting from the length of the region where instability of the hinge is observed. In the case of Fig. 2a, such length can associated with the buckling length L_{buck} or the length of the concrete wedge L_{wdg}, whichever may condition the problem (see Chapter 6).

Conversely to Fig. 2a, Fig. 2b shows the case where part of the hinge is in tension. Accordingly, concrete cracks will be responsible for discrete rotations, particularly when a fan-type crack pattern is observed. In this case, the reinforcing steel bars are subjected to additional strains to accommodate the crack process due to the resulting tension shift effect, adding an additional moment (and therefore rotation) to the hinge region. Goodnight *et al.* [25] transformed equivalent strains into displacements of RC columns by adopting a triangular hinge length with height $L_{PH,t}$ when tensile strains are considered and a triangular compressive hinge length with height $L_{PH,c}$ when compressive strains are used as limit state variables for circular columns. By inverting the view of the plastic hinge integration methods suggested by Goodnight *et al.* [25], the mechanical approach previously described is obtained, in the sense that equivalent strains resulting from a monotonic load will be proportional to the two different displacements d_c and d_t over a single integration length, resulting in an objective rotation of the hinge. Conversely, in the local approach followed by Goodnight *et al.* [25], the local curvature is considered the objective metric and, therefore, the local strains are translated into global rotations by considering different L_{hinge} values depending on the mechanism generating the strains.

A further aspect that needs to be highlighted with respect to the damage accumulation in a hinge similar to that shown in Fig. 2b is the influence of cyclic effects. Due to these effects, a symmetric damaged pattern is observed in experimental tests, with the height of the damaged region (L_D) varying depending on the specimen and the loading properties. Chapter 6 analysed the damaged patterns of several rectangular columns tested experimentally and showed that there is a duality in the quantification of L_D (or, more specifically, in the number of stirrups mobilized in the damage pattern, L_D/s_w, where s_w is the stirrup spacing). Accordingly, for a column with longitudinal bars that have a slenderness ratio $\lambda = s_w/d_b$ (where d_b is the longitudinal bar diameter) larger than 6, and particularly for cases where it is larger than 8, L_D/s_w provided a good approximation for the damaged length as a function of the local buckling length, i.e. s_w. Conversely, when lower λ values are involved, L_D extends over several stirrup levels, although in many cases lower s_w values are also found. That fact implies that, although the damage mode

$L_D/\mathrm{s_w}$ increases with $\mathrm{s_w}/\mathrm{d_b}$, the real value of L_D may exhibit smaller variations. From the analysis conducted in Chapter 6, it was seen that $L_D/\mathrm{s_w} = 17.91\cdot\left(\mathrm{s_w}/\mathrm{d_b}\right)^{-1}$ which implies that $L_D \approx 18\cdot\mathrm{d_b}$ defines a simplified empirical model where the diameter of the longitudinal bars is used as a scale factor for the damage length.

By assuming that large rotations can delimitate the length of the damaged region, L_D, this length can then be used s a predictor for L_{hinge}. Hence, the equivalent strains will depend on the local mechanisms generating the d_c and d_t displacements. For the case of d_c, this displacement is correlated with the shear friction properties of concrete and its corresponding softening of the stress-strain curve and with the softening of the reinforcing steel stress-strain curve in compression due to the shortening with buckling, as shown in Figs. 1 and 2b. Each one of these processes is also dependent on the geometry of the concrete prism and of the reinforcing steel bar segment over which the transverse deformations occur.

7.2.2 Equivalent strains in concrete prisms under concentric compression

By considering a concrete hinge under concentric compression, as shown in Fig. 3, plane sections verifying the EBH are considered to be located at the boundaries of the test setup. For material strains associated to stress levels below the peak stress $f_{c,peak}$ (see Fig. 3a), the contraction (*S*) of the hinge over L_{hinge} (approximately equal to L_{core}) provides real strains. After reaching the maximum contraction S_{peak} (i.e. $\varepsilon_{c,peak}\cdot L_{hinge}$), an increase in the vertical displacement must be accommodated by the sliding of concrete wedges over diagonal planes as the critical shear-friction capacity is attained. The sliding on the diagonal planes occurs due to the interaction between the stresses normal to the diagonal crack (σ_{cr}), the shear stresses along the crack plane (τ_{cr}), the crack widening (h_{cr}) and the sliding displacement (Δ_{wdg}).
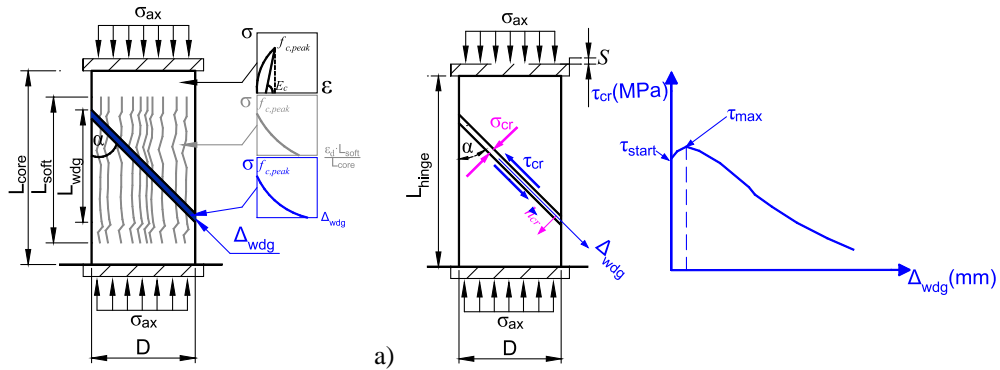
Figure 3. Components of the deformations and damage localization in a concrete core under concentric compression (a) and shear-friction properties of a concrete core (b), including the correlation between the stress normal to the diagonal crack plane (σ_{cr}), the shear stress along the diagonal crack plane (τ_{cr}), the shear stress at the initiation of the sliding (τ_{start}), the maximum shear stress (τ_{max}), the crack widening (h_{cr}) and the sliding displacement (Δ_{wdg}).

By considering the possibility of having a uniform confinement stress σ_{con}, Chen *et al.* [26] defined the shear and normal stresses at the diagonal crack as a function of the sliding plane slope angle α, of σ_{con} and of the axial stress σ_{ax}:

$$\tau_{cr} = \left(\sigma_{ax} - 2 \cdot \sigma_{con}\right) \cdot \sin\alpha \cdot \cos\alpha . \tag{2}$$

$$\sigma_{cr} = \sigma_{ax} \cdot \sin^2\alpha - 2 \cdot \sigma_{con} \cdot \cos^2\alpha . \tag{3}$$

Due to the effect of confinement, the lateral strains can be obtained by adding the dilation strain associated to σ_{ax} (based on the coefficient of Poisson) to the contraction strain associated to the equivalent confinement stress σ_{con}. Consequently, by adding the expansion related to the sliding along the wedge, the nonlocal strain ε_{lat} becomes [26]:

$$\varepsilon_{lat} = \gamma_c \cdot \frac{\sigma_{ax}}{E_c} - \frac{\sigma_{con}}{E_c} + \frac{\beta \cdot \left(\Delta_{wdg} \cdot \sin\alpha + \dfrac{h_{cr}}{\cos\alpha}\right)}{D} . \tag{4}$$

where D is the diameter of the concrete hinge and β is a factor that is equal to 1 if a single sliding plane forms (Fig. 2a) leading to the development of an elliptical wedge and 2 if a circumferential wedge is observed instead, as discussed in Chen *et al.* [26]. The angle of the sliding plane to the longitudinal axis has been defined by Visintin *et al.* [27] as:

$$\alpha = 26^{\circ} + \frac{\sigma_{con}}{f_{c0}} 20^{\circ} . \tag{5}$$

Teng *et al.* [28] proposed a model to quantify the axial strains based on ε_{lat} as:

$$\varepsilon_{c,eq} = 0.85 \cdot \varepsilon_{c0} \cdot \left\{\left[1 + 0.75\left(\frac{-\varepsilon_{lat}}{\varepsilon_{c0}}\right)\right]^{0.7} - \exp\left[-7 \cdot \left(\frac{-\varepsilon_{lat}}{\varepsilon_{c0}}\right)\right]\right\} \cdot \left(1 + 8 \cdot \frac{\sigma_{con}}{f_{c0}}\right). \tag{6}$$

where f_{c0} and ε_{c0} are the peak strength and strain of the unconfined concrete, respectively.

7.2.3 Equivalent strains in reinforcing steel coupons under compression

Similar to the size-dependence of equivalent concrete strains in a concrete prism, the instability of reinforcing steel bars in compression leads to nonlocal effects, as shown in Fig. 4a. A common set of assumptions made in the mechanical analysis of the buckling of reinforcing bars involves

adopting a sinusoidal deformed shape for the bar [29] and assuming that the maximum transverse displacement (Δ_{tra}) occurs at the centre of the unsupported length L_{buck}. The magnitude of the bar slenderness ratio $\lambda = s_w / d_b$ is the key parameter influencing the buckling sensitivity of the bar, as illustrated in Fig. 4b (based on [30]).
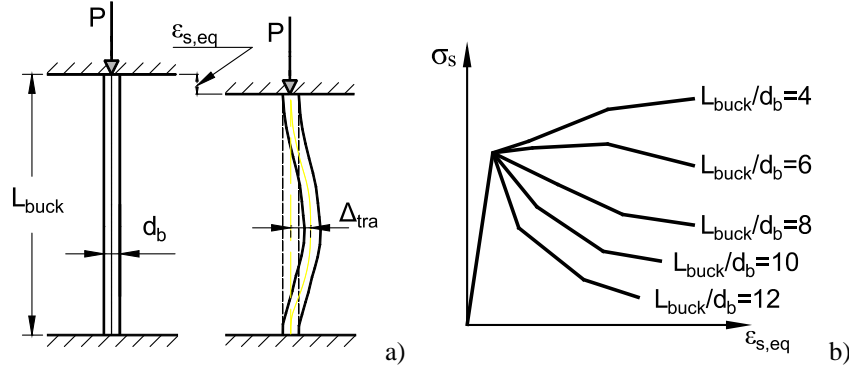
Figure 4. Shortening of a reinforcing steel bar due to buckling (a) and sensitivity of the potential softening of the steel stress-strain curve in compression due to different slenderness ratios (b).

Bae *et al.* [30] introduced a three-branch model correlating the axial stress and Δ_{tra}. The strength degradation in this model initiates at a transverse displacement Δ_{tra} equal to 4% of the unsupported length L_{buck}. The corresponding steel stress, σ_s^*, can be estimated based of the steel overstrength ratio in tension ($\xi = f_u / f_y$, where f_y is the reinforcing steel yielding strength and f_u the corresponding maximum strength value in tension, respectively) by:

$$\sigma_s^* = \min\left[-0.45 \cdot \xi^{1.5} \cdot \ln\left(\frac{\lambda}{4}\right) + \xi; \; \xi \right]. \tag{7}$$

The slope of the descending branch *A* (see Fig. 5) can also be quantified based on ξ as:

$$A = 4 \cdot \left(\xi - 1\right)^2 - 5. \tag{8}$$

Since the total vertical displacement of the bar can be assumed to be the sum of the material deformations and the axial shortening due to the transverse deformations, the axial strains can also be defined by the equivalent strain $\varepsilon_{s,eq}$ given by the sum of the real material strain ε_{mat} due to the axial stress and the axial strain resulting from the transverse displacement ε_{tra}.

7.9
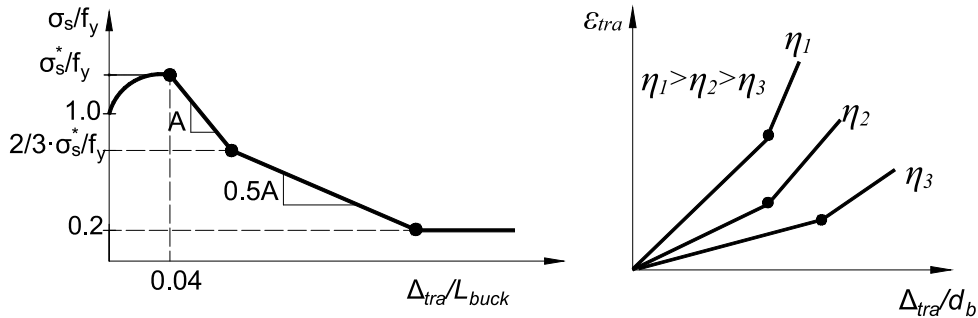
Figure 5. Stress-displacement model of reinforcing steel bars in compression according to Bae *et al.* [30].

Bae *et al.* [30] proposed a model correlating ε_{tra} and Δ_{tra} (See):

$$\varepsilon_{tra} = \max \begin{cases} \left(\dfrac{0.035 \cdot \cos(\eta) + \eta}{\cos(\eta) - 0.035 \cdot \eta} \right) \cdot \left(\dfrac{\Delta_{tra}}{d_b} \right) \\[4mm] \left(\dfrac{0.07 \cdot \cos(\eta) + \eta}{\cos(\eta) - 0.07 \cdot \eta} \right) \cdot \left(\dfrac{\Delta_{tra}}{d_b} - 0.035 \right) \end{cases} . \tag{9}$$

where η can be estimated from:

$$\eta = \frac{6.9}{\left(L_{buck} / d_b \right)^2} - 0.05 . \tag{10}$$

Hence, the equivalent reinforcing steel strains can be estimated based Eqs. (7)-(9) and Fig. 5 using a general model to define the stress-strain diagram of steel in tension/compression without buckling, such as the model of Mander *et al.* [30], leading to the final strain values given by:

$$\varepsilon_{eq} = \varepsilon_{mat} + \varepsilon_{tra} . \tag{11}$$

7.2.4 Integration of material damage localization with the concrete cover spalling

Spalling strains represent the conditions at which the layers of unconfined concrete located in the region outside the stirrup detach from the hinge region. Hence, the average behaviour of the unconfined concrete layer will be affected not only by the material properties but also by the hinge characteristics. Dhakal and Maekawa [32] analysed the mechanical effects behind the spalling of the concrete cover, associating it to the longitudinal cracks that develop in compression (Fig. 3a) followed by the widening of the section induced by the lateral displacement Δ_{tra} of the reinforcing bars in compression. Figure 6 illustrates the two deformation components triggering the spalling of the concrete cover.
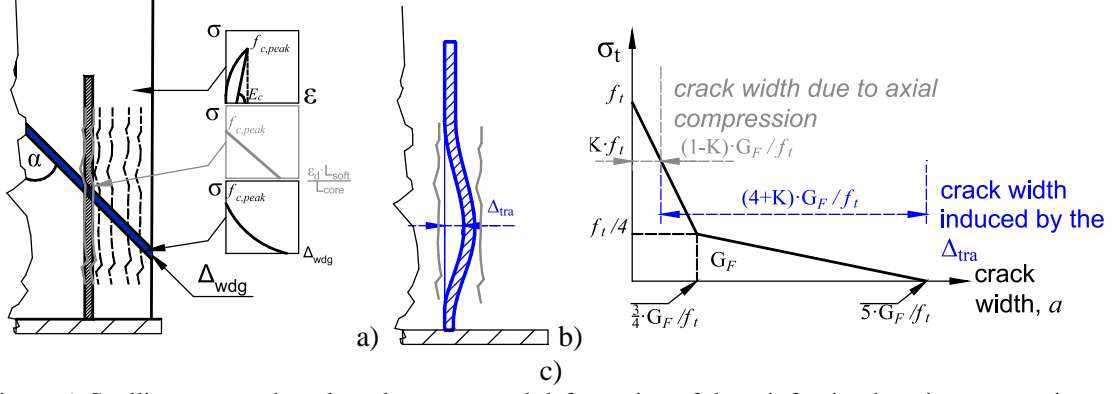
Figure 6. Spalling process based on the transversal deformation of the reinforcing bars in compression as formulated by Dhakal and Maekawa [32]: longitudinal cracking width due to axial compression (a), longitudinal crack width due to lateral deformations of the reinforcing bars (b) and resulting equivalent deterioration of the concrete cover tensile strength in the transversal direction (c).

Based on the approach followed by Dhakal and Maekawa [32], the critical crack width at the centre of the deformed shape of the reinforcing bars a_{cr} can be estimated as:

$$a_{cr} = (4 + K) \cdot \frac{G_F}{f_t}. \qquad (12)$$

where f_t is the tensile concrete strength, G_F is the concrete fracture energy in tension and K is a fracture parameter (between 0.25 and 1.0) that reflects the equivalent damage induced by the compressive strains. Parameter K can be estimated based on the ratio between the compressive strain ε_c and the strain corresponding to the peak compressive strain ε_0 as:

$$K = e^{-0.73 \cdot \frac{\varepsilon_c}{\varepsilon_0} \left(1 - e^{-1.25 \frac{\varepsilon_c}{\varepsilon_0}} \right)} \approx 1 - 0.364 \cdot \frac{\varepsilon_c}{\varepsilon_0} \leq 0.25. \qquad (13)$$

Thus, using the critical crack width a_{cr} proposed by Dhakal and Maekawa [32] based on the reinforcing steel buckling and combining it with the stress-deformation diagram proposed by Bae *et al.* [30] enables the explicit modelling of the spalling phenomenon including all the nonlocal geometrical effects between the concrete cover and the reinforcing steel bars.

7.3 Proposed strategy to incorporate damage localization and material nonlocal (size-dependent) strains using local force-based beam theories

7.3.1 Element modelling strategy and local rotation-based regularization scheme

The modelling strategy proposed herein incorporates the effects of violating the EBH into widely used local beam theories, such as the formulations behind DP-FB elements. As recognized by

recent proposals that also incorporate nonlocal effects into DPs (e.g. see [12, 14]), the sectional response of each IP is not independent of the response of the other IPs, as assumed in local DP-FB formulations. Hence, to be able to use a simplified local DP-FB formulation in a consistent way, it is necessary to ensure that: 1) the sections bounding the region where the EBH is valid (i.e. the region with a length L_{hinge} between e-e and f-f in Fig. 1) represent the geometry of the hinge responsible for the relevant rotations of the element; 2) equivalent local material stress-strain laws are adopted in order to ensure that the integration of the size-dependent material response over L_{hinge} provides objective rotations accounting for all the partial rotations resulting from the nonlocal effects shown in Fig. 1.

The element modelling approach proposed herein consistently accounts for these two conditions. In order to address condition (1), the proposed numerical model involves an assemblage in series of a moment-rotation spring accounting for the rigid-body fixed-end rotations and strain penetration effects with a FLPH distributed inelasticity model. The moment-rotation spring was established based on [33] as an elastic spring with stiffness K_θ given by:

$$K_\theta = 3 \cdot EI \cdot \frac{L_s^2}{\left[\left(L_s + L_{sp} \right)^3 - L_s^3 \right]} \tag{14}$$

where EI is the section flexibility determined based on the yielding moment M_y and the yielding curvature ϕ_y calculated following the proposal made by Panagiotakos and Fardis [34], L_s is the shear span of the element and L_{sp} is the strain-penetration length which can be obtained from [8]:

$$L_{sp} = 0.022 \cdot f_y \cdot d_b \tag{15}$$

Thus, by combining the elastic spring in series with the distributed inelasticity, the rigid body rotations associated to the discrete rotations at the joint-element interface (detail A in Fig. 1) can be included without affecting the internal equilibrium of the beam-column element. This last element must reflect the fact that the main discrete rotations associated to the nonlocal deformations are localized within L_{hinge}. In order to achieve this consistent localization of the equivalent curvatures, the FLPH force-based formulation proposed by Scott and Fenves [10] was adopted herein. The model uses a modified Gauss-Radau integration scheme which defines the positions x and the weights w of the 6 IPs that are considered as:

$$x = \left\{ 0, \frac{8}{3} \cdot L_{hinge,1}, x_3, x_4, L - \frac{8}{3} \cdot L_{hinge,2}, L \right\} \tag{16}$$

$$w = \left\{ L_{hinge,1}, 3 \cdot L_{hinge,1}, 0.5 - 2 \cdot \left(L_{hinge,1} + L_{hinge,2} \right), 0.5 - 2 \cdot \left(L_{hinge,1} + L_{hinge,2} \right), 3 \cdot L_{hinge,2}, L_{hinge,2} \right\} \tag{17}$$

where $L_{hinge,1}$ and $L_{hinge,2}$ refer to the tributary lengths of the IPs located at the extreme ends of the component, where the maximum moment usually occurs in RC frame buildings subjected to earthquake loading. The use of this fixed integration scheme provides a simplified approach to derive rotations that are compatible with the damage patterns found in experimental tests. Since estimates for $L_{hinge,1}$ and $L_{hinge,2}$ need to be defined, the analyses performed in Chapter 6 addressing the length of the damaged region were used to define the potential length between the sections where the EBH is assumed to be valid. Hence, for flexure-dominated components, $L_{hinge,1}$ and $L_{hinge,2}$ were assigned an initial estimate based on the relation $L_{hinge} = 18 \cdot d_b$.

Although the proposed modelling approach enables a consistent quantification of forces and deformations by assigning the length of the damaged region to the characteristic length (condition 1), constitutive models that are able to provide adequate estimates of the equivalent local strains still have to be defined, given that the adopted beam theory considers uncoupled IPs. The main principles outlined in condition 2 were adopted in order to transform the curvatures calculated with local fibre sections into equivalent size-dependent values. Although the previous discussion on this issue suggests a way of analysing explicitly the nonlocal effects (i.e. by determining Δ_{wdg} and Δ_{tra}), an alternative efficient approach was adopted herein instead. This approach uses equivalent local material stress-strain laws correlated with the stress-strain laws derived in experimental tests and the equivalent values that are associated with the damage localization at L_{hinge}, following similar principles proposed by Coleman and Spacone [16] and Pugh *et al.* [7]. The selected approach adopts a size-dependent models for the concrete cover (unconfined concrete), for the confined concrete core and for the reinforcing steel bars, each one connected to the properties of the experimental tests conducted to estimate the material stress-strain properties and their consistent transformation to the real scale defined by L_{hinge}.

7.3.2 Size-dependent properties of concrete cover spalling

In the proposed modelling approach, the unconfined concrete layer outside the reinforcing steel is modelled using the backbone curve introduced by Karthik and Mander [35]. Nevertheless, since the local rotations associated to the horizontal cracks are not explicitly modelled, the unconfined concrete stress-strain model has no tensile strength. The main properties of the uniaxial stress-strain curve adopted herein are shown in the right-hand side plot of Fig. 7.
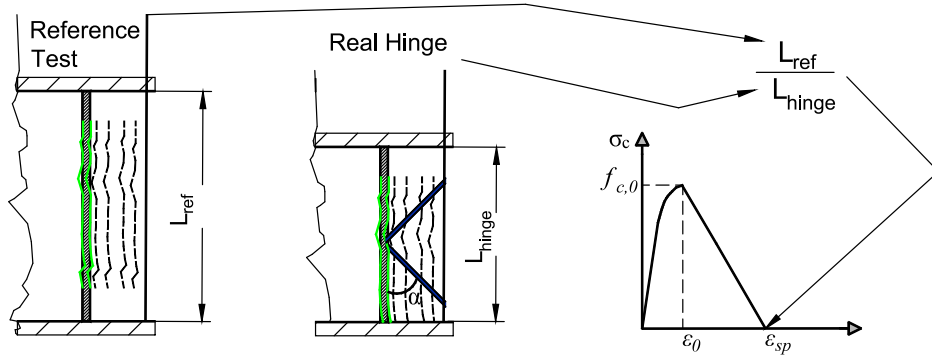
Figure 7. Adjustment of the ultimate strain of the unconfined concrete model to account for the size dependence of the softening stress-strain branch.

Karthik and Mander [35] re-evaluated several experimental tests and recommended the adoption of the Collins and Mitchel [36] approach to compute the strain corresponding to the peak compressive strength $f_{c,0}$ as:

$$\varepsilon_0 = 0.0015 + \frac{f_{c0}}{70000}.$$ (18)

Following the approach proposed by Karthik and Mander [35], the strain corresponding to the failure stress (i.e. a stress of 0 MPa) can be simply estimated by:

$$\varepsilon_f = 0.012 - \frac{f_{c0}}{10000}.$$ (19)

The simplified approach that is proposed herein for calculating the spalling strain ε_{sp} (illustrated in Fig. 7) is based on the strain obtained for a zero stress defined by Eq. (19), assuming this model can be associated to experimental data obtained for specimens with a reference height L_{ref}. Accordingly, ε_{sp} can be adjusted to reflect the size-dependence of the concrete softening properties, namely by including the size effects that will influence the longitudinal crack formation, as pointed by Markeset and Hillerborg [37] and Samani and Attard [38]. Hence, following the interpretation made by Chen *et al.* [39], the spalling strain was defined by:

$$\varepsilon_{sp} = \varepsilon_0 + \left(\varepsilon_f - \varepsilon_0\right) \cdot \frac{L_{ref}}{L_{hinge}}$$ (20)

where L_{ref} was assumed to be equal to 0.400 m given its compatibility with experimental data such as the tests results reported in Mander *et al.* [40] and Scott *et al.* [41].

7.14

7.3.3 Size-dependent uniaxial model for the confined concrete core

The size dependency of the softening branch of the stress-strain envelope is a direct consequence of the nonlocal effects arising mainly from the deterioration of the shear-friction properties of concrete. Several authors have proposed stress-strain curves to account for the size-dependency of the material (e.g. [42-45]) without modelling the sliding deformations. The main considerations involved in the definition of these models are similar to the concepts adopted by Coleman and Spacone [16] and Pugh *et al.* [7] for the regularization of the element response. The approach proposed herein involves similar concepts but not as a numerical convenience but rather as way to represent a physical size-effect. The main principle of the approach proposed herein involves adjusting the fracture energy in order to derive a stress-strain model that is consistent with the finite dimensions of the hinge. The process used to quantify the size-dependent stress-strain law is illustrated in Fig. 8. Essentially, the starts by defining the softening branch of the stress-strain model for the reference test and by quantifying the area under the softening branch (shaded area in Fig. 8) that defines the fracture energy, G_{fcc}. This fracture energy is based on strains associated to a reference length L_{ref} and must then be factored in order to represent a hinge with a size L_{hinge}
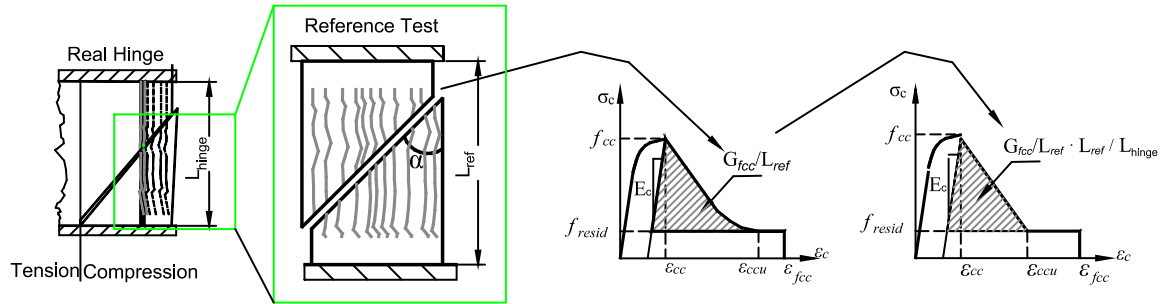
Figure 8. Calibration of the equivalent confined concrete uniaxial stress-strain model based on core tests by adjusting the fracture energy.

Samani and Attard [38] defined a model for the fracture energy G_{fcc} of columns confined by reinforcing steel bars as a function of residual stress levels f_{resid} that is given by:

$$f_{resid} = f_{cc} - \frac{f_{cc}}{1+\left(795.8 - 3.291 \cdot f_{c,0}\right) \cdot \left(\frac{f_l}{f_{c,0}}\right)^{\left\{5.79 \cdot \left(\frac{f_l}{f_{c,0}}\right)^{0.694} + 1.301\right\}}}, \qquad (21)$$

where f_{cc} is the peak confined concrete strength and f_l is the confinement stress. The confinement stress f_l can be quantified based on Mander *et al.* [31], while the confined concrete peak strength f_{cc} can be established based on Bing *et al.* [46] for rectangular confinement and for normal and high strength concrete as:

$$f_{cc} = f_{c0} + 2.1 \cdot f_l \quad , \quad f_{c0} \leq 50\,\text{MPa} \,, \tag{22}$$

$$f_{cc} = f_{c0} + 1.9 \cdot f_l \quad , \quad f_{c0} > 50\,\text{MPa} \,. \tag{23}$$

These values of f_{cc} are associated to a strain defined by Mander *et al.* [40] as:

$$\varepsilon_{cc} = \varepsilon_0 \cdot \left(1 + 5 \cdot \left(\frac{f_{cc}}{f_{c0}} - 1 \right) \right). \tag{24}$$

Based on the residual confined concrete stress, the size-dependent fracture energy G_{fcc} can be quantified by [38]:

$$\frac{G_{fcc}}{L_{ref}} = \frac{1}{2} \cdot \frac{\sqrt{\pi} \cdot \left(\varepsilon_{ic} - \varepsilon_{cc} \right) \cdot \left(f_{cc} - f_{resid} \right)}{\sqrt{\ln\left(f_{c0}\right) - \ln\left(f_{ic}\right)}} + \frac{1}{2} \cdot \frac{\left(f_{cc} - f_{resid} \right)^2}{E_c} \tag{25}$$

where ε_{ic} and f_{ic} are the coordinates of the inflection point and are given by:

$$\frac{\varepsilon_{ic}}{\varepsilon_{cc}} = \frac{f_{resid}}{f_{cc}} \cdot \left(1.26 + \frac{2.89}{\sqrt{f_{c0}}} \right) + \left(1 - \frac{f_{resid}}{f_{cc}} \right) \cdot \left(2.76 - 0.35 \cdot \ln\left(f_{c0}\right) \right), \tag{26}$$

$$\frac{f_{ic}}{f_{cc}} = \frac{f_{resid}}{f_{cc}} + \left(1 - \frac{f_{resid}}{f_{cc}} \right) \cdot \left(1.41 - 0.17 \cdot \ln\left(f_{c0}\right) \right). \tag{27}$$

Finally, by using the fracture energy quantified in Eq. (25) and adopting a value of L_{ref} equal to 0.400 m (consistent with the unconfined concrete model and with the distance between gauges defined in [31]), the adjusted size-dependent strain corresponding to the residual stress can be computed by:

$$\varepsilon_{ccu} = \frac{2 \cdot \left(\dfrac{G_{fcc}}{L_{ref}} \cdot \dfrac{L_{ref}}{L_{hinge}} \right)}{\left(f_{cc} - f_{resid} \right)} + \varepsilon_{cc} - \frac{\left(f_{cc} - f_{resid} \right)}{E_c} \,. \tag{28}$$

The proposed model for confined concrete has a residual strength plateau whose ductility has to be limited in order to simulate the failure mechanism. Scott *et al.* [41] and Bing *et al.* [46] used the first hoop fracture to limit the strain ductility of the stress-strain law. Hence, the ultimate strain ε_{fcc} corresponding to a rectangular confinement can be established based on this condition by [46]:

7.16

$$\varepsilon_{fcc} = \left\{ 2 + \left(122.5 - 0.92 \cdot f_{c0}\right) \cdot \sqrt{\frac{f_l}{f_{c0}}} \right\} \cdot \varepsilon_{c0} \cdot \frac{L_{ref}}{L_{hinge}} \quad , \quad f_{c0} < 80\text{MPa}$$

$$\varepsilon_{fcc} = \left\{ 2 + \left(82.75 - 0.37 \cdot f_{c0}\right) \cdot \sqrt{\frac{f_l}{f_{c0}}} \right\} \cdot \varepsilon_{c0} \cdot \frac{L_{ref}}{L_{hinge}} \quad , \quad f_{c0} \geq 80\text{MPa}$$

(29)

where L_{ref} is equal to 0.300 m in order to be consistent with the experimental data reported by Bing *et al.* [46].

7.3.4 Size-dependent uniaxial model for the reinforcing steel

The instability of the reinforcing steel bars due to necking, local buckling and fracture, and how to include these aspects into uniaxial stress-strain models for reinforcing steel have been studied in the past ([7;29-32; 50; 51]). In the current proposal, the selected steel models are the idealized quadrilinear backbone model of the reinforcing steel bar in compression and the corresponding trilinear backbone model in tension shown in Fig. 9.
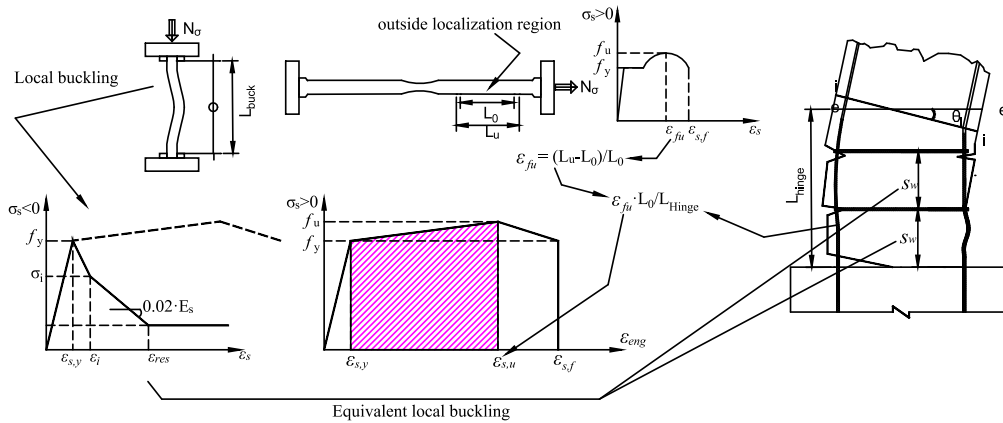
Figure 9. Calibration of the equivalent reinforcing steel uniaxial stress-strain model based on experimental tests to quantify the bar response under monotonic tension and compression.

The response of the reinforcing steel bar in tension (Fig. 9, $\sigma_s > 0$) involves a trilinear backbone representing the expected monotonic response of the bar. The yielding strength f_y and strain ε_y are values that can typically be extracted directly from experimental tests and that are considered reliable values. The Young modulus E_s is usually around 200 GPa, and can be used to quantify ε_y based on f_y. The second point of the proposed backbone model requires the quantification of two points that are more difficult to accurately determine from experimental tests since they are associated to the necking phenomenon. As discussed for example by Dodd and Restrepo [47], stress is obtained by the ratio between the force N_σ that is applied and the initial area of the cross section of the bar A_0. The corresponding strains can be quantified by dividing the measured

7.17

displacements by the considered gauge length L_0. These coordinates are valid in a phase where the bar is strained homogenously, until the maximum stress f_u is achieved. After this stress level, the strain hardening is insufficient to compensate the reduction of cross-section area due to radial contraction, leading to a phenomenon designated by necking. The necking strain can be defined as the strain ε_{fu} corresponding to the maximum uniform deformation along the bar measured before the beginning of the constriction, usually associated to the stress f_u. In order to have a parametric definition of these properties, the models provided by Pipa [48], correlating ε_{fu} and f_u with f_y, can be adopted:

$$\varepsilon_{fu} = 0.238 - 0.000244 \cdot f_y. \tag{30}$$

$$f_u = 161 + 0.88 \cdot f_y. \tag{31}$$

The strain ε_{fu} is correlated with the test setup and depends on the gauge length L_0 that is used to measure the strains. European norms (e.g. [49]) recommend adopting L_0 equal to 0.10 m, although it is also common to adopt a value between $5 \cdot d_b$ and $10 \cdot d_b$. As shown in Fig. 9, the proposed model considers a value of $5 \cdot d_b$ for L_0 and adjusts the plastic part of $\varepsilon_{s,u}$ in order to account for the size effects. A similar strategy was adopted by Pugh *et al.* [7] by adjusting the fracture energy (shaded area in Fig. 9) to account for the size effects. Accordingly, the adjusted strain corresponding to the maximum stress f_u becomes:

$$\varepsilon_{s,u} = \varepsilon_y + \left(\varepsilon_{fu} - \varepsilon_y\right) \cdot \frac{L_0}{L_{hinge}}. \tag{32}$$

As also seen in Fig. 9, a linear branch between the necking strain and the post-necking strain is considered to model the monotonic post-necking behaviour. As discussed by Kolwankar *et al.* [50], deformations exceeding 1.25 times the true necking deformation are consistent with those required to induce fracture. As a result, after $\varepsilon_{s,u}$, strength deteriorates linearly until a stress level around f_y is reached, with a corresponding deformation $\varepsilon_{s,f}$ given by:

$$\varepsilon_{s,f} = 1.25 \cdot \varepsilon_{s,u}. \tag{33}$$

Under monotonic loading, this strain can be used as a limit value for the bar ductility in tension, whereas under cyclic loading the interaction between isotropic hardening, necking and low cycle

fatigue/cyclic degradation can lead to a smoother degradation of the strength with different ductility levels, instead of leading to immediate fracture.

With respect to the reinforcing steel in compression, the model selected to represent its response is the quadrilinear backbone model proposed by Dhakal and Maekawa [51], as shown in Fig. 9 (i.e. for $\sigma_s < 0$). After the yielding point defined by the stress f_y and the strain ε_y, as detailed for the tension case, a linear branch is assumed to represent the behaviour until the point $(\varepsilon^*, \sigma^*)$ is attained. The intermediate strain ε_i is defined by Dhakal and Maekawa [51] by:

$$\varepsilon_i = \max\left(55 - 2.3 \cdot \sqrt{\frac{f_y}{100}} \cdot \frac{s_w}{d_b}; 7\right) \cdot \varepsilon_y. \tag{34}$$

which depends on the local buckling behaviour since the results are based only on the slenderness ratio of the rebar, s_w / d_b. The corresponding stress level is obtained from:

$$\sigma_i = \left(1.1 - 0.016 \cdot \sqrt{\frac{f_y}{100}} \cdot \frac{s_w}{d_b}\right) \cdot \sigma_{pos} \geq 0.20 \cdot f_y. \tag{35}$$

where σ_{pos} is assumed to be the equivalent stress in tension for the strain ε_i given by:

$$\sigma_{pos} = f_y + \left(\varepsilon_i - \varepsilon_y\right) \cdot E_{hard} \geq 0.20 \cdot f_y. \tag{36}$$

where E_{hard} represents the slope of the hardening branch between f_u and f_y. According to Dhakal and Maekawa [51], after this intermediate point, a linear branch with a constant slope equal to $0.02 \cdot E_s$ can be used to determine ε_{20}, the strain corresponding to a stress level of $0.20 \cdot f_y$.

7.4 Comparison of the proposed modelling approach with experimental results

7.4.1 Selected database of experimental tests and numerical models

A database containing 36 RC columns tested in laboratory was considered to assess the adequacy of the proposed modelling approach combining the nonlocal uniaxial stress-strain material models for reinforcing steel and concrete, the fundamentals behind the damaged region length and the regularized force-based formulation proposed by Scott and Fenves [10]. The properties of the tested columns are presented in Table 1 and were collected from the database presented in [52, 53]. In Table 1, B represents the section width, H is the section height, d_w is the diameter of

the stirrup, $f_{y,w}$ and $f_{y,1}$ are the yielding reinforcing steel strength of transversal and longitudinal bars, and L is the shear span of the element. This database was selected in order to cover all the potential different flexural mechanisms. The criteria to assess the expected type of ductile flexural response proposed in Chapter 6 were used to ensure that of all the 3 regions (see I, II and III in Fig. 10) were covered.

Figure 10 shows the distribution of the selected specimens on the $s_w/d_b - \nu$ spectrum along with the different regions that identify the expected mechanism leading to damage accumulation. As can be seen, the selected specimens exhibit a large variety of buckling-restraining capacities and confinement levels (as indirectly measured by s_w/d_b), as well as a variety of axial load levels.
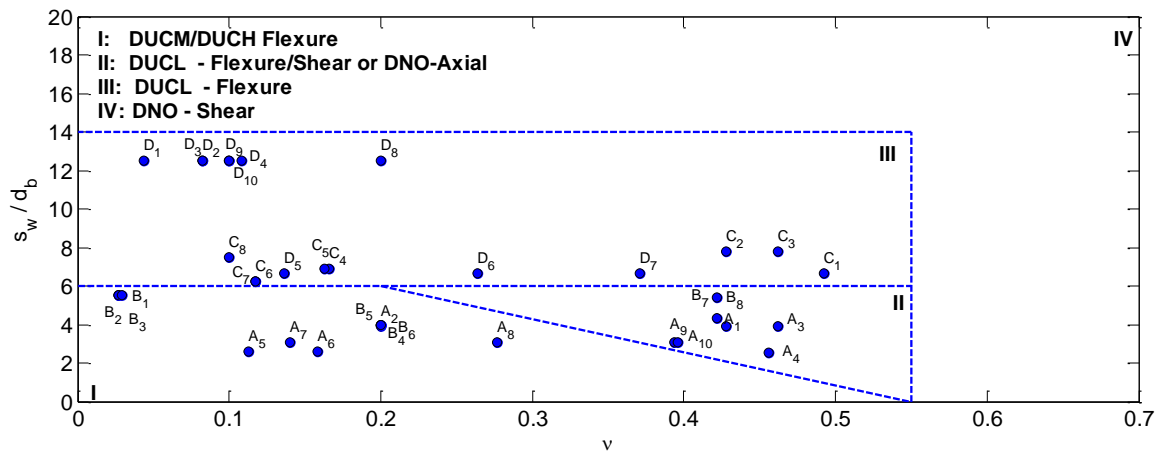
Figure 10. Classification of the expected mechanism controlling the cyclic response of the specimens based on the criteria developed in Chapter 6: DUCM/DUCH Flexure refer to specimens with moderate to high ductility, DUCL-Flexure/Shear are specimens with low ductility governed by flexure/shear failure modes, DNO-Axial are non-ductile specimens due to excessive axial load levels that lead to softening after yielding, DUCL-Flexure are specimens with low-ductility and flexural behaviour controlled by buckling of the reinforcement and DNO-Shear are non-ductile specimens governed by shear capacity.

OpenSees [64] was used to perform the numerical analyses in the present study. A *zerolengthelement* was used to simulate the fixed-end rotations considering an elastic moment-rotation spring. A force-based element was used considering the modified Gauss-Radau integration approach proposed by Scott and Fenves [10] and a characteristic length L_c defined according to the average length of the damaged region estimated in Chapter 6 (i.e. $18 \cdot d_b$). Fibre sections were assigned the integration points to model their behaviour. The fibre section mesh was defined considering a fibre width of 0.01m. The unconfined concrete was modelled using the *Concrete01* model considering the parametrization previously discussed. The uniaxial stress-strain model of confined concrete was defined by a combination of the *Concrete01* model with residual stress and equivalent strains as defined in Eqs. (21) and (28) with a *MinMax* criteria which enforces the stiffness and strength of the fibre to become zero when the compressive strain

defined by Eq. (29) is attained. At this strain, a residual stress of 5% of f_{cc} was added in the cyclic analyses to increase the numerical stability of the model.

Table 1. Physical properties of the RC frame components considered in the study

Code	Ref.	Specimen	B	H	υ	s_w	$\emptyset_w$	λ	f_c	f_{yw}	L	f_{yl}
-	-	-	mm	mm	-	mm	mm	-	MPa	MPa	mm	MPa
A_1	54	BG-2	350	350	0.43	76	9.5	3.9	34.0	570	1645	456
A_2	54	BG-3	350	350	0.20	76	9.5	3.9	34.0	570	1645	456
A_3	54	BG-5	350	350	0.46	76	9.5	3.9	34.0	570	1645	456
A_4	54	BG-6	350	350	0.46	76	9.5	2.5	34.0	570	1645	478
A_5	55	C1-1	400	400	0.11	50	6.35	2.6	24.9	460	1400	497
A_6	55	C1-2	400	400	0.16	50	6.35	2.6	26.7	460	1400	497
A_7	55	C2-1	305	305	0.14	60	11.3	3.9	92.4	391	2000	451
A_8	55	C2-2	305	305	0.28	60	11.3	3.9	93.3	391	2000	430
A_9	55	C3-1	305	305	0.39	60	11.3	3.9	98.2	418	2000	451
A_{10}	55	C3-2	305	305	0.40	60	11.3	3.9	78.7	438	2000	446
B_1	56	Test1	400	400	0.03	70	6	5.5	35.9	368	1245	363
B_2	56	Test2	400	400	0.03	70	6	5.5	35.7	368	1245	363
B_3	56	Test3	400	400	0.03	70	6	5.5	34.3	368	1245	363
B_4	57	No. 1	400	400	0.20	80	12	4.0	25.6	333	1600	474
B_5	57	No. 2	400	400	0.20	80	12	4.0	25.6	333	1600	474
B_6	57	No. 3	400	400	0.20	80	12	4.0	25.6	333	1600	474
B_7	58	Sp.1	550	550	0.04	50	6	5.0	23.5	300	2250	300
B_8	58	Sp.1	550	550	0.04	50	6	5.0	23.5	300	2250	300
C_1	54	BG-1	350	350	0.43	152	9.5	7.8	34.0	570	1645	455
C_2	54	BG-4	350	350	0.46	152	9.5	7.8	34.0	570	1645	455
C_3	59	S24-4UT	610	610	0.17	152	12.7	6.9	36.5	455	3050	400
C_4	59	S24-5UT	610	610	0.16	152	12.7	6.9	41.4	434	3050	400
C_5	53	N05	300	400	0.12	75	6	6.3	21.4	450	1500	450
C_6	53	N06	400	300	0.12	75	6	6.3	21.4	450	1500	450
C_7	60	T3	250	250	0.10	120	8	7.5	59.0	480	950	480
C_8	61	No.7	400	400	0.22	117	10	7.3	28.3	466	1600	440
D_1	53	N01	200	400	0.04	150	6	12.5	48.4	450	1500	450
D_2	53	N09	300	500	0.08	150	6	12.5	24.4	450	1500	450
D_3	53	N10	500	300	0.08	150	6	12.5	24.4	450	1500	450
D_4	53	N13	300	300	0.11	150	6	12.5	21.6	450	1500	450
D_5	62	C100B130N15	305	305	0.14	130	11.3	8.1	94.8	391	2150	469
D_6	62	C100B130N25	305	305	0.26	130	11.3	8.1	97.7	404	2150	456
D_7	62	C100B130N40	305	305	0.37	130	11.3	8.1	104.3	418	2150	457
D_8	63	S300D-c	300	300	0.20	150	8	12.5	18.8	520	1500	520
D_9	63	R300D-c	500	300	0.10	150	8	12.5	18.8	520	1500	520
D_{10}	63	R500D-c	300	500	0.10	150	8	12.5	18.8	520	1500	520

Finally, the reinforcing steel stress-strain curve was simulated using the *Hysteretic Material* model. A pinching factor for strain of 0.20 and a pinching factor for stress of 0.60 were considered during reloading. For cyclic analyses, a ductility-based cyclic damage parameter d_1 with a value of 1% was also included as part of the *Hysteretic Material* parameters. This model was defined for specimens where buckling is not dominant, i.e. for tests with $s_w/d_b < 8$, considering a symmetric backbone model with the same behaviour in tension and in compression. Specimens with $s_w/d_b \geq 8$ were simulated with the quadrilinear backbone model previously defined.

The performance of the proposed modelling approach was analysed for both monotonic and cyclic analyses. For the monotonic analyses, lateral displacements were imposed at the top of each cantilever column (specimens that have double curvature configurations were reduced to the corresponding equivalent cantilever column). For the cyclic analyses, the experimental cyclic lateral displacements were imposed at the top of each cantilever column. For both types of analyses, the numerical behaviour curves were compared with the cyclic curves collected from the experimental campaigns.

7.4.2 Damage and buckling length

Figure 11 shows the estimates obtained for the length of the damaged region L_D that were used to establish the strain characteristic length and the corresponding bucking length L_{buck}. As seen in Fig. 11a, on average, L_D reduces as λ increases. Variations around this average behaviour are due to the differences in the longitudinal reinforcement diameter d_b. These variations reflect the delay in the occurrence of the longitudinal reinforcement buckling due to its larger diameter and the corresponding influence of the damaged concrete region (i.e. the length of the region where concrete fracture mechanisms are observed). Such observations are corroborated by the values of L_{buck} shown in Fig. 11b, in which a more stable pattern where L_{buck} converges to s_w is observed. Furthermore, the fact that when L_D increases, the intermediate strain ε_i also increases (Fig.11c), indicates that, in these cases, the buckling phenomenon is less relevant and the deterioration of the shear-friction properties of concrete becomes the governing failure mechanism. As also seen in Figs. 11b and 11c, adopting the buckling model to define the damage length of specimens assigned code D in Table 1 (i.e. specimens with $\lambda \geq 8$) is sufficient since these specimen exhibit the smaller levels of ductility ($\varepsilon_i / \varepsilon_y$). Cases from this group of specimens that exhibit some deviations with respect to the hypotheses that were assumed can be justified by the fact they involve a higher concrete strength. This higher compressive capacity of the concrete surrounding the reinforcing bars will enable the development of larger values of L_D. In these cases, as shown in Fig. 11d, the material becomes very brittle and, consequently, exhibits a very low fracture

ductility ($\varepsilon_{fcc}/\varepsilon_0$, where ε_{fcc} was calculated by Eq. 29 assuming $L_{ref}/L_{hinge}=1$). This will, therefore, lead to a slight increase of L_D. This feature is however not captured by the empirical model adopted for L_D.
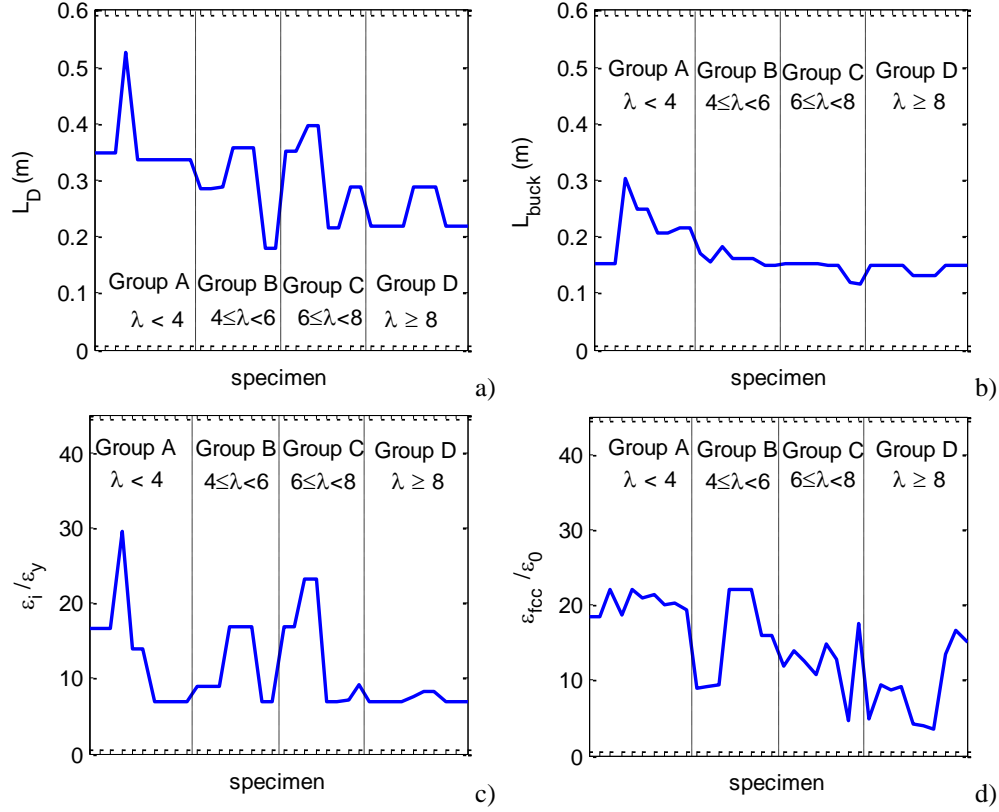

Figure 11. Estimates for the length of the damaged region used for the quantification of the strain localization phenomenon (a), estimates obtained for the buckling length (b), estimated strain ductility for the reinforcing steel obtained by normalizing the values of the intermediate obtained using Eq. (34) by the yielding strain (c) and estimated ratio between the peak strain of confined concrete and the peak strain of unconfined concrete (d) for each specimen.

7.4.3 Results obtained for the monotonic analyses

Figures 11-13 show the results obtained with the modelling approach defined in Section 7.3 considering the empirical model for the length of the damaged region developed in Chapter 6. In this first set of analyses, the maximum lateral displacement that is imposed corresponds to the maximum displacement of the experimental test, and the strain limit corresponding to the criterion for steel bar fracture defined by Eq. (33) was not considered.

By analysing the monotonic response of the column it is possible to assess the ability of the proposed modelling approach to capture the initial in cycle degradation induced by concrete softening. As seen in the 36 simulations that were performed, the backbone model is able to capture most of the initial degradation effects of the specimens, particularly when referring to the within-cycle degradation of the capacity.in the majority of the specimens.

Figure 12. Comparison of the experimental lateral load-drift cyclic results with the monotonic response results obtained with the proposed modelling approach for specimens A1-B5, when the strain limit corresponding to the criterion for steel bar fracture was not considered.

Figure 13. Comparison of the experimental lateral load-drift cyclic results with the monotonic response results obtained with the proposed modelling approach for specimens B6-D4, when the strain limit corresponding to the criterion for steel bar fracture was not considered.
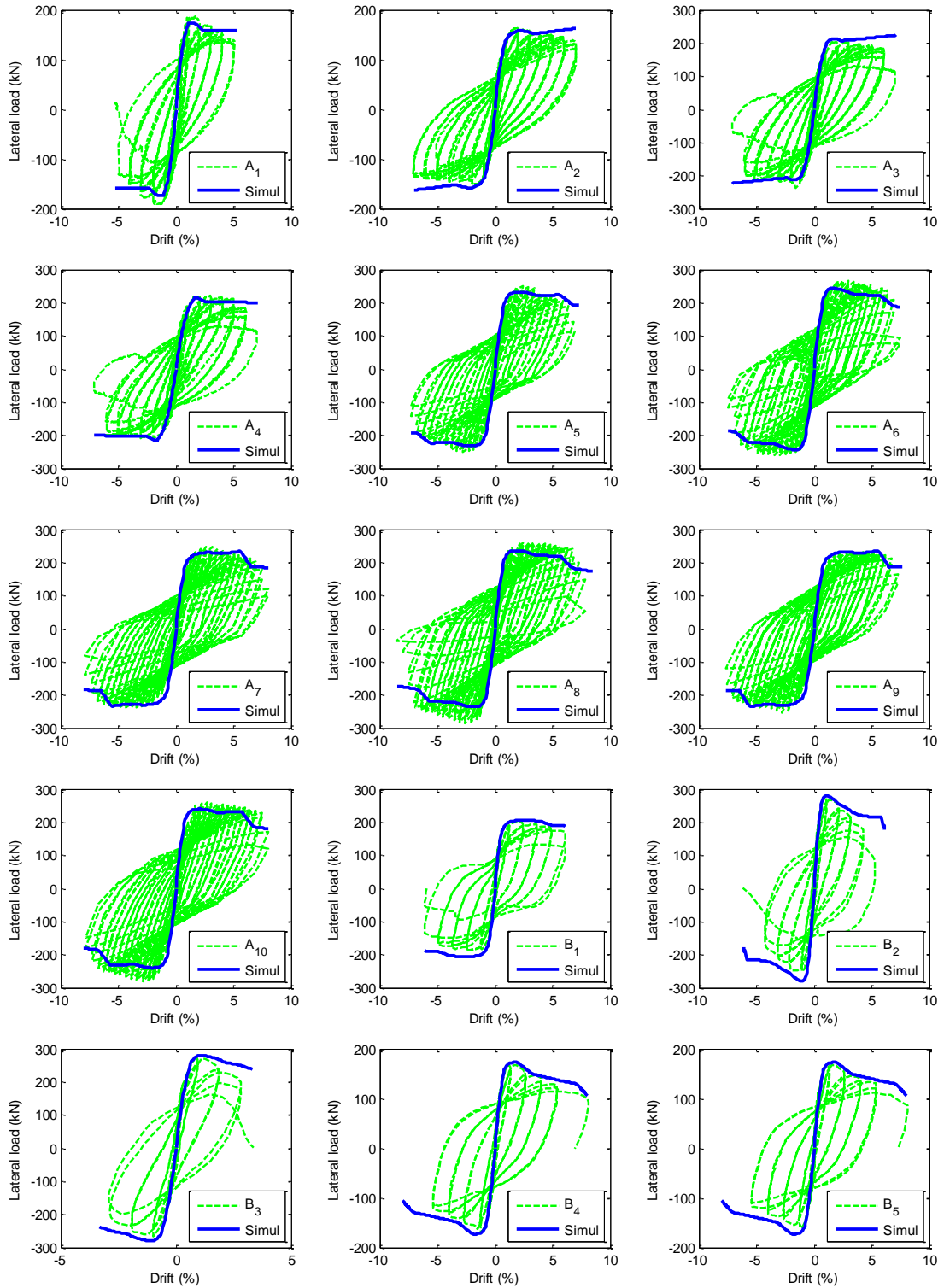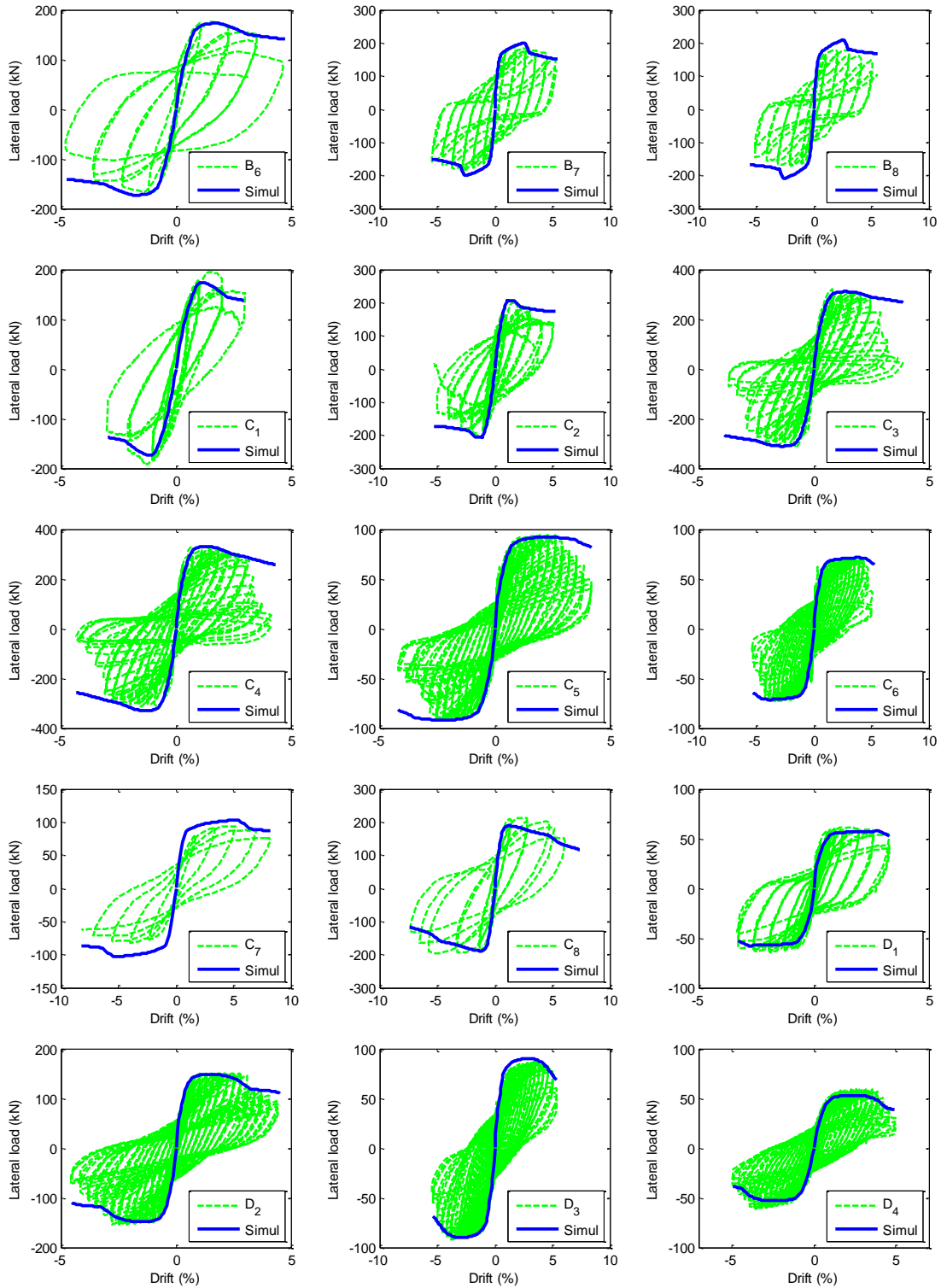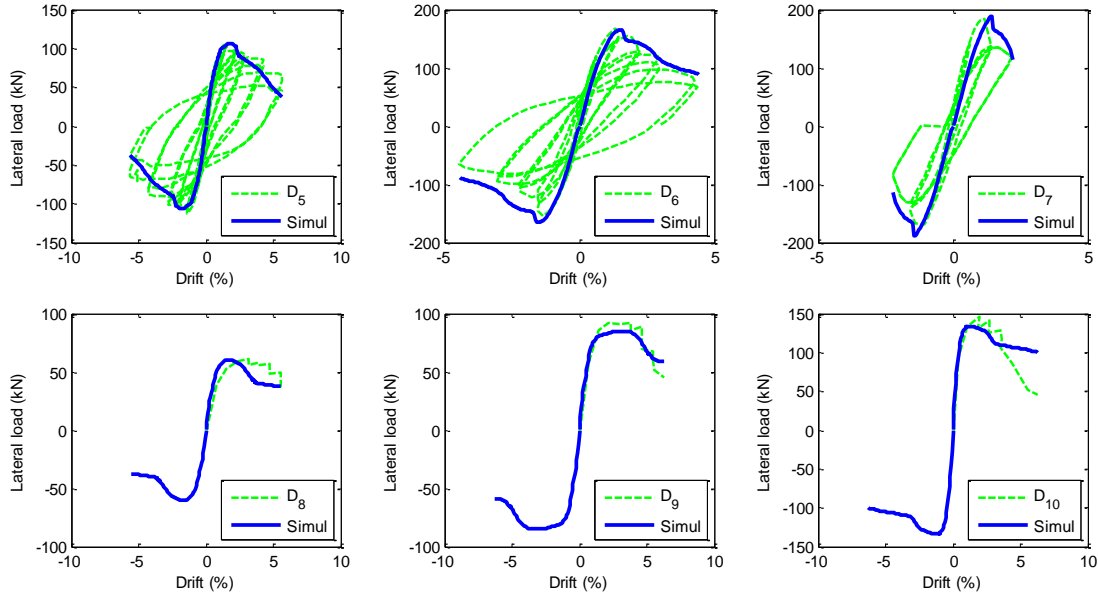
Figure 14. Comparison of the experimental lateral load-drift cyclic results with the monotonic response results obtained with the proposed modelling approach for specimens D5-D10, when the strain limit corresponding to the criterion for steel bar fracture was not considered.

The backbone model is, nevertheless, unable to capture the major contributions of the cycle-to-cycle degradation, which can be related to the fatigue properties and the combination between the steel elongation in tension and buckling in compression, namely the bar strength deterioration due to the reduction of the bar area and the instability that follows due to the load reversals.

In some of the tested specimens (A1-A4, B3, C2-C4, D1), the cyclic degradation of the experimental test is not captured by the model. In specimens C2-C4, the softening of the global load-displacement envelope is captured, which can be seen to be the result of the in-cycle and a minor cyclic degradation related to the softening of the concrete fibres (see e.g. [68] for a distinction between cyclic and in-cycle strength deterioration in RC components). In the majority of the tests, the initial softening in the post-yielding stage is simulated accurately, as can be seen from the results of tests B2, B4-B5 and D6. Since the hysteretic behaviour of unconfined and confined concrete models does not include any damage parameter based on energy or ductility, the results obtained from the monotonic analyses show directly the adequacy of the selected combination of element and uniaxial concrete stress-strain curve to capture concrete crushing and spalling. This fact is particularly relevant in specimens belonging to groups A, B and C where the reinforcing steel stress-strain model adopted is symmetric. For specimens of group D, the buckling of the reinforcement influences the backbone of the model in compression and, therefore, the simulated response is based on the peak-oriented response of both concrete and reinforcing steel softening in compression.

To analyse the differences in the results of the monotonic analyses that would be obtained by enforcing the criterion for steel bar fracture, Figs. 15-17 show the monotonic results obtained when the lateral displacement of each specimen is increased until strain $\varepsilon_{s,u}$ (defined by Eq. (33))

occurs. As seen in these new results, the modelling approach is able to capture the monotonic failure of the specimens and provides an adequate backbone curve for the cyclic capacity of the specimens. Thus, based on these general observations, the proposed modelling approach appears to be adequate for the static nonlinear analysis of RC frame buildings.

Figure 15. Comparison of the experimental lateral load-drift cyclic results with the monotonic response results obtained with the proposed modelling approach for specimens A1-B2, when the strain limit corresponding to the criterion for steel bar fracture was considered.

Figure 16. Comparison of the experimental lateral load-drift cyclic results with the monotonic response results obtained with the proposed modelling approach for specimens B3-D1, when the strain limit corresponding to the criterion for steel bar fracture was considered.
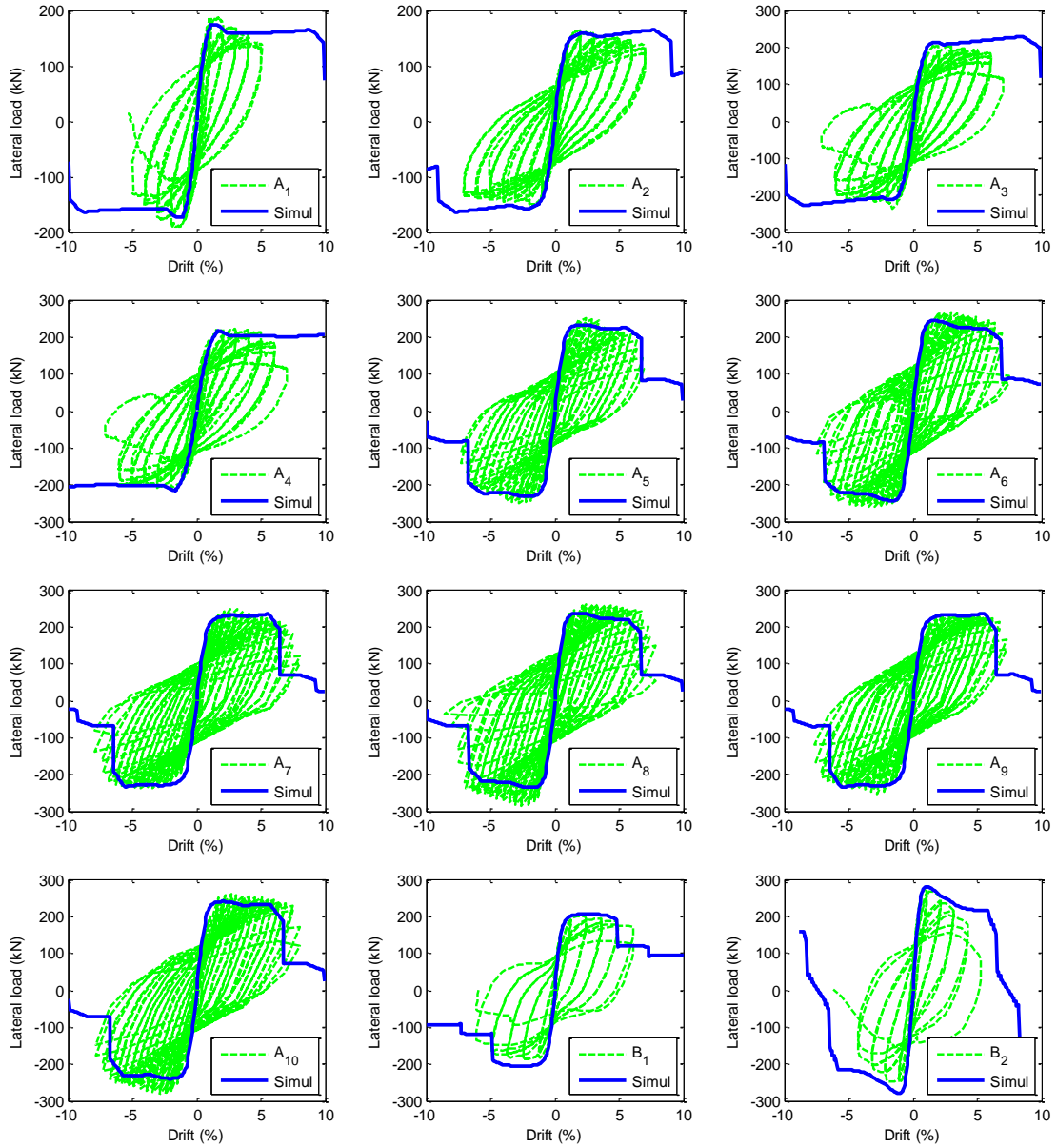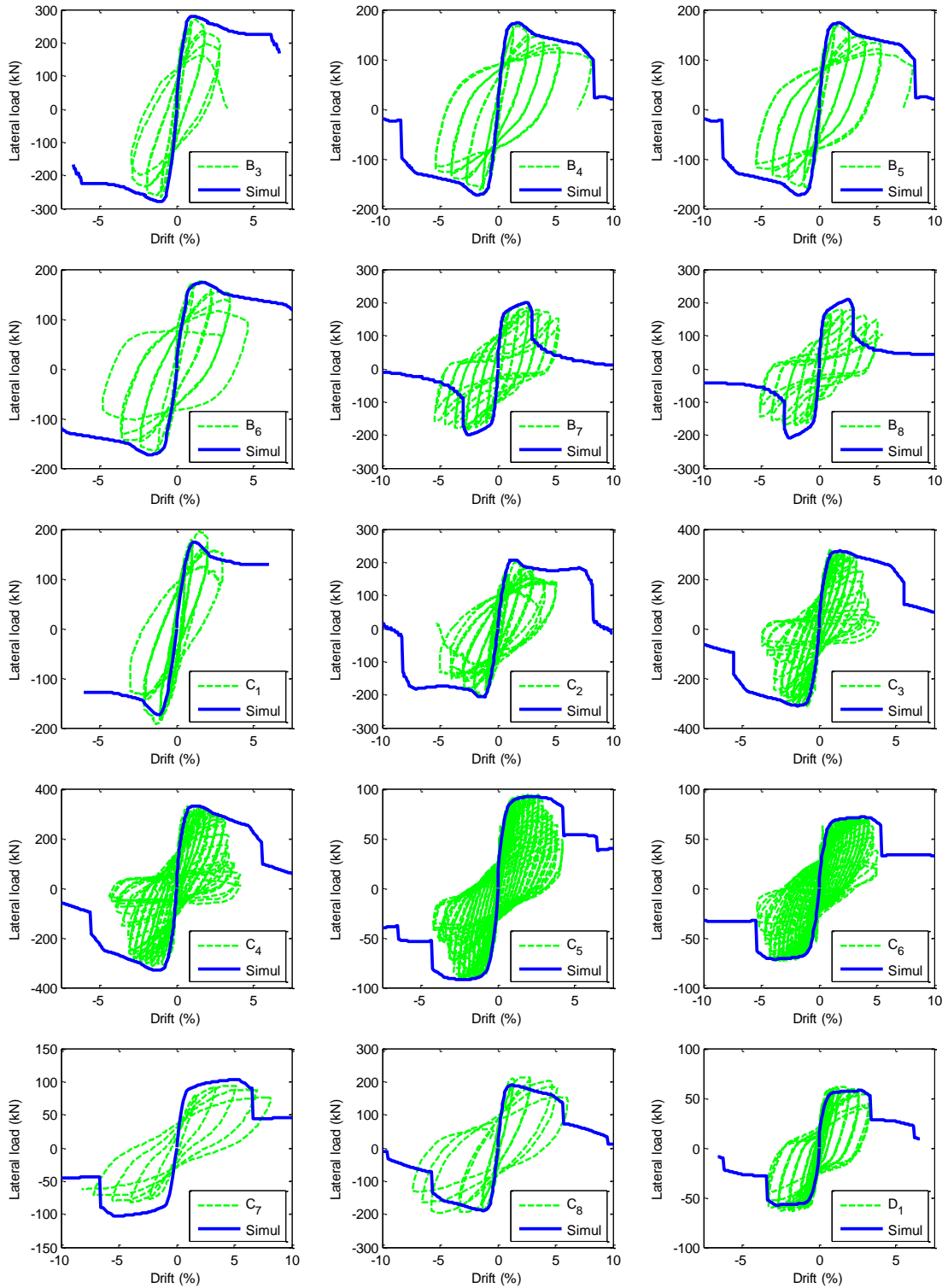
Figure 17. Comparison of the experimental lateral load-drift cyclic results with the monotonic response results obtained with the proposed modelling approach for specimens D3-D10, when the strain limit corresponding to the criterion for steel bar fracture was considered.

7.4.4 Results obtained for the cyclic analyses

In order to evaluate the effects of load-reloading cycles on the efficiency of the proposed modelling approach, Figs. 14-16 show the comparison of the numerical load-displacement histories with the corresponding experimental results. The selected modelling approach includes cyclic degradation parameters but did not consider the criterion for steel bar. The overall results show an adequate performance of the proposed modelling approach.

Convergence issues were identified in the simulation of specimen B2 where the rapid strength degradation caused the failure of the analysis for a drift of 4%. Some deviations between the numerical and experimental responses were also identified in loading stages closer to failure, although the numerical responses are still seen to exhibit degradations rate similar to those of the experimental test data. Furthermore, it is noted that the pinching parameters adopted for the reinforcing steel model based on the parametric study performed by Kashani *et al.* [65] have shown to be effective in capturing the reloading path of the global force-displacement history.
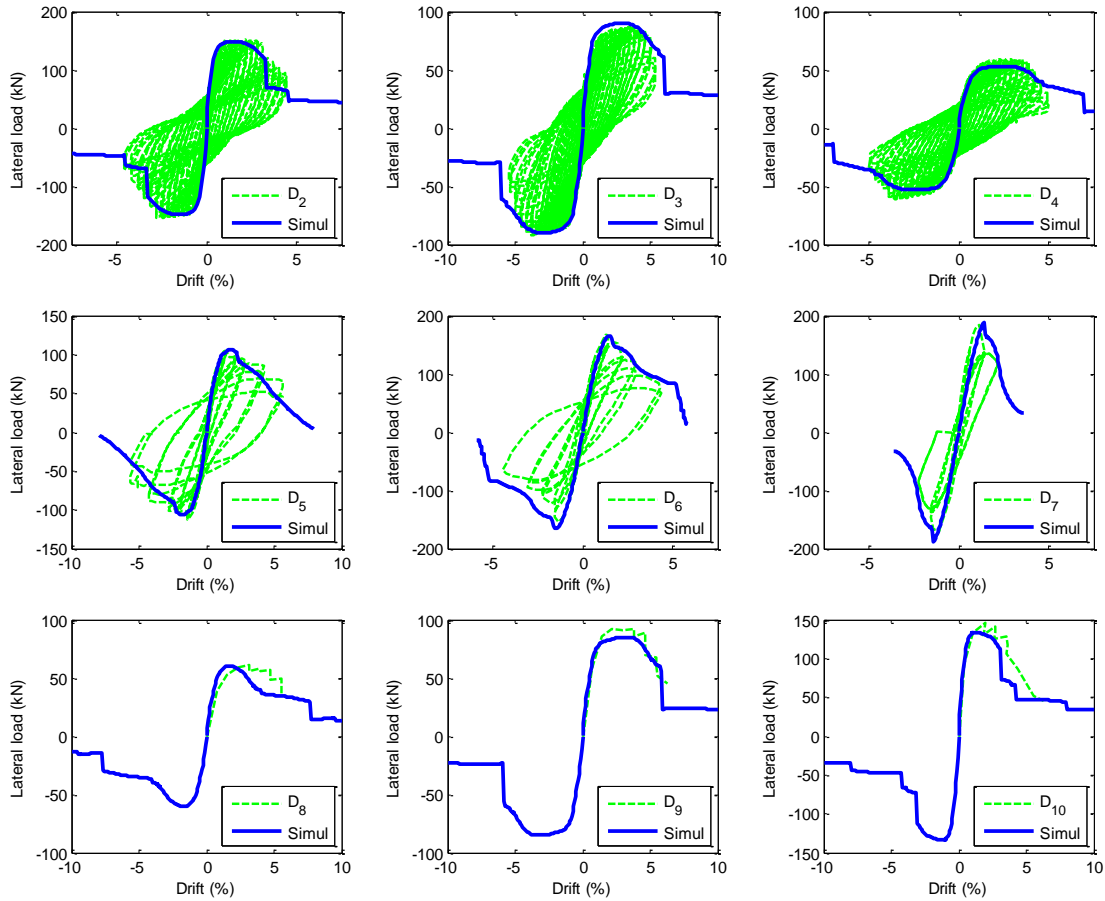
Figure 18. Comparison of the experimental lateral load-drift cyclic results with the cyclic response results obtained with the proposed modelling approach for specimens A1-B5.
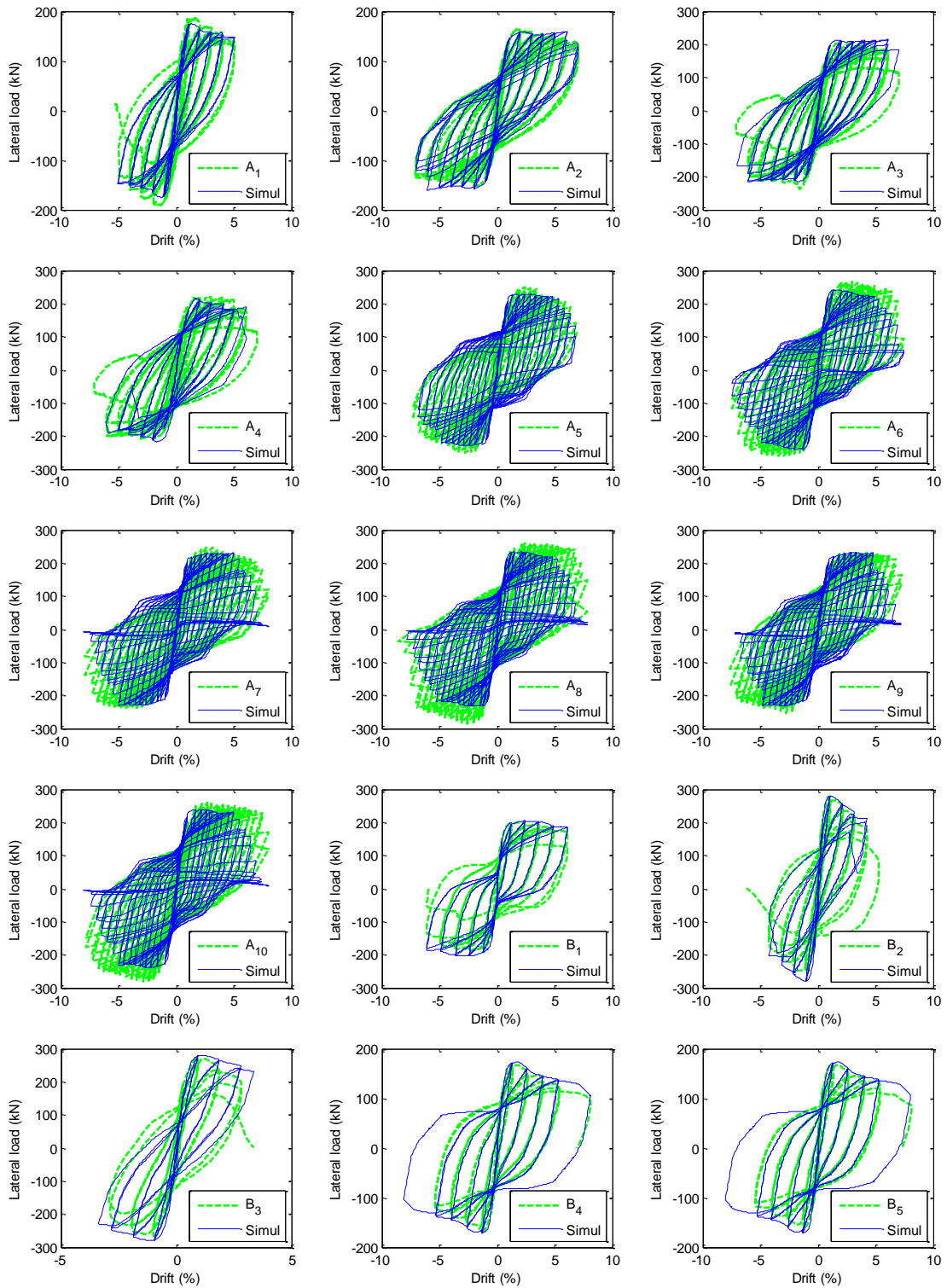
Figure 19. Comparison of the experimental lateral load-drift cyclic results with the cyclic response results obtained with the proposed modelling approach for specimens B6-D4.
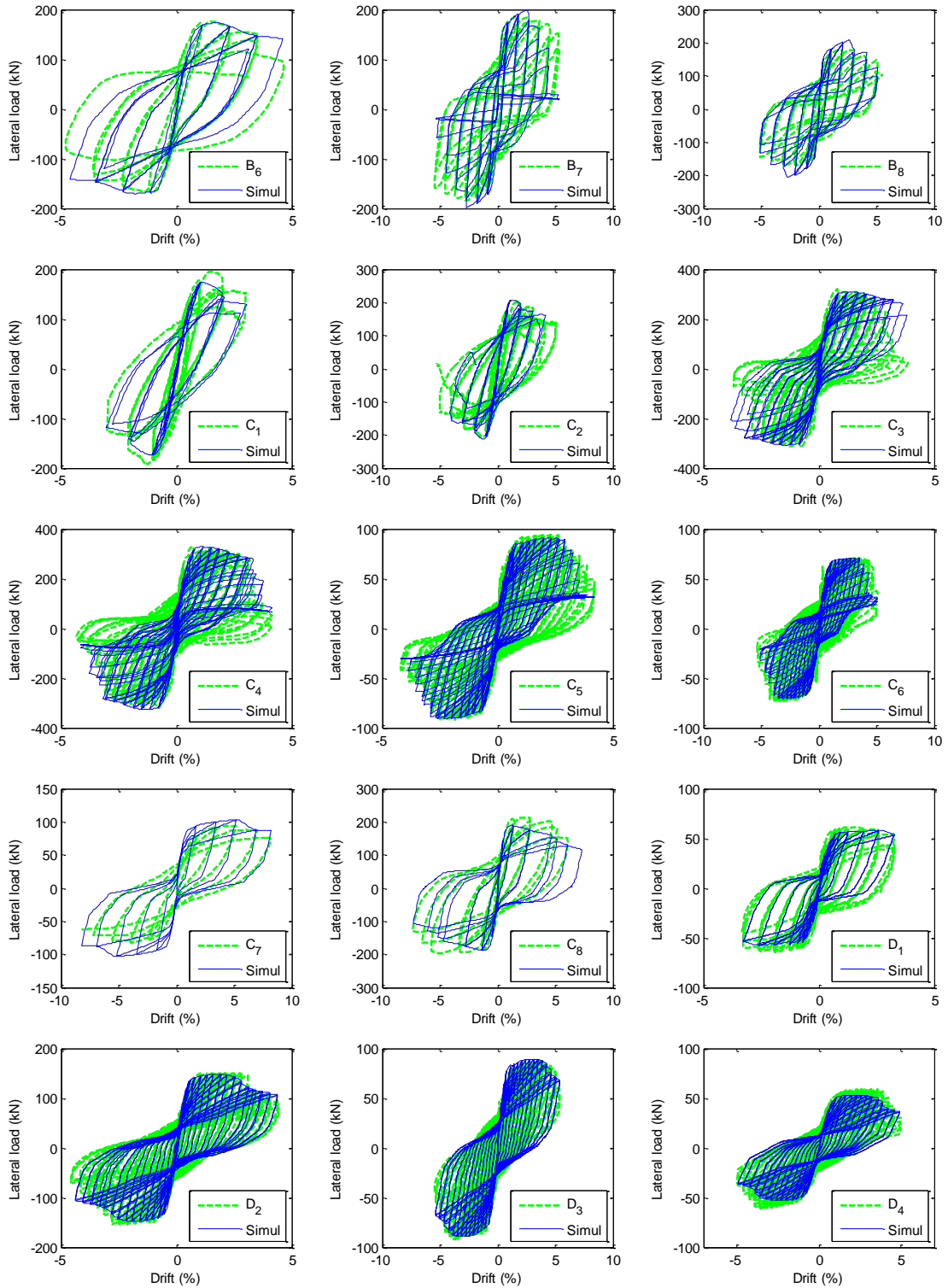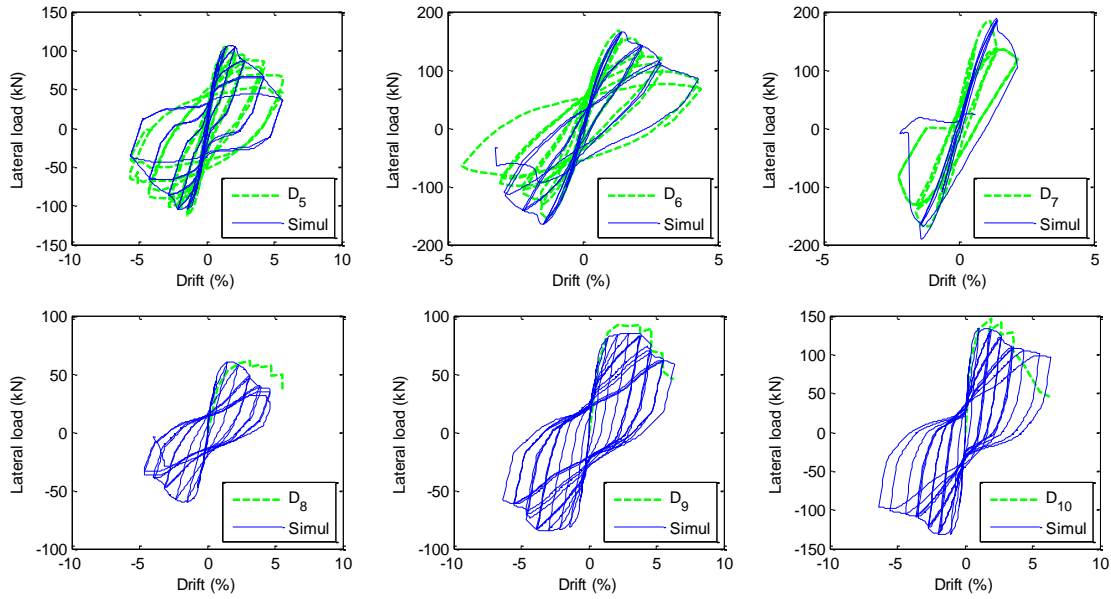
7.31

Figure 20. Comparison of the experimental lateral load-drift cyclic results with the cyclic response results obtained with the proposed modelling approach for specimens D5-D10.

For specimens of group D and in most of the specimens of groups A-C that involve a small number of cycles, the degradation of the cyclic response is essentially governed by the monotonic behaviour curve. Specimens A3, A4, B1-B6, C1, C7-C8 are clear examples of cases where the small number of cycles of the loading protocol lead to a cyclic response whose envelope follows the monotonic curve. On the other hand, introducing the effect of cyclic degradation was seen to be adequate, as observed in tests A3-A10, B7-B8 and C4-C6. Still, the cyclic degradation simulated for specimen C3 was unable to capture the effect of the reinforcing steel instability.

7.4.5 Implications of the observed results for selecting an adequate DP modelling approach
Even though the proposed modelling approach is able to capture the most important features of the experimental responses over a wide range of behaviour states, in particular close to collapse, the results that were obtained also highlight that an inconsistent selection of uniaxial material models and beam formulations are likely to generate unrealistic results. This aspect is particularly relevant when the softening response close to collapse needs to be simulated. Although similar discussions regarding this issue have been extensively highlighted in past research (e.g. see [4, 10-11]), a significant amount of studies still perform comparisons of seismic behaviour and measure seismic demand using an element formulation, an element mesh, a number of IPs and material models that appear to have been almost randomly selected. As a contribution to overcome this issue, Fig. 17 presents a flowchart that was developed to facilitate and ensure an adequate model selection.
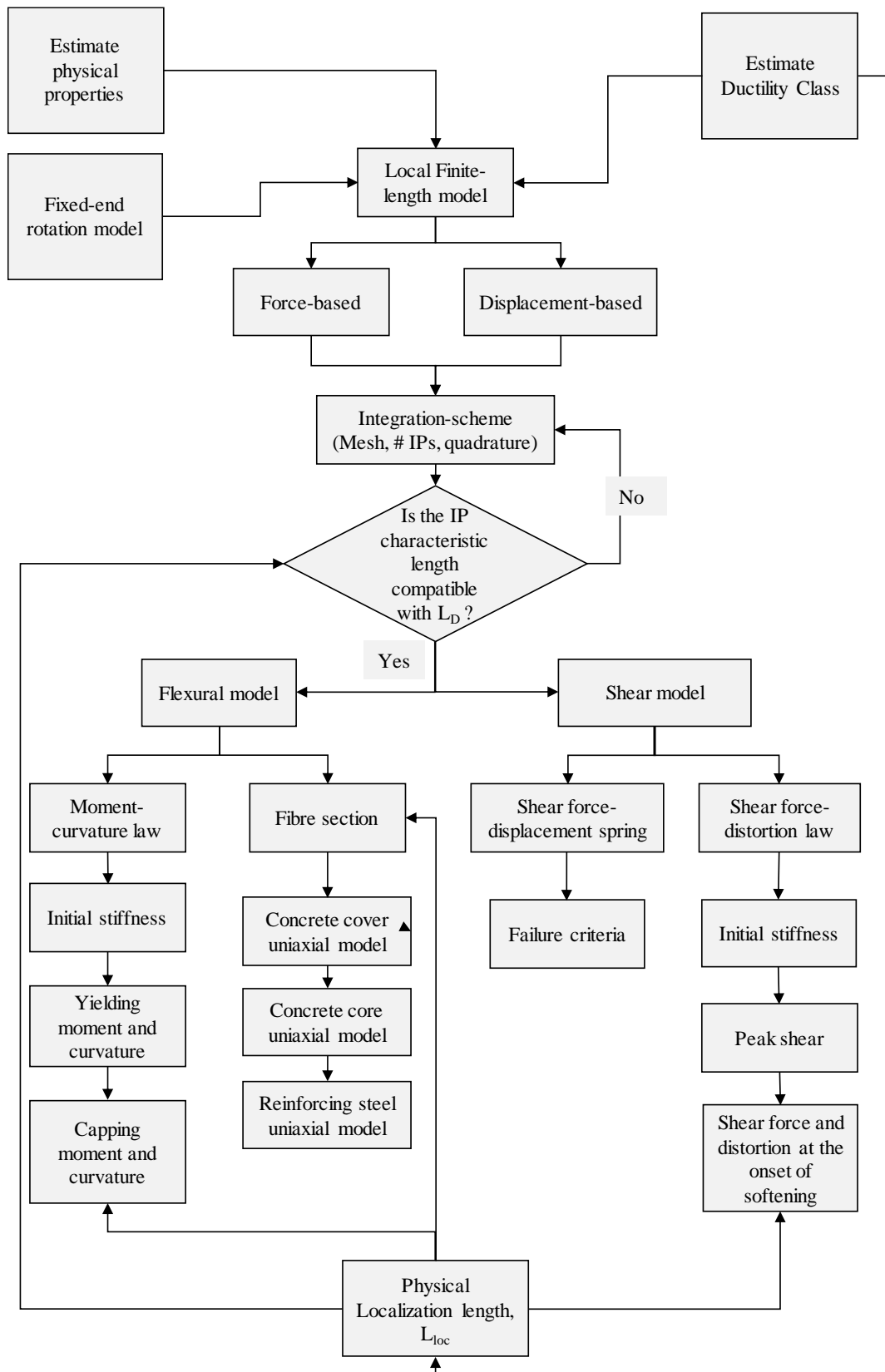
Figure 21. Flowchart for selecting and adequate local formulation for distributed inelasticity elements according to the ductility, the expected failure mode and the length of the damaged region defined in Chapter 6.

The flowchart aggregates the main properties of the modelling approach that was used herein, but it also allows the use of other formulations if the compatibility condition $L_c = L_D$ is verified. When behaviour is governed by flexural failure modes, the selected beam formulation should be either a FB formulation or an axially equilibrated displacement-based formulation [66]. An additional branch is added at the start of the flowchart based on Chapter 6 to assess the expected failure mode. When non-ductile failure governs the response, shear becomes dominant and the shear characteristic length proposed by Zimos *et al.* [67] should be adopted. Furthermore, fibre sections should include, at least, an uncoupled shear distortion-shear force law to ensure that shear failure before or close to flexural yielding is captured.

7.5 Conclusions

This study introduced a consistent local formulation modelling approach for the simulation of the post-peak response of RC beam-columns combining the relevant principles analysed in Chapter 6 regarding the localization of damage in RC frame elements, the regularization techniques available for force-based elements and the mechanics associated to hinge formation and rotation. The proposed modelling approach is a regularized local FB frame element and a modified fibre-based local plasticity model that generates equivalent strains and curvatures after softening of the uniaxial materials occur. The stress-strain curves of these materials were defined based on the rationale behind the expected failure mode of the component and include a regularization of the strains based on the size-dependent properties of the materials given the differences between the size of the specimen tested to evaluate the uniaxial material properties and the real size of the plastic hinge. The proposed modelling framework was developed using the models available in the software OpenSees and the performance of the modelling approach was analysed using a suite of 36 experimental tests.

The main findings of this study can be summarized as follows:

• The proposed approach successfully simulates the numerical strain localization in the presence of concrete and reinforcing steel softening in compression. The modelling approach is able to capture the combined effect of fixed-end rotations and of flexural deformations based on the length of the damaged region L_D that is observed in experimental tests and on the hinge mechanics related to nonlocal material deformations such as rebar necking and buckling and the formation and spalling of concrete wedges.

• The proposed framework is able to predict the in-cycle strength degradation of the response of RC beam-columns subjected to axial loads and cyclic lateral displacements with reasonable accuracy. The numerical examples shown in this study demonstrate that the global numerical response is in good agreement with the corresponding experimental response, which implies that

the chord rotations of structural elements defined based on the equivalent curvature and L_D are compatible with the plastic deformations of the element.

• The beam formulation that was adopted is the modified Hinge-Radau regularized FB finite element formulation proposed by Scott and Fenves [10] instead of using an arbitrary number of IPs and integration schemes as found in many studies. When using local formulations, and as opposed to recently proposed nonlocal theories [12-14], only adaptive (e.g. [20]) or regularized FB formulations [10] are able to always provide objective global deformations, i.e. chord rotations and member end deformations.

• The adopted regularized formulation considers a characteristic length associated with the damage accumulation due to the sliding of concrete wedges, the reinforcing steel lateral deformations and necking, increasing the rotation of a region between two sections where the EBH is approximately valid. Since the characteristic length accounts for the global rotation of the damaged region, the numerical results that were obtained exhibit a good agreement with the peak and post peak response of the experimental tests that were analysed. The empirical characteristic length that was used and its connection to the size-dependent material models leads to adequate results since the mechanisms contributing to the equivalent curvatures and the rotation of the hinge are captured by the equivalent stress-strain models.

• The results show that the numerical localization simulated with the proposed modelling approach is compatible with the damage localization found in experimental tests. The inconsistency of local response (curvatures), which are only valid in an average sense, is in agreement with the mechanical analysis made by Visintin *et al.* [27] where only the hinge rotations were defined as objective results. Furthermore, the physical effects that lead to the size-dependent uniaxial material models are captured by the averaging strategy that is performed for the hinge since the nonlocal effects are directly connected to the size of the region that develops these nonlocal effects and to the sequence of phenomena leading to the inelastic rotations (i.e. concrete diagonal cracks that develop before nonlocal steel effects may increase the characteristic length).

As an extension of the proposed study, a quantitative comparison of the proposed modelling approach with recent gradient-based frame element formulations should be performed in the future, in order to analyse how the mechanical rationale that was adopted herein can be incorporated within these beam theories. Furthermore, specimens with more earthquake-like cyclic load protocols and with time-history analysis should be assessed to verify the impact that undershooting and overshooting issues can have in the reliability of the proposed approach.

7.6 References

1. Berry MP, Eberhard MO, (2004). Performance modelling strategies for modern reinforced concrete bridge columns. Pacific Earthquake Engineering Research Center Report. University of California, Berkeley, USA.

2. Mitra N, (2008). Uncertainty in analytical structural response associated with high level modelling decisions. Proceedings of the 14th World Conference on Earthquake Engineering October 12-17, 2008, Beijing, China.

3. Heo Y, Kunnath SK, (2009). Sensitivity to constitutive modeling in fiber-based discretization of reinforced concrete members for performance-based seismic evaluation. Adv Struct Eng 12(1):37–51.

4. Calabrese A, Almeida JP, Pinho R, (2010). Numerical issues in distributed inelasticity modeling of RC frame elements for seismic analysis. Journal of Earthquake Engineering;14(S1):38-68.

5. Yazgan U, Dazio A, (2011). Simulating maximum and residual displacements of RC structures: II. Sensitivity. Earthquake Spectra; 27(4):1203-18

6. Huang X, Kwon O, (2015). Numerical Models of RC Elements and their Impacts on Seismic Performance Assessment. Earthquake Engineering and Structural Dynamics, 44(2):283-298.

7. Pugh JS, Lowes LN, Lehman DE, (2015). Nonlinear line-element modeling of flexural reinforced concrete walls. Engineering Structures; 104:174-92.

8. Sousa R, Almeida JP, Correia AA, Pinho R, (2018). Shake Table Blind Prediction Tests: Contributions for Improved Fiber-based Frame Modelling. Journal of Earthquake Engineering; 13:1-42.

9. Terzic V, Schoettler MJ, Restrepo JI, Mahin SA, (2015). Concrete column blind prediction contest 2010: outcomes and observations. PEER Report; 1:1-45.

10. Scott MH, Fenves GL, (2006). Plastic hinge integration methods for force-based beam–column elements. Journal of Structural Engineering; 132(2):244-52.

11. Li S, Zhai CH, Xie LL, (2012). Evaluation of displacement-based, force-based and plastic hinge elements for structural non-linear static analysis. Advances in Structural Engineering;15(3):477-88

12. Feng D, Ren X, Li J, (2015). Implicit gradient delocalization method for force-based frame element. Journal of Structural Engineering; 142(2):04015122.

13. Sideris P, Salehi M, (2016). A gradient inelastic flexibility-based frame element formulation. Journal of Engineering Mechanics; 142(7):04016039.

14. Kenawy M, Kunnath S, Kolwankar S, Kanvinde A, (2018). Fiber-based nonlocal formulation for simulating softening in reinforced concrete beam-columns. Journal of Structural Engineering; 144(12):04018217.

15. Valipour HR, Foster SJ, (2009). Nonlocal damage formulation for a flexibility-based frame element. Journal of structural engineering; 135(10):1213-21.

16. Coleman J, Spacone E, (2001). Localization issues in force-based frame elements. Journal of Structural Engineering; 127(11):1257-65.

17. Addessi D, Ciampi V, (2007). A regularized force-based beam element with a damage–plastic section constitutive law. International Journal for Numerical Methods in Engineering; 70(5):610-29.

18. Scott MH, Hamutçuoğlu OM, (2008). Numerically consistent regularization of force-based frame elements. International journal for numerical methods in engineering; 76(10):1612-31.

19. Lee CL, Filippou FC, (2009). Efficient beam-column element with variable inelastic end zones. Journal of structural engineering; 135(11):1310-9.

20. Almeida JP, Das S, Pinho R, (2012). Adaptive force-based frame element for regularized softening response. Computers and Structures;102:1-3.

21. Ribeiro FL, Neves LA, Barbosa AR, (2017). Implementation and calibration of finite-length plastic hinge elements for use in seismic structural collapse analysis. Journal of Earthquake Engineering;21(8):1197-219.

22. Visintin P, Oehlers DJ, Haskett M, Wu C, (2012). Mechanics-based hinge analysis for reinforced concrete columns. Journal of Structural Engineering;139(11):1973-80

23. Paret T, Shuck A, (2018). Performance-Based Design Procedures: Beware Uncharted Waters. Proceedings of the 16th European Conference on Earthquake Engineering, Thessaloniki, Greece.

24. Head M, Dennis S, Muthukumar S, Nielson B, Mackie K, (2014). Nonlinear analysis in modern earthquake engineering practice. ASCE Structure Magazine:16–20.

25. Goodnight JC, Kowalsky MJ, Nau JM, (2016). Modified plastic-hinge method for circular RC bridge columns. Journal of Structural Engineering; 142(11): 04016103.

26. Chen Y, Visintin P, Oehlers DJ, (2015). Extracting Size-Dependent Stress–Strain Relationships from FRP-Confined Concrete Cylinders for Varying Diameters and Heights. Journal of Materials in Civil Engineering; 28.5: 04015182.

27. Visintin P, Chen Y, Oehlers DJ, (2015) Size dependent axial and lateral stress strain relationships for actively confined concrete. Advances in Structural Engineering; 18(1):1-20.

28. Teng J, Huang YL, Lam L, Ye LP, (2007). Theoretical model for fiber-reinforced polymer-confined concrete. Journal of composites for construction; 11(2):201-10.

29. Pantazopoulou SJ, (1998). Detailing for reinforcement stability in RC members. Journal of Structural Engineering; 124(6):623-32

30. Bae S, Mieses AM, Bayrak O, (2005). Inelastic buckling of reinforcing bars. Journal of Structural Engineering; 131(2):314-21.

31. Mander JB, Panthaki FD, Kasalanati A, (1994). Low-cycle fatigue behavior of reinforcing steel. Journal of Materials in Civil Engineering; 6(4):453-68.

32. Dhakal RP, Maekawa K, (2002). Reinforcement stability and fracture of cover concrete in reinforced concrete members. Journal of Structural Engineering; 128(10):1253-62.

33. Correia AA, (2011). A pile-head macro-element approach to seismic design of monoshaft-supported bridges. Ph.D. Dissertation, Istituto Universitario di Studi Superiori, University of Pavia, Pavia, Italy.

34. Panagiotakos TB, Fardis MN, (2001). Deformations of reinforced concrete members at yielding and ultimate. Structural Journal; 98(2):135-48.

35. Karthik MM, Mander JB, (2010). Stress-block parameters for unconfined and confined concrete based on a unified stress-strain model. Journal of Structural Engineering; 137(2):270-3.

36. Collins MP, Mitchell D, (1994). Prestressed concrete structures, Prentice-Hall, Englewood Cliffs, NJ, USA.

37. Markeset G, Hillerborg A, (1995). Softening of concrete in compression—localization and size effects. Cement and Concrete Research; 25(4):702-8.

38. Samani AK, Attard MM, (2012). A stress–strain model for uniaxial and confined concrete under compression. Engineering Structures; 41:335-49.

39. Chen Y, Visintin P, Oehlers DJ, Alengaram UJ, (2013). Size-dependent stress-strain model for unconfined concrete. Journal of Structural Engineering; 140(4):04013088.

40. Mander JB, Priestley MJ, Park R, (1988). Theoretical stress-strain model for confined concrete. Journal of structural engineering; 114(8):1804-26.

41. Scott BD, Park R, Priestley MJN, (1982). Stress-strain behaviour of concrete confined by overlapping hoops at low and high strain rates. American Concrete Institute; 79(1): 13-27.

42. Binici B, (2005). An analytical model for stress–strain behavior of confined concrete. Engineering structures; 27(7):1040-51.

43. Akiyama M, Suzuki M, Frangopol DM, (2010). Stress-Averaged Strain Model for Confined High-Strength Concrete. ACI Structural Journal; 107(2).

44. Wei YY, Wu YF, (2012). Unified stress–strain model of concrete for FRP-confined columns. Construction and Building Materials; 26(1):381-92.

45. Tung ND, Tue NV, (2016). A fracture mechanics-based approach to modeling the confinement effect in reinforced concrete columns. Construction and Building Materials; 102:893-903.

46. Li B, Park R, Tanaka H, (2001). Stress-strain behavior of high-strength concrete confined by ultra-high-and normal-strength transverse reinforcements. ACI Structural Journal; 98(3): 395-406.

47. Dodd LL, Restrepo-Posada JI, (1995). Model for predicting cyclic behavior of reinforcing steel. Journal of structural engineering;121(3):433-45.

48. Pipa M, (1994). Ductility of reinforced concrete elements subjected to cyclic and reverse-cyclic loads: influence of the mechanical properties of reinforcing bars (in Portuguese). PhD Dissertation. Technical University of Lisbon, Lisbon, Portugal.

49. CEN, (2005). EN 10080: Steel for the reinforcement of concrete, weldable, ribbed reinforcing steel. comité européen de normalisation, Brussels, Belgium.

50. Kolwankar S, Kanvinde A, Kenawy M, Kunnath S, (2017). Uniaxial Nonlocal Formulation for Geometric Nonlinearity–Induced Necking and Buckling Localization in a Steel Bar. Journal of Structural Engineering; 143(9):04017091.

51. Dhakal R., Maekawa K, (2002). Path-dependent cyclic stress–strain relationship of reinforcing bar including buckling. Engineering Structures 24:1383–1396.

52. Peruš, I, Fajfar. P. Biskinis D. et al. (2013). Enrichment of the distributed database with existing data. Background report accompanying SERIES project Deliverable D2.7. Version: 1.2.

53. Rodrigues H, Arêde A, Varum H, Costa AG, (2013) Experimental evaluation or rectangular reinforced concrete column behaviour under biaxial cyclic loading. Earthquake Eng struct Dyn 42:236–259.

54. Saatcioglu M, Grira M, (1999) Confinement of reinforced concrete columns with welded reinforced grids. ACI Structural Journal; 96(1):29-39.

55. Mo YL, Wang SJ, (2000) Seismic behavior of RC columns with various tie configurations. Journal of Structural Engineering; 126(10):1122-30

56. Soesianawati MT, (1986), Limited ductility design of reinforced concrete columns, Research Report 86-10, Department of Civil Engineering, University of Canterbury, Christchurch, New Zealand

57. Tanaka H, Park R, (1990). Effect of lateral confining reinforcement on the ductile behavior of reinforced concrete columns. Rep. 90-2, Dept. of Civil Engineering, Univ. of Canterbury, Christchurch, New Zealand.

58. Tsuno K, Park R, (2004). Experimental study of reinforced concrete bridge piers subjected to bi-directional quasi-static loading. Struct Eng Struct JSCE 21(1):11s–26s

59. Bae S, Bayrak O, (2008). Plastic hinge length of reinforced concrete columns. ACI Structural Journal; 105(3):290.

60. De Stefano A, Sabia D, (1988). Tests up to Failure on High Strength Concrete elements subjected to Bending and Axial Load, Special Discussion Session: Design Aspects of High Strength Concrete", Dubrovnik, Croatia.

61. Zahn FA, Park R, Priestley MJN, (1986). Design of Reinforced Bridge Columns for Strength and Ductility, Report 86-7, Department of Civil Engineering, University of Canterbury, Christchurch, New Zealand.

62. Paultre P, Légeron F, (2000). Behavior of high-strength concrete columns under cyclic flexure and constant axial load. ACI Structural Journal, 97(4): 591–601.

63. Di Ludovico M, Verderame GM, Prota A, Manfredi G, Cosenza E, (2013). Cyclic Behavior of Nonconforming Full-Scale RC Columns. Journal of Structural Engineering; 140(5).

64. McKenna F, Scott MH, Fenves GL, (2009). Nonlinear finite-element analysis software architecture using object composition. Journal of Computing in Civil Engineering; 24(1):95-107.

65. Kashani M, Lowes L, Crewe A, Alexander N, (2016). Nonlinear fibre element modelling of RC bridge piers considering inelastic buckling of reinforcement. Engineering Structures; 116:163-177.

66. Tarquini D, Almeida J, Beyer K, (2017). Axially equilibrated displacement-based beam element for simulating the cyclic inelastic behaviour of RC members. Earthquake Engineering and Structural Dynamics; 46(9):1471-1492

67. Zimos DK, Mergos PE, Kappos AJ, (2018). Modelling of R/C members accounting for shear failure localisation: Finite element model and verification. Earthquake Engineering and Structural Dynamics;47:1631–1650.

68. Haselton CB, Liel AB, Deirlein GG, (2009). Simulating structural collapse due to earthquakes: model idealization, model calibration, and numerical solution algorithms. Proceedings of COMPDYN 2009: ECCOMAS thematic conference on computational methods in structural dynamics and earthquake engineering, Rhodes, Greece.

[This page was intentionally left blank]

Chapter 8

Development and calibration of compatibility factors between nonlinear analysis methods and their impact in the seismic safety assessment of existing RC frame buildings

Scope and objectives

The safety assessment framework developed in Chapter 5 was based on the definition of a safety factor SF_R for the capacity of RC frame components that must be considered in the context of component-based limit state verifications. The focus of that approach was on developing a strategy that explicitly incorporates the effect of the uncertainty associated with lack of knowledge about the structural components. In this context, an alternative format for the limit state conditions was introduced that considers a lower quantile of the capacity of each structural component based on the existing uncertainties and the knowledge gathered during the assessment. The empirical models that were adopted to define the shear capacity and the chord rotation capacity of frame components correspond to specific points across the behaviour ranges, and SF_R reflects the probability of having a certain damage pattern at a given performance level. To ensure the consistency of this safety assessment framework, structural demand must be defined by a numerical model that is compatible with the quantification approach that was adopted for the selected performance levels. This means the safety verification would only be fully valid when using the same modelling approach to compute demand. This chapter addresses this issue in more detail and defines a set of compatibility factors that modify the demand obtained with a certain modelling approach to make it compatible with the one underlying the semi-probabilistic limit state conditions defined in Chapter 5.

8.1 Introduction

According to current standard-based methods, the seismic safety assessment of existing buildings involves the comparison of component-level seismic demand values with the corresponding capacities. These comparisons are established for different damage limit states (LSs) or performance levels, and refer to behaviour states of the structural components that can be associated with a given set of repair actions. Component demands are determined by creating a numerical model of the building and performing a set of static or dynamic analyses involving earthquake-like loading. The use of nonlinear methods of analysis is suggested in these standard-based seismic safety evaluations, given that, in many cases, existing buildings may have not been designed to sustain severe ground motions in the elastic range and will therefore exhibit levels of inelastic demand requiring more advanced approaches to be estimated. From these analyses, the building-level demand (roof drifts, inter-storey drifts and floor accelerations) and the component-level demand (chord rotations, shear and axial forces in beams and columns or joint deformations and forces) that are obtained can be used as engineering demand parameters, i.e. metrics representing the damage state or performance level of the overall system for a given level of the seismic action.

Usually, standard-based methods addressing the seismic safety assessment of existing RC frame buildings focus on evaluating the structural response of individual components. Therefore, LS conditions are set for each structural component and a chain rule where the weakest link of the chain defines the critical state of the structure is usually adopted. Hence, existing standards such as Part 3 of Eurocode 8 (EC8/3) [1] and ASCE 41-13 [2] define the structural capacity at the component level, indicating specific ways of estimating capacity according to the type of component. These standards provide empirical and semi-empirical models defining the capacity in terms of chord rotation (to evaluate the flexural/ductile capacity of the component) and shear demand (to verify the safety of the component against brittle failure modes).

A new safety assessment framework was proposed in Chapter 5 that combines the strengths of ASCE 41-13 and EC8/3 with state of the art models and survey strategies. One particular feature of the proposed framework is that it considers a direct compatibility between the numerical modelling approach adopted to analyse the building response and the uncertainty about the LS. ASCE 41-13 considers the same moment-rotation model to analyse demand and to quantify the rotation capacity of the component, which implies that the same type of modelling uncertainty is involved on the side of capacity when formulating the LS condition. Consequently, when the numerical modelling approach that is used to analyse demand is based on the empirical models that are used to quantify capacity, the modelling uncertainty is implicitly accounted for in the LS conditions. Therefore, using a different frame modelling approach (e.g. distributed inelasticity models) will lead to an inconsistent treatment of the modelling uncertainty, since the referred uncertainty propagation assumption is lost. A new formulation is therefore necessary to account

for differences between the demand quantified using a component model that is different from the reference one (i.e. the model selected to define the flexural capacity of components) whose uncertainty is fully known. In light of this, the present chapter establishes a procedure defining compatibility factors that modify the demand obtained with a certain modelling approach to make it compatible with the reference one.

8.2 Proposed limit-state assessment framework including modelling compatibility factors

8.2.1 Definition of a single strategy to define seismic demand and capacity

The safety assessment format defined by current seismic safety assessment standards that analyses the compliance with a certain LS was examined in Chapter 5. A revised framework was then proposed based on the use of a standard model to define both the demand and the capacity of RC components. This framework considered two moment-rotation (M-θ) models characterizing the hinge response: one for the case where the reinforcement of structural component has smooth bars and one for the case where it has ribbed bars. Furthermore, it was established that, given the properties of components with smooth bars and the features of the empirical models developed by Haselton *et al.* [3], brittle failure modes (defined by the maximum shear force V_n) could be analysed independently of the flexural modes. It is therefore assumed that the adopted M-θ envelopes and the corresponding LSs can implicitly account for flexure-shear failure modes. The model developed by Haselton *et al.* [3] is based on the results of a database that includes 220 tests of RC components that failed in flexure and 35 tests of RC components that failed in a combined flexure-shear mode. Thus, the parametrization proposed in [3] reflects the strength degradation resulting from multiple effects such as fixed-end rotations due to bar slip, the degradation associated with ductile shear failure and the degradation due to material degradation in flexure. Figure 1 shows the backbone of the analytical model and the corresponding LSs adopted in Chapter 5 for the case where the reinforcement of structural component has ribbed bars.
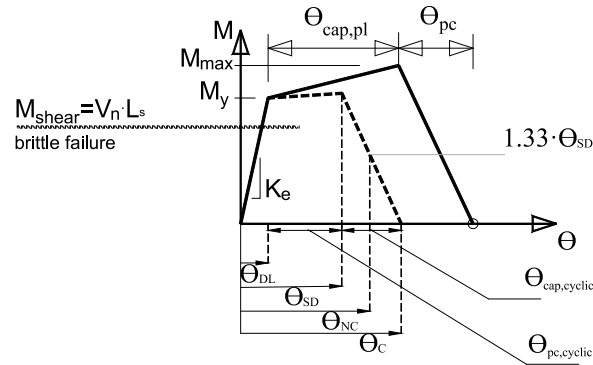

Figure 1. Backbone of the models proposed in Chapter 5 for demand evaluation and LS verification.

The basis for the LS verification is an empirical model that simulates the M-θ envelopes of RC beam-column components based on 6 key parameters: the yielding moment M_y, the effective initial rotation stiffness K_e, computed using the effective stiffness defined as the secant stiffness to 40% of the yield moment, the hardening ratio M_{max}/M_y, the capping plastic rotation capacity $\theta_{cap,pl}$, the post-capping rotation capacity, θ_{pc}, and the cyclic degradation factor, λ. The λ factor is able to account for the cyclic degradation based on the cyclic response enforced by ground motions. In order to include this effect in the capacity, it was assumed in Chapter 5 that the limits proposed by Haselton *et al.* [3] for the equivalent cyclic envelope ($\theta_{cap,pl,cyclic}$ $\theta_{pc,pl,cyclic}$) based on PEER-ATC 72 [4] could be adopted to establish the rotation capacity of beams and columns. The referred rotation capacity limits (for Damage Limitation (DL), Significant Damage (SD), Near Collapse (NC) and Collapse (C) LSs) were therefore defined as portions of the reference M-θ envelope model that is used to quantify the seismic demand, as shown in Fig. 1.

8.2.2 Accounting for the demand uncertainty in the LS assessment framework

Based on the definition of demand and capacity in RC frame components highlighted in the previous section, a consistent safety assessment framework can be established using the following condition:

$$R \geq D, \tag{1}$$

in which D is the demand and R is the capacity of the component for a given LS. Since the formulae used to establish the numerical model and the LS conditions have an empirical basis, there is uncertainty in the component M-θ envelope model. This uncertainty can be indirectly accounted for by defining a factored capacity, an estimate that is lower than the corresponding median. The factored capacity must then be compared with the demand:

$$\frac{\hat{R}}{SF_R} \geq \hat{D}, \tag{2}$$

where $\hat{D}$ is the median value of the demand (standard-based methods often indicate that an estimate of the central value of the demand can be used to assess seismic safety), $\hat{R}$ is the median value of the capacity, and SF_R is a safety factor that reflects the total uncertainty about the model defining $\hat{R}$. Considering the modelling uncertainty by including SF_R implicitly assumes the record-to-record variability of the demand and the uncertainty about the damage state of the component are independent. Under this condition, the median value of the demand is an unbiased estimator of the expected structural response, but its uncertainty depends on the number of ground

motions adopted in the analysis. As a result, a robust estimate for $\hat{D}$ must be determined considering the distribution of the sampling median. By assuming that demand follows a lognormal distribution and the inherent relation between the mean of the logarithms and the median, a confidence interval for the median can be defined following principles similar to those adopted by Bradley [5]. Hence (see Ang and Tang [6], p.264):

$$\hat{D} = \exp\left(\bar{x}_{\ln D} \pm t_{1-\alpha/2, N_{gm}-1} \cdot \frac{s_{\ln D}}{\sqrt{N_{gm}}} \right), \tag{3}$$

where $\bar{x}_{\ln D}$ and $s_{\ln D}$ are the sample mean and sample standard deviation of $\ln D$, respectively, $t_{1-\alpha/2, N_{gm}-1}$ is the $1-\alpha/2$ quantile of the t-distribution with $N_{gm}-1$ degrees of freedom, considering that α is the selected confidence level adopted and N_{gm} is the number of ground motion records adopted in the analysis. By considering that only the upper bound of the interval is of interest within the context of the safety assessment, Eq. (3) can be re-written as:

$$\hat{D} \leq \exp\left(\bar{x}_{\ln D} + t_{1-\alpha/2, N_{gm}-1} \cdot \frac{s_{\ln D}}{\sqrt{N_{gm}}} \right), \tag{4}$$

which, by considering the critical case that maximizes the estimate for $\hat{D}$, yields:

$$\hat{D} = \exp\left(\bar{x}_{\ln D} \right) \cdot \exp\left(t_{1-\alpha/2, N_{gm}-1} \cdot \frac{s_{\ln D}}{\sqrt{N_{gm}}} \right), \tag{5}$$

Hence, a revised version of Eq. (2) can be established by:

$$\frac{\hat{R}}{SF_R} \geq \exp\left(\bar{x}_{\ln D} \right) \cdot SF_D, \tag{6}$$

where SF_D is an uncertainty factor given by

$$SF_D = \exp\left(t_{1-\alpha/2, N_{gm}-1} \cdot \frac{s_{\ln D}}{\sqrt{N_{gm}}} \right), \tag{7}$$

8.5

8.2.3 Compatibility factors for alternative modelling strategies or analysis methods

As addressed before, the LS conditions defined in Chapter 5 are fully connected to the modelling approach that is adopted. This fact implies that full consistency between demand and capacity is only ensured when they are both quantified using the same empirical model for chord rotation. Furthermore, the ability of this empirical model to implicitly account for flexure-shear failure, and the independence between pure shear and flexure failure modes needs to be assumed for the verification of limit states involving the shear force. Consequently, using an alternative component modelling approach will bias the safety assessment since the previously defined factor SF_R will be unable to reflect the modelling uncertainty in this case. As a result, Eqs. (4)-(7) must be revised to include a factor accounting for the inconsistency introduced by the use of a different numerical modelling approach. This can be done by considering that the seismic demand D_{ref} obtained with the reference model can be expressed as a function of the demand quantified using an alternative modelling strategy (D_{alt}) as:

$$D_{ref} = D_{alt} \cdot \varepsilon_{Co}, \tag{8}$$

where ε_{Co} is the compatibility factor defined by the ratio between D_{ref} and D_{alt}. Since ε_{Co} can be defined as the distribution of the residuals of a linear regression in the logarithmic space between D_{ref} and D_{alt}, its distribution is assumed to be lognormal. Hence, since the distribution of the demand D_{alt} obtained with N_{gm} ground motion records is also assumed to be lognormal with logarithmic mean and standard deviation $\mu_{\ln D_{alt}}$ and $\sigma_{\ln D_{alt}}$, respectively, $D_{alt} \cdot \varepsilon_{Co}$ is also lognormal with logarithmic mean:

$$\mu_{\ln D_{alt} \cdot \varepsilon_{Co}} = \mu_{\ln D_{alt}} + \mu_{\ln \varepsilon_{Co}}, \tag{9}$$

and logarithmic standard deviation:

$$\beta_{\ln D_{alt} \cdot \varepsilon_{Co}} = \sqrt{\sigma_{\ln D_{alt}}^2 + \sigma_{\ln \varepsilon_{Co}}^2 + 2 \cdot \rho_{D_{alt} \cdot \varepsilon_{Co}} \cdot \sigma_{\ln D_{alt}} \cdot \sigma_{\ln \varepsilon_{Co}}}, \tag{10}$$

where $\rho_{\ln D_{alt} \cdot \ln \varepsilon_{Co}}$ is the coefficient of correlation between the $\ln D_{alt}$ and $\ln \varepsilon_{co}$. Hence, the uncertainty factor must be re-defined to account for the use of alternate modelling approaches as:

$$SF_D = \exp\left(t_{1-\alpha/2, N_{gm}-1} \cdot \frac{\sqrt{s_{\ln D_{alt}}^2 + \sigma_{\ln \varepsilon_{Co}}^2 + 2 \cdot \rho_{D_{alt} \cdot \varepsilon_{Co}} \cdot s_{\ln D_{alt}} \cdot \sigma_{\ln \varepsilon_{Co}}}}{\sqrt{N_{gm}}} \right). \tag{11}$$

The overall limit state condition presented in Eq. (6) can be finally written as:

$$\frac{\hat{R}}{SF_R} \geq \exp\left(\mu_{\ln \varepsilon_{Co}}\right) \cdot \exp\left(\bar{x}_{\ln D}\right) \cdot \exp\left(t_{1-\alpha/2,N_{gm}-1} \cdot \frac{\sqrt{s_{\ln D_{alt}}^2 + \sigma_{\ln \varepsilon_{Co}}^2 + 2 \cdot \rho_{D_{alt} \cdot \varepsilon_{Co}} \cdot s_{\ln D_{alt}} \cdot \sigma_{\ln \varepsilon_{Co}}}}{\sqrt{N_{gm}}}\right), \quad (12)$$

which, by assuming that $\ln D_{alt}$ and $\ln \varepsilon_{co}$ are independent (i.e. $\rho_{\ln D_{alt} \cdot \ln \varepsilon_{Co}} = 0$) simplifies to:

$$\frac{\hat{R}}{SF_R} \geq \exp\left(\mu_{\ln \varepsilon_{Co}}\right) \cdot \exp\left(\bar{x}_{\ln D}\right) \cdot \exp\left(t_{1-\alpha/2,N_{gm}-1} \cdot \frac{\sqrt{s_{\ln D_{alt}}^2 + \sigma_{\ln \varepsilon_{Co}}^2}}{\sqrt{N_{gm}}}\right). \quad (13)$$

It can be seen that the Eq. (13) involves the real values of $\mu_{\ln \varepsilon_{Co}}$ and $\sigma_{\ln \varepsilon_{Co}}$ since average values for these statistical parameters can be established based on calibration procedures, particularly when assuming independence between $\ln D_{alt}$ and $\ln \varepsilon_{co}$. Finally, when the reference modelling approach is used, $\mu_{\ln \varepsilon_{Co}}$ is 1.0 and $\sigma_{\ln \varepsilon_{Co}}$ is equal to 0.0, since it is assumed that SF_R is able to capture the uncertainty in the definition of the LS condition.

To illustrate the calibration of $\mu_{\ln \varepsilon_{Co}}$ and $\sigma_{\ln \varepsilon_{Co}}$ for different types of analysis methods, distributed inelasticity models (DP) were adopted herein as the alternative modelling approach, given their widespread use in earthquake engineering. When using these models, chord rotations are not directly obtained in the analysis and an additional set of steps is required to quantify their values, as summarized in the following section.

8.3 Quantification of chord rotation in RC frames

8.3.1 Quantification of chord rotation using the reference modelling approach

The reference modelling approach discussed in Chapter 5 and Section 8.2 is a concentrated plasticity (CP) component model that enables a direct quantification of the rotations since they are explicitly considered by the numerical model. CP models are characterized by an assemblage in series of two discrete zero-length springs, located at the ends of the component, with an interior elastic element between the springs. The corresponding flexibility matrix of the component is therefore defined by:

$$\mathbf{f}_{comp} = \mathbf{f}_{spring,1} + \mathbf{f}_{interior} + \mathbf{f}_{spring,2}, \quad (14)$$

where $\mathbf{f}_{comp}$ is the component flexibility matrix, i.e. the inverse of the stiffness matrix of the component, $\mathbf{f}_{interior}$ is the flexibility of the interior linear elastic element and $\mathbf{f}_{spring,1}$ and $\mathbf{f}_{spring,2}$, are the flexibility terms introduced by the springs located at the ends of the component, at nodes 1 and 2. The spring flexibility term includes a set of deformations and mechanisms, namely the deformations related to flexural deformations, shear deformations and interface effects such as bar pull-out (which lead to rigid body rotations [7]). As illustrated by Zimos *et al.* [8], the global flexibility matrix $\mathbf{f}_{comp}$ can be written as:

$$\mathbf{f}_{comp} = \mathbf{f}_{shear} + \mathbf{f}_{flexure} + \mathbf{f}_{slip,tens} + \mathbf{f}_{anchorage,slip} \,, \tag{15}$$

where $\mathbf{f}_{shear}$, $\mathbf{f}_{flexure}$, $\mathbf{f}_{slip,tens}$ and $\mathbf{f}_{anchorage,slip}$ represent components of the flexibility assigned to shear deformations, flexural deformations, deformations that are associated with slippage of the bars in cracks developing along the element shear span and anchorage-slip deformations, respectively.

The quantification of chord rotations θ at nodes 1 and 2 located at the ends of the component is paramount in earthquake engineering due to the typical localization of damage in these regions. The chord rotation at a given point A of a structural component can be defined as the angle between the chord connecting the centroid of A and a second point B located at a given distance with respect to A and the tangent to the component axis at point A [9]. Accordingly, if the exact integral method (EIM) is used and the flexibility of the component is obtained by combining the contributions of rotations due to flexural, shear and slip deformations (assumed to be uncoupled), the chord rotations at nodes 1 and 2 located at the ends of the component can be obtained by:

$$\theta_1 = \int_0^{x_{L_s}} \chi(x) \cdot \left(\frac{x_{L_s} - x}{x_{L_s}} \right) dx + \int_0^{x_{L_s}} \gamma(x) \cdot \left(\frac{x_{L_s} - x}{x_{L_s}} \right) dx + \theta_{slip,tens,0-x_{L_s}} + \theta_{anchorage,slip,1} \,, \tag{16}$$

$$\theta_2 = \int_{x_{L_s}}^{L} \chi(x) \cdot \left(\frac{x_{L_s} - x}{L - x_{L_s}} \right) dx + \int_{x_{L_s}}^{L} \gamma(x) \cdot \left(\frac{x_{L_s} - x}{L - x_{L_s}} \right) dx + \theta_{slip,tens,x_{L_s}-L} + \theta_{anchorage,slip,2} \,, \tag{17}$$

where x_{L_s} is the abscissa x of the point of contra-flexure, which is 0 at node 1 and L at node 2, $\chi(x)$ is the curvature of the section located at the abscissa x, $\gamma(x)$ is the shear distortion of the section located at the abscissa x due to a shear force $V(x)$ associated to moment $M(x)$, $\theta_{slip,tens}$ is the rotation associated to slip deformations in flexural cracks along the shear span x_{L_s}, $\theta_{anchorage}$ is the rotation associated to strain-penetration effects and bond-slip issues at the interface between

the component and beam-column joints or footings, and L is the length of the component. By considering the global flexibility matrix from Eq. (15), the chord rotations θ_1 and θ_2 can be defined by [8]:

$$\begin{bmatrix} \theta_1 \\ \theta_2 \end{bmatrix} = \mathbf{f}_{component} \cdot \begin{bmatrix} M_1 \\ M_2 \end{bmatrix}, \tag{18}$$

where M_1 and M_2 are the bending moments at the abscissas x_1 and x_2 of the length of the structural component. From the analysis of Eqs. (16)-(17), three types of component behaviour can be distinguished. In flexure-governed components, the deformations defined by $\chi(x)$ can be used to quantify the chord rotations. On the other hand, when there is a combined flexure-shear behaviour, the chord rotations are a consequence of the combined effect of residual deformations caused by the flexural inelastic deformations and of the shear distortions along the element. Finally, when a pure-shear failure is observed, curvatures are within the elastic range since the element has not yielded yet and, consequently, chord rotations can be represented mainly by the measured inelastic shear distortions. In CP models, all these mechanisms are lumped into springs located at nodes 1 and 2. Therefore, the rotations obtained from these springs can be used directly as estimates for the chord rotations.

8.3.2 Quantification of chord rotations using DP models

Analytical models for the quantification of chord rotations involve multiple levels of approximation, pre- and post-processing, and also involve different assumptions regarding the expected behaviour of the component. Some alternatives also consider springs in order to reflect rigid body movements such as those related with fixed-end rotations ($\mathbf{f}_{anchorage,slip}$), which are not part of the internal equilibrium of the component when considering distributed inelasticity (DP) models. Similar considerations regarding this assumption have been made by Zhao and Sritharan [10], Goodnight *et al.* [11], Mergos and Kappos [12], Zimos *et al* [8]; Megalooikonomou *et al.* [13].

Conversely to CP models, quantifying chord rotations in DP models requires post-processing, since global deformations such as inter-storey drifts, node displacements and chord rotations are determined based on section-level demand. Typically, the formulation of DP models is based on the response of several sections and the component flexibility is computed as:

$$\mathbf{f}_{member} = \int_L \mathbf{b}(x)^T \cdot \mathbf{f}_{sec}(x) \cdot \mathbf{b}(x) dx, \tag{19}$$

where $\mathbf{b}(x)$ is the interpolation matrix function and $\mathbf{f}_{\text{sec}}$ is the flexibility of a given section. Fibre models are generally considered in DP models to establish the interaction between moments and axial forces at the section level. Alternatively, these internal forces can be assumed to be uncoupled and phenomenological moment-curvature laws have to be adopted in this case. With respect to the ability to account for shear failure in DP modelling approaches, two alternatives are usually considered. On the one hand, some studies (e.g. see [14-16]) proposed modifications to include the effect of shear deformations into the formulation of DP models involving fibre sections. These approaches normally adopt triaxial material constitutive laws for concrete which require considerable larger computational costs. On the other hand, other studies (e.g. see [17] considered a shear-distortion (V-γ) law that is uncoupled at the section level from the axial and bending behaviour. Still, in this approach, moments and shear forces are coupled at component level through the verification of equilibrium conditions [17].

DP models can have multiple numerical formulations and these can then lead to significantly different chord rotation estimates. These formulations can be generally divided into displacement-based (DB), force-based (FB) and mixed formulations, but earthquake engineering practice uses mostly DB and FB formulations in nonlinear seismic analyses. Both DB and FB models are known to exhibit considerably different accuracy levels, depending on weather strain hardening or strain-softening responses are involved.

In components models using FB formulations, chord-rotations are calculated by solving Eqs. (16) and (17) using the numerical integration schemes that are part the DP model. In general terms, the numerical solution of the integrals in Eqs (16)-(17) can be written as a function of the number of integration points (*IP*s) and based on a quadrature rule. Considering U as the vector of nodal displacements at nodes 1 and 2, it can be written as:

$$U = \int_0^L N_Q^T(x) \cdot e(x) dx \approx \sum_{IP=1}^{nIP} w_{IP} \cdot L \cdot N_Q^T(x_{IP}) \cdot e(x_{IP}), \qquad (20)$$

where $N_Q(x)$ is an interpolation function, $e(x)$ is the deformation vector of section x, w_{IP} and x_{IP} are the weight and position of the integration point IP, respectively, and nIP is the number of integration points in one component. The term $w_{IP} \cdot L$ corresponds to the tributary length L_{IP} associated with each IP. Chapter 7 discussed the issue of localization in DP formulations and proposed a generic strategy for model selection. The modelling approach defined in Chapter 7 involves a physical and mechanical rationale that considers size-dependent experimental data to enhance the consistency of the model, assuming that L_{IP} is the length over which the nonlocal material response and the nonlocal deformations are developed.

By assuming that $L_{IP,1}$ and $L_{IP,2}$ refer to the characteristic lengths (i.e. lengths where the inelastic rotations are concentrated) associated with the IPs located at or near nodes 1 and 2 associated with the critical mechanism governing the component response (flexural, flexural-shear or pure shear failure), Eqs. (16) and (17) can be re-defined as:

$$\theta_1 = \chi^{soft}\left(x_{IP,1}\right) \cdot L_{IP,1} + \gamma^{soft}\left(x_{IP,1}\right) \cdot L_{IP,1} + \theta_{slip,tens,0-x_{L_s}} + \theta_{anchorage,slip,1}, \tag{21}$$

$$\theta_2 = \chi^{soft}\left(x_{IP,2}\right) \cdot L_{IP,2} + \gamma^{soft}\left(x_{IP,2}\right) \cdot L_{IP,2} + \theta_{slip,tens,x_{L_s}-L} + \theta_{anchorage,slip,2}, \tag{22}$$

where $\chi^{soft}\left(x_{IP,i}\right)$ and $\gamma^{soft}\left(x_{IP,i}\right)$ are the curvature and shear distortion of the section at $x_{IP,i}$. DPs are often associated with the use of fibre sections, which enable bending moments axial forces to be coupled. Shear deformations, however, are usually considered as uncoupled from the flexural/axial counterparts. Nonetheless, section-level shear force-distortion laws can be used in the component equilibrium, thus enabling the adequate consideration of cases where shear failure and degradation may govern the response of the section. In this last situation, strain localization issues also apply since the softening of the shear response will lead to unloading of the moment-curvature response and, consequently, strain localization to occur at the tributary length of the section. Thus, irrespectively of the considered failure mode (flexure, flexure-shear or pure shear) strain localization needs to be accounted for when using DP models, otherwise alternative formulations need to be considered for solving the non-objectivity of these models under softening of the response.

8.3.3 Numerical computation of chord rotation using consistent regularized force-based methods
The principles outlined before, and that are the source of Eqs. (16) and (17), were used to define the so-called Finite Length Plastic Hinge (FLPH) models adopted and tested in Chapter 7. Given that a RC frame component loaded until collapse will exhibit a softening response, since strain localization issues will always affect the numerical response of the component (e.g. see [18]). Several regularization techniques have been proposed for DP models to address these localization issues and determine objective estimates of the chord rotations of frame components. Some of the proposed regularization techniques are based on the modification of material properties or on the use of specific integration schemes. Regularization techniques based on the modification of material properties were proposed by Coleman and Spacone [19]. Regularization techniques using the properties of integration schemes are termed FLPH methods and can be disaggregated into those that include a fixed characteristic length (e.g. see [20-21]) and those that include an adaptive integration scheme (e.g. see [12-22]). The characteristic length defines the strain localization length of the component where curvatures localize after the response of the section enters into the

softening range of its response. Coleman and Spacone [19] associated this characteristic length with the physical properties of concrete failure. The main principle they followed requires setting a constant fracture energy to enforce the concrete softening to occur along the localization (softening) length. Apart from adjusting the material properties to ensure a constant fracture energy, an additional procedure was proposed by Coleman and Spacone [19] to post-process the curvature results for the cases where L_{IP} at nodes 1 and 2 do not coincide with the expected strain localization region (thereon termed plastic zone length and plastic chord region). The authors used Paulay and Priestley's [23] equivalent plastic chord length in the application of the proposed regularization technique. In order to avoid the post-processing that is necessary to obtain objective responses, Scott and Fenves [20] adopted a FLPH model that uses the so-called plastic chord integration methods. These authors adopted the modified two-point Gauss-Radau integration scheme considering 6 IPs distributed along the characteristic length near point 1 $L_{D,1}$, the characteristic length near point 2 $L_{D,2}$ and the length L_{int} of the interior region between $L_{D,1}$ and $L_{D,2}$. The positions of these IPs (vector ξ) and the corresponding weights (vector w) are given by:

$$\xi = \left\{ \left\{ 0; \frac{8L_{D,1}}{3} \right\}, \left\{ 4L_{D,1} + \frac{L_{\text{int}}}{2}\left(1 - \frac{1}{\sqrt{3}}\right); 4L_{D,2} + \frac{L_{\text{int}}}{2}\left(1 + \frac{1}{\sqrt{3}}\right) \right\}, \left\{ L - \frac{8L_{D,2}}{3}; L \right\} \right\} \qquad (23)$$

$$w = \left\{ \left\{ L_{D,1}; 3L_{D,1} \right\}\Big|_{w_1}, \left\{ \frac{L_{\text{int}}}{2}; \frac{L_{\text{int}}}{2} \right\}\Big|_{w_{\text{int}}}, \left\{ L_{D,2}; 3L_{D,2} \right\}\Big|_{w_2} \right\} \qquad (24)$$

implying that the component flexibility matrix can be obtained based on ξ and w as:

$$\mathbf{f}_{component} = \sum_{i=1}^{6} \left(\left\langle \mathbf{b}^T \cdot \mathbf{f}_s \cdot \mathbf{b} \right\rangle\Big|_{x=\xi_i} \right) \cdot w_i \qquad (25)$$

where $\mathbf{f}_s$ is the flexibility matrix of the section and $\mathbf{b}$ is the interpolation function at an abscissa $x = \xi_i$. The chord rotations can then be defined based on the response χ of the section (assuming that deformations associated with shear effects can be neglected) as:

$$\begin{bmatrix} \theta_1 \\ \theta_2 \end{bmatrix} \approx \begin{bmatrix} \left\langle \chi \right\rangle\big|_{x=\xi_1} \cdot L_{D,1} + \theta_{slip,tens,0-x_{L_s}} + \theta_{anchorage,slip,1} \\ \left\langle \chi \right\rangle\big|_{x=\xi_2} \cdot L_{D,2} + \theta_{slip,tens,x_{L_s}-L} + \theta_{anchorage,slip,2} \end{bmatrix} \qquad (26)$$

Contrary to the single element strategy followed by Scott and Fenves [20], Kashani *et al.* [24] adopted a mesh of three FB elements with a Gauss-Lobatto integration scheme. Two of the

elements have 3 IPs and a length of $6 \cdot L_{eff}$ where L_{eff} represents the buckling length proposed by Dhakal and Maekawa [25], thus implying that localization will occur at L_{eff}. These elements are located at the ends of the component and the third element is a FB element with 5 IPs located in between the previous two. Therefore, the main differences between the two approaches are the higher complexity of the latter, since it requires three elements to model a single component, and the fact that Kashani *et al.* [24] uncoupled the fixed-end rotations from the internal equilibrium of the element.

Although the approaches followed by Scott and Fenves [20], Adessi and Ciampi [26] and Kashani *et al.* [24] can be used to determine a regularized response when strain-softening behaviour is observed, they overestimate the flexibility when elastic response or strain hardening is observed. This comes from the fact that a regularized modelling approach assumes a fully formed mechanism. A similar concept was also adopted by Zimos *et al.* [8] who set the characteristic length equal to a constant length based on the shear localization length, i.e. the length where the nonlocal shear distortions are concentrated.

8.4 Methodology adopted to calibrate generic $\mu_{\ln \varepsilon_{Co}}$ and $\sigma_{\ln \varepsilon_{Co}}$ factors

8.4.1 Numerical models and structural systems analysed

A set of 48 archetype frame structures was considered herein in order to capture the response of systems engaging into different failure modes. The properties of these archetype frames were defined by varying key design parameters such as the level of flexibility of joints, design assumptions regarding the lateral capacity of the building, beam ductility, beam-to-column strength ratios, confinement and shear capacity of beams and columns. A summary of the properties of the frames is presented in Table 1. The main reason for adopting of all these variations consisted in aggregating a set of chord rotation, shear demands in structural elements with the reference CP model that is associated with multiple global response levels and mechanisms, to be compared with those estimated using the DP models. For simplicity, and since the objective of the present study is to analyse the potential applicability of a set of generalized model compatibility factors, a single frame configuration with four storeys and three bays was considered. The frames were defined with a beam span of 5m, a ground storey height of 4.0m and upper storey heights of 3.5m (measured at the centreline of the frame geometry). The concrete compressive strength was assumed to be on average 28MPa, and the average reinforcing steel yield strength was taken as 400MPa, both for longitudinal and transverse reinforcement. A scenario corresponding to full knowledge about the material properties and structural details was considered herein, which leads to the case where all structural components were surveyed and, therefore, the safety factor SF_R (as defined in Chapter 5) only depends on the uncertainty about

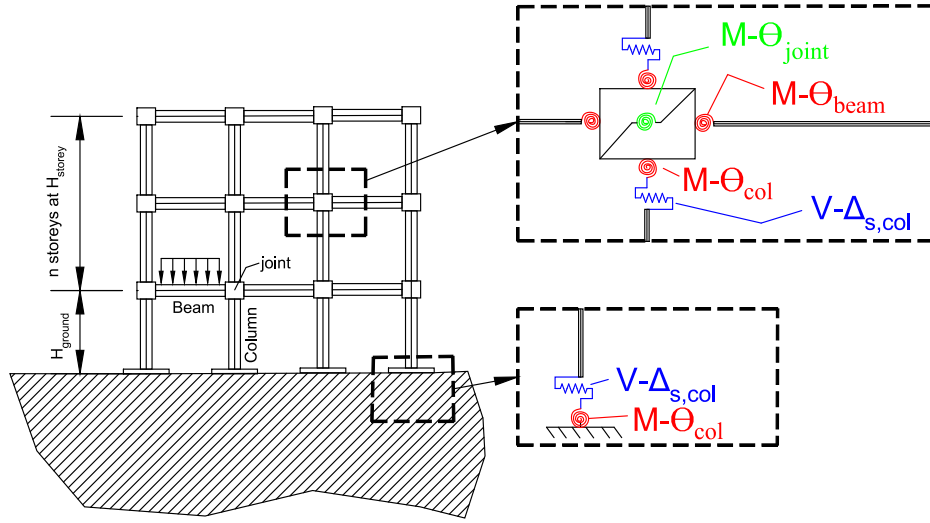the capacity model. The main characteristics of the reference CP model that was adopted are shown in Fig. 2.

Figure 2. Schematic representation of the reference (CP) model considered in the study, including the sections (V-Δs,col) used to control the shear failure during post-processing.

The 48 frames were defined considering two types of beam-column joints: 1) a case where the beam-column joints are assumed to be rigid (RIG) and 2) a case where nonlinear joint deformations are considered (NL). As seen in Fig. 2, numerical models were constructed using frame elements and using a scissor model for the beam-column joints, following the proposal and numerical implementation details of Altoontash [27]. Small deformations and constant geometry were considered for the joints in order to reduce numerical instability issues. The NL beam column joint model was defined based on the proposal made by O'Reilly and Sullivan [28].

In the reference CP model, moment-rotation springs where modelled using the parametrization defined in [3]. A detailed description of the model parametrization and conditions can be found in [3]. The effective stiffness of the frame elements was taken as 50% of the gross section value for beams, while in columns a ratio between 0.35 and 0.80 was considered, depending on the properties of the column. This stiffness was defined as the secant stiffness to 40% of the yield force of the component. A damping factor of 1% of the critical damping in the first and third modes of the structure was adopted using the Rayleigh damping model. Initial stiffness proportional damping was assigned to the elastic segments of the component assembly following the indications in Zareian and Medina [29].

Table 1. Properties of the RC frames that were adopted

Frame	Columns			Beams			
	B x H (m x m)	$\rho_{tot,col}$ (-)	s_w (m)	B x H (mxm)	ρ_{top} (top)	ρ_{bot} (bottom)	s_w (m)
F1	30x30	0.018	0.075	30x50	0.008	0.004	0.15
F2	30x30	0.018	0.075	30x50	0.008	0.008	0.15
F3	30x30	0.018	0.075	30x50	0.005	0.003	0.15
F4	30x30	0.018	0.075	30x50	0.005	0.005	0.15
F5	30x30	0.010	0.075	30x50	0.008	0.004	0.15
F6	30x30	0.010	0.075	30x50	0.008	0.008	0.15
F7	30x30	0.010	0.075	30x50	0.005	0.003	0.15
F8	30x30	0.010	0.075	30x50	0.005	0.005	0.15
F9	30x30	0.005	0.075	30x50	0.008	0.004	0.15
F10	30x30	0.005	0.075	30x50	0.008	0.008	0.15
F11	30x30	0.005	0.075	30x50	0.005	0.003	0.15
F12	30x30	0.005	0.075	30x50	0.005	0.005	0.15
F13	30x30	0.018	0.15	30x50	0.008	0.004	0.15
F14	30x30	0.018	0.15	30x50	0.008	0.008	0.15
F15	30x30	0.018	0.15	30x50	0.005	0.003	0.15
F16	30x30	0.018	0.15	30x50	0.005	0.005	0.15
F17	30x30	0.010	0.15	30x50	0.008	0.004	0.15
F18	30x30	0.010	0.15	30x50	0.008	0.008	0.15
F19	30x30	0.010	0.15	30x50	0.005	0.003	0.15
F20	30x30	0.010	0.15	30x50	0.005	0.005	0.15
F21	30x30	0.005	0.15	30x50	0.008	0.004	0.15
F22	30x30	0.005	0.15	30x50	0.008	0.008	0.15
F23	30x30	0.005	0.15	30x50	0.005	0.003	0.15
F24	30x30	0.005	0.15	30x50	0.005	0.005	0.15
F25	50x50	0.015	0.075	30x50	0.008	0.004	0.15
F26	50x50	0.015	0.075	30x50	0.008	0.008	0.15
F27	50x50	0.015	0.075	30x50	0.005	0.003	0.15
F28	50x50	0.015	0.075	30x50	0.005	0.005	0.15
F29	50x50	0.010	0.075	30x50	0.008	0.004	0.15
F30	50x50	0.010	0.075	30x50	0.008	0.008	0.15
F31	50x50	0.010	0.075	30x50	0.005	0.003	0.15
F32	50x50	0.010	0.075	30x50	0.005	0.005	0.15
F33	50x50	0.006	0.075	30x50	0.008	0.004	0.15
F34	50x50	0.006	0.075	30x50	0.008	0.008	0.15
F35	50x50	0.006	0.075	30x50	0.005	0.003	0.15
F36	50x50	0.006	0.075	30x50	0.005	0.005	0.15
F37	50x50	0.015	0.15	30x50	0.008	0.004	0.15
F38	50x50	0.015	0.15	30x50	0.008	0.008	0.15
F39	50x50	0.015	0.15	30x50	0.005	0.003	0.15
F40	50x50	0.015	0.15	30x50	0.005	0.005	0.15
F41	50x50	0.010	0.15	30x50	0.008	0.004	0.15
F42	50x50	0.010	0.15	30x50	0.008	0.008	0.15
F43	50x50	0.010	0.15	30x50	0.005	0.003	0.15
F44	50x50	0.010	0.15	30x50	0.005	0.005	0.15
F45	50x50	0.006	0.15	30x50	0.008	0.004	0.15
F46	50x50	0.006	0.15	30x50	0.008	0.008	0.15
F47	50x50	0.006	0.15	30x50	0.005	0.003	0.15
F48	50x50	0.006	0.15	30x50	0.005	0.005	0.15

In the case of the DP model, the modelling scheme proposed in Chapter 7 was adopted. A force-based element was assigned to each frame component that includes the modified Gauss-Radau integration proposed by Scott and Fenves [20]. The localization length was defined based on the damage mode analysed in Chapter 6 using the approximation of $18 \cdot d_b$, where d_b represents the longitudinal bar diameter, whose performance was evaluated in Chapter 7. The size-dependent uniaxial material models developed in Chapter 7 were considered and fixed-end rotations were simulated using the simplified strategy proposed in [30] and [31]. Also in this case, a damping factor of 1% of the critical damping in the first and third modes of the structure was adopted, using a damping model proportional to the initial stiffness. This damping model was considered following the observations made by Sousa *et al.* [31] whereby including a low amount of equivalent critical damping was seen to limit the differences in the structural response obtained using different damping models. The use of damping proportional to the initial stiffness was mostly defined in order to ensure compatibility with the CP model, and was preferred against mass-proportional damping due to the higher numerical stability of this model that was observed in preliminary sensitivity analyses. Table 2 summarizes the four modelling strategies analysed in the study.

Table 2. Modelling strategies analysed in the study

Model	Frame element model	Beam-column joint model	Damping	Fixed-end rotations
DP-RIG	FLPH	Rigid	1% ISD	Spring
DP-NL	FLPH	Nonlinear	1% ISD	Spring
CP-RIG	CP	Rigid	1% ISD	Implicit
CP-NL	CP	Nonlinear	1% ISD	Implicit

8.4.2 Calibration of $\mu_{\ln \varepsilon_{Co}}$ and $\sigma_{\ln \varepsilon_{Co}}$ using pushover analysis

The calibration of the generic values of $\mu_{\ln \varepsilon_{Co}}$ and $\sigma_{\ln \varepsilon_{Co}}$ was first carried out by performing nonlinear static analyses of the 48 frames. An inverted triangular load pattern proportional to the first mode of vibration was used to assess the response of each frame. Each analysis was performed until a full drop of the base shear from the peak value or a maximum roof drift of 10% was observed. After performing the analysis, the chord-rotations and the shear forces of the DP models and of the CP models were determined. All the pairs of demand values ($D_{CP,j}$; $D_{DP,j}$) that were obtained with the two modelling strategies were determined for each component (j) of each frame and for the modelling combinations defined in Table 2. These demand values were defined for specific values of roof drift between 0.5% and 10%, in steps of 1%. Subsequently, a filter was applied to remove all the demand pairs of each component where at least one of the models reached the maximum response and started unloading. Furthermore, in order to avoid biasing the

results by including ratios corresponding to early elastic response stages, pairs including chord rotations lower than 0.005 radians and shear forces below 20kN were excluded. Using the filtered dataset, the ε_{Co} factors were determined for chord rotations in columns, chord rotations in beams and shear forces in columns at each structural component j by:

$$\varepsilon_{\theta_c} = \frac{\theta_{c,CP,j}}{\theta_{c,DP,j}}, \tag{27}$$

$$\varepsilon_{\theta_b} = \frac{\theta_{b,CP,j}}{\theta_{b,DP,j}}, \tag{28}$$

$$\varepsilon_{V_c} = \frac{V_{c,CP,j}}{V_{c,DP,j}} \tag{29}$$

A lognormal distribution was fitted to the sets of ratios using the maximum likelihood estimation method. After a global model was fitted, the results were disaggregated among bins defined in terms of values of $\theta_{c,DP}$, $\theta_{b,DP}$ and $V_{c,DP}$. For chord rotations, these bins were defined with a bin width of 0.01 radians. In the case of shear force, a bin width of 20kN was established. Lognormal distributions were then also fitted to the disaggregated datasets, and the evolution of the statistical parameters of these distributions was analysed. In order to control the shear response of columns, the median shear capacity V_n as defined in Chapter 5 (see p. 5.22) was also determined.

8.4.3 Calibration of $\mu_{\ln \varepsilon_{Co}}$ and $\sigma_{\ln \varepsilon_{Co}}$ using time history analysis

Since the main objective of this study was to assess the possible adoption of generic factors that could be applicable within the scope of standard-based procedures, general values for the total variability ($s^2_{\ln D_{alt}} + \sigma^2_{\ln \varepsilon_{Co}}$) defined in Eq. (13) need to be developed. With this in mind, a generic set of ground motions was selected in order to include multiple types of ground motions and multiple intensity levels. The 21-ground motion record involving far-field scenarios defined by Miano *et al.* [32] for cloud analysis with no or limited scaling was considering herein. Details of the ground motion records are presented in [32]. Average spectral acceleration ($AvgSa$) calculated at periods from 0.4s to 4s in steps of 0.2s was used as the intensity measure (IM). $AvgSa$ was selected due to the sufficiency, robustness and lower site dependence observed in recent studies ([33]), which may benefit the general character of the $\mu_{\ln \varepsilon_{Co}}$ and $\sigma_{\ln \varepsilon_{Co}}$ factors under analysis. Two separate sets of analyses were performed using nonlinear dynamic analysis. The first set assumes independence between the record-to-record variability and the uncertainty about the use of an alternative structural modelling approach. In this set the maximum values of $\theta_{c,CP}$, $\theta_{b,CP}$, $\theta_{c,CP}$, $\theta_{b,DP}$ and $V_{c,DP}$ were determined for each ground motion, for each frame and for the two joint modelling scenarios (i.e. rigid or with nonlinear behaviour). The ε_{Co} factors were

defined using the maximum responses obtained for each modelling approach and the corresponding probability distributions were analysed. By doing so, the factors ε_{θ_c}, ε_{θ_b} and ε_{V_c} of Eqs. (27) -(29) were obtained considering a critical safety condition defined by the maximum demand observed in the frame, without enforcing (unlike for the pushover case) that the maximum demand obtained for each modelling approach is from the same component of the frame. Hence, factors $\varepsilon_{\theta_{c,\max}}$, $\varepsilon_{\theta_{b,\max}}$ and $\varepsilon_{V_{c,\max}}$ were defined as:

$$\varepsilon_{\theta_{c,\max}} = \frac{max\{\theta_{c,CP}(j):j=1:n_{columns}\}}{max\{\theta_{c,DP}(j):j=1:n_{columns}\}}, \qquad (30)$$

$$\varepsilon_{\theta_{b,\max}} = \frac{max\{\theta_{b,CP}(j):j=1:n_{beams}\}}{max\{\theta_{b,DP}(j):j=1:n_{beams}\}}, \qquad (31)$$

$$\varepsilon_{V_{c,\max}} = \frac{max\{V_{c,CP}(j):j=1:n_{columns}\}}{max\{V_{c,DP}(j):j=1:n_{columns}\}} \qquad (32)$$

In the second set of analyses, cloud analysis was performed for each frame and a power model was considered to correlate the maximum rotation in columns ($\theta_{c,DP}$) and the maximum rotation in beams ($\theta_{b,DP}$) with the IM of the ground motion (i.e. $AvgSa$). Consequently, for each frame, a linear model in logarithmic space given by:

$$\log\left(max\{\theta_c(j):j=1:n_{columns}\}\right) = a + b\cdot\log\left(AvgSa\right) + \varepsilon_{\ln c,\max}, \qquad (33)$$

$$\log\left(max\{\theta_b(j):j=1:n_{cbeams}\}\right) = a + b\cdot\log\left(AvgSa\right) + \varepsilon_{\ln b,\max}, \qquad (34)$$

was established for the models CP-RIG, CP-NL, DP-RIG and DP-NL, where $\varepsilon_{\ln c,\max}$ and $\varepsilon_{\ln b,\max}$ are zero-mean normal variables with standard deviation $\sigma_{\ln c,\max}$ and $\sigma_{\ln b,\max}$, respectively. Hence, $\sigma_{\ln c,\max}$ and $\sigma_{\ln b,\max}$ represent the record-to-record variability, which is assumed to be constant across all IM levels following assumptions of the cloud analysis method (e.g. see [35]). Hence, by establishing a relation between $\sigma_{\ln c,\max,CP}$ and $\sigma_{\ln c,\max,DP}$, and between $\sigma_{\ln b,\max,CP}$ and $\sigma_{\ln b,\max,DP}$, the total variability ($\beta_{\ln c,DP\cdot\varepsilon_{Co}}$ and $\beta_{\ln b,DP\cdot\varepsilon_{Co}}$) defined in Eq. (10) can be approximated by:

$$\beta_{\ln c,DP\cdot\varepsilon_{Co}} \cong \left.\frac{\sigma_{\ln c,\max,CP}}{\sigma_{\ln c,\max,DP}}\right|_{cloud} \cdot \sigma_{\ln c,\max,DP}, \qquad (35)$$

$$\beta_{\ln b,DP\cdot\varepsilon_{Co}} \cong \left.\frac{\sigma_{\ln b,\max,CP}}{\sigma_{\ln b,\max,DP}}\right|_{cloud} \cdot \sigma_{\ln b,\max,DP}, \qquad (36)$$

where $\left.\dfrac{\sigma_{\ln c,\max,CP}}{\sigma_{\ln c,\max,DP}}\right|_{cloud}$ and $\left.\dfrac{\sigma_{\ln b,\max,CP}}{\sigma_{\ln b,\max,DP}}\right|_{cloud}$ were defined in order to represent average compatibility

factors that can be used to convert a generic value of $\sigma_{\ln c,\max,DP}$ or $\sigma_{\ln b,\max,DP}$ into the corresponding record-to-record variability expected to be observed, on average, with the reference model (i.e. $\sigma_{\ln c,\max,CP}$ and $\sigma_{\ln b,\max,CP}$).

8.5 Results

8.5.1 Results from the pushover analyses

8.5.1.1 Global response

Figure 3 shows the capacity curves obtained with the four modelling combinations defined in Table 2 for the 48 frames analysed in the study. Independently of the adopted modelling approach, the pushover curves show that the 48 buildings can be divided in two classes separated by the size of the columns presented in Table 1.
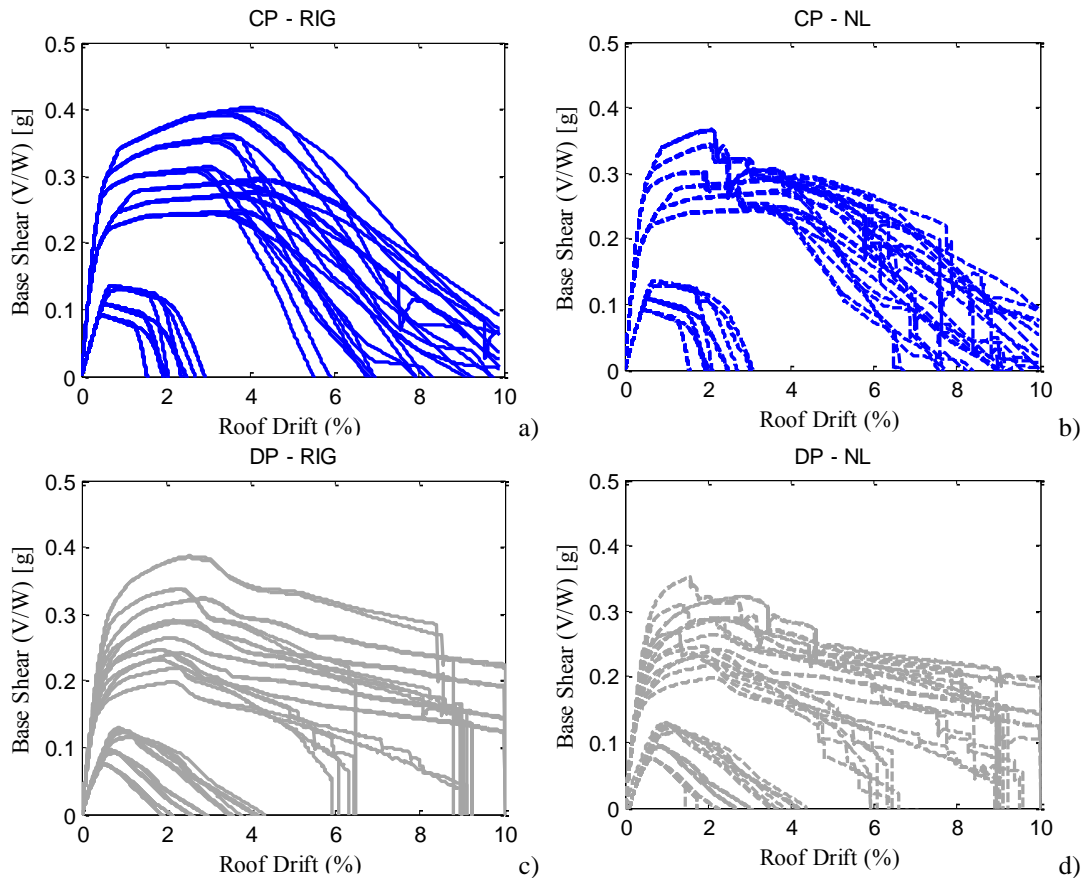
Figure 3. Capacity curves of the 48 frames with properties listed in table 1 considering the CP-RIG (a), CP-NL (b), DP-RIG (c) and CP-NL (d) models (V/W refers to the base shear force normalized by the weight of the structure).

The first set of curves refers to cases F1 to F24 (see Table 1) and were seen to have a yielding lateral capacity (defined by the ratio of the base shear to the weight of the structure, V/W) in the

range of 5%-15%. Conversely, the second set of curves refers to frames F25-F48 (the frames with larger column sections) and exhibit a yielding lateral capacity between 15% and 35%. In terms of ductility, it can be seen that frames F1-F24 exhibit a behaviour that is typical of buildings with low ductility, with yielding roof drifts around 1% and collapse ductility between 2 and 4. By analysing the properties of the frames using the column density (defined by the ratio between the sum of the area of all columns of the frame by the corresponding tributary area of the floor for the gravity loads), it can be seen that frames F1-F24 have a column density of 0.40, while frames F25-F48 have a density of 1.1%. The effect of the different structural details is reflected in the maximum capacity of each frame, as seen in the probability plots shown in Fig. 4.
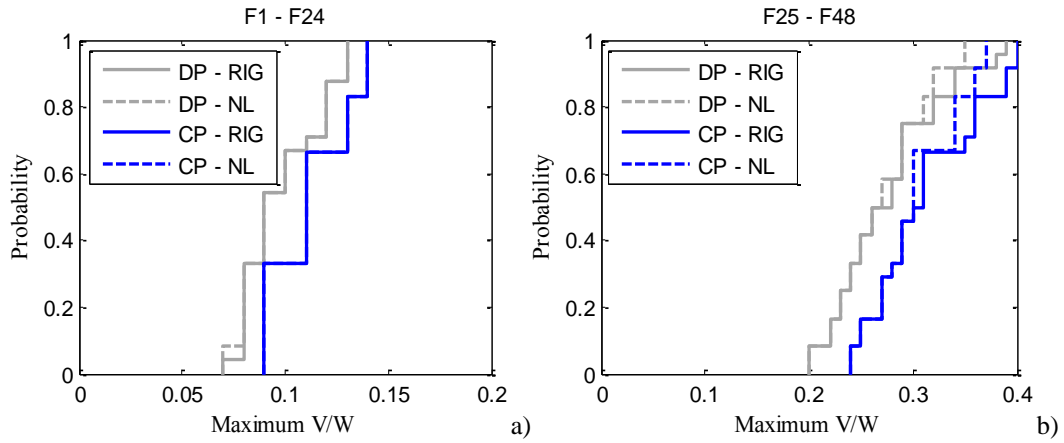
Figure 4. Empirical cumulative distribution functions of the maximum base shear estimated with the four modelling strategies defined in Table 2 for frames F1-F24 (a) and F25-F48 (b).

From Fig. 4, it can be seen that, for a given typology of frames, the probability distributions of V/W obtained for the different modelling approaches are similar. Still, models involving CP elements provide, in general, a slightly higher V/W capacity than that estimated with DP models. These differences may be related to the constant values of the yielding and maximum moments that need to be assumed for each spring of the CP models while, for the DP models, the axial-flexure interaction seems to lead to a faster softening of the capacity curve. These observations are corroborated by the distribution of the collapse ductility of the system, as seen in the probability plots of the roof drift quantified at the end of each analysis shown in Fig. 5. The roof drift values estimated at the last converged step of the pushover analysis shown in Fig. 5a are those of structures F1-F24 and it can be seen that similar collapse roof drifts are obtained with all modelling techniques. Still, a lower collapse ductility is observed in some of the results obtained with model DP-NL. The differences between the results obtained with the DP and CP component models are larger for frames F25-F48. In this case, the empirical distributions of collapse roof drifts obtained with DP models exhibit a significant number of lower values than those of obtained with the CP component models. This fact indicates that larger values of the chord rotations can

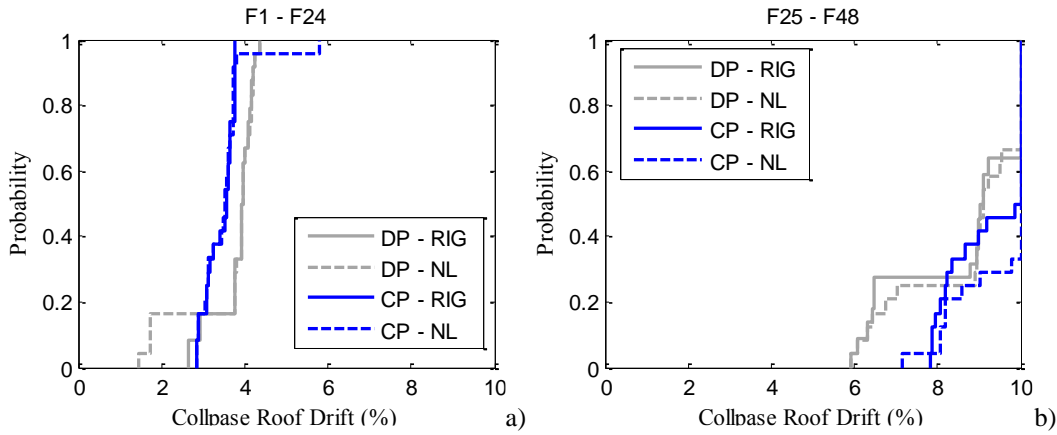be expected with a DP model and when comparing them with the values obtained with the CP model.

Figure 5. Empirical cumulative distribution functions of the collapse roof drift (corresponding to the analysis step at which the base shear is zero or when a maximum roof drift of 10% was achieved) for frames F1-F24 (a) and F25-F48 (b).

8.5.1.2 Chord rotation in columns

Figure 6 shows the relation between the chord rotation of columns obtained with the CP model and those obtained with the DP model. As seen in Fig. 6a, a linear correlation with a slope of 1.03 is obtained when comparing the DP-RIG and the CP-RIG models. The mean ratio has a value of 1.068, a median of 1.061 and a standard deviation of 0.259. When comparing the response obtained for the DP-NL and CP-NL models (Fig. 6b), the linear regression has now a slope of 1.0, with a mean ratio of 1.023, a median of 1.011 and a standard deviation of 0.234.
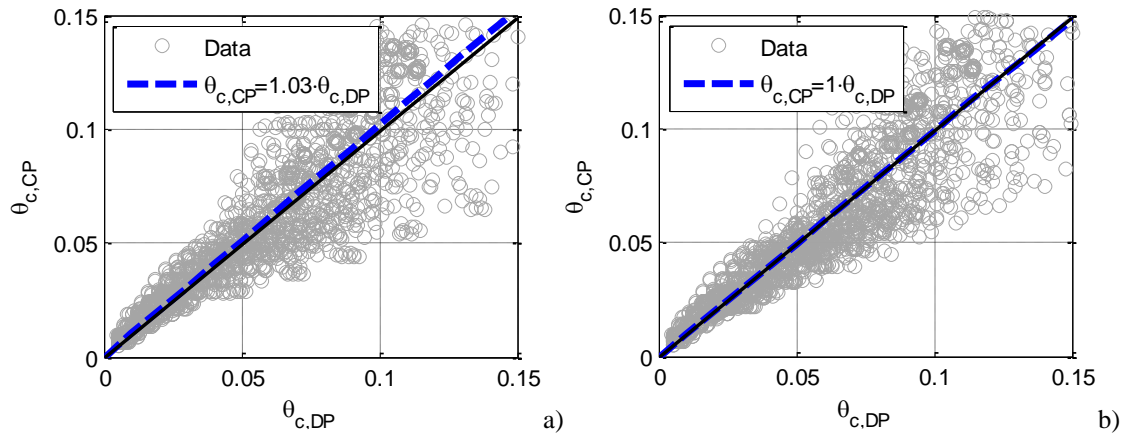
Figure 6. Comparison of the column chord rotations obtained using the CP and the DP models for the case where joints are considered rigid (RIG; a) and for the case where joints are assumed to have nonlinear behaviour (NL; b)

Figure 7 shows the probability plots of the ratios defined between the chord rotations obtained in columns when the frames are modelled with the CP and DP modelling approaches, assuming these ratios follow a lognormal distribution. Fig. 7a shows the probability plot obtained for the case where RIG joints are used, while the probability plot obtained for the case where NL joints

are used is shown in Fig. 7b. The fit of a lognormal distribution shown in Fig. 7a can be seen to be adequate for the range defined between the quantiles of 5% and 95%. The lognormal model fitted to the data using the maximum likelihood method has a mean $\mu_{\ln \varepsilon_{\theta_c}}$ of -0.035 and a standard deviation $\sigma_{\ln \varepsilon_{\theta_c}}$ of 0.250. For the case where NL joints (Fig. 7b) are considered, the quality of the fit to the ratios that were observed increases. The parameters of the fitted lognormal distributions are now $\mu_{\ln \varepsilon_{\theta_c}} = -0.003$ and $\sigma_{\ln \varepsilon_{\theta_c}} = 0.228$.
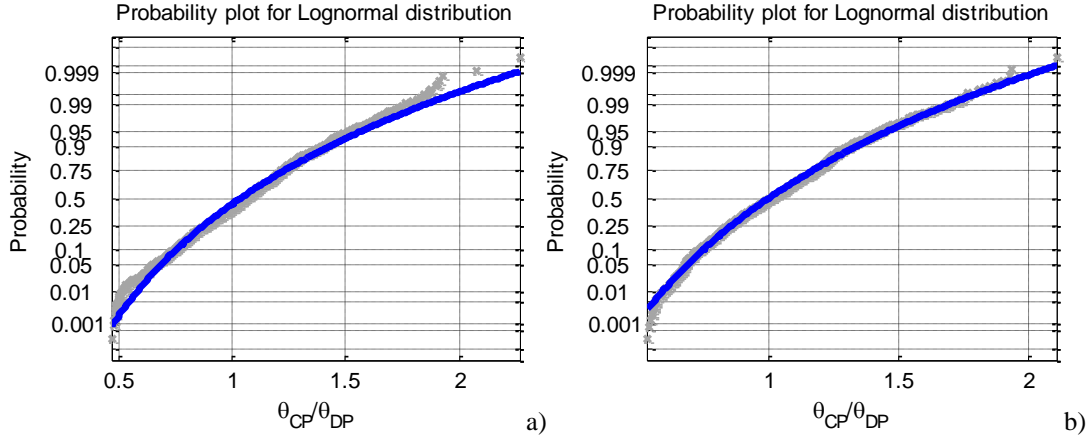
Figure 7. Probability plots of the ratios between the chord rotations values obtained using the CP and the DP models for the case where joints are considered rigid (RIG; a) and for the case where joints are assumed to have nonlinear behaviour (NL; b)

Figure 8 shows the disaggregation of the distribution of the values of ε_{θ_c} considering the previously defined bins determined by values of $\theta_{c,DP}$. As seen in Fig. 8, for lower values of $\theta_{c,DP}$ near the yielding rotation values (i.e. between 0.005 and 0.010 for the column sections analysed in this study), there is an increase in the values of ε_{θ_c} that reach values above 2 in both cases (Fig. 8a and Fig. 8b). After this initial stage, the median of ε_{θ_c} stabilize at values close to 1.0.

The observations made in Fig. 8 are more clearly seen in Fig. 9 that presents the variations of the parameters of the fitted lognormal models, $\mu_{\ln \varepsilon_{\theta_c}}$ and $\sigma_{\ln \varepsilon_{\theta_c}}$, using the values of $\theta_{c,DP}$ in each bin. As seen in Fig. 9, for values of $\theta_{c,DP}$ close to the linear elastic range, the values of $\mu_{\ln \varepsilon_{\theta_c}}$ vary between 0.26 and 0.09 for the models with RIG joints, and between 0.22 and 0.05 for the models that consider NL joints. After this, a reduction is observed in the results obtained for the model with RIG joints that end up concentrating at values around $\mu_{\ln \varepsilon_{\theta_c}} = 0$. When using the NL joint model, the same reduction is observed, however the results end up converging to a value of $\mu_{\ln \varepsilon_{\theta_c}}$ close to -0.05. The opposite of this trend is observed when analysing the variation of $\sigma_{\ln \varepsilon_{\theta_c}}$ in Fig. 9b. For early elastic stages, $\sigma_{\ln \varepsilon_{\theta_c}}$ increases up to 0.25 and then decreases until $\theta_{c,DP}$

values in the range of 0.02 to 0.04. After this range, $\sigma_{\ln \varepsilon_{\theta_c}}$ increases again up to a value close to 0.27, in the case of the models with RI joints, and up to a value close to 0.23 for the models with NL joints.
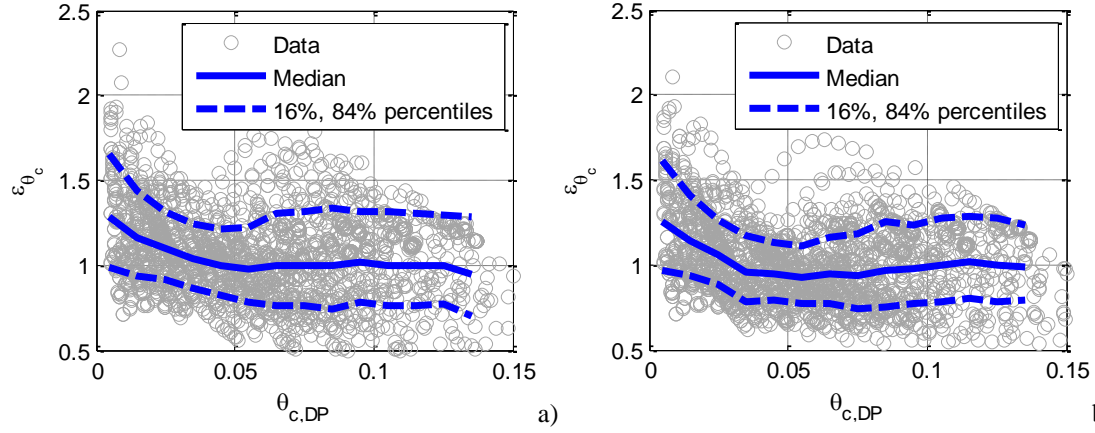

Figure 8. Disaggregation of ε_{θ_c} among bins of $\theta_{c,DP}$ values centred at specific values of the arithmetic progression between 0.005 and 0.135, in steps of 0.01, for the frames with RIG (a) and NL (b) joints.
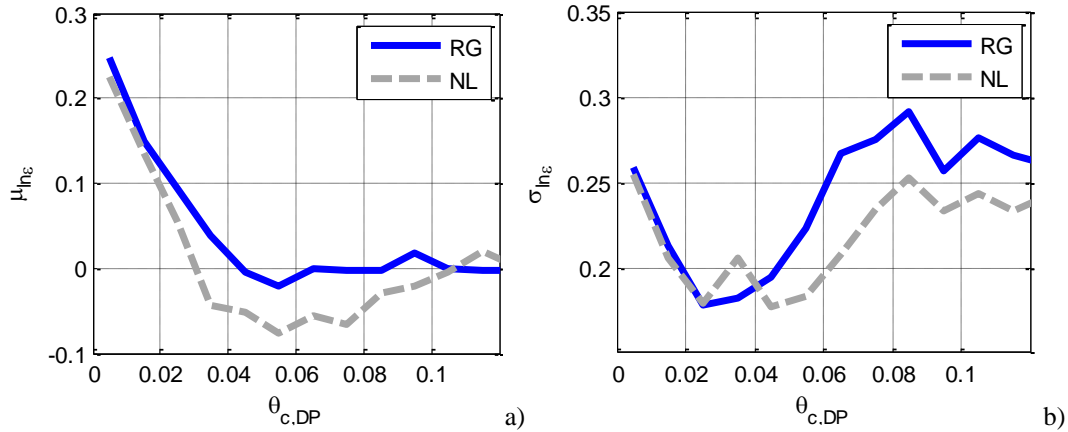

Figure 9. Variation of the mean $\mu_{\ln \varepsilon_{\theta_c}}$ (a) and of the standard deviation $\sigma_{\ln \varepsilon_{\theta_c}}$ (b) of $\ln \theta_c$ obtained from the lognormal fits to the data disaggregated among bins delimited by specific $\theta_{c,DP}$ values.

Based on these general observations, particularly those for Fig. 9, generic $\mu_{\ln \varepsilon_{\theta_c}}$ and $\sigma_{\ln \varepsilon_{\theta_c}}$ values of 0.15 and 0.25, respectively, can be suggested for cases where the $\theta_{c,DP}$ corresponds to a behaviour range close to the corresponding yielding value. For values above the yielding region, generic $\mu_{\ln \varepsilon_{\theta_c}}$ and $\sigma_{\ln \varepsilon_{\theta_c}}$ of -0.05 and 0.25, respectively, can be suggested instead. It must be noted that detecting the yielding region can be done in models using DP elements either by monitoring the uniaxial behaviour of the materials, or by assessing the curvature of the end IP and comparing its demands with the expected value of the yielding curvature.

8.5.1.3 Chord rotation in beams

Figure 10 shows the comparison of the beam chord rotations obtained using the models RIG-CP and RIG-DP (Fig. 10a) and using models NL-CP and NL-DP (Fig. 10b). As can be seen, the linear regression analysis leads to average ratios that are now larger than those previously obtained for columns. For beam chord rotations, the slopes of the linear regression are 1.15 and 1.11 for the cases where RIG and NL joints were considered, respectively. The mean $\theta_{b,CP} / \theta_{b,DP}$ ratios that were obtained are 1.28 and 1.29 for the model with RIG and NL joints, respectively, and the corresponding medians are 1.20 (for the RIG model; Fig. 10a) and 1.17 (for the NL model; Fig. 10b). The standard deviations of the $\theta_{b,CP} / \theta_{b,DP}$ ratios are also higher than the values observed for $\theta_{c,CP} / \theta_{c,DP}$, increasing up to 0.35 (for the RIG model; Fig. 10a) and to 0.41 (for the NL model; Fig. 10b).

The probability plots of the ratios defined between the chord rotations obtained in beams when the frames are modelled with the CP and DP modelling approaches, assuming these ratios follow a lognormal distribution are shown in Fig. 11. As for the columns, the lognormal approximation is also visually acceptable in both cases (i.e. for the models with RIG and NL joints) up to the 95% quantile, above which both cases exhibit a deviation between the theoretical (lognormal) and the empirical distributions. For the case where RIG joints were used, the fitted lognormal distribution has a mean $\mu_{\ln \varepsilon_{\theta_b}}$ of 0.226 and a standard deviation $\sigma_{\ln \varepsilon_{\theta_b}}$ of 0.223. On the other hand, in the case where NL joints were used, the lognormal fit has parameters $\mu_{\ln \varepsilon_{\theta_b}}$ and $\sigma_{\ln \varepsilon_{\theta_b}}$ equal to 0.212 and to 0.259, respectively.
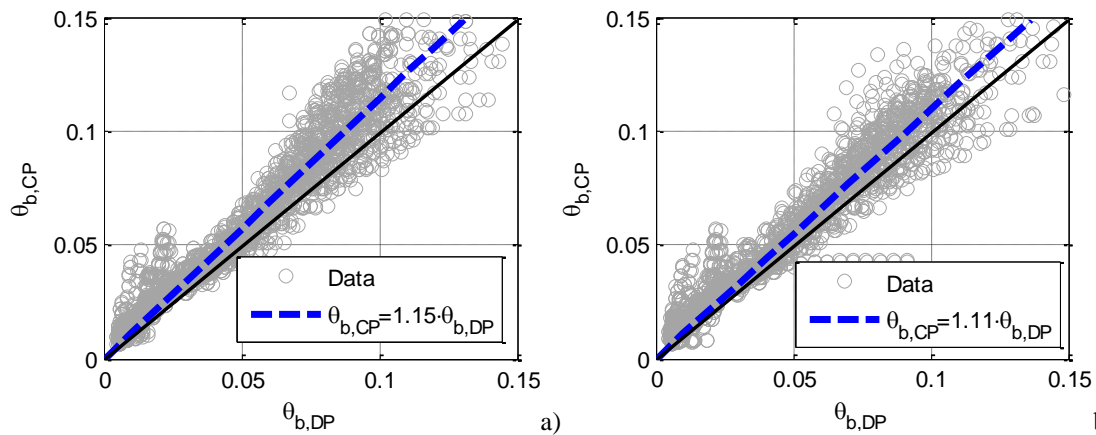

Figure 10. Comparison of the beam chord rotations obtained using the CP and the DP models for the case where joints are considered rigid (RIG; a) and for the case where joints are assumed to have nonlinear behaviour (NL; b).
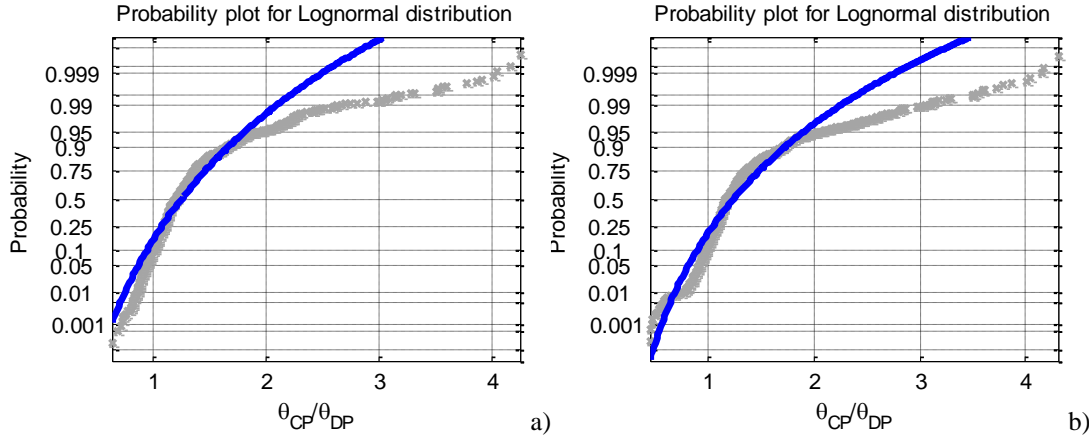
Figure 11. Probability plots of the ratios between the chord rotations values obtained using the CP and the DP models for the case where joints are considered rigid (RIG; a) and for the case where joints are assumed to have nonlinear behaviour (NL; b)

In order to analyse the source of the discrepancies between the right hand side tails of the theoretical and empirical distributions of $\theta_{b,CP}/\theta_{b,DP}$ shown in Fig. 11, Fig. 12 presents the disaggregation of the values of ε_{θ_b} in bins separated based on values of $\theta_{b,DP}$, as done before to the case of columns to obtain Fig. 8. Ratios equal or higher than 2.0 are seen to be concentrated at the initial stages of the response and are associated to the deviations previously identified in the lognormal probability plots. Since the geometry of the beams of all frames is the same (0.3x0.50 m^2), the yielding rotation can be seen to be in the range of 0.65%-0.80% (by computing the yielding rotation following Eq. A10b of [CEN, 2005Ec8/3] and assuming a shear span in the range of L/3 to L/2 where L is the beam span). Hence, it can be seen that the major differences that are observed between the response of the two models come from the rotations measured in the elastic range or in early post yielding stages of the components response. By analysing the median ratios of the bins centred at ε_{θ_b} values of 0.5% (0%-1%), 1.5% (1%-2%) and 2.5% (2%-3%), the median factor is seen to reduce from 1.75 to 1.32 and from 1.81 to 1.32 in the models with RIG and NL joints, respectively. All the bins defined with centres larger than a chord rotation of 3% exhibit less variable ε_{θ_b} ratios, with median and standard deviation values that remain approximately constant. These values converge to a ratio with an average value of 1.11 in the case of the models with RIG joints, and with a slightly lower average value of 1.07 in the case of the models with NL joints. These differences can be associated to the different approaches that were defined to establish the initial stiffness of CP and DP beam components. In the CP model, the stiffness was assumed to be 50% of the flexure stiffness of the gross cross-section. Furthermore, a shear span of L/2 was also adopted. Since the shear span in the DP model varies during the analysis according to the loading conditions, a larger secant-to-yield stiffness may be expected in this modelling approach. For example, if the length of the shear span was assumed to be 30% of L in the CP modelling approach, the secant stiffness would be 1.67 times the one computed with

L/2. It is noted that, during the initial elastic stages of the analyses, the effect of the gravity loads reduces the length of the shear span. With the increase of lateral displacements, plastic rotations become more important and the length of the shear span increases progressively and converges to L/2. This fact may justify the convergence of the results that is observed when $\theta_{b,DP}$ increases.
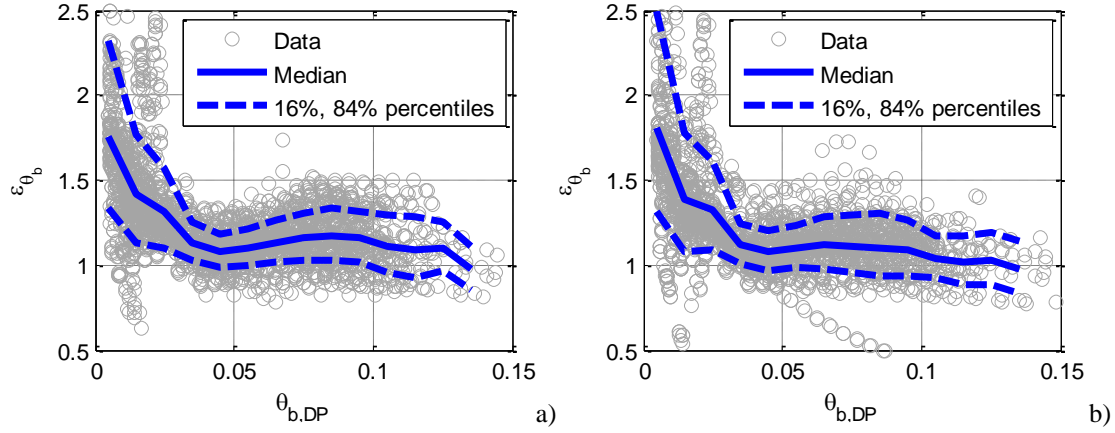

Figure 12. Disaggregation of ε_{θ_b} among bins of $\theta_{b,DP}$ values centred at specific values of the arithmetic progression between 0.005 and 0.135, in steps of 0.01, for the frames with RIG (a) and NL (b) joints.

The distribution of the parameters ($\mu_{\ln \varepsilon_{\theta_b}}$ and $\sigma_{\ln \varepsilon_{\theta_b}}$) of the lognormal models fitted to the ratios disaggregated according to the value of $\theta_{b,DP}$ is shown in Fig. 13. These results show a reduction of the mean $\mu_{\ln \varepsilon_{\theta_b}}$ and of the standard deviation $\sigma_{\ln \varepsilon_{\theta_b}}$ of the logarithm of ε_{θ_b}, $\ln \varepsilon_{\theta_b}$, as the value of $\theta_{b,DP}$ increases. The mean value $\mu_{\ln \varepsilon_{\theta_b}}$ is seen to be between 0.60 and 0.27 for $\theta_{b,DP}$ values lower than 0.02, and is seen to converge to an average value of 0.10 (for the RIG model) and of 0.06 (for the NL model) after this point. With respect to the standard deviation $\sigma_{\ln \varepsilon_{\theta_b}}$, values between 0.30 and 0.20 are observed for $\theta_{b,DP}$ values lower than 0.02, and its value is seen to converge to an average value of 0.12 (for the RIG model) and of 0.14 (for the NL model) after that. Based on these general observations, generic $\mu_{\ln \varepsilon_{\theta_b}}$ and $\sigma_{\ln \varepsilon_{\theta_b}}$ values of 0.40 and 0.25 can be suggested for cases where $\theta_{b,DP}$ is close to the corresponding yielding value. For chord rotations above the yielding range, suggesting generic $\mu_{\ln \varepsilon_{\theta_b}}$ and $\sigma_{\ln \varepsilon_{\theta_b}}$ values of 0.10 and 0.15 appears to be appropriated.
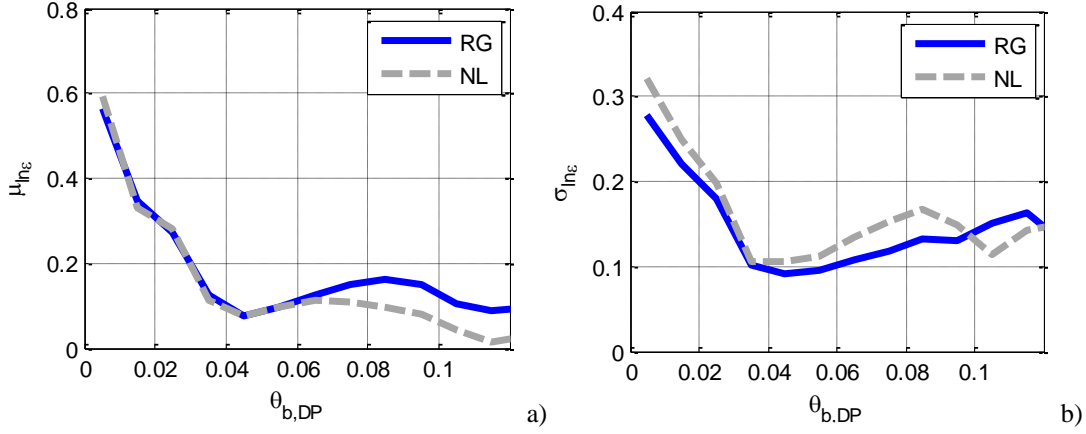
Figure 13. Variation of the mean $\mu_{\ln \varepsilon_{\theta_b}}$ (a) and of the standard deviation $\sigma_{\ln \varepsilon_{\theta_b}}$ (b) of $\ln \theta_b$ obtained from the lognormal fits to the data disaggregated among bins delimited by specific $\theta_{b,DP}$ values.

8.5.1.4 Shear forces in columns

As for the results presented in Figs. 6 and 10, Fig. 14 shows the direct comparison of the shear forces calculated using the CP and DP modelling approaches combined with the use of RIG joints (Fig. 14a) and NL joints (Fig. 14b). As can be seen, the correlation found between shear forces obtained with the DP and CP models is on average 1.02 and 1.03 when using RIG or NL joints, respectively. The mean, median and standard deviation values found for the shear force ratio $V_{c,CP}/V_{c,DP}$ are 1.1, 1.09 and 0.21, respectively, for the case involving RIG joints (Fig. 14a). For the case where the NL joint were used, the mean, median and standard deviation values of the $V_{c,CP}/V_{c,DP}$ ratios were 1.1, 1.09 and 0.21, respectively.
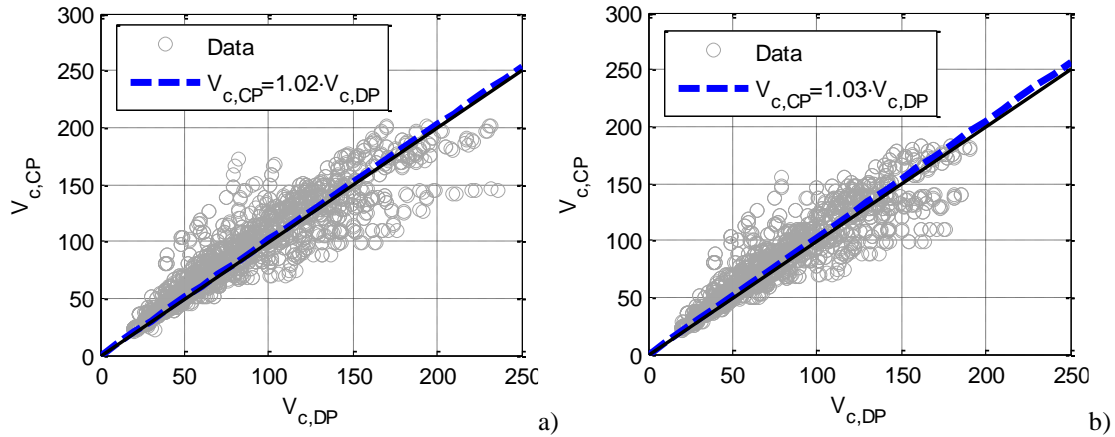

Figure 14. Comparison of the column shear forces obtained using the CP and the DP models for the case where joints are considered rigid (RIG; a) and for the case where joints are assumed to have nonlinear behaviour (NL; b).

Figure 15 shows the probability plots of the $V_{c,CP}/V_{c,DP}$ ratios obtained in models involving RIG joints (Fig. 15a) and NL joints (Fig. 15b), assuming these ratios follow a lognormal distribution. As in the previous cases, the visual assessment of the probability plots shows a deviation between the theoretical lognormal model fitted to the data and the corresponding empirical distribution for

quantiles with a probability equal or large than 0.95. The parameters ($\mu_{\ln \varepsilon_{V_c}}$, $\sigma_{\ln \varepsilon_{V_c}}$) of the fitted lognormal models are (0.077, 0.0184), for the case of Fig. 15a, and (0.079, 0.176) for the case of and Fig. 15b. Figure 16 shows the disaggregation of the shear force ratios $V_{c,CP}/V_{c,DP}$ according to the bins of $V_{c,DP}$ centred at specific values of the arithmetic progression between 30kN and 200kN, in steps of 20kN. As can be seen, the ε_{V_c} values concentrate around the global median values previously referred. The dashed lines representing the plus and minus one standard deviation thresholds are also seen to be equidistant for different values of $V_{c,DP}$. Median ratios above 1.0 are observed for lower shear force values, while values lower than 1.0 are found for $V_{c,DP}$ above 130kN.
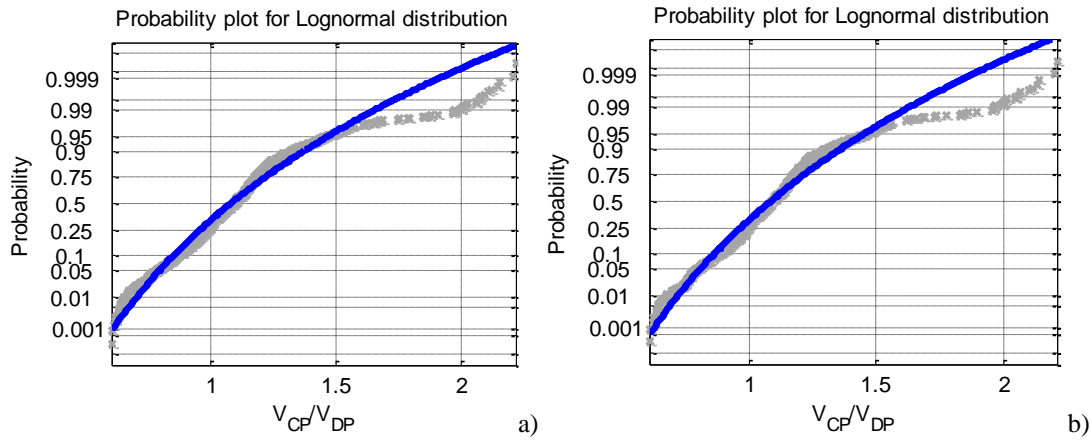

Figure 15. Probability plots of the ratios between the shear forces obtained using the CP and the DP models for the case where joints are considered rigid (RIG; a) and for the case where joints are assumed to have nonlinear behaviour (NL; b)
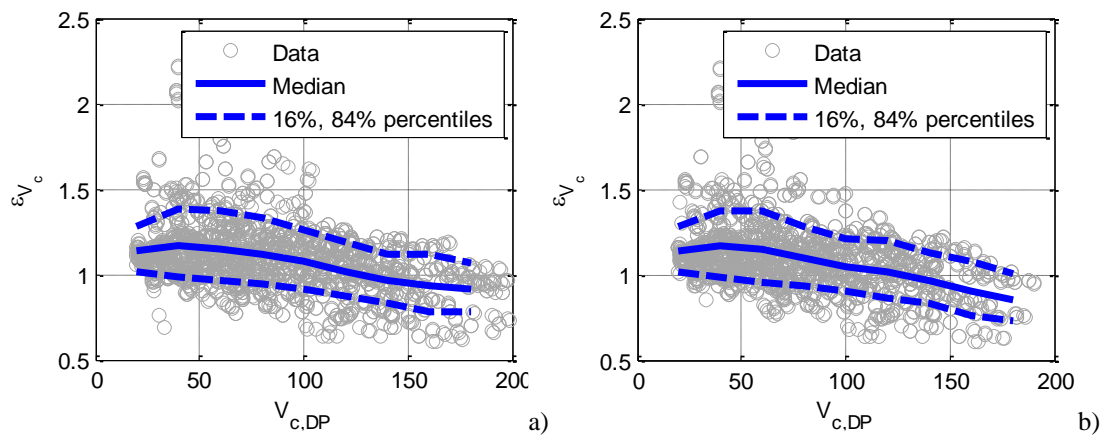

Figure 16. Disaggregation of ε_{V_c} among bins of $V_{c,DP}$ values centred at specific values of the arithmetic progression between 30kN and 200kN, in steps of 20kN, for the frames with RIG (a) and NL (b) joints.

Finally, Fig. 17 disaggregates the results shown in Fig. 16 based on the shear force ductility determined by the ratio between $V_{c,DP}$ and the capacity V_n of each column. The results that were

obtained demonstrate that the analysed frames have a response that is mostly within the flexural domain since the ratio $V_{c,DP}/V_n$ is below 0.6. It is noted that the stirrup diameter is equal to 0.008m for all beams and columns, thus satisfying the minimum condition for ductile failure modes based on the transverse reinforcement ratio ($\rho_{sh} \geq 0.002$) defined in Chapter 6 (see p. 6.6). Figure 17 also shows that a constant $\sigma_{\ln \varepsilon_{V_c}}$ of 0.15 can be adopted irrespectively of the $V_{c,DP}/V_n$ value when shear is not governing the response. Conversely, the mean value $\mu_{\ln \varepsilon_{V_c}}$ exhibits a large variation, decreasing almost linearly with $V_{c,DP}/V_n$. For $V_{c,DP}/V_n$ values lower than 0.40, a conservative approach suggests the use of a $\mu_{\ln \varepsilon_{V_c}}$ factor with a value of 0.10. For $V_{c,DP}/V_n$ that are larger than 0.4, a value of -0.10 can also be suggested as a conservative estimate for $\mu_{\ln \varepsilon_{V_c}}$.
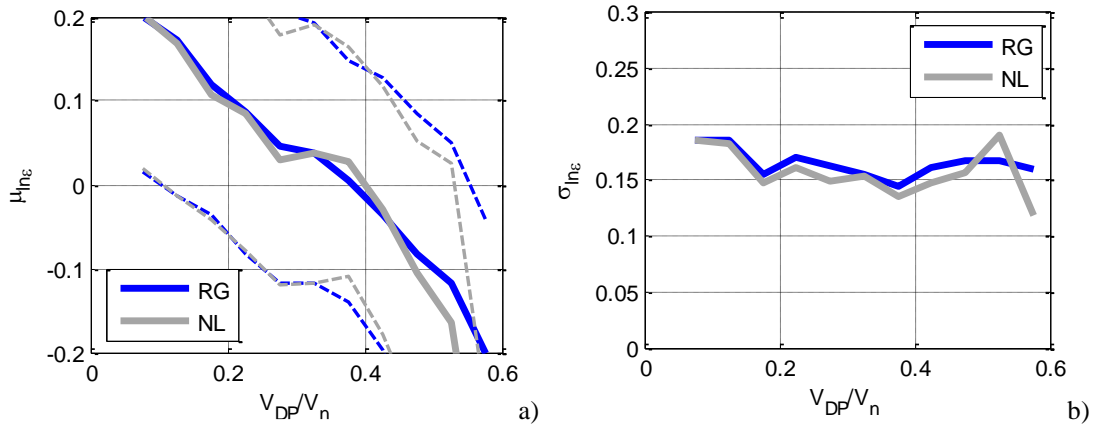

Figure 17. Variation of the mean $\mu_{\ln \varepsilon_{V_c}}$ (a) and of the standard deviation $\sigma_{\ln \varepsilon_{V_c}}$ (b) of $\ln V_c$ obtained from the lognormal fits to the data disaggregated among bins delimited by specific values of $V_{c,DP}/V_n$

8.5.2 Results from nonlinear time history analysis
8.5.2.1 Global response

Figure 18 shows the results of the maximum interstorey drift ratio (*IDR*) over all storeys obtained for the 48 frames analysed with the set of 21 far-field ground motions previously described. Given that some of the analyses that were performed with the DP modelling approach experienced numerical instability issues, leading to an early termination of the process, the corresponding results were not included in the following statistical analyses. However, these results are presented in Fig. 18 with those obtained with the CP modelling approach. Furthermore, irrespective of the modelling approach, all the converged analyses that lead to a maximum interstorey drift above 10% were treated as possible collapses, following the assumption made by Vamvatsikos and Cornel (2002), Gokkaya *el al.* (2017) and O'Reilly and Sulivan (2017).

For the frames with RIG joints, mean, median and standard deviation values of the ratio $IDR_{\max,CP}/IDR_{\max,DP}$ equal to 0.875, 0.846 and 0.273, respectively, were found. For the frames

8.29

modelled with NL joints, the values found for these same statistical parameters 0.879 (mean), 0.841 (median) and 0.284 (standard deviation). Figure 19 shows the results of the ratio $IDR_{k,CP} / IDR_{k,DP}$ between the $IDRs$ at the kth storey of the frames ($k = 1,2,3,4$), obtained with the CP and the DP modelling approaches. As can be seen, there are many cases where a certain ground motion leads to a different global mechanism just as a result of using a different modelling approach. This can be seen by the fact that, for a given frame and ground motion, maximum $IDRs$ concentrate at different storeys for the two modelling approaches.
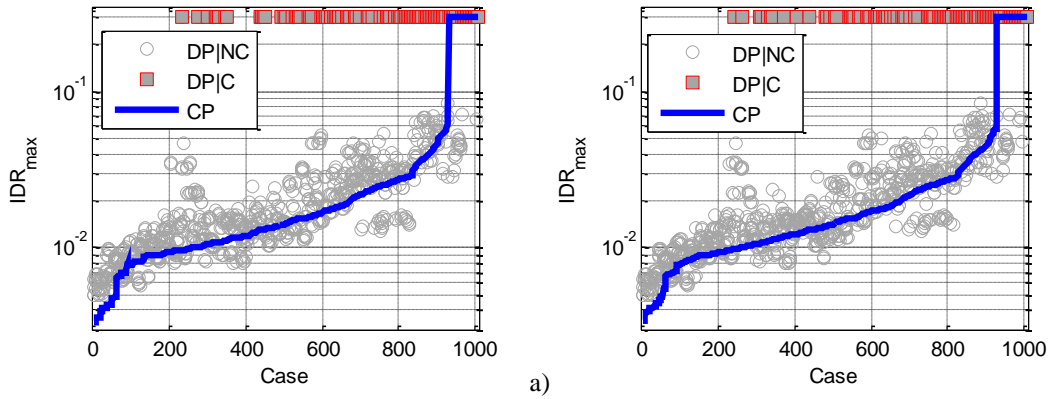

Figure 18. Comparison of the maximum interstorey drift ratios over all storeys estimated using the CP and DP modelling approaches for all frames and all ground motions; C and NC stand for collapse and non-collapse cases.

As shown in Fig. 19a, there is a moderate agreement between the IDR predictions obtained with the two modelling approaches for the first storey (i.e. the ground storey). The results obtained for the upper storeys indicate the CP modelling approach is more prone to generate a plastic mechanism that concentrates maximum $IDRs$ at the second floor (see the concentration of points on the left hand side region of Fig. 19b). On the contrary, the DP modelling approach appears to distribute the damage over the third and fourth storeys. Evidence of this can be seen in some cases of Figs. 19c and 19d, where larger $IDRs$ are observed in these two storeys for this modelling approach, while those obtained with the CP model are negligible. These differences are not generalized, which means that in some cases the type of mechanism observed for the two models is the same. Hence, these different deformation patterns of the frames suggest these differences are occurring for some of the ground motions because hinges are not developing in the same beams and in columns, thus creating a different post elastic response of the frames.
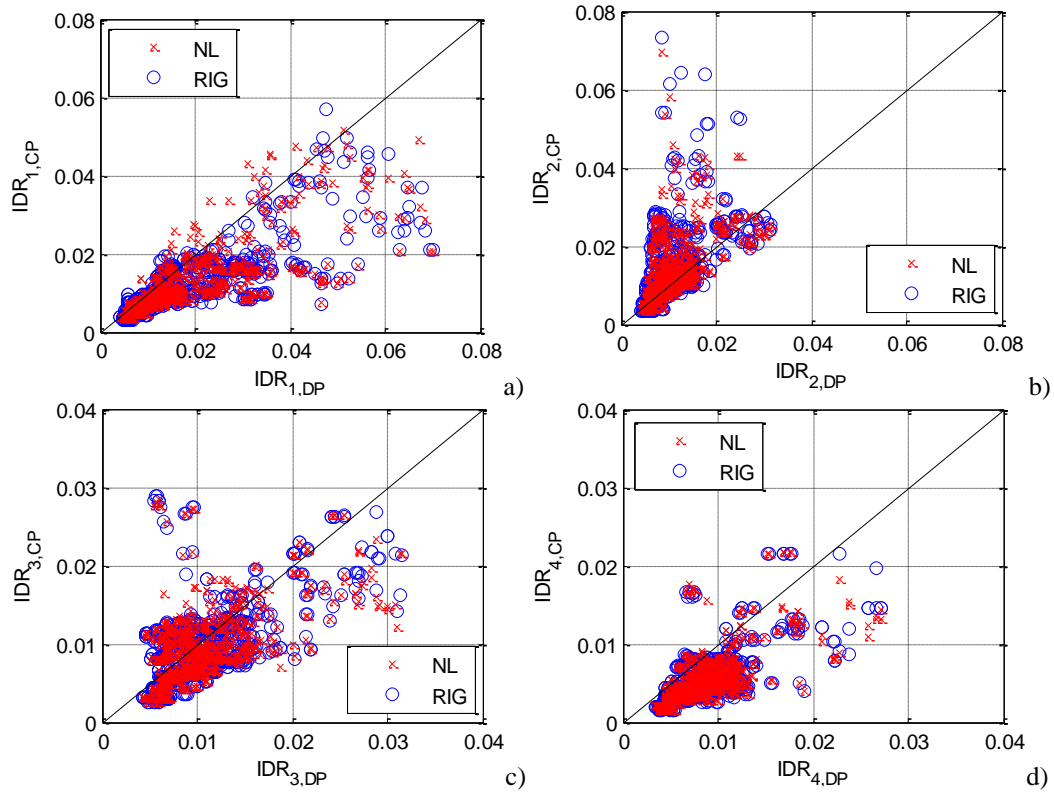
Figure 19. Comparison of the interstorey drift ratios at each storey estimated using the CP and DP modelling approaches for all frames and all ground motions.

Table 3 shows the central values and the dispersion estimates calculated for the results shown in Fig. 19. Mean ratios of 0.72 and 0.75 were observed for the first storey in models with RIG and NL joints, respectively, corroborating the apparent moderate correlation mentioned before for this case. As seen in Table 3, for the second storey, the standard deviation of $IDR_{2,CP} / IDR_{2,DP}$ is large, which also points to the lack of DP models concentrating deformations at this storey. Instead, the damage accumulation of DP models (due to excessive IDR) is concentrated at the first floor in some cases while, in others, damage occurs along the upper storeys. Still, the number of cases where the latter is observed is lower than the cases where deformations are concentrated at the first floor, since the means of $IDR_{3,CP} / IDR_{3,DP}$ and $IDR_{4,CP} / IDR_{4,DP}$ are in the range 0.97-1.09.

Table 3. Statistical results of the $IDR_{k,CP} / IDR_{k,DP}$ ratios presented in Fig. 19

Joints	RIG			NL		
Storey	Mean	Median	σ	Mean	Median	σ
1	0.721	0.705	0.225	0.748	0.723	0.228
2	1.328	1.097	0.779	1.314	1.100	0.794
3	0.959	0.806	0.542	0.942	0.820	0.536
4	0.624	0.586	0.251	0.640	0.590	0.260

8.5.2.2 Chord rotation in columns

Figure 20 shows the results of the comparison between the maximum chord rotations obtained in the converged analyses using the wo modelling approaches and considering also the previously referred condition limiting the admissible maximum *IDR*. Fig. 20a shows the linear correlation between the maximum chord rotation in columns obtained with the CP and DP models and RIG joints. When analysing the linear trend between the maximum chord rotations, a slope of 0.72 is observed, which is not entirely consistent with the 1.03 value found for the results obtained with pushover analyses.
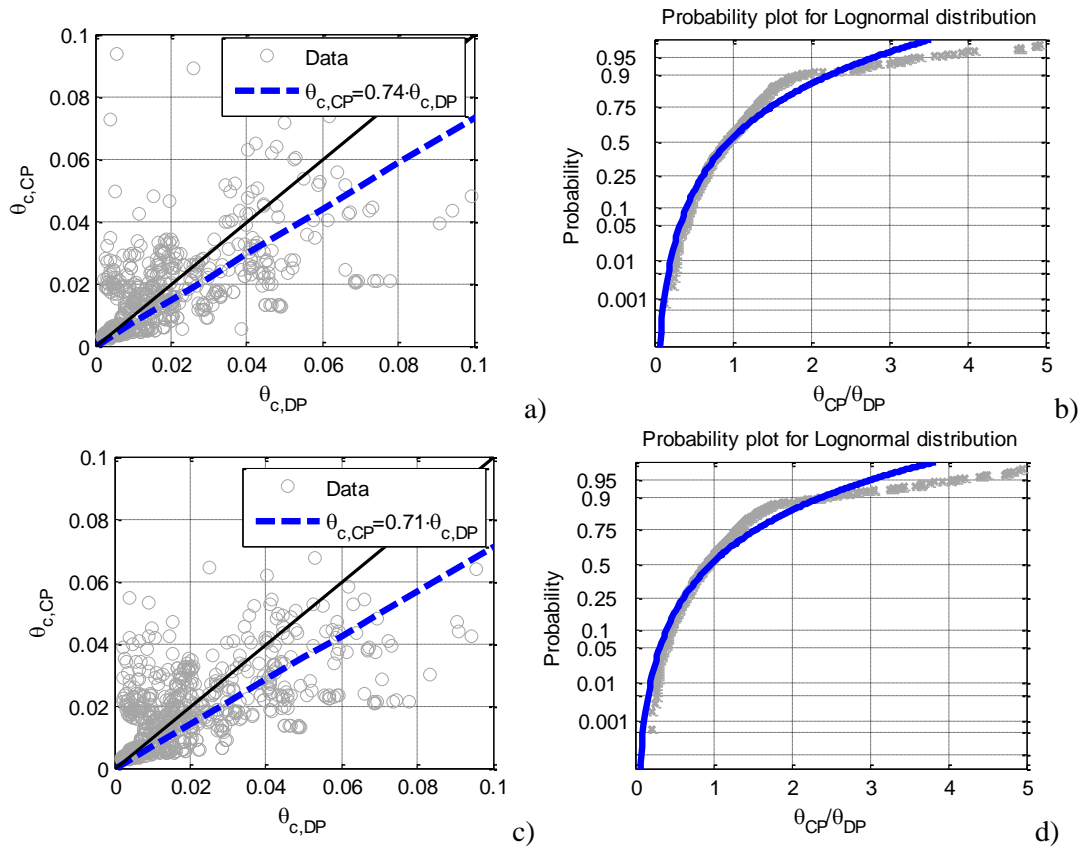

Figure 20. Comparison of the chord rotations in columns obtained with CP and DP models for frames with RIG (a) and NL joints (c), and representation of the corresponding probability plots of the ratios $\theta_{c,CP} / \theta_{c,DP}$ ((b) and (d), respectively for models with RIG and NL joints).

This difference can be interpreted in light of the previous discussion addressing the *IDR*s. There are cases (Fig. 20a) where the predictions of the CP model increase and there is no similar increase in the deformations obtained with the DP model, while in other cases the opposite occurs. Similar observations are made in the results obtained with the NL joints. The lognormal model fitted to the data using the maximum likelihood method has a mean $\mu_{\ln \varepsilon_{\theta_c}}$ of -0.043 (median of 0.958) and a standard deviation $\sigma_{\ln \varepsilon_{\theta_c}}$ of 0.654, for the results obtained with RIG joints, and a mean $\mu_{\ln \varepsilon_{\theta_c}}$ equal to -0.025 (median of 1.026) and a standard deviation $\sigma_{\ln \varepsilon_{\theta_c}}$ equal to 0.686, for the results

obtained with the NL joints. The corresponding probability plots are shown in Fig. 20b and in Fig. 20d. Although these values of $\mu_{\ln \varepsilon_{\theta_c}}$ are consistent with those found with the pushover analysis (-0.035 and -0.003 for models with RIG and NL joints, respectively), variability increases significantly in the results of the dynamic analysis ($\sigma_{\ln \varepsilon_{\theta_c}}$ increases from 0.250 to 0.654 and from 0.228 to 0.686 for the results obtained with RIG and NL joints, respectively).

Due to the different global behaviour observed in Section 8.5.1.1 between frames F1-F24 and frames F25-F48, a separated analysis of the ε_{θ_c} ratios was performed, disaggregating the obtained results between these two classes and attempting to disaggregate the different component behaviour and the global deformation mechanisms that causes the referred increase of $\sigma_{\ln \varepsilon_{\theta_c}}$.

Figure 21 shows the same comparisons made in Fig. 20 but separating the chord rotation and ε_{θ_c} values of frames F1-F24 from those of frames F25-F48. The results shown in Fig. 21 confirm the existence of two governing mechanisms: one that exhibits large column chord rotations (F1-F24) and another where smaller values are found (F25-F48). The results corresponding to frames F1-F24 (Fig. 21a; Fig. 21e) can be seen to involve large inelastic deformations in columns, while in frames F25-F48 (Fig. 21c; Fig. 21g) the maximum column chord rotation is either still elastic or involves a small level of inelasticity. Differences between the behaviour of the columns of frames F24-F48 are nonetheless observed. The generality of the rotations obtained using the DP model are up to 0.020rad, which indicates that columns are in the elastic range. On the other hand, in some cases, the CP model presents higher inelastic incursions, a trend that increases when NL joints are considered (see Fig. 21g). These facts indicate that the CP model leads to higher inelastic demands in beams while, at the same type, it explores the ductility of the columns, mostly on the second floor, as discussed in the previous section. With respect to the probability plots shown in Figs. 21b, 21d, 21f and 21h, it can be seen that the ε_{θ_c} ratios obtained for the disaggregated sets of results have different variability levels depending on the extent of the inelastic rotations that are observed.
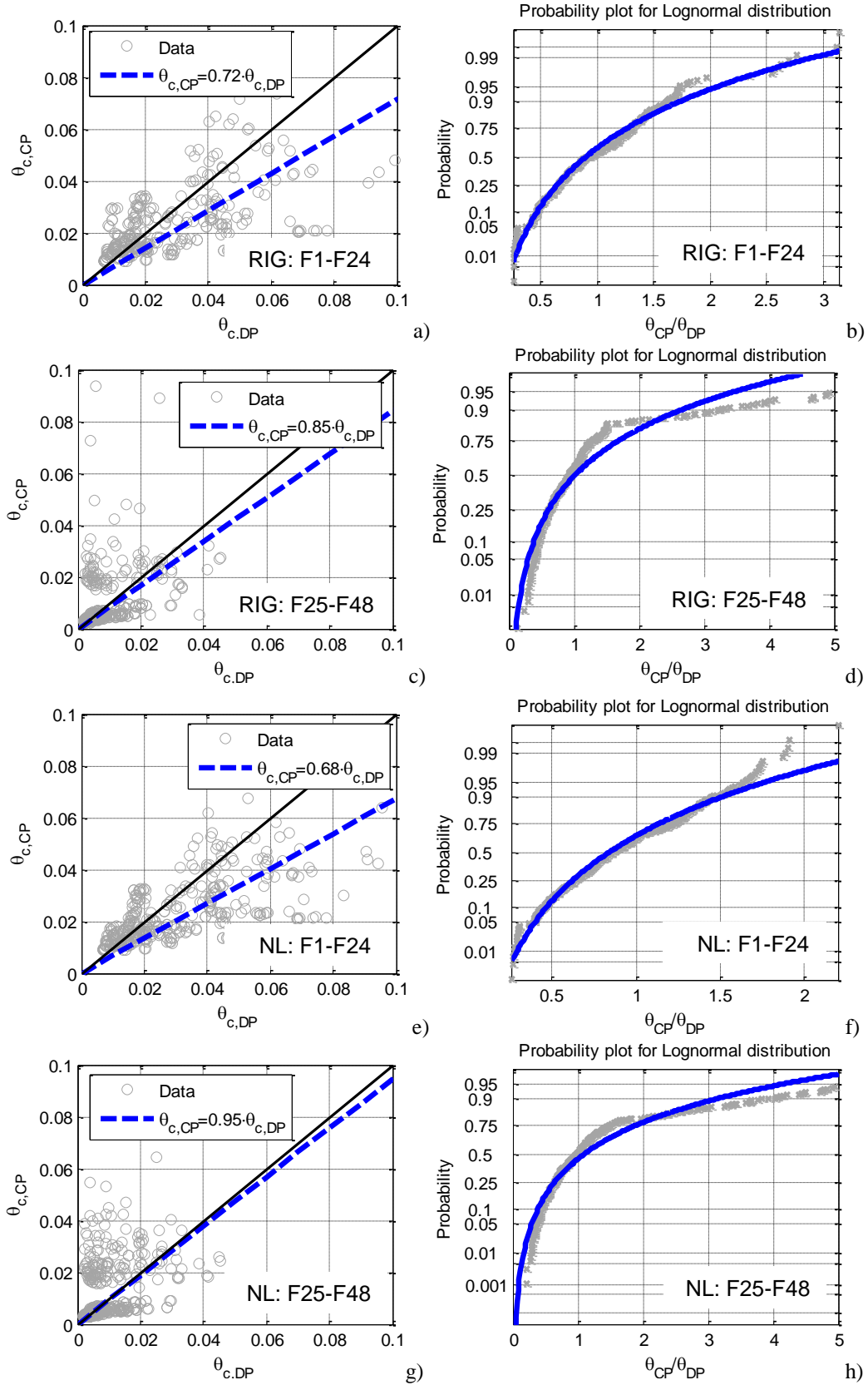
Figure 21. Comparison of the chord rotations obtained with CP and DP models for frames F1-F24 with RIG (a) and NL joints (e), and representation of the corresponding probability plots of the ratios $\theta_{c,CP} / \theta_{c,DP}$ ((b) and (f), respectively for models with RIG and NL joints), for frames F25-F48 with RIG (c) and NL joints (g), and representation of the corresponding probability plots of the ratios $\theta_{c,CP} / \theta_{c,DP}$ ((d) and (h), respectively for models with RIG and NL joints).

8.34

The statistical parameters of the lognormal distributions fitted to the ε_{θ_c} ratios are shown in Table 4. As can be seen, there is a reduction of $\sigma_{\ln \varepsilon_{\theta_c}}$ when comparing these results with those obtained when using the entire dataset. Still, the magnitude of $\sigma_{\ln \varepsilon_{\theta_c}}$ for frames F1-F24 is approximately 2 times the value that was obtained when using pushover analysis. Nevertheless, the dispersion of the regression lines found in Fig. 6 for the pushover analyses results is now seen to be larger for higher values of θ_c, thus partially justifying the differences seen in the nonlinear dynamic analysis case. Based on Table 4, if the frame is expected to have a failure mode governed by the behaviour of columns, a conservative value of 0.45 can be suggested for $\sigma_{\ln \varepsilon_{\theta_c}}$ for cases with NL joints and of 0.50 for cases with RIG joints. These factors target structures whose expected failure mechanism involves a concentration of damage in the columns. It must be noted that the proposed factor includes not only the variability associated with the use of the model $\sigma_{\ln \varepsilon_{\theta_c}}$ but also the influence of the record-to-record variability. Therefore, it can be seen as conservative estimate for the modelling compatibility dispersion factor, i.e. the term $\sigma^2_{\ln \varepsilon_{Co}} + 2 \cdot \rho_{D_{alt} \cdot \varepsilon_{Co}} \cdot s_{\ln D_{alt}} \cdot \sigma_{\ln \varepsilon_{Co}}$ in Eq. (10).

Table 4. Statistical results of the $\theta_{c,CP} / \theta_{c,DP}$ ratios presented in Fig. 21

Joints	Frames	$\mu_{\ln \varepsilon_{\theta_c}}$	Median ε_{θ_c}	$\sigma_{\ln \varepsilon_{\theta_c}}$
RIG	F1-F24	-0.104	0.902	0.503
RIG	F25-F48	-0.006	1.006	0.752
NL	F1-F24	-0.176	0.838	0.452
NL	F25-F48	0.095	1.099	0.808

8.5.2.3 Chord rotation in beams

Similar to the analysis performed in the previous section, Fig. 22 (for models with RIG joints) and Fig. 23 (for models with NL joints) shows the results of $\theta_{b,CP} / \theta_{b,DP}$ for frames F1-F24 and frames F25-F48. It can be seen that results observed for frames F1-F24 are concentrated mostly in the region for which larger differences between the beam chord rotations were observed in the pushover analyses (i.e. below 0.02rad). As a result, the responses obtained for frames F1-F24 are mostly within the range where ε_{θ_b} was higher (1.50) in the pushover analyses. Consequently, large values for the $\theta_{b,CP} / \theta_{b,DP}$ ratios were observed. For the case of frames F25-F48, Figs. 22c and 23c, the number of points with larger deformations increases (with respect to the results obtained with pushover analyses) and, consequently, a larger value of the slope is observed (in both cases above 1.0).
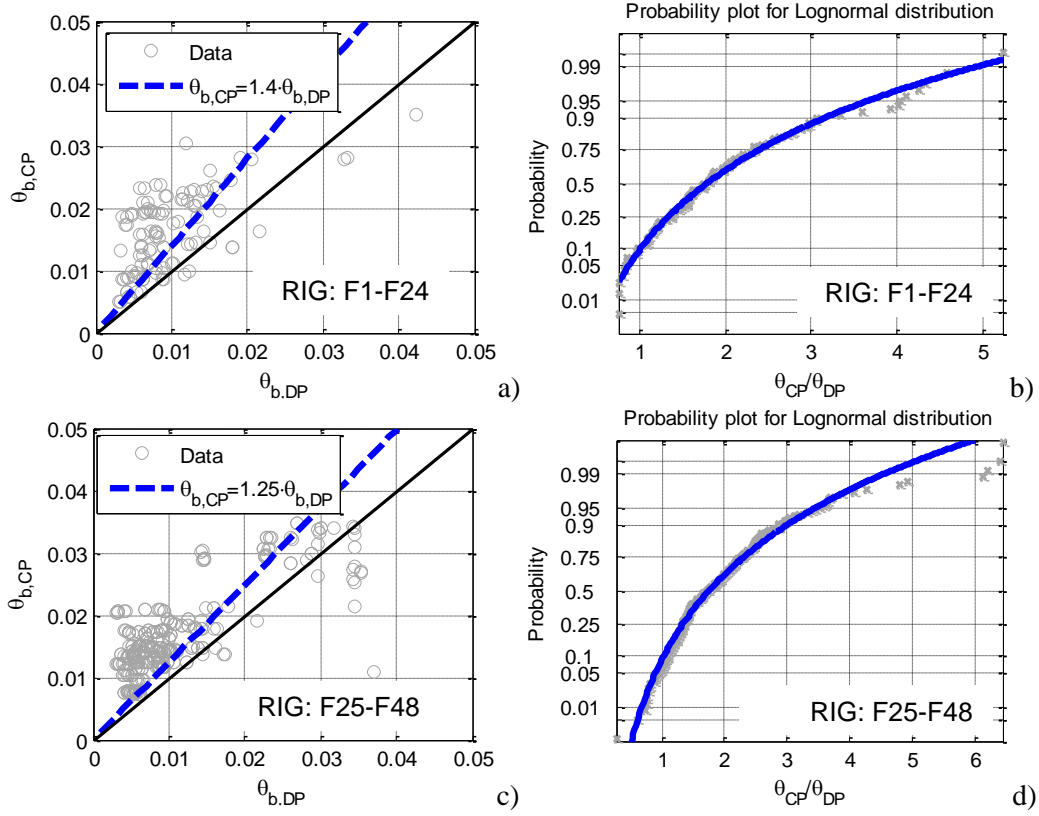
Figure 22. Comparison of the chord rotations obtained in beams with CP and DP models for frames F1-F24 (a) and frames F2-F48 (c) with RIG joints, and representation of the corresponding probability plots of the ratios $\theta_{b,CP} / \theta_{b,DP}$ for frames F1-F24 (b) and frames F2-F48 (d).
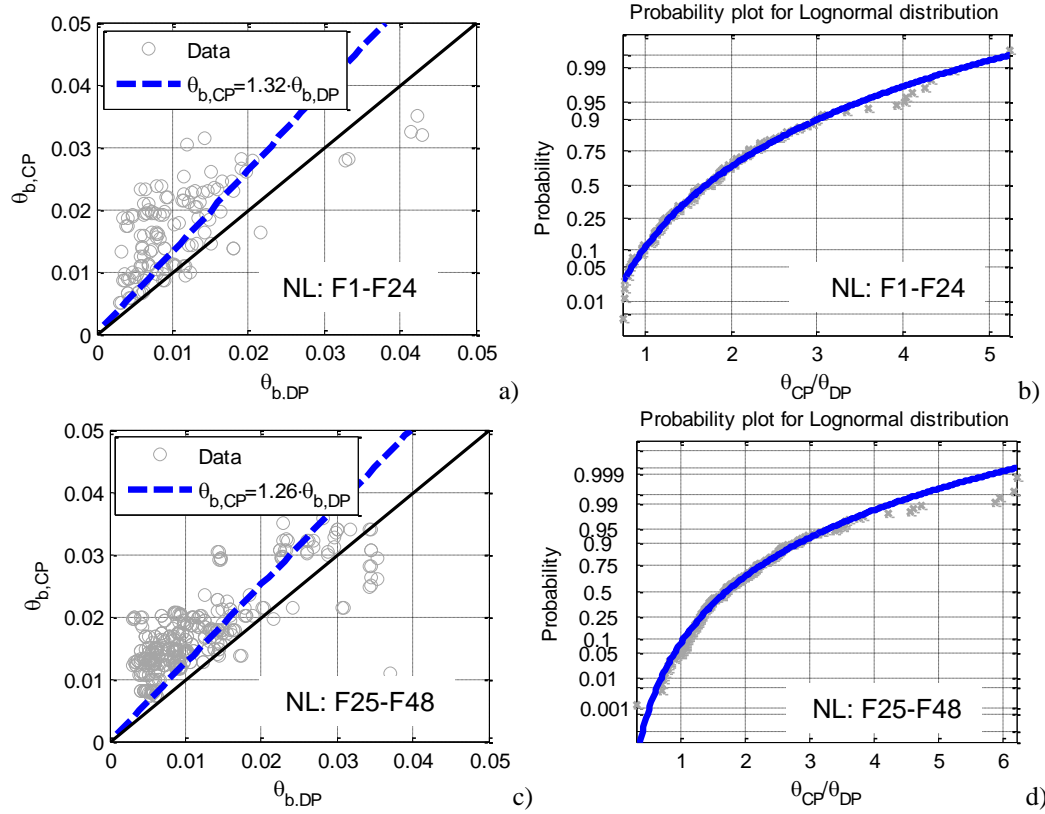

Figure 23. Comparison of the chord rotations obtained in beams with CP and DP models for frames F1-F24 (a) and frames F2-F48 (c) with NL joints, and representation of the corresponding probability plots of the ratios $\theta_{b,CP} / \theta_{b,DP}$ for frames F1-F24 (b) and frames F2-F48 (d).

Table 5 provides the statistical parameters of the lognormal curves fitted to the $\theta_{b,CP}/\theta_{b,DP}$ ratios in the probability plots shown in Figs. 22 and 23. It must be noted that the results obtained are biased by the fact that all datasets include a large concentration of points within the range of responses where ε_{θ_b} is larger, as identified during the analysis of the results obtained for the pushover analyses. Bearing that in mind, the range of values observed for the dispersion (0.40-0.44) was seen to be unaffected by the dynamic analysis, especially when compared with variations observed between the nonlinear static and dynamic analyses results.

Table 5. Statistical results of the $\theta_{b,CP}/\theta_{b,DP}$ ratios presented in Figs 22 and 23.

Joints	Frames	$\mu_{\ln \varepsilon_{\theta_c}}$	Median ε_{θ_c}	$\sigma_{\ln \varepsilon_{\theta_c}}$
RIG	F1-F24	0.536	1.709	0.435
RIG	F25-F48	0.561	1.752	0.410
NL	F1-F24	0.519	1.680	0.417
NL	F25-F48	0.535	1.707	0.395

The fact that the response of beams is less affected by the hysteretic behaviour during dynamic analyses is also connected with the fact that the unscaled ground motion set is not able to induce sufficiently large deformation levels in the stronger frames to mobilize the nonlinear cyclic response of the frames. Furthermore, the differences between the response of beams obtained with the two models becomes less relevant when NL joints are considered as they reduce the rotations obtained in these components with the CP model. As discussed before for the pushover analysis results, differences associated with the shear span (which is fixed in the CP models) appear to play a significant role in the behaviour of beams. This role may even be more important in the results of dynamic analyses due to the changes in the global deformation pattern of frames that was observed between the results of CP and DP models that could be induced by the early yielding of beams.

8.5.3 Results from cloud analysis

8.5.3.1 Chord rotation in columns

Figure 24 shows four examples of the probabilistic seismic demand models (PSDMs) developed using linear regression analysis in the log-log space and correlating the value of AvgSa of each ground motion record with the value of the maximum chord rotation obtained in columns. As can be seen, considering the generic far-field set of ground motions adopted by Moeli *et al.* (2018) leads to a PSDM for each frame that involves different types of demand evolutions depending on the properties of the frame. Figures 24a and 24b show two cases where the variability of the regression model fitted to the data is similar, as illustrated by the 95% confidence bounds

represented by dashed lines. The cases where numerical collapse or excessive *IDR*s were observed with the DP (C_{DP}) or in the CP (C_{CP}) models are also identified in Fig. 24.
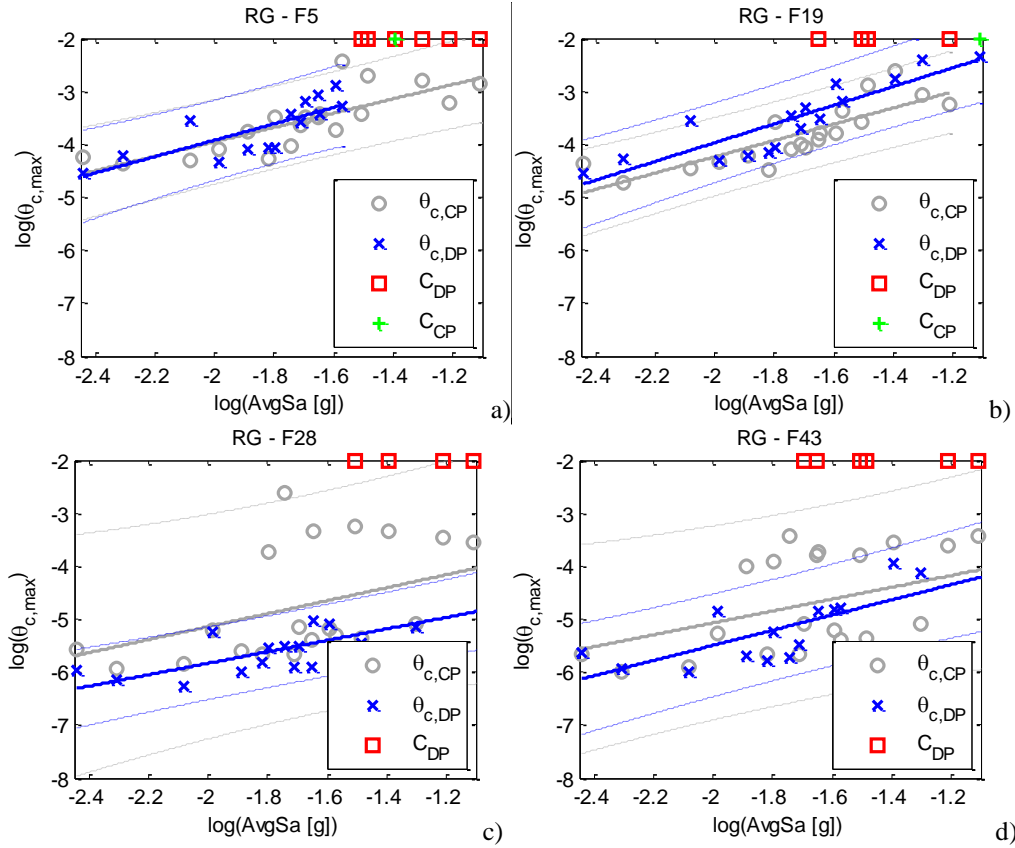

Figure 24. Examples of regression models fitted to establish the power model correlating the maximum chord rotation of columns $\theta_{c,max}$ obtained with DP and CP models for frames F5 (a), F19 (b), F43 (c) and F28 (d) with RIG joints; C stands for cases considered as collapse.

The complete set of PSDMs (regression models fitted to the AvgSa-$\theta_{c,max}$) for frames with RIG joints is shown in Appendix A. Similar trends were observed for models simulated with NL joints, and the corresponding complete set of PSDMs that were obtained is shown in Appendix B. Similar slopes and standard deviations of the fitting error are observed Figs. 24a and 24b. On the other hand, the plots of Figs. 24c and 24d present the cases where part of the analysis results of the CP model follow the same trend of those obtained with the DP model, while another part of these results exhibit column chord rotations with large values (around 0.05rad) that are not reached by the DP model and cases of C_{DP} are obtained instead. The fact that two types of responses are obtained for Frame F28 is clear in Fig. 24c, where three ground motions induce larger rotations than those observed with the DP model for AvgSa values between 0.15g and 0.20g, while four other records induce $\theta_{c,max,CP}$ values that in the linear elastic range ($\theta_{c,max,CP}$ values around 0.003rad). Similar observations can be made for Fig. 24d that also exhibits some values of $\theta_{c,max,DP}$ that are in the elastic range while others are much larger.

Figure 25 shows the estimates obtained for the ratio $\sigma_{\ln \theta_{c,max,CP}} / \sigma_{\ln \theta_{c,max,DP}}$ (used as a direct conversion factor in Eq. (35) to calculate $\beta_{\ln \theta_c, DP \cdot \varepsilon_{Co}}$ of Eq. (10) using only $\sigma_{\theta_{c,max,DP}}$) by comparing the PSDMs developed for each frame. The results shown in Figs. 25a and 25b refer to models with RIG and NL joints, respectively.
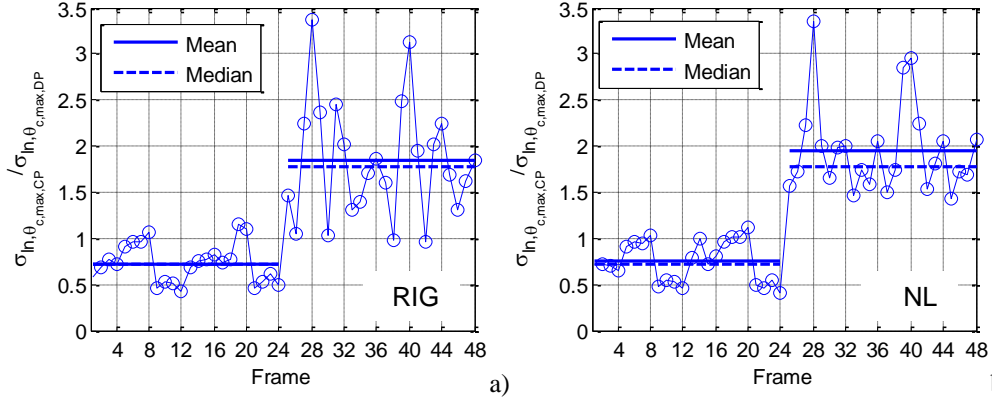

Figure 25. Estimates obtained for $\sigma_{\ln \theta_{c,max,CP}} / \sigma_{\ln \theta_{c,max,DP}}$) using the PSDMs for the maximum chord rotation observed in columns ($\theta_{\ln c,max}$) for each frame assuming that beam-column joints are RIG (a) or NL (b).

In the previous sections, significant differences were observed in the estimates of $\beta_{\ln D_{alt} \cdot \varepsilon_{Co}}$ between frames F1-F24 and frames F25-F48. As seen in Fig. 25, these differences are also observed in the RMSE of the regression models (used to represent $\sigma_{\ln c,max,CP}$ and $\sigma_{\ln c,max,DP}$). In both Fig. 25a and Fig. 25b, large $\sigma_{\ln \theta_{c,max,CP}} / \sigma_{\ln \theta_{c,max,DP}}$ ratios are observed for frames F25-F48, while the results of frames F1-F24 have lower frame-to-frame variability and are closer to 1.0. Table 6 summarizes the values of the statistical parameters of the $\sigma_{\ln \theta_{c,max,CP}} / \sigma_{\ln \theta_{c,max,DP}}$ factors obtained by the cloud analysis for column chord rotations.

Table 6. Statistical results of the $\sigma_{\ln \theta_{c,max,CP}} / \sigma_{\ln \theta_{c,max,CP}}$ ratios presented in Fig. 25

Joints	Frames	Mean $\sigma_{\ln \theta_{c,max,CP}} / \sigma_{\ln \theta_{c,max,CP}}$	Median $\sigma_{\ln \theta_{c,max,CP}} / \sigma_{\ln \theta_{c,max,CP}}$	SD of $\sigma_{\ln \theta_{c,max,CP}} / \sigma_{\ln \theta_{c,max,CP}}$
RIG	F1-F24	0.755	0.747	0.204
RIG	F25-F48	1.832	1.769	0.553
NL	F1-F24	0.771	0.775	0.227
NL	F25-F48	1.903	1.728	0.477

Figure 26 shows the disaggregation of the results presented in Fig. 25 according to the value of the geometrical reinforcement ratio adopted for the columns of each frame, $\rho_{tot,col}$ (see Table 1). The results show (Figs. 26a; 26c) that for cases where the column density is lower (frames F1-

F24), considering a low value for $\rho_{tot,col}$ leads to the previously referred concentration of damage and large inelastic deformations at these elements, potentially at the first storey. In this case (i.e. for $\rho_{tot,col}$ approximately 0.5%, which is typical of columns with non-ductile/low ductility) and since pure shear failure mechanisms were not observed, the value of $\sigma_{\ln\theta_{c,max,CP}} / \sigma_{\ln\theta_{c,max,DP}}$ that is observed is around 0.50, which indicates that the record-to-record variability determined by DP models can be assumed to be 2 times the reference value $\sigma_{\ln\theta_{c,max,CP}}$. For frames with the same properties but with larger column ductility with respect to the previous case, due to an increase of $\rho_{tot,col}$ to 1%, $\sigma_{\ln\theta_{c,max,CP}} / \sigma_{\ln\theta_{c,max,DP}}$ is on average 1.0. The variations observed in this case are larger in models with RIG joints. Finally, columns with even larger ductility ($\rho_{tot,col}$ equal to 1.8%), a consistent decay of the value of $\sigma_{\ln\theta_{c,max,CP}} / \sigma_{\ln\theta_{c,max,DP}}$ is observed, going down to an average value close to 0.80.

The results obtained for frames F25-F28 (that have 0.50x0.50m^2 columns instead of 0.30x0.30m^2) shows that there is a larger influence of factors other than $\rho_{tot,col}$. Particularly in the case where NL joints were considered (Fig. 26d), it is clear that the effect of the beam ductility induces different levels of column responses, although the importance of these elements in the safety assessment may be lower than for frames F1-F24.
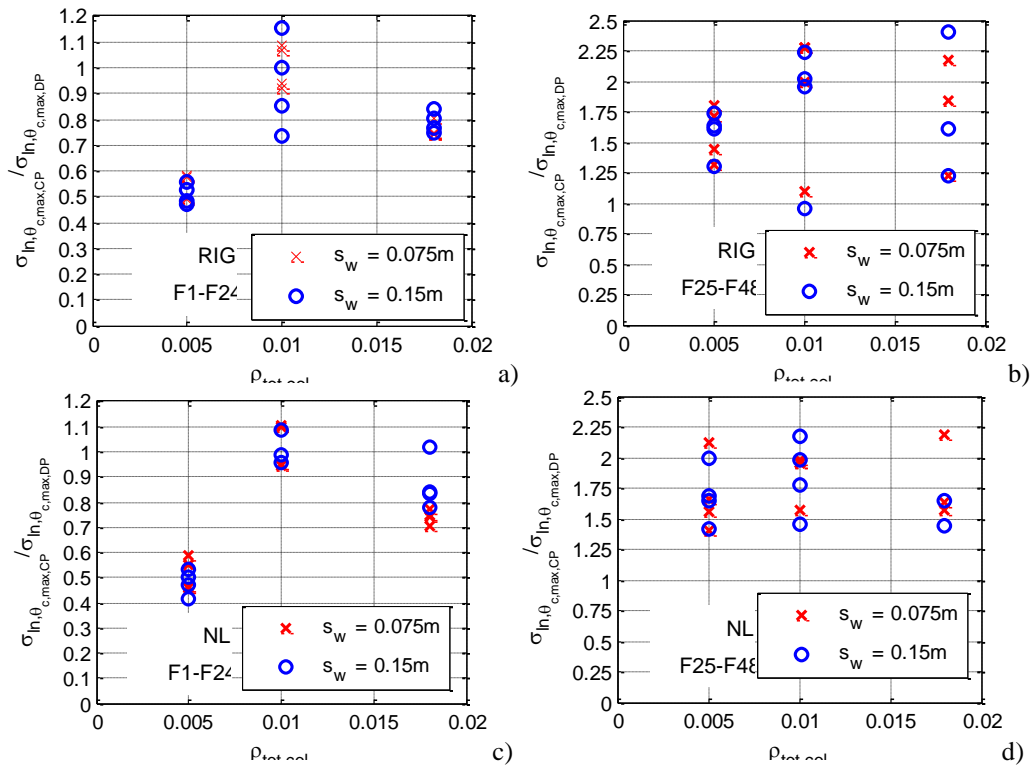

Figure 26. Disaggregation of the results presented in Fig. 25 according to the value of the geometrical reinforcement ratio adopted for the columns of each frame, $\rho_{tot,col}$ for frames F1-F24 (a, c) and for frames F25-F48 (b, d) considering the cases with RIG (a, b) and NL (c, d) joints.

8.5.3.2 Chord rotation in beams

To complement the previous discussion addressing the variations of $\sigma_{\ln\theta_{b,max,CP}}/\sigma_{\ln\theta_{b,max,DP}}$ with the behaviour and the design properties of frames F1-F24 and F25-F48, Fig. 27 shows the PSDMs obtained for $\theta_{b,max,DP}$ and $\theta_{b,max,CP}$ for the same cases analysed before in Fig. 24. The results show that frames F5 and F19 have PSDMs that are very similar, with beam rotations mostly within the elastic range, and where the same variability parameters $\sigma_{\ln\theta_{b,max,CP}}$ and $\sigma_{\ln\theta_{b,max,CP}}$ have similar magnitudes, as can be seen by the amplitude of the confidence bounds. Nevertheless, the regression lines indicate that different power factor are applicable for the CP and DP PSDM models (0.913 (RG-F5) and 0.98 (RG-F19) for the DP models and 0.845 (RG-F5). and 1.23 (RG-F19) for the CP models).

Figure 28 shows the disaggregation of the ratio $\sigma_{\ln b,max,CP}/\sigma_{\ln b,max,DP}$ according to the frame and the type of joint model used in the simulations. Conversely to the observations made for $\theta_{\ln c,max}$, frames F1-F24 lead to large values of $\sigma_{\ln b,max,CP}/\sigma_{\ln b,max,DP}$, often larger than 1.50. No pattern can be identified for the different frames. On the other hand, a lower variation is observed for frames F25-F48 which ranges between 0.40 and 1.00. Table 7 summarizes the data presented in Fig. 28.
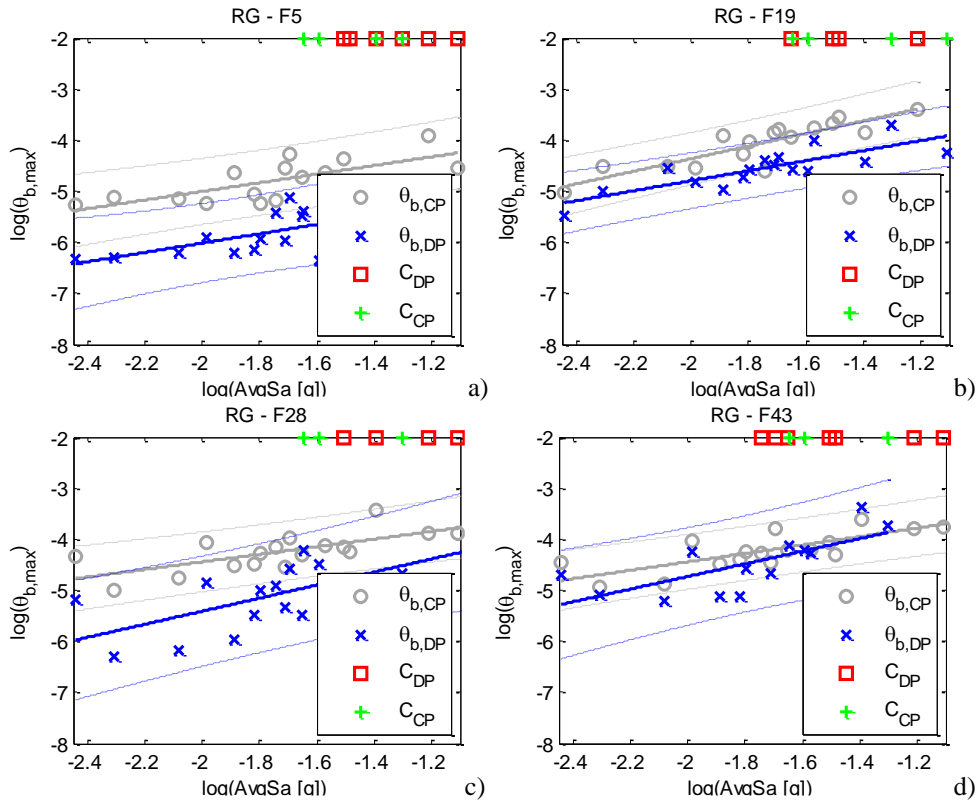

Figure 27. Examples of regression models fitted to establish the power model correlating the maximum chord rotation of beams $\theta_{b,max}$ obtained with DP and the CP models for frames F5 (a), F19 (b), F28 (c) and F43 (d) with RIG joints; C stands for cases considered as collapse.
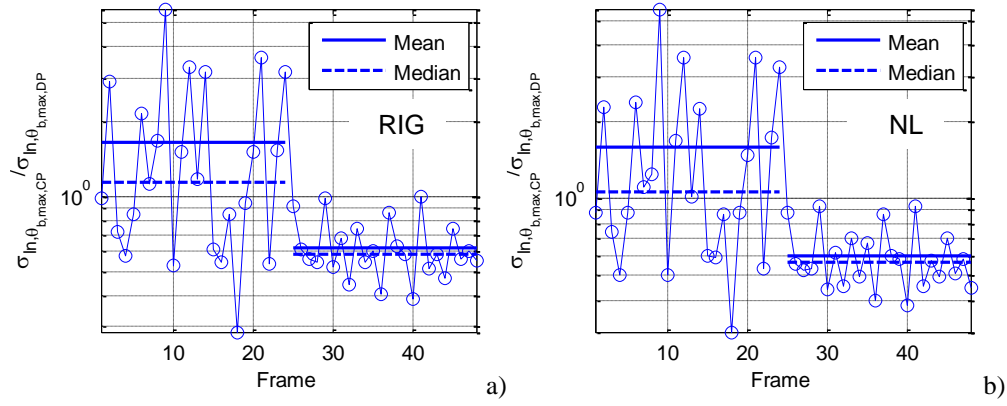
Figure 28. Estimates obtained for $\sigma_{\ln b,\max,CP} / \sigma_{\ln b,\max,DP}$) using the PSDMs for the maximum chord rotation observed in beams ($\theta_{\ln b,\max}$) for each frame assuming that beam-column joints are RIG (a) or NL (b).

Table 7. Statistical results of the $\sigma_{\ln \theta_{b,\max,CP}} / \sigma_{\ln \theta_{b,\max,CP}}$ ratios presented in Fig. 28

Joints	Frames	Mean $\sigma_{\ln \theta_{b,\max,CP}} / \sigma_{\ln \theta_{b,\max,DP}}$	Median $\sigma_{\ln \theta_{b,\max,CP}} / \sigma_{\ln \theta_{b,\max,DP}}$	SD of $\sigma_{\ln \theta_{b,\max,CP}} / \sigma_{\ln \theta_{b,\max,DP}}$
RIG	F1-F24	1.662	1.146	1.133
RIG	F25-F48	0.625	0.587	0.168
NL	F1-F24	1.956	1.780	0.490
NL	F25-F48	0.750	0.722	0.222

The results shown in Fig. 28 and Table 7 are clear indicators that contrary to the response of columns, the maximum chord rotation in beams is more compatible in cases where significant nonlinear response is observed in these elements (i.e. frames F25-F48). In order to analyse the variation of these results with $\rho_{tot,col}$ and with the beam reinforcement ratios, Fig. 29 shows the variations of the results for frames F25-F48 considering the cases of RIG joints (Fig. 29a; b) and NL joints (Fig. 29c;d).

As can be seen, the variation of $\sigma_{\ln \theta_{b,\max,CP}} / \sigma_{\ln \theta_{b,\max,DP}}$ is insensitive to the column reinforcement ratios $\rho_{tot,col}$. On the other hand, a variation is observed as a function of the ratio between the area of the reinforcing bars adopted at the top and bottom of beam sections. The $\sigma_{\ln \theta_{b,\max,CP}} / \sigma_{\ln \theta_{b,\max,DP}}$ ratios are closer to 1.0 when the bottom reinforcement is defined as 50% of the top one. Conversely, considering a symmetric reinforcement leads to a larger over prediction of the variability obtained by the DP model. It must be noted that these results, which converge to mean ratios of 0.50 and 0.75 for cases of symmetric and non-symmetric reinforcement configurations, did not account for the effective width of the beams.
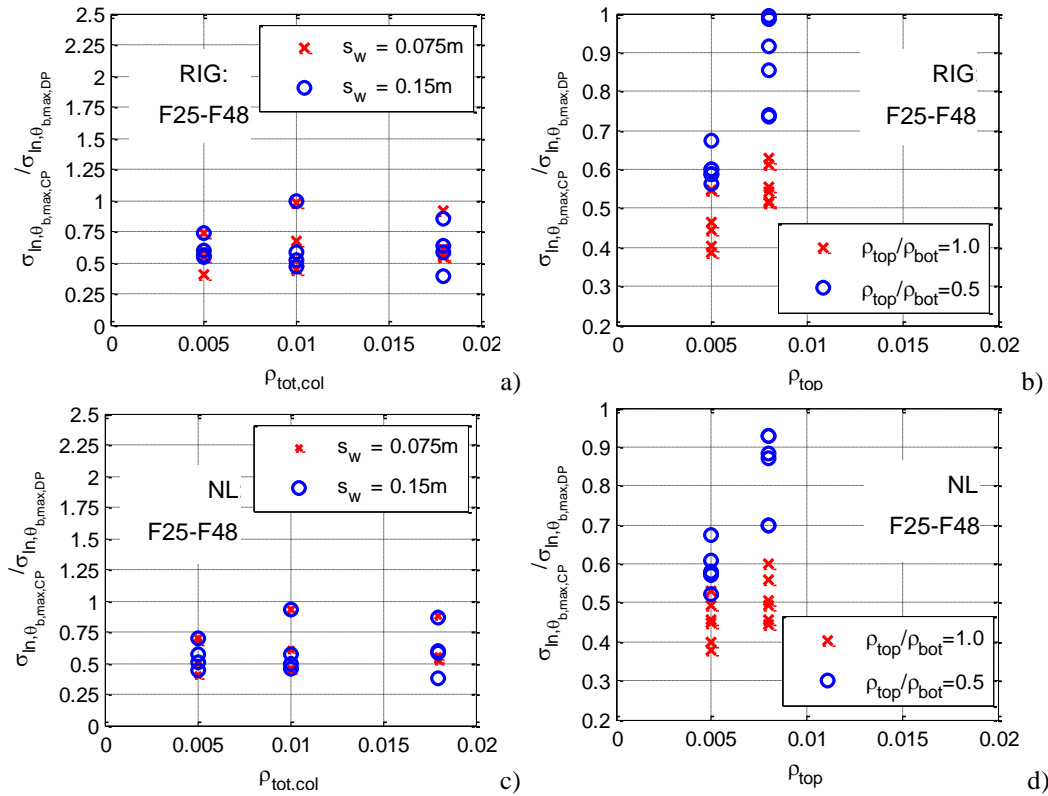
Figure 29. Disaggregation of the results presented in Fig. 28 for frames F25-F48 according to the value of the geometrical reinforcement ratio adopted for the columns of each frame, $\rho_{tot,col}$ and the beam reinforcement ratios ρ_{top} and ρ_{bot} for the cases with RIG joints (a; b) and NL joints (c; d).

8.6 Conclusions

The presented study formulates and develops a methodology to calibrate modelling compatibility factors to be used with global safety factors that reduce the chord rotation capacity of columns and beams and the shear force capacity of columns in standard-based approaches. Due to the empirical nature of the capacity models usually adopted by seismic safety assessment standards, capacities were considered to be defined by an empirical model that is also used to simulate the structural response, as established for ASCE 41-13. Given this condition, it is possible to assume that modelling uncertainties for the local-level demands (chord rotations, shear forces) can be approximated by the uncertainty about the capacity, since the same model is used in both sides of the safety equation. Since alternative response modelling techniques can be used, it is necessary to establish a compatibility factor that allows converting the demands computed with this alternative modelling approach into those that would be obtained by the reference model. Bearing that in mind, a factor SF_D was proposed, which includes a random compatibility factor with parameters $\mu_{\ln \varepsilon_{Co}}$ and $\sigma_{\ln \varepsilon_{Co}}$ assuming to follow lognormal distribution, that is used to factor the results of the alternative modelling approach. A three-stage study including 48 four-storey RC frames with different levels of column and beam ductility and capacity was performed to establish

8.43

proposals for these parameters, considering the modelling approach proposed in Chapter 7 as the alternative one.

The first stage included the calibration of $\mu_{\ln \varepsilon_{C_o}}$ and $\sigma_{\ln \varepsilon_{C_o}}$ for the case where nonlinear static analysis is used to determine the structural response. The results of the pushover analysis indicated that the compatibility factors for column chord rotations have $\mu_{\ln \varepsilon_{\theta_c}}$ and $\sigma_{\ln \varepsilon_{\theta_c}}$ values of 0.15 and 0.25, respectively, applicable when the chord rotation demands $\theta_{c,DP}$ obtained from the alternative model are within the yielding rotation range. For demand values above the yielding region, $\mu_{\ln \varepsilon_{\theta_c}}$ and $\sigma_{\ln \varepsilon_{\theta_c}}$ values of -0.05 and 0.25 are suggested instead, respectively. For beam chord rotations, it was seen that the compatibility factor also varies significantly depending on the magnitude of the plastic deformations. Values of 0.40 and 0.25 are suggested for $\mu_{\ln \varepsilon_{\theta_b}}$ and $\sigma_{\ln \varepsilon_{\theta_b}}$ for cases where $\theta_{b,DP}$ is close to the corresponding yielding value, and values of 0.10 and 0.15 are suggested instead for $\mu_{\ln \varepsilon_{\theta_b}}$ and $\sigma_{\ln \varepsilon_{\theta_b}}$ when $\theta_{b,DP}$ is larger than the yielding rotation or some level of inelasticity is already observed in these components.

The second stage of the study analysed the case where nonlinear dynamic analysis is used to determine the structural response. In this situation, the compatibility between the record-to-record demand distribution of the reference model and that of the alternative model has to be accounted for. It was seen that using different modelling approaches and different ground motions may lead, in some cases, to the occurrence of different deformation patterns of the structure, namely patterns that concentrate deformations at different storeys or in different types of components. The value of parameter $\mu_{\ln \varepsilon_{\theta_c}}$ found in this case is smaller than the one obtained from the results of the pushover analyses, while the value of $\sigma_{\ln \varepsilon_{\theta_c}}$ was found to be larger instead. For the chord rotations of columns, the overall values that were observed for $\mu_{\ln \varepsilon_{\theta_c}}$ and $\sigma_{\ln \varepsilon_{\theta_c}}$ are -0.10 and 0.50, respectively, when rigid joints are considered, and -0.18 and 0.45, respectively, when flexible joints are considered instead. These values correspond to the set of frames whose deformation patter exhibited larger demand values in columns. For the case of beams, following the same principles, it was seen that $\sigma_{\ln \varepsilon_{\theta_b}}$ also increased with respect to the value obtained from the pushover analyses (from 0.25 to 0.40), and that $\mu_{\ln \varepsilon_{\theta_b}}$ is in line with the proposal for the elastic range in pushover analyses. It must be noted that the values of these parameters derived using dynamic analysis indirectly account simultaneously for the variation of the compatibility factor and the record-to-record variability of the demand.

Finally, the third stage of the study analysed a calibration strategy based on $\sigma_{\ln \theta_{c,\max,CP}} / \sigma_{\ln \theta_{c,\max,DP}}$, a simple factor able to directly modify the demand dispersion obtained with the alternative modelling approach. Several aspects were highlighted in the results, namely the importance of

the design properties of the building, which were seen to contribute significantly to the variations found in $\sigma_{\ln \theta_{b,\max,CP}} / \sigma_{\ln \theta_{b,\max,DP}}$. For cases involving mechanisms based on weak columns, a value of 0.80 for $\sigma_{\ln \theta_{c,\max,CP}} / \sigma_{\ln \theta_{c,\max,DP}}$ was seen to be adequate. The use of the cloud method as a way to calibrate generic factors was seen to be limited due to the moderate number of ground motions that was used and the variations in the deformation patterns that were observed. Therefore, future studies should focus more robust techniques to include multiple ground motion scenarios and assess the record-to-record variability based on incremental dynamic analysis or stripe analysis for certain seismic scenarios. By doing so, the possible systematization of the differences between the behaviours of the reference and of the alternate modelling strategies may allow for a clearer (i.e. less general but more robust) interpretation of $\sigma_{\ln \theta_{b,\max,CP}} / \sigma_{\ln \theta_{b,\max,DP}}$. Nevertheless, this study shows that the systematic inclusion of multiple types of buildings, consequently different levels and classes of seismic design, is instrumental for the correct calibration of these factors.
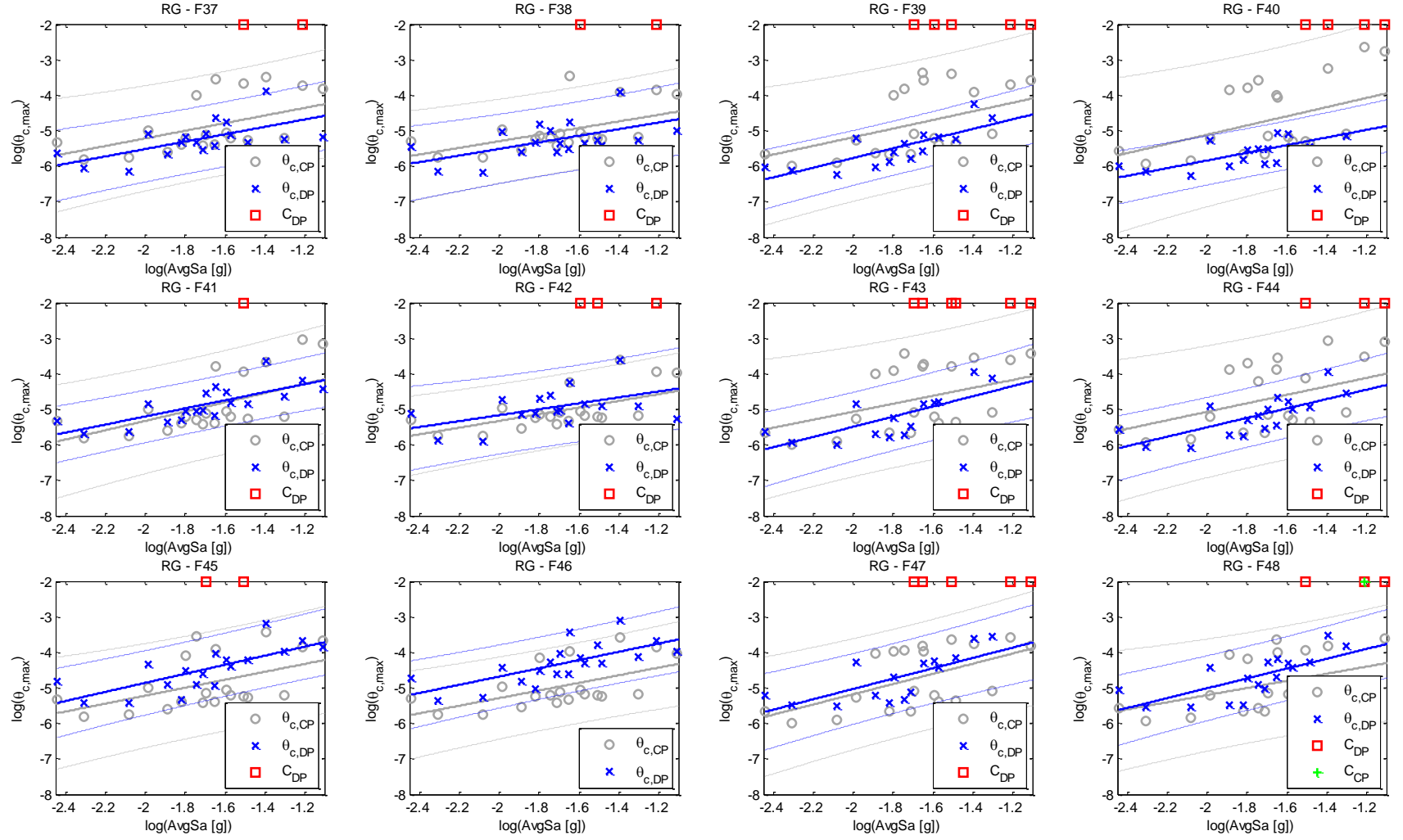
8.7 Appendixes

Appendix A. Results obtained with cloud analysis for the maximum chord rotation in columns using models DP-RIG and CP-RIG
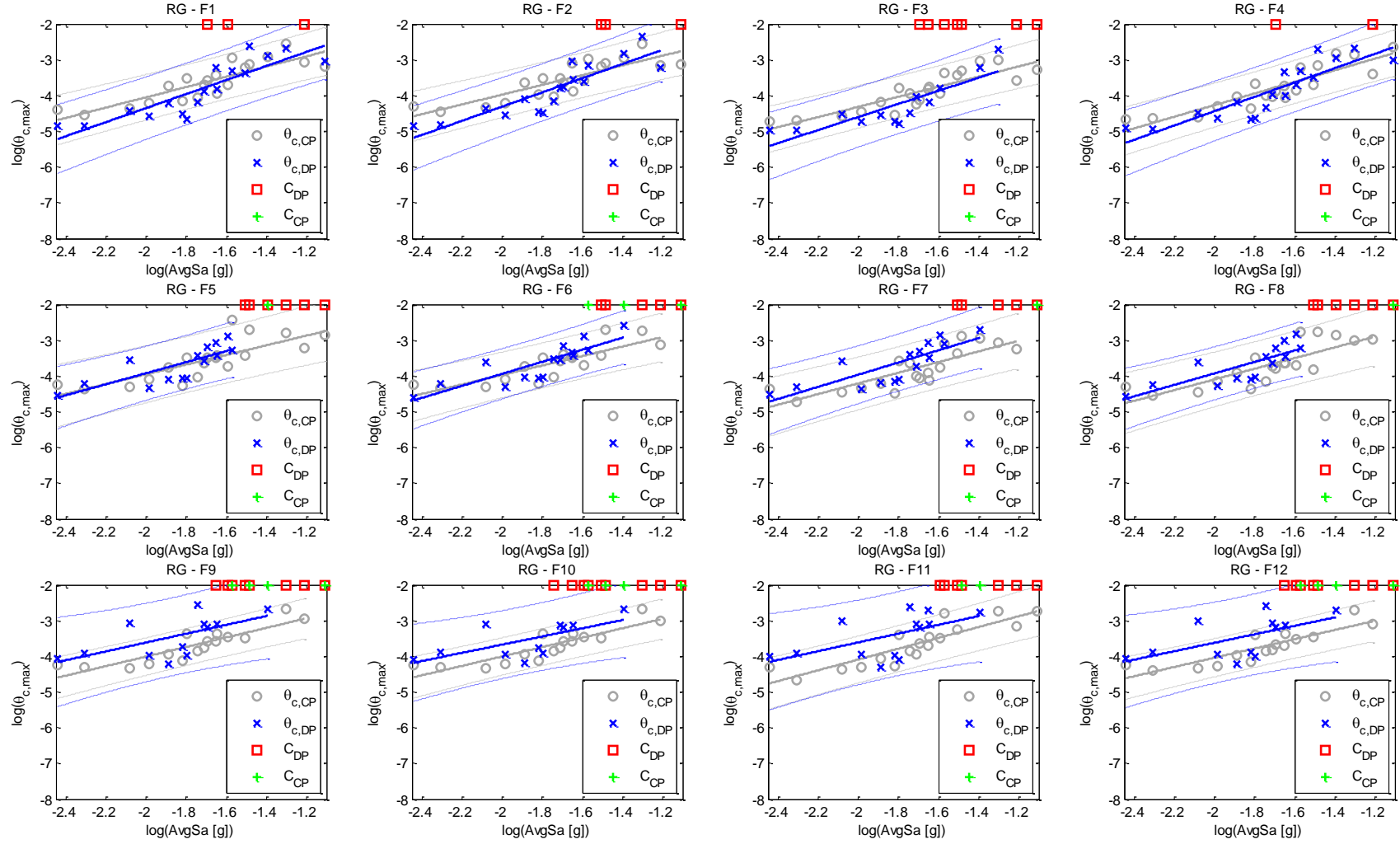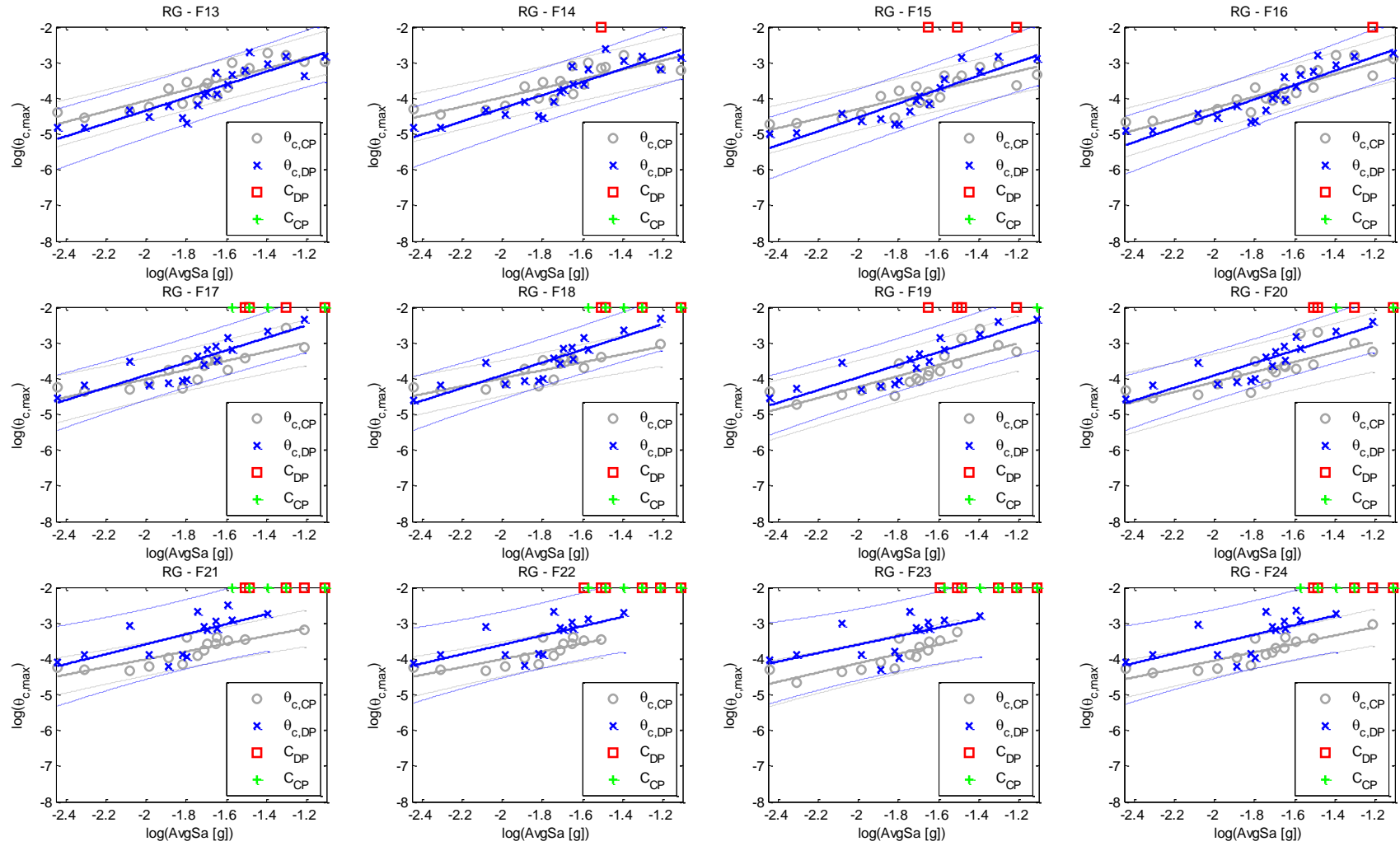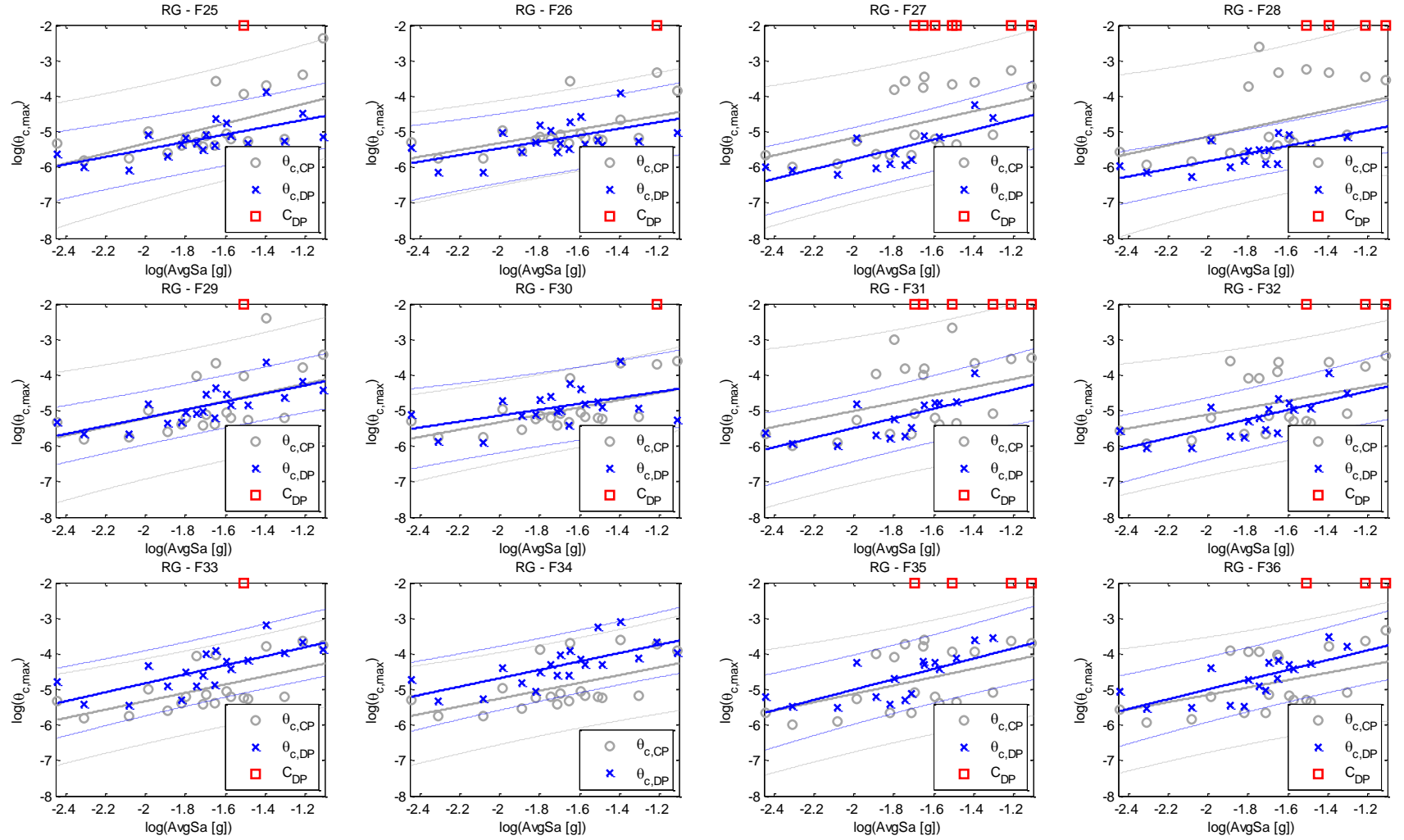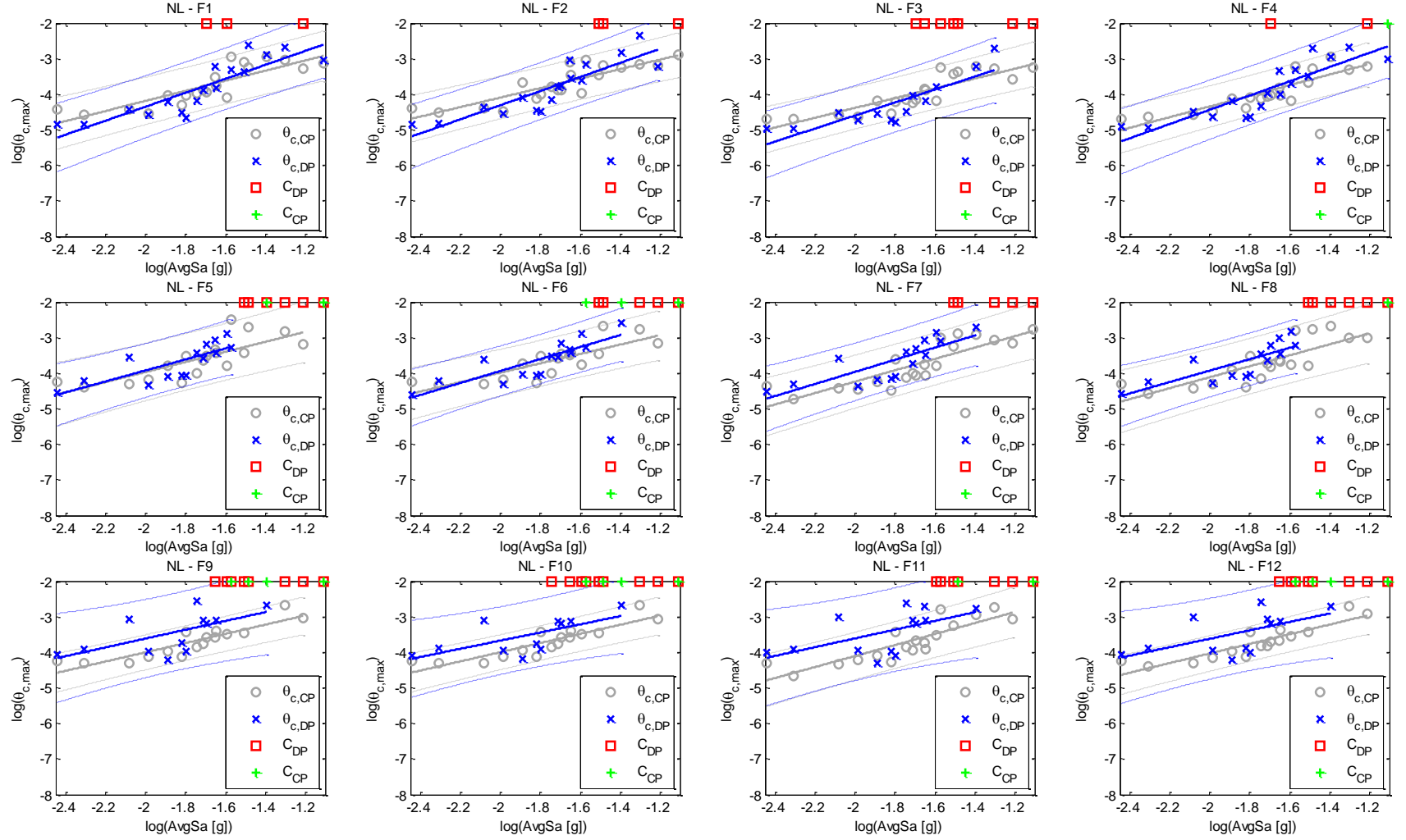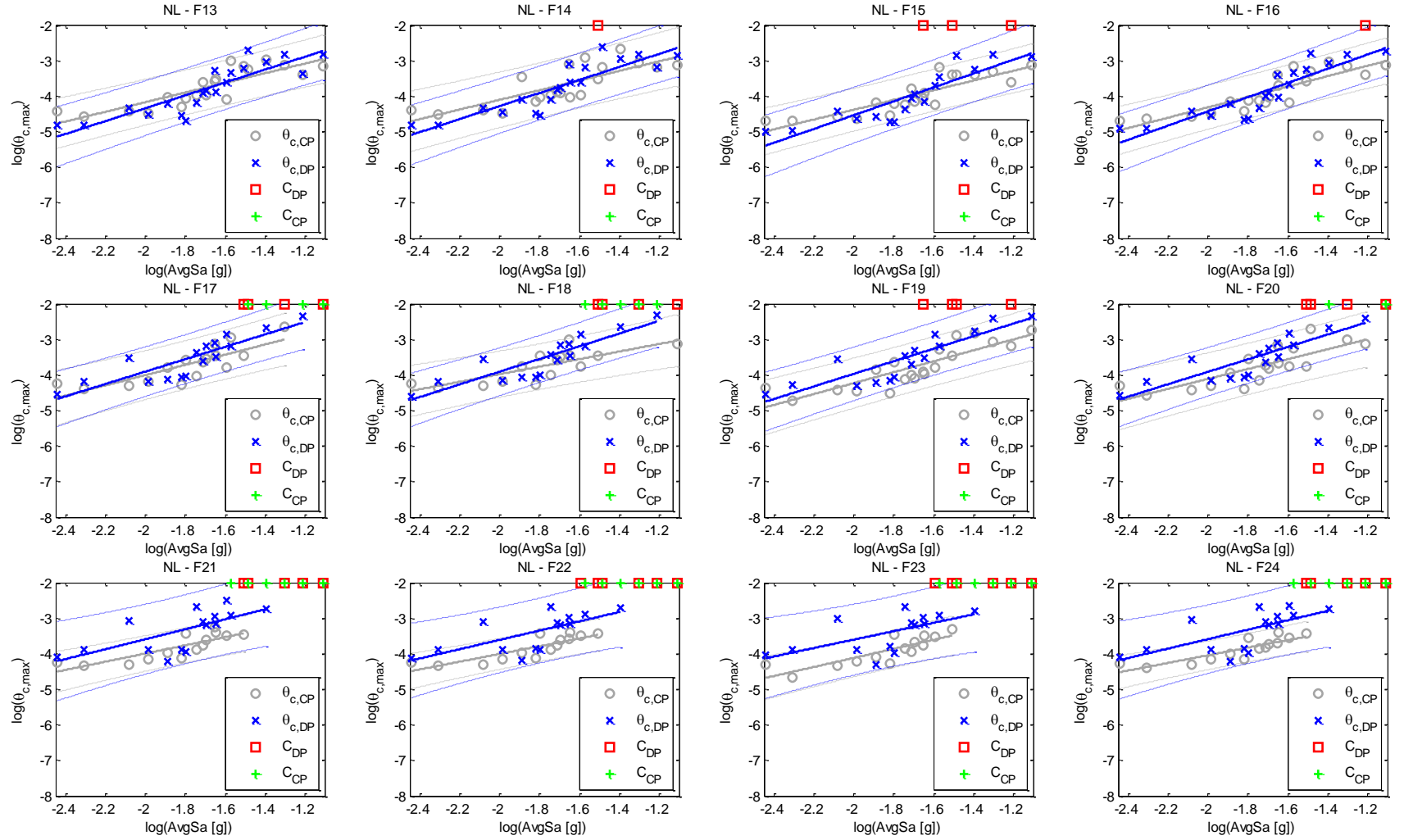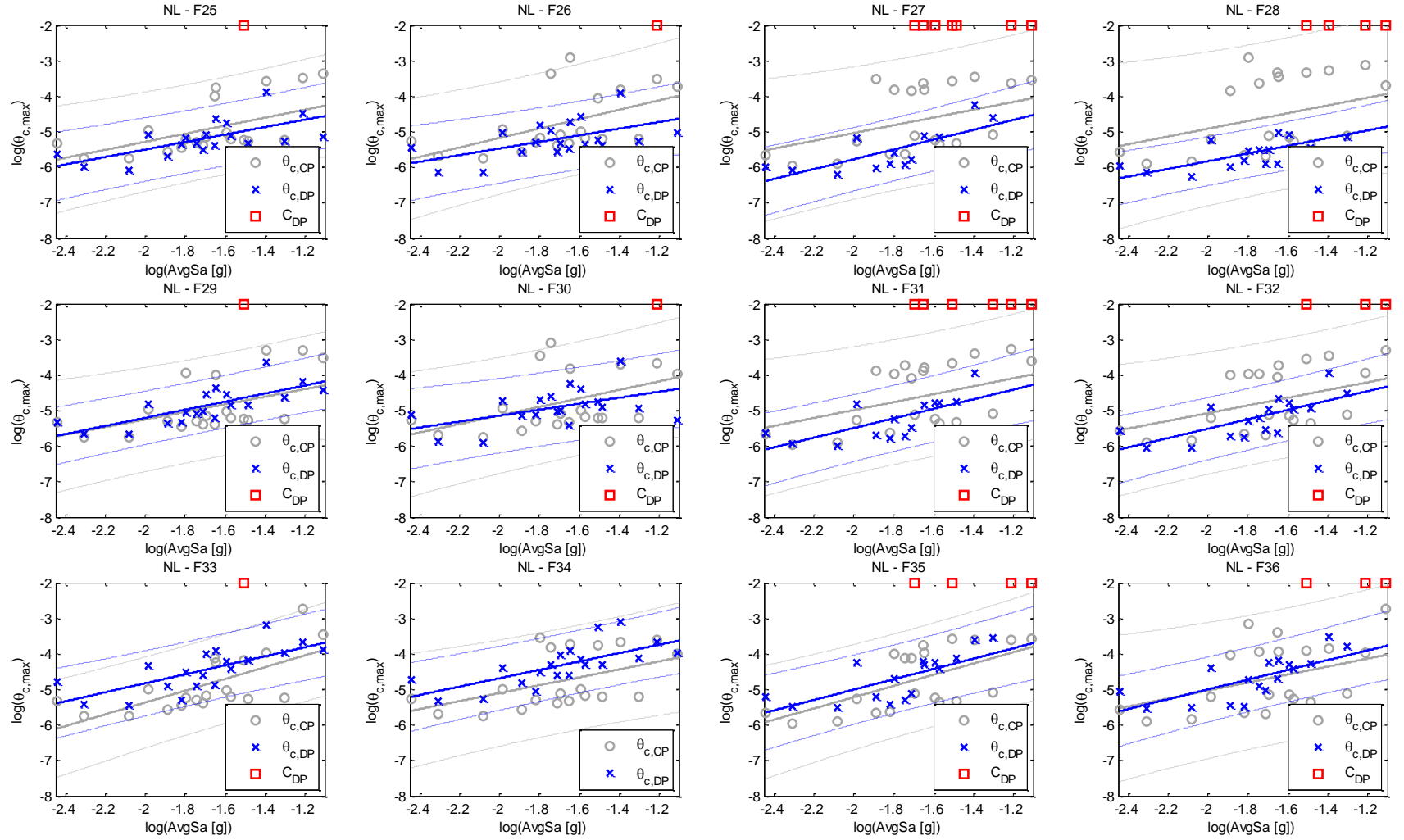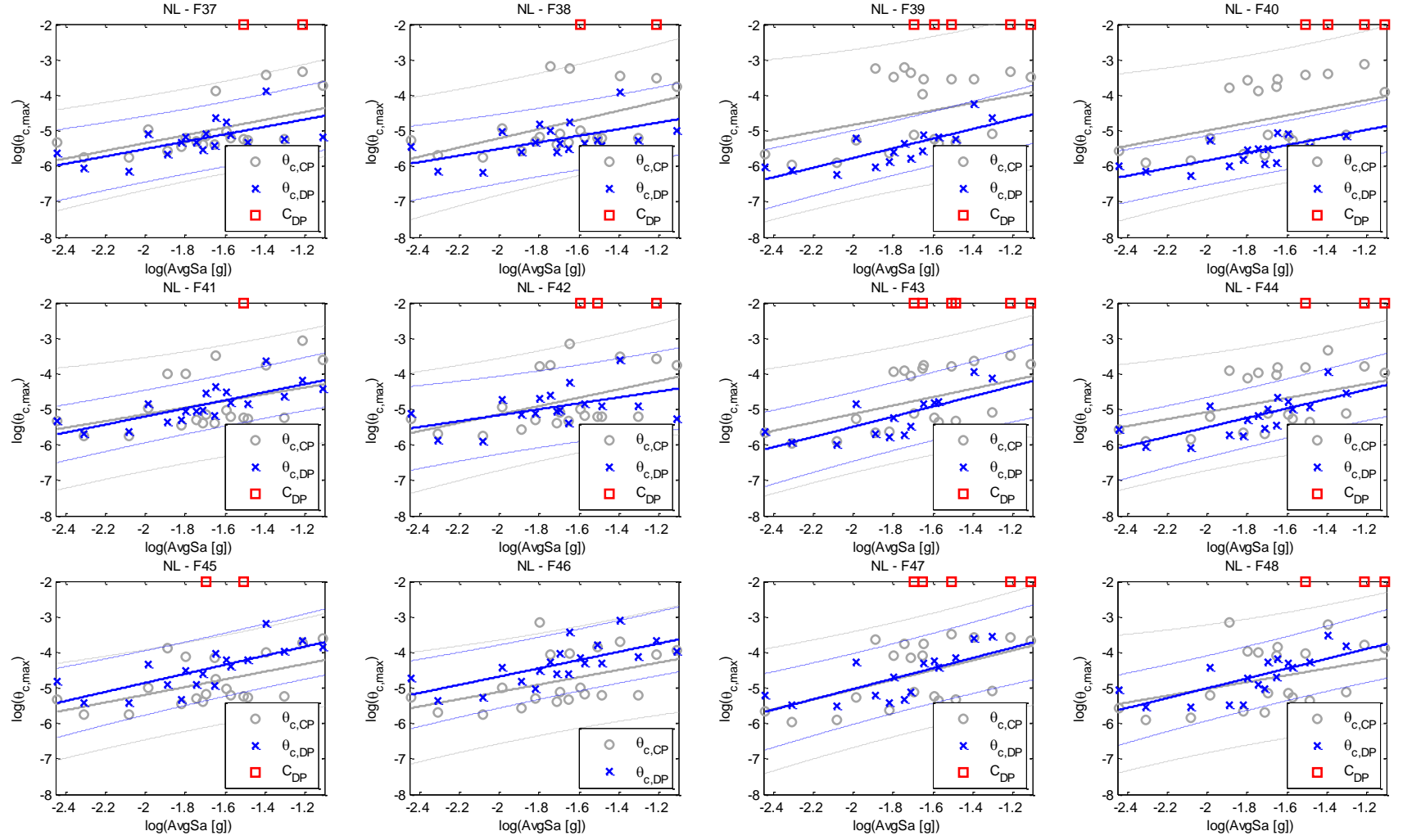
Appendix B. Results obtained with cloud analysis for the maximum chord rotation in columns using models DP-NL and CP-NL

References

1   CEN (2005). Eurocode 8: design of structures for earthquake resistance. Part 3: Assessment and retrofitting of buildings. Brussels, 2005.

2   American Society of Civil Engineers (ASCE), (2014). Seismic Evaluation and Retrofit of Existing Buildings (ASCE/SEI 41-13), Reston, VA, USA.

3   Haselton CB, Liel AB, Taylor-Lange SC, Deierlein GG. (2016). Calibration of model to simulate response of reinforced concrete beam-columns to collapse. ACI Structural journal. 113(6): 1141-1152.

4   PEER/ATC-72-1 (2010). Modeling and Acceptance Criteria for Seismic Design and Analysis of Tall Buildings. Pacific Earthquake Engineering Research Center, Berkeley, CA, and Applied Technology Council, Redwood City, CA, USA.

5   Bradley B A, (2011). Design seismic demands from seismic response analyses: a probability-based approach. Earthquake Spectra; 27(1): 213-224.

6   Ang AHS, Tang WH, (2006). Probability Concepts in Engineering: Emphasis on Applications to Civil and Environmental Engineering (vol.1), second ed., John Wiley and Sons.

7   LeBorgne MR, Ghannoum WM, (2014). Calibrated analytical element for lateral-strength degradation of reinforced concrete columns. Engineering Structures; 81: 35-48.

8   Zimos DK, Mergos PE, Kappos AJ, (2018). Modelling of R/C members accounting for shear failure localisation: Finite element model and verification. Earthquake Engineering & Structural Dynamics; 47:1631–1650.

9   CEB (1996). RC frames under earthquake loading. Bulletin No. 231, Comité Euro-International du Béton.

10 Zhao J, Sritharan S, (2007). Modeling of strain penetration effects in fiber-based analysis of reinforced concrete structures ACI Structural Journal; 104(2): 133–141.

11 Goodnight JC, Kowalsky MJ, Nau JM, (2016). Modified plastic-hinge method for circular RC bridge columns. Journal of Structural Engineering; 142(11): 04016103.

12 Mergos PE, Kappos AJ (2012). A gradual spread inelasticity model for R/C beam–columns, accounting for flexure, shear and anchorage slip. Engineering Structures, 44, 94-106.

13 Megalooikonomou KG, Tastani SP, Pantazopoulou SJ, (2018). Effect of yield penetration on column plastic hinge length. Engineering Structures; 156:161–174.

14 Ranzo G, Petrangeli M. (1998). A fibre finite beam element with section shear modelling for seismic analysis of RC structures. Journal of Earthquake Engineering; 2(3): 443-473.

15 Ceresa P, Petrini L, Pinho R, Sousa R, (2009). A fibre flexure–shear model for seismic analysis of RC-framed structures. Earthquake Engineering & Structural Dynamics; 38(5): 565-586.

16 Ferreira D, Bairán J, Marí A, Faria R, (2014). Nonlinear analysis of RC beams using a hybrid shear-flexural fibre beam model. Engineering Computations; 31(7): 1444-1483.

17 Marini A, Spacone E, (2006). Analysis of reinforced concrete elements including shear effects. ACI Structural Journal; 103(5): 645.

18 Calabrese A, Almeida JP, Pinho R, (2010). Numerical issues in distributed inelasticity modeling of RC frame elements for seismic analysis. Journal of Earthquake Engineering;14(S1):38-68.

19 Coleman J, Spacone E, (2001). Localization issues in force-based frame elements. Journal of Structural Engineering; 127(11):1257-65.

20   Scott MH, Fenves GL, (2006). Plastic hinge integration methods for force-based beam–column elements. Journal of Structural Engineering; 132(2):244-52.

21   Scott MH, Hamutçuoğlu OM, (2008). Numerically consistent regularization of force- based frame elements. International journal for numerical methods in engineering; 76(10):1612-31.

22 Almeida JP, Das S, Pinho R, (2012). Adaptive force-based frame element for regularized softening response. Computers & Structures; 102: 1-13.

23 Paulay T, Priestley MN, (1992). Seismic design of reinforced concrete and masonry buildings. John Wiley and Sons; New York, USA

24   Kashani M, Lowes L, Crewe A, Alexander N, (2016). Nonlinear fibre element modelling of RC bridge piers considering inelastic buckling of reinforcement. Engineering Structures; 116:163-177.

25   Dhakal R., Maekawa K, (2002). Path-dependent cyclic stress–strain relationship of reinforcing bar including buckling. Engineering Structures 24:1383–1396.

26   Addessi D, Ciampi V, (2007). A regularized force- based beam element with a damage–plastic section constitutive law. International Journal for Numerical Methods in Engineering; 70(5):610-29.

27 Altoontash A, (2004). Simulation and damage models for performance assessment of reinforced concrete beam-column joints. PhD Dissertation, Stanford University, California, USA.

28 O'Reilly GJ, Sullivan TJ, (2017). Modeling techniques for the seismic assessment of the existing Italian RC Frame Structures. Journal of Earthquake Engineering: 1-35.

29 Zareian F, Medina RA (2010): A practical method for proper modeling of structural damping in inelastic plane structural systems. Computers and structures; 88(1): 45-53.

30 Correia AA, (2011). A pile-head macro-element approach to seismic design of monoshaft-supported bridges. Ph.D. Dissertation, Istituto Universitario di Studi Superiori, University of Pavia, Pavia, Italy.

31 Sousa R, Almeida JP, Correia AA, Pinho R, (2018). Shake Table Blind Prediction Tests: Contributions for Improved Fiber-based Frame Modelling. Journal of Earthquake Engineering; 13:1-42.

32 Miano A, Jalayer F, Ebrahimian H, Prota A, (2018). Cloud to IDA: Efficient fragility assessment with limited scaling. Earthquake Engineering & Structural Dynamics, 47(5), 1124-1147.

33 Kohrangi M, Vamvatsikos D, Bazzurro P, (2017). Site dependence and record selection schemes for building fragility and regional loss assessment. Earthquake Engineering and Structural Dynamics; 46(10): 1625-1643

34 Vamvatsikos D, Cornell CA, (2002). Incremental dynamic analysis. Earthquake Engineering and Structural Dynamics; 31 (3): 491-514.

35 Jalayer F, Cornell CA, (2003). A technical framework for probability-based demand and capacity factor design (DCFD) seismic formats. PacificEarthquake Engineering Center (PEER)2003/08.

36 Gokkaya BU, Baker JW, Deierlein GG, (2016) Quantifying the impacts of modeling uncertainties on the seismic drift demands and collapse risk of buildings with implications on seismic design checks. Earthquake Engineering and Structural Dynamics; 45: 1661–1683

[This page was intentionally left blank]

Chapter 9

Implications and adequacy of performance objectives in existing standards for the seismic safety assessment of RC frame buildings

Scope and objectives

The previous chapters introduced a new format that can be used within the scope of the seismic safety assessment of existing RC frame buildings. A set of tools, methods and coefficients have been proposed allowing for a consistent definition of the limit state criteria and an efficient management of the uncertainties affecting the assessment results. By following the traditional safety equation that forms the basis of standard-based methods, a set of probabilistic modifications were formulated for different limit states, both factorizing the estimated made for the capacity and the demands of individual structural components of the existing building. The importance of to have a consistent definition of the component response and capacity stems from the fact that they are used as benchmarks to classify the damage states and the overall seismic performance of the building. Seismic safety assessment standards associate to each limit state condition a set of performance objectives, which define the minimum requirements for the structure and define the conditions that are covered by the code when the limit states are verified. These objectives are defined in terms of decision variables (DV) for stakeholder information, and include references to the overall damage state, reparability and expected losses, but are only implicit in the LS verifications. This chapter aims to analyse the compatibility between the component-based LS verifications and the qualitative performance objectives defined in current seismic safety assessment standards such as the Eurocode 8 part 3 (EC8/3).

9.1 Introduction

Performance-based seismic assessment of buildings is a methodology that targets the evaluation of the seismic performance of a system when it is subjected to earthquake ground motions with different intensities. The main reason for the development of these methods stemmed from the observations made in the aftermath of the 1989 Loma Prieta and the 1994 Northridge earthquakes in California. After these events, stakeholders started to express some concerns regarding the performance of buildings, namely about the losses resulting from the damage in structural and non-structural components, despite ensuring life-safety conditions. Within this context, the main principles of performance-based earthquake engineering (PBEE) were developed, including explicit or implicit references to the human and economic consequences of the ground motion effects. One of the outcomes of this new philosophy was the definition of performance matrices as a complement to traditional safety assessment methods. These matrices, which were first introduced in American standards ([1-2]), define the maximum damage that is allowed to occur in the structure as a key consequence of a ground motion with a given intensity.

In Europe, one of the main developments introduced to create a unified approach to assess the seismic safety of existing reinforced concrete (RC) buildings was the publication of Part 3 of Eurocode 8 (EC8/3) ([3]). Similar to other standards available worldwide, EC8/3 establishes three classes of performance objectives termed, in a decreasing order of expected damage, as Near Collapse (NC), Significant Damage (SD) and Damage Limitation (DL). These performance levels are qualitatively described in the standard in terms of admissible damage levels and deformations, and each class of performance objectives is connected to a specific level of seismic hazard (represented by a specific average return period). For NC, the performance objectives require the structure to still be able to sustain gravity loads after the ground motion, even though it may exhibit heavy damage and large permanent deformations. Conversely, the performance objectives associated with SD refer that non-structural components are expected to exhibit significant damage (although without out-of-the-plane collapse of infill walls). A structure compatible with the SD level is also expected to exhibit residual interstorey drifts with a moderate magnitude while still being able to sustain a moderate intensity aftershock without collapsing. EC8/3 also states that a structure exceeding the limit conditions associated with SD has a significant probability of being uneconomic to repair. Finally, the performance objectives associated with DL establish that no damage is expected in the structural elements while only minor damage, such as cracking of the infill walls, is expected for the non-structural components. Consequently, DL implies a post-earthquake state of the building with very low repair needs and assumes that no residual deformation has occurred in the building. The transitions between the performance or damage levels defined in EC8/3 are characterized by limit state conditions that establish limits above which the building is no longer compatible with a given performance class. Table 1 presents the referred damage states and the limits of the corresponding compliance criteria.

Table 1. Damage states and performance objectives defined in the current version of EC8/3.

Performance Objectives	Structural Components	Non-structural Components	Permanent deformations	Reparable structure?	Compliance criteria
Damage Limitation, DL	Light	Economical repair	Negligible	Yes	θ_{DL}
Significant Damage, SD	Significant	Damaged	Visible	Uneconomic	θ_{SD}
Near Collapse, NC	Heavy	Collapsed	Large	No	θ_{NC}, V_{NC}

As shown in Table 1, the compliance criteria for ductile elements defining the transition between the several damage limit states are defined in terms of local deformations (chord rotations, θ). Similar principles are also present in ASCE 41-13 ([4]) and other codes. However, for the case of NC, the fragile failure of structural elements must also be analysed by assessing shear demand. These verifications are defined only for structural elements and connected to a specific level of seismic hazard compatible with the limit states, establishing the separation between the performance classes. If a single component exceeds a given limit state condition, the overall building is classified as non-compliant with that limit state. Hence, the considerations made regarding the state of non-structural components, the level of residual deformations, the capacity reserve against collapse or the level of repair losses are implicitly included in the limit state verifications.

The Pacific Earthquake Engineering Research Centre (PEER) methodology was developed to answer the need for communicating seismic risk to stakeholders involving metrics that reflect seismic consequences and are different than the engineering terms usually adopted in earthquake engineering. This methodology allows for the quantification, in probabilistic terms, of different decision variables (DVs) such as monetary losses, repair time or number of fatalities. The basis of the PEER methodology lies in the probabilistic characterization of several performance metrics along with the multiple sources of uncertainty that are inherent to seismic assessment (e.g. the uncertainty about the hazard, the ground motions representing a seismic scenario, the modelling and knowledge-based uncertainties of the building components and properties). The PEER methodology can be summarized into the framing equation representing the rate of a certain DV exceeding a value *dv* ([5]):

$$\lambda\left(DV>dv\right) = \int_{IM}\int_{EDP}\int_{DM} G\left(DV|DM\right) \cdot \left|dG\left(DM|EDP\right)\right| \cdot \left|dG\left(EDP|IM\right)\right| \cdot \left|d\lambda\left(IM\right)\right| \qquad (1)$$

where DM represents a damage measure, generally discretised into several damage states, EDP represents a measure of the structural response that can be correlated with DM, IM is a ground motion intensity measure and G(·) is the complementary cumulative distribution function. The

numerical integration of Eq. (1) can be used to estimate the annual losses. A discrete solution of Eq. (1) requires the quantification of the expected loss value, $E(L|IM_i)$, for each ground motion intensity IM_i, and can be estimated from the proposal of Ramirez and Miranda ([6]), based on previous work by Aslani ([7]):

$$
\begin{aligned}
E\left(L \mid IM_i\right) = & \ E\left(L \mid \overline{C} \cap R, IM_i\right) \cdot p\left(\overline{C} \cap R \mid IM_i\right) + \\
& + E\left(L \mid \overline{C} \cap D, IM_i\right) \cdot p\left(\overline{C} \cap D \mid IM_i\right) + \\
& + E\left(L \mid C, IM_i\right) \cdot p\left(C \mid IM_i\right)
\end{aligned}
\tag{2}
$$

where $E(L|\overline{C} \cap R, IM_i)$, $E(L|\overline{C} \cap D, IM_i)$ and $E(L|C, IM_i)$ are the expected value of the losses for IM_i given that the structure is still reparable (without collapsing), the expected value of the losses for IM_i given that the structure is not reparable (without collapsing) and the expected value of the losses for IM_i given that the structure will collapse, respectively. The probabilities of having a reparable and an irreparable building without collapsing can be calculated by factorizing the corresponding probability of demolition $p\left(D \mid \overline{C}, IM_i\right)$ by the probability of collapse, $p\left(C \mid IM_i\right)$. Finally, the expected value of the losses for a given ground motion intensity IM_i can be quantified considering a relative quantity, the loss ratio, defined by the ratio between the obtained losses and the cost of replacing the structure. This implies that the loss ratio is 1.0 when the structure is considered irreparable or when structural collapse is observed, and Eq. (2) becomes:

$$
\begin{aligned}
E\left(L \mid IM_i\right) = & \ E\left(L \mid \overline{C} \cap R, IM_i\right) \cdot \left[1 - p\left(D \mid \overline{C}, IM_i\right)\right] \cdot \left[1 - p\left(C \mid IM_i\right)\right] + \\
& + p\left(D \mid \overline{C}, IM_i\right) \cdot \left[1 - p\left(C \mid IM_i\right)\right] \\
& + p\left(C \mid IM_i\right)
\end{aligned}
\tag{3}
$$

A closer analysis of EC8/3 performance objectives (Table 1) shows that most variables currently used to estimate losses, as those included in Eq. (3), have to be controlled for each limit state. Hence, in principle, thresholds associated with maximum expected losses can be defined in the same way that local demand limits are employed in current standards, since they explicitly represent the conditions qualitative defined by the performance objectives. Nevertheless, to the authors' knowledge, a solid conceptual and statistical evaluation of the equivalence between the implicit and the explicit verification of the performance objectives described in EC8/3 has not yet been conducted. As such, the proposed study aims to assess the extent of this equivalence, analysing the conceptual similarities between current code methods and the PEER-PBEE, and

evaluating the statistical equivalence between the results obtained with both formulations for the specific case of existing mid-rise RC moment resisting frame (RC-MRF) buildings.

9.2 Methodology

9.2.1 General approach

Three RC-MRF buildings were considered in the present study. These buildings consist of structures regular in plan and in elevation designed without capacity design rules. The plan view of the building and of the structure, the sectional details (common to all buildings) and the elevation view of the buildings with 3 (REG3), 4 (REG4) and 5 (REG5) storeys can be found in Fig. 1. The three buildings analysed have masonry infill walls with a thickness of 0.15m and openings in all spans apart from that of the staircase façade where glass panels were considered. The stairs are composed of slabs simply supported by beams, unloading on the beams of the floor levels and on mid-height beams located at each storey. Regarding the material properties, a mean concrete compressive strength and a mean reinforcing steel yielding strength of 25 MPa and 500 MPa were adopted, respectively. The masonry compressive strength was assumed with the value of 3.10 MPa. A permanent load equal to 4 kN/m^2 was uniformly distributed across all slabs, in addition to the self-weight of the horizontal elements. A uniform live load of 3 kN/m^2 was also assigned to all slabs, with the exception of the roof where the live load was reduced to 1 kN/m^2. The stair slabs were only considered through their equivalent permanent and live loading distributed on the supporting beams. The short columns at this element have improved shear capacity, thus being sufficient to hold the shear demands imposed by the ground motions. The weight of the masonry infills was defined as a uniform load (7 kN/m) applied to the supporting beams of the peripheral frames. The fundamental periods of the analysed buildings are 0.31sec; 0.25 sec (REG3), 0.41 sec; 0.31 sec (REG4) and 0.52 sec; 0.39 sec (REG5) for the fully infilled building and 0.73sec; 0.72 sec (REG3), 0.96 sec; 0.93 sec (REG4) and 1.18 sec; 1.15sec (REG5) when the masonry infills were not considered for the initial stiffness (i.e. bare frame conditions).

A 3D nonlinear model of each building was created using the OpenSees platform ([8]). Beam-column elements were modelled using nonlinear moment-rotation springs at the ends of all elements. The axial load and the moment interaction between the two orthogonal directions of the transversal sections of the columns was not considered, with independent flexural springs calibrated using the axial loads from the gravity load analysis being assigned to each direction.
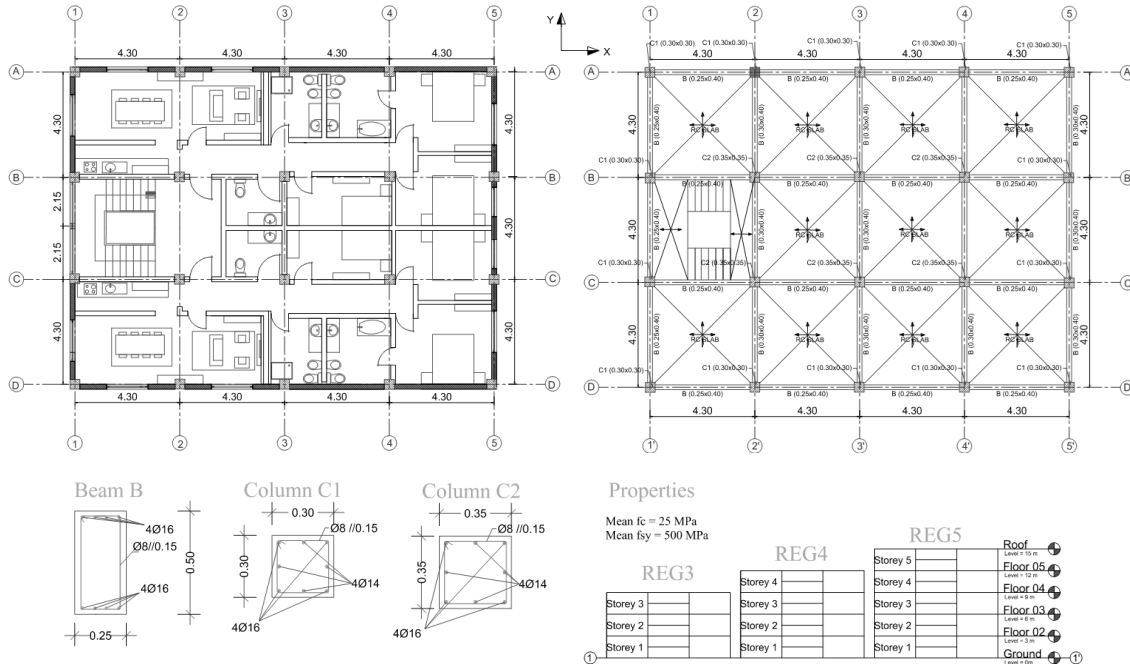
Figure 1. Properties of the three selected buildings analysed in this study.

The moment rotation behaviour of each spring was defined using a trilinear curve defined by the yielding moment approximation (M_y) and yielding rotation (θ_y) proposed by Panagiotakos and Fardis ([9]), the capping rotation θ_c (corresponding to a maximum moment of $1.14 \cdot M_y$) and the post-capping rotation (θ_{pc}) following the proposal of Haselton *et al.* ([10]). Damping and stiffness of the structural elements were adjusted based on the recommendations of Zareian and Medina ([11]). Beam-column joints were assumed rigid. This assumption was made since it corresponds to the most commonly considered approach made by analysts applying current seismic safety assessment methods. Finally, the infills located at peripheral frames (apart from the staircase façade) were modelled using a single strut model, following the recommendations of Dolšek and Fajfar ([12]).

The three-benchmark buildings were considered located in Lisbon, Portugal, with foundations in a soil of type B ([13]). Incremental dynamic analysis ([14]) was used to evaluate the response of the buildings for increasing values of the ground motion intensity level (IML). Each building was analysed up to collapse, this being defined by numerical instability of the nonlinear model for a given IML of each ground motion record. The IML corresponding to the selected performance criteria was determined using the hunt and fill algorithm ([15]). In total, 160 pairs of ground motion records were used in each IDA analysis. Due to the specificities of the Portuguese seismic hazard, 40 (40) pairs of records were selected using SelEQ ([16]) matching the average of the geometric mean of the two as-recorded components to the Type I (II) response spectrum as presented in the national annex to the Eurocode 8-Part 1 ([13]). Individual control of the goodness of fit of each pair of records was also imposed. The response spectra of the round motion sets and

the corresponding code-target spectra defined for Lisbon considering a 475 years average return period are shown in Fig. 2.
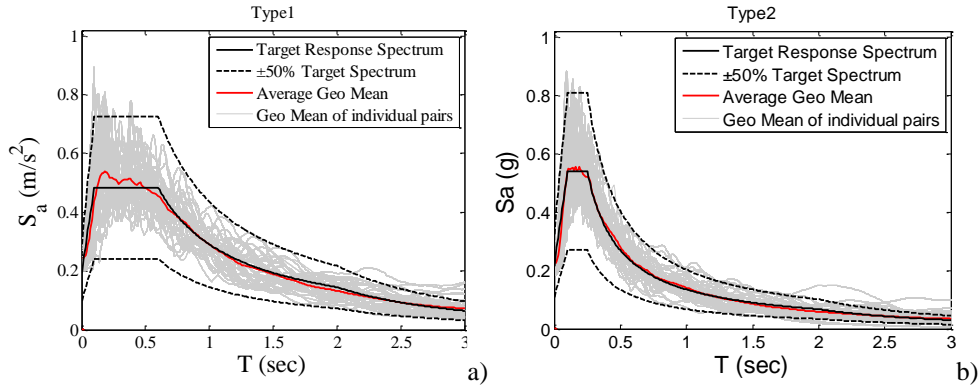

Figure 2. Response spectra of the ground motion sets used to perform the incremental dynamic analysis.

The selected pairs of records were applied to each structure considering incidence angles of 0º and 90º, following the recommendations of current guidelines (i.e. FEMA-P58 [17]). The intensity measure adopted in the IDA consisted in the geometric mean of the 5% damped spectral acceleration, $AvgS_a$, considering the periods T_{1xinf} (T_{1yinf}) computed using the infilled frame structure (see x and y directions in Fig. 1), $T_{1x,bare}$ ($T_{1y,bare}$) and $2T_{1x,bare}$ ($2T_{1y,bare}$) computed using only the bare frame structure. In that way, a period corresponding to different behaviour ranges of the structure is included in the IM definition. Details about the more generic use of $AvgS_a$ can be found e.g. in Kohrangi *et al.* ([18]). The results of the IDA were post-processed considering as decision variables the maximum (over all structural elements) chord rotation demand-to-capacity ratio attained for each ground motion case and for each IML (implicit approach) and the expected value of the losses due to the damage induced by each ground motion case and each IML (explicit approach). The adoption of the different criteria aimed at establishing an objective approach that could be used to compare the results of different limit state conditions defined using implicit (based on current standard-based methods) or explicit (based on the loss-based approach) verifications of the performance objectives described in Table 1. After the processing of the EDP-based and loss-based criteria, IDA curves for all the 160 ground motion pairs were computed and the distribution of the $AvgS_a$ levels leading to the performance criterion was computed. Finally, a statistical comparison between the $AvgS_a$ distributions obtained using the implicit and the explicit performance-based criteria was performed.

9.2.2 Implicit verifications of the performance objectives

The implicit approach adopted for the post-processing of the IDA results involved the analysis of local demands, which are considered to be a proxy for the building performance, as assumed in current seismic safety assessment standards. Scalar damage variables were analysed with a generic format given by:

$$Y_{LS} = \frac{\theta_D}{\theta_{R,LS}} = \max\left(\frac{\theta_{D,x}}{\theta_{R,LS,x}} ; \frac{\theta_{D,y}}{\theta_{R,LS,y}} \right) \qquad (4)$$

where θ_D represents the maximum demand in terms of chord rotations, $\theta_{R,LS}$ is defined as a damage limit state threshold and x and y represent the main sectional directions of each element. Scalar damage variables were calculated for every component of the building. Several proposals can be found in the literature to establish $\theta_{R,LS}$ (e.g. [3; 10; 19]). As defined in Table 1, three damage limit states (damage limitation, DL, significant damage, SD and near collapse, NC) are available in EC8/3 that are compatible with different performance objectives (see Table 1). Accordingly, these damage limit states were adopted in the implicit approach. The θ_{DL} limit was computed according to the proposal of EC8/3. The remaining limits were computed using the empirical models derived by Haselton *et al.* [10], according to which θ_{SD} is computed by adding $\theta_{cap,pl}$ (see [10] to θ_{DL}; θ_{NC} was defined as 4/3 of θ_{DL} following a similar principle to that of EC8/3. In addition to these cases, the ultimate limit θ_C was defined as the sum of θ_{DL} and θ_{pc} (see Haselton *et al.* (2016). Figure 3 summarizes the Y_{LS} conditions adopted and presents vertical lines representing the demand-to-capacity ratios that correspond to the condition $Y_{LS}=1$ for DL, SD, NC and C. For each ground motion record and IML, the maximum of Y_{DL}, Y_{SD}, Y_{NC} and Y_C was computed, yielding 160 IDA curves used to determine the probability distribution of the AvgSa leading to $Y_{LS}=1$.
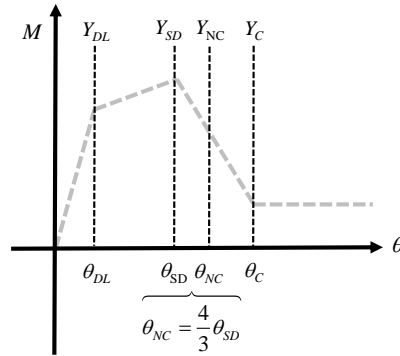
Figure 3. Capacity of each spring defined according to the concentrated plasticity (CP) model adopted and definition of the code-compatible ductile limit states

9.2.3 Explicit verifications of the performance objectives

For the case of the explicit verification of performance objectives, a similar rationale was adopted to define a new Y_{LS} condition using a direct loss-based approach. Accordingly, Y_{LS} was defined as the ratio between the expected loss value and a limit value representing the corresponding limit state capacity:

$$Y_{LS} = \frac{L \mid m}{L_{m,LS}} \qquad (5)$$

where L/m represents the expected value of the losses induced to the structure due to the occurrence of a given ground motion m and $L_{m,LS}$ represents a threshold for the expected value of the losses. Both quantities can be normalized by the replacement cost, leading to loss values between 0 and 1.0. For each ground motion, the quantification of L/m was defined using the principles outlined in Eq. (6). The condition that explicitly evaluates the performance objectives described before is defined as:

$$L \mid m = \begin{cases} E\big[L \mid m\big] \cdot \left[1 - \Phi\left(\dfrac{\ln\big[RIDR\big] - \ln\big[0.015\big]}{0.3}\right)\right] + \Phi\left(\dfrac{\ln\big[RIDR\big] - \ln\big[0.015\big]}{0.3}\right) & \text{if } \overline{C} \\ 1.0 & \text{if } C \end{cases} \quad (6)$$

which includes the expected value of the repair costs $E[L|m]$, the loss component related to the probability of demolition given the permanent deformations (RIDR) exhibited by the building when subjected to ground motion m and, indirectly, the probability of collapse by assigning a value of 1.0 to $L|m$ if the collapse criterion defined by the numerical instability condition is attained. In the explicit approach, the probability of demolition was represented according to Ramirez and Miranda ([27]). Hence, the probability of demolition was calculated using the value of the maximum residual IDR (RIDR) considering that the referred probability follows a lognormal distribution with a mean RIDR of 0.015 and a dispersion of 0.30. The approach adopted to quantify the repair losses was based on the storey-based approach proposed by Zareian and Krawinkler (820]) and Ramirez and Miranda ([6]). To derive these functions, three classes of building components were selected: interstorey drift (ISR) -sensitive structural elements (S|IDR), IDR-sensitive non-structural components (NS|IDR) and peak floor acceleration (PFA) -sensitive non-structural components (NS|PFA). The development of engineering demand parameters to loss (EDP-to-Loss) functions for these three classes was done following the strategy adopted by Ramirez *et al.* ([21]). Fragility functions for these classes of components were collected from HAZUS-MH MR4 ([22]) for low-code C3L (low-rise concrete frame with unreinforced masonry infill walls with 1-3 storeys) and C3M (mid-rise concrete frame with unreinforced masonry infill walls with 4-7 storeys) buildings. These fragility functions were crossed with the median consequence models proposed in HAZUS-MH MR4 ([22]) for multi-family dwellings (RES3). By assuming the expected value of the consequences and simulating the fragility functions for different values of IDR and PFA. A normalized E [L|EDP] curve (between 0 and 1 where 1 represents the total loss of the class of components) were created for each class of components. The resulting EDP-to-Loss functions are shown in Fig.4.
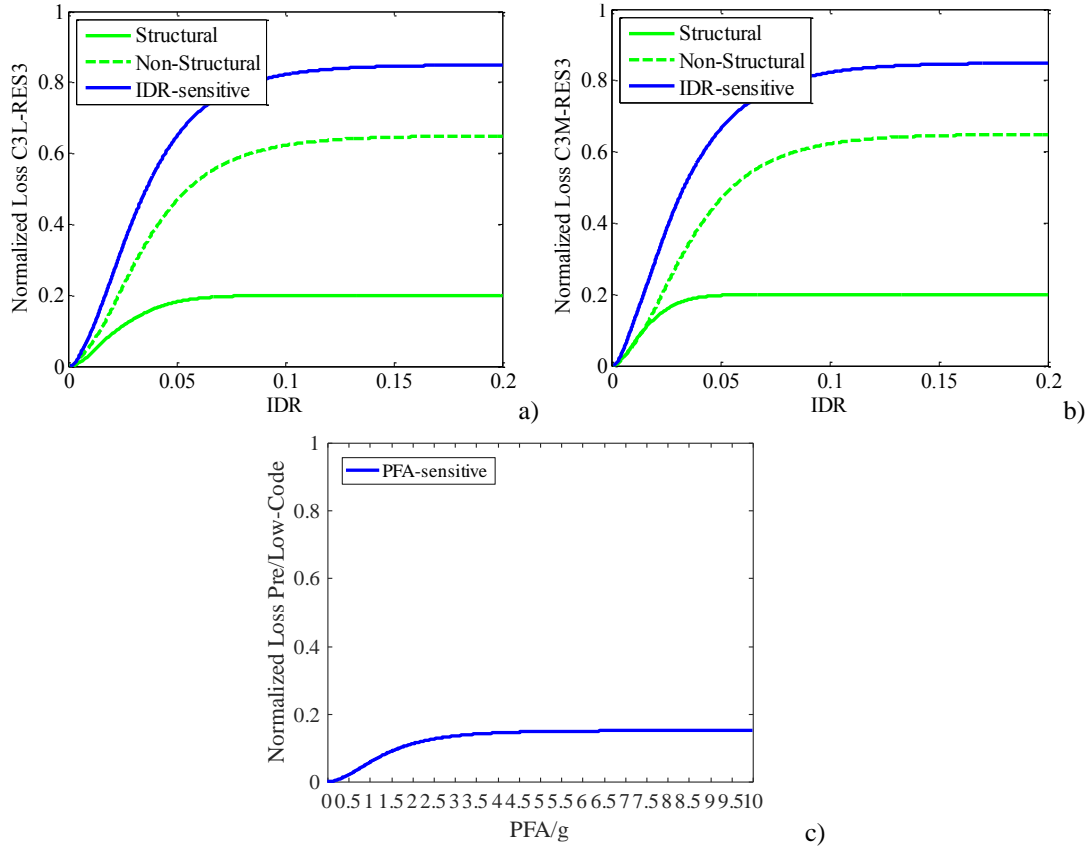
Figure 4. EDP-to-Loss curves adopted for the evaluation of the expected loss value due to the maximum IDR and PFA values resulting from a given ground motion.

As mentioned, the principles adopted by Ramirez *et al.* ([21]) were followed, thus leading to EDP-to-Loss curves not at the building level but at the storey-level. Therefore, $E[\mathrm{L}|m]$ was calculated using:

$$E\left[L\,|\,m\right] = \frac{1}{n_{storeys}} \cdot \sum_{i=1}^{nstoreys} \frac{1}{2} \cdot \left(L\,|\,IDR_{x,i} + L\,|\,IDR_{y,i}\right) + \frac{1}{n_{floors}} \cdot \sum_{j=1}^{nfloors} \max\left(L\,|\,\mathrm{PFA}_{x,j}, L\,|\,\mathrm{PFA}_{y,j}\right) \quad (7)$$

which implies the assumption that all storeys have the same configuration (and therefore value), the averaging of the losses between the two directions of the building, thus assuming a similar distribution of drift- sensitive non-structural elements along the *x* and *y* as well as an average damage level induced to structural elements. In Eq.(7), n_{floors} refers to the number of ceilings (see Fig. 1) that have acoustic panels and lighting equipment. In total, 160 vulnerability curves were generated for all the pairs of the considered ground motion records and, based on these IDA curves, $\mathrm{AvgS_a}$ distributions corresponding to normalized loss thresholds from 0.01 to 1.00 in steps of 0.01 were computed.

9.2.4 Statistical analysis

The AvgS$_a$ distributions were analysed using median and standard deviation (SD) values. The comparison between the distributions of the AvgS$_a$ values leading to the conditions $Y_{DL}=1$, $Y_{SD}=1$, $Y_{NC}=1$, $Y_C=1$ and those associated to the 100 normalized loss thresholds was made considering three different strategies. The comparison of the medians of the distributions was done using the Kruskal-Wallis test (KW; Kruskal and Wallis, [25]) to evaluate if the EDP-based and the loss-based AvgS$_a$ distributions could be assumed has samples of the same distribution. Similarly, the Brown–Forsythe test (BF, Brown and Forsythe, [24]) was adopted to evaluate the equality of the variances of the different samples of AvgS$_a$. A critical value of 0.05 for the p-value was considered in these tests. Additionally, the two-sample Kolmogorov-Smirnov (KS, Marsaglia *et al.*, [26]) distance was also adopted to measure the overall differences between the EDP-based and the loss-based AvgS$_a$ distributions.

9.3 Results

Figure 5 presents the IDA curves obtained for the maximum values of Y_{DL}, Y_{SD}, Y_{NC} and Y_C for structures REG3, REG4 and REG5. The limit lines corresponding to $Y_{DL}=1$, $Y_{SD}=1$, $Y_{NC}=1$, $Y_C=1$ are also presented. The median (SD) AvgS$_a$ leading to the condition $Y_{DL}=1$ was found to be 0.176g (0.046g), 0.149g (0.037g) and 0.117g (0.030g) for the REG3, REG4 and REG5, respectively. For the $Y_{SD}=1$ condition, the median (SD) values obtained for building REG3 was 0.666g (0.151g), while lower values were observed for REG4 (0.477g (0.113g)) and for REG5 (0.392g (0.080g)). The NC limit state condition $Y_{NC}=1$ was observed for median (SD) AvgS$_a$ values of 0.798g (0.198g), 0.602g (0.148g) and 0.457g (0.111g), with similar values being also observed for the $Y_C=1$ (0.900g (0.243g), 0.694g (0.174g) and 0.536g (0.126g) for the REG3, REG4 and REG5, respectively).

Figure 6 shows the evolution of the distributions of the AvgS$_a$ values obtained for incremental levels of the admissible normalized loss ($L_{m,LS}$) for buildings REG3 to REG5. An approximate trilinear curve was obtained for the median $L_{m,LS}$ - AvgS$_a$ curve in all cases. The first branch of the curve develops until a $L_{m,LS}$ value of 0.20. Similarly, in all cases, a subsequent linear branch with a smaller slope is observed until a value of $L_{m,LS}$ around 0.50 is reached. Finally, the third branch of the curve represents a region with a very small increment of the AvgS$_a$ and a large increase of the losses.

Figure 7 shows the comparison of the distributions of the AvgS$_a$ values leading to the condition $Y_{LS}=1$ with the 100 distributions of the same IML for different $L_{m,LS}$ thresholds. The results presented refer to the evolution of the p-values of the Kruskal-Wallis and of the Brown.-Forsythe tests and their corresponding comparison with the assumed critical value (0.05). As seen in Figs. 7a-7c, the KW test applied to the distribution associated with $Y_{DL}=1$ yields maximum p-values of

0.08, 0.69 and 0.91 for values of the normalized loss $L_{m,DL}$ of 0.03, 0.04 and 0.04, for buildings REG3, REG4 and REG5, respectively. Similar results are observed for the BF test.
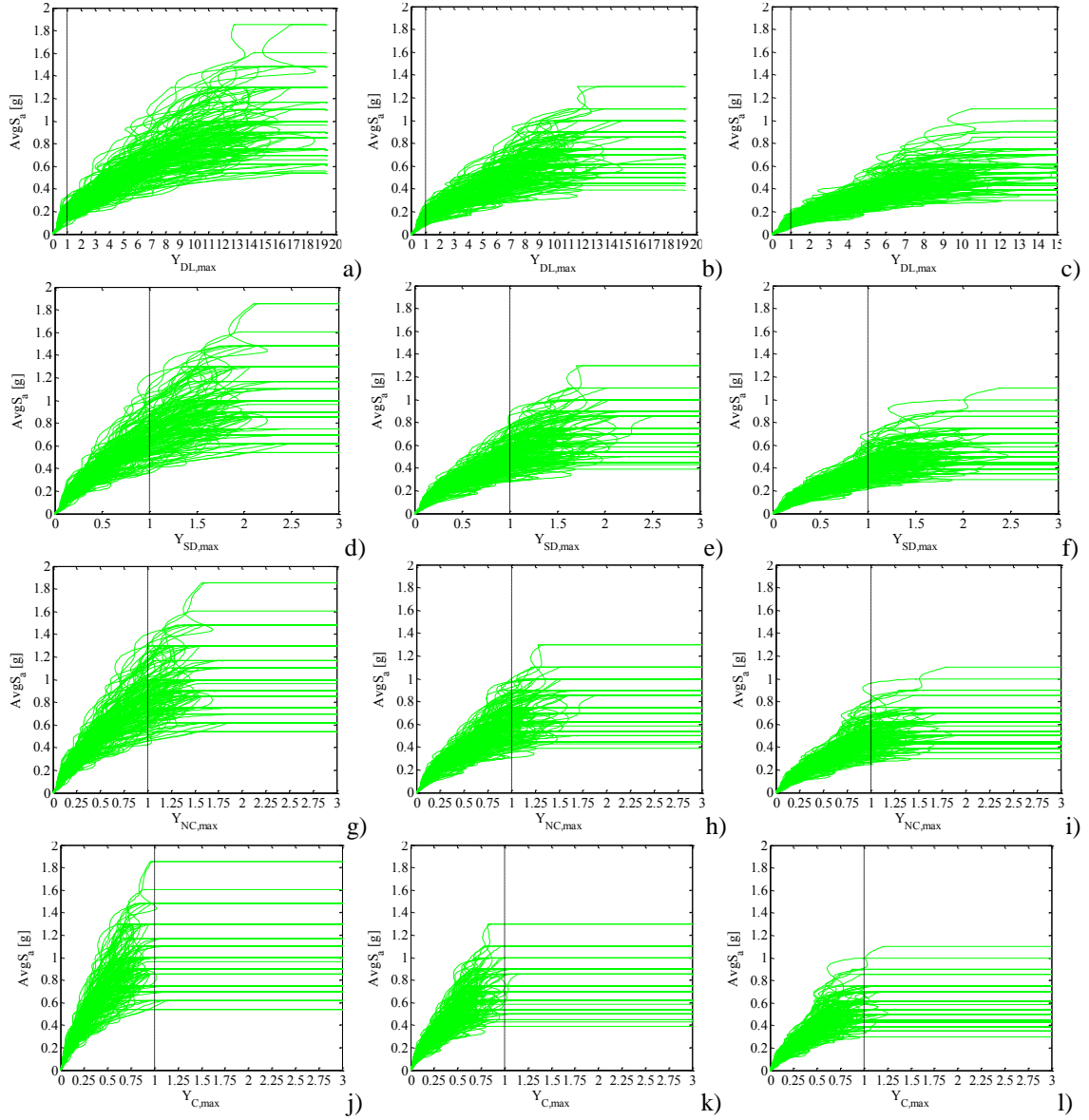
Figure 5. IDA curves for the maximum values of the Y_{DL} (a, b, c), Y_{SD} (d, e, f), Y_{NC} (g, h, i) and Y_C (j, k, l) for building REG3 (a, d, g, j), REG4 (b, e, h, k) and REG5 (c, f, i, l).

Figure 6. Evolution of the $AvgS_a$ values associated with different normalized loss limits for buildings REG3 (a), REG4 (b) and REG5 (c).

Figure 7. Results of the KW and BF tests applied when using as a reference the distribution of AvgSa values compatible with Y_{DL} (a, b, c), Y_{SD} (d, e, f), Y_{NC} (g, h, i) and Y_C (j, k, l) for building REG3 (a, d, g, j), REG4 (b, e, h, k) and REG5 (c, f, i, l).
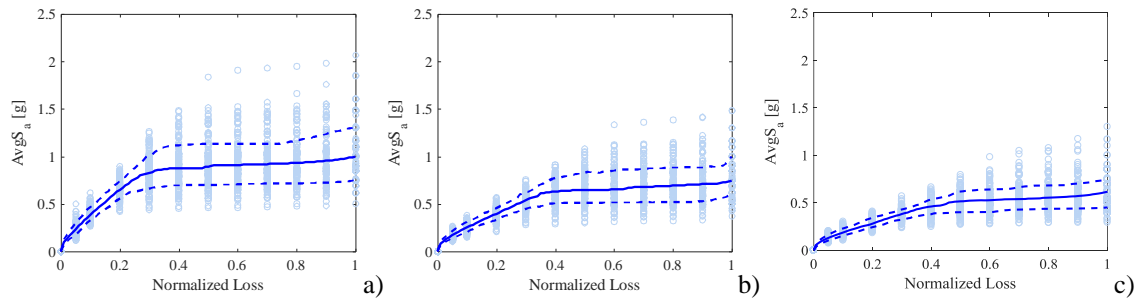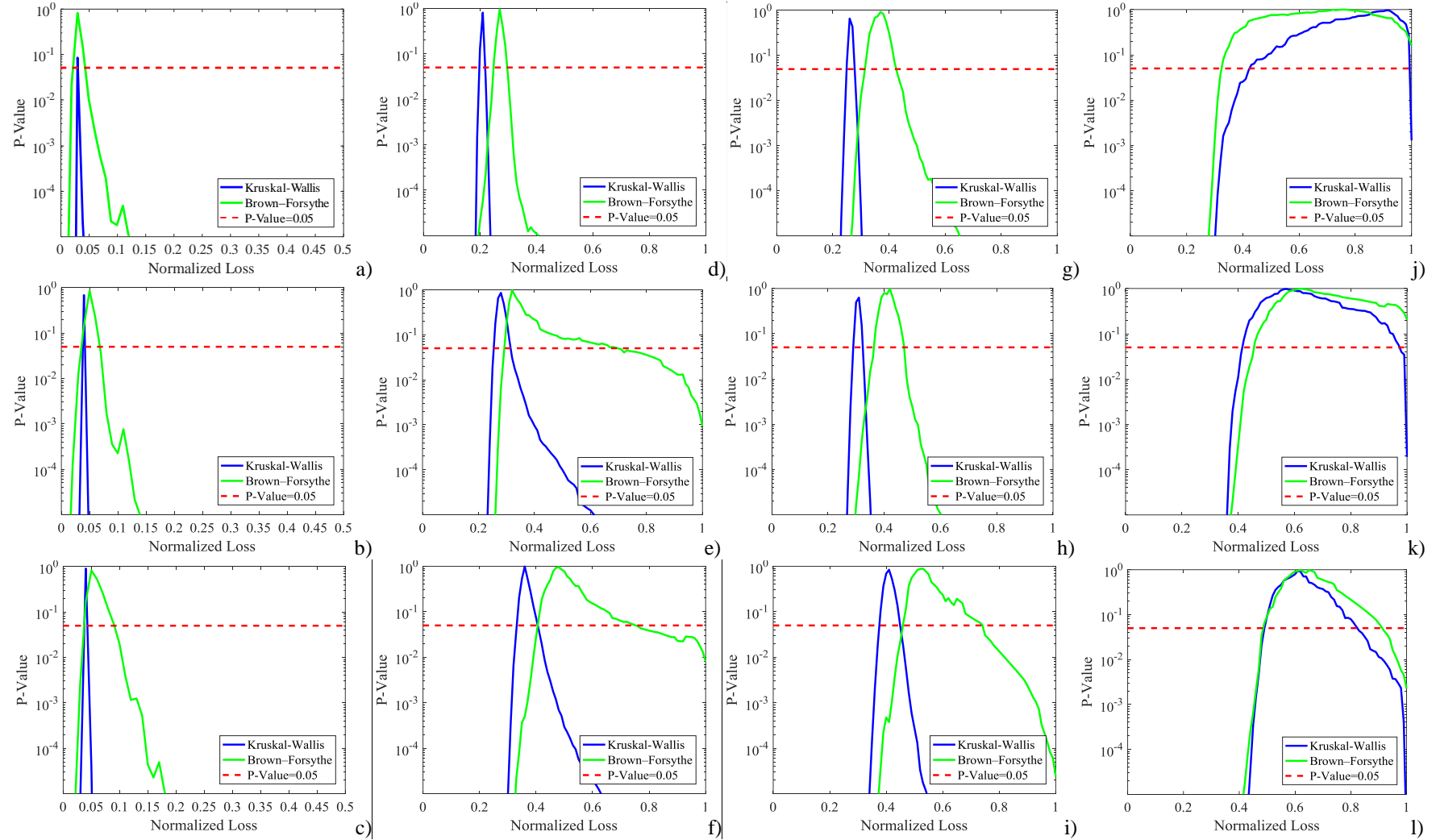
The p-value range above the critical limit is wider (around 0.03-0.09 instead of 0.03-0.04). The maximum p-values observed (0.81, 0.86 and 0.83) correspond to $L_{m,DL}$ limits of 0.03, 0.05 and 0.05 for REG3, REG4 and REG5, respectively. Figures 7d-7f present the evolution of the p-values of the KW and BF tests for increasing levels of the normalized loss considering as a reference the condition $Y_{SD}=1$. In this case, $L_{m,SD}$ values of 0.20-0.31 are found to be compatible with the higher p-values of the KW test (0.81; 0.66; 0.63). Similar values of $L_{m,SD}$ (0.27; 0.37; 0.42) are also observed when analysing the maximum p-values obtained when applying the BF test. The range of the $L_{m,SD}$ values above the critical p-value (0.25-0.47) is wider than the one obtained for the DL limit state.

The results for the NC limit state condition $Y_{NC} = 1$ are shown in Figs. 7g-7i. The $L_{m,NC}$ limit values that are seen to have a higher compatibility with the $Y_{NC}=1$ condition are 0.28, 0.36 and 0.41 according to the results of the KW test (p-values of 0.85, 0.99, and 0.84), and 0.32, 0.48 and 0.53 according to the BF test (p-values of 0.96, 0.96 and 0.89), for REG3, REG4 and REG5, respectively. Nevertheless, for the BF test, the range of values compatible with the critical p-value are wider and range from 0.30, 0.41 and 0.46 to 0.69, 0.75 and 0.74, respectively. For the KW test, the range of values compatible with the critical p-value is limited to 0.46-0.75. Different results are obtained when the condition $Y_C = 1$ is evaluated (Figs. 7j-7l).). In this case, it can be seen that p-values above 0.95 are obtained for all cases and for both tests. The $L_{m,C}$ values that are statistically compatible with the condition $Y_C = 1$ are 0.92, 0.57 and 0.61 according to the maximum p-value obtained using the KW test, and 0.76, 0.62 and 0.62 when the BF test is used (for REG3, REG4 and REG5, respectively). The range of $L_{m,C}$ values obtained using both tests that verify the selected critical p-value are within the range 0.49-0.91.

Figure 8 complements the above information by showing the maximum absolute difference between the ordinates of the cumulative distribution functions (CDFs) of the AvgS$_a$ values corresponding to the Y_{LS} conditions and those obtained assuming different $L_{m,LS}$ limits (KSstat), using the KS distance. As seen in Fig. 8, for $Y_{DL} = 1$, the minimum value of KSstat occurs for a $L_{m,DL}$ value of 0.03, 0.04 and 0.04, for REG3, REG4 and REG5, respectively. For the $Y_{SD} = 1$, the $L_{m,SD}$ values that minimize KSstat are now 0.21, 0.26, 0.31, while for $Y_{NC} = 1$ they are 0.28, 0.35 and 0.41. For $Y_C = 1$, it can be seen that the minimum distance between the CDFs does not change considerably after reaching $L_{m,C} = 0.40$, thus corroborating the main results presented in Figs. 7j-7l. Figure 9 shows the disaggregation of the losses corresponding to the mean AvgS$_a$ leading to the condition $Y_{DL}=1$. It can be seen that losses associated with the PFA-sensitive non-structural components (NST-PFA) are responsible for the largest contribution, whose global value is in the order of 3-4%. Structural losses (ST) and losses in drift-sensitive components (NST-IDR) have a very low contribution. The difference between the average loss value and the sum of the losses attributed to IDR and PFA-sensitive components (Total - ST&NST, used as a proxy for collapse

and residual deformations) has an insignificant or null value in all cases (in both cases represented as <1%).
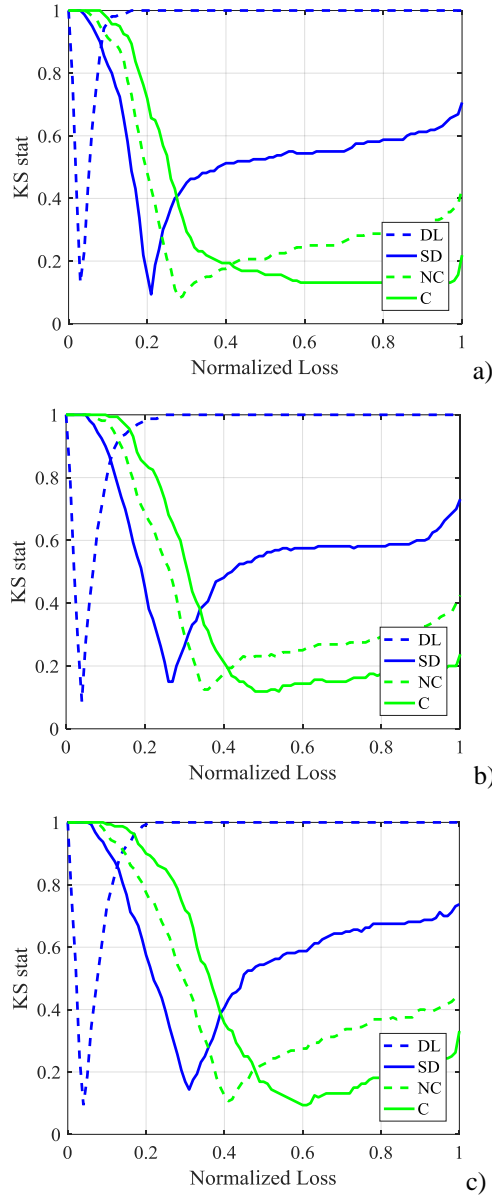
Figure 8. Evolution of the distance obtained using the two-sample Kolmogorov-Smirnov distance between the distribution of $AvgS_a$ values referring to the $Y_{LS} = 1$ conditions that are obtained for different levels of the admissible normalized loss for buildings REG3 (a), REG4 (b) and REG5 (c).

Figure 10 shows results similar to those of Fig. 9 for the condition $Y_{SD}=1$. In this case, 20-30% of the total average loss can be associated with structural components, but the major component (40-45%) is due to the repair needs of IDR-sensitive non-structural components. In total, the losses of non-structural components account for 60-70% of the total average loss. The component Total-ST&NST has a low contribution, reflecting the lower influence of collapse in the total losses.

Figure 9. Disaggregation of the losses corresponding to the mean AvgS$_a$ leading to the condition Y_{DL}=1 in buildings REG3 (a), REG4 (b) and REG5 (c).

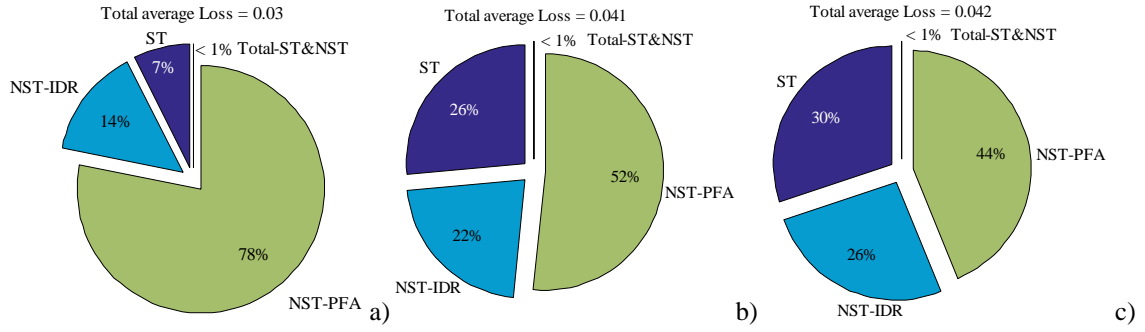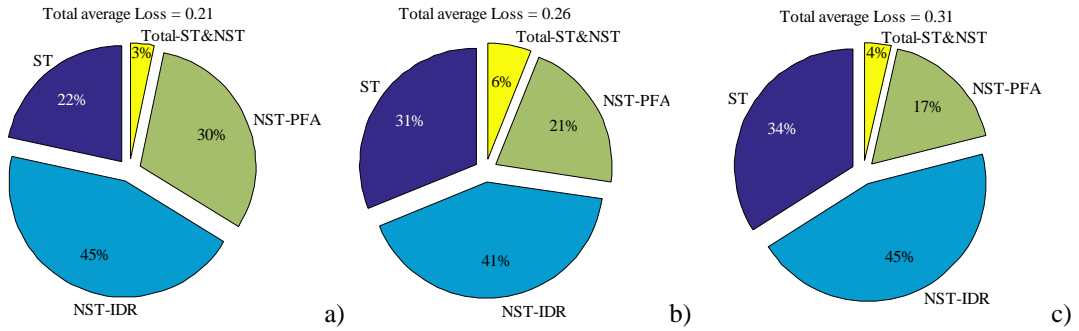Figure 10. Disaggregation of the losses corresponding to the mean AvgS$_a$ leading to the attainment of the condition Y_{SD}=1 in buildings REG3 (a), REG4 (b) and REG5 (c).

9.4 Discussion

The statistical analyses and comparisons performed in the present study indicate that, for the selected structures, i.e. mid-rise RC infilled frames, regular in plan and in elevation, and designed without capacity-design, there is a compatibility between the philosophy adopted in present seismic safety assessment standards and the full probabilistic PBEE principles. As referred by EC8/3, the DL limit state considers a low level of damage in structural elements and damage to non-structural components that is economical to repair. Results show that the $Y_{DL} = 1$ condition is statistically equivalent to a normalized loss $L_{m,DL}$ close to 5% of the replacement cost. Previous studies ([28]) using 2D frames reached similar conclusions regarding the amount of losses (6% of the total loss was computed for $Y_{DL} = 1$). Due to the properties of the $Y_{DL} = 1$ condition, limited losses are induced to structural elements, which may only present minor cracking due to the pre-yielding state of most components. Therefore, most of the losses are attributed to the damage in non-structural elements, particularly since plastic deformations are not expected for $Y_{DL} = 1$. The considerable level of damage found for NST-PFA components implies that some repairs may be required, although their expected extent is still expected to be compatible with the DL performance objectives.

9.16

For the SD limit state, the computed $L_{m,SD}$ values were seen to be within the range 0.20-0.40. Interestingly, these values are in line with the recommendations made by FEMA P-58 ([17]) and the results provided by Ramirez and Miranda ([27]). FEMA ([17]) suggests that 40% can be seen as a reasonable limit for many buildings. Hence, the results obtained for the three buildings imply that the $Y_{SD} = 1$ condition can be seen as equivalent to the performance objectives defined for SD in Table 1, since the governing condition is related with the fact that a building in such state may be uneconomic to repair. Romão *et al.* ([28]) found a loss value of 0.17 compatible with the $Y_{SD} = 1$ condition. Nevertheless, these authors did not include the losses in the PFA-sensitive components, which can contribute to the lower values that were found. As shown in Fig. 9, the amount of losses attributed to the structural elements is in the range 20-35% of the overall total, thus approximately 1/4 of the total replacement value of these elements. Similar relative values (25%) were found for the losses induced to NST-IDR. The PFA-sensitive elements showed loss values of about 1/3 of their total replacement. These values are compatible with the SD performance objectives, where non-structural elements are expected to be significantly damaged.

9.5 Conclusions

Current standard-based methods for seismic performance assessment use compliance criteria that are expected to aggregate the main probabilistic principles inherent to performance objectives. However, analysing the equivalence of standard-based methods and probabilistic approaches in a more global way instead of on a case-by-case situation is not straightforward. The loss assessment procedure considered in the current Chapter addresses this issue by involving a simplified loss assessment approach derived from storey-based loss assessment methods. The use of this simplified method supports the development of a more generalized analysis of the referred equivalences, since it considers general loss functions that avoid the need for an extensive inventory of building components.

The conceptual comparison presented herein shows that performance objectives currently defined in EC8/3 include a qualitative description of all the main principles also adopted in probabilistic PBEE methods. The performance objectives are clearly defined in terms of decision variables that are also used in modern PBEE methods (repair costs) and include explicit settings which resemble the weighting scheme associated with demolition and collapse probabilities. This study as shown that for the three analysed regular RC-MRF buildings with infill walls, the compliance criteria based on chord rotations have a statistical equivalence with expected loss values (defined based on conditions of general methods such as the HAZUS approach) found in the literature as representative of similar performance levels. Furthermore, despite potential limitations that may be associated with the proposed storey-based approach, it nevertheless provides a more consistent correlation between the building-specific assessments proposed by current standards and the more generalized seismic risk assessment strategies.

9.6 References

1   SEAOC Vision 2000 Committee (1995). Performance-based seismic engineering. SEAOC, Sacramento, CA.

2   FEMA (2000). FEMA-356: Pre-standard and commentary for the seismic rehabilitation of buildings. Report No. FEMA-356, Washington, D.C.

3   CEN (2005). ENV 1998-3. Eurocode 8: Design of structures for earthquake resistance - Part 3: Assessment and retrofitting of buildings. European Committee for Standardization, Brussels, Belgium.

4   ASCE (2013). Seismic Evaluation and Retrofit of Existing Buildings (ASCE/SEI 41-13). American Society of Civil Engineers, Reston, Virginia, USA.

5   Cornell CA, Krawinkler H, (2000). Progress and challenges in seismic performance assessment, PEER Centre News 3(2):1-3.

6   Ramirez CM, Miranda E, (2009): Building-specific loss estimation methods & tools for simplified performance-based earthquake engineering. Report No. 171. John A. Blume Earthquake Engineering Research Centre. Stanford University. Stanford, California.

7   Aslani H, (2005): Probabilistic earthquake loss estimation and loss disaggregation in buildings. PhD Dissertation. Stanford University. CA,USA.

8   McKenna F, Scott MH, Fenves GL, (2009). Nonlinear finite-element analysis software architecture using object composition. Journal of Computing in Civil Engineering; 24(1):95-107

9   Panagiotakos TB, Fardis MN, (2001). A displacement-based seismic design procedure for RC buildings and comparison with EC8. Earthquake Engineering and Structural Dynamics; 30: 1439–1462.

10 Haselton CB, Liel AB, Taylor-Lange SC, Deierlein GG, (2016). Calibration of model to simulate response of reinforced concrete beam-columns to collapse. ACI Structural journal. 113(6): 1141-1152.

11 Zareian F, Medina RA (2010): A practical method for proper modeling of structural damping in inelastic plane structural systems. Computers and structures; 88(1): 45-53.

12 Dolšek M, Fajfar, P (2008). The effect of masonry infills on the seismic response of a four-storey reinforced concrete frame – a deterministic assessment, Engineering Structures; 30: 1991-2001.

13 CEN, (2004). Eurocode 8 : Design of structures for earthquake resistance - Part 1: General rules, seismic actions and rules for buildings (EN 1998-1:2004). European Standard NP EN. CEN, Brussels, Belgium.

14 Vamvatsikos D, Cornell CA, (2002). Incremental dynamic analysis. Earthquake Engineering and Structural Dynamics; 31(3): 491-514.

15 Vamvatsikos D, Cornell CA, (2004). Applied Incremental Dynamic Analysis. Earthquake Spectra, 20(2): 523-553. (http://users.ntua.gr/divamva/software.html).

16 Macedo L, Castro JM, (2017). SelEQ: An advanced ground motion record selection and scaling framework. Advances in Engineering Software; 114: 32–47.

17 FEMA (2012). Next-Generation Methodology for Seismic Performance Assessment of Buildings, prepared by the Applied Technology Council for the Federal Emergency Management Agency, Report No. FEMA P-58, Washington, D.C.

18 Kohrangi M, Bazzurro P, Vamvatsikos D, (2016). Vector and scalar IMs in structural response estimation: Part II - Building Demand Assessment. Earthquake Spectra. Earthquake Spectra; 32(3): 1525-1543.

19   Grammatikou S, Biskinis D, Fardis MN (2017). Flexural rotation capacity models fitted to test results using different statistical approaches. Structural Concrete: 1–17.

20   Zareian F, Krawinkler H (2006): Simplified performance-based earthquake engineering. Report No. 169. John A. Blume Earthquake Engineering Research Centre. Stanford University. Stanford, California.

21   Ramirez CM, Gupta A, Myers A, (2012). Detailed seismic loss estimation for a tall building in Japan. 15th World Conference on Earthquake Engineering, Lisbon, Portugal.

22   FEMA (2003). HAZUS-MH MR4, Technical manual, Department of Homeland Security - Federal Emergency Management Agency.

23   Martins L, Silva V, Marques M, Crowley H, Delgado R, (2015). Development and assessment of damage-to-loss models for moment-frame reinforced concrete buildings, Earthquake Engineering and Structural Dynamics; 45(5): 797-817.

24   Brown MB, Forsythe AB, (1974). Robust tests for the equality of variances. Journal of the American Statistical Association; 69: 364–367.

25   Kruskal WH, Wallis WA, (1952). Use of Ranks in One-Criterion Variance Analysis. Journal of the American Statistical Association; 47 (260): 583–621.

26   Marsaglia G, Tsang W, Wang J, (2003). Evaluating Kolmogorov's Distribution. Journal of Statistical Software; 8(18).

27   Ramirez CM, Miranda E, (2012). Significance of residual drifts in building earthquake loss estimation. Earthquake Engineering and Structural Dynamics; 41: 1477–1493.

28   Romão X, Delgado R, Guedes J, Costa A, (2014). Probabilistic performance analysis of existing buildings under earthquake loading. Journal of Earthquake Engineering; 18(8): 1241-1265.

[This page was intentionally left blank]

Chapter 10

Closure

10.1 Conclusions

The present thesis addressed several topics related to the development and application of seismic safety assessment methodologies focusing, in particular, the compatibility between simplified standard-based methods and full probabilistic approaches such as the PEER performance-based earthquake engineering (PBEE) framework. Although observations and conclusions drawn from the research were discussed in each Chapter, the most relevant findings, conclusions and proposals are summarized in the following. Aspects related to further research needs, limitations and possible future works are also discussed.

10.1.1 Uncertainty about the physical and measurable properties of RC buildings

Chapters 2, 3 and 4 focused on evaluating the adequacy of current standard-based methods for the survey and quantification of physical properties of existing reinforced concrete (RC) buildings. A finite population statistics-based approach was proposed to be the core of the new survey framework that is established. This approach was first implemented for assessing the concrete strength of existing RC buildings, since this is one of the variables that involves larger levels of aleatory uncertainty. The proposed approach is able to effectively control the uncertainty in the estimate of the variability of the concrete strength in a population as well as the uncertainty in the estimate of its mean value. Furthermore, it relies on a discretization of the material and

structural properties distribution within the building, focusing on the component-to-component variability.

Chapter 2 focusses on assessing the mean of a finite population of concrete strength values. The use of non-destructive tests to estimate the coefficient of variation (CoV) of the concrete strength was analysed as an alternative way of to estimate the component-to-component variability. The use of an empirical model to estimate the CoV of the concrete strength using indirect measurements was proposed as an alternative method that can provide significant insights for controlling the epistemic uncertainty. The effectiveness of the approach was tested against the use of a limited number of destructive tests and was seen to efficiently improve the quality of the estimates that were obtained.

This concept was further enhanced in Chapter 3 where the concept of a bi-objective approach for developing a correlation between destructive and non-destructive tests was addressed in light of the proposed finite-population approach. Prior models were developed for the estimate of the statistical parameters of the concrete strength of a finite population of structural members. These prior models highlighted some of the key issues usually faced when developing a correlation model between the concrete strength and indirect measurements, namely the form of the mathematical model that is fitted. A new set of prior estimators was proposed which require the test results in 30% of the structural elements within a given region in order to have a prior estimate about the central value and the aleatory uncertainty of the concrete strength in the region.

The fact that reinforcing steel properties usually exhibit lower aleatory uncertainty, as confirmed in Chapter 4, leads to different proposals for the survey of concrete and steel properties. These proposal minimize the number of tests that need to be carried out for each material and lead to different values of the material safety factor CF_{mat} that is established. An adaptive probability-based framework defining testing plans for existing RC buildings and new CF_{mat} factors used for defining mean concrete strength values that are on the "safe side" was also proposed.

10.1.2 Modelling uncertainties

Chapter 6 focused on evaluating the effect of the correlation between the physical and measurable properties and the constitutive parameters, while Chapter 7 discussed the relation between the selected constitutive model and the seismic performance of RC beam-column members. The response is often characterized by the damage that accumulates at the end regions of the component and, in the numerical simulation of this phenomenon, inelastic behaviour is often concentrated into a single spring in series with an elastic interior element or assigned to a finite-length region of the component. In any case, understanding the assumptions underlying each modelling strategy implies the need to understand how the so-called plastic hinge mechanism is developed.

Chapter 6 analysed how hinges occur in RC frame components and examines from a physical viewpoint the process according to which it damage and deformations develop. The interpretation of the hinge development mechanism and of the damage accumulation were made based by analysing the physical effects that may invalidate the Euler-Bernoulli hypothesis. It was seen that violating this hypothesis can be mainly associated to the instability effects that occur in the longitudinal steel bars and with the diagonal cracking of the concrete core, particularly the diagonal macro-cracks that develop and the consequent sliding of wedges. Thus, the damaged region length $L_{D,flex}$ can be associated with the reinforcement buckling length, the concrete wedge size, the diagonal cracking associated with concrete shear failure and tension shift effects. It was concluded, based on statistical analyses, that only the models based on the steel bar slenderness λ could provide, on average, adequate estimates of $L_{D,flex}/s_w$, the damage mode based on the number of stirrups mobilized by the damage mechanism. Nevertheless, a posterior analysis has shown that the buckling length L_{buck} can also be considered as an estimate for the length of the damaged region for specimens with $\lambda \geq 6$, while parameters involving the tension shift effect due to the development of diagonal failure planes in concrete ($L_{PH,t}$ and $L_{D,flex,ts}$) can also provide adequate estimates for specimens with $\lambda < 6$. Hence, for frame components with low ductility (classified as DUCL), the length of the damaged region can be estimated by L_{buck} following [8], while the tension shift based model $L_{PH,t}$ adapted from the proposal in [3] seems to provide more adequate estimates for DUCM/DUCH components. For DNO components with flexural failure modes, due to the potential shear failure diagonal planes, $L_{PH,t}$ and $L_{D,flex,ts}$ can provide adequate alternatives, but the use of the model proposed in [5] for flexure-shear failure may also be considered in this case. It was highlighted that damage localization will always occurr in RC frame components loaded until collapse, and that the nonlocal effects violating the Euler Bernoulli hypotheses must always be considered in numerical modelling. As a result, the selected modelling approach must always account for the expected mechanisms affecting the component behaviour, for the component ductility class and for the corresponding damage localization.

Chapter 7 proposed a model selection scheme for distributed inelasticity elements using fibre sections, since these models are, among the common alternatives adopted in earthquake engineering, those requiring a larger number of decisions to be made by an analyst. The model selection scheme adopts size-dependent uniaxial material models that regularize the material and curvature responses in order to provide adequate estimates for the hinge rotations and, consequently, for the global deformation of the component. The size dependent model that is proposed for reinforcing steel uses a compression branch that is based on the buckling length in [8] when $\lambda \geq 6$. The tensile envelope considers the fracture energy and adjusts the necking strain to reflect a localization of the tensile strain at the length of the damaged region, i.e. the length over which the nonlocal deformations occur. This fact was seen to reduce the strains observed in tensile tests of steel coupons, since the rotation will force the straining in tension of the bars given

the instability in steel and the fracture in concrete at the compression side of the sections. For the modelling of concrete, the fracture energy in compression was defined using a size dependent model proposed in the literature [9], and ultimate strains leading to the complete loss of strength were defined based on the expected length of the damaged region. Hence, the proposed modelling strategy avoids the random adoption of material models for distributed inelasticity elements, whose effects can lead to considerable uncertainties in the local response (e.g. see [6, 7]). Furthermore, the proposed modelling strategy provides a direct correlation between the physical aspects discussed in Chapter 6 about the development and the rotation of hinges and the numerical localization issues that affect local formulations of distributed inelasticity elements. The criteria defined for estimating the length of the damaged region can therefore be used as an adequate strategy to specify consistent uniaxial material models. Furthermore, the results that were obtained in the simulations that were performed highlighted the adequacy of the proposed strategy to regularize the response of the component.

10.1.3 Uncertainties about the objectives and the methodology adopted for seismic safety assessment

Chapters 5 and 8 define a complete framework for the seismic safety assessment of existing RC frames that interconnects the type of method used to estimate the demand, the capacity of each structural component and the level of knowledge available about the properties of a given component. The framework was defined following the demand-capacity factor design (DCFD) format typically adopted in standard-based approaches, and introduces a set of uncertainty and compatibility factors that must be used in component-by-component verifications. The proposed DCFD format involves comparing a reliable estimate for the median seismic demand of each component of a building with a lower quantile of the distribution of its capacity.

Chapter 5 analysed the capacity side of the proposed DCFD methodology. Based on previous research, a new formulation for the limit state verification that shifts from the use of CF or CF_{mat} values to a format that involves global safety factors (SF_R) that factor the capacity of RC building components. These safety factors were calibrated for RC beams and columns with smooth and ribbed bars and were formulated for different levels of uncertainty of the parameters involved in the assessment. The selected parameters were divided in classes corresponding to the concrete strength, reinforcing steel strength, geometric properties and reinforcement details. The calibration that was performed provides a direct link between the testing and inspection plans that can be adopted and the admissible range of values for the mean properties of the variables. The finite population paradigm introduced in Chapters 2, 3 and 4 was used to define a set of predefined testing and inspection plans, ultimately leading to the corresponding value of SF_R that must be adopted for each component (that depends on the level of information collected about each component). SF_R values were defined for moment rotation spring models defined for components

with smooth and ribbed steel bars, and cases where pure shear failures occurs prior to yielding in flexure.

Chapter 8 analysed the demand side of the proposed DCFD methodology. A factor SF_D was proposed to define a reliable estimate for the median demands using the distributions of the demands obtained using a given set of ground motions. When the modelling approach that is used to compute the demands is based on the one discussed in Chapter 5 (i.e. the reference modelling approach), it was seen that SF_D only depends on the number of ground motions considered in the analysis and on the corresponding estimate for the record-to-record variability. When a different modelling approach is used (the alternative modelling approach), the use of a compatibility factor ε_{Co} was proposed to convert the median and the variability of the demand obtained with this model into estimates that can be directly compared with the median capacity factored by SF_R that is based on the reference modelling approach. This compatibility factor has parameters $\mu_{\ln \varepsilon_{Co}}$ and $\sigma_{\ln \varepsilon_{Co}}$ which were assumed to follow a lognormal distribution. Estimates for these parameters were developed based on pushover analyses. Furthermore, a calibration strategy was tested to convert the dispersion of the demands obtained with the alternative modelling approach directly into that of the reference model, thus also accounting for the covariations of ε_{Co} with record-to-record variability. Furthermore, it was seen that including multiple types of buildings, i.e. buildings with different levels of seismic design, is instrumental to perform a correct calibration of these factors. Hence, the generic factors that were proposed must be further analysed in the future by performing additional simulations that can be disaggregated by different design classes and ground motion scenarios.

Finally, Chapter 9 presented a conceptual comparison between the component-based DCFD conditions, the performance objectives that are defined in current standards (i.e. Part 3 of Eurocode (EC8/3)) and loss-based seismic performance assessments. The comparison showed that performance objectives currently defined in EC8/3 include a qualitative description of all the main principles also adopted in probabilistic PBEE methods. The performance objectives are clearly defined in terms of decision variables that are also used in modern PBEE methods (repair costs) and include explicit settings which resemble the weighting scheme associated to demolition and collapse probabilities. It was observed that for infilled RC buildings with a deformation mechanism governed by column deformations (therefore within the class of frames F1-F24 analysed in Chapter 8), the statistical distribution of the spectral accelerations leading to Damage Limitation, Significant Damage and Near Collapse limit states are compatible with expected losses that, on average, are around 5%, 30% and 45% of the replacement cost, thus conforming with the qualitative description of losses found in standards. Nevertheless, it was also observed that the use of a storey-based loss assessment approach using generic functions associated with

building classes provided a generic compatibility between the evolution of column chord rotations, inter-storey drifts and consequently losses. Therefore, it must be noted that the results obtained should not be generalized and that the proposed methodology for verifying the compatibility between performance objectives and limit state criteria must be extended to different building typologies, particularly using well defined taxonomies that include aspects that clearly differentiate the building seismic capacity, such as the seismic design class and the expected design seismic intensity.

10.2 Limitations and future work

10.2.1 Uncertainty about the physical and measurable properties of RC buildings

An entirely new framework was proposed for the assessment of structural properties of existing buildings. Nevertheless, several approximations and issues were left outside the scope of the research that was developed. These should be addressed in future research since it can significantly improve the proposed methodology. Some of the relevant topics are referred in the following.

With respect to material properties, the spatial variability of the concrete strength was not addressed in this study, as the main focus was defining the mean concrete strength in a region of a building (e.g. a storey). The spatial variability may lead to a different redistribution of the loads in 3D analysis and must be carefully assessed in future studies.

Chapter 5 assumes that the response and capacity of structural components that are not surveyed can be modelled using the expected values of the material properties and of the conformity indices. This assumption must be re-evaluated in the future to assess its main implications in the outcome of the seismic safety assessment.

10.2.2 Modelling uncertainties

The assessment of modelling uncertainties in component response only focused beam-column elements under flexural or flexure-shear response. Therefore, some of the limitations addressed in the following derive from the research that was carried out.

The analysis performed in the Chapter 6 is based on a database of experimental results that involve mostly qualitative descriptions of the observed damage observations. Future experimental studies should adopt more robust damage monitoring techniques such as those found in [3]. The use of these techniques will reduce the uncertainty/subjectivity of the damage classification that can be found in existing experimental observations. Furthermore, the cyclic load patterns that were adopted in some of these tests may not resemble those imposed by earthquakes. Hence, future experimental studies should try to mimic this type of cyclic loading, since the cyclic effects may

drastically change the damage patterns. Furthermore, since the database that was adopted had a limited number of biaxial tests conducted in columns, additional biaxial test cases should be considered to validate the results that were obtained.

The measurement of curvatures and effective rotations of plastic hinges in experimental tests requires advanced experimental setups, such as those used in [3]. A database including these reliable observations must be assembled in order to perform a consistent evaluation of nonlocal and local frame element formulations in terms of equivalent curvature demands. The values that are currently available in the literature do not separate the effects of fixed-end rotations and flexural deformations in a consistent manner.

Nonlocal frame element formulations were not evaluated in this study. Their development still requires the definition of the characteristic length, which is similar by definition to the damage localization length analysed in Chapter 6. Hence, future studies should evaluate the performance of these numerical formulations in association with the observations made in Chapter 6. The potential benefits of exploring these issues is related to improvements in the convergence of the element and structural responses due to the formulation of nonlocal models.

The effectiveness of using two independent moment rotation springs, defined herein as the reference modelling strategy, must be evaluated to observe its sensitivity to biaxial effects. Furthermore, the cyclic deterioration of these models is based on experimental tests with well-defined cycles. Therefore, despite the reported uncertainty about the parameters proposed in [4] and shown in [1], this approach may overestimate the rate at which cyclic degradation occurs, especially when ground motions with a longer duration are used. Some of these issues may be at the core of the differences found in Chapter 8.

Most of the studies performed to date considering modelling uncertainties involve 2D frames. Similar studies should be performed for 3D buildings to assess the importance of modelling uncertainties for global (drifts, peak floor accelerations) and local demands.

10.2.3 Uncertainties about the objectives of the seismic performance assessment

A revised seismic safety assessment framework compatible with current standards was analysed in this thesis, focusing on the ability to include different sources of uncertainty. The seismic safety equation that is proposed is based on several assumptions that require further validation.

Beam-column joint capacities and safety factors were not considered in the limit state conditions that were considered in the proposed framework. Although the response of these elements may not lead directly to structural collapse or extensive damage without the corresponding damage of frame components, joints may play a significant role in the compatibility between performance objectives since they may lead to probabilities of demolition that are larger for low-to-moderate levels of the ground motion intensity. Future studies should add these elements in the numerical

simulations to cover the lack of safety factors for these elements. Furthermore, such studies should also analyse the compatibility of the limit state condition for joints with the probability of demolition determined based on residual drifts.

The assumption that modelling uncertainties can be directly accounted for by factoring the capacity by SF_R and by adopting the mean properties in the model that is used to evaluate seismic demand needs to be verified. Such verification implies performing a simulation study starting from a fully known 3D model, i.e. a model where all the component properties are known, and assess if, on average, the use of SF_R is enough to cover the two referred sources of uncertainty. The basis for this assumption is that there is a full correlation of the errors in all components. Nevertheless, studies including correlations such as the one performed in [1] should also be conducted to assess the impact these correlations may have in local demands and in the limit state conditions that were adopted herein.

Regarding the modelling compatibility factors, it was seen there is a strong dependence of the factors on the properties of the ground motions and on the type of mechanism that develops in the structure. Although these differences may be expected to be smaller if infill walls are included, future studies must address the use of compatibility factor using specific building typologies and classes, in order to allow for a more rigorous selection of the factors that should be applied.

Future studies must also analyse these factors using intensity-based assessments, for specific locations and using sets of ground motions with less variability than the one adopted herein in order to have a better characterisation of the correlation between the ground motions and the differences between modelling techniques.

10.3 References

1 Gokkaya BU, Baker JE, Deierlein GG, (2016). Quantifying the impacts of modeling uncertainties on the seismic drift demands and collapse risk of buildings with implications on seismic design checks. Earthquake Engineering and Structural Dynamics; 45(10): 1661–1683.

2 Galanis P, Shin YB, Moehle JP (2016). Laboratory and computer simulations of reinforced concrete frames with different ductility. Earthquake Engineering and Structural Dynamics 45(10): 1603–1619.

3 Goodnight JC, Kowalsky MJ, Nau JM, (2016). Modified plastic-hinge method for circular RC bridge columns. Journal of Structural Engineering; 142(11): 04016103.

4 Haselton CB, Liel AB, Taylor Lange S, Deierlein GG, (2016). Calibration of Reinforced Concrete Beam-Columns for Simulating Seismic Response to Collapse. ACI Structural Journal, 113(6):1141-1152.

5 Zimos DK, Mergos PE, Kappos AJ, (2018). Modelling of R/C members accounting for shear failure localisation: Finite element model and verification. Earthquake Engineering & Structural Dynamics; 47:1631–1650.

6 Terzic V, Schoettler MJ, Restrepo JI, Mahin SA, (2015). Concrete column blind prediction contest 2010: outcomes and observations. PEER Report; 1:1-45.

7   Pereira N, Romão X, Delgado R, (2013) Epistemic uncertainty of the structural response of reinforced concrete members under cyclic loading due to different material modelling choices. *ICOSSAR2013 - 11th International Conference on Structural Safety & Reliability,* New York, USA.

8   Dhakal R, Maekawa K, (2002). Reinforcement stability and fracture of cover concrete in reinforced concrete members. Journal of Structural Engineering; 128(10): 1253–1262.

9   Samani AK, Attard MM, (2012). A stress–strain model for uniaxial and confined concrete under compression. Engineering Structures; 41:335-49.

[This page was intentionally left blank]